# KINEMATICS AND STELLAR

# POPULATIONS IN BRIGHTEST

# CLUSTER GALAXIES

Susan Ilani Loubser

A THESIS SUBMITTED IN PARTIAL FULFILMENT
OF THE REQUIREMENTS FOR THE DEGREE OF
DOCTOR OF PHILOSOPHY

Jeremiah Horrocks Institute for Astrophysics and Supercomputing
School of Computing, Engineering and Physical Sciences
University of Central Lancashire

June 2009

# Student Declaration

**Concurrent registration for two or more academic awards**

I declare that while registered as a candidate for the research degree, I have not been a registered candidate or enrolled student for another award of the University or other academic or professional institution

**Material submitted for another award**

I declare that no material contained in the thesis has been used in any other submission for an academic award and is solely my own work

**Collaboration**

Where a candidate's research programme is part of a collaborative project, the thesis must indicate in addition clearly the candidate's individual contribution and the extent of the collaboration. Please state below:
The entire thesis is the work of the candidate, Susan Ilani Loubser.

Signature of Candidate _____

Type of Award          Doctor of Philosophy

School                 School of Computing, Engineering and Physical Sciences

# Abstract

This thesis is devoted to the investigation of a new, large sample of brightest cluster galaxies (BCGs), their kinematic and stellar population properties and the relationships between these and the properties of the host clusters. Some of the questions addressed are: how the kinematic and stellar population properties differ from those of ordinary giant elliptical galaxies; and whether these properties are more influenced by the internal parameters of the BCGs or the properties of the host clusters.

In order to do this, high signal-to-noise, long-slit spectra of 49 BCGs (concentrating on those classified as cD galaxies) in the nearby Universe were obtained with the Gemini and WHT telescopes. The radial velocity and velocity dispersion profiles were measured, and the Lick/IDS system of absorption indices was used to derive Single Stellar Population (SSP)-equivalent ages, metallicities and $\alpha$-abundance ratios. A systematic comparison was made between the indices and derived parameters for this sample of BCGs and those of large samples of ordinary elliptical galaxies in the same mass range. The derived properties were tested for possible correlations with the internal properties of the galaxies (mass and luminosity) and the properties of the host clusters (density, mass, distance to X-ray peak and the presence of cooling flows).

Clear rotation curves were found for a number of BCGs. In particular,

NGC6034 and NGC7768 are rapidly rotating ($> 100$ km s$^{-1}$ as measured from their major axis spectra), indicating that it is unlikely that they formed through dissipationless mergers. Velocity substructure in the form of kinematically decoupled cores was detected in 15 BCGs, and five BCGs were found with velocity dispersion increasing with radius. In general, the amount of rotation and the velocity substructure detected in this sample, and the position of the BCGs as a class of objects on the anisotropy–luminosity diagram, are similar to those of ordinary giant ellipticals in high density environments. No significant discrepancies between the index–velocity dispersion relations of this sample and those of normal ellipticals were found, but subtle differences between the derived SSP-parameters do exist. The BCGs show, on average, higher metallicity ([Z/H]) and $\alpha$-abundance ([E/Fe]) values. The SSP-parameters show very little dependence on the mass or luminosity of the galaxies, or the mass or density of the host clusters. The derived ages of these massive galaxies are consistent with being old, as expected. Overall, the star formation histories in BCGs, and the connection to the processes in the cluster centres, are very complex.

# Contents

# List of Tables

9

11

# List of Figures

15

# Acronyms and abbreviations

ADU      Analogue Digital Unit

AGN      Active Galactic Nuclei

BCG      Brightest Cluster Galaxy

CCD      Charge-coupled Device

CDM      Cold Dark Matter

EPS      Evolutionary Population Synthesis

FWHM      Full Width Half Maximum

GC      Globular Cluster

GCE      Galactic Chemical Evolution

GMOS      Gemini Multi-object Spectrograph

HST      Hubble Space Telescope

IDS      Image Dissecting Scanner

IFU      Integral Field Unit

IMF      Initial Mass Function

IR      Infrared

ISM      Interstellar Medium

KDC      Kinematically Decoupled Core

LINERS      Low Ionization Nuclear Emission Regions

| | |
|---|---|
| MA | Major Axis |
| M/L | Mass-to-light Ratio |
| NED | NASA/IPAC Extragalactic Database |
| PA | Position Angle |
| RC3 | The Third Reference Catalogue of Bright Galaxies |
| RMS | Root Mean Square |
| SDSS | Sloan Digital Sky Survey |
| SED | Spectral Energy Distribution |
| SFH | Star Formation History |
| S/N | Signal-to-noise Ratio |
| SNIa | Supernovae Ia |
| SNII | Supernovae II |
| SSP | Simple/Single Stellar Population |
| UV | Ultraviolet |
| WHT | William Herschel Telescope |

# Publications

**Refereed**

Loubser S.I., Sansom A.E., Sánchez-Blázquez P., Soechting I.K. & Bromage G. *Radial kinematics of brightest cluster galaxies.* 2008, MNRAS, 391, 1009 – 1028.

Loubser S.I., Sánchez-Blázquez P., Sansom A.E. & Soechting I.K. *Stellar populations is the centres of brightest cluster galaxies.* 2009, MNRAS, 398, 133 – 156.

**Proceedings**

Loubser S.I., Sansom A.E. & Soechting I.K. 2007, *IAU symp. 241: Stellar Populations as Building Blocks of Galaxies,* ed. Vazdekis A. & Peletier R.F., IAUS, 241, 422 (ISBN 9780521863506).

Loubser S.I., Sansom A.E. & Soechting I.K. 2007, *Proceedings of the Gemini Science Meeting 2007* (ISBN 9788598138039).

Sansom A.E., Loubser S.I., Sánchez-Blázquez P. & Soechting I.K. 2008, *IAU symp. 245: Spiral Bulges,* ed. Bureau M., Athanassoula E. & Barbuy B., IAUS, 245, 141 (ISBN 9780521874670).

# Acknowledgements

Countless people have contributed to make my PhD study both a very enriching and enjoyable experience. First and foremost, I thank Patricia Sánchez-Blázquez for the selfless and enthusiastic way in which she shared her knowledge and time with me. Her example helped me work more effectively and her friendliness, advice, and motivation was endless. I highly value the input and kind manner of Gordon Bromage, who made this voyage possible. I also thank Ilona Soechting for the contribution she made to my experience here, and to this project, as well as for her continued interest and the many hours she dedicated to me.

I thank Rob Proctor, for very helpful discussions and for making his software available to me, along with Scott Trager for his interest and suggestions. I greatly appreciate the help of Anne Sansom with the initial data collection and WHT observations, and that of Bryan Miller with the observations at Gemini South. Steven Chapman and Xiaohu Guo provided me with much valued computer and network assistance. I also thank Alfonso Aragón-Salamanca and Roger Clowes for their constructive suggestions and comments during the examination of this work.

During the past few years I've thoroughly enjoyed the company of many friends at the CfA/JHI. I especially thank all the students and postdocs for all the good times (in and out of the office), from our never-ending quest to find the

best lunch in town to discovering new cocktails, and from exercise classes and squash games to walks in the Lakes and abseiling from trees. Special mention must go to Hannah, who has endured climbing, cycling and even shopping with me. My gratitude to Brad and Kate, for their friendship and advice throughout, and to Katie, for her help and humour. I also thank Don, the honorary South African, for reminding me of home. Thank you all!

*Jan en Ananka, dankie vir julle onvoorwaardelike ondersteuning en bemoediging, maak nie saak wat ek doen, of hoe ver dit weg was nie. Al die oproepe, boodskappe en foto's het julle baie nader laat voel. Jan – dankie vir al jou opofferings, en al jou liefde en sorg. Ananka – dankie dat jy vir my uitkyk.*

# Chapter 1

# INTRODUCTION

The most massive of early-type galaxies – central galaxies in clusters – are special. They have extremely high luminosities, diffuse and extended structures, and dominant locations in clusters. Because of their special location in the cluster, they are believed to be sites of very interesting evolutionary phenomena (e.g. dynamical friction, galactic cannibalism, cooling flows). This special class of objects may well require there to have been a special process of formation. The terms *central cluster galaxy* and *brightest cluster galaxy* (BCG) have become synonymous in recent literature. According to the above definition, for a small fraction of clusters the BCG might not strictly be the brightest galaxy in the cluster. For consistency, we adopt the definition to comply with recent literature (for example De Lucia & Blaizot 2007; Von der Linden et al. 2007), where the central, dominant galaxy in a cluster is referred to as the BCG, and the sample of galaxies investigated in this study will hereafter be referred to as a BCG sample.

Even with increased telescope size and improved instrumentation, resolving individual stars in the vast majority of extragalactic sources will remain impossible. Nevertheless, the unresolved stellar populations are important because they contain signatures, locked in their age and chemical composition, of the processes that were important in the formation of the galaxy. Careful observations

and interpretations of these signatures can constrain the formation and evolution of these systems. In this study, stellar populations are investigated and used to probe the formation scenarios, ages and star formation histories (SFHs) of BCGs. This will add to our general understanding of how giant spheroidal galaxies in high density environments form.

## 1.1   Galaxy formation

The two basic models for galaxy formation are the following:

- Monolithic collapse. The majority of galaxies were formed through the gravitational collapse of clouds of primordial gas, very early in the history of the Universe ($z > 3$).

- Hierarchical merging. Galaxies are gradually assembled through multiple mergers of small subgalactic units, and in the current accepted paradigm of $\Lambda$CDM, this process continues to the current epoch.

These differences extend to our ideas about galaxy evolution. In the monolithic collapse scenarios, galaxies of different morphological types are "born" intrinsically different (the nature argument), whereas in the hierarchical merging scenario, galaxies transform to ellipticals or spirals depending on the details of their merger history (the nurture argument). The two scenarios appear to contradict each other, but accumulating observational evidence has made the models less distinct in recent years.

Hierarchical models of galaxy formation now provide a closer match to observations than a few years ago. This has been partly achieved by adjusting the description of baryonic processes such as star formation and supernovae/active galactic nuclei (AGN) feedback in the models, while leaving the evolution of the underlying dark matter haloes the same. It is believed that star formation

is quenched by supernovae in galaxies with stellar mass $M \leqslant 10^{10} M_{\odot}$, while other processes such as AGN feedback are necessary to stop star formation at $M \geqslant 10^{10} M_{\odot}$, where AGNs become abundant locally (see review by Renzini 2007). In the $\Lambda$CDM paradigm, most massive galaxies originate from the highest primordial overdensities, and hence are the first to collapse (Blumenthal et al. 1984). The more massive a galaxy, the older the stellar content (this is often called downsizing). Alongside downsizing in star formation, the continuous merging of dark matter haloes should result in an increase in mass assembly, with the most massive galaxies being the last to be fully assembled. Thus, the apparent anti-hierarchical formation of stars in giant elliptical galaxies can be reconciled with the hierarchical formation of structures by decoupling the epochs of star formation from mass assembly. In this scenario, there is a decrease in the relative amount of dissipation (and therefore star formation) with increasing mass, experienced by the baryonic mass components when they assemble (Sánchez-Blázquez et al. 2007, and references therein).

The hierarchical galaxy formation scenario predicts the following concerning the ages of massive early-type galaxies (as summarised in Trager, Faber & Dressler 2008):

- Early-type galaxies of a given stellar mass form stars earlier, and thus should have older stellar population ages, in the highest-density environments than those in the lower-density environments.

- The most massive early-type galaxies in the densest environments should have a small spread in stellar population ages.

- In all environments, more massive early-type galaxies should have older stars (downsizing).

Increasing support for the hierarchical merger scenario comes from studies involving galactic chemical evolution (GCE) models (De Lucia et al. 2006; Trager & Somerville 2009), and ongoing and recent mergers that are observed in the local Universe (for example in Schweizer 1998).

### 1.1.1 Galactic archaeology

The most direct route to investigate the evolution of early-type galaxies is to observe their mass growth at different redshifts. Unfortunately, it is very difficult to find the progenitors of early-type galaxies by direct observations at high redshift (Van Dokkum et al. 2000). This method also demands large amounts of observing time, even on the current generation of 10m-class telescopes, as one needs to observe high-redshift objects which are fainter. An alternative method is to employ galactic archaeology – to look at the local population of galaxies and infer their SFH from their current dynamical, structural and stellar population properties. Bright nearby galaxies are far more accessible observationally, thus allowing larger numbers to be studied with high signal-to-noise ratios (S/N). Here, the archaeology approach will be followed.

## 1.2 Brightest cluster galaxies

The central supergiant galaxies in clusters, called BCGs, are massive ($\sim 10^{13} M_\odot$) and extended. Some BCGs are called cD galaxies indicating that they have an extended stellar halo. Approximately 20 per cent of rich clusters of galaxies contain a dominant central cD galaxy (Dressler 1984; Oegerle & Hill 2001), although they can be found in poor clusters as well (Giacintucci et al. 2007). The surface-brightness profiles of cD galaxies show enhanced brightness above the De Vaucouleurs law ($r^{\frac{1}{4}}$ law proposed by Gérard de Vaucouleurs in De Vaucouleurs
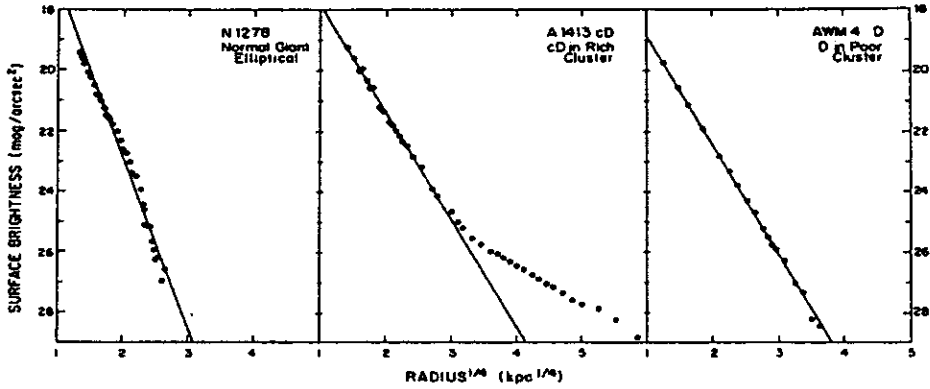
Figure 1.1: Typical surface brightness profile of a cD galaxy (middle) compared with that of an ordinary elliptical galaxy (left). It shows the typical break in the cD surface brightness profile between 24 and 26 mag/arcsec$^2$ (in the $V$-band). The right panel shows the surface brightness profile of a D galaxy, which lacks the stellar halo but has the same slope as a cD galaxy (according to the Schombert 1987 definition). The figure was adapted from Sarazin (1988).

1948) at large radii $r$, typically $50 - 500$ $h^{-1}$ kpc, from the galaxy centre (Figure 1.1; Schombert 1988). The interpretation of this deviation is that the galaxy is embedded in an extensive luminous halo. Some clusters have more than one cD galaxy (e.g. Hercules and Coma), but a cD galaxy is always the dominant member of a local subcluster. In these cases where a cD galaxy is not the BCG in the main cluster, the BCG in the main cluster is always of the cD type as well (Schombert 1987). At low redshift, BCGs have very little dispersion in their aperture luminosities, and were used as "standard candles" in the past (Sandage 1972; Postman & Lauer 1995).

Oemler (1976) was one of the first to study the differences between BCGs (cD and non-cD) and normal elliptical galaxies. He fitted surface brightness profiles to an exponentially truncated Hubble law of the form

$$I = \frac{I_0 e^{(r/\alpha)^{-2}}}{(r + \beta)^2} \tag{1.1}$$

where $\alpha$ describes the exponential falloff, $\beta$ the Hubble law core radius and $I_0$ the

reduced intensity (a number which represents a core-independent and envelope-independent parameter describing the power-law section of a galaxy profile). This is a convenient method of comparing structures between different types of galaxies but has no physical significance.

There exists a great deal of confusion over the exact meaning of the classifications gE, D and cD. Matthews, Morgan & Schmidt (1964) outlined the following definition: "D galaxies have an elliptical-like nucleus surrounded by an extensive envelope. The supergiant D galaxies observed near the centre of a number of Abell's rich clusters have diameters 3 − 4 times larger than the ordinary lenticulars in the same clusters. These very large D galaxies observed in clusters are given the prefix "c", in a manner similar to the notation for supergiant stars in stellar spectroscopy."

Equation 1.1 offers another way of distinguishing between the different types. According to Schombert (1987), D galaxies are typified by their large diffuse appearance and their shallow profile slopes ($\beta = -1.7$ to $-1.2$)[1]. The cD galaxies have all the above properties but with a large extended envelope (Oemler 1976), forming a distinct break in the profile. In contrast, giant elliptical galaxies have profiles with $\beta$ between $-1.9$ and $-1.7$. In summary, gE galaxies are distinguished from other early-type galaxies by their large size; D galaxies are gE galaxies with a shallow surface brightness profile slope; and cD galaxies are D galaxies with large extended stellar haloes (Figure 1.1). These cD galaxies are also more diffuse than normal ellipticals (Schombert 1986)[2].

The surface brightness profiles of elliptical galaxies are now fitted with single or double Sérsic profiles ($r^{\frac{1}{n}}$), rather than fixing $n = 4$ as used in De Vaucouleurs law. Kormendy et al. (2009) translate Schombert's definition of a cD galaxy in terms of Sérsic profiles as: "cD galaxies are gEs that have cluster-sized extra

---

[1]Note that these values were derived with $H_0 = 100$ km s$^{-1}$ Mpc$^{-1}$.

[2]The term diffuse means here that cD galaxies have larger half-light radii than normal ellipticals with the same effective surface brightness.

27

light at large radii with respect to the outward extrapolation of a Sérsic function fitted to the inner profile." Because of the lack of generally accepted definitions, and the fact that D galaxies are rarely considered to be a separate type in modern literature, the present study will only differentiate between cD and non-cD BCGs (containing a halo or not) where necessary for the introduction and sample selection.

## 1.2.1  Formation mechanisms

Early-type galaxies exhibit well-known, tight correlations between many of their observables, such as luminosity, half-light radii, mean surface brightness, colours, and velocity dispersion. As an exception, BCGs often deviate from these scaling relations (Oegerle & Hoessel 1991; Postman & Lauer 1995; Von der Linden et al. 2007; Hyde & Bernardi 2009). This leads to the suggestion that BCGs had a formation history different from other massive ellipticals.

In this section, the three main theories proposed over the last four decades to explain the properties of BCG, and also cD galaxies, together with the observational evidence will be discussed.

### Theory 1 – Cooling flows

In the first theory, BCG formation is caused by the presence of cooling flows in clusters of galaxies (Cowie & Binney 1977). Cooling-flow clusters are common in the local Universe and BCGs are often found at the centres of these systems (Edwards et al. 2007). If the central cluster density is high enough, intracluster gas can condense and form stars at the bottom of the potential well. Since the radiative cooling times for intracluster gas are short enough that gas can cool and settle to the cluster centre, it has been suggested that cD envelopes may arise from the gradual deposition of this cool gas.

Observations that support this idea are blue- and ultraviolet-colour (UV-colour) excesses observed (indicative of star formation) in the central galaxy of Abell 1795 by McNamara et al. (1996) and molecular gas detected in 10 out of 32 central cluster galaxies by Salomé & Combes (2003). Cardiel, Gorgas & Aragón-Salamanca (1998a) obtained radial gradients for the $D_{4000}$ (the $\sim 4000$ Å break defined in Bruzual 1983) and $Mg_2$ (introduced in Section 1.3.1) spectral features in 11 central cluster galaxies. Their observations were consistent with an evolutionary sequence in which star formation bursts, triggered by radio sources, take place several times during the lifetime of the cooling flow in the centre of the cluster. However, McNamara & O'Connell (1992) found only colour anomalies with small amplitudes, implying star formation rates that account for at most a few percent of the material that is cooling and accreting onto the central galaxy. Cooling-flow models for BCG formation also imply the formation of larger numbers of new stars, for which there is no good observational evidence (Athanassoula, Garijo & García-Gómez 2001).

More recently, high spectral resolution *XMM-Newton* observations showed that the X-ray gas in cluster centres does not cool significantly below a threshold temperature of $kT \sim 1 - 2$ keV (Jordán et al. 2004, and references therein). Cool gas below this threshold is necessary to form stars, and this is sometimes referred to as the "cooling flow problem". The central cluster galaxies often host radio-loud AGN which may account for the necessary heating to counteract radiative cooling (Von der Linden et al. 2007).

In conclusion, although BCGs are probably not completely formed in cooling flows, the flows play an important role in regulating the rate at which gas cools at the centres of groups and clusters.

CHAPTER 1

## Theory 2 – Primordial origin

The second theory was proposed by Merritt (1983) and suggests that the essential properties of cD galaxies were determined when the clusters collapsed. This is referred to as the primordial origin theory. After the cluster collapsed, frequent mergers of galaxies are inhibited by the relatively high velocities between galaxies. Merritt (1983) argued that all galaxies had large haloes early in the life of the cluster. These haloes were then removed by the mean cluster tidal field during the initial collapse and returned to the cluster potential, except for the central member which remained unaffected because of its special position with respect to the cluster potential.

## Theory 3 – Galactic cannibalism

The third, and most widely accepted, theory has been proposed in the context of the $\Lambda$CDM cosmology. It relates the formation of the central galaxy to mergings with, or captures of, less massive galaxies, and is known as galactic cannibalism. It was first proposed by Ostriker & Tremaine (1975) and developed by Ostriker & Hausman (1977).

A related theory, called *tidal stripping*, was proposed by Gallagher & Ostriker (1972). Cluster galaxies that pass near the gravitational centre of the cluster may be stripped of some of their material by the tidal forces from the cluster potential or the central galaxy potential. The stripped material falls to the centre of the potential well, and could contribute to the observed haloes of cD galaxies. The most massive galaxies surrounding the central galaxy would be preferentially depleted as they are most strongly affected by dynamical friction (Jordán et al. 2004). The difference between stripping and primordial origin is that stripping (and cD halo formation) begins after cluster collapse whereas primordial origin assumes that the tidal events occur before collapse, and that the cD halo is not

a consequence of tidal stripping (Schombert 1988).

**Galactic cannibalism – model predictions:** Using the Millennium Simulation, De Lucia et al. (2006) studied how formation histories, ages and metallicities of elliptical galaxies depend on environment and on stellar mass. Their figure 9 shows the effective number of progenitors of early-type galaxies as a function of galaxy stellar mass. The number of effective progenitors is less than two for galaxies up to stellar masses of $\simeq 10^{11}$ $M_\odot$. This function then increases up to a value of approximately five effective progenitors for the mass of a typical BCG.

Dubinski (1998) showed that a central cluster galaxy forms naturally when a cluster collapses along the filaments. Gao et al. (2004), using numerical simulations, predicted that central galaxies in clusters would have experienced a significant number of mergers since $z \sim 1$. The most complete quantitative simulations of the formation of BCGs are by De Lucia & Blaizot (2007). They used semi-analytic techniques to study the formation and evolution of BCGs and found that, in a model where cooling flows are suppressed at late times by AGN activity, the stars of BCGs are formed very early (50 per cent at $z \sim 5$, which means that they are older than 12.5 Gyr, and 80 per cent at $z \sim 3$) and in many small galaxies. They also found that BCGs assemble late: half of their final mass is typically locked up in a single galaxy after $z \sim 0.5$ (as illustrated in their figure 9). A very similar conclusion was reached by Romeo et al. (2008), who performed N-body and hydrodynamical simulations of the formation and evolution of galaxy groups and clusters in a $\Lambda$CDM cosmology. According to the above-mentioned simulations, we expect to see evidence of dissipationless mergers in these galaxies, little dependence of metallicity on mass and old stellar populations.

Athanassoula et al. (2001) found with their $N$-body simulations that in all cases a giant galaxy is formed in the central parts by merging of secondary galaxies and by accreting material stripped from the rest of the galaxies by tidal forces.

They also found that only certain density distributions give rise to the excess over the $r^{\frac{1}{4}}$ law in the outer parts of cD galaxies.

**Galactic cannibalism – observations:** Aragón-Salamanca, Baugh & Kauffmann (1998) examined the $K$-band Hubble diagram for BCGs for redshifts up to $z = 1$, and found that the BCGs had grown by a factor of two to four since $z = 1$. Brough et al. (2002) found a similar result, and discovered that the mass growth depended on X-ray luminosity (indicative of the cluster density) of the host cluster. They found that BCGs in low X-ray luminosity clusters grew by a factor of four as opposed to BCGs in high X-ray luminosity clusters which showed no mass accretion since $z = 1$.

However, the recent near-infrared (near-IR) photometric study of 42 BCGs by Whiley et al. (2008) in the $0.2 < z < 1$ range contradicts this. They studied the colour and rest-frame $K$-band luminosity evolution of BCGs and found it to be in good agreement with population synthesis models of stellar populations which formed at $z \sim 2$ and evolved passively thereafter. They do not detect any significant change in the stellar mass of the BCGs since $z \sim 1$. Stott et al. (2008) also concluded from the near-IR colour evolution of BCGs that their stellar populations have been in place since $z = 2$ or earlier, and that a shorter period of star formation is expected than that predicted by the hierarchical models.

These contradictory results may be partially attributed to differences in environment for the different samples (Brough et al. 2002; see also Chapter 5), and to the difficulty in the sample selection and in making comparisons between aperture magnitudes (observations) and total magnitudes (models; see Whiley et al. 2008). Aperture magnitudes used so far in the literature include less than 50 per cent of the total mass of the BCGs. Furthermore, it is not clear if intracluster light should be considered when comparing observations with the models (González, Zaritsky & Zabludoff 2007).

The observations of multiple nuclei in BCGs also favour the cannibalism theory (Tonry 1984; Tonry 1985; Postman & Lauer 1995). The fraction of BCGs containing multiple nuclei is reported to be around 40 – 50 per cent (Schneider, Gunn & Hoessel 1983; Laine et al. 2003), regardless of the richness of the cluster. This, according to Schneider et al. (1983), is greatly in excess of the number of chance projections expected in a cluster where galaxies are distributed as an isothermal sphere with a typical core radius of 200 $h^{-1}$ kpc.

Other studies also favour the cannibalism theory. For example, Jordán et al. (2004) studied the globular cluster (GC) systems in cD galaxies with the Hubble Space Telescope (HST). They concluded that the observed GC metallicity distributions are consistent with those expected if cD galaxies form through cannibalism of numerous galaxies and protogalactic fragments that formed their stars and GCs before capture and disruption. However, they state that the cannibalism scenario is not the only possible mechanism to explain these observations. Jordán et al. (2004) also speculate that cD galaxies experienced their mergers prior to cluster virialisation (arguing that the GCs formed before the bulk of the stars), yet the presence of tidal streams (which are not yet erased) suggest otherwise (Seigar, Graham & Jerjen 2007). Recent results on the evolution in the sizes of BCGs are also consistent with models which assume that the galaxies formed through predominantly dissipationless, minor mergers (Bernardi 2009).

Further indication that mergers had taken place comes from observations of the luminosities and alignments of central cluster galaxies. Oemler (1976) determined the luminosities of cD envelopes and showed them to be correlated with the total luminosities of their parent clusters ($L_{env} \propto L_{cluster}^{2.2}$), emphasising the close connection between halo formation and cluster processes. Loh & Strauss (2006) found the luminosity gap between the first and second brightness-ranked galaxies

to be large ($\sim 0.8$ mag), larger than could be explained by an exponentially decaying luminosity function of galaxies. They found that the large luminosity gap showed little evolution with redshift since $z = 0.4$, and ruled out the possibility that BCGs grew by recent cannibalism of cluster members. Instead, they suggest that the BCGs must have become the dominant cluster members by $z > 0.4$.

Carter & Metcalfe (1980) and West (1989) showed that the major axis of BCGs tends to be aligned with the principal axis of their host clusters (see also Fuller, West & Bridges 1999, who found the same for poor clusters). Recent studies of the Coma cluster (Torlina, De Propris & West 2007) show strong evidence that there are no large-scale galaxy alignments other than for the BCGs. This might imply that BCGs form via a mechanism related to radial infall and the growth of the cluster from the surrounding large scale structure (Boylan-Kolchin, Ma & Quataert 2006). Observations that support BCG formation by predominantly radial mergers include those by Bernardi et al. (2008), who showed that the shapes of the most massive ($\sigma \geq 350$ km s$^{-1}$), high luminosity objects (with properties similar to BCG properties) are consistent with those expected if the objects formed through radial mergers.

These theories are not mutually exclusive. For instance, Carter, Bridges & Hau (1999) suggested that mergers/cannibalism create the central body of the BCG, while tidal stripping accounts for the extended haloes of cD galaxies. In the $\Lambda$CDM cosmology it is now understood that local massive haloes assemble late through the merging of smaller systems. In this picture, cooling flows seem to be the main fuel for galaxy mass growth at high redshift. This source is removed only at low redshifts in group or cluster environments, due to AGN feedback (De Lucia & Blaizot 2007; Voit et al. 2008). Indeed, if AGN feedback is not properly assumed in hydrodynamical simulations, an apparently bluer BCG is formed as a result of an accelerated late stellar birthrate even after the epoch of quiescent

star formation (Romeo et al. 2008).

## 1.3   Investigating stellar populations

Stars and gas in galaxies exhibit diverse chemical element abundance patterns that are shaped by their SFHs. The aim of stellar population analysis is to use the ages and abundances through observed spectral line strengths to gain insight into the mechanisms of galaxy formation.

The basis of modern stellar population models consists of a method pioneered by B. Tinsley (1968) and called evolutionary population synthesis (EPS). In this method, hypothesised populations are modelled from the starting point of an isochrone (a line on the Hertzsprung–Russell diagram connecting stars of constant age) and a luminosity function, and then matched to spectral observations. This is in contrast to other methods consisting of attempts to extract a stellar colour–magnitude diagram and stellar luminosity function from resolved stellar observations. The simplest example of an EPS model, called a simple stellar population (SSP), assumes that all stars are coeval and have the same chemical composition. SSPs can then be compared with GC data since GCs are good approximations to SSPs, and this offers the advantage of calibrating the SSPs in the range of abundances present in GCs. This is a necessary step to account for the model ingredients that can not be derived from first principles, such as convection, mass loss, and mixing (Maraston 2003). Then, complex stellar population systems are modelled by luminosity weighting the sum of the SSPs from an adopted SFH. A description of modern SSP-methods and models follows in Sections 1.3.1 and 1.3.2.

The calculation of the model spectrum (or individual indices) of the galaxy, with which the observed spectrum will be compared, requires knowledge of the stars that the galaxy is supposed to consist of. Accurate stellar evolution models

are needed to understand the properties of different stellar populations present in galaxies. The reliability of stellar models depends mostly on the accuracy of the adopted physical inputs, as well as on the physical processes accounted for. Cassisi (2007) reviewed the various building blocks of stellar models and the constraints imposed on the models by observations of stars in various mass regimes and evolutionary stages. The equations that describe the physical behaviour of stellar structures are well known (Cassisi 2007), and as shown by Weiss et al. (2007), when the physical scenario has been homogeneously fixed then stellar evolution codes provide similar results.

### 1.3.1 Lick indices

A widely used set of absorption-feature indices in studies of stellar populations is the Lick system. This system is based on a large survey of individual stars in the solar neighbourhood, carried out with the image dissecting scanner (IDS) at the Lick Observatory (Burstein et al. 1984; Faber et al. 1985; Gorgas et al. 1993; Worthey et al. 1994). The set of 110 stars, observed in the range $4000 < \lambda < 6200$ Å with $\sim 8.6$ Å full width half maximum (FWHM) resolution, consisted of K giants and subgiants, as well as some giants in metal poor GCs. The system identifies spectroscopic absorption features sensitive to photospheric effective temperature $(T_{\text{eff}})$, surface gravity $(g)$ and metallicity $([\text{Fe/H}])$[3]. The measurements of these indices in local stars are used to predict the indices in SSPs for comparison to observations. Table 1.1 gives the definitions of the Lick indices. The original Lick system consisted of 21 indices from $CN_1$ to $TiO_2$ (Faber et al. 1985; Worthey 1994; Trager et al. 1998 – hereafter T98). Worthey & Ottaviani (1997) later contributed the $H\delta_{A+F}$ and $H\gamma_{A+F}$ indices. This collection of 25 indices will be used in the present study, and will hereafter be referred to as the Lick indices. Other

---

[3]The standard notation of $[\text{X/Y}]=[\log(\text{X/Y}) - \log(\text{X}_\odot/\text{Y}_\odot)]$ is being used, where X and Y are mass fractions.
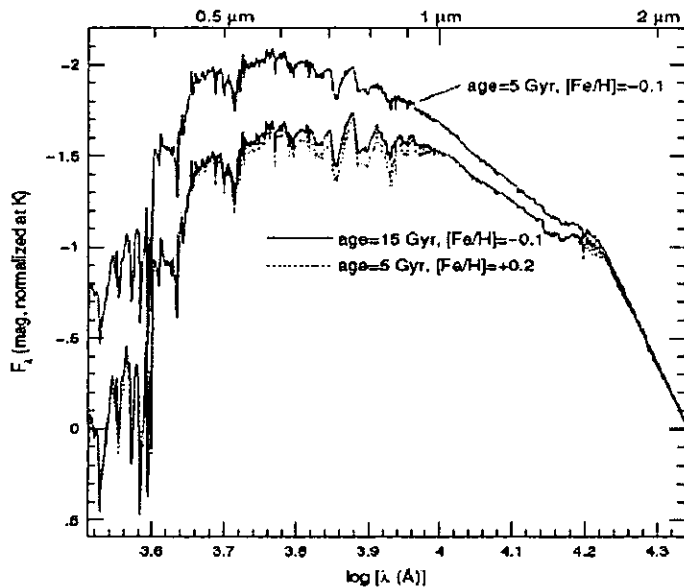
Figure 1.2: Figure illustrating the age–metallicity degeneracy (taken from Worthey 2001). Note that the spectrum of an object with age 15 Gyr and metallicity [Fe/H] = −0.1 looks similar to the spectrum of an object with an age a factor of three times younger but double the metallicity.

popular indices include the near-IR CaII triplet at $\sim$ 8600 Å and the MgI index (Diaz, Terlevich & Terlevich 1989).

The study of integrated light from stellar populations suffers from the *age–metallicity degeneracy* effect. A metal-rich population can be approximated by decreasing the mean temperature (that is, increasing the age) of a more metal-poor population (as illustrated in Figure 1.2). Worthey (1994) quantified the age–metallicity degeneracy as the ratio $\partial \log t / \partial \log Z = 3/2$ (i.e. a factor of three change in age looks like a factor of two change in metallicity in an SSP).

The Lick indices can be divided into three groups with varying sensitivities to age and metallicity (Proctor 2002), and hence measuring different age and metallicity sensitive indices permits one to break the age–metallicity degeneracy:

- Indices with degeneracy $\leq$ 1.3, which are primarily sensitive to age. For example, G4300 and the Balmer lines.

| Name | Index Band | Blue Continuum | Red Continuum | Unit | Measures | Degeneracy |
|---|---|---|---|---|---|---|
| Hδ$_A$ | 4083.5 – 4122.3 | 4041.6 – 4079.8 | 4128.5 – 4161.0 | Å | | 1.1 |
| Hδ$_F$ | 4091.0 – 4112.3 | 4057.3 – 4088.5 | 4114.8 – 4137.3 | Å | | 0.9 |
| CN$_1$ | 4142.1 – 4177.1 | 4080.1 – 4117.6 | 4244.1 – 4284.1 | mag | C,N,(O) | 1.9 |
| CN$_2$ | 4142.1 – 4177.1 | 4083.9 – 4096.4 | 4244.1 – 4284.1 | mag | C,N,(O) | 2.1 |
| Ca4227 | 4222.3 – 4234.8 | 4211.0 – 4219.8 | 4241.0 – 4251.0 | Å | Ca,(C) | 1.5 |
| G4300 | 4281.4 – 4316.4 | 4266.4 – 4282.6 | 4318.9 – 4335.1 | Å | C,(O) | 1.0 |
| Hγ$_A$ | 4319.8 – 4363.5 | 4283.5 – 4319.8 | 4367.3 – 4419.8 | Å | | 1.0 |
| Hγ$_F$ | 4331.3 – 4352.3 | 4283.5 – 4319.8 | 4354.8 – 4384.8 | Å | | 0.8 |
| Fe4383 | 4369.1 – 4420.4 | 4359.1 – 4370.4 | 4442.9 – 4455.4 | Å | Fe,C,(Mg) | 1.9 |
| Ca4455 | 4452.1 – 4474.6 | 4445.9 – 4454.6 | 4477.1 – 4492.1 | Å | (Fe),(C),Cr | 2.0 |
| Fe4531 | 4514.3 – 4559.3 | 4504.3 – 4514.3 | 4560.5 – 4579.3 | Å | Ti,(Si) | 1.9 |
| C$_2$4668 | 4634.0 – 4720.3 | 4611.5 – 4630.3 | 4742.8 – 4756.5 | Å | C,(O),(Si) | 4.9 |
| Hβ | 4847.9 – 4876.6 | 4827.9 – 4847.9 | 4876.6 – 4891.6 | Å | | 0.6 |
| Fe5015 | 4977.8 – 5054.0 | 4946.5 – 4977.8 | 5054.0 – 5065.3 | Å | (Mg),Ti,Fe | 4.0 |
| Mg$_1$ | 5069.1 – 5134.1 | 4895.1 – 4957.6 | 5301.1 – 5366.1 | mag | C,Mg,(O),(Fe) | 1.8 |
| Mg$_2$ | 5145.1 – 5196.6 | 4895.1 – 4957.6 | 5301.1 – 5366.1 | mag | C,Mg,(O),(Fe) | 1.8 |
| Mg$_b$ | 5160.1 – 5192.6 | 5142.6 – 5161.4 | 5191.4 – 5206.4 | Å | Mg,(C),(Cr) | 1.7 |
| Fe5270 | 5245.7 – 5285.7 | 5233.2 – 5248.2 | 5285.7 – 5318.2 | Å | Fe,C,(Mg) | 2.3 |
| Fe5335 | 5312.1 – 5352.1 | 5304.6 – 5315.9 | 5353.4 – 5363.4 | Å | Fe,(C),(Mg),Cr | 2.8 |
| Fe5406 | 5387.5 – 5415.0 | 5376.3 – 5387.5 | 5415.0 – 5425.0 | Å | Fe | 2.5 |
| Fe5709 | 5696.6 – 5720.4 | 5672.9 – 5969.6 | 5722.9 – 5736.6 | Å | (C),Fe | 6.5 |
| Fe5782 | 5776.6 – 5796.6 | 5765.4 – 5775.4 | 5797.9 – 5811.6 | Å | Cr | 5.1 |
| NaD | 5876.9 – 5909.4 | 5860.6 – 5875.6 | 5922.1 – 5948.1 | Å | Na,C,(Mg) | 2.1 |
| TiO$_1$ | 5936.6 – 5994.1 | 5816.6 – 5849.1 | 6038.6 – 6103.6 | mag | C | 1.5 |
| TiO$_2$ | 6189.6 – 6272.1 | 6066.6 – 6141.6 | 6372.6 – 6415.1 | mag | C,V,Sc | 2.5 |
| CaII$_1$ | 8483.0 – 8513.0 | 8447.5 – 8462.5 | 8842.5 – 8857.5 | Å | | 6.7 |
| CaII$_2$ | 8527.0 – 8557.0 | 8447.5 – 8462.5 | 8842.5 – 8857.5 | Å | | 6.7 |
| CaII$_3$ | 8647.0 – 8677.0 | 8447.5 – 8462.5 | 8842.5 – 8857.5 | Å | | 6.7 |
| MgI | 8799.5 – 8814.5 | 8775.0 – 8787.0 | 8845.0 – 8855.0 | Å | | – |

Table 1.1: The Lick indices, with the wavelengths, defined by T98. The elements contributing to the strength of each index are given in the second to last column (elements in brackets increase the line strength when their abundance decreases). The degeneracy is described in the text. Table adapted from Salaris & Cassisi (2005; table 11.1).
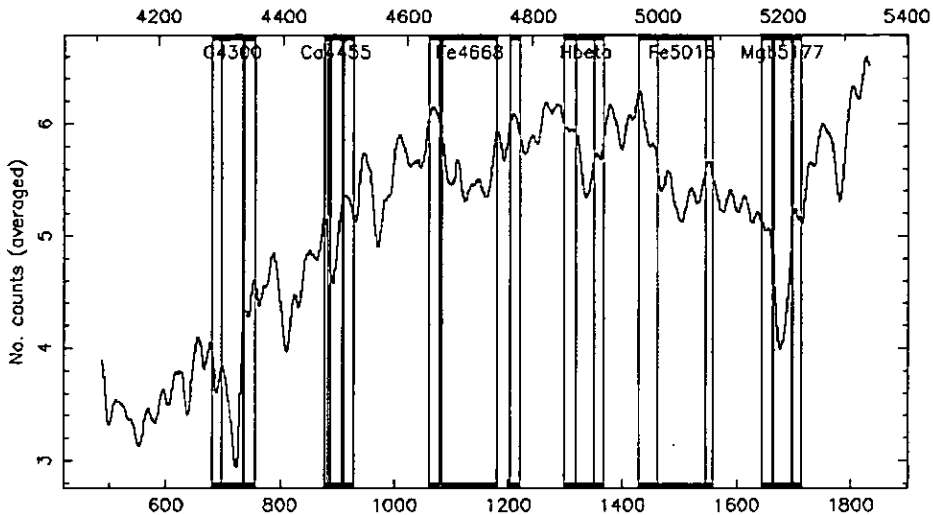
Figure 1.3: Figure illustrating the measurement of some of the Lick indices in NGC1399 (spectrum taken from this galaxy sample). The central bands (green) and sidebands (blue and red) are indicated on the figure.

- Indices with degeneracy $\sim$ 1.6, which are degenerate and can not differentiate between the effects of age and metallicity. For example, Ca4227 and $Mg_b$. Some of these indices may be sensitive to specific element abundances.

- Indices with degeneracy $\gg$ 1.6, which are highly sensitive to metallicity. For example, Fe5015.

Absorption-feature indices are composed of measurements of the flux in a central wavelength interval corresponding to the absorption feature considered, and two sideband intervals (as illustrated in Figure 1.3) that provide a reference level, which is called the pseudocontinuum. The average fluxes in the sidebands are found and a line is drawn between the mid-points to represent the reference pseudocontinuum level. The difference in flux between this line and the observed spectrum within the feature wavelength interval determines the index. The sidebands also contain absorption features, and therefore, the value of an index is dependent on the strength of the lines in the central feature as well as the sidebands.

For narrow atomic features, the indices are expressed in Å whereas for broad molecular bands, in magnitudes. If $F_{I,\lambda}$ represents the observed flux per unit wavelength in the central wavelength range $\lambda_1 - \lambda_2$, and $F_{C,\lambda}$ that of the pseudo-continuum level, then the numerical value for a narrow absorption-feature ($I_{Ang}$) is defined as:

$$I_{Ang} = \int_{\lambda_1}^{\lambda_2} \left(1 - \frac{F_{I,\lambda}}{F_{C,\lambda}}\right) d\lambda \tag{1.2}$$

(Salaris & Cassisi 2005). The value of an index measured in magnitudes ($I_{Mag}$) is:

$$I_{Mag} = 2.5 \log \left[\left(\frac{1}{\lambda_1 - \lambda_2}\right) \int_{\lambda_1}^{\lambda_2} \frac{F_{I,\lambda}}{F_{C,\lambda}} d\lambda\right] \tag{1.3}$$

$I_{Ang}$ and $I_{Mag}$ are therefore related by:

$$I_{Mag} = 2.5 \log \left[\frac{I_{Ang}}{(\lambda_2 - \lambda_1)} - 1\right] \tag{1.4}$$

To compute the model values for indices of an unresolved SSP, an isochrone representing an SSP of a certain age and chemical composition is required. This isochrone is populated according to the assumed initial mass function (IMF) and, together with a spectral library with the adequate resolution, the integrated spectrum can be determined by applying

$$F_{I,\lambda}(t, Z) = \int_{M_l}^{M_u} f_\lambda(M, t, Z) \Phi(M) \, dM \tag{1.5}$$

to all relevant wavelengths (Salaris & Cassisi 2005). Here $f_\lambda(M, t, Z)$ is the flux emitted at a specific wavelength by a star of mass $M$, metallicity $Z$ and age $t$, $\Phi(M) \, dM$ is the IMF as a function of mass, and $M_l$ and $M_u$ is the mass of the lowest-mass and highest-mass star respectively, in the SSP (see Salaris & Cassisi 2005 for details). This process is known as isochrone synthesis if integration is over mass for all stars (for example in Bruzual & Charlot 2003), and as the "fuel consumption" method if integration over mass is changed to integration over

luminosity in post main-sequence stars (for example in Maraston 2005). The indices can then be determined from the integrated spectrum according to their wavelength definitions given in Table 1.1.

The measured values of the Lick indices in stars have been parametrised as functions of $T_{\text{eff}}$, $g$ and [Fe/H], to produce a series of fitting functions. A detailed description of the process to determine the integrated index values, in order to compare them with observed galaxy index measurements, is given in Tantalo & Chiosi (2004).

The advantages of using the Lick indices are: they are well calibrated against GCs; using a combination of age and metallicity-sensitive indices can partially break the age–metallicity degeneracy; due to their narrow wavelength definitions, the indices are not affected by dust (MacArthur 2005); and their sensitivity to different chemical elements has been calculated using model atmospheres (Tripicco & Bell 1995; Korn, Maraston & Thomas 2005).

The Lick/IDS indices are defined at low resolution, and since a galaxy spectrum is broadened by the internal kinematics, the indices are a blend of many spectral lines. Careful calibrations are needed to fully understand their sensitivity to age and metallicity (Korn et al. 2005; Koleva et al. 2008). New indices are also being defined to improve the sensitivity of an index to either age or metallicity, such as a new definition for H$\delta$ (Vazdekis & Arimoto 1999), and for the Ca triplet (Cenarro et al. 2001).

An alternative to fitting the spectrophotometric indices is fitting the whole spectral energy distribution (SED; for example Panter, Heavens & Jimenez 2003; Cid Fernandes et al. 2005; Koleva et al. 2008). SED fitting has the advantage that all the information in the spectrum is used simultaneously (see Section 4.5). However, due to the lack of libraries of synthetic spectra with different abundance ratios, care needs to be taken when interpreting the results. Furthermore, all

the lines can not be fitted simultaneously, and information about the chemical abundance ratios can not be extracted.

## 1.3.2 SSP-models

Stellar libraries are based on stars in the solar neighbourhood. Though these measurements provide good estimates of iron abundance [Fe/H], solar-neighbourhood stars possess considerable scatter in the abundance ratios of individual elements. Giant early-type galaxies show non-solar abundance ratios such as [Mg/Fe] $> 0$ (Worthey, Faber & González 1992). The new generation of SSP-models include non-solar abundance ratios by taking into account the variations in $\alpha$-element abundance (O, Mg, Ar, Ca, Ne, S, Si and Ti) with respect to Fe-peak elements (Cr, Mn, Fe, Co, Ni, Cu and Zn) and their effect on the Lick index measurements. Tripicco & Bell (1995) computed these effects on the 21 indices modelled by Worthey (1994). Korn et al. (2005) revisited these response functions, calculated them at different metallicities, and added sensitivity calculations for the higher order Balmer lines. The inclusion of these $\alpha$-element abundances in SSP-models solved part of the problem observed in elliptical galaxies where ages and metallicities depend on the indices used to measure those parameters (Sánchez-Blázquez et al. 2006b).

If galaxies experienced a SFH more complicated than a single burst, the SSP-fitted values should be carefully interpreted. The youngest stellar populations dominate the light from galaxies which causes the SSP-fitted stellar population ages to be biased towards the younger stellar populations and not the dominating stellar populations by mass (Li & Han 2007; Trager & Somerville 2009). The SSP-metallicity, on the other hand, will be more biased to the metallicity of the old population, depending on the mass fraction of the burst (Serra & Trager 2007; Sánchez-Blázquez et al. 2007).

CHAPTER 1

## Popular SSP-models

**Thomas, Maraston & Korn (2004)** provided the full set of Lick indices in the wavelength range $4000 \lesssim \lambda \lesssim 6500$ Å (covering all 25 Lick indices in this range) for SSPs with variable element abundance ratios $[\alpha/\mathrm{Fe}] = 0.0, 0.3, 0.5$; $[\alpha/\mathrm{Ca}] = -0.1, 0.0, 0.2, 0.5$ and $[\alpha/\mathrm{N}] = -0.5, 0.0$. The models cover ages in the range 1 to 15 Gyr, and metallicities between 0.005 and 3.5 solar (further described in Section 4.4).

Other widely used SSP-models include that of **Bruzual & Charlot (2003)**, which uses the fitting functions of Worthey (1994) and Worthey & Ottaviani (1997). The **Lee & Worthey (2005)** models includes $\alpha$-element enhancement calculated by Houdashelt et al. (2002), and the **Vazdekis (1999)** and **Vazdekis (in preparation)** models predict the full SED for SSPs of different ages and metallicities (but comparison to individual absorption lines is also possible). The latter models makes use of the new stellar library, MILES (Sánchez-Blázquez 2006d)[4], which covers the wavelength range from 3525 to 7500 Å, and has superior flux calibration to the previous stellar libraries included in models. The Vazdekis models provides synthetic spectra with spectral resolution of 1.8 Å, which is much higher than the resolution of the Lick indices, and thus has the advantage that observed spectra can be compared with models without degrading their resolution. The **Schiavon (2007)** models predict the Lick index measurements for a grid of ages between $0.1 \leq t \leq 15.8$ Gyr, with $-1.3 \leq [\mathrm{Fe/H}] \leq 0.2$ for solar-scaled isochrones and $-0.8 \leq [\mathrm{Fe/H}] \leq 0.3$ for the $\alpha$-enhanced isochrones, though only models older than 0.8 Gyr are computed with variable abundance ratios. Graves & Schiavon (2008) implemented the Schiavon (2007) models into a publicly available code, called EZ_AGES, which can determine the mean light-weighted abundances of Fe, Mg, C, N, and Ca from medium resolution spectra.

---

[4]http://www.ucm.es/info/Astrof/miles/miles.html.

### 1.3.3 Previous work

Numerous previous authors used the Lick/IDS line-strength indices to derive mean ages and abundances of galaxies over the past two decades: González (1993); Davies, Sadler & Peletier (1993); Worthey (1994); Fisher, Franx & Illingworth (1995b); Gorgas et al. (1997); Worthey & Ottaviani (1997); T98; Jørgensen (1999); Vazdekis (1999); Mehlert et al. (2000); Schiavon, Barbuy & Bruzual (2000); Trager et al. (2000a,b); Kuntschner et al. (2001); Proctor & Sansom (2002); Moore et al. (2002); Bruzual & Charlot (2003); Thomas, Maraston & Bender (2003); Nelan et al. (2005); Thomas et al. (2005); Sánchez-Blázquez et al. (2006a, 2006b, 2006c, 2007); Trager et al. (2008); Ogando et al. (2008), and many others. Most of these authors have concentrated on early-type galaxies because of their higher surface brightness, and the fact that they contain less nebular emission which complicates the measurement of absorption lines. The vast majority of stellar population studies of early-type galaxies treat all ellipticals, S0s and BCGs together.

Until now BCGs have been imaged extensively (Malumuth & Kirshner 1985; Schombert 1986, 1987, 1988; Postman & Lauer 1995; Collins & Mann 1998; Aragón-Salamanca et al. 1998; Brough et al. 2002; Laine et al. 2003; Patel et al. 2006; Liu et al. 2008; Whiley et al. 2008), but spectroscopic data have been limited to very small samples or narrow wavelength ranges. Tonry (1984); Tonry (1985); Fisher, Illingworth & Franx (1995a); Fisher et al. (1995b); Cardiel et al. (1998a); and Carter et al. (1999) each investigated 18 or fewer galaxies, and moreover measured only three or fewer spectral indices. Brough et al. (2007) used a wide wavelength range but only for six brightest group and cluster galaxies. Spectroscopic data from the Sloan Digital Sky Survey (SDSS) are not ideal for stellar population analysis of individual sources, because the S/N ratio is often not high enough, and the spatial information is lacking since fibres were used.

Recently, Von der Linden et al. (2008) carried out a study of 625 brightest group and cluster galaxies to relate their stellar population properties to those of ordinary elliptical galaxies of the same mass. They found that stellar populations of BCGs are not different from the stellar populations in elliptical galaxies, except for the $\alpha$-abundance ratios, which are higher in BCGs. Brough et al. (2007) with a smaller sample, did not find this difference.

The study of Von der Linden et al. (2008) constitutes a benchmark in the study of stellar populations in BCGs. However, they did not have spatially resolved information. The merger history of a galaxy determines the kinematic and stellar population properties and, therefore, can be used as a probe for the assembly history of those galaxies. Brough et al. (2007) showed that BCGs present a large spread in their metallicity gradients, probably reflecting differences in their assembly history and the dissipation during the interaction.

## 1.4 Scientific motivation and thesis outline

BCGs have been modelled dynamically and imaged extensively. However, their formation mechanism is still unknown. Mergers between smaller galaxies, massive star formation in the early stages of the formation of the cluster due to (the now extinguished) cooling flows, or monolithic collapse that may originate from unusually large primordial fluctuations, are all possible candidates. These processes will leave different imprints in the dynamical properties and in the detailed chemical abundances of the stars. High S/N ratio spectroscopy is needed to characterise their composite stellar populations. Testing these theories has important consequences for models of galaxy formation in clusters since it affects both the brightest galaxies and the population of nearby galaxies.

The connection between the formation of a galaxy cluster and the formation of its most dominant inhabitant also remains a mystery. It is still unresolved

whether these bright giants are products of cluster evolution, whether they form at the same time as the cluster or whether these galaxies are the seeds around which clusters accreted. The great densities in the rich clusters in which they are found causes the probability of interactions to be far greater than in the field, in spite of large relative velocities causing interaction time-scales to be small.

To address some of these issues, long-slit spectroscopy of a large and statistically significant sample of BCGs were obtained. This provides a complete dataset of spectral indices, covering a wide wavelength range. These luminous central galaxies are contrasted with ordinary early-type galaxies to look for relative differences in their evolution, using features sensitive to stellar population age and abundances of various elements.

The objectives and outlines of this study are the following:

- Compile a statistically significant sample of nearby BCGs, concentrating on those previously classified as cD galaxies, suitable for long-slit observations. Obtain, and reduce, the long-slit spectra of the BCGs, covering a wide wavelength range. *–Chapter 2.*

- Determine the central and spatially-resolved stellar kinematics through derivation of radial velocity and velocity dispersion profiles. *–Chapter 3.*

- Measure all the Lick/IDS indices, and calibrate them onto the Lick system. Contrast the BCG central indices with those of ordinary ellipticals over the same mass range. Derive luminosity-weighted average properties (ages, metallicities and $\alpha$-enhancement ratios) in the cores of the galaxies using SSP-fitting. Systematically contrast the stellar population parameters derived for the BCGs with those of ordinary ellipticals in the same mass range. Firstly, BCGs are suspected to have a formation and evolution history different to that of ordinary elliptical galaxies, and secondly, this comparison will help distinguish whether mass is the main influence on BCG kinematic

and stellar population properties, or the privileged location in the cluster. Derive the BCG SFHs using full-spectrum fitting. *−Chapter 4.*

- Investigate the context of the cluster environment, and correlate the stellar population properties of BCGs with the properties of the host clusters (cluster density, mass, distance to X-ray peak, presence of cooling flows). *−Chapter 5.*

# Chapter 2

# BCGs: SAMPLE AND OBSERVATIONS

## 2.1  Galaxy sample

The initial intention of this project was to study cD galaxies in particular. However, the confusion regarding the classification of cD galaxies, and the lack of deep photometry which would enable a conclusive distinction to be made between BCGs with and without a halo, made the sample selection extremely challenging. Aiming at compiling a representative cD sample, rather broad selection criteria were adopted, although the sample is intrinsically a BCG sample. It is expected that deep photometric information will be added in the future which will allow a test to be made for the presence of a faint halo and discriminate between cD and non-cD BCGs. For the purpose of this thesis the sample will be referred to as a BCG sample. Two ordinary elliptical galaxies were also observed (one E and one E/S0) and the resulting data are presented here.

The sample selection combines three methods, making the best use of available information from the literature and astronomical databases. The three search methods are described below:

CHAPTER 2

## Method 1

Two well-known galaxy cluster classification systems that distinguish clusters containing a cD galaxy in the centre from other galaxy clusters, are those of Rood & Sastry (1971, hereafter RS) and Bautz & Morgan (1970, hereafter BM). The RS classification is based on the projected distribution of the brightest 10 members, and recognises the following cluster types:

- **cD** – Single dominant cD galaxy.

- **B** – Dominant binary, for example the Coma cluster.

- **L** – Linear array of galaxies, for example the Perseus cluster.

- **C** – Single core of galaxies.

- **F** – Flattened.

- **I** – Irregular distribution, for example the Hercules cluster.

The BM classification is based on the brightness contrast between the brightest member and the typical bright galaxies in the cluster (i.e. the slope of the luminosity function at the bright end), and recognises the following cluster types:

- **I** – Dominated by a central cD galaxy.

- **II** – Intermediate E/cD galaxy.

- **III** – No dominant galaxy.

Hoessel, Gunn & Thuan (1980) derived the BM types for all the nearby Abell clusters of galaxies, which made it possible to obtain a list of Abell clusters with BM types I and I-II (a type intermediate between I and II) with the vizieR

service[1]. Struble & Rood (1987) compiled a catalogue of the morphological properties of 2712 Abell clusters, derived from visual inspection of the Kitt Peak National Observatory photographic plates. This made it possible to obtain a list of Abell clusters with RS cluster classification type cD. These two lists contained the coordinates of the centre of the cluster, but not the names or coordinates of the BCGs. The NASA/IPAC Extragalactic Database (NED)[2] was then used to search for the brightest galaxies closest to the centre of each cluster. If the brightest member was classified as either a cD or D galaxy in NED (in the NED morphology or notes of previous observations), it was included in the list of BCGs. The RS and/or BM classifications are frequently used as a method to identify possible cD galaxies (for example Hill & Oegerle 1992; Baier & Wipper 1995; Giacintucci et al. 2007).

**Method 2**

The De Vaucouleurs Third Reference Catalogue (RC3; De Vaucouleurs et al. 1995) classifies cD galaxies as T-type $= -4$, where the T-type is a numerical index of different classes of objects on the Hubble sequence (for example: $-6 =$ compact elliptical; $-5 =$ elliptical; $-4 =$ cD galaxy; $-3$ to $-1 =$ S0 etc.). The HyperLEDA[3] catalogue collected T-type determinations for galaxies from different sources and lists the mean T-type in their database. Unfortunately, the original sources are not listed in the catalogue. Therefore, the uncertainty is the only indication of ambiguity in the classification of galaxies from different sources; when several determinations agree, the uncertainty is small (Georges Paturel, private communication). The second search was carried out by doing

---

[1]Electronic catalogue search service, hosted and maintained by Centre de Données Astronomiques de Strasbourg (http://vizier.u-strasbg.fr/).

[2]http://nedwww.ipac.caltech.edu/.

[3]HyperLEDA is an extended version of the Lyon–Meudon Extragalactic Database operated by the Centre de Recherche Astronomique de Lyon (http://leda.univ-lyon1.fr/).

an all-sky search in the HyperLEDA database for galaxies with the following properties:

- T-type between -3.7 and -4.3.

- Apparent $B$-magnitude brighter than 16.

- Distance closer than 340 Mpc[4].

- Further than 15 degrees from the Galactic plane.

It was found that RC3 T-type (as listed in HyperLeda) alone is not a reliable classification of galaxy types. Figure 2.1 shows the absolute magnitude range of the galaxies found with T-type $= -4$. It shows that low luminosity galaxies are also categorised as galaxies with T-type $= -4$. This prompted an absolute magnitude cutoff of $M_B = -20$ to be applied throughout the sample selection. The galaxies obtained with this search were added to the list of BCGs galaxies if they were classified as either cD or D galaxies in NED.

**Method 3**

The third search was undertaken by choosing galaxies with published surface brightness profiles that had a slope consistent with cD/D galaxies, and in the case of cD galaxies, that also broke the De Vaucouleurs $r^{\frac{1}{4}}$ law at large radii. Galaxies were chosen from the series of papers by Schombert (1986; 1987; and 1988) and from Malumuth & Kirshner (1985). Galaxies with surface brightness slopes and profiles conforming to the cD/D criteria set in Schombert (1987) were included in the list of BCGs, since that forms the basis of most definitions of cD galaxies.

The complete list of galaxies and their properties is given in Table 2.1. The following global criteria were applied to the sample: apparent $B$-magnitude brighter

---

[4]An $H_0$ value of 75 km s$^{-1}$ Mpc$^{-1}$ is assumed.
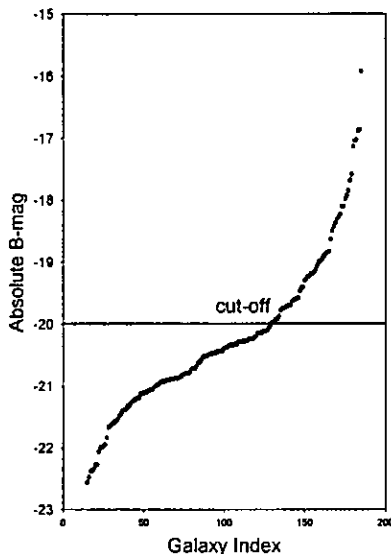
Figure 2.1: The absolute magnitudes of all the galaxies selected by the T-type search criteria explained in method 2. It shows the cut-off magnitude chosen here for eliminating all the lower luminosity galaxies, and illustrates the T-type misclassification.

than 16; distance closer than 340 Mpc; and absolute magnitude brighter than $M_B$ = -20. In addition, the Galactic plane was avoided. Method 1 delivered 13 galaxies, method 2 delivered 32 galaxies and method 3 delivered 29 galaxies (indicated in Table 2.1). With 11 of the merged list being duplicates present from more than one method, this provided an unbiased, all-sky list of 63 galaxies.

In summary: these 63 galaxies were classified as cD/D in NED (in the morphological classification or in the notes of previous observations) and/or have profiles breaking the $r^{\frac{1}{4}}$ law. With the exception of NGC4946 and NGC6047 which are included in the sample as control galaxies (known to be an E and E/S0 galaxy respectively), all BCGs have been categorised as containing a halo, albeit very inhomogeneously. Despite the confusion regarding the halo classification, all these galaxies are the dominant central galaxies in clusters and groups. If selection methods 1 and 3 above are assumed to be more robust methods of identifying a BCG with a halo, then 67 per cent of the BCG sample are confirmed cD galaxies.

**BCG Galaxy Distribution**
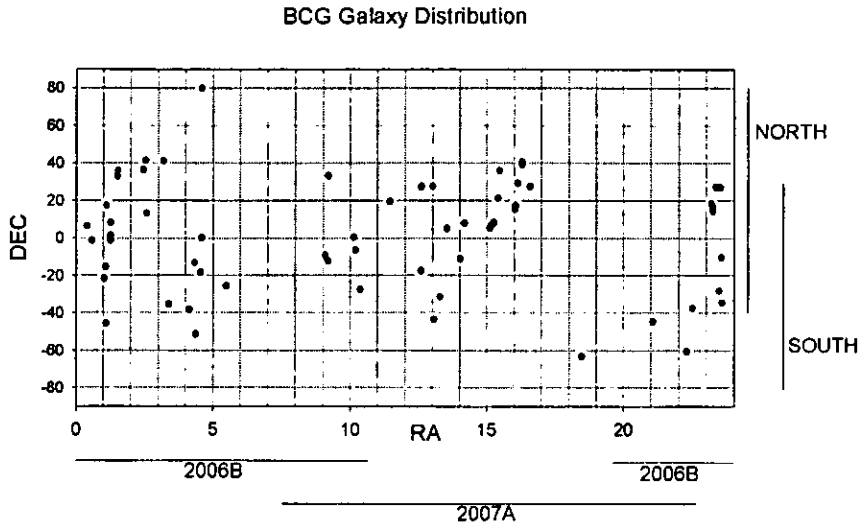


Figure 2.2: All-sky distribution of the BCG sample. The right ascension distribution over two observing semesters (with Gemini) and the declination distribution over Gemini North and South are indicated. The gaps in the all-sky sample distribution, caused by the selection condition stating that all galaxies should be further than 15 degrees from the Galactic plane, can clearly be seen.

In all the conclusions of this study, it will be clearly stated whether a statement applies only to BCGs or also includes the two elliptical galaxies. Figure 2.2 shows the all-sky distribution of the BCGs.

The BCG sample has a common overlap of 10 galaxies with the Fisher et al. (1995a) sample of 13 BCGs. For four Abell clusters (Abell 0194, 0548, 4038 and 2151), the choice of BCG differs from that made by Postman & Lauer (1995). In each of the first three cases, the choice of BCG in this sample is the dominant galaxy closest to the cluster centre (compared with the BCGs in the Postman & Lauer (1995) sample, which were chosen to be strictly the brightest galaxies in the cluster). In the case of Abell 2151, NGC6034 was chosen to be the BCG (following previous authors e.g. Aragón-Salamanca et al. 1998), as it has a very prominent cD halo (Schombert 1987, 1988), and is close to an X-ray peak.

Some of the clusters in this sample are known to have substructure (Rines et al. 2002; Adami et al. 2005) and, in these cases, there may be more than one local

X-ray maximum, which can host a dominant galaxy central to that substructure. Hence, according to the BCG definition adopted here, there can be more than one BCG per cluster. In particular, three BCGs selected (NGC4889, NGC4874 and NGC4839) are hosted by the Coma cluster, all of them showing pronounced envelopes (Schombert 1987; Andreon et al. 1996). The first two are the dominant galaxies in the cluster, although it is not clear which one is the original central galaxy of the main cluster (see e.g. Adami et al. 2005). The third BCG, NGC4839, is the dominant galaxy of a group that appears to be falling into the main cluster (Neumann et al. 2001). Two galaxies (NGC6173 and NGC6160) from the cluster Abell 2197 are also included in the sample. These two galaxies are believed to be the dominant galaxies of two main groups in the process of merging (Abell 2197E and Abell 2197W; Schombert 1987).

Of the 63 galaxies in the merged list, a total of 49 were observed over multiple semesters for this thesis, together with the two control ellipticals. The observed galaxies have a brightness range from $M_{\rm B} = -20.71$ to $M_{\rm B} = -23.54$ and are hosted by clusters with X-ray luminosities from $L_{\rm X} = 0.03 \times 10^{44}$ to $17.07 \times 10^{44}$ erg s$^{-1}$. The observed sample is the largest spectroscopic sample of BCGs to date for which spatially-resolved stellar populations can be analysed.

## 2.2 Observations and data reduction

Observations of the 49 BCGs and two normal elliptical galaxies were taken over a 20 month period from June 2006 to January 2008, using the William Herschel Telescope (WHT)[5] and Gemini North and South telescopes[6].

---

[5]http://www.ing.iac.es/Astronomy/telescopes/wht.
[6]http://www.gemini.edu.

| Object | $\alpha$(J2000) | $\delta$(J2000) | Cluster | NED-type | T-type | MA | $m_B$ | $M_B$ | Ref | Run |
|---|---|---|---|---|---|---|---|---|---|---|
| IC1565 | 0 39 26.3 | +06 44 03 | A0076 | cD;E | −3.9±1.2 | − | 14.41 | −21.96 | 2 | |
| UGC00579 | 0 56 16.2 | −01 15 22 | A0119 | cD;E | −4.8±0.4 | 41 | 14.40 | −22.34 | 3 | 6 |
| ESO541-013 | 1 02 41.8 | −21 52 55 | A0133 | cD;E+3 pec | −4.0±0.7 | 16 | 14.71 | −22.54 | 2 | 6 |
| PGC004072 | 1 08 50.8 | −15 24 31 | A0151 | D | −4.2±1.0 | 83 | 14.75 | −22.37 | 2 | 6 |
| IC1633 | 1 09 55.6 | −45 55 52 | A2877 | cD;E+1 | −3.9±0.5 | 97 | 12.57 | −22.60 | 2, 3 | 3 |
| IC1634 | 1 11 02.9 | +17 39 46 | A0154 | MLT SYS | −4.1±1.0 | 153 | 15.27 | −22.64 | 1 | |
| IC1695 | 1 25 07.6 | +08 41 58 | A0193 | cD;S? | − | 103 | 14.87 | −21.98 | 1 | |
| NGC0533 | 1 25 31.5 | +01 45 33 | A0189B | cD;E3: | −4.8±0.6 | 50 | 12.45 | −22.25 | 3 | 6 |
| NGC0541 | 1 25 44.3 | −01 22 46 | A0194 | cD;S0−: | −3.9±0.9 | 69 | 13.09 | −21.62 | 2 | 6 |
| IC1733 | 1 50 42.9 | +33 04 55 | A0260 | cD;E: | −4.9±0.8 | − | 14.14 | −22.16 | 1 | |
| NGC0708 | 1 52 46.3 | +36 09 12 | A0262 | cD;E | −4.9±0.4 | 39 | 13.63 | −20.98 | 3 | |
| UGC02232 | 2 46 03.9 | +36 54 19 | A0376 | cD;E/D | −3.9±1.3 | − | 15.50 | −21.64 | 2 | 2 |
| NGC1129 | 2 54 27.4 | +41 34 46 | AWM7 | E;BrClG | −4.7±1.2 | 73 | 13.34 | −21.67 | 3 | |
| UGC02450 | 2 58 57.8 | +13 34 59 | A0401 | cD | 2.8±5.0 | 29 | 15.24 | −23.50 | 1 | |
| NGC1275 | 3 19 48.2 | +41 30 42 | A0426 | cD;pec;NLRG | −2.2±1.7 | 110 | 12.55 | −22.69 | 3 | |
| NGC1399 | 3 38 29.0 | −35 26 58 | RBS454 | cD;E1 pec | −4.5±0.5 | − | 10.42 | −20.81 | 3 | 3 |
| ESO303-005 | 4 13 58.8 | −38 05 50 | RBS521 | cD? | −4.0±0.5 | − | 15.38 | −21.51 | 2 | 3 |
| MCG-02-12-039 | 4 33 37.8 | −13 15 40 | A0496 | cD;E+? | −3.9±0.9 | 180 | 13.95 | −22.50 | 2, 3 | 3 |
| ESO202-043 | 4 37 47.6 | −51 25 23 | A S0479 | E+ | −3.8±0.8 | 133 | 14.45 | −21.72 | 2 | 6 |
| ESO552-020 | 4 54 52.3 | −18 06 53 | CID 28 | cD;E+ | −3.9±0.7 | 148 | 13.54 | −22.51 | 2 | 3 |
| NGC1713 | 4 58 54.6 | +00 29 20 | CID 27 | cD;E+ | −4.3±0.6 | 39 | 13.88 | −20.71 | 2 | 2 |
| UGC03197 | 4 59 55.8 | +80 10 43 | A0505 | cD | −4.9±0.9 | 85 | 15.25 | −22.26 | 3 | |
| ESO488-027 | 5 48 38.5 | −25 28 44 | A0548 | cD;E+1 | −3.8±0.6 | 68 | 14.22 | −22.22 | 2 | 3 |
| PGC025714 | 9 08 32.4 | −09 37 47 | A0754 | D | −4.2±1.4 | 122 | 14.32 | −23.04 | 2 | 6 |
| PGC026269 | 9 18 05.7 | −12 05 44 | A0780 | (R')SA0−:;BrClGSy3 | −2.6±1.0 | 133 | 14.38 | −22.84 | 1 | 3 |

Table 2.1 – Continued

| Object | $\alpha$(J2000) | $\delta$(J2000) | Cluster | NED-type | T-type | MA | $m_B$ | $M_B$ | Ref | Run |
|---|---|---|---|---|---|---|---|---|---|---|
| NGC2832 | 9 19 46.9 | +33 44 59 | A0779 | E+2:;cD | −4.3±0.6 | 172 | 12.79 | −22.38 | 2, 3 | 2 |
| UGC05515 | 10 13 38.3 | +00 55 32 | A0957 | E+pec: | −4.0±0.7 | 83 | 14.49 | −22.28 | 2, 3 | 5 |
| PGC030223 | 10 20 26.6 | −06 31 35 | A0978 | D | −3.9±1.2 | 1 | 15.40 | −21.85 | 2 | 6 |
| NGC3311 | 10 36 42.9 | −27 31 37 | A1060 | cD;E+2 | −3.3±1.3 | − | 12.69 | −21.33 | 1 | 5 |
| NGC3842 | 11 44 02.2 | +19 56 59 | A1367 | E;BrClG | −4.8±0.7 | 177 | 12.80 | −22.18 | 3 | 1 |
| PGC044257 | 12 57 11.4 | −17 24 36 | A1644 | cD;E+4 | −4.1±1.0 | 44 | 13.50 | −23.54 | 1, 2 | 5 |
| NGC4839 | 12 57 24.2 | +27 29 54 | A1656 | cD;SA0 | −4.0±0.8 | 64 | 13.05 | −22.26 | 2, 3 | 4 |
| NGC4874 | 12 59 35.5 | +27 57 36 | A1656 | cD;Di | −3.7±0.9 | 45 | 12.75 | −22.50 | 2, 3 | 1 |
| NGC4884(9) | 13 00 07.9 | +27 58 41 | A1656 | cD;E4;Db | −4.3±0.5 | 82 | 12.48 | −22.56 | 2 | 1 |
| NGC4946* | 13 05 29.4 | −43 35 28 | A3526 | E+? | −3.8±0.8 | 135 | 13.41 | −20.27 | | 5 |
| ESO444-046 | 13 27 56.9 | −31 29 44 | A3558 | cD;E+4 | −3.7±1.0 | 161 | 14.07 | −22.86 | 2, 3 | 5 |
| LEDA094683 | 13 53 06.4 | +05 08 59 | A1809 | cD | −2.3±5.0 | 46 | 15.30 | −22.35 | 1 | 5 |
| GSC555700266 | 14 01 36.4 | −11 07 43 | A1837 | cD | − | − | 14.59 | − | 1 | 5 |
| NGC5539 | 14 17 37.8 | +08 10 46 | A1890 | cD | 0.7±5.0 | 39 | 14.92 | −22.62 | 1 | |
| IC1101 | 15 10 56.1 | +05 44 41 | A2029 | cD;S0-: | −2.9±1.1 | 25 | 15.10 | −23.05 | 3 | 5 |
| UGC09799 | 15 16 44.6 | +07 01 16 | A2052 | cD;E | −4.7±1.3 | 30 | 14.34 | −21.84 | 3 | |
| PGC054913 | 15 23 05.3 | +08 36 33 | A2063 | cD;S | −3.8±1.6 | − | 14.71 | −21.46 | 2 | |
| UGC09958 | 15 39 39.1 | +21 46 58 | A2107 | cD;S0-: | −2.9±0.7 | 98 | 14.76 | −22.00 | 3 | |
| UGC10012 | 15 44 59.0 | +36 06 36 | A2124 | cD;E | −4.9±0.6 | 143 | 14.54 | −23.15 | 3 | |
| UGC10143 | 16 02 17.3 | +15 58 28 | A2147 | cD;E+ | −4.0±0.8 | 12 | 14.27 | −21.97 | 2, 3 | 1 |
| NGC6034 | 16 03 32.1 | +17 11 55 | A2151 | E+ | −4.0±0.4 | 59 | 14.58 | −21.60 | 2, 3 | 1 |
| NGC6047* | 16 05 09.1 | +17 43 48 | A2151 | E+ | −3.5±0.8 | 117 | 14.58 | −21.45 | | 1 |
| NGC6086 | 16 12 35.6 | +29 29 06 | A2162 | cD;E | −4.8±0.6 | 3 | 13.81 | −22.19 | 3 | 4 |
| NGC6160 | 16 27 41.1 | +40 55 37 | A2197 | cD;E | −4.8±0.6 | 72 | 14.17 | −21.70 | 3 | 4 |

Table 2.1 – Continued

| Object | α(J2000) | δ(J2000) | Cluster | NED-type | T-type | MA | $m_B$ | $M_B$ | Ref | Run |
|--------|----------|----------|---------|----------|--------|-----|-------|-------|-----|-----|
| NGC6166 | 16 28 38.5 | +39 33 04 | A2199 | cD;E | −4.2±1.4 | 38 | 12.88 | −22.92 | 2, 3 | 1 |
| NGC6173 | 16 29 44.9 | +40 48 42 | A2197 | cD;E | −4.8±0.6 | 138 | 13.13 | −22.58 | 3 | 4 |
| NGC6269 | 16 57 58.1 | +27 51 16 | AWM5 | cD;E | −4.7±0.7 | 80 | 13.38 | −22.98 | 3 | 4 |
| IC4765 | 18 47 18.5 | −63 19 50 | A S0805 | cD;E+4 | −3.9±0.5 | 123 | 12.46 | −21.97 | 2 | 5 |
| NGC7012 | 21 06 45.8 | −44 48 49 | A S0921 | E+4 pec | −3.9±0.5 | 100 | 13.93 | −21.79 | 2 | 3 |
| ESO146-028 | 22 28 51.1 | −60 52 55 | RXCJ2228.8-6053 | E+3 | −3.8±0.8 | 154 | 13.94 | −22.54 | 2 | 5 |
| ESO346-003 | 22 49 22.0 | −37 28 20 | A S1065 | E+2 pec: | −3.8±0.8 | 118 | 14.00 | −21.59 | 2 | 5 |
| NGC7597 | 23 18 30.3 | +18 41 20 | A2572 | cD;S? | −2.0±0.8 | 133 | 15.00 | −21.52 | 1 | 2 |
| NGC7647 | 23 23 57.4 | +16 46 38 | A2589 | cD;E | −4.7±0.8 | 174 | 14.61 | −21.93 | 3 | 1 |
| NGC7649 | 23 24 20.1 | +14 38 49 | A2593 | cD;E | −4.6±1.1 | 78 | 15.65 | −20.99 | 3 | 2 |
| PGC071807 | 23 35 01.5 | +27 22 20 | A2622 | cD | − | 138 | 15.28 | −22.05 | 1 | 4 |
| NGC7720 | 23 38 29.5 | +27 01 51 | A2634 | cD;E+pec: | −4.3±0.6 | − | 13.43 | −22.63 | 2 | 1 |
| IC5358 | 23 47 45.0 | −28 08 26 | A4038 | cD;E+4 pec | −3.8±1.1 | 114 | 13.64 | −22.00 | 2 | 3 |
| NGC7768 | 23 50 58.3 | +27 08 51 | A2666 | cD;E | −4.9±0.5 | 55 | 13.28 | −22.39 | 3 | 1 |
| PGC072804 | 23 54 13.7 | −10 25 09 | A2670 | cD;XBONG | −4.4±2.4 | 76 | 15.32 | −22.82 | 1 | 5 |
| ESO349-010 | 23 57 00.7 | −34 45 33 | A4059 | cD;E+4 | −3.7±1.2 | 155 | 14.18 | −22.69 | 2 | 3 |

Table 2.1: The new sample of BCG galaxies, and the two ordinary ellipticals (marked ⋆). Columns 2, 3, 6 – 9 are from the HyperLeda catalogue, and 4 and 5 from NED. The T-type column is described in the text (see Method 2). MA is the galaxy major axis (in degrees). Ref 1,2 and 3 correspond to the three search methods for the objects (column 10). Observing run number (column 11) 1 = WHT, 2 = Gemini N 2006B, 3 = Gemini S 2006B, 4 = Gemini N 2007A, 5 = Gemini S 2007A, 6 = Gemini S 2007B. Besides the galaxies classified as cD/D in the NED morphology (column 5), NGC6034, UGC05515 and NGC1129 were classified as cD/D in Schombert (1987), and NGC7012, ESO146-028, ESO346-003, ESO202-043, NGC3842, PGC026269 and IC1634 were classified as cD/D in the NED notes by previous observations.

## 2.2.1 WHT observations

Longslit spectroscopy of 10 of the 51 galaxies (listed in Table 2.2) was carried out by the author and A. Sansom during the period 23 to 26 June 2006, using the 4.2m WHT, equipped with the ISIS double spectrograph mounted at the $f/11$ Cassegrain focus. The Marconi2 charge-coupled device (CCD) was employed on the red arm; and the EEV12, on the blue. The spatial scale of the spectrograph was 0.4 arcsec/pixel (with $2 \times 2$ binning which was used here) and the slit width was 1.0 arcsec. Dispersion in the blue arm was 0.90 Å/pixel (grating R600B) and 0.88 Å/pixel (grating R600R) in the red. The spectral resolution ranged between 3.3 and 4.0 Å, depending on the dichroic and arm used. In most cases, the slit was placed on the major axis (MA) of the galaxy. Two exceptions occurred where there was another early-type galaxy (unrelated to the sample) in close proximity, in which case the slit was positioned to go through the centres of both galaxies to observe the two galaxies simultaneously.

Two different dichroics were used. The 5300 Å dichroic was used for three nights and delivered an unvignetted spectral range of 3900 – 5460 Å in the blue arm and 5730 – 6960 Å in the red arm, covering most of the optical Lick absorption features (as introduced in Section 1.3.1). The 6100 Å dichroic was used for one night, delivering an unvignetted spectral range of 4500 – 6120 Å in the blue arm and 7950 – 9600 Å in the red arm. This combination yielded observations of a total of 29 absorption indices, consisting of the original 21 Lick indices from $CN_1$ to $TiO_2$, the four H$\delta$ and H$\gamma$ indices, the near-IR CaII triplet at $\sim$ 8600 Å and the MgI index. The exposure times are listed in Table 2.2. Multiple spectra, instead of long exposures, of the objects were taken and combined after reduction to minimise the effects of cosmic rays on images.

Seeing was always better than 1.0 arcsecond throughout all four nights, and the following calibration frames were obtained: bias frames; arc frames provided

by Cu/Ar and Cu/Ne arcs; dome flat-field illumination by a tungsten lamp; and sky flat-field frames. The sets of bias and sky flat-field frames were taken before and after each observing night. Before and/or after every star or object spectrum, an arc spectrum and flat-field frame were obtained in the red and blue arm at each telescope pointing. This was done to allow accurate wavelength calibration and the removal of the response function of the dichroics, respectively. Five spectrophotometric standard stars were also observed for flux calibration (see Table 2.3). These stars were observed, on average, three times throughout the night, at different airmasses.

A total of 22 Lick calibration stars (G and K type stars, which are considered the main contributors to the visible light in early-type galaxies) were also observed with the 5300 Å dichroic, and 10 with the 6100 Å dichroic. These stars are used as templates for the kinematic measurements, as well as to transform the line-strength indices to the Lick system. A neutral density filter was used for the Lick stars with both dichroics. Table 2.4 details the stars that were observed with the WHT for calibration to the Lick system. Particular care was taken to include stars with a wide range of [Fe/H] values, including above-solar metallicity as they are most similar to the expected properties of the BCGs.

## 2.2.2   Gemini observations

Gemini Multi-object Spectrograph (GMOS) observations were performed in queue scheduling mode, by Gemini Astronomers, over a period of three semesters (see below). Executable observing programmes were prepared in accordance with the Gemini telescope systems. These consist of very detailed descriptions of the instrumental set-up, the procedure to be followed, definition of the objects and guide stars, placement and rotation of the slit, description of the calibration stars, etc. During the observing semester these programmes can be fetched from the

| Object | Exposure (5300 Å) seconds | Exposure (6100 Å) seconds | Slit PA degrees | Axis MA degrees | $r_e$ arcsec | $\epsilon$ | $a_e$ arcsec | Number of $a_e$ observed |
|---|---|---|---|---|---|---|---|---|
| NGC3842 | 6×1200 | 2×900 | 5 | 177 | 16.4 | 0.29 | 16.3 | 1.22 |
| NGC4874 | 6×1200 | 3×900 | 82 | 45 | 20.0 | 0.00 | 20.0 | 0.60 |
| NGC4889 | 6×1200 | 2×900 | 80 | 82 | 25.7 | 0.34 | 25.7 | 0.89 |
| NGC6034 | 6×1200 | 3×900 | 50 | 59 | 8.2 | 0.27 | 8.1 | 1.23 |
| NGC6047 | 3×1200 | – | 88 | 117 | 7.4 | 0.27 | 7.0 | 0.61 |
| NGC6166 | 6×1200 | 3×900 | 35 | 38 | 22.6 | 0.26 | 22.6 | 0.22 |
| NGC7647 | 6×1200 | 3×900 | 174 | 174 | 11.2 | 0.49 | 11.2 | 1.21 |
| NGC7720 | 6×1200 | 3×900 | 10 | – | 9.3 | 0.19 | 9.3 | 0.65 |
| NGC7768 | 3×1200 | 3×900 | 60 | 55 | 14.7 | 0.19 | 14.7 | 0.82 |
| UGC10143 | 6×1200 | 3×900 | 12 | 12 | 10.5 | 0.41 | 10.5 | 0.65 |

Table 2.2: Exposure times for each of the two dichroics for the WHT observations of the BCGs. MA indicates the major axis, and the slit position angle (PA) is given as deg E of N. The half-light radii ($r_e$) were calculated from the 2MASS catalogue, except NGC6166 and NGC7720 for which they were calculated with the VAUCOUL task in the REDUCE package. The last column lists the number of effective half-light radii ($a_e$) spanned by the radial kinematic profiles measured in this work (calculated using the ellipticity $\epsilon$; see Section 3.2 for the detailed derivations of $r_e$ and $a_e$). Table 2.1 contains more properties for the galaxies.

| Star | $\alpha$(J2000) | $\delta$(J2000) | $m_V$ | Spectral type |
|---|---|---|---|---|
| Feige 98 | 14 38 15.8 | +27 29 33 | 11.84 | B7 |
| Feige 92 | 14 11 31.9 | +50 07 04 | 11.62 | Bp |
| BD +33 2642 | 15 51 59.9 | +32 56 54 | 10.74 | B2IVp |
| BD +40 4032 | 20 08 24.1 | +41 15 04 | 10.45 | B2III |
| BD +28 4211 | 21 51 11.0 | +28 51 50 | 10.56 | sdOp |

Table 2.3: Spectrophotometric standard stars used in WHT observations.

| Name | $\alpha$(J2000) | $\delta$(J2000) | $m_V$ | Spec. type | $T_{\text{eff}}$ | log $g$ | [Fe/H] | Dichroic |
|---|---|---|---|---|---|---|---|---|
| HD002665 | 00 30 45.45 | +57 03 53.63 | 7.75 | G5III | 5000 | 2.50 | −2.00 | 1 |
| HD003546 | 00 38 33.35 | +29 18 42.31 | 4.37 | G8III | 4957 | 2.60 | −0.66 | 1 & 2 |
| HD003651 | 00 39 21.81 | +21 15 01.70 | 5.80 | K0V | 5487 | 4.50 | −0.18 | 1 & 2 |
| HD004656 | 00 48 40.94 | +07 35 06.29 | 4.44 | K4III | 3953 | 1.10 | −0.07 | 1 & 2 |
| HD125560 | 14 19 45.24 | +16 18 25.01 | 4.85 | K3III | 4381 | 1.65 | 0.31 | 1 & 2 |
| HD129312 | 14 41 38.75 | +08 09 42.35 | 4.87 | G7III | 4834 | 1.55 | 0.00 | 1 & 2 |
| HD132142 | 14 55 11.04 | +53 40 49.25 | 7.73 | K1V | 5057 | 4.60 | −0.55 | 1 |
| HD132345 | 14 58 53.58 | −11 08 38.45 | 5.87 | K3III | 4374 | 1.60 | 0.42 | 1 & 2 |
| HD135722 | 15 15 30.16 | +33 18 53.40 | 3.47 | G8III | 4834 | 2.45 | −0.44 | 1 |
| HD145328 | 16 08 58.30 | +36 29 27.40 | 4.76 | K1III-IV | 4687 | 2.50 | 0.01 | 1 |
| HD149161 | 16 32 36.29 | +11 29 16.95 | 4.84 | K4III | 3940 | 1.45 | −0.13 | 1 & 2 |
| HD175743 | 18 56 06.12 | +18 06 19.48 | 5.71 | K1III | 4635 | 2.45 | −0.09 | 1 |
| HD184406 | 19 34 05.35 | +07 22 44.19 | 4.45 | K3III | 4428 | 2.45 | 0.22 | 1 |
| HD184492 | 19 35 07.26 | −10 33 37.60 | 5.14 | G8III | 4536 | 1.50 | −0.20 | 1 |
| HD188056 | 19 50 37.72 | +52 59 16.81 | 5.03 | K3III | 4355 | 2.15 | 0.42 | 1 |
| HD188512 | 19 55 18.79 | +06 24 24.35 | 3.71 | G8IV | 5062 | 3.70 | −0.35 | 1 |
| HD199580 | 20 56 48.02 | +42 53 44.39 | 7.19 | K0III-IV | 5039 | 3.50 | −0.10 | 1 |
| HD203344 | 21 21 04.39 | +23 51 21.48 | 5.57 | K1III | 4669 | 2.60 | −0.09 | 1 & 2 |
| HD217476 | 23 00 05.10 | +56 56 43.35 | 5.10 | G0Iab | 5100 | 0.00 | 0.07 | 1 |
| HD219134 | 23 13 16.98 | +57 10 06.08 | 5.56 | K3V | 4824 | 4.65 | 0.01 | 1 |
| HD219449 | 23 15 53.49 | −09 05 15.85 | 4.21 | K0III | 4635 | 2.55 | −0.13 | 1 & 2 |
| HD221148 | 23 29 32.08 | −04 31 57.89 | 6.25 | K3III | 4643 | 3.05 | 0.55 | 1 & 2 |

Table 2.4: The Lick calibration stars used in the WHT observations. Dichroic 1 refers to the 5300 Å dichroic and 2 to the 6100 Å dichroic. Columns 2 – 4 are from the Simbad Astronomical Database (http://simbad.u-strasbg.fr/simbad/) and columns 5 – 8 are from the Lick Database available in electronic form from the webpage of G. Worthey (http://astro.wsu.edu/worthey/).

CHAPTER 2

Gemini database and stored again, making it possible to monitor the progress of each particular observing programme.

Miller et al. (private communication) performed a series of Gemini North and South observing programmes from 2002 to 2004 in which they acquired long-slit spectroscopic data of some of the Lick stars. These were well suited as calibration data for the BCG observing programmes, and the instrumental set-up used here was the same as the set-up used for observations of the Lick stars (with the single exception of the binning – the Lick stars were unbinned in the spatial and spectral direction). The GMOS B600 grating was used (2.7 Å resolution) with a 0.5 arcsec slit width. Dispersion was 0.914 Å/pixel, and the spatial scale was 0.146 arcsec/pixel (with 2 × 2 binning which was used here).

The first 10 galaxies were observed at Gemini South in semester 2006B (August 2006 to January 2007) and five galaxies at Gemini North in the same observing semester. A further 12 galaxies were observed at Gemini South and six at Gemini North in 2007A (February 2007 to July 2007). The final eight galaxies in the sample presented here were observed at Gemini South in 2007B (August 2007 to January 2008). The observed galaxies are listed in Table 2.5. The spectrograph slit was positioned along the MA of the galaxies in most cases. Exceptions occurred if there were no suitable bright guide stars in the area in front of the mask plane, which forced the slit to be rotated. This is due to the limited movement of the On-Instrument Wavefront Sensor (OIWFS) used for guiding.

Spectral dithering was carried out between two central wavelengths at 5080 Å and at 5120 Å for both the Lick stars and the galaxy data described here. This was done in order to obtain the full spectrum uninterrupted by the gaps between the three GMOS CCDs. The three CCDs mosaiced together delivered a spectral range from 3700 to 6500 Å, covering all 25 Lick indices from H$\delta$ to TiO (depending on the redshift of the individual galaxies). Exposure times were 2 ×

900 seconds at each position for each galaxy, except for ESO444-046, where only one 900 second exposure at each position was taken due to time constraints in the Gemini queue; and for NGC0533 and NGC0541, which were observed with double the exposure time due to additional available time in the queue. Imaging sequences of 5.5 × 5.5 arcmin images of the galaxies (3 × 20 seconds for each of $g$ and $r$ filters) were performed to allow insight into the possible presence and location of dust lanes or gas relative to the slit position.

The observations were mostly executed in dark time (which aided accurate sky subtraction), and assigned to Gemini-band[7] 3. The seeing typically ranged from 0.6 to 1.2 arcsec, and very rarely went up to 2.2 arcsec, although none of the results obtained in this study is particularly dependent on the seeing conditions. Calibration arc (CuAr) and flat-field spectra were also routinely observed, alongside the object spectra and at the two different central wavelengths, as part of the observing queue. General bias frames and imaging flat-field frames were also obtained throughout each semester. The spectrophotometric standard stars that were observed for relative flux calibration as part of the Gemini programmes are shown in Table 2.6. Only one spectrophotometric standard star is usually observed per Gemini programme; where more than one is observed it is charged to the allocated programme time. Similar programmes were undertaken in the 2006B observing semester, investigating stellar populations in spiral bulge galaxies, using exactly the same instrumental set-up, thus enabling two spectrophotometric standard stars to be used per hemisphere, for that semester. However, one spectrophotometric standard star per hemisphere per semester is deemed sufficient for flux calibration of the data. One spectrophotometric standard star was observed for the Lick star observations.

Table 2.7 details the stars that had been observed with the Gemini telescopes

---

[7]Gemini queue observations are ranked by priority, and large observing programmes that do not necessarily need the best photometric seeing conditions are normally assigned to band 3.

in previous programmes (PI: B. Miller) and used here for calibration to the Lick system. From the previous Gemini South programmes, stars of spectral type G and K were chosen as being most appropriate for calibrating early-type galaxies to the Lick system. In the previous Gemini North programmes, very few stars had been observed, none of them were G- or K-type stars, and only two were chosen as most applicable to this study.

For the Gemini data, information on the slit placements during observations was used to reconstruct the slit position on images of the galaxies. In each case, the slit location on the target was determined using the slit acquisition images and the target positions from the imaging sequences. The images were taken with the same telescope pointing, and used to measure the offsets of the slit position from the galaxy centre. In the few cases where the same galaxy was observed on two different nights, this was done separately for each night. Offsets from the galaxy centres are shown in Table 2.5. The majority of the galaxies were centred correctly or with very small offsets. For the minority of the galaxies which were not centred correctly, the data are still valuable for the derivation of the kinematics and stellar populations, as discussed in Section 3.3.

## 2.2.3 WHT data reduction

The WHT data reduction was performed with the IRAF[8] and STARLINK[9] reduction packages. Figure 2.3 shows the sequence in which the data reduction processes were executed.

Overscan correction, analogue-to-digital (ADU) conversion, bias subtraction and trimming of the image edges were done first. ADU conversion was done by

---

[8]IRAF is distributed by the National Optical Astronomy Observatories, which are operated by the Association of Universities for Research in Astronomy Inc., under cooperative agreement with the National Science Foundation.

[9]STARLINK is an interactive reduction and analysis facility that was developed in the UK, funded by the PPARC/STFC Research Council.

| Object | Slit PA | Major Axis MA | $r_e$ arcsec | $\epsilon$ | $a_e$ arcsec | Number of $a_e$ observed | Offset arcsec |
|---|---|---|---|---|---|---|---|
| | | | 2006B South | | | | |
| ESO303-005 | 55 | – | 9.1 | 0.25 | 9.1 | 0.50 | 0.70 |
| ESO349-010 | 14 | 155 | 15.3 | 0.52 | 12.3 | 1.18 | 0.30 |
| ESO488-027 | 88 | 68 | 10.3 | 0.15 | 10.1 | 0.94 | 2.20 |
| ESO552-020 | 148 | 148 | 18.3 | 0.43 | 18.3 | 0.76 | 0.64 |
| IC1633 | 97 | 97 | 23.9 | 0.17 | 23.9 | 0.75 | 0.00 |
| IC5358 | 40 | 114 | 17.4 | 0.60 | 8.3 | 1.44 | 0.26 |
| MCG-02-12-039 | 166 | 180 | 15.2 | 0.19 | 15.1 | 1.13 | 0.64 |
| NGC1399 | 222 | – | 42.2 | 0.06 | 42.2 | 0.44 | 0.45 |
| NGC7012 | 289 | 100 | 15.8 | 0.44 | 15.6 | 0.96 | 0.00 |
| PGC026269 | 313 | 133 | 7.3 | 0.00 | 7.3 | 0.89 | 0.00 |
| | | | 2006B North | | | | |
| NGC1713 | 330 | 39 | 15.5 | 0.14 | 14.0 | 1.07 | 0.00 |
| NGC2832 | 226 | 172 | 21.2 | 0.17 | 19.6 | 1.12 | 0.50 |
| NGC7597 | 46 | 133 | 9.4 | 0.00 | 9.4 | 0.64 | 0.00 |
| NGC7649 | 78 | 78 | 12.8 | 0.31 | 12.8 | 0.82 | 0.20 |
| UGC02232 | 60 | – | 9.7 | 0.00 | 9.7 | 0.82 | 0.00 |
| | | | 2007A South | | | | |
| ESO146-028 | 154 | 154 | 12.4 | 0.35 | 12.4 | 0.48 | 0.15 |
| ESO346-003 | 297 | 118 | 11.9 | 0.18 | 11.9 | 0.29 | 0.15 |
| ESO444-046 | 196 | 161 | 16.0 | 0.29 | 14.9 | 0.24 | 0.45 |
| GSC555700266 | 204 | – | 10.6 | 0.30 | 10.6 | 0.47 | 0.00 |
| IC1101 | 204 | 25 | 12.2 | 0.50 | 12.2 | 0.39 | 0.20 |
| IC4765 | 287 | 123 | 28.0 | 0.46 | 27.1 | 0.13 | 0.75 |
| LEDA094683 | 226 | 46 | 7.3 | 0.33 | 7.3 | 0.54 | 2.00 |
| NGC3311 | 63 | – | 26.6 | 0.17 | 26.6 | 0.53 | 0.40 |
| NGC4946 | 134 | 135 | 17.0 | 0.20 | 17.0 | 0.74 | 0.00 |
| PGC044257 | 267 | 44 | 15.3 | 0.63 | 10.5 | 0.38 | 0.00 |
| PGC072804 | 76 | 76 | 7.6 | 0.16 | 7.6 | 0.52 | 0.00 |
| UGC05515 | 293 | 83 | 12.0 | 0.13 | 11.8 | 0.38 | 0.00 |
| | | | 2007A North | | | | |
| NGC4839 | 63 | 64 | 17.2 | 0.52 | 17.2 | 0.61 | 0.00 |
| NGC6086 | 270 | 3 | 11.2 | 0.29 | 8.1 | 0.51 | 0.10 |
| NGC6160 | 140 | 72 | 13.9 | 0.47 | 9.0 | 0.41 | 0.00 |
| NGC6173 | 139 | 138 | 15.0 | 0.26 | 15.0 | 0.47 | 0.10 |
| NGC6269 | 306 | 80 | 14.1 | 0.20 | 13.1 | 0.50 | 0.35 |
| PGC071807 | 138 | 138 | 6.7 | 0.70 | 6.7 | 0.71 | 0.10 |
| | | | 2007B South | | | | |
| ESO202-043 | 137 | 133 | 12.9 | 0.40 | 12.9 | 0.39 | 0.20 |
| ESO541-013 | 114 | 16 | 10.6 | 0.31 | 7.7 | 0.63 | 1.50 |
| NGC0533 | 350 | 50 | 23.7 | 0.39 | 18.0 | 0.44 | 0.00 |
| NGC0541 | 64 | 69 | 15.1 | 0.06 | 15.1 | 0.40 | 0.00 |
| PGC004072 | 204 | 83 | 10.2 | 0.33 | 8.2 | 0.50 | 0.00 |
| PGC025714 | 302 | 122 | 10.0 | 0.30 | 10.0 | 0.25 | 0.00 |
| PGC030223 | 145 | 1 | 8.4 | 0.00 | 8.4 | 0.60 | 0.00 |
| UGC00579 | 221 | 41 | 13.0 | 0.14 | 13.0 | 0.31 | 0.10 |

Table 2.5: Galaxies observed with the Gemini North and South telescopes. Table 2.1 contains more properties of the galaxies. MA indicates the major axis, and the PA is given as deg E of N. The half-light radii, $r_e$, were calculated from the 2MASS catalogue, except ESO303-005 and PGC004072 for which it was calculated with the VAUCOUL task in the REDUCE package. The second last column lists the fraction of the effective half-light radii, $a_e$, spanned by the radial profiles measured in this work (see Section 3.2 for the calculations), and the last column lists the offsets as described in the text.

| Star | $\alpha$(J2000) | $\delta$(J2000) | $m_V$ | Spectral type |
|------|-----------------|-----------------|-------|---------------|
| | | Lick Stars | | |
| LTT9239 | 22 52 40.9 | −20 35 26.3 | 12.07 | F |
| | Gemini North 2006B Semester | | | |
| BD +28 4211 | 21 51 11.1 | +28 51 53 | 10.56 | sdOp |
| G191B2B | 05 05 30.6 | +52 49 56 | 11.85 | DAw |
| | Gemini South 2006B Semester | | | |
| LTT1788 | 03 48 22.2 | −39 08 33.6 | 13.16 | F |
| LTT7987 | 20 10 57.4 | −30 13 01.2 | 12.23 | DA |
| | Gemini North 2007A Semester | | | |
| EG131 | 19 20 34.93 | −07 40 00.05 | 12.28 | DAw |
| | Gemini South 2007A Semester | | | |
| LTT7379 | 18 36 25.95 | −44 18 36.94 | 10.22 | G0 |
| | Gemini South 2007B Semester | | | |
| EG131 | 19 20 34.93 | −07 40 00.05 | 12.28 | DAw |

Table 2.6: Spectrophotometric standard stars used in Gemini observations.

multiplying by the factor relating the digital units in the spectrum back to the number of photo-electrons that were stored in the pixels of the CCD instrument. Flat-field spectra were normalised by dividing by the lamp response function, and all star and galaxy spectra were then appropriately flat-fielded. The dichroics introduced an intermediate spectral-frequency pattern which varied with the position of the telescope. This was successfully removed by flat-fielding, using the flat-field images taken directly before and/or after the science frames (i.e. at the same telescope pointing). The flat-fielding correctly calibrated the relative pixel responses locally, but a residual large scale illumination pattern was present in the frames. It was necessary to perform an illumination correction using normalised twilight flat-field spectra to correct for spatial gradients in the star and galaxy frames. Wavelength calibration was performed in two dimensions, including correcting for C-distortion (the geometrical distortions along the spatial direction). Star and galaxy spectra were then transformed to spectra with equal linear spectral bin spacings. A cosmic ray cleaning algorithm was applied to all

| Name | $\alpha$(J2000) | $\delta$(J2000) | $m_V$ | Spec. type | $T_{\mathrm{eff}}$ | log $g$ | [Fe/H] |
|---|---|---|---|---|---|---|---|
| | | Gemini South | | | | | |
| HD004307 | 00 45 28.69 | −12 52 50.92 | 6.15 | G0V | 5650 | 3.93 | −0.52 |
| HD004628 | 00 48 22.98 | +05 16 50.21 | 5.75 | K2V | 4960 | 4.64 | — |
| HD004656 | 00 48 40.94 | +07 35 06.29 | 4.44 | K4III | 3953 | 1.10 | −0.07 |
| HD010380 | 01 41 25.89 | +05 29 15.41 | 4.45 | K3IIIb | 4133 | 1.20 | −0.11 |
| HD013043 | 02 07 34.27 | −00 37 02.71 | 6.87 | G2V | 5730 | 4.01 | 0.07 |
| HD020630 | 03 19 21.70 | +03 22 12.71 | 4.83 | G5Vv | 5528 | 4.40 | 0.23 |
| HD036003 | 05 28 26.10 | −03 29 58.40 | 7.64 | K5V | 4465 | 4.61 | — |
| HD037160 | 05 36 54.39 | +09 17 26.42 | 4.09 | K0IIIb | 4751 | 2.90 | −0.55 |
| HD054810 | 07 10 13.68 | −04 14 13.58 | 4.92 | K0III | 4697 | 2.35 | −0.30 |
| HD064606 | 07 54 34.18 | −01 24 44.13 | 7.44 | G8V | 5120 | 4.11 | −0.92 |
| HD069267 | 08 16 30.92 | +09 11 07.96 | 3.54 | K4III | 4032 | 1.60 | −0.36 |
| HD114946 | 13 14 10.90 | −19 55 51.41 | 5.33 | G6V | 4930 | 3.61 | −0.44 |
| HD145148 | 16 09 11.21 | +06 22 43.30 | 5.94 | K0IV | 4849 | 3.45 | 0.13 |
| HD165760 | 18 07 18.36 | +08 44 01.92 | 4.65 | G8III | 4957 | 2.00 | −0.05 |
| HD175751 | 18 57 03.67 | −05 50 46.73 | 4.83 | K2III | 4697 | 2.20 | 0.03 |
| HD184406 | 19 34 05.35 | +07 22 44.19 | 4.45 | K3III | 4428 | 2.45 | 0.22 |
| HD184492 | 19 35 07.26 | −10 33 37.60 | 5.14 | G8III | 4536 | 1.50 | −0.20 |
| HD195633 | 20 32 23.99 | +06 31 03.27 | 8.54 | G0V | 5830 | 3.78 | −1.12 |
| | | Gemini North | | | | | |
| HD 140283 | 15 43 03.10 | −10 56 00.59 | 7.24 | F3VI | 5650 | 4.24 | −2.45 |
| HD 168720 | 18 20 17.91 | +21 57 40.67 | 4.95 | M1III | 3810 | 1.10 | — |

Table 2.7: Lick calibration stars used to calibrate the Gemini observations. Columns 2 – 4 are from the Simbad Astronomical Database and columns 5 – 8 are from the Lick Database available in electronic form from the webpage of G. Worthey (http://astro.wsu.edu/worthey/).

the two-dimensional spectra[10].

All star and galaxy spectra were sky-subtracted and corrected for S-distortion (the geometrical distortions along the spectral direction). The S-distortion correction was performed by finding the maximum luminosity peak (in the spatial direction) at the centre of the galaxy and then tracing it as a function of wavelength. These traces were fitted using low-order polynomials which were then used to transform the spectra. For sky subtraction, a sky region consisting of 40 rows was chosen on each side of the galaxy, in each individual galaxy frame, and averaged to obtain an extracted sky spectrum for each frame. This was expanded into a two-dimensional spectrum and subtracted from the data frame.

The effective airmass at all exposures was calculated using the parameters appropriate for the La Palma site. All two-dimensional galaxy spectra and extracted Lick star spectra were flux-calibrated and corrected for atmospheric extinction. The galaxy frames were then co-added (also removing any remaining cosmic ray effects in the process) to form a single frame for each galaxy in each of the blue and red arms and for each of the two dichroics.

## Errors

There are many common causes of systematic errors in line-strength indices. These include: flux calibration effects; spectral resolution and velocity dispersion corrections; sky subtraction uncertainties; scattered light effects; wavelength calibration and radial velocity errors; seeing and focus corrections; deviation from linear response of the detectors; and contamination by nebular emission lines (Cardiel et al. 1998b).

Therefore, a careful error analysis was undertaken, considering both Poisson (photon) noise and systematic errors in the data. Variance frames were created from the data frames after bias subtraction and ADU conversion, and reduced in a

---

[10]Here, a two-dimensional spectrum means a spatially-resolved spectrum.
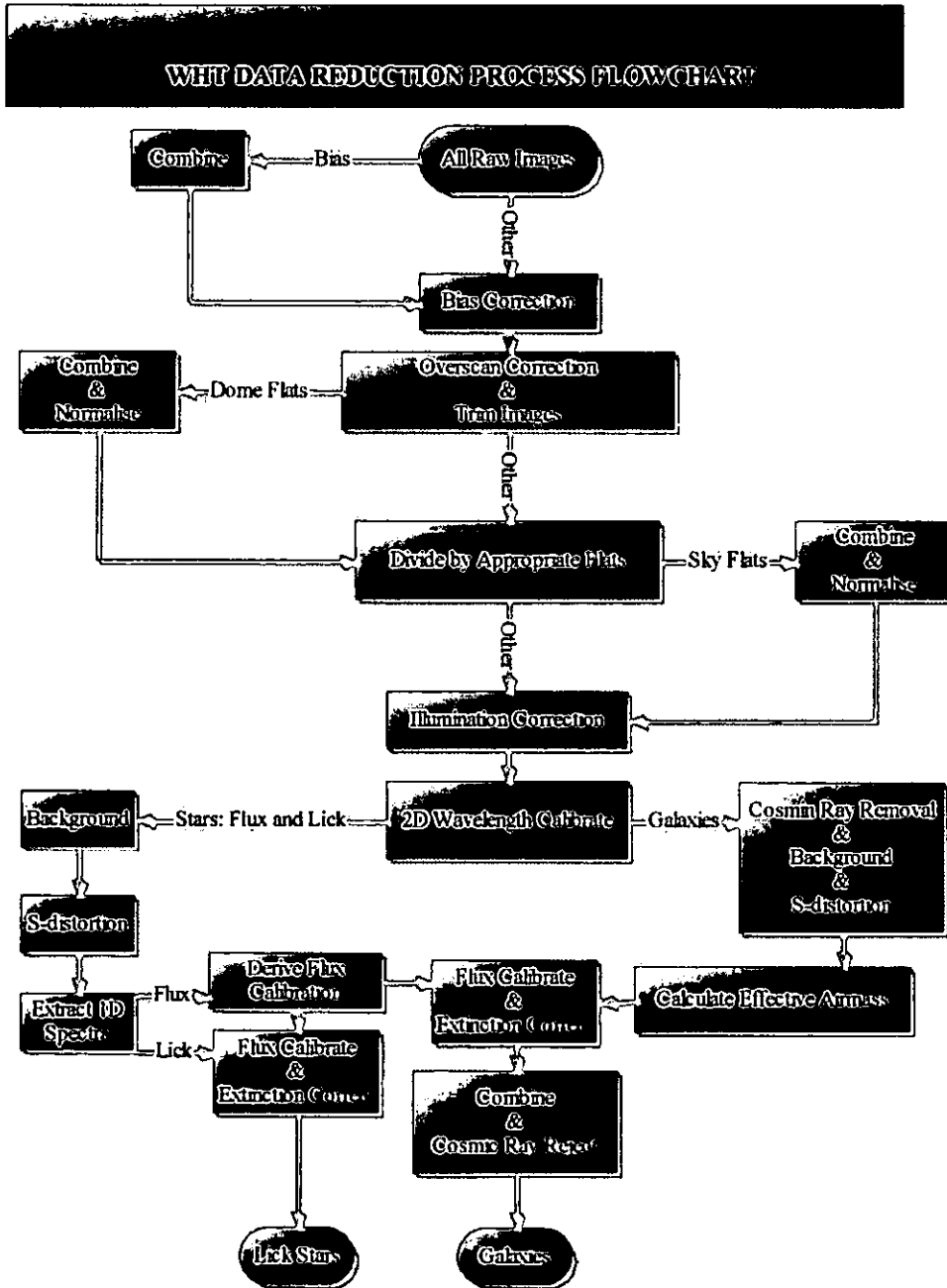
Figure 2.3: Stages in the WHT data reduction process. The dome flat-field and sky flat-field images were normalised in the spatial and spectral dimensions. All the reduction procedures were carried out in IRAF except for three reduction procedures (cosmic ray removal, background subtraction and S-distortion) which were done in STARLINK. Rectangular boxes indicate the reduction steps and the ellipses at the end indicate the fully reduced galaxy (two-dimensional) and Lick star (one-dimensional) data.

way similar to the data frames, but the arithmetic manipulations were performed by incorporating the usual error propagation laws. Thus, the variance frames represent the square of the Poisson noise at the start of this reduction process, and are then propagated along all the reduction steps.

The Poisson noise per average pixel was measured at certain wavelength intervals (in the blue and red spectra of both dichroics) in example data frames. Then, throughout this reduction process, the contributions of the systematic errors were estimated and compared with the Poisson noise to see whether it considerably increases the errors. Flat-fielding produced negligible systematic errors with the exception of the WHT flat-field spectra taken in the upper wavelength region (red spectra of dichroic 6100 Å on night four) which contained fringe patterns caused by the dichroic. This contributed about four per cent to the overall errors, and was found to be constant in the spatial as well as spectral directions of the frames, and was appropriately propagated in the variance frame. Errors contributed by the illumination correction proved negligible. Wavelength calibration was accurate to within 0.1 Å in all cases and the variance frames were wavelength-calibrated in exactly the same two-dimensional manner as the galaxy data frames. This also ensured that the variance frames had the same start wavelength, end wavelength and wavelength increment as the data frames. After that, the variance frames were also S-distortion corrected, following the procedure used for the corresponding data frames.

The sky subtraction process added to the systematic errors in the data and was properly taken into account by averaging its contribution over the number of spatial cross sections used for the sky determination. Because the observations were obtained in dark time, the variability in the sky was minimal. Relative flux calibration was accurate to within five per cent (determined by using the different standard stars), and the variance frames were also co-added so that

they could be treated alongside the galaxy data in further analysis. At the end of this reduction process, each two-dimensional galaxy data frame had an associated two-dimensional variance array.

## 2.2.4 Gemini data reduction

The basic Gemini data reduction was carried out within the Gemini-specific GMOS data reduction package[11] that can be added to the standard IRAF reduction package. Spectra with different central wavelengths (5080 and 5120 Å) and spectra taken with GMOS-North and GMOS-South were treated in similar parallel streams of data reduction. Figure 2.5 shows the sequence in which the Gemini data reduction processes were executed. The raw Lick star data were obtained from the Gemini Science Archive[12].

The basic data reduction was conducted in a similar manner to the WHT data reduction (with the exception of the illumination correction which was not necessary for the Gemini data) but with parameters appropriate for the Gemini observations. For each of the two central wavelength settings, a "bad pixel spectrum" was made in order to avoid interpolation between the CCD gaps. This is a one-dimensional Boolean spectrum which was created with values of one everywhere except in the CCD gaps. These spectra were expanded into two-dimensional spectra with the dimensions of the galaxy data. When the spectra of the two different wavelength settings were combined, these bad pixel masks were used to ensure that only true data were averaged.

As a test to see if the regions chosen for background subtraction are flat, bright sky lines were used to extract cross sections (perpendicular to the wavelength dispersion direction) that could be compared with the shape and gradients

---

[11]http://www.gemini.edu/sciops/data-and-results/processing-software.

[12]http://www4.cadc-ccda.hia-iha.nrc-cnrc.gc.ca/gsa/.
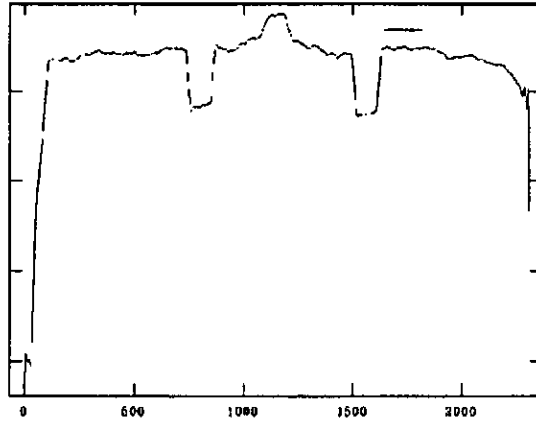
Figure 2.4: Flat-field spectrum extracted using sky lines. The black line indicates the region used for sky subtraction.

of the dome flats that were used. Figure 2.4 shows an example of a flat-field spectrum extracted from a bright sky line. The black line shows the area used for background subtraction. The peak in the centre is the galaxy spectrum and the CCD gaps can be seen on either side. This figure shows that the galaxy data, and the data used for background subtraction, are not in the region of the flat-field frame that is tapering off at the ends. Hence, there were no gradients present in the regions chosen for background subtraction.

## Errors

The error determination for the Gemini data reduction procedures was done in a similar manner to the WHT error determination, by appropriately reducing variance frames. Variance frames were created from the data frames after bias subtraction, assuming Poisson noise, and then propagated through all the reduction steps.

The systematic errors arising from sky subtraction were estimated as follows. An extracted spectrum representing the error contribution of the sky subtraction was made for each case, taking into account the number of spatial cross sections averaged when sky was subtracted and the Poisson error on the average
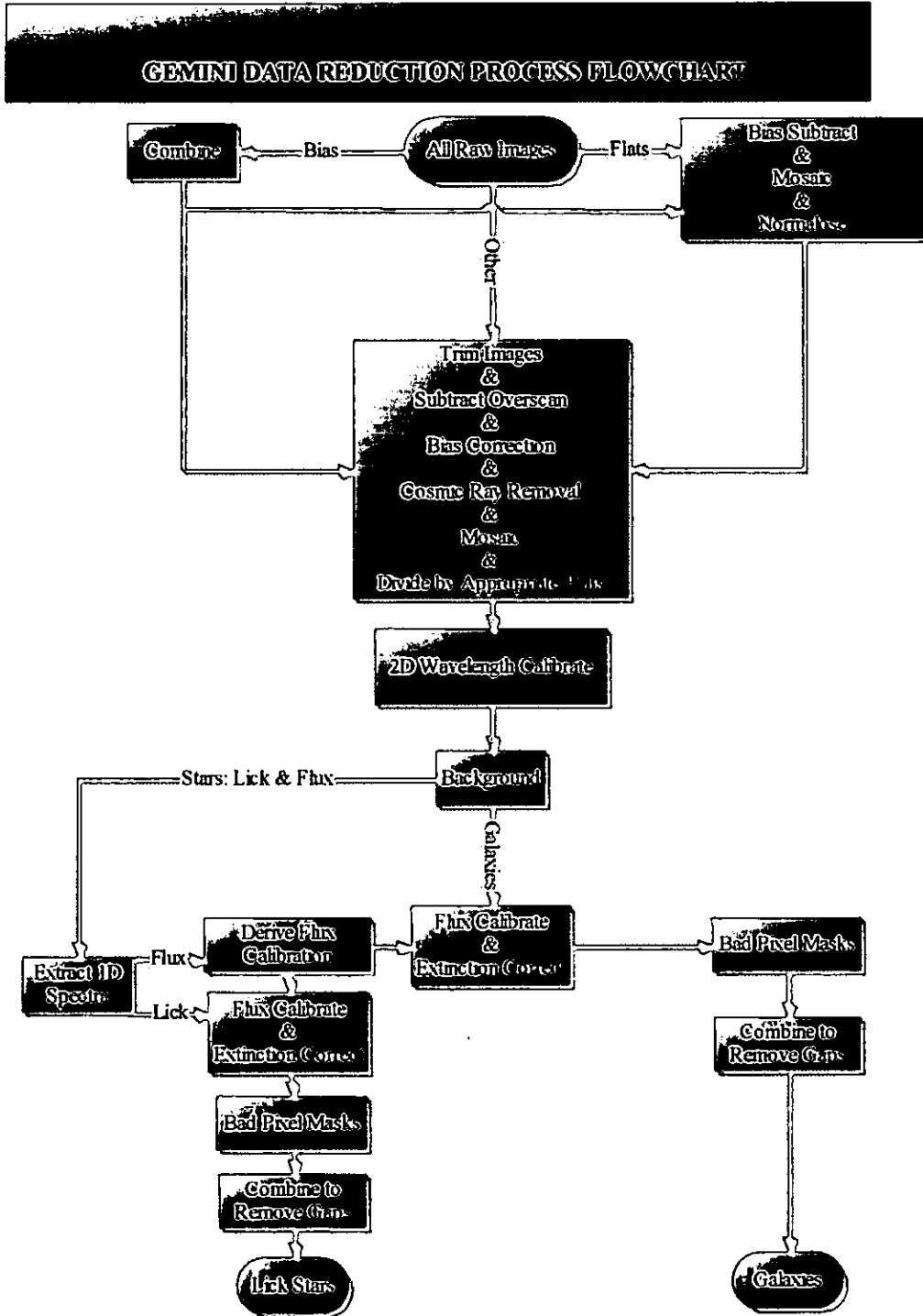
Figure 2.5: Stages in the Gemini data reduction process. All the reduction procedures were carried out in the GEMINI GMOS package in IRAF.
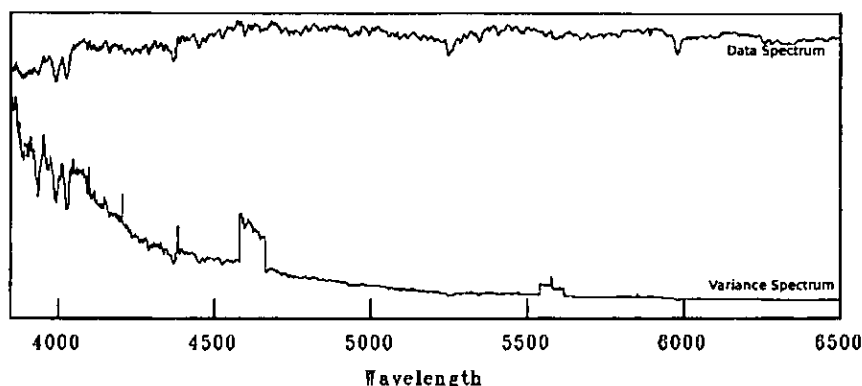
Figure 2.6: NGC1713 spectrum and its associated variance spectrum (flux in arbitrary units versus wavelength in Å). The vertical scale is relative as follows: the square root of the variance (the error) is equal to about 15 per cent of the data at 4500 Å in this galaxy. The effect of the CCD gaps can be seen at 4600 and 5550 Å. The lower S/N at the blue end of the spectrum is amplified in the variance spectrum.

one-dimensional sky spectrum. This extracted spectrum was then grown into a two-dimensional spectrum and added onto the variance frames in all cases, representing the systematic noise added in the sky subtraction process.

The variance frames were appropriately flux-calibrated, wavelength-calibrated, and binned to the same start wavelength and wavelength increment. The variance frames were then co-added for each galaxy by dealing with the CCD gaps in the same manner as in the data reduction of the object frames described above, to avoid interpolation of the data. The fact that only half as many frames as usual were added in the regions where the gaps occur, was taken into account in the variance frames. Figure 2.6 shows the spectra from the data and variance frames of NGC1713, as an example.

# Chapter 3

# KINEMATICS

The kinematic properties can give insight into the formation and evolutionary histories of BCGs. For example, the remnants left by mergers with or without dissipation are expected to differ in their kinematical structure (as discussed in Section 3.4). In addition, kinematic measurements ensure correct conversion to the Lick/IDS system (as discussed in Section 4.1), will be used in the SSP-fitting routines, and will be investigated for possible correlations with line strengths and derived properties (see Chapters 4 and 5).

## 3.1   Measurements

### 3.1.1   Lick star spectra

The IRAF FXCOR routine was used to measure the radial velocities of the Lick stars from the WHT and Gemini data separately. The wavelength axis of the spectra was rebinned to a logarithmic scale, which causes them to be equivalent to intervals of constant radial velocity. The FXCOR routine uses Fourier cross-correlation to do the radial velocity measurements by cross-correlating stellar spectra against a template, and fitting a Gaussian to the peak in the cross-correlation function

to give the radial velocity shift. In each case, one of the stars (HD129312 for the WHT data and HD020630 for the Gemini data) was chosen as template. For the template star, the radial velocity was calculated by identifying and measuring the positions (by fitting Gaussians to ensure accurate measurements) of five or more of the absorption lines. The radial velocities of the other stars were then measured relative to the template. Heliocentric corrections were applied using IRAF RVCORRECT to give radial velocity measurements independent of the time and location of the observations. The results are shown in Table 3.1 and Figure 3.1. The quoted uncertainties are attributed to the errors in wavelength calibration, uncertainties in the laboratory wavelengths of the absorption lines and blending of some of the absorption lines. In the case of the WHT data, errors were decreased by averaging up to four separate measurements from the 5300 Å and 6100 Å dichroic, and the red and blue spectra. Overall, the measurements compared well with the published values in the Simbad astronomical database (as shown in Figure 3.1). The Lick spectra were shifted to zero radial velocity before using them as templates for the galaxies.

## 3.1.2 BCG spectra

Radial velocities and velocity dispersions of the galaxies were measured using the MOVEL and OPTEMA algorithms, as described by González (1993) and integrated into the RED$_{uc}^{uc}$E data reduction package[1].

The MOVEL routine embodies an improvement on the widely-used Fourier Quotient Technique originally described by Sargent et al. (1977). In summary, this routine models the galaxy spectra as the convolution of a Gaussian broadening function with an appropriate template stellar spectrum. The ratio of the

---

[1]RED$_{uc}^{uc}$E is an astronomical data reduction package, specially devoted to the analysis of long-slit spectroscopy data. It was developed by N. Cardiel and J. Gorgas (Cardiel 1999). http://www.ucm.es/info/Astrof/software/reduceme/reduceme.html.

| Star | Published Simbad (km s$^{-1}$) | This analysis IRAF (km s$^{-1}$) |
|---|---|---|
| WHT | | |
| HD002665 | −379±2 | −392±9 |
| HD003546 | −84±1 | −91±6 |
| HD003651 | −34±2 | −39±7 |
| HD004656 | 32±1 | 29±3 |
| HD125560 | −8±1 | −8±3 |
| HD129312 | −22±1 | −24±2 |
| HD132142 | −15±2 | −25±11 |
| HD132345 | −12±2 | −21±4 |
| HD135722 | −12±1 | −30±10 |
| HD145328 | −19±2 | −21±2 |
| HD149161 | 3±1 | 1±5 |
| HD175743 | 44±5 | 13±2 |
| HD184406 | −24±1 | −55±3 |
| HD184492 | −31±1 | −46±2 |
| HD188056 | −20±2 | −36±6 |
| HD188512 | −40±1 | −53±11 |
| HD199580 | −19±1 | −34±5 |
| HD203344 | −89±2 | −96±5 |
| HD217476 | −58±1 | −60±12 |
| HD219134 | −18±2 | −32±5 |
| HD219449 | −26±1 | −28±3 |
| HD221148 | −25±2 | −49±3 |
| Gemini | | |
| HD004307 | −13±2 | −10±10 |
| HD004628 | −13±2 | −10±11 |
| HD004656 | 32±1 | 32±29 |
| HD010380 | 0±1 | 2±19 |
| HD013043 | −40±2 | −84±3 |
| HD020630 | 20±1 | 15±4 |
| HD036003 | −54±5 | −59±33 |
| HD037160 | 99±1 | 103±9 |
| HD054810 | 79±1 | 82±15 |
| HD064606 | 93±1 | 102±9 |
| HD069267 | 22±1 | −8±25 |
| HD114946 | −45±5 | −45±7 |
| HD140283 | −171±1 | −162±32 |
| HD145148 | −4±2 | −3±13 |
| HD165760 | −3±1 | −1±7 |
| HD168720 | −33±2 | −60±35 |
| HD175751 | −93±1 | −101±11 |
| HD184406 | −24±1 | −16±21 |
| HD184492 | −31±1 | −27±13 |
| HD195633 | −46±1 | −38±12 |

Table 3.1: Radial velocity measurements of the Lick calibration stars (including heliocentric corrections) compared with the published values in Simbad.
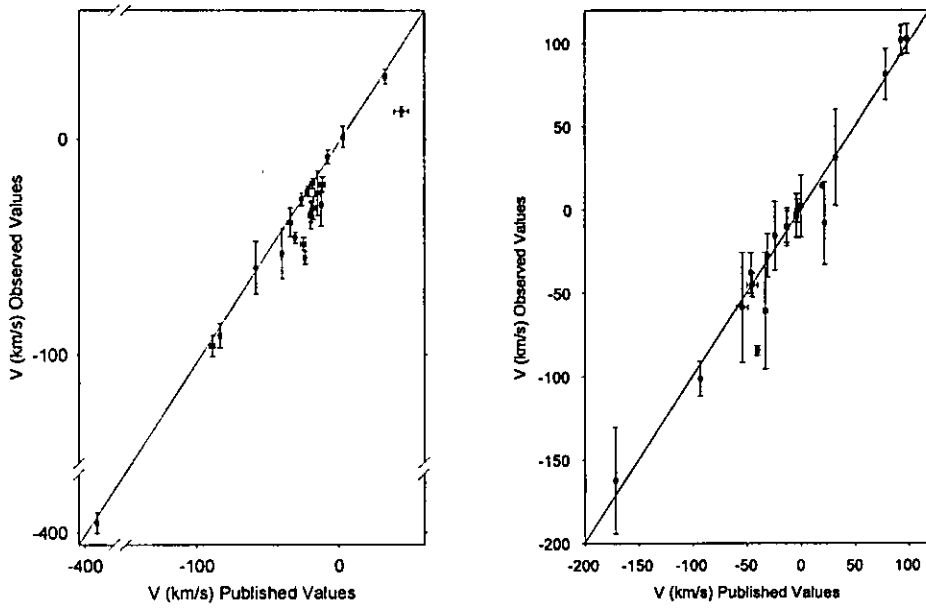
(a) WHT Lick stars: radial velocity measurements. The −350 to −150 km s$^{-1}$ region is omitted in the graph as none of the stars have velocities in that range.

(b) Gemini Lick stars: radial velocity measurements.

Figure 3.1: Radial velocity measurements of the Lick stars. The published values are from Simbad, and the straight lines are the lines $x = y$.

Fourier transforms of the galaxy and stellar template (the Fourier quotient) is the transform of the broadening function, which then yields the galaxy's velocity dispersion and radial velocity, hence effectively removing the effects of the instrumental response (González 1993).

Since there are many absorption features in the wide wavelength range used here, the fitted broadening function is very sensitive to spectral mismatches between template and object spectra (Rix & White 1992; Van der Marel & Franx 1993). The OPTEMA algorithm is able to overcome this template mismatch problem by constructing an optimal template as a linear combination of stellar spectra of different spectral types and luminosity classes that best matches each galaxy (González 1993; Sánchez-Blázquez et al. 2006a – hereafter SB06). It is an iterative procedure in which a galaxy model is processed in parallel with the galaxy spectrum. In this way, the model spectrum is also processed, which allows one to take any imperfections of the data handling procedures in Fourier space into account. The galaxy and template spectra are binned onto a logarithmic wavelength scale (for equal velocity bins). A new optimal template was constructed for each spatial bin in the galaxy spectra. The best template is determined with a non-linear least-squares algorithm, and scaled, shifted and broadened to match the galaxy kinematic parameters and is then fed to the MOVEL algorithm. The output kinematic parameters are then used to create and improve composite templates and the process continues until it converges.

Sky line residuals and emission lines were masked when the wavelength range for the fit was chosen. The template, galaxy and model spectra were divided by a low-order polynomial to subtract the mean, and then multiplied by a tapering cosine-bell. In addition, the model fits are weighted using an optimal Wiener filter, as high frequencies are dominated by noise which is dependent on the velocity dispersion and S/N of the galaxy spectrum (the tapering cosine-bell and

Wiener filter are fully described in González 1993).

For the Gemini data, 20 of the Lick stars were used to make the optimal template (excluding the stars not of G or K spectral type), and all 22 Lick stars for the WHT data. Figure 3.2 shows a typical fit (magnified over a small range) between the observed central spectrum of a galaxy and the optimal template for that galaxy corrected by the derived kinematic parameters.

The errors were computed through 50 Monte–Carlo numerical simulations and using the appropriate error spectra. In each simulation, Gaussian noise was added to the galaxy spectra in accordance with the error spectra and the radial velocity and velocity dispersion derived. Errors in the radial velocities and velocity dispersions were calculated as the unbiased standard deviation of the different solutions. The errors computed in this manner are expected to incorporate all the uncertainties, from the basic reduction process (which is accounted for in the error spectra) to the final measurement of the parameters.

## 3.2 Central radial velocity and velocity dispersion values

As mentioned in Sections 2.2.1 and 2.2.2, some of the galaxies were observed at a slit position angle (PA) other than the MA. Thus, the effective half-light radii ($a_e$) were calculated from the half-light radii ($r_e$). Tables 2.2 and 2.5 list the $r_e$ along the semimajor axis of the galaxies, computed from the 2MASS $K$-band 20th magnitude arcsec$^{-2}$ isophotal radius, following Brough et al. (2007), and using the formula by Jarrett et al. (2003): $\log r_e \sim \log r_{K20} - 0.4$. Using the ellipticities ($\epsilon$) of the galaxies (data from NED), the $a_e$ values were computed according to

$$a_e = \frac{r_e(1 - \epsilon)}{1 - \epsilon \mid cos(\mid \text{PA} - \text{MA} \mid) \mid}. \tag{3.1}$$
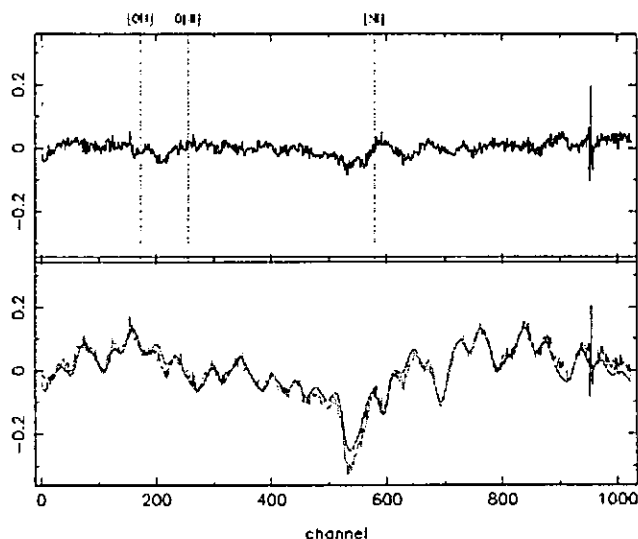
Figure 3.2: Example of the calculation of the derived kinematics for NGC7768 using the MOVEL algorithm. In the lower panel, the smooth line corresponds to the optimal template spectrum, plotted together with the galaxy spectrum which has been shifted and broadened to the derived parameters. The upper panel shows the residuals of fit (in relative flux units), with the dotted lines indicating the positions of typical emission lines. This illustration spans 4900 to 5400 Å.

The derivation of accurate half-light radii is known to be problematic for BCGs (Graham et al. 1996). The present investigation, however, is not affected by this issue as the half-light radii are only used to define the central apertures (see below), and small aperture differences are negligible. The number of $a_e$ which the radial profiles measured in this work spans is also listed in Tables 2.2 and 2.5. For those galaxies for which MA information was not available in HyperLeda, the PA is assumed to be the same as the MA (as intended during the observation preparations).

The central radial velocity and velocity dispersion values of the galaxies were derived for central bins $a_e/8$ arcsec in size, and with the galaxy centres defined as the luminosity peaks. Thus, the central values are for an aperture of $1 \times a_e/8$ arcsec$^2$ for the WHT data and $0.5 \times a_e/8$ arcsec$^2$ for the Gemini data, limited by the slitwidth in one dimension. The results of the central kinematical

measurements are shown in Table 3.2.

When comparing measured central velocity dispersion values with those from the literature, emphasis must be placed on the fact that published values are measurements from within different apertures. Because the velocity dispersion profile changes with radius (as seen in Figure 3.12 for example), this can produce differences in the values measured in different apertures. Accurate comparison is further limited because of different effective spatial resolution, data of different quality and different analysis techniques.

Figure 3.3 shows the comparison (i.e. not taking into account the above differences) between the velocity dispersion values from HyperLeda (if available) and those derived in this study. For most of the galaxies, more than one velocity dispersion value is listed in HyperLeda and in those cases the most recent was used for this comparison. In the case of NGC1399, for example, published values range between 233 km s$^{-1}$ and 420 km s$^{-1}$, which illustrates the effects of different apertures and measurements. This can be seen in the steep change in the measured velocity dispersion profile of NGC1399 in Figure 3.12. No systematic differences between the measurements in this study and previous measurements were found. The absolute mean difference between the velocity dispersion values measured here and the literature is $|\sigma(\text{here}) - \sigma(\text{lit, uncorrected})| = 33 \pm 29$ km s$^{-1}$, which is mainly because of the large errors on the literature measurements. This is acceptable for the purposes of this project.

Relativistic effects were taken into account in the derivation of the radial velocities of the galaxies:

$$z = (1 + \frac{V}{c})\gamma - 1 \qquad (3.2)$$

where $\gamma = \frac{c}{\sqrt{c^2 - V^2}}$, $z$ is the redshift, $V$ is the radial velocity and $c$ the speed of light. The relativistic effect is very significant ($\sim 800$ km s$^{-1}$) for the highest redshift galaxies in the sample ($z \sim 0.07$). In the comparison of the derived radial
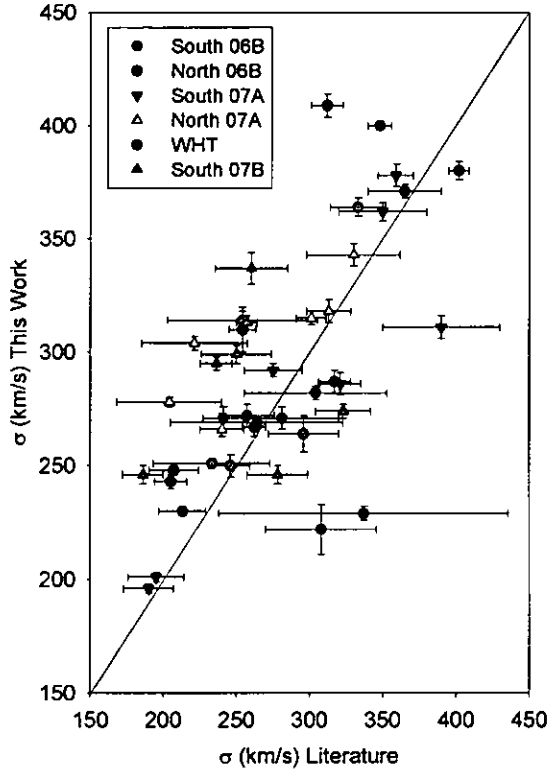
Figure 3.3: Velocity dispersion results compared with literature values. The latter values are the most recent ones from HyperLeda as described in the text.

velocities with the values listed in HyperLeda, the case $V \ll z$ (thus $z = \frac{V}{c}$) was used. This comparison is shown in Figure 3.4.

## 3.3    Spatially resolved kinematics

The galaxy spectra were binned in the spatial direction to ensure a minimum S/N of 20 per Å in the H$\beta$ region of the spectrum for kinematical measurements as a function of radius. A S/N ratio of 20 per bin was chosen to resolve the optimal number of possible points, whilst still having acceptable errors on the kinematical measurements (on average $< 20$ km s$^{-1}$). Thus, the spatial cross-sections are broader with increasing radius from the centre of the galaxy. The

CHAPTER 3

| Galaxy | $\sigma$ km s$^{-1}$ Observed | $V$ km s$^{-1}$ Observed | $V_{max}$ km s$^{-1}$ | $\log(V_{max}/\sigma_0)^*$ |
|---|---|---|---|---|
| ESO146-028 | 299±3 | 12061±3 | 14±18 | −1.2±0.9 |
| ESO202-043 | 256±3 | 10942±4 | 46±10 | −0.7±0.2 |
| ESO303-005 | 276±5 | 14526±4 | 23±17 | −0.8±0.4 |
| ESO346-003 | 226±4 | 8459±9 | 51±13 | −0.3±0.1 |
| ESO349-010 | 282±3 | 14420±3 | 46±19 | −0.8±0.4 |
| ESO444-046 | 292±3 | 13741±3 | 26±16 | −0.9±0.4 |
| ESO488-027 | 248±2 | 11754±4 | 53±12 | −0.3±0.1 |
| ESO541-013 | 295±3 | 16440±8 | 138±24 | −0.2±0.2 |
| ESO552-020 | 229±3 | 9128±5 | 20±19 | −1.0±0.8 |
| GSC555700266 | 312±9 | 20059±6 | 49±14 | −0.6±0.2 |
| IC1101 | 378±5 | 22585±9 | 41±31 | −1.0±0.8 |
| IC1633 | 400±2 | 7061±2 | 20±17 | −1.0±0.4 |
| IC4765 | 286±5 | 4403±6 | 50±28 | −0.8±0.6 |
| IC5358 | 243±3 | 8539±9 | 55±13 | −0.7±0.3 |
| LEDA094683 | 332±5 | 22748±5 | 32±26 | −0.9±0.6 |
| MCG-02-12-039 | 271±5 | 9648±3 | 59±28 | −0.3±0.3 |
| NGC0533 | 299±4 | 5488±2 | 36±8 | −0.8±0.2 |
| NGC0541 | 246±4 | 5339±2 | 10±6 | −0.8±0.6 |
| NGC1399 | 371±3 | 1406±2 | 24±11 | −0.6±0.1 |
| NGC1713 | 251±2 | 4472±2 | 30±11 | −0.5±0.1 |
| NGC2832 | 364±4 | 6841±4 | 64±22 | −0.4±0.2 |
| NGC3311 | 196±2 | 3709±2 | 25±9 | −0.6±0.2 |
| NGC3842 | 287±5 | 6211±2 | 11±13 | −1.2±0.8 |
| NGC4839 | 278±2 | 7380±2 | 44±14 | −0.8±0.3 |
| NGC4874 | 267±4 | 6953±2 | 15±12 | −0.4±0.1 |
| NGC4889 | 380±4 | 6266±5 | 40±19 | −0.8±0.3 |
| NGC4946 | 201±2 | 3148±9 | 62±9 | −0.2±0.1 |
| NGC6034 | 325±4 | 10113±28 | 134±15 | −0.2±0.1 |
| NGC6047 | 230±2 | 9031±8 | 59±16 | −0.4±0.2 |
| NGC6086 | 318±5 | 9483±2 | 13±18 | −1.2±0.9 |
| NGC6160 | 266±3 | 9428±3 | 12±18 | −1.3±1.4 |
| NGC6166 | 310±10 | 9100±2 | 31±20 | −0.7±0.4 |
| NGC6173 | 304±3 | 8766±2 | 24±16 | −0.9±0.4 |
| NGC6269 | 343±5 | 10363±3 | 26±35 | −0.8±0.7 |
| NGC7012 | 240±3 | 8653±3 | 24±16 | −0.9±0.6 |
| NGC7597 | 264±8 | 10907±5 | 63±20 | 0.2±0.1 |
| NGC7647 | 271±5 | 11842±7 | 36±14 | −0.9±0.4 |
| NGC7649 | 250±5 | 12258±5 | 41±14 | −0.6±0.2 |
| NGC7720 | 409±5 | 9034±5 | 50±18 | −0.6±0.2 |
| NGC7768 | 272±5 | 7875±24 | 114±11 | −0.1±0.1 |
| PGC004072 | 313±3 | 15458±6 | 93±24 | −0.2±0.3 |
| PGC025714 | 274±3 | 15986±2 | 29±11 | −0.8±0.4 |
| PGC026269 | 222±11 | 15816±8 | 51±20 | 0.2±0.1 |
| PGC030223 | 337±7 | 15806±5 | 90±22 | −0.6±0.3 |
| PGC044257 | 247±9 | 14014±6 | 20±16 | −1.2±1.0 |
| PGC071807 | 315±3 | 17911±5 | 16±13 | −1.5±1.2 |
| PGC072804 | 311±5 | 22433±4 | 50±24 | −0.4±0.2 |
| UGC00579 | 246±4 | 13025±6 | 36±14 | −0.5±0.4 |
| UGC02232 | 314±4 | 14208±3 | 42±18 | 0.0±0.1 |
| UGC05515 | 362±4 | 13103±7 | 56±18 | −0.4±0.1 |
| UGC10143 | 262±2 | 10344±5 | 19±11 | −1.1±0.5 |

Table 3.2: Central velocity dispersions ($\sigma$) and radial velocities ($V$) of all the galaxies. The rotational velocity $V_{max}$ was measured as half the difference between the minimum and maximum peaks of the rotation curve. The determination of $(V_{max}/\sigma_0)^*$ is described in Section 3.3.
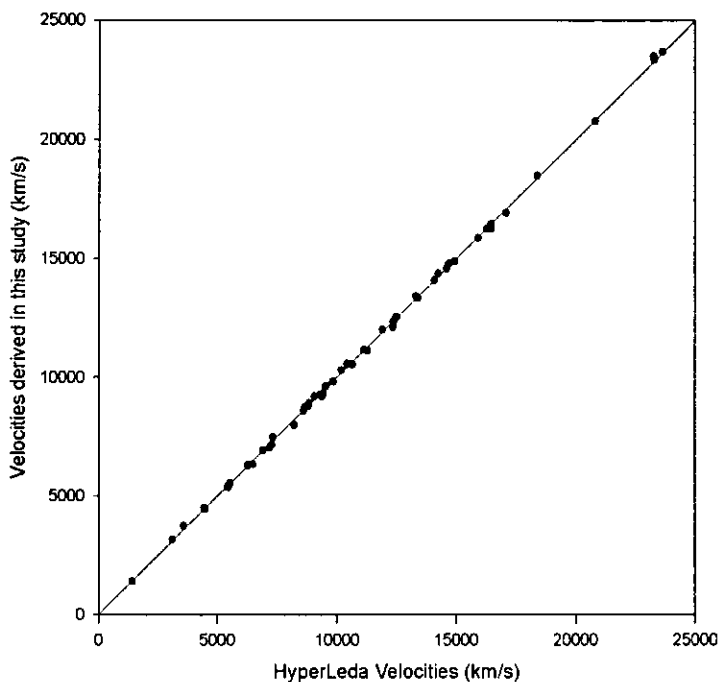
Figure 3.4: Radial velocity results compared with HyperLeda values.

radial kinematics (radial velocities and velocity dispersions) were measured with the same MOVEL and OPTEMA algorithms in the RED<sub>m</sub>E package and with the same optimal Lick star templates as used for the central kinematics. In all the kinematic profiles plotted here, the values of the velocities and velocity dispersions are plotted at the luminosity-weighted centres of the spatial bins used to derive the parameters.

Dark time at both Gemini telescopes is highly oversubscribed. To speed up the completion of this multi-semester project, the observing conditions were relaxed to accept grey time as well. However, as a consequence it was not possible to extract radial profiles to very large radii for those targets observed during grey time. Eight galaxies (three WHT and five Gemini) could be extracted to radii $>$ $1a_e$, but 17 galaxies (one WHT and 16 Gemini) could only be extracted to radii $< 0.5a_e$ (shown in Tables 2.2 and 2.5).

A number of the galaxies initially showed a "U"-shaped radial velocity profile

85
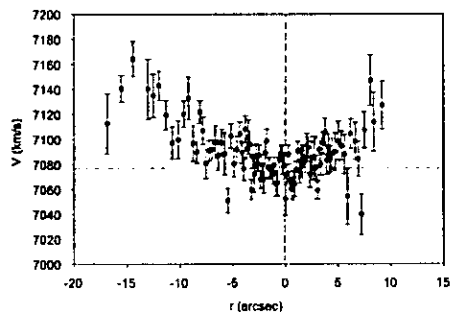
Figure 3.5: IC1633: radial velocity profile before modifications were made to the software.

which spurred further investigation. An extreme example of this (IC1633) is shown in Figure 3.5. The two-dimensional wavelength calibration was carefully checked and proved to be accurate. Such a profile shape can also be caused by placing the slit slightly off-centre during observations (Sánchez-Blázquez et al. 2007). This motivated the investigation into the slit placements in the Gemini queue observations, as described in Section 2.2.2 and tabulated in Table 2.5, but this proved not to have a large influence on the kinematic profiles. The problem was solved by improvements to the software used in the derivation of the profiles, made by the original authors (Cardiel et al., private communication). The improvements centred around achieving a better fit for the continuum, with the continuum in the modified routine only fitted in the wavelength region selected to calculate the kinematics. An updated version of the MOVEL software has been released, and accurate radial profiles were then derived for all the galaxies. The radial velocity profile derived for IC1633 using the improved software follows in Figure 3.12.

The spatially-resolved kinematic profiles of some of the galaxies could be compared with previous measurements in the literature. Four comparisons are shown in Figures 3.6 to 3.9. Two of the Coma cluster BCGs (NGC4839 and NGC4889) were compared with results from Fisher et al. (1995a) and Mehlert et al. (2000). The third Coma BCG (NGC4874) was not compared as it was observed at a
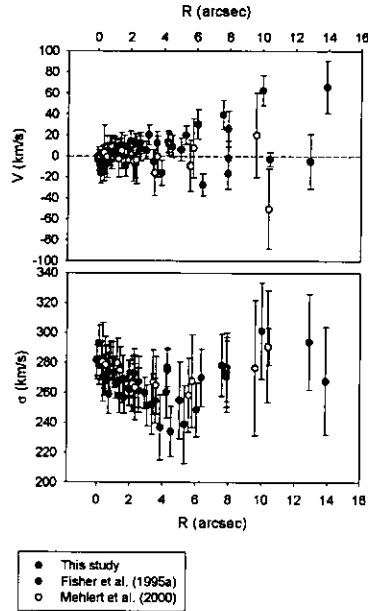
Figure 3.6: NGC4839: kinematic profiles compared with previous literature. The data are folded with respect to the centre of the galaxy, and the radial velocities are given as relative to the central radial velocity.

different slit PA from that used in the other studies. No systematic differences, within the error bars, were found for the measurements of this study compared with the previous studies. The velocity dispersion measurements of NGC4889 in Fisher et al. (1995a) are lower than the other studies. This discrepancy was already reported in Mehlert et al. (2000). Measurements for NGC6166 were compared with results of Fisher et al. (1995a): they agree within the errors. IC1101 results were compared with those of Fisher et al. (1995a), who found the velocity dispersion profile to be increasing. As can be seen from Figure 3.9, the velocity dispersion profile measured here does not extend out to the same radius as that from Fisher et al. (1995a) but the central measurements are in good agreement.

A comparison was also made between the spatially-resolved kinematics measured with the method described here, and profiles measured with a different method called the "pixel-penalising" technique. The latter method does not assume that the data points in the spectra follow a Poisson distribution or that
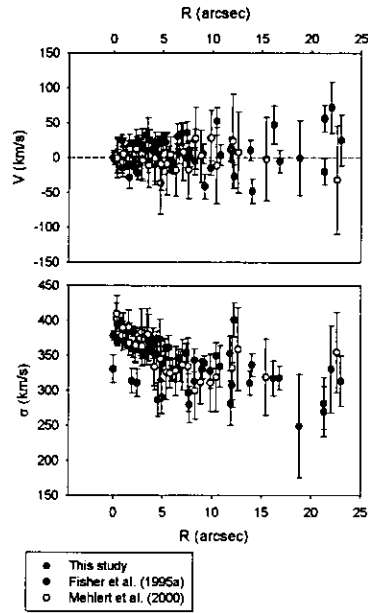
Figure 3.7: NGC4889: kinematic profiles compared with previous literature.
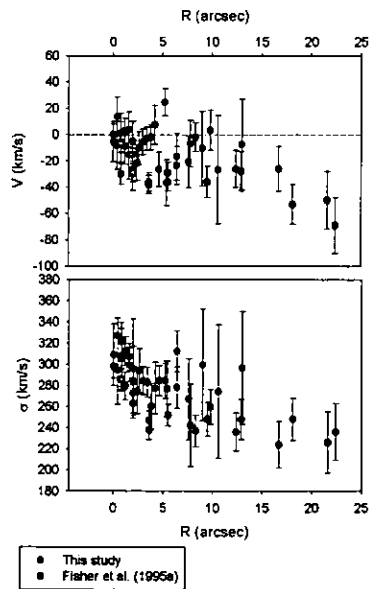


Figure 3.8: NGC6166: kinematic profiles compared with previous literature.
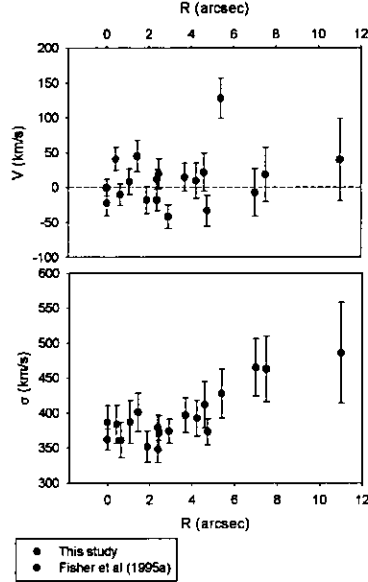
Figure 3.9: IC1101: kinematic profiles compared with previous literature.

the noise levels in adjacent pixels are independent (De Bruyne et al. 2003). This comparison is shown in Figures 3.10 and 3.11 for ESO146-028. The velocity dispersions derived using the pixel penalising technique (pPXF – from Cappellari & Emsellem 2004) are systematically lower than those derived using MOVEL, as shown in Figure 3.11. However, the MOVEL velocity dispersions are in very good agreement with those from previous studies (Figures 3.6 to 3.9).

The spatially-resolved kinematics profiles of all the galaxies are shown in Figure 3.12, and the individual profiles are discussed in Appendix A.

## 3.4   Results and discussion

**Velocity dispersion gradients**

- Five out of 49 BCGs (ESO349-010, ESO444-046, ESO552-020, NGC3311 and PGC026269) were found to have a positive velocity dispersion gradient. The radial kinematic studies undertaken previously on early-type galaxies
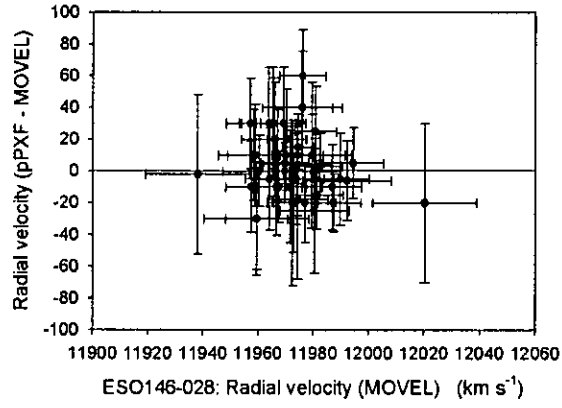
Figure 3.10: ESO146-028 radial velocities: comparison with pPXF.
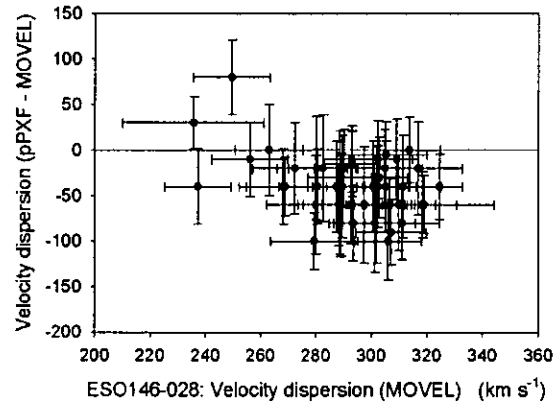


Figure 3.11: ESO146-028 velocity dispersions: comparison with pPXF.
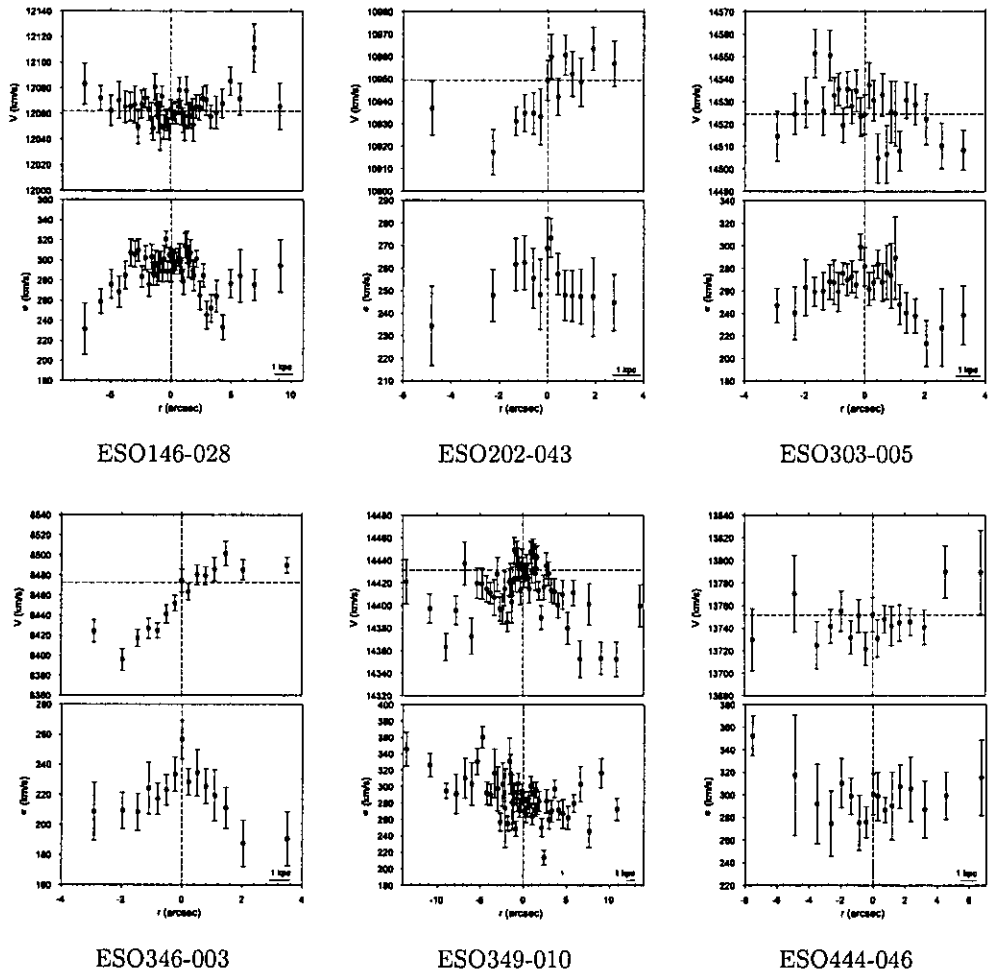
Figure 3.12: Radial velocity ($V$) and velocity dispersion ($\sigma$) profiles. The vertical lines indicate the centre of the galaxy, and the horizontal line the radial velocity of the central bin.
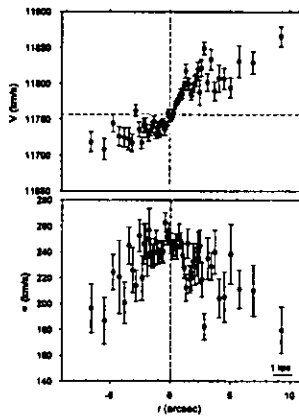
ESO488-027
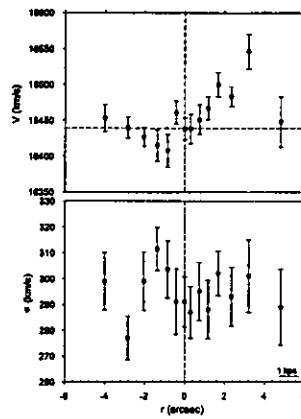
ESO541-013
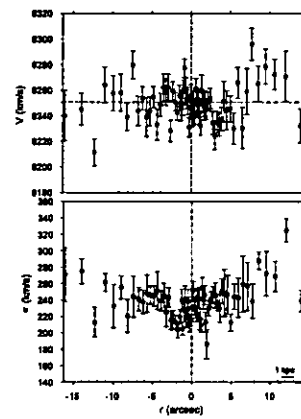
ESO552-020
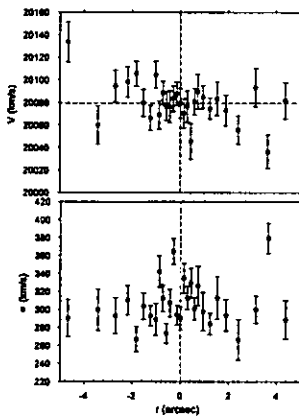
GSC555700266
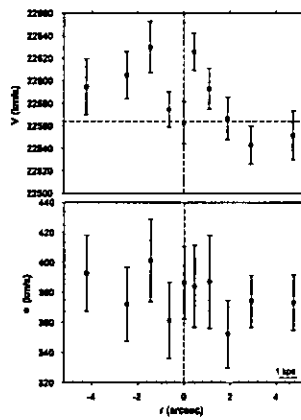
IC1101
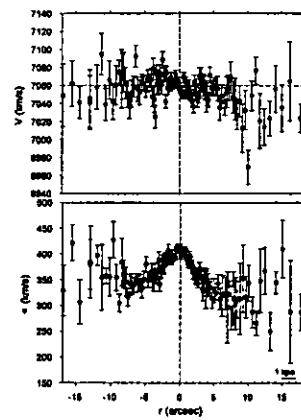
IC1633

Figure 3.12 continued.
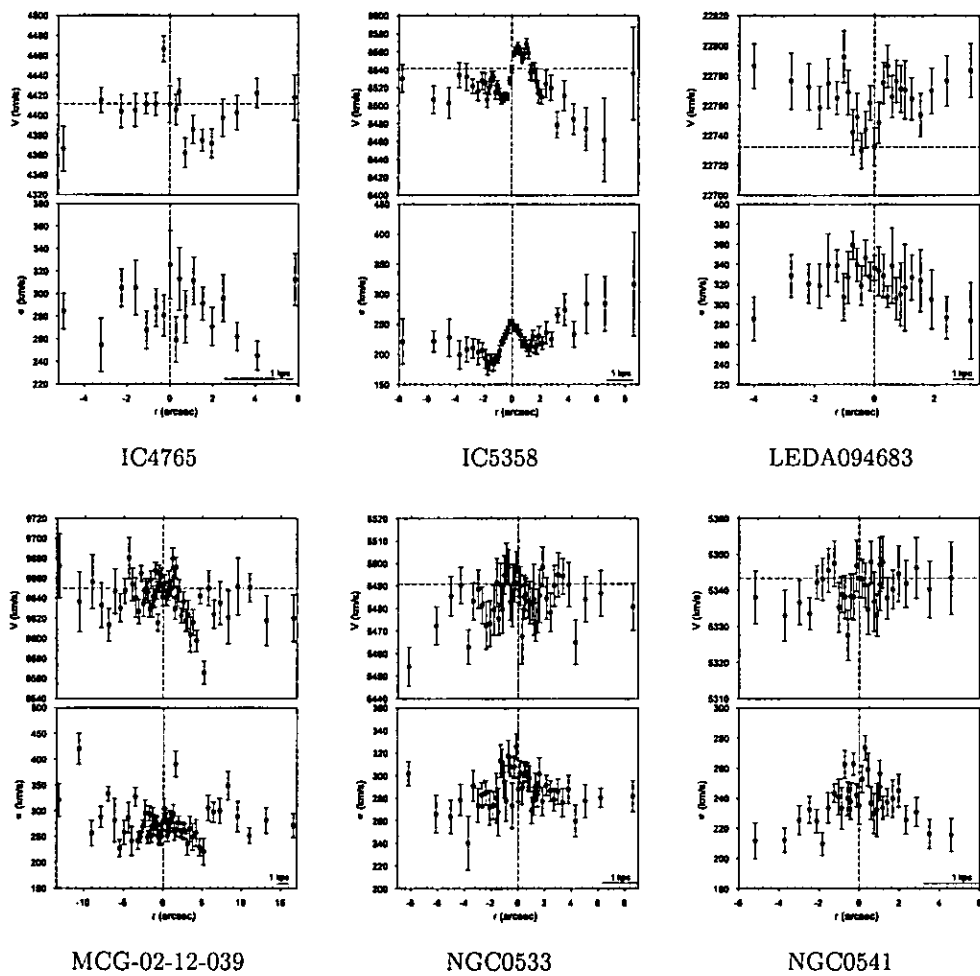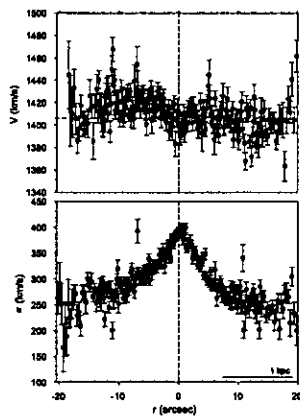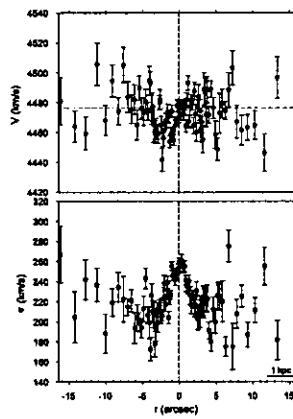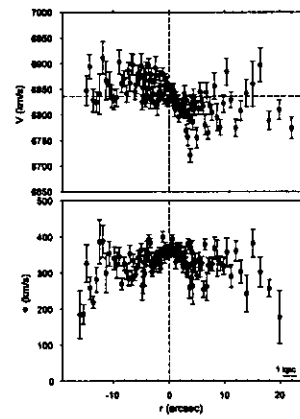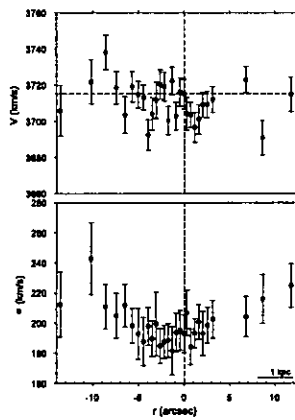
IC4765        IC5358        LEDA094683

MCG-02-12-039        NGC0533        NGC0541
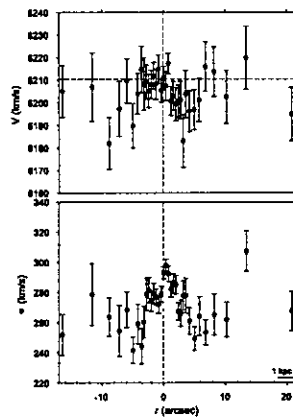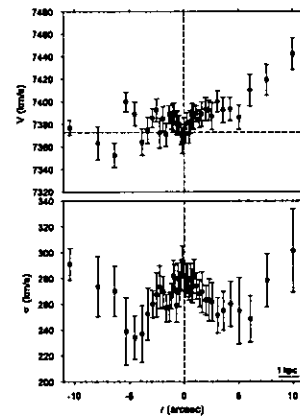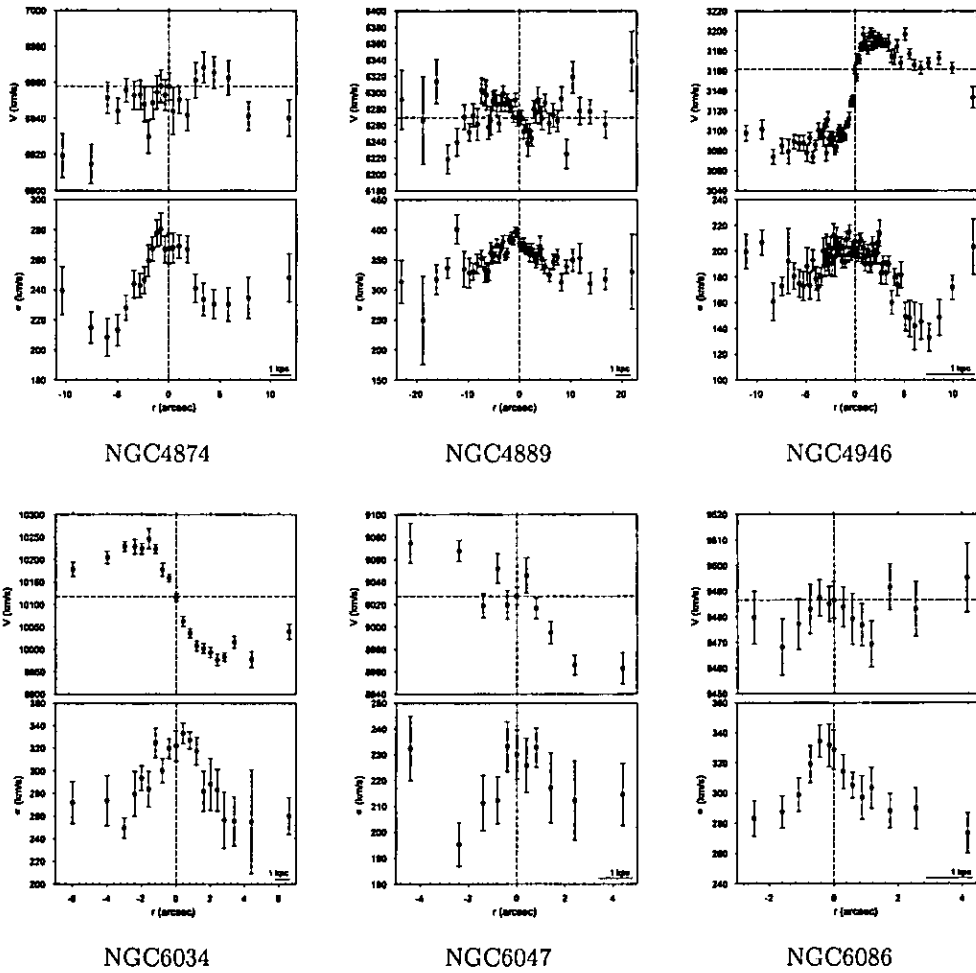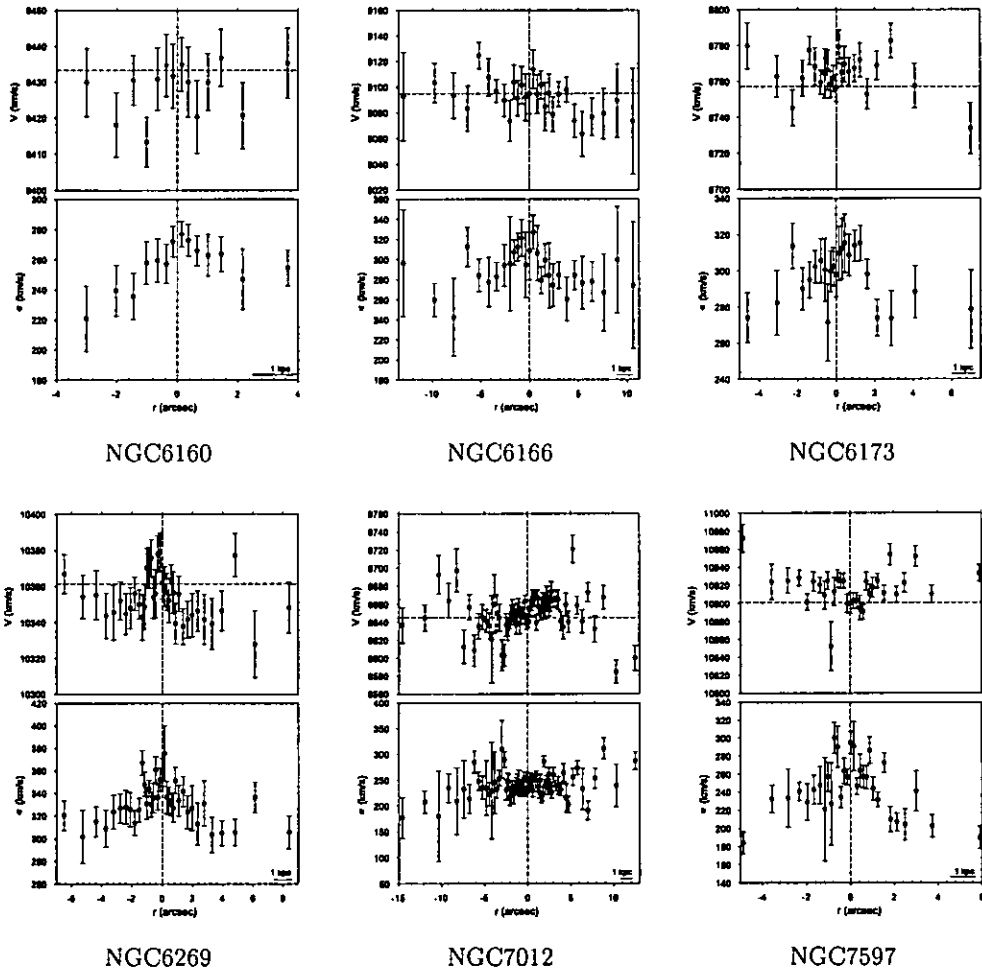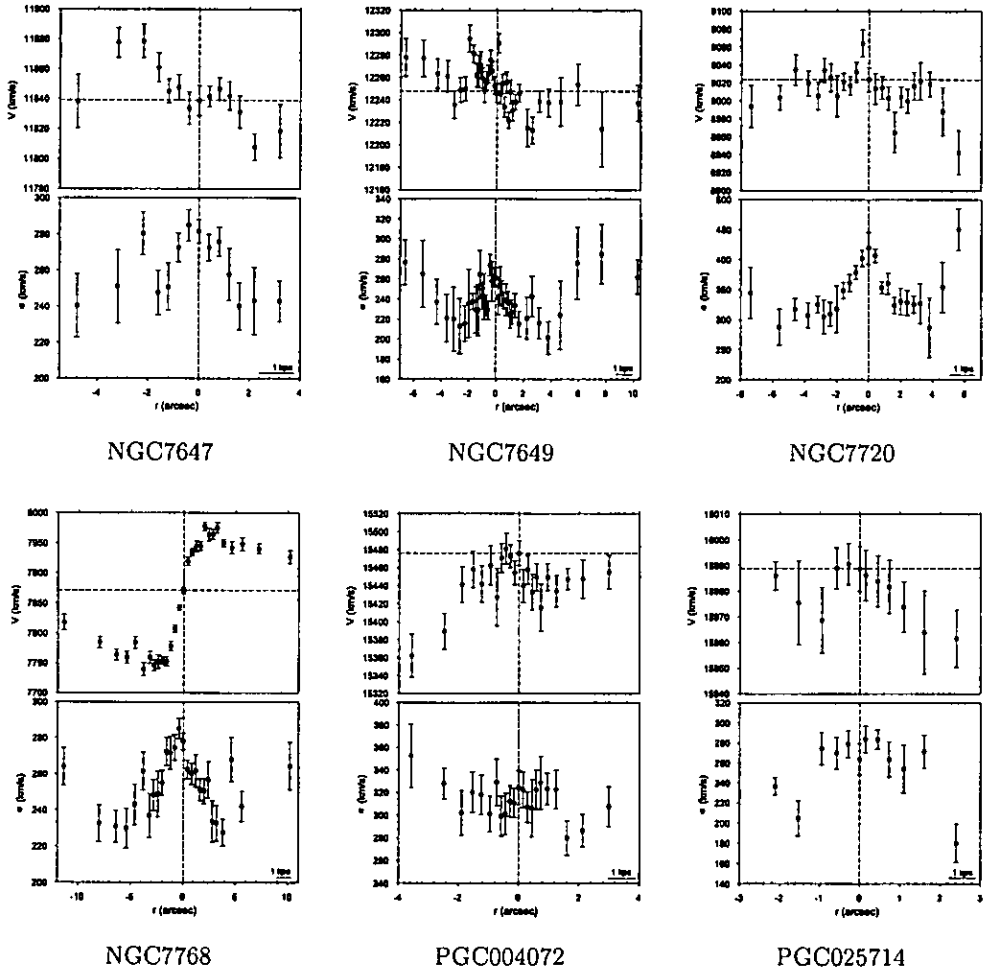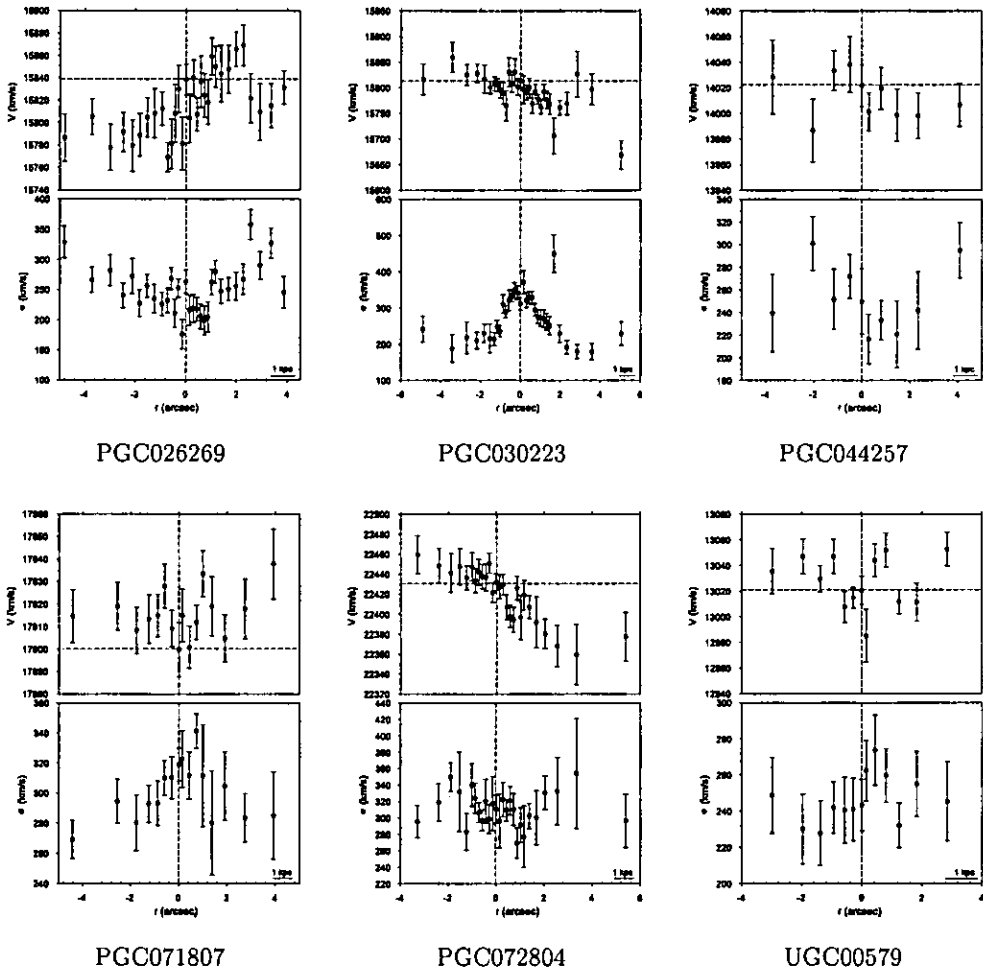
Figure 3.12 continued.

Figure 3.12 continued.

NGC4874          NGC4889          NGC4946

NGC6034          NGC6047          NGC6086

Figure 3.12 continued.

NGC6160          NGC6166          NGC6173

NGC6269          NGC7012          NGC7597

Figure 3.12 continued.

96

NGC7647            NGC7649            NGC7720

NGC7768            PGC004072          PGC025714

Figure 3.12 continued.

PGC026269            PGC030223            PGC044257

PGC071807            PGC072804            UGC00579

Figure 3.12 continued.

UGC02232          UGC05515          UGC10143
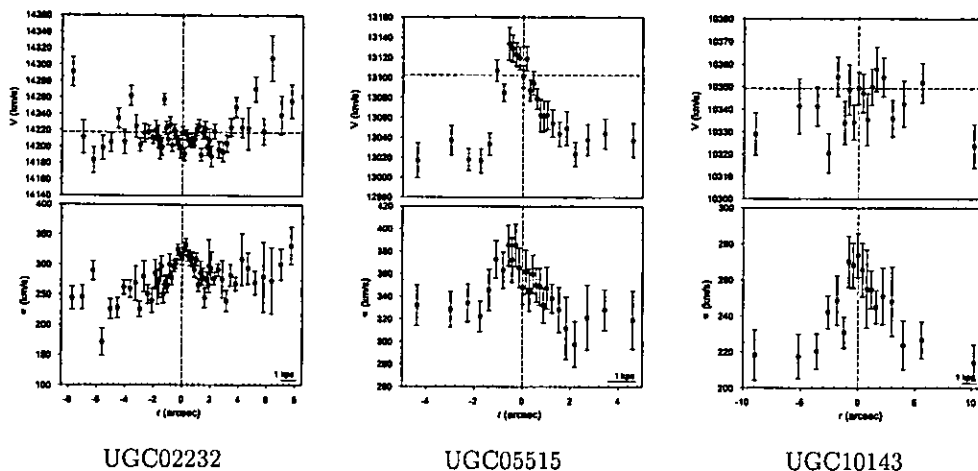
Figure 3.12 continued.

were mostly limited to normal ellipticals, for which flat or decreasing ve-
locity dispersion profiles are found (Franx, Illingworth & Heckman 1989;
Bender, Saglia & Gerhard 1994; Mehlert et al. 1998; Koprolin & Zeilinger
2000). The majority of the results previously obtained for very small sam-
ples of BCGs are similar to those of normal ellipticals, with a few exceptions:
Fisher et al. (1995a) and Carter et al. (1999) each found one galaxy (IC1101
and NGC6166, respectively) in their samples of BCGs to have a positive
velocity dispersion gradient, although Fisher et al. (1995a) did not find this
for NGC6166. Brough et al. (2007) found no positive velocity dispersion
gradients for their sample of brightest group and cluster galaxies.

Both IC1101 and NGC6166 form part of the sample of BCGs studied here,
but in both cases the measured velocity dispersion profiles do not reach the
radius achieved in the much smaller samples in the above-mentioned studies
(see Figures 3.8 and 3.9). Thus, the positive velocity dispersion gradients
could not be confirmed for IC1101 or NGC6166. However, as mentioned
above, five other BCGs were found to have a positive velocity dispersion
gradient, though admittedly the slope is only marginally positive in the

first two cases (ESO349-010, ESO444-046). Positive velocity dispersion gradients imply rising mass-to-light (M/L) ratios with distance from the centre of the galaxies. In a recent cosmological simulation, Ruszkowski & Springel (2009) found faster dark matter mass growth within the half-light radius of the BCG in their simulated cluster, compared with the increase in stellar mass inside the same radius.

**Kinematically decoupled cores**

- Clear velocity substructure was found in the profiles of 15 BCGs (ESO488-027, IC5358, MCG-02-12-039, NGC0533, NGC1713, NGC2832, NGC3842, NGC4839, NGC4889, NGC6269, NGC7647, NGC7649, PGC004072, PGC030223 and UGC05515).

From studies of elliptical galaxies in high density environments (e.g. Koprolin & Zeilinger 2000), the incidence of kinematically decoupled cores (KDCs) is observed to be about 33 per cent, rising to 50 per cent when projection effects are considered. Hau & Forbes (2006) found KDCs in 40 per cent of their isolated elliptical galaxies. Here, at least 15 BCGs show velocity substructure, amounting to 31 per cent of the sample. This is a lower limit since the cases where the kinematic profiles show a large amount of scatter, which makes it difficult to conclusively confirm the presence of a KDC, were not included in the count.

KDCs can be the result of a merger event (Koprolin & Zeilinger 2000), but can also occur when the galaxy is triaxial and supports different orbital types in the core and main body (Statler 1991). The fact that the incidence of KDCs in BCGs is comparable with that found for normal elliptical galaxies in high density environments suggests that the two classes have the same fraction of galaxies with triaxial shapes.

CHAPTER 3

## Rotation

- NGC6034 and NGC7768 show rapid rotation of 134 and 114 km s$^{-1}$, respectively (major axis spectra). ESO541-013 shows rotation of 138 km s$^{-1}$ (minor axis spectrum). Several other BCGs show rotation that is > 40 km s$^{-1}$ and more than three times the error on the rotation measurement ($V_{max}$): ESO202-043, ESO346-003, GSC555700266 and NGC4839 (major axis spectra); ESO488-027, IC5358, PGC004072, PGC030223 and UGC05515 (intermediate axis spectra); as do the two E galaxies NGC4946 (major axis spectra) and NGC6047 (intermediate axis spectra).

Carter et al. (1999) found small rotation (< 40 km s$^{-1}$) along the major axis at large radii (30 – 40 arcsec) for their sample of three BCGs, which is consistent with the nearly complete lack of rotation found near the centres of the sample of 13 BCGs by Fisher et al. (1995a). According to Fisher at al. (1995a), the lack of rotation found in samples of BCGs is in agreement with the expectation of declining importance of rotation with increasing luminosity for elliptical galaxies. The lack of rotation is also compatible with the idea that these objects formed through dissipationless mergers (Boylan-Kolchin et al. 2006). The remnants left by mergers with dissipation and those without dissipation are expected to differ in their kinematical structure. In a merger which involves gas-rich galaxies, the gas will form a disc. After the gas has been removed from the system at the end of the merger through ejection and conversion into stars, the remnant will show significant rotation (Bournaud, Jog & Combes 2005). Conversely, in a merger where dissipationless processes dominate, the remnant will show little or no rotation (Naab & Burkert 2003; Cox et al. 2006). In the present study, clear major axis rotation above 100 km s$^{-1}$ was found for NGC6034 and

NGC7768, while most other BCGs showed little or no rotation. This kinematical differentiation (the existence of slow and fast rotators) in normal elliptical galaxies is also clearly visible in the SAURON data presented by Emsellem et al. (2007).

The amount of flattening due to rotation in a galaxy depends on the balance between ordered and random motions, and this can be quantified using the anisotropy parameter. The rotation of elliptical galaxies is conventionally expressed as this anisotropy parameter, which is defined as $(V_{max}/\sigma_0)^* = (V_{max}/\sigma_0)/\sqrt{\epsilon/1-\epsilon}$ (Kormendy 1982), where the rotational velocity $(V_{max})$ is half the difference between the minimum and maximum peaks of the rotation curve, and $\sigma_0$ is the measured central velocity dispersion (as listed in Table 3.2). A value of $(V_{max}/\sigma_0)^* \approx 1$ would be expected if a galaxy is flattened by rotation. Measurement of the anisotropy parameter $(V_{max}/\sigma_0)^*$ can conveniently be used to distinguish galaxies that are rotationally supported from those that are supported by velocity dispersion anisotropy, for which the value is substantially less than unity. The division occurs at about $(V_{max}/\sigma_0)^* = 0.7$ (Bender, Burstein & Faber 1992).

Figure 3.13 shows values of the anisotropy parameter as a function of galaxy $B$-band luminosity. The above-mentioned division is indicated by the horizontal dashed line. Note that the errors indicated are only propagated from the errors on the velocity measurements taken to be the extreme radial velocity points (minimum and maximum of the rotation curve), and the errors on the central velocity dispersion. They do not take into account the general uncertainties involved in determining the most extreme velocity measurements. Therefore, care has to be taken when interpreting individual points on the diagram. The only notable BCG data point that lies significantly above the dashed line is for the galaxy PGC026269, which

possesses moderate rotation (51 km s$^{-1}$) and surprisingly low central velocity dispersion (222 km s$^{-1}$). However, the ellipticity of this galaxy is zero and it is not rotationally supported.

All galaxies for which major axis spectra were observed are plotted on the ($\epsilon$, $V_{max}/\sigma_0$) plane in Figure 3.14. This diagram has also classically been used to analyse the level of rotational support of galaxies with respect to their flattening. The theoretical "isotropic oblate rotator" line ($V_{max}/\sigma_0$)$=\sqrt{\epsilon/(1-\epsilon)}$ is also plotted in Figure 3.14 as is commonly done (e.g. Bender 1988). This line is for an oblate spheroid in which the velocity dispersion is isotropic everywhere and the rotation is responsible for the galaxy's flattening. Galaxies with points below the line are supported by anisotropy.

A factor that complicates the dynamical interpretation of individual points in such diagrams is that the observed ellipticity is a global property of the galaxy, whereas the kinematic measurements taken here only reflect the kinematics along the axis where the slit was placed, and only close to the centre of the galaxy. For example, a disc component may dominate the measured kinematics but will have little effect on the overall ellipticity, making the galaxy appear to rotate faster than its global ellipticity would suggest (Merrifield 2004).

For comparison with the major-axis BCG datapoints, data from a sample of isolated ellipticals (Hau & Forbes 2006) are also plotted in Figure 3.13. The central velocity dispersions of these galaxies were derived from the bins closest to the galaxy cores. The BCGs show less rotational support than these isolated elliptical galaxies, as a class of objects. In addition, data on spiral bulges (typically rotationally supported) and giant ellipticals (Bender et al. 1992) are also plotted. Their central velocity dispersions were derived
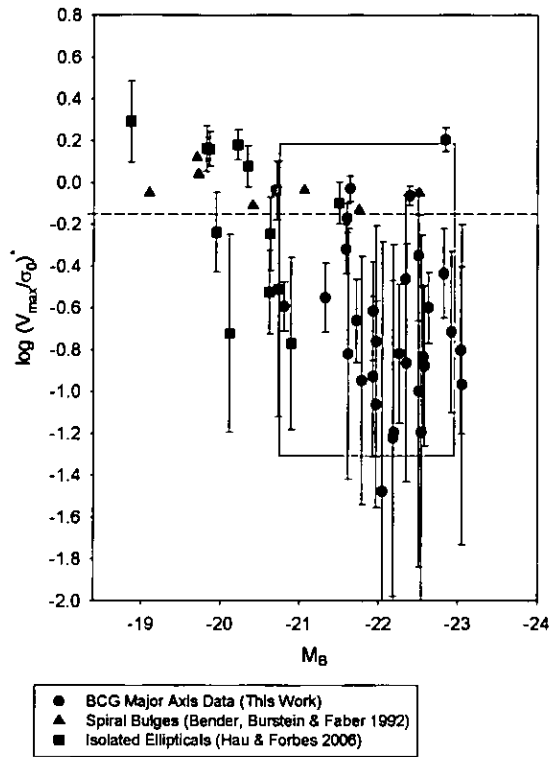
Figure 3.13: The anisotropy–luminosity diagram. The horizontal dashed line separates the rotationally supported galaxies from the anisotropic galaxies as described in the text. Only the BCGs for which major axis spectra were taken (within 10 degrees) are plotted. The box plotted in the figure outlines the region containing data on giant ellipticals from Bender et al. (1992).

over the whole half-light radii of the galaxies. Even though large rotation velocities were found for a few individual cases, the BCGs are consistent with the general trend for very massive galaxies.

**Faber–Jackson relation**

- BCGs lie above the Faber–Jackson relation.

Several previous studies have shown that BCGs lie above the Faber–Jackson relation (Faber & Jackson 1976) followed by elliptical galaxies (Tonry 1984;
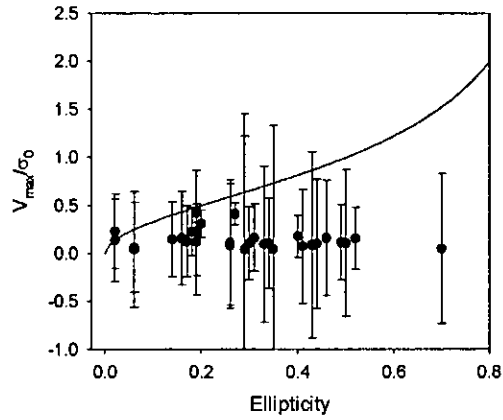
Figure 3.14: The $(V_{max}/\sigma_0)$ versus ellipticity diagram showing the BCGs for which major axis spectra were observed.

Oegerle & Hoessel 1991; Bernardi et al. 2007; Lauer et al. 2007; Desroches et al. 2007; Von der Linden et al. 2007). Their central velocity dispersions are almost constant with increasing luminosity while their effective radii increase very rapidly with luminosity. Figure 3.15 shows the luminosity–velocity dispersion relation fitted with a linear least-squares fit to the $B$ and $K$ magnitude BCG data, even though the data exhibit a large amount of scatter. The magnitudes used here were not corrected for passive evolution. However, a typical correction using the Bruzual & Charlot (2003) stellar population synthesis code with the assumption that the galaxies are 10 Gyr old and formed in an instantaneous burst, is only −0.2 mag for a galaxy at $z \sim 0.054$ (in the $K$-band). Figure 3.15 also shows the Faber–Jackson relation for normal ellipticals, corresponding to the slope $L \propto \sigma^4$, for comparison. A t-test was run on the correlation fitted to the BCG data to assess if a real slope is present in the scatter, or if $b = 0$ (as a null hypothesis). A $t$ value larger than 1.96 means that there is a true correlation between the variables ($b \neq 0$), at a 95 per cent confidence level. $P$ is the probability of being wrong in concluding that there is a true correlation (i.e. the probability of falsely rejecting the null hypothesis). For the BCG

105

$B$ magnitude data slope, a $t$ value of 2.11 and a $P$ value of 0.04 were found. Similarly, a $t$ value of 2.30 and a $P$ value of 0.03 were found for the $K$ magnitude data slope. Thus, the correlations are weak as a result of the large scatter in the data.

For the BCG data, the slope of the best-fitting straight line equates to $L \propto \sigma^{11.27 \pm 5.32}$ when $B$ magnitudes are used, and $L \propto \sigma^{9.05 \pm 6.55}$ when $K$ magnitudes are used. Measurements in the literature for BCGs also report $L \propto \sigma^{\beta}$ with $\beta > 4$. Von der Linden et al. (2007) found $\beta$ to be $5.32 \pm 0.37$ in the $R$ band at an isophotal limit of 23 mag arcsec$^{-2}$ using SDSS data, compared with a $\beta$ of $3.93 \pm 0.21$ for comparable elliptical galaxies. Liu et al. (2008) found a $\beta$ of 5.6 (surface brightness limit of 25 mag arcsec$^{-2}$), and Lauer et al. (2007) a $\beta$ of $6.5 \pm 1.3$ (with $M_v < -21$).

The scatter in Figure 3.15 is large, and in the $B$ magnitudes it might, in principle, be due to inhomogeneous magnitude measurements taken from the HyperLeda catalogue. However, the scatter when the 2MASS $K$ magnitudes are used is just as large. Thus, usage of $B$ or $K$ magnitudes both lead to the same conclusion: the BCGs do not follow the Faber–Jackson relation defined by elliptical galaxies, and exhibit a large amount of scatter.

Boylan-Kolchin et al. (2006) performed a series of major merger simulations to investigate the spatial and velocity structure of the remnants of such mergers. They found that the luminosity–velocity dispersion relation depended strongly on the merger orbit and that $\beta$ increased significantly for mergers on radial orbits. Thus, dissipationless merging of elliptical galaxies provides a natural mechanism for increasing the $\beta$ of the relation, provided that the merger orbits become preferentially more radial for the most massive galaxies. This is supported by the observation that the alignment of BCGs corresponds to that of the host cluster (example West 1989).
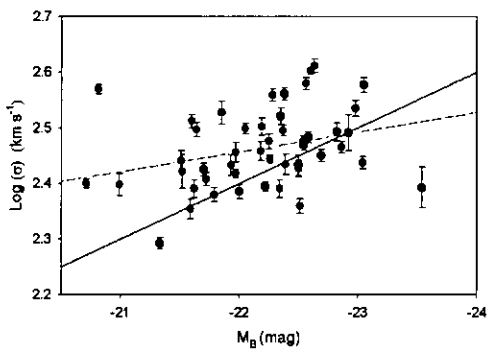
The BCG luminosity–velocity dispersion relation using $B$ magnitudes from the Hyper-Leda catalogue.
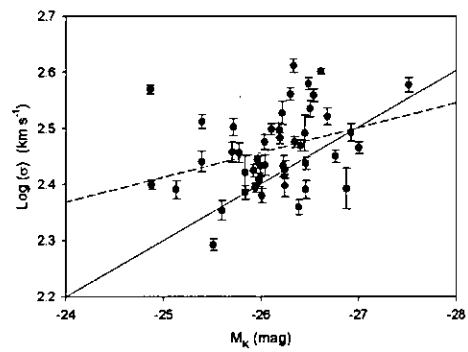
The BCG luminosity–velocity dispersion relation using $K$ magnitudes from the 2MASS catalogue.

Figure 3.15: The Faber–Jackson relation for normal elliptical galaxies is shown by the black line. Most of the BCGs lie above this relation. The BCG data are fitted with the red lines but show a large amount of scatter.

# Chapter 4

# STELLAR POPULATIONS

BCGs are unique not only in their location at the bottom of the cluster potential well, but also because they occupy the massive end of the galaxy luminosity function. Thus, their properties can be influenced both by their masses and by the cluster environment. What drives the stellar population properties of BCGs: internal (e.g. mass) or external (environment) factors?

In this chapter, the stellar populations of the galaxies are analysed by measuring Lick/IDS spectral indices from emission-line corrected spectra. The results are compared with SSP-models to derive the ages and abundances for the central parts of the BCGs. To address the question posed above, the SSP-parameters are compared with the central indices of ordinary ellipticals over the same mass range.

## 4.1   Calibration to the Lick system

Index measurements depend on the broadening of the absorption lines caused by both the instrumental spectral resolution and the line-of-sight velocities of the stars. In order to use model predictions based on the Lick system (see Section 1.3.1), the observed spectra need to be degraded to the wavelength-dependent

resolution of the Lick/IDS spectrograph, and the indices need to be corrected for the broadening caused by the velocity dispersion of the galaxies.

Three effects need to be accounted for to derive the intrinsic index-values and compare them with those predicted by models:

- The difference in spectral resolution between the observational data, and that of the Lick stars observed with the Lick set-up (Faber et al. 1985).

- The internal velocity dispersion of the galaxies.

- Small systematic differences caused by the fact that the Lick/IDS spectra were not flux-calibrated.

The following two sections describe these corrections, following the prescriptions of Worthey & Ottaviani (1997).

## 4.1.1  Correction to the Lick spectral resolution and velocity dispersion corrections

A total of 22 Lick calibration stars observed with the 5300 Å dichroic, and 10 with the 6100 Å dichroic at the WHT (as described in Section 2.2.1) were used here. Of the Gemini Lick star spectra retrieved from the Gemini Science Archive, 17 were used here (the ones that most closely resembled the galaxy spectra). All line strengths were measured through the procedure detailed in Section 4.3.

The instrumental broadening ($\sigma_{Inst}$) of the WHT telescope and ISIS CCD was measured from the emission lines of the arc spectra. The lines were fitted with Gaussian functions from which the FWHMs were measured: 5300 Å Blue $\sigma_{Inst}$ = 1.62 Å; 5300 Å Red $\sigma_{Inst}$ = 1.73 Å; 6100 Å Blue $\sigma_{Inst}$ = 1.56 Å; and 6100 Å Red $\sigma_{Inst}$ = 1.39 Å. Using the same technique, the instrumental broadening of Gemini and GMOS was determined to be $\sigma_{Inst}$ = 1.09 Å (for both Gemini North and South).

As the first step, the Lick star spectra observed here (both WHT and Gemini data) were shifted to zero radial velocity (Doppler correction) and broadened to the wavelength-dependent resolution of the original Lick/IDS spectra ($\sigma_{\text{Lick}}$ measured in Å; taken from figure 7 in Worthey & Ottaviani (1997) and listed in Table 4.1). A Gaussian of width $\sqrt{\sigma_{\text{Lick}}^2 - \sigma_{\text{Inst}}^2}$, was used to broaden the Lick stellar spectra to $\sigma_{\text{Lick}}$.

Depending on whether the observed galaxy spectra had a combined broadening, $\sqrt{\sigma_{\text{Inst}}^2 + \sigma_{\text{Gal}}^2}$ (where $\sigma_{\text{Gal}}$ is the velocity dispersion of the galaxy), smaller or greater than the Lick resolution ($\sigma_{\text{Lick}}$), two different procedures were followed:

1) If the total broadening $\sqrt{\sigma_{\text{Inst}}^2 + \sigma_{\text{Gal}}^2}$ was smaller than $\sigma_{\text{Lick}}$, a Gaussian of width $\sqrt{\sigma_{\text{Lick}}^2 - \sigma_{\text{Gal}}^2 - \sigma_{\text{Inst}}^2}$, was used to broaden the galaxy spectra to $\sigma_{\text{Lick}}$.

2) If the galaxies had a total broadening ($\sqrt{\sigma_{\text{Inst}}^2 + \sigma_{\text{Gal}}^2}$) greater than $\sigma_{\text{Lick}}$, then their indices could not be broadened to $\sigma_{\text{Lick}}$ and were corrected for the broadening effect caused by the velocity dispersion of the galaxies, using the polynomials calculated as follows:

The stellar spectra were smoothed to various widths in the range $\sigma_c = 0$ to 300 km s$^{-1}$, in intervals of 20 km s$^{-1}$ where $\sigma_c$ is the width of the broadening Gaussian. This was done by rebinning the spectra onto a logarithmic wavelength scale, calculating the appropriate width of the broadening Gaussian in pixels and artificially broadening the spectra by convolving them with the broadening Gaussian, and then rebinning the spectra back to a linear wavelength scale. Following Proctor & Sansom (2002), correction factors $C_i(\sigma_c)$ were determined as follows:

For molecular line indices (CN$_1$, CN$_2$, Mg$_1$, Mg$_2$, TiO$_1$ and TiO$_2$) and for indices with ranges which include negative values (i.e. H$\gamma$ and H$\delta$):

$$C_i(\sigma_c) = I_0 - I_c, \qquad (4.1)$$

where $I_0$ is the index value at the calibration resolution and $I_c$ the index value measured in the broadened star spectrum.

For all the other atomic line indices:

$$C_i(\sigma_c) = I_0/I_c. \tag{4.2}$$

For each of the indices, $C_i$ was plotted against $\sigma_c$, and the best-fitting third order polynomial $(C_i = x_0 + x_1\sigma_c + x_2\sigma_c^2 + x_3\sigma_c^3)$ was derived from the data with all the stars equally weighed. The value of $x_0$ was fixed at zero for the molecular, $H\gamma$ and $H\delta$ indices and at one for the other atomic indices.

The polynomial coefficients are plotted in Figures 4.1 (WHT data) and 4.2 (Gemini data). These figures illustrate how the different indices depend on the broadening. For example, $TiO_2$ index line strengths are essentially independent, whilst those for Ca4455 depend very strongly on resolution. Some of the indices, for example $CN_1$, show a large variation in the datapoints derived using different stars, however, the derived correction is very small. The derived broadening functions agreed very well when compared with those derived by Proctor & Sansom (2002) and Kuntschner (2004). The derived broadening functions were extrapolated to 410 km s$^{-1}$ when applied to the BCG spectra index measurements, to cover the whole range of velocity dispersions derived for the BCGs. This extrapolation and the fact that all stars were equally weighed in the derivation of the broadening functions will not affect the index measurements as the uncertainties are negligible compared to the large errors on the index measurements. Indeed, in Section 4.3 it will be shown that using calibrations to the Lick system derived from a completely different set of stars (taken from the MILES library) does not influence the SSP results. Details of all the Lick calibrations are tabulated in Tables 4.1 and 4.2.
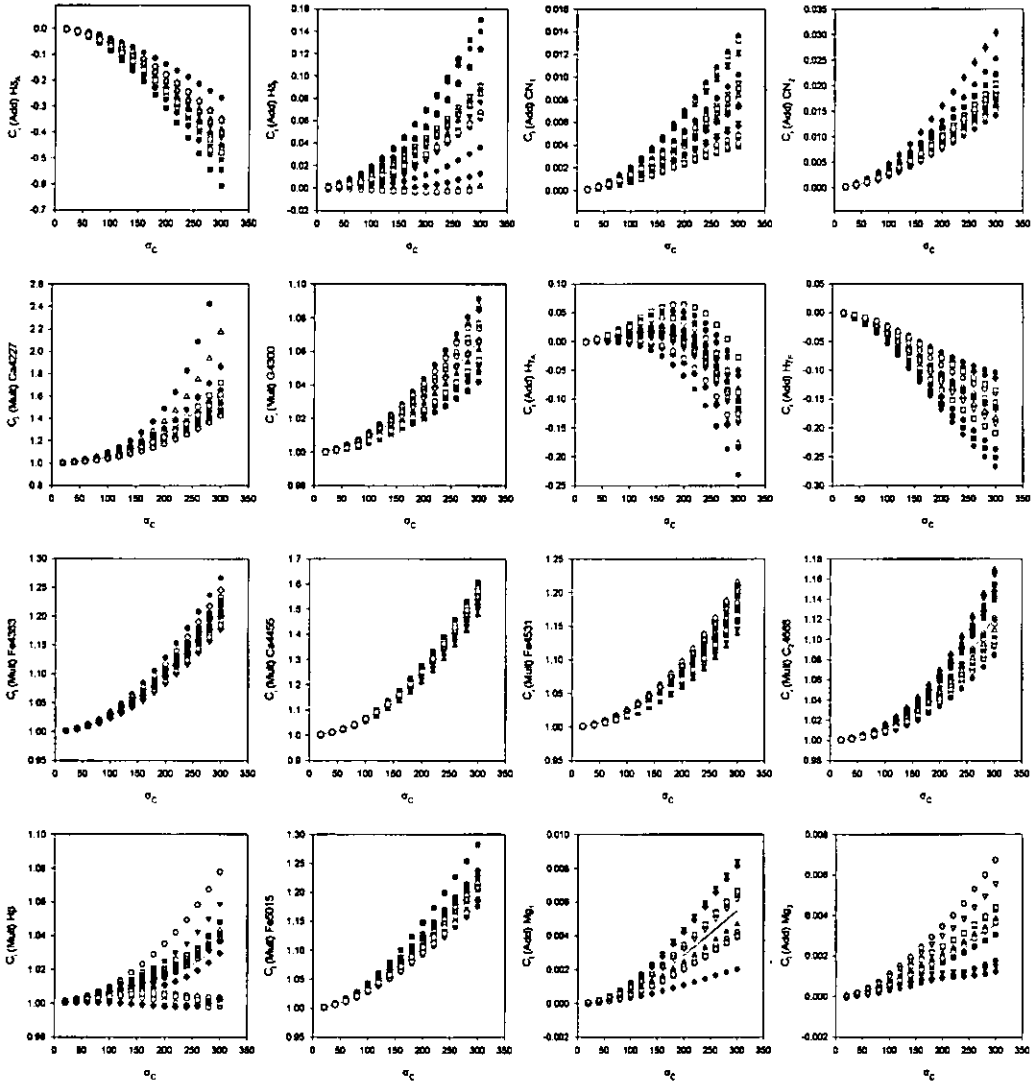
Figure 4.1: Broadening functions: $C_i$ plotted as a function of $\sigma_c$ (WHT data) for all the indices. The best-fitting third order polynomial is indicated in each figure by the continuous curve. The different symbols represent the different stars used to obtain the best-fitting curve. The abbreviations "Add" and "Mult" indicates whether the index values were added (molecular and higher order Balmer indices) or multiplied (atomic indices) to calculate $C_i$, and $\sigma_c$ is in km s$^{-1}$.
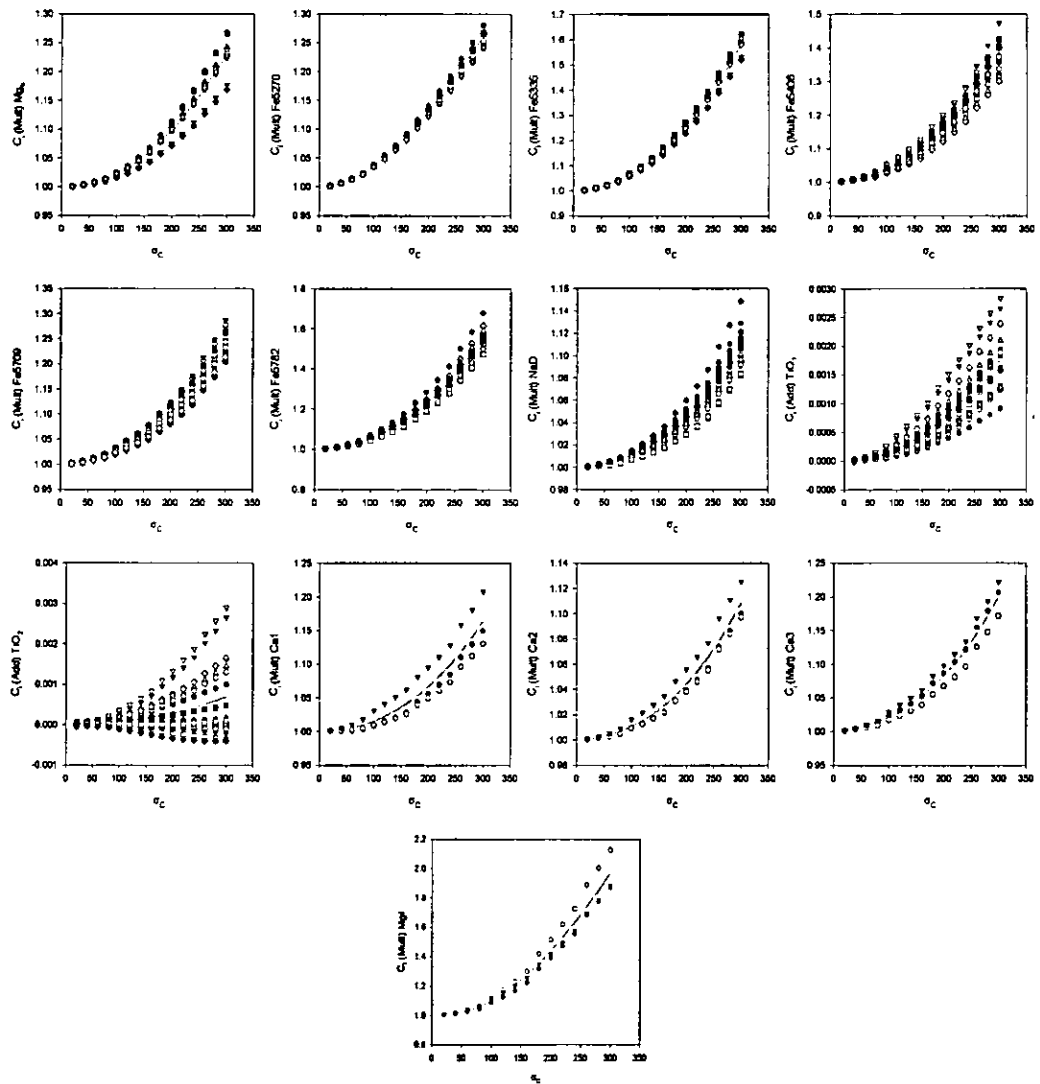
Figure 4.1 continued.
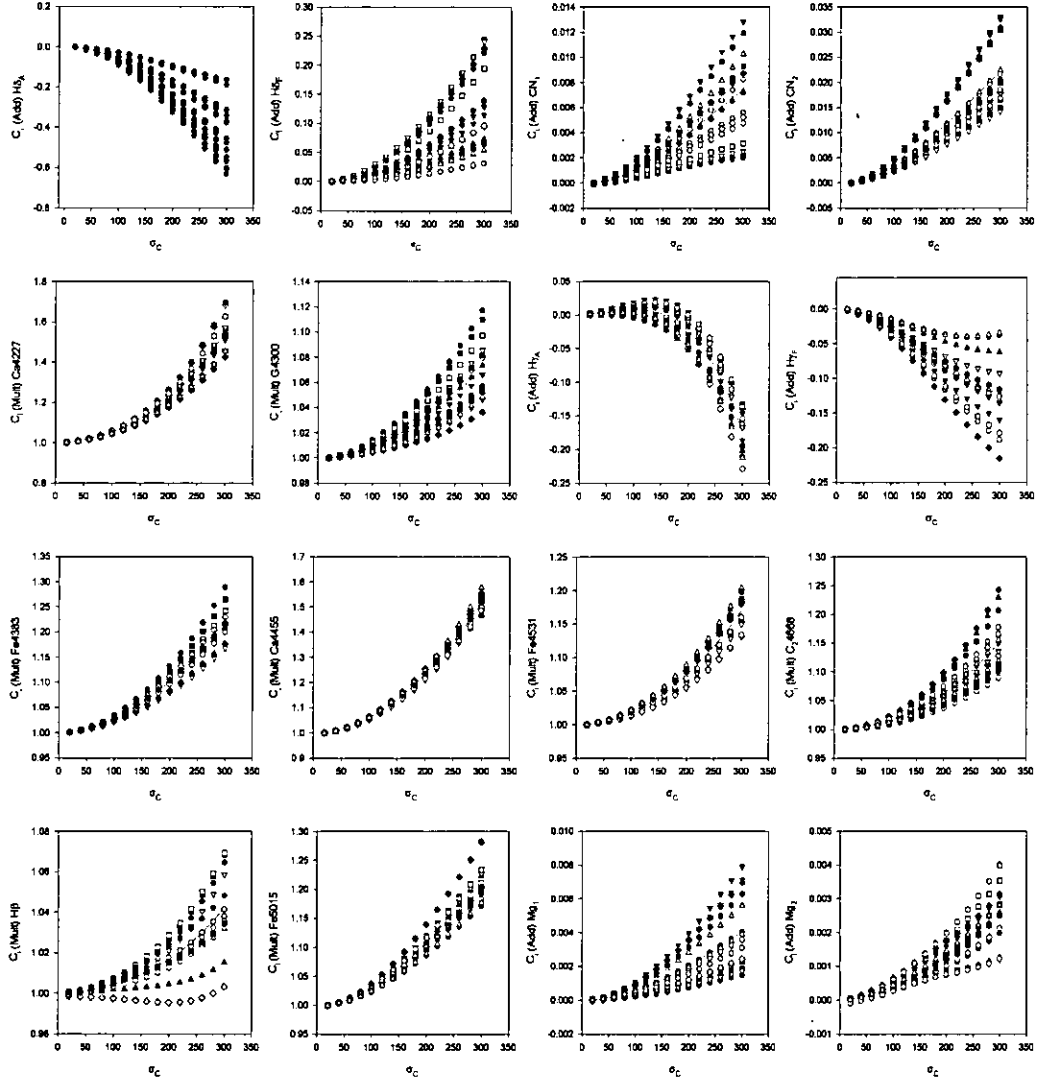
Figure 4.2: Broadening functions: $C_i$ plotted as a function of $\sigma_c$ (Gemini data). The best-fitting third order polynomial is indicated in each figure by the continuous curve. The different symbols represent the different stars used to obtain the best-fitting curve. The abbreviations "Add" and "Mult" indicates whether the index values were added (molecular and higher order Balmer indices) or multiplied (atomic indices) to calculate $C_i$, and $\sigma_c$ is in km s$^{-1}$.
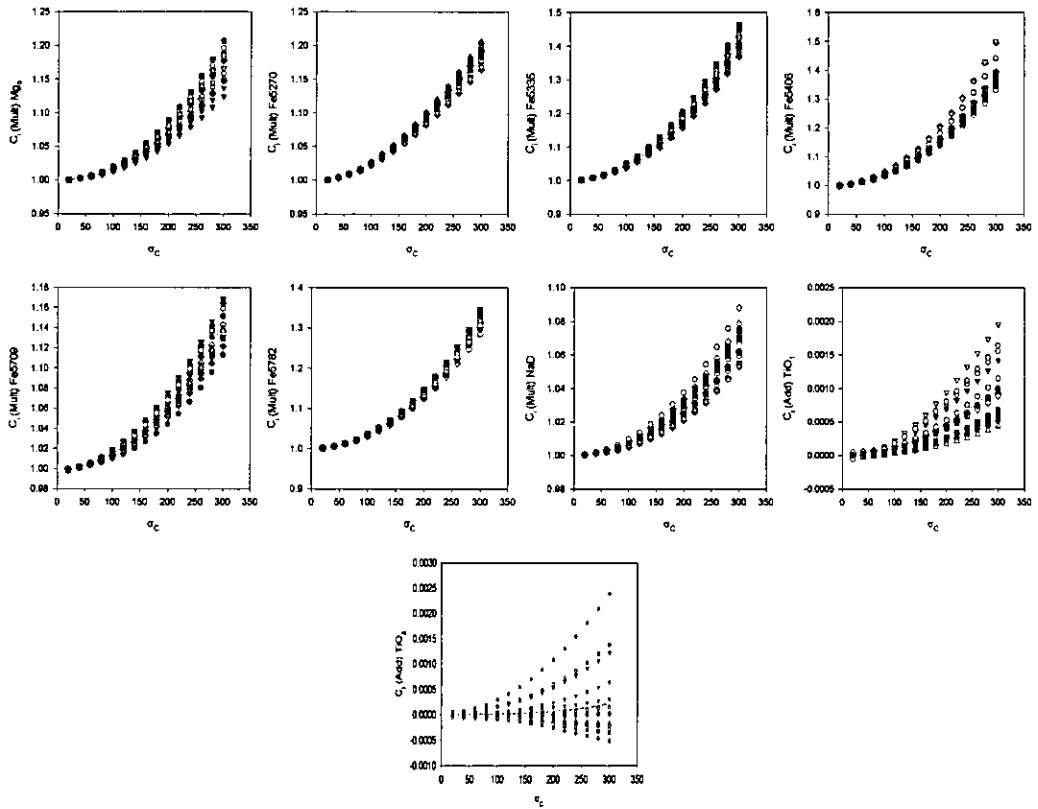
Figure 4.2 continued.

| Index | FWHM | $x_0$ | $x_1$ | $x_2$ | $x_3$ | $\Delta I$ | RMS |
|---|---|---|---|---|---|---|---|
| $H\delta_A$ | 10.9 | 0 | 1.4376e-5 | -7.0050e-6 | 6.7430e-9 | -1.186 | 0.089 |
| $H\delta_F$ | 10.9 | 0 | 2.1742e-5 | 5.1146e-7 | 1.0149e-9 | -0.386 | 0.083 |
| $CN_1$ | 10.6 | 0 | 1.1628e-6 | 1.3401e-7 | -1.5542e-10 | -0.025 | 0.006 |
| $CN_2$ | 10.6 | 0 | 2.7297e-6 | 3.0690e-7 | -3.2468e-10 | -0.028 | 0.006 |
| Ca4227 | 10.2 | 1 | -2.6640e-4 | 6.6143e-6 | 4.6085e-9 | -0.031 | 0.062 |
| G4300 | 9.8 | 1 | 1.7427e-5 | 8.5111e-7 | -5.8318e-10 | -0.081 | 0.089 |
| $H\gamma_A$ | 9.5 | 0 | -4.0111e-5 | 3.2212e-6 | -1.4626e-8 | 0.369 | 0.128 |
| $H\gamma_F$ | 9.5 | 0 | 1.9519e-5 | -4.7505e-6 | 9.0335e-9 | 0.074 | 0.037 |
| Fe4383 | 9.2 | 1 | -2.0730e-5 | 3.0180e-6 | -1.9781e-9 | 0.280 | 0.131 |
| Ca4455 | 9.1 | 1 | 5.6573e-5 | 5.8261e-6 | 5.1207e-10 | 0.278 | 0.055 |
| Fe4531 | 9.0 | 1 | 1.9200e-5 | 1.9685e-6 | 4.4126e-11 | -0.082 | 0.102 |
| $C_2$4668 | 8.8 | 1 | -1.2262e-5 | 1.1718e-6 | 7.5142e-10 | 0.009 | 0.191 |
| $H\beta$ | 8.5 | 1 | 7.8786e-5 | -1.6245e-7 | 9.2492e-10 | -0.131 | 0.061 |
| Fe5015 | 8.4 | 1 | 5.5061e-5 | 3.2590e-6 | -3.4812e-9 | -1.024 | 0.118 |
| $Mg_1$ | 8.4 | 0 | -8.4147e-7 | 9.8180e-8 | -1.1490e-10 | 0.121 | 0.001 |
| $Mg_2$ | 8.4 | 0 | 2.6909e-6 | 4.9189e-8 | -6.2815e-11 | 0.125 | 0.004 |
| $Mg_b$ | 8.4 | 1 | -1.1510e-4 | 3.0409e-6 | -4.8406e-10 | 0.051 | 0.088 |
| Fe5270 | 8.4 | 1 | -3.2223e-5 | 4.2668e-6 | -4.2445e-9 | -0.066 | 0.039 |
| Fe5335 | 8.4 | 1 | -9.1612e-6 | 5.9912e-6 | 1.6145e-9 | -0.125 | 0.094 |
| Fe5406 | 8.4 | 1 | -2.6486e-5 | 3.5295e-6 | 2.4828e-9 | 0.057 | 0.099 |
| Fe5709 | 9.1 | 1 | 1.2167e-4 | 1.3390e-6 | 3.2135e-9 | -0.012 | 0.036 |
| Fe5782 | 9.3 | 1 | 6.7022e-5 | 4.0766e-6 | 6.1807e-9 | -0.035 | 0.028 |
| NaD | 9.5 | 1 | 7.2965e-5 | 8.2817e-7 | 2.1684e-9 | 0.077 | 0.046 |
| $TiO_1$ | 9.7 | 0 | -4.6528e-7 | 2.6727e-8 | -1.8833e-11 | 0.008 | 0.002 |
| $TiO_2$ | 10.3 | 0 | 3.1823e-7 | 3.1277e-9 | 1.1340e-11 | 0.054 | 0.001 |
| $CaII_1$ | 8.2 | 1 | 1.5487e-5 | 1.2149e-6 | 1.8415e-9 | -0.648 | 0.160 |
| $CaII_2$ | 8.2 | 1 | 2.4419e-5 | 6.9414e-7 | 1.4441e-9 | -1.459 | 0.236 |
| $CaII_3$ | 8.2 | 1 | 1.1674e-4 | 9.1068e-7 | 3.1945e-9 | 0.243 | 0.171 |
| MgI | 8.2 | 1 | -7.7710e-4 | 1.6918e-5 | -1.2632e-8 | -0.022 | 0.052 |

Table 4.1: Values of the offsets and polynomial coefficients used in the calibration of the WHT data to the Lick system. The values of the Lick spectral resolution ($\sigma_{Lick}$; Worthey & Ottaviani 1997) are given as FWHM values, where FWHM = $2.35\sigma_{Lick}$ in Å. The values of the offsets $\Delta I$ are (Lick – this work), and the root mean square (RMS) is the error on the offset.

| Index | FWHM | $x_0$ | $x_1$ | $x_2$ | $x_3$ | $\Delta$I | RMS |
|---|---|---|---|---|---|---|---|
| H$\delta_A$ | 10.9 | 0 | 3.5695e-5 | −7.7694e-6 | 8.5777e-9 | −0.139 | 0.154 |
| H$\delta_F$ | 10.9 | 0 | −3.0135e-5 | 1.7720e-6 | −5.6082e-10 | −0.065 | 0.073 |
| CN$_1$ | 10.6 | 0 | −1.3830e-6 | 1.4721e-7 | −2.0204e-10 | * | 0.013 |
| CN$_2$ | 10.6 | 0 | −3.6741e-6 | 4.2346e-7 | −5.5390e-10 | * | 0.015 |
| Ca4227 | 10.2 | 1 | 1.7865e-4 | 2.9655e-6 | 9.0006e-9 | 0.021 | 0.050 |
| G4300 | 9.8 | 1 | 3.2797e-5 | 6.4488e-7 | 1.7805e-10 | −0.058 | 0.061 |
| H$\gamma_A$ | 9.5 | 0 | 2.8251e-6 | 2.0551e-6 | −1.3255e-8 | 0.344 | 0.087 |
| H$\gamma_F$ | 9.5 | 0 | −1.4965e-5 | −3.3005e-6 | 6.6191e-9 | 0.071 | 0.061 |
| Fe4383 | 9.2 | 1 | 4.7860e-6 | 2.7446e-6 | −1.2824e-9 | −0.016 | 0.094 |
| Ca4455 | 9.1 | 1 | 5.0919e-5 | 5.8155e-6 | −8.1350e-10 | 0.452 | 0.041 |
| Fe4531 | 9.0 | 1 | 3.1621e-5 | 1.5188e-6 | 8.8514e-10 | −0.045 | 0.072 |
| C$_2$4668 | 8.8 | 1 | −1.9459e-6 | 1.3580e-6 | 1.0041e-9 | 0.018 | 0.106 |
| H$\beta$ | 8.5 | 1 | 4.5530e-5 | 2.4319e-9 | 1.0960e-9 | −0.051 | 0.041 |
| Fe5015 | 8.4 | 1 | 1.5787e-5 | 3.2697e-6 | −3.0301e-9 | −0.066 | 0.090 |
| Mg$_1$ | 8.4 | 0 | −2.9836e-7 | 6.4496e-8 | −6.1692e-11 | 0.005 | 0.003 |
| Mg$_2$ | 8.4 | 0 | 1.0236e-6 | 3.3235e-8 | −3.0902e-11 | 0.005 | 0.003 |
| Mg$_b$ | 8.4 | 1 | −4.1861e-5 | 2.0200e-6 | 4.1426e-11 | −0.001 | 0.042 |
| Fe5270 | 8.4 | 1 | −8.9369e-6 | 2.8442e-6 | −2.4675e-9 | −0.073 | 0.053 |
| Fe5335 | 8.4 | 1 | 2.0324e-5 | 4.1990e-6 | 1.1364e-9 | −0.017 | 0.045 |
| Fe5406 | 8.4 | 1 | 3.1157e-5 | 3.2510e-6 | 3.1952e-9 | 0.001 | 0.043 |
| Fe5709 | 9.1 | 1 | 5.4235e-5 | 1.0542e-6 | 1.2787e-9 | 0.005 | 0.030 |
| Fe5782 | 9.3 | 1 | 3.3839e-5 | 2.9915e-6 | 1.3392e-9 | −0.003 | 0.041 |
| NaD | 9.5 | 1 | 3.0030e-5 | 3.4807e-7 | 9.2784e-10 | 0.097 | 0.055 |
| TiO$_1$ | 9.7 | 0 | −2.8748e-7 | 1.4645e-8 | −7.8336e-12 | 0.006 | 0.002 |
| TiO$_2$ | 10.3 | 0 | 2.7041e-7 | −1.8201e-9 | 1.1353e-11 | −0.007 | 0.003 |

Table 4.2: Values of the offsets and polynomial coefficients used in the calibration of the Gemini data to Lick system. $\sigma_{Lick}$ are given as FWHM values, where FWHM = $2.35\sigma_{Lick}$ in Å. The values of $\Delta$I are (Lick − this work), and RMS is the error on the offset.

* Relations were derived for the two CN offsets (as described in Section 4.1.2), whereas all the other offsets were found to be independent of the strength of the index.

## 4.1.2 Correction to the Lick flux scale

The original Lick/IDS spectra were not flux-calibrated by means of spectrophotometric standard stars but instead were normalised to a calibration lamp. This causes small differences in the indices compared with those measured from flux-calibrated data. This effect needs to be taken into account by transforming the measurements to the same system as the Lick data, so that the models based on the Lick system can be used. By comparing the measured indices in the observed, flux-calibrated stars with those in the Lick/IDS database, the mean differences in index measurements (hereafter called offsets $\Delta I$) caused by this flux scale difference can be derived for all the indices.

Index values were measured from the Lick star spectra observed in this work (WHT and Gemini data) broadened to the Lick/IDS spectral resolution. These values were then compared with published Lick standards to obtain offsets. Comparisons to the data presented in Worthey (1994) and Worthey & Ottaviani (1997) for the same stars enabled the calculation of the mean offsets. For the near-IR indices in the WHT data, the stellar data of Diaz et al. (1989) were used to calculate the correction. The error on the near-IR measurements was given as typically five per cent in Diaz et al. (1989), but since these indices are not used for the purpose of age or metallicity measurements, this uncertainty has been excluded in the current error analysis. Only three stars of the WHT Lick star sample were in common with Diaz et al. (1989), and could be used to derive the offsets for the near-IR indices.

All the offsets derived for the WHT and Gemini data were independent of the strength of the index itself, with the exception of the two Gemini CN indices. For all other indices the average differences were computed and used as final corrections. For the CN indices, correlations between the offsets and the measured

index values (from this work) were found:

$$\Delta I = -0.0109 + 0.201 \times CN_1 \qquad (4.3)$$

$$\Delta I = -0.0150 + 0.184 \times CN_2 \qquad (4.4)$$

For all indices, the error on the mean offset was calculated as $RMS/\sqrt{N-1}$, where $N$ is the number of calibration stars ($N = 17$ for the Gemini data; $N = 22$ for the WHT data 5300 dichroic; $N = 10$ for the WHT data 6100 blue dichroic; and $N = 3$ for the WHT data 6100 red dichroic). The WHT offsets are shown in Figure 4.3, and the Gemini offsets in Figure 4.4. As can be seen in both datasets, the offsets are typically smaller than the error on the index measurement. For all the galaxy index measurements, this correction was performed by adding the appropriate $\Delta I$ to the measured index value.

Lick offsets are applied to correct measurements that were flux-calibrated using the spectrophotometric system to the Lick/IDS system and, therefore, should be identical for all flux-calibrated studies. Thus, the offsets derived here were compared with other sources to test the robustness of the Lick transformation. Figure 4.5 shows a comparison of the Gemini offsets derived in this work with those derived by M. Norris (private communication), also using archive data from the same Lick star observation programme. All the indices were converted to Å using equation 1.4. The CN indices are not plotted since correlations were applied in this work (equations 4.3 and 4.4) and not in the set derived by Norris. Most of the offsets used here are in agreement with those derived by Norris, with the exception of $C_24668$ and Ca4455, which are slightly higher in this study. The differences in the $Mg_1$ and $Mg_2$ index offsets are large, but the offsets (in magnitudes) are very small (see Table 4.2). No systematic differences between the two sets of offsets are apparent.

Since the BCG data are being compared with SB06 (from Section 4.3.2 onwards), the Lick offsets were also compared for these two datasets. The offsets

119

agree very well within the errors. As a final test, the offsets were also compared with the offsets derived by comparing the 242 stars in common between the flux-calibrated MILES library (Sánchez-Blázquez et al. 2006d; Sánchez-Blázquez et al. 2009) and the Lick/IDS library, and no systematic differences were found. Any remaining systematics in the galaxy spectra (for example flux calibration problems) would not have been corrected by the usual Lick calibration offsets, as the systematic effect would have had a different effect on stars and on galaxies (at different redshifts).

## 4.2 Emission-line contamination

Emission lines originate from the hot ionised gas in the galaxies. There is important astrophysical information contained in emission lines concerning the environment and the ionisation mechanism, as well as the physical conditions of the gas. However, their presence leads to problems in analysing the absorption lines in stellar populations. Some of the key absorption indices like $H\beta$, $H\gamma$ and $H\delta$ suffer from emission-line in-filling. Fe5015 is also affected by $[OIII]\lambda5007$[1] emission, while $Mg_b$ is affected by $[NI]\lambda5199$ emission. In the case of the Balmer lines, for example, emission fill-in can substantially weaken the line strength and lead to older derived ages.

### 4.2.1 Emission-line measurement and correction

González (1993) derived the correlation $\frac{H\beta}{[OIII]\lambda5007} = 0.7$ for his sample of elliptical galaxies. Subsequently, authors have used this together with the correlations for $H\gamma$ and $H\delta$, to estimate the emission in the affected line indices from the

---

[1]The standard notation is used, where the spectral identification is written between two square brackets for forbidden lines.
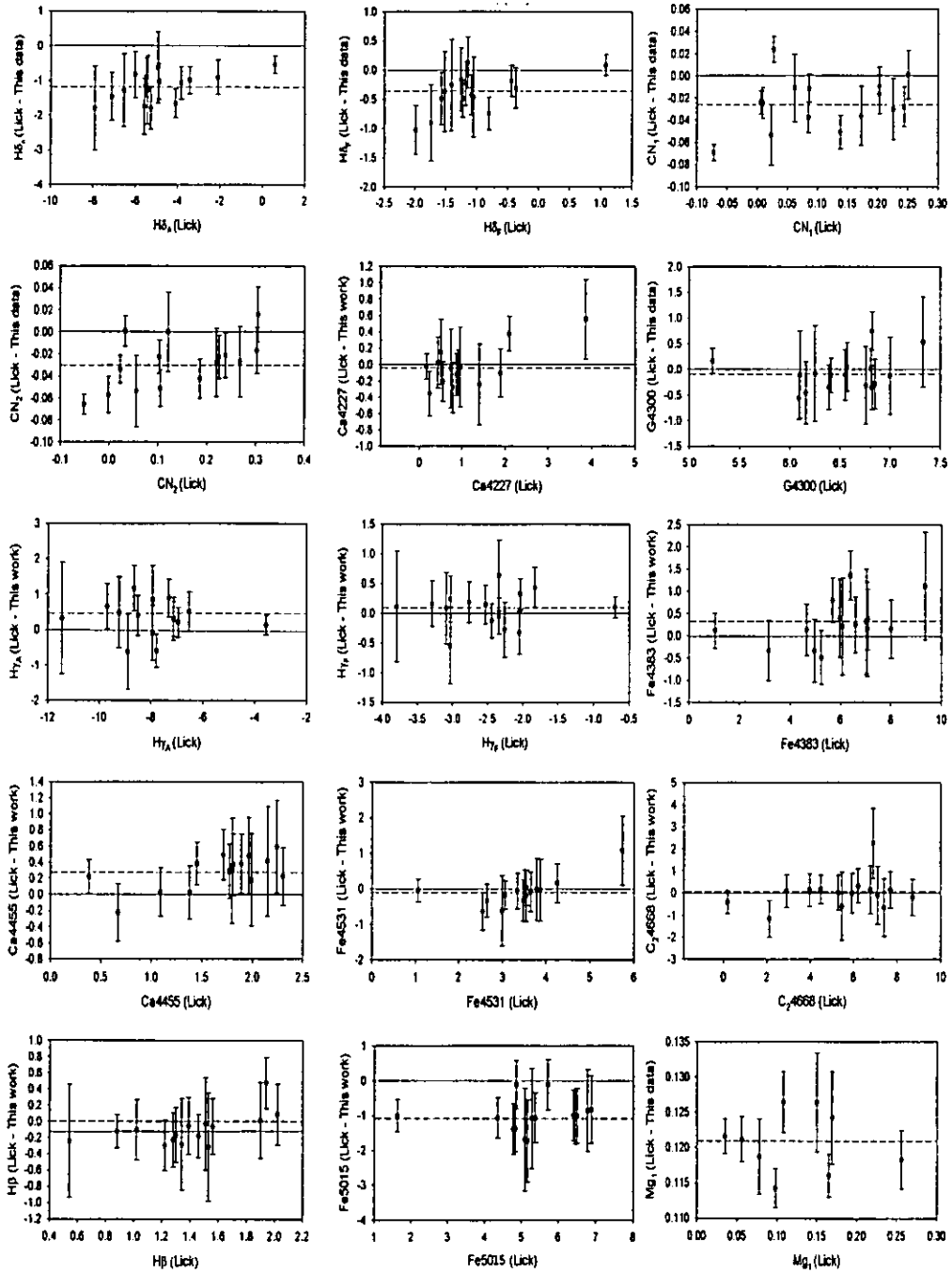
Figure 4.3: WHT offsets ($\Delta$I) derived from index measurements (original Lick data – this work) plotted against the original Lick measurements. The dashed horizontal line represents the Lick offset.
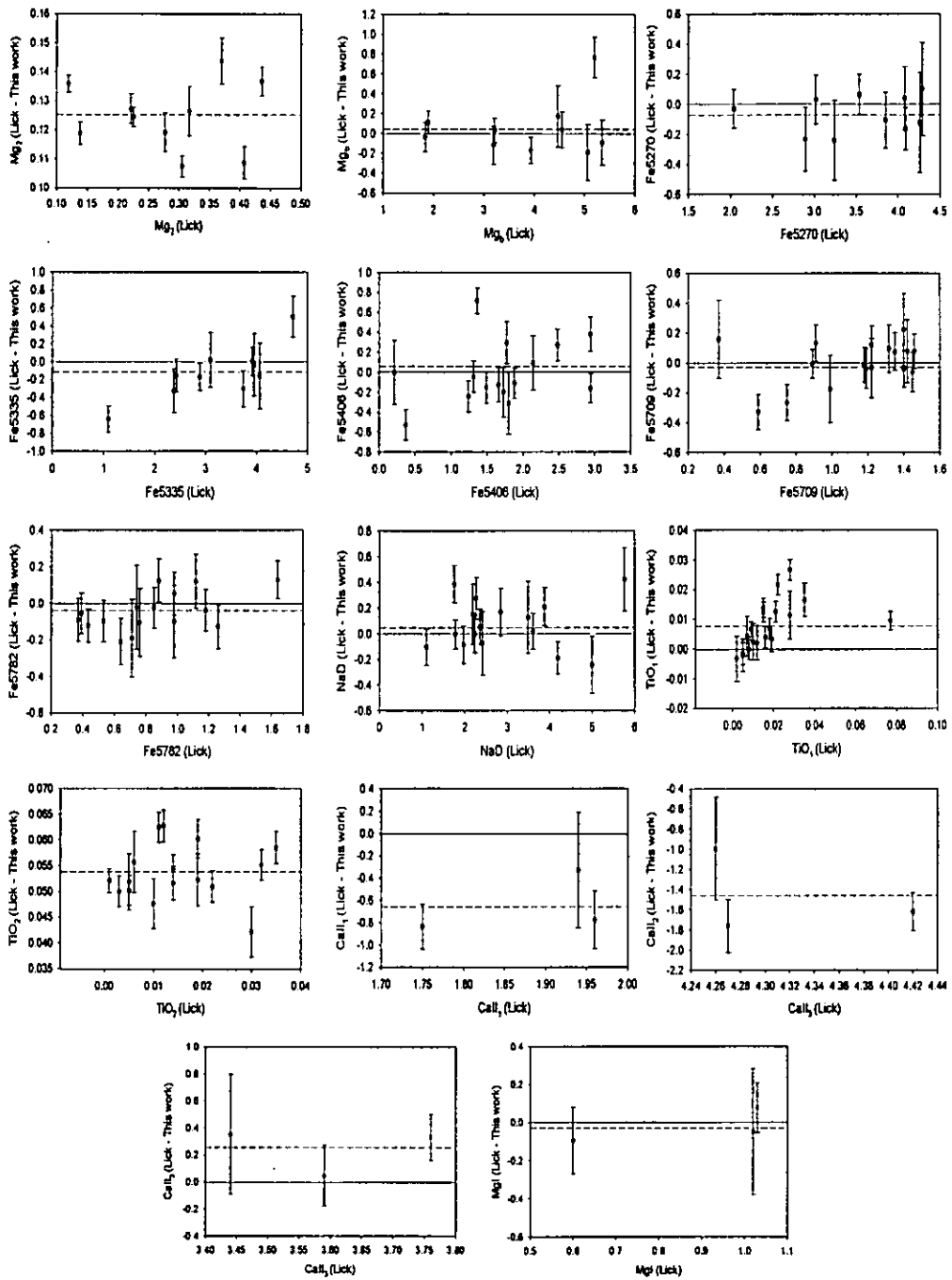
Figure 4.3 continued.
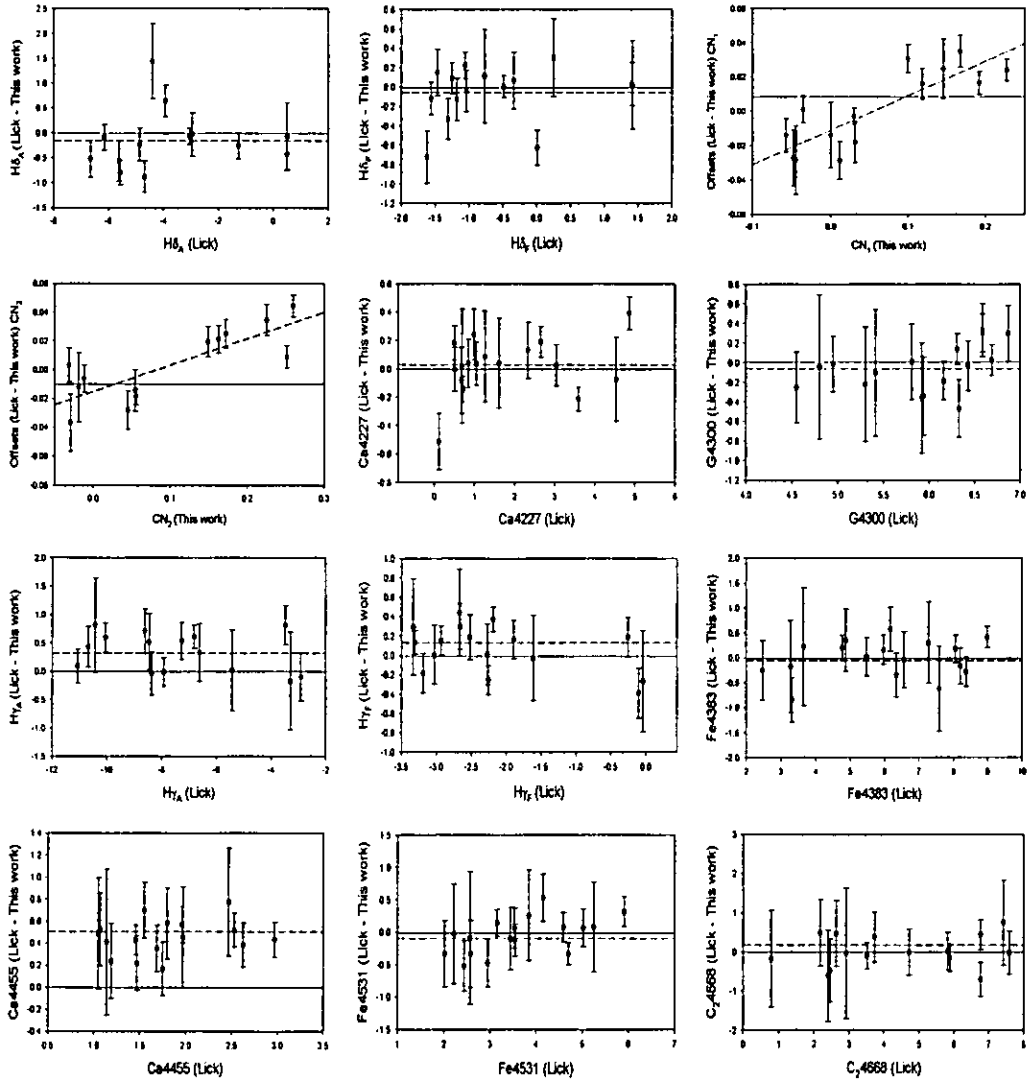
Figure 4.4: Gemini offsets ($\Delta I$) derived from index measurements (original Lick data – this work) plotted against the original Lick measurements. The dashed horizontal line represents the Lick offset.
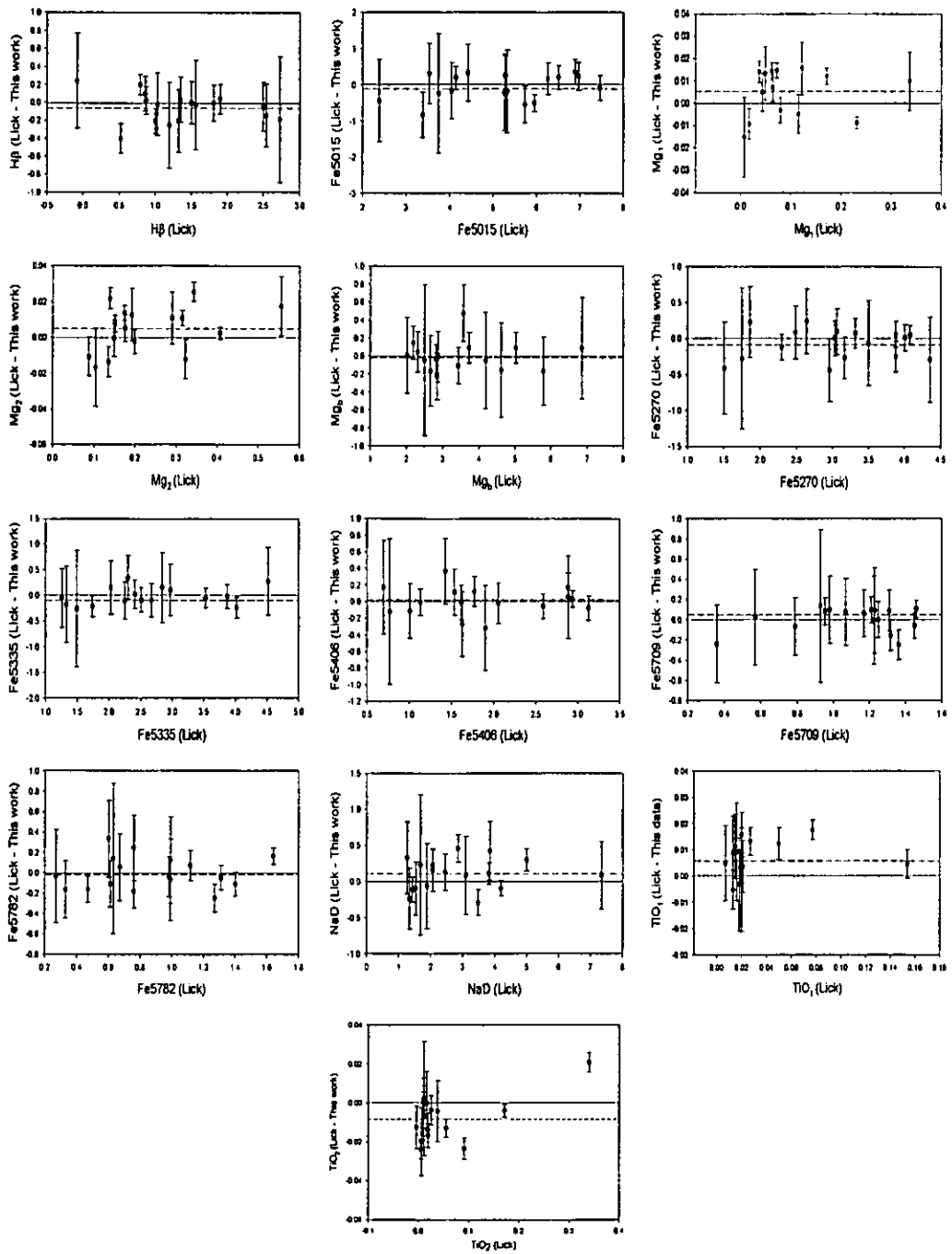
Figure 4.4 continued.
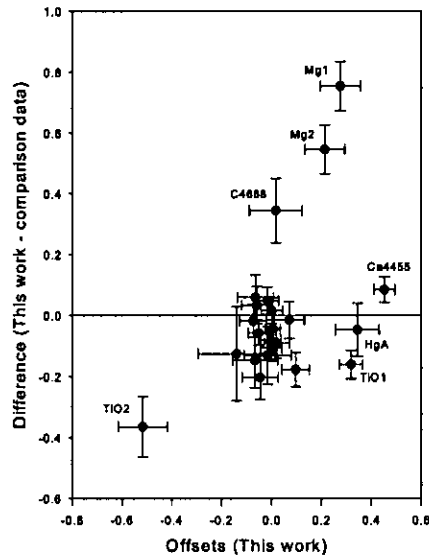
Figure 4.5: Gemini offsets (in Å) compared with M. Norris (private communication).

[OIII]$\lambda$5007 emission. Trager et al. (2000a) investigated this further, and increased the sample with more early type galaxies, to find that the $\frac{H\beta}{[OIII]\lambda5007}$ ratio varied from 0.33 to 1.25, with a median value of 0.6. They proposed a correlation of H$\beta$ = 0.6 × [OIII]$\lambda$5007; however, the correlation remains very uncertain for individual galaxies (Mehlert et al. 2000; Nelan et al. 2005). The reason is that a simple relation between H$\beta$ and [OIII] is only expected for star forming galaxies, but emission in red elliptical galaxies is very often due to AGN and low ionization nuclear emission regions (LINERS; Yan et al. 2006).

To measure the emission-line flux of the BCG spectra, an improved method called the GANDALF routine (Sarzi et al. 2006) was used. This software treats the emission lines as additional Gaussian templates, and solves linearly at each step for their amplitudes and the optimal combination of stellar templates, which are convolved by the best stellar line-of-sight velocity distribution. The stellar

continuum and emission lines are fitted simultaneously. The stellar templates used were based on the MILES stellar library (Sánchez-Blázquez et al. 2006d). The [OIII]$\lambda$5007 line was fitted first. Where H$\beta$ emission was relatively weak, the kinematics of all the other lines were tied to [OIII]$\lambda$5007, following the procedure described in Sarzi et al. (2006). This was done to avoid any spurious detections of H$\beta$ lines that might have been caused by the presence of a number of metal features around 4870 Å. However, in cases where H$\beta$ was strong enough to measure velocity and velocity dispersion, this was calculated independently as there is no a priori reason to expect the kinematics measured from the [OIII]$\lambda$5007 and H$\beta$ lines to be the same (as they can originate in different regions). After the kinematics are fixed, a Gaussian template is constructed for each emission line at each iteration, and the best linear combination of both stellar and emission-line templates (with positive weights) is determined. This is done without assuming line ratios, except in the case of doublets where their relative strength is fixed by the ratio of the corresponding transition probabilities.

The spectra of ESO349-010, MCG-02-12-039, NGC0541, NGC1713, NGC3311, NGC4874, NGC4946, NGC6166, NGC6173, NGC7012, NGC7649, NGC7720 and PGC044257 all have detectable emission lines. For these galaxies, a purely-stellar spectrum was derived by subtracting the best-fitting emission-line spectrum from the observed one. As an example, Figure 4.6 shows the H$\beta$ region of the spectrum of NGC6166 before and after the emission-line correction.

## 4.2.2 The nature of BCG emission lines

A commonly used method to distinguish between the sources of ionisation uses the emission-line diagrams pioneered by Baldwin, Phillips & Terlevich (1981) which separate the two major origins of emission: star formation and AGN. The diagrams use pairs of emission line ratios, of which the most commonly
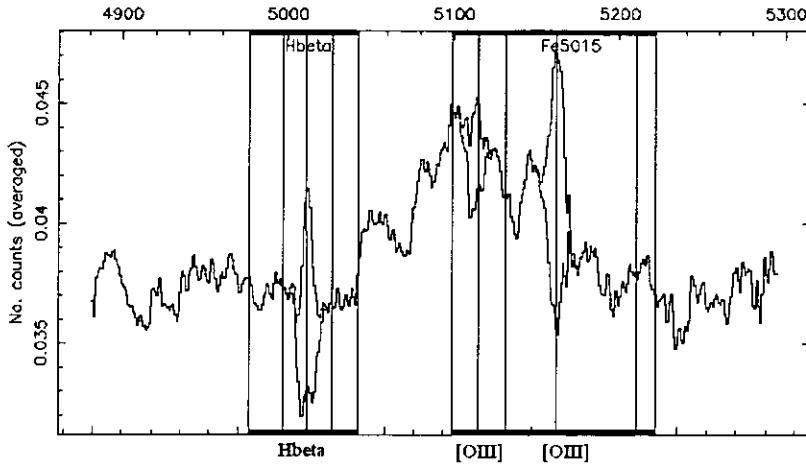
Figure 4.6: Illustration of emission line correction of NGC6166. The original spectrum (red) is plotted over the emission-corrected spectrum (black) with the affected indices (H$\beta$ and Fe5015) and their sidebands indicated.The H$\beta$ and [OIII]$\lambda\lambda$4958, 5007 emission lines are indicated by black vertical lines.
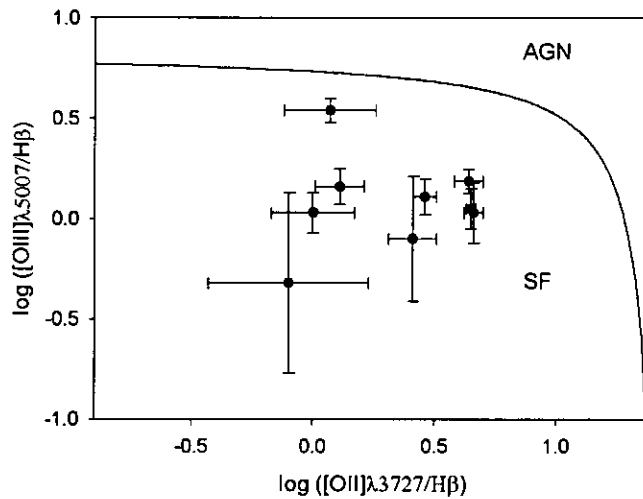


Figure 4.7: Diagnostic diagram using emission-line flux ratios to aid separation of star forming galaxies from AGN. Star forming galaxies should be located preferentially below the continuous curve (taken from Lamareille et al. 2004).

used is [OIII]$\lambda$5007/H$\beta$ against [NII]$\lambda$6584/H$\alpha$. A diagram of [OIII]$\lambda$5007/H$\beta$ against [OII]$\lambda$3727/H$\beta$ can also be used but is much less effective (Stasińska et al. 2006). The latter diagram will nevertheless be used here, due to the limits of the wavelength range. Figure 4.7 shows this diagnostic plot with all the galaxies for which H$\beta$, [OII]$\lambda$3727 and [OIII]$\lambda$5007 could be measured with at least 2$\sigma$ detections. Line fluxes, obtained with GANDALF, are used. Star forming galaxies are located preferentially below the continuous curve (Lamareille et al. 2004).

To quantify the effect of interstellar extinction on the emission line ratios plotted in Figure 4.7, the DEREDDEN task in IRAF was used together with the extinction function by Cardelli, Clayton & Mathis (1989). The parameter E($B$–$V$), i.e. the colour excess between 4350 Å and 5550 Å, for each of the galaxies plotted in Figure 4.7 was taken from the NED database (Schlegel, Finkbeiner & Davis 1998), and ranged between 0.013 and 0.140 mag. The parameter $R_V$, i.e. the ratio of the absolute extinction at 5550 Å ($A_V$) to the colour excess E($B$-$V$), was taken as 3.1 for the interstellar medium (Cardelli et al. 1989).

A similar procedure was followed to quantify the effect of galactic extinction by dust in the galaxies themselves on the line ratios plotted in Figure 4.7. The individual internal extinction parameters of the galaxies are not known. As an approximation, an average value of E($B$-$V$)$_{int}$ = 0.3 for BCGs was used. This value was calculated using the Balmer decrement measurements in the nearby BCG sample of Crawford et al. (1999). Following Edwards et al. (2009), $R_V$ = 3.1 was assumed, similar to the calculations of the galactic extinction. The DEREDDEN task was also used to estimate the effect of the internal extinction on the line ratios, and it was found that both the galactic and internal extinction corrections were not significantly large to move any of the datapoints plotted in Figure 4.7 above the continuous curve, and hence, does not influence the result.

All nine emission-line galaxies in the present work for which these three lines

could be measured should be star forming galaxies according to this test. BCGs are known to be more likely to host radio-loud AGN than any other galaxy with the same stellar mass (Burns 1990; Best et al. 2007). This is especially true if they are hosted by cooling-flow clusters (Burns et al. 1997). However, Best et al. (2007) argue that radio-loud AGN and emission-line AGN (detectable through optical emission lines) are independent, unrelated phenomena. Edwards et al. (2007) found, in their sample of BCGs, that the emission was mostly LINER-like or a combination of LINER and star formation, and concluded that this emission was directly related to the cooling of X-ray gas at the cluster centre. Von der Linden et al. (2007) found emission lines in more than 50 per cent of their sample, although the four lines that they used as a diagnostic could only be measured with a S/N > 3 in 30 per cent of their sample. From this subsample, only 6 per cent were star forming galaxies, 70 per cent LINERs and 24 per cent composite objects (star forming and LINER).

Because the diagnostic diagram used here in Figure 4.7 is much less effective at separating different sources of ionisation (Stasińska et al. 2006), and because the fraction of the current sample containing emission lines is relatively small, and with weak emission lines, it is too early to draw detailed conclusions about the nature of emission lines in BCGs.

Of the nine emission-line galaxies in this sample for which cooling-flow information is available (see Table 5.1), five are hosted by clusters with cooling flows and four are hosted by clusters without cooling flows. Edwards et al. (2007) found that the frequency of BCGs showing optical emission lines in their sample increased in cooling-flow clusters (70 per cent versus 10 per cent in non-cooling flow clusters), regardless of the mass density or velocity dispersion of the cluster. This is also true here, where the corresponding fractions are 33 per cent in

cooling-flow clusters and 21 per cent in non-cooling clusters, although the difference in the fractions are not as pronounced. One possible cause of this difference could be that the fraction of BCGs with emission lines changes with the distance between the BCG and the cluster X-ray centre (Edwards et al. 2007; Best et al. 2007; also see Section 5.4).

## 4.3 Indices

The Lick indices were measured according to the equations set out in Section 1.3.1 and their errors according to the error equations presented in Cardiel et al. (1998b), Vazdekis & Arimoto (1999) and Cenarro et al. (2001).

To investigate the possible effects different software codes and different offsets can have on the derived SSP-parameters, index measurements obtained from two different codes and with two different sets of applied offsets were compared. Figures 4.8 and 4.9 show some examples (for one molecular and one atomic index), comparing the index measurements obtained with two publicly available codes: LECTOR (by A. Vazdekis and used here) and offsets derived here, and IN-DEX (Cardiel 1999) and the MILES offsets (Sánchez-Blázquez et al. 2009). The RED$_{\text{m}}^{\text{uc}}$E index measurement software (INDEX) uses velocities which have been relativistically corrected, whereas the software used here (LECTOR) needs the classical velocities as input values. These velocity differences were taken into account during the comparison and throughout the index measurement process to ensure accurate measurements. The differences in the measurements are plotted as a function of velocity dispersion and radial velocities. In order to clearly detect the difference caused by using two different sets of offsets (the offsets derived here versus the MILES offsets), only the Gemini data are plotted. Different sets of offsets were derived for the WHT and Gemini data (Tables 4.1 and 4.2), and
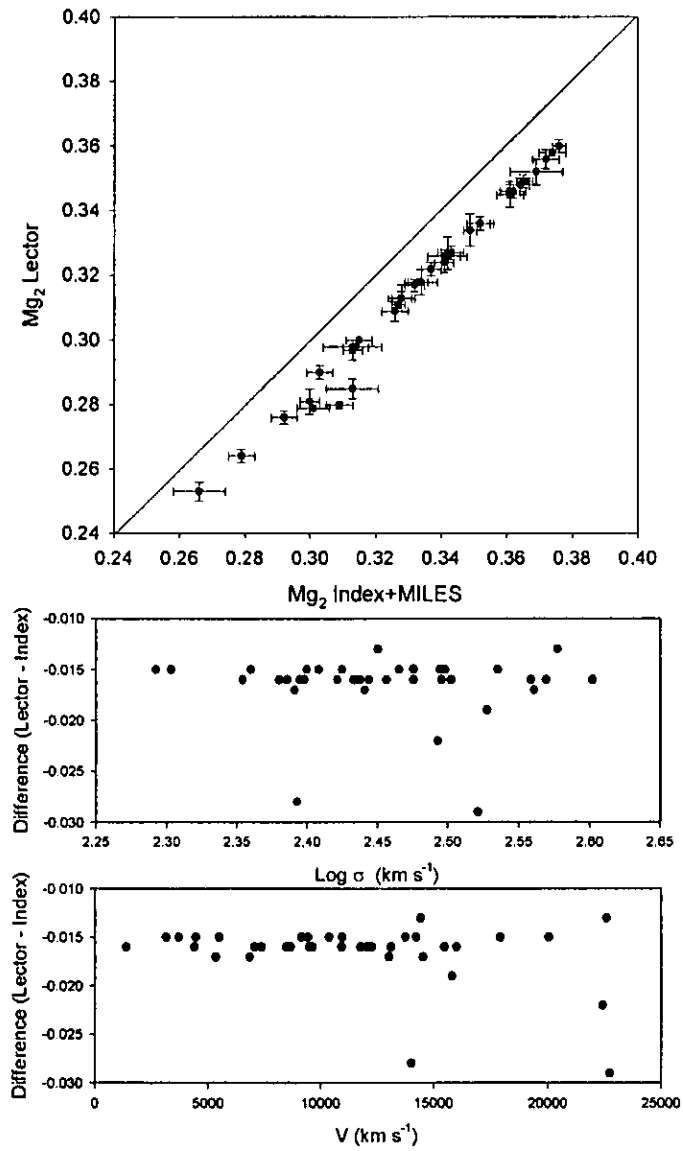
Figure 4.8: Comparison of $Mg_2$ index values using different index measurement software and offsets.
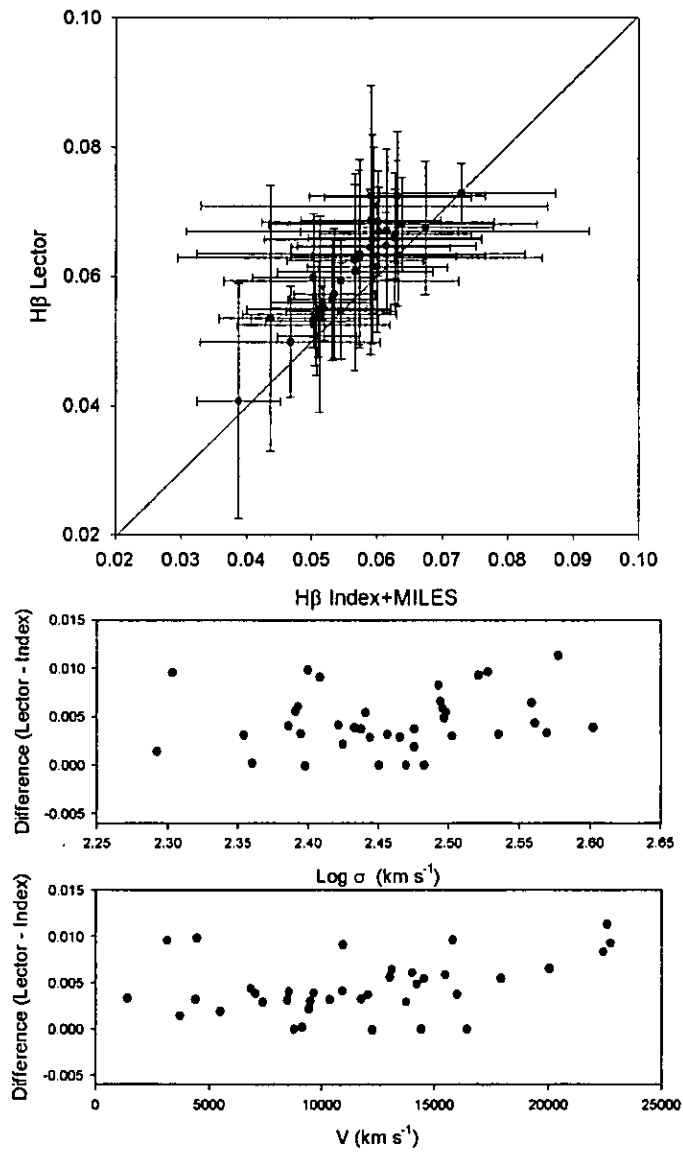
Figure 4.9: Comparison of H$\beta$ index values using different index measurement software and offsets.

they were separately compared with the MILES offsets. Except for the obvious systematic difference caused by the different offsets, no difference could be detected between the molecular indices measured with the two different codes. The differences in the atomic indices appear more scattered, but no strong, clear relationship with velocity or velocity dispersion could be seen. To test the effect these small index differences will have on the results derived in this study, SSP-parameters were derived with both sets of index measurements (using $H\beta$, $Mg_b$, Fe5270 and Fe5335 according to the method described in Section 4.4). The SSP-parameters were compatible within their errors, and it was concluded that the choice of index measurement software and offsets applied in this study did not influence the results.

As in the case of the central kinematic measurements, the central indices were measured for regions with the size of $a_e/8$, and with the galaxy centres defined as the luminosity peaks. The index error measurements were obtained using the variance frames and thus take into account both Poisson and systematic errors (flux calibration effects; velocity dispersion errors; sky subtraction uncertainties; and radial velocity errors). The errors derived on the offsets (shown in Tables 4.1 and 4.2) are not taken into account for the index measurements; they are however taken into account in the SSP-analysis in the case where the multi-index method is used. Table 4.3 shows the S/N ratios in the central apertures ($a_e/8$) of all the galaxies, as measured in the $H\beta$ wavelength region in the spectrum.

## 4.3.1 Comparison with previous measurements

All the central index values and corresponding errors are presented in Table C.1 (index measurements from $H\delta_A$ to $C_24668$) and Table C.2 ($H\beta$ to $TiO_2$) in Appendix C. Five indices ($Mg_1$, $Mg_2$, $Mg_b$, Fe5270 and Fe5335) could not be measured in NGC6047 since no spectrum of this galaxy was taken with the 6100 Å

| Galaxy | S/N ratio | Galaxy | S/N ratio | Galaxy | S/N ratio |
|---|---|---|---|---|---|
| ESO146-028 | 93 | NGC0541 | 83 | NGC7012 | 107 |
| ESO202-043 | 26 | NGC1399 | 502 | NGC7597 | 41 |
| ESO303-005 | 75 | NGC1713 | 109 | NGC7647 | 66 |
| ESO346-003 | 63 | NGC2832 | 148 | NGC7649 | 56 |
| ESO349-010 | 84 | NGC3311 | 60 | NGC7720 | 80 |
| ESO444-046 | 43 | NGC3842 | 142 | NGC7768 | 94 |
| ESO488-027 | 131 | NGC4839 | 88 | PGC004072 | 32 |
| ESO541-013 | 16 | NGC4874 | 87 | PGC025714 | 28 |
| ESO552-020 | 90 | NGC4889 | 173 | PGC026269 | 52 |
| GSC555700266 | 72 | NGC4946 | 138 | PGC030223 | 46 |
| IC1101 | 27 | NGC6034 | 100 | PGC044257 | 38 |
| IC1633 | 299 | NGC6047 | 48 | PGC071807 | 42 |
| IC4765 | 63 | NGC6086 | 49 | PGC072804 | 71 |
| IC5358 | 165 | NGC6160 | 42 | UGC00579 | 24 |
| LEDA094683 | 70 | NGC6166 | 63 | UGC02232 | 69 |
| MCG-02-12-039 | 94 | NGC6173 | 57 | UGC05515 | 75 |
| NGC0533 | 96 | NGC6269 | 80 | UGC10143 | 48 |

Table 4.3: S/N ratios in the central apertures ($a_e/8$) of all the galaxies, as measured in the H$\beta$ region in the spectrum.

dichroic during the WHT observations (due to time constraints). For most of the Gemini galaxies, the TiO$_2$ sideband is redshifted out of the spectral range. For three of these galaxies, their recession velocity is also large enough to cause the sideband of TiO$_1$ to be shifted outside the spectral range, and for the rest of the Gemini galaxies TiO$_1$ is very close to the edge of the spectrum. The spectra were visually inspected, and five galaxies (LEDA094683, NGC7649, NGC6166, PGC025714 and PGC030223) showed either residuals of sky line removal or residuals where the gaps between the CCDs were added in the important indices Mg$_b$, Fe5270 or Fe5335; hence they were also excluded from any further analysis using those indices.

The central index measurements were compared with those of T98 and Lee & Worthey (2005, hereafter LW05) for 14 galaxies which the samples had in common (Figure 4.10). The measurements of the original 21 Lick indices were presented in T98, and the four higher-order Balmer indices (of the same galaxy sample) in

LW05. The central values of the T98 sample were measured in an aperture of 1.4 × 4 arcsec$^2$. Only one of the 14 galaxies had TiO$_2$ measurements in both T98 and this sample, so no comparison of TiO$_2$ measurements were made. Galaxies with large differences in certain indices (for example a few Fe5270 measurements) were compared on an individual basis (S. Trager, private communication), and can be attributed to lower S/N data in the T98 sample.

The central index measurements were also compared with those of SB06 for five galaxies in common (also indicated in Figure 4.10). For this comparison, the same central aperture of the galaxies was extracted and 16 indices measured by P. Sánchez-Blázquez (private communication). Nine index measurements for five galaxies were also compared with those in Ogando et al. (2008, hereafter OG08). The indices from OG08 were measured within a metric circular aperture equivalent to 1.19 kpc at the distance of the Coma cluster. No flux calibration was applied to these galaxies. No separate comparisons between the six different observing runs (WHT, Gemini North 06B and 07A, Gemini South 06B, 07A and 07B) and T98, SB06 or OG08 could be made since there were too few galaxies in common.

In total, index measurements of 15 galaxies (some of the galaxies being in common with more than one of the above-mentioned samples) could be compared, and are all shown in Figure 4.10. This comparison shows that the H$\delta_A$ index measurements in the Gemini data are systematically higher (by 1 − 2 Å) compared with previous measurements, and shows a large amount of scatter. This index will not be used here in the stellar population analysis, since it will lead to overestimated SSP-equivalent ages. No other systematic differences were found. With the exception of the TiO$_1$ index, which was often very close to the edge of the spectrum in the BCG data, all the index comparison plots show scatter that is smaller than that expected from the errors on the index measurements.
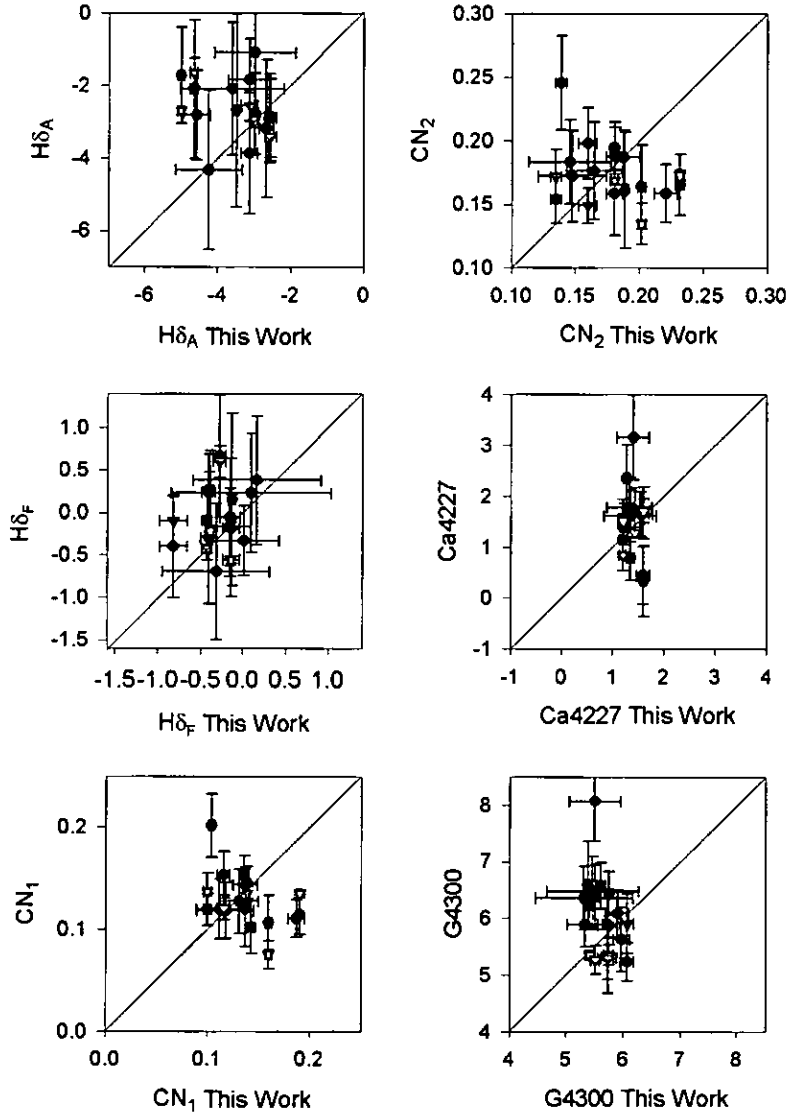
Figure 4.10: Central index measurements compared with T98 and LW05 (black circles) for 14 galaxies in common, SB06 (red triangles) for five galaxies in common and OG08 (green circles) for five galaxies in common. All index measurements are in Å, except CN, $Mg_{1+2}$, and TiO which are in magnitudes.
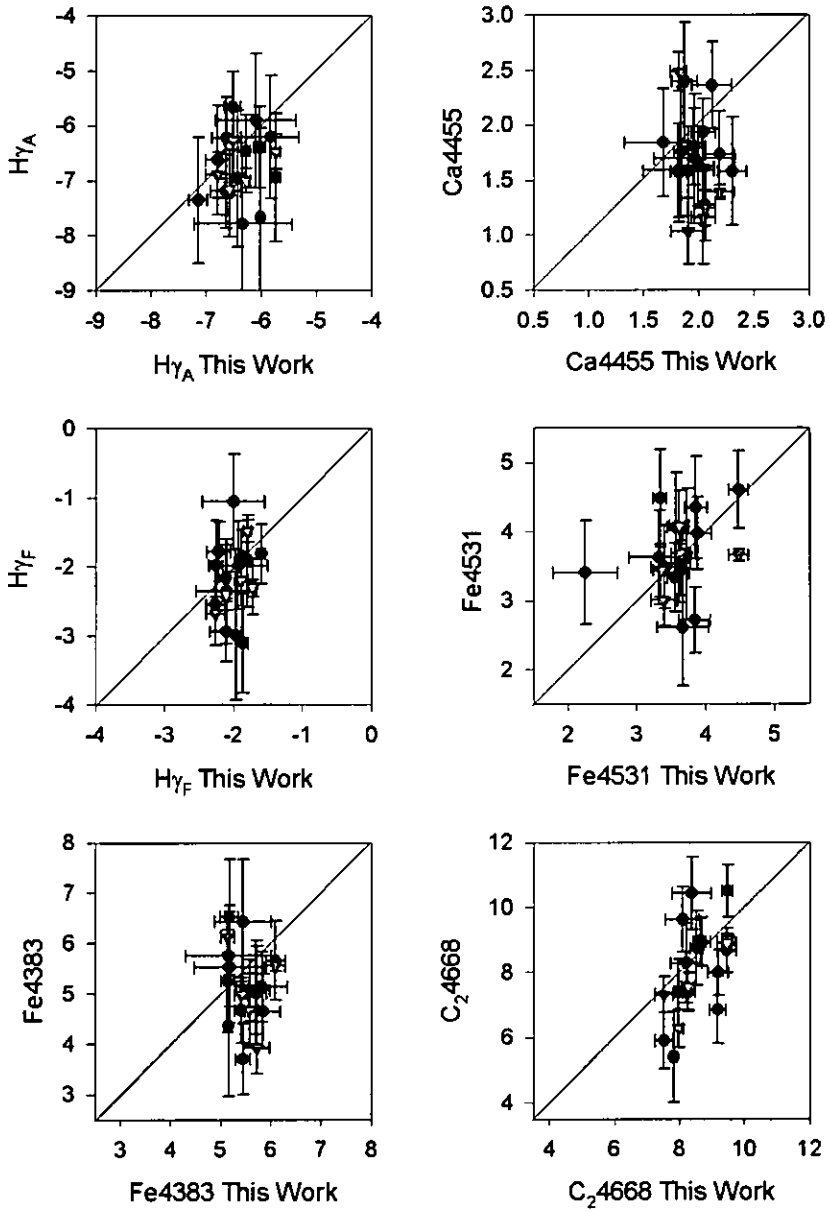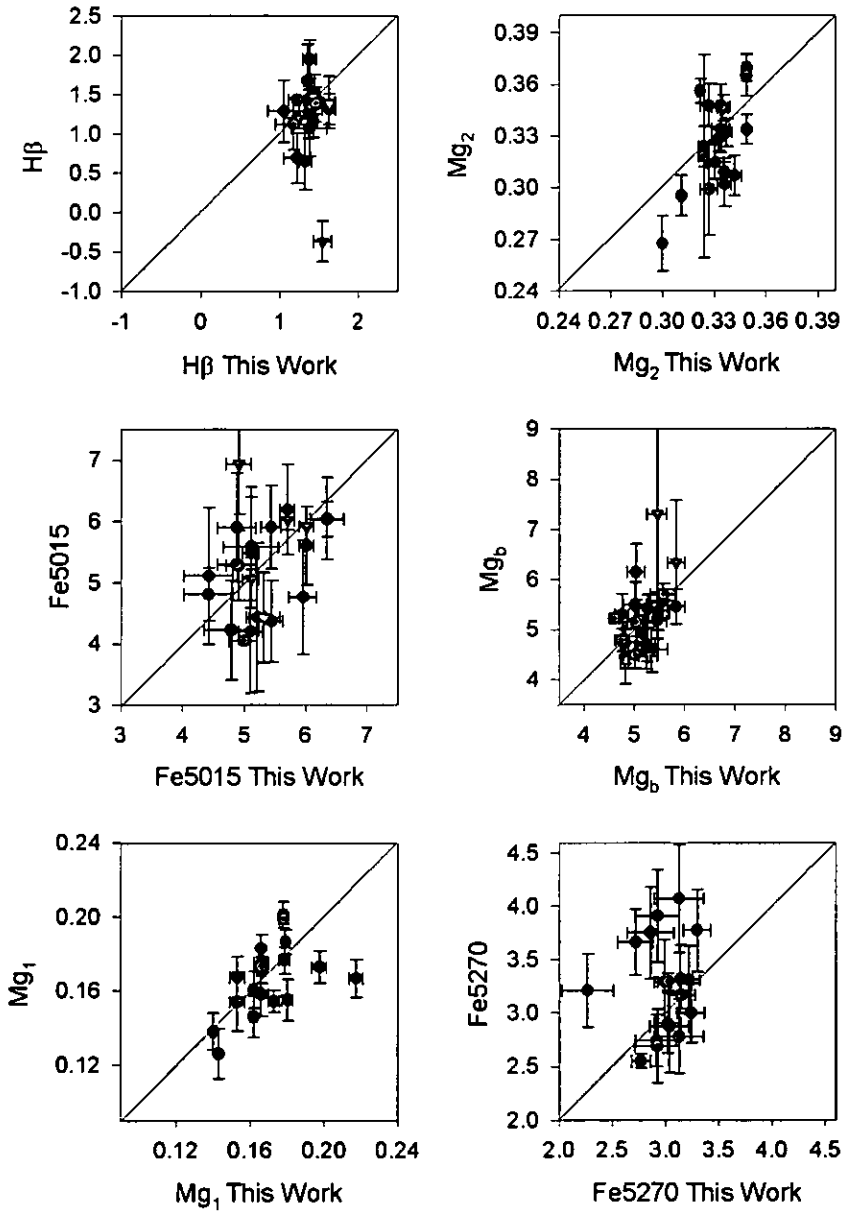
Figure 4.10 continued.

Figure 4.10 continued.
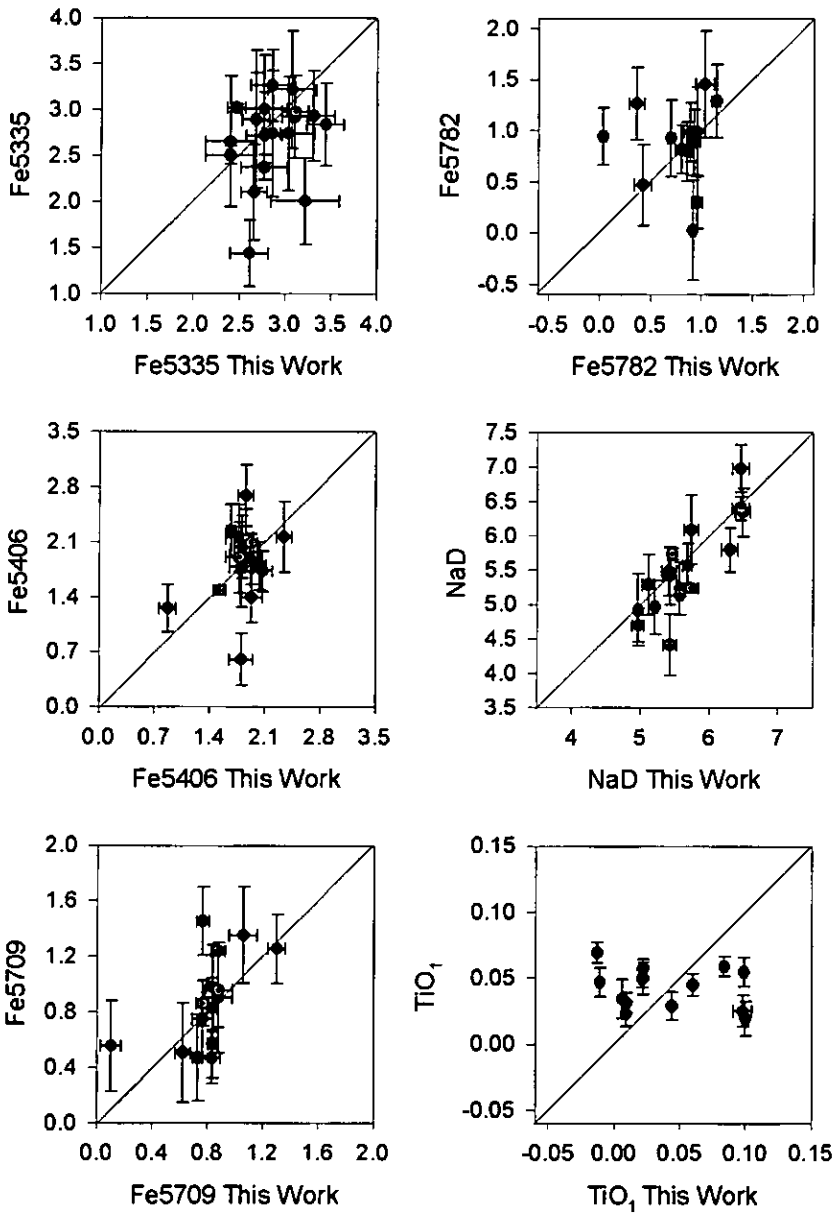
Figure 4.10 continued.

The above-mentioned studies did not include any near-IR index measurements, so no comparison could be made. Since these near-IR indices are not part of the system of 25 Lick indices for which the models used in this study were derived, they are excluded from further analysis.

## 4.3.2 Correlations between kinematics and indices

In this section, the least-squares best-fitting straight lines found for the relations between the indices and velocity dispersion of the BCGs will be compared with those found for ordinary ellipticals.

Early-type galaxies show a well-known positive correlation between the $Mg_2$ index and the velocity dispersion (González 1993; Concannon, Rose & Caldwell 2000; Proctor & Sansom 2002; Vazdekis 2005). Classically, this $Mg_2$–velocity dispersion relation has been interpreted as a relation between mass and metallicity, though much debate exists as to whether this relation reflects trends in stellar ages, in metallicities or in the relative abundance of different heavy elements (e.g. SB06, and references therein). The mass–metallicity relation is thought to exist because more massive galaxies have larger amounts of enriched gas expelled in supernova events, which in turn increases the metallicity of the material from which new stars are formed. The low scatter in this relation has also been used to suggest that all early-type galaxies have nearly-coeval stellar populations (Bernardi et al. 1998). However, later studies conclude that the low scatter is due to the degeneracy between the age and metallicity, i.e. that younger galaxies are also more metal rich (SB06).

The slopes of such correlations between indices and velocity dispersion measured by different authors are generally found to be in agreement, but offsets vary from author to author. This could be due to differences in calibration, or differences in aperture size and orientation or in methods of estimating velocity

dispersion (as previously discussed in Section 3.2).

Following various other authors, and to compare with the elliptical galaxy sample of SB06, the atomic indices are expressed here in magnitudes. These are denoted by the index name followed by a prime sign, and their values were obtained by using Equation 1.4.

Figure 4.11 shows all indices (except $TiO_2$) plotted against the velocity dispersion of the galaxies. For 16 of these indices, the index–velocity dispersion relation found by SB06 for a large sample of elliptical galaxies are also indicated. The complete SB06 sample consists of 98 galaxies, of which 35 belong to the Coma cluster, and the rest are galaxies in the field, in groups or in the Virgo cluster. Two relations per index were derived by SB06: one for ellipticals in a higher density environment, and one for ellipticals in a lower density environment. Here, both the higher and lower density samples are combined for comparison with the BCG data, since some of the BCGs are in Virgo-equivalent environments. As mentioned in the previous section, five galaxies were in common with SB06. Four of those are in the higher density sample and one in the lower density sample.

The BCG data are spread over a much narrower range in velocity dispersion ($\log \sigma = 2.3$ to $2.6$ km s$^{-1}$) than the SB06 sample ($\log \sigma = 1.4$ to $2.6$ km s$^{-1}$). This makes a quantitative comparison with the SB06 sample more difficult, as the slopes of the SB06 correlations could be heavily influenced by the lower velocity dispersion galaxies. The velocity dispersion distributions of the two samples are shown in Figure 4.12. A Kolmogorov-Smirnov test was performed on the velocity dispersion distributions of the two samples within the $\log \sigma = 2.3$ to $2.6$ km s$^{-1}$ range, where the null hypothesis is that the distributions were drawn from an identical parent population. Within this limited range, the two velocity dispersion distributions are consistent (see Section 4.4.1 for the detailed description and results of this test). New straight-line least-squares fits between the indices

and velocity dispersion were derived for the SB06 sample, including only those elliptical galaxies in the same mass range as the BCG sample, and excluding the five known BCGs in the SB06 sample (P. Sánchez-Blázquez, private communication). Details of these are given in Table 4.4. Both relations derived for the SB06 sample are shown in Figure 4.11: the new relation found for the SB06 elliptical sample over the same mass range as the BCG sample, as well as the relation for the complete SB06 elliptical sample (high and low density samples combined).

The amount of scatter in the $CN_1$, $CN_2$, $Mg_1$, $Mg_2$, NaD and $TiO_1$ plots is large. The molecular indices are known to show only a small amount of scatter (Concannon et al. 2000), but are frequently affected by systematic flux calibration errors since the index definitions span a broad wavelength range.

Straight line fits ($I' = a + b \times \log \sigma$) were made to the BCG data plotted in Figure 4.11 with a least-squares fitting routine, and are given in Table 4.4. Statistical t-tests were run on all the fits to assess if a significant slope was present or if $b = 0$ (as a null hypothesis). A $t$ value larger than 1.96 indicates that there is a true correlation between the variables ($b \neq 0$), at a 95 per cent confidence level. $P$ is the probability of being wrong in concluding that there is a true correlation (i.e. the probability of falsely rejecting the null hypothesis). As can be seen form Table 4.4 only six out of 18 indices (excluding CN, $Mg_{1+2}$, NaD, TiO) show a statistically significant correlation with velocity dispersion. Those are Ca4227, $H\gamma_F$, Ca4455, Fe4531, $C_24668$ and $Mg_b$.

Most of the fitted relations for BCGs agree with those for the SB06 elliptical galaxies. The only indices where there is a significant difference is in G4300 and $C_24668$, where the BCG datapoints are on average higher than the SB06 elliptical data. For $C_24668$, this may be explained by the offsets applied to the data, as the $C_24668$ offset applied to the BCG data is higher than the equivalent offset in SB06 by $\sim 0.025$ Å. The offsets, however, do not explain the discrepancy in
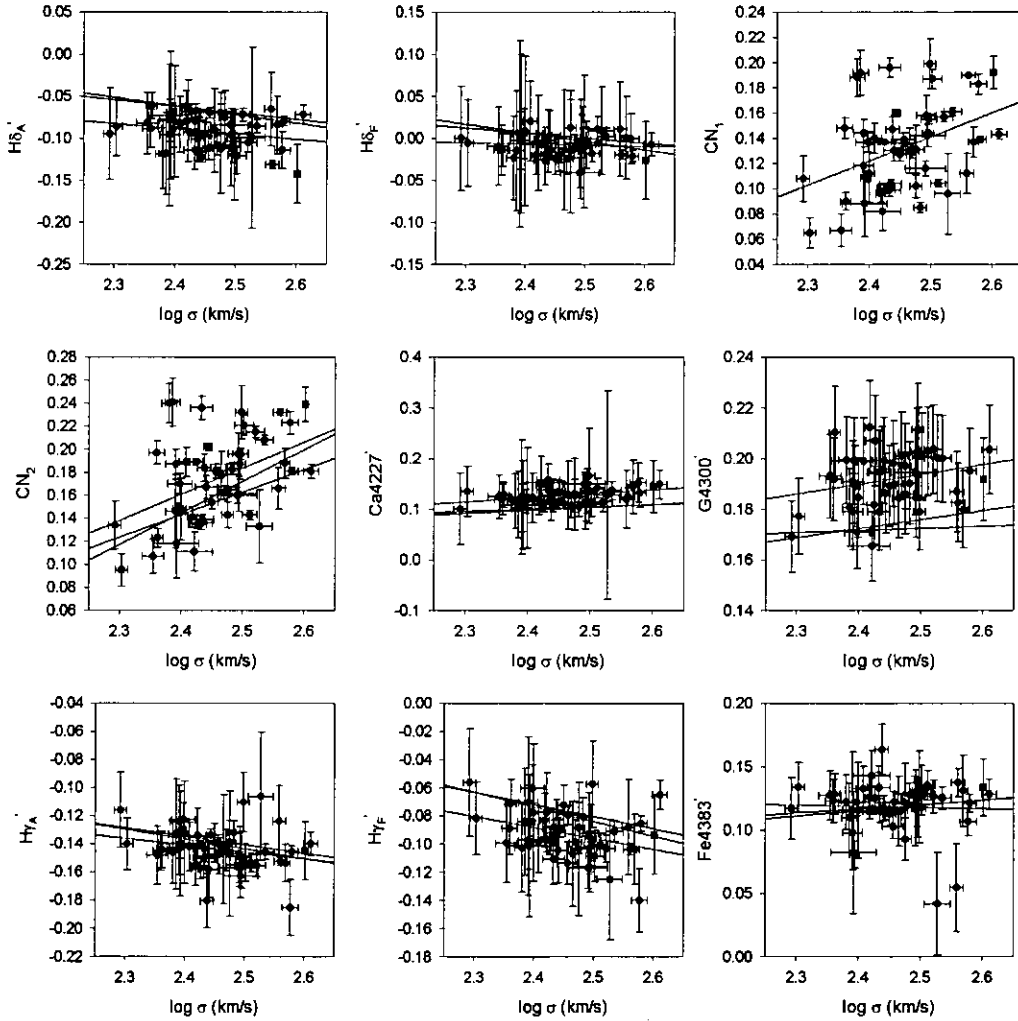
Figure 4.11: Central index measurements against velocity dispersion. The straight lines fitted to the BCG data are in red. The blue lines denote the relations found for the SB06 elliptical sample in the same mass range, and the green line the relation for the complete SB06 elliptical sample (high and low density samples combined).
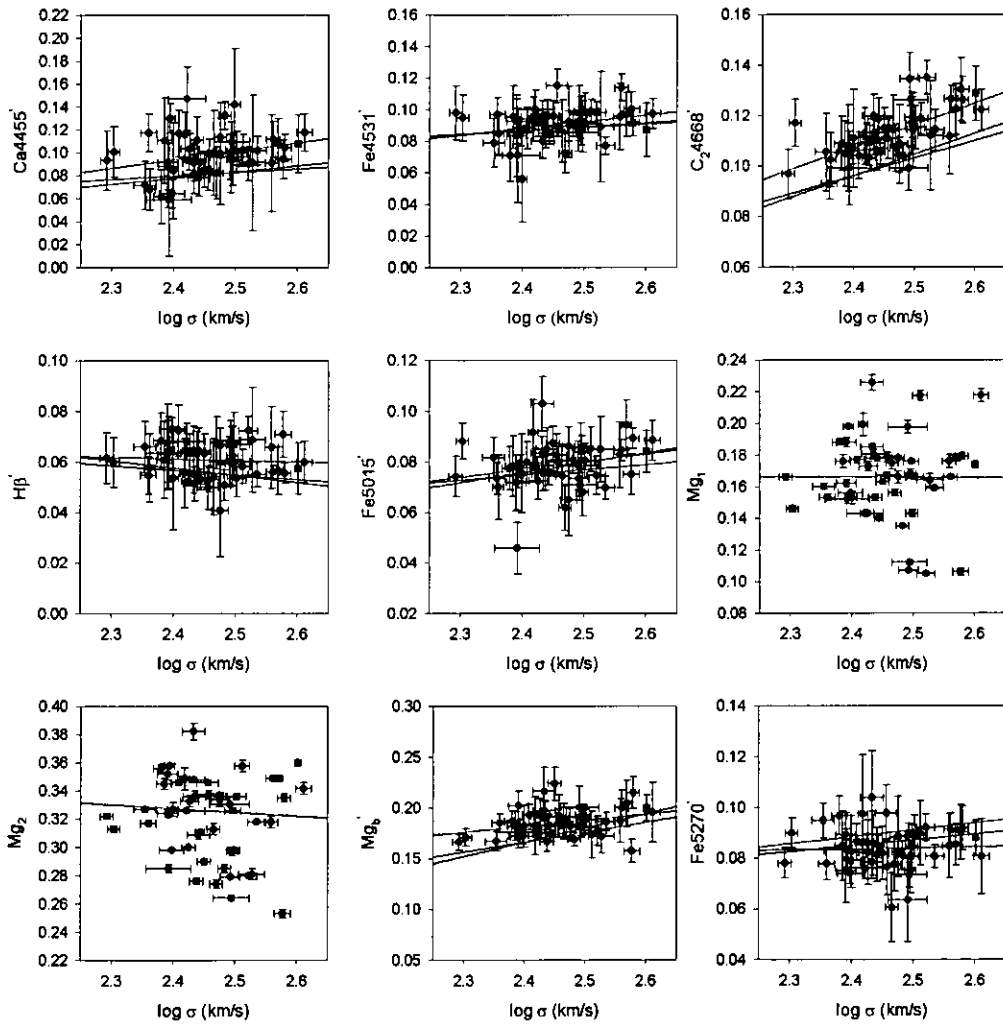
Figure 4.11 continued.
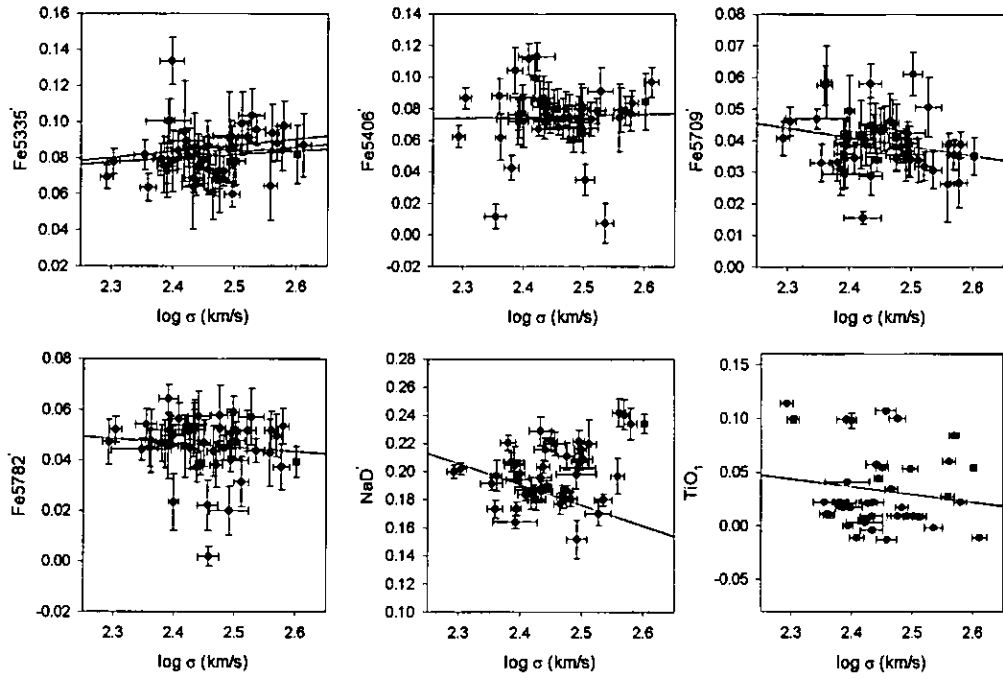
Figure 4.11 continued.
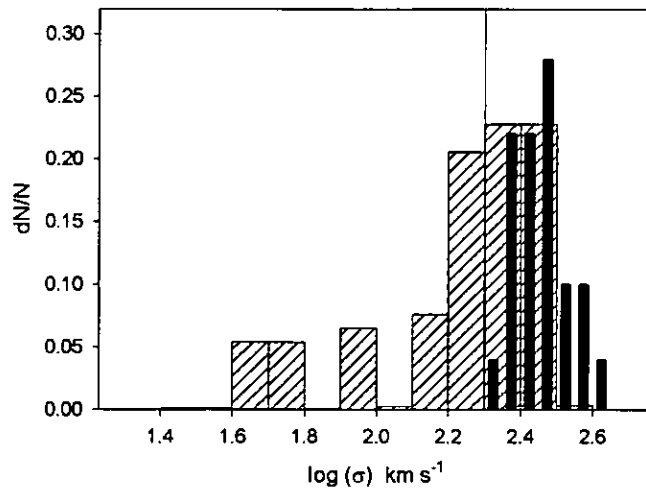


Figure 4.12: The velocity dispersion distributions of the complete SB06 (red) and the BCG sample (cyan). The vertical line indicates the lower limit in velocity dispersion ($\log \sigma = 2.3$ km s$^{-1}$) of the SB06 subsample used here for comparison.

the G4300 index where the BCG data offset is even lower than the one applied to the elliptical data. The BCG G4300 measurements are on average 0.017 mag higher than the elliptical galaxy measurements, independent of the set of offsets (MILES offsets or the offsets derived here) applied to the data. In summary, with the exception of G4300, there are no significant discrepancies between the index–velocity dispersion relations for the BCG data and those for normal ellipticals in the same mass range.

The only Balmer index–velocity dispersion plot with a statistically significant (negative) slope is $H\gamma_F$. All the other Balmer indices are consistent with being flat. None of the other index–velocity dispersion plots with significant slopes were found to be decreasing. This is consistent with the results of previous work, for example SB06 and OG08, who found that the Balmer indices are the only ones that decrease with increasing velocity dispersion. The previously well-known $Mg_2$–velocity dispersion relation can not be seen in Figure 4.11 because the mass range is very limited compared with the previously mentioned studies of normal elliptical galaxies.

Values for the intrinsic scatter in the measured indices values were derived by comparing the measured standard error on the mean index value with that expected from the mean index errors (Table 4.5). $\sigma_{std}$ is the standard deviation on the mean index value, $\sigma_{exp}$ is the standard deviation expected from the mean errors on the index values, and $\sigma_{res} = \sqrt{\sigma_{std}^2 - \sigma_{exp}^2}$ is the residual scatter not explained by the errors on the index measurements. Those indices marked with $\star$ have $\sigma_{std} \leq \sigma_{exp}$, indicating that the errors on at least some index measurements were slightly overestimated. The table also shows that the intrinsic scatter in the molecular indices is large.

The same process was then repeated, but this time calculating the intrinsic scatter of the points around the fitted straight lines for the BCGs and the SB06

| Index | BCG Galaxies | | | | | Ellipticals | |
|---|---|---|---|---|---|---|---|
| | $a \pm$ std err($a$) | $b \pm$ std err($b$) | $t$ | $P$ | Mean $\pm$ std err | $a \pm$ std err($a$) | $b \pm$ std err($b$) |
| $H\delta_A'$ | 0.060±0.090 | -0.062±0.037 | 1.687 | 0.098 | -0.093±0.020 | 0.184±0.016 | -0.102±0.007 |
| $H\delta_F'$ | 0.028±0.059 | -0.015±0.024 | 0.603 | 0.550 | -0.008±0.016 | 0.251±0.018 | -0.102±0.008 |
| $CN_1$ | -0.337±0.151 | 0.191±0.061 | 3.115 | 0.003 | 0.133±0.035 | | |
| $CN_2$ | -0.383±0.159 | 0.227±0.065 | 3.500 | 0.001 | 0.174±0.038 | -0.514±0.033 | 0.274±0.015 |
| $Ca4227'$ | -0.070±0.068 | 0.080±0.028 | 2.887 | 0.006 | 0.127±0.016 | -0.044±0.015 | 0.059±0.007 |
| $G4300'$ | 0.097±0.050 | 0.039±0.020 | 1.893 | 0.065 | 0.192±0.011 | 0.152±0.016 | 0.008±0.007 |
| $H\gamma_A'$ | -0.026±0.067 | -0.048±0.027 | 1.758 | 0.085 | -0.144±0.015 | 0.009±0.017 | -0.060±0.007 |
| $H\gamma_F'$ | 0.099±0.075 | -0.078±0.030 | 2.570 | 0.013 | -0.093±0.017 | 0.135±0.023 | -0.086±0.010 |
| $Fe4383'$ | 0.140±0.095 | -0.009±0.039 | 0.235 | 0.815 | 0.118±0.020 | 0.014±0.008 | 0.042±0.003 |
| $Ca4455'$ | -0.083±0.084 | 0.074±0.034 | 2.142 | 0.037 | 0.098±0.019 | -0.049±0.009 | 0.053±0.004 |
| $Fe4531'$ | -0.014±0.046 | 0.042±0.019 | 2.266 | 0.028 | 0.090±0.010 | 0.027±0.005 | 0.025±0.002 |
| $C_24668'$ | -0.099±0.033 | 0.086±0.014 | 6.317 | <0.001 | 0.113±0.009 | -0.103±0.011 | 0.083±0.005 |
| $H\beta'$ | 0.075±0.033 | -0.006±0.013 | 0.448 | 0.656 | 0.061±0.001 | 0.100±0.012 | -0.018±0.005 |
| $Fe5015'$ | 0.004±0.041 | 0.031±0.017 | 1.819 | 0.075 | 0.079±0.010 | -0.018±0.013 | 0.039±0.006 |
| $Mg_1$ | 0.172±0.125 | -0.003±0.051 | 0.051 | 0.960 | 0.166±0.026 | | |
| $Mg_2$ | 0.407±0.137 | -0.035±0.056 | 0.630 | 0.532 | 0.321±0.029 | | |
| $Mg_b'$ | 0.041±0.061 | 0.059±0.025 | 2.383 | 0.021 | 0.185±0.014 | -0.169±0.015 | 0.140±0.007 |
| $Fe5270'$ | 0.074±0.040 | 0.004±0.016 | 0.253 | 0.801 | 0.084±0.008 | 0.029±0.007 | 0.023±0.003 |
| $Fe5335'$ | 0.013±0.063 | 0.028±0.026 | 1.093 | 0.280 | 0.082±0.014 | 0.030±0.044 | 0.009±0.004 |
| $Fe5406'$ | 0.055±0.091 | 0.008±0.037 | 0.225 | 0.823 | 0.075±0.019 | | |
| $Fe5709'$ | 0.111±0.040 | -0.029±0.016 | 1.783 | 0.081 | 0.040±0.009 | | |
| $Fe5782'$ | 0.088±0.052 | -0.017±0.021 | 0.812 | 0.421 | 0.046±0.011 | | |
| $NaD'$ | 0.543±0.331 | -0.146±0.135 | 1.090 | 0.282 | 0.183±0.071 | | |
| $TiO_1$ | 0.208±0.172 | -0.071±0.070 | 1.026 | 0.311 | 0.033±0.036 | | |

Table 4.4: Parameters of the indices versus velocity dispersion linear relationships. $P$ and $t$ are the parameters of the $t$-tests run on the linear relationships. The average index measurements (mean $\pm$ std err) for the BCGs are also given.

elliptical sample in the mass range considered here. For all indices for which the intrinsic scatter around the straight line could be calculated for both samples, the BCG data are intrinsically more scattered than the elliptical data (column 5 compared with column 6 in Table 4.5). This might indicate that the BCGs are more affected by properties other than mass than are elliptical galaxies over this mass range.

## 4.4 SSP-equivalent parameters

In order to derive mean ages and metallicities, the line-strength indices were compared with the SSP-models of Thomas et al. (2003), together with Thomas et al. (2004) for the extension to the higher order Balmer lines (hereafter referred to as the KMT models). These models are based on the EPS models of Maraston (1998; 2005). Variations of the indices with chemical partitions departing from solar are computed with the Tripicco & Bell (1995) and Korn et al. (2005) model atmospheres, using a method slightly modified from the one presented by Trager et al. (2000a). The models are presented for metallicities $[Z/H] = -2.25, -1.35,$ $-0.33, 0.0, 0.35, 0.67$, ages between 1 and 15 Gyr evenly spaced in logarithmic steps of 0.025, and $\alpha$-abundance $[E/Fe] = 0.0, 0.3$ and $0.5$, where E represents the sum of the elements: O, Ne, Mg, Si, S, Ar, Ca, Ti, Na and N. The models are computed at constant metallicity in such a way that an increase in the "E" group is compensated by a decrease of the abundances of the elements Fe and Cr (see Thomas et al. 2003 and Trager et al. 2000a for a more detailed discussion), because the total metallicity is dominated by oxygen (included in the E group).

Two techniques were used and the results compared. In the first technique, ages, metallicities and [E/Fe] were derived for the BCG sample using only the indices $<Fe>^2$, H$\beta$ and Mg$_b$. The model grids were interpolated in increments

---

$^2<Fe> = (Fe5270 + Fe5335)/2$, (González 1993).

| | Scatter in BCG data points. | | | Scatter around the best-fitting straight line (BCGs) | Scatter around the best-fitting straight line (Es) |
|---|---|---|---|---|---|
| Index | $\sigma_{std}$ | $\sigma_{exp}$ | $\sigma_{res} = \sqrt{\sigma_{std}^2 - \sigma_{exp}^2}$ | $\sigma_{res}$ | $\sigma_{res}$ |
| $H\delta'_A$ | 0.020 | 0.029 | ⋆ | 0.023 | 0.005 |
| $H\delta'_F$ | 0.016 | 0.036 | ⋆ | ⋆ | 0.006 |
| $CN_1$ | 0.035 | 0.010 | 0.034 | 0.060 | |
| $CN_2$ | 0.038 | 0.012 | 0.036 | 0.064 | ⋆ |
| $Ca4227'$ | 0.016 | 0.042 | ⋆ | ⋆ | 0.006 |
| $G4300'$ | 0.011 | 0.016 | ⋆ | 0.013 | 0.006 |
| $H\gamma'_A$ | 0.015 | 0.017 | ⋆ | 0.021 | 0.006 |
| $H\gamma'_F$ | 0.017 | 0.022 | ⋆ | 0.021 | 0.008 |
| $Fe4383'$ | 0.020 | 0.019 | 0.006 | 0.034 | ⋆ |
| $Ca4455'$ | 0.019 | 0.023 | ⋆ | 0.025 | ⋆ |
| $Fe4531'$ | 0.010 | 0.016 | ⋆ | 0.010 | ⋆ |
| $C_24668'$ | 0.009 | 0.010 | ⋆ | 0.009 | ⋆ |
| $H\beta'$ | 0.001 | 0.010 | ⋆ | 0.009 | 0.004 |
| $Fe5015'$ | 0.010 | 0.009 | 0.004 | 0.014 | 0.005 |
| $Mg_1$ | 0.026 | 0.002 | 0.026 | 0.051 | |
| $Mg_2$ | 0.029 | 0.003 | 0.029 | 0.056 | |
| $Mg_b'$ | 0.014 | 0.014 | ⋆ | 0.020 | ⋆ |
| $Fe5270'$ | 0.008 | 0.009 | ⋆ | 0.013 | ⋆ |
| $Fe5335'$ | 0.014 | 0.013 | 0.005 | 0.022 | ⋆ |
| $Fe5406'$ | 0.019 | 0.011 | 0.015 | 0.036 | |
| $Fe5709'$ | 0.009 | 0.006 | 0.007 | 0.015 | |
| $Fe5782'$ | 0.011 | 0.008 | 0.008 | 0.019 | |
| $NaD'$ | 0.071 | 0.007 | 0.071 | 0.135 | |
| $TiO_1$ | 0.036 | 0.002 | 0.036 | 0.070 | |

Table 4.5: Scatter of the index measurements (in magnitudes) compared with that expected from the errors on the index measurements. $\sigma_{std}$ is the standard deviation on the mean index value, $\sigma_{exp}$ is the standard deviation expected from the mean errors on the index values, and $\sigma_{res} = \sqrt{\sigma_{std}^2 - \sigma_{exp}^2}$ is the residual scatter not explained by the errors on the index measurements. The indices marked with ⋆ have $\sigma_{std} \leq \sigma_{exp}$. The first three columns are for the scatter in the BCG data points. The last two columns are for the intrinsic scatter around the straight line fit for the BCG and elliptical data, respectively, over the same mass range.

of 0.05 dex in both metallicity and [E/Fe], and of 0.1 dex in age. Then, a $\chi^2$-minimisation was applied to find the combination of SSPs that best reproduced the four indices simultaneously. Errors on the parameters were calculated by performing 50 Monte–Carlo simulations in which, each time, the indices were displaced by an amount given by a Gaussian probability distribution with a width equal to the errors on these indices.

In the second technique, the multi-index $\chi^2$-fitting technique (described in Proctor, Forbes & Beasley 2004), any number of the 25 Lick indices can be used together to derive mean ages and metallicities. A comparison was made between results obtained using these two techniques, namely a) only H$\beta$, Mg$_b$, Fe5270 and Fe5335 (as described above), and b) the results obtained from the multi-index $\chi^2$-fitting technique using most of the indices[3] (following the procedure described below). The errors on the derived parameters in the multi-index $\chi^2$-method were also obtained with 50 Monte–Carlo simulations. The advantage of the multi-index $\chi^2$-fitting technique is that most indices contain information on each of the derived parameters (age, metallicity and [E/Fe]) and this technique makes maximum use of the available data.

A major problem in deriving SSP-parameters by multi-index $\chi^2$-fitting is related to the zero-points of the models (Kelson et al. 2006). Despite transforming observations to the Lick/IDS system, the models have problems reproducing some of the measured indices for Galactic GCs (Thomas et al. 2003) as well as for elliptical galaxies where it has been shown that the derived SSP-parameters depend on the indices used (Sánchez-Blázquez et al. 2006b, and references therein). Part of this problem has been resolved with the inclusion of non-solar $\alpha$-element abundance ratios, but some difficulties with using multiple-indices procedures remain unsolved. The major issue is that different indices have different sensitivities to

---

[3]Note that the same KMT models were used in the multi-index fitting routine, but the modified method of deriving [E/Fe] has not yet been introduced in the routine (R. Proctor, private communication).

different chemical species, and some elements (apart from the ones already considered in the models) may have non-solar abundances, whilst not all elements are equally enhanced (Sánchez-Blázquez et al. 2007).

The procedure followed for the multi-index $\chi^2$-fitting routine was as follows. NaD is known to be affected by interstellar absorption, and was excluded in all cases. $TiO_1$ and $TiO_2$ were also excluded in both the WHT and Gemini datasets. The five indices not measured for NGC6047 ($Mg_1$, $Mg_2$, $Mg_b$, Fe5270 and Fe5335) were excluded in that galaxy only. The average $\chi$ deviations for each index obtained using the KMT models are shown in Figures 4.13 and 4.14 (described below). As seen in Figure 4.13, the $Mg_1$ index values lie off the model grid, especially in the case of the WHT data because of the dichroic configuration. As mentioned before, the CN and $Mg_{1+2}$ indices were excluded (because of their large scatter), so no molecular indices were used for SSP-parameter derivations of the galaxies. Figure 4.10 shows that there are discrepancies in the $H\delta_A$ measurements (of the Gemini data) compared with those measured by previous authors, so $H\delta_{A+F}$ were also excluded in all galaxies. Figures 4.13 and 4.14 also show Fe5709 to have high $\chi$ deviations when compared with the models, and so this was also excluded.

An effort was made to use the same indices to derive SSP-parameters in all galaxies. Figures 4.13 (WHT data) and 4.14 (Gemini data) shows the average $\chi$ residuals to the best fit for all the indices (i.e. the observed value minus the best fitting value normalised by the error on the index). The box boundaries in Figures 4.13 and 4.14 indicates the 25th and 75th percentiles. The line in the box represents the median, and the circles are the individual outliers. The error bars are the 10th and 90th percentiles. The individual outliers (circles) were not included in the multi-index fitting routine for that particular galaxy if they had a $\chi > 5$.
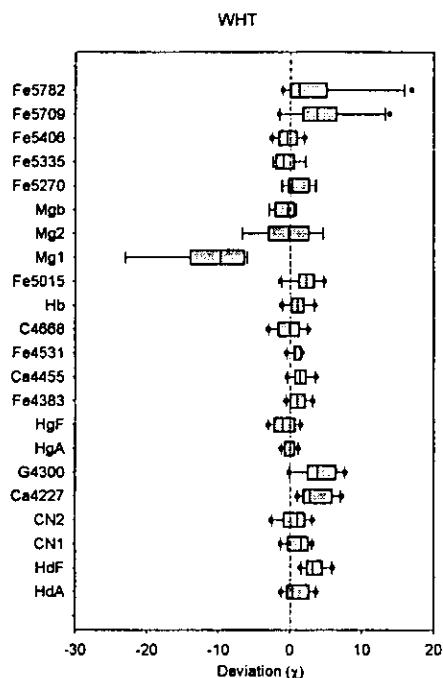
Figure 4.13: WHT: average $\chi$ residuals to the best fit for all the indices (i.e. the observed value − the best fitting value normalised by the error on the index).
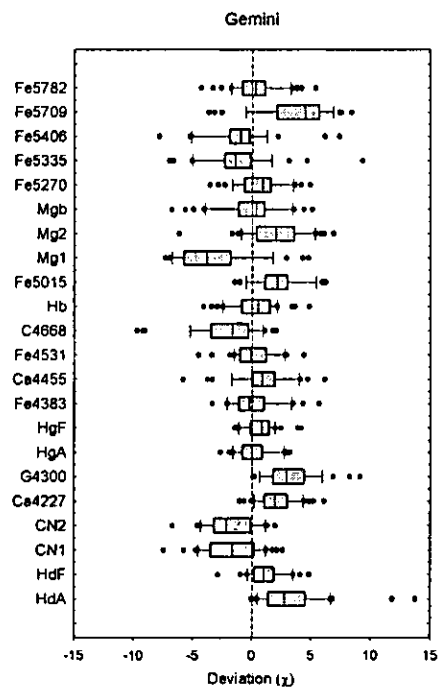


Figure 4.14: Gemini: average $\chi$ residuals to the best fit for all the indices (i.e. the observed value − the best fitting value normalised by the error on the index).
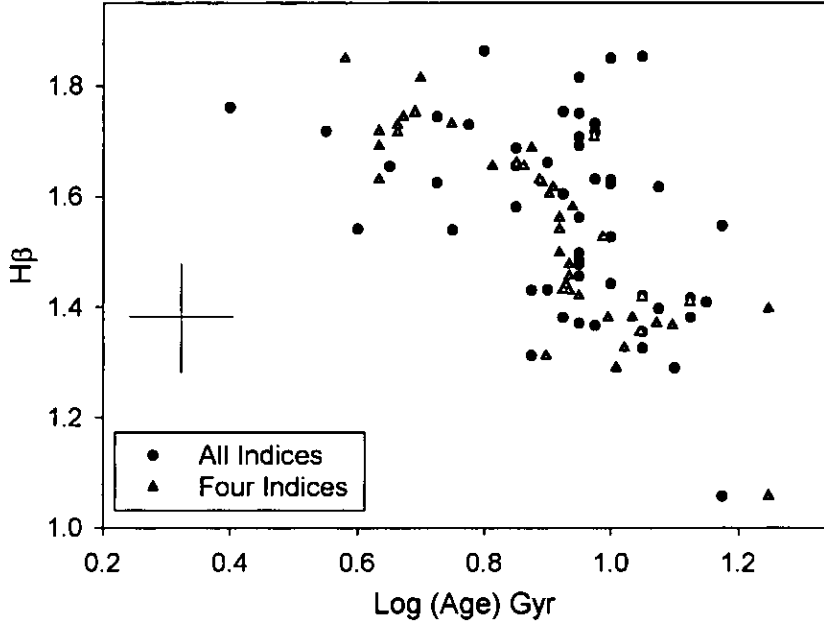
Figure 4.15: H$\beta$ against ages of the galaxies derived using the two different methods. The average error bar is shown on the left.

Figure 4.15 shows the correlation between H$\beta$ index measurement and the derived ages for both methods (with four indices and with all indices). The correlation is very clear for the ages derived using only H$\beta$, Mg$_b$, Fe5270 and Fe5335, whereas there is a very large scatter in the ages derived using all the indices. As the molecular indices were excluded, this is not due to flux calibration. In the case where only four indices are used, H$\beta$ is the strongest contributor to the derived age, whereas other indices also contribute to the derived age when more indices are used (although H$\beta$ is still the strongest contributor). Therefore, the above correlation is expected to be slightly more scattered when more indices are used.

The comparison between all three derived parameters is shown in Figure 4.16. All the parameters derived using the multi-index fitting routine show a large amount of scatter compared with the parameters derived using only four indices. Figure 4.16 also shows that the [E/Fe] values are systematically higher when only
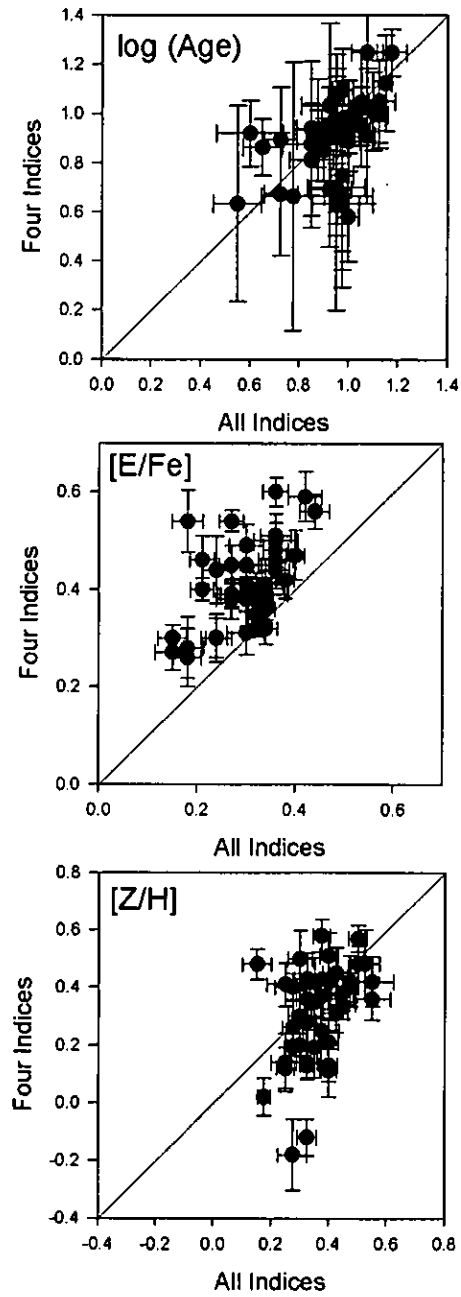
Figure 4.16: Comparison of SSP-results using all indices (except H$\delta$, CN, Mg$_{1+2}$, Fe5709, TiO and NaD) and using four indices (H$\beta$, Mg$_b$, Fe5270 and Fe5335).

four indices are used, due to the modified method used to derive them (described at the beginning of this section, and not yet incorporated into the multi-index fitting routine). This will not influence the comparison to the SSP-parameters of the elliptical samples, as the same method was used to recalculate the SSP-parameters of the elliptical samples (Section 4.4.1).

As a further check on the robustness of these SSP-results and to see how well the above-mentioned models fit the BCG observational data, index-index plots were created (Figures 4.17 to 4.19). On the plane of Figure 4.17, age and metallicity are efficiently decoupled, with H$\beta$ being a good indicator of age and [Mg<Fe>][4] a good tracer of metallicity. In Figure 4.17a, the ages derived with four indices are marked in different colours (as explained in the caption). As in Figure 4.15, it can be seen that the derived ages in Figure 4.17a correspond better to the H$\beta$ grid than in Figure 4.17b, where all the indices were used to derive the ages.

It was very difficult to use the same sets of indices for all galaxies in the multi-index fitting method (to keep the results homogeneously determined), without compromising on the goodness of the fits and getting unacceptably high $\chi^2$ values for the results. For this reason, and because of the zero-point problem in multi-index fitting techniques discussed earlier in this section, all SSP-parameter results in the following discussions, and for the rest of this thesis, will be the ones derived using only the four indices (shown in Table 4.6). Figure 4.18 shows more index-index plots with the ages derived using only four indices.

In index-index plots which are most degenerate in age and metallicity (Figure 4.19), the model grids describe narrow regions and will show whether the models accurately describe the properties of BCGs and if there are problems with the data, for example flux calibration. Figure 4.19 confirms that the models do not describe observed values of the $Mg_1$ index very well.

---

[4][Mg<Fe>]=$\sqrt{Mg_b} \times <Fe>$
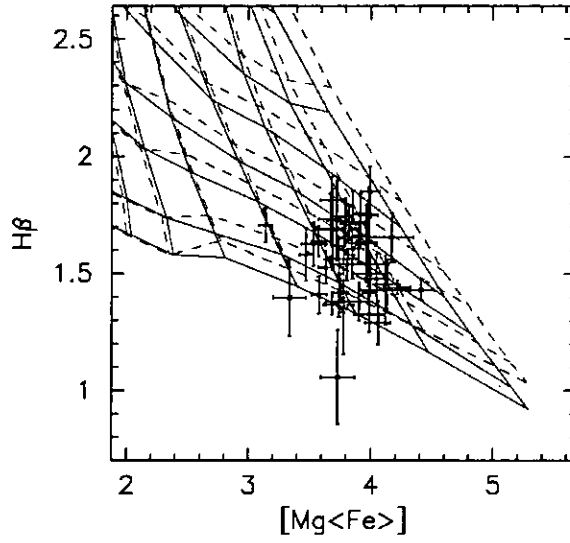
a) With four indices.
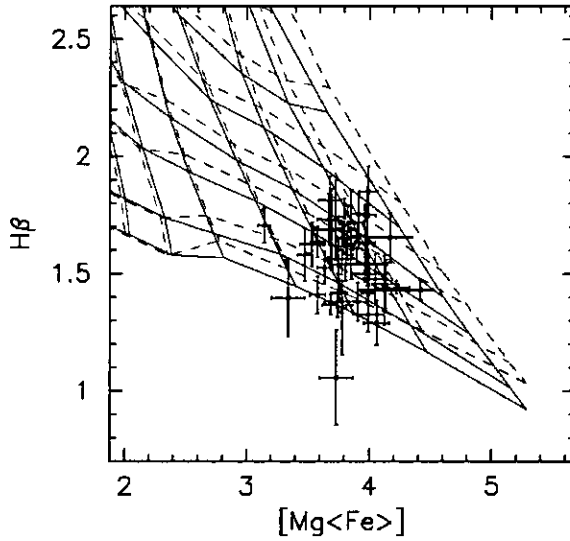


b) With all indices.

Figure 4.17: [Mg<Fe>] – H$\beta$ index plot using four indices (a), and all indices (b). The grids correspond to the KMT models, with $\alpha$-enhancement [E/Fe] = 0 (solid – black) and 0.3 (dashed – blue). Age lines are 15, 12, 8, 5 and 3 Gyr (from the bottom) and metallicities from [Z/H] = 0.80 decreasing in steps of 0.25 dex towards the left. The galaxies with derived ages log (age) < 0.7 are in black, with ages 0.7 $\leqslant$ log (age) $\leqslant$ 0.9 in green, and log (age) > 0.9 in red. All index measurements are in Å. The galaxy point which lies below the H$\beta$ grid is that of NGC0533, which reached the upper age limit of the models, but does not contain emission.
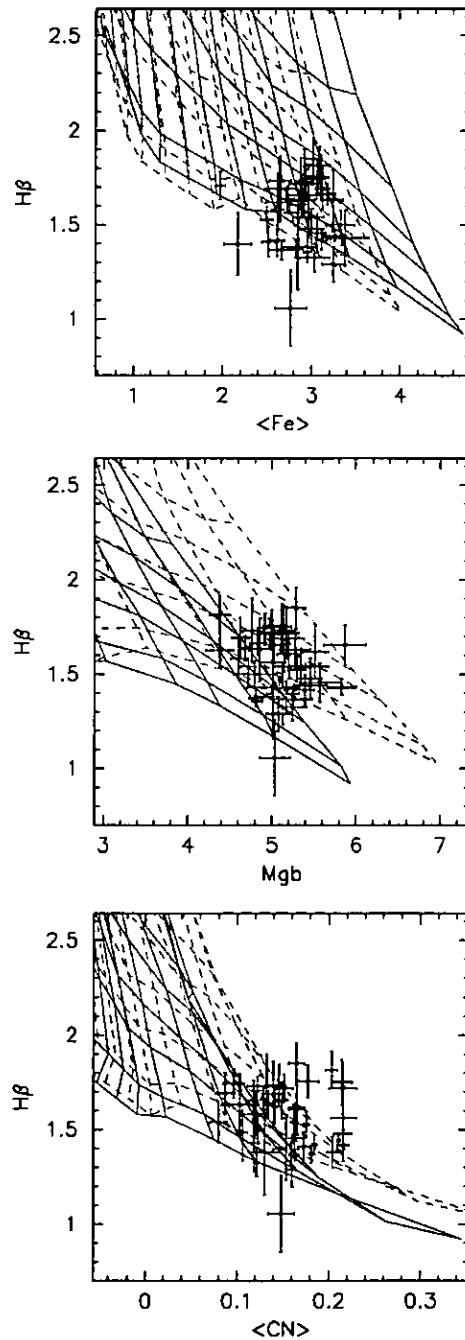
Figure 4.18: Example index-index plots: non-degenerate grids. The grids and colours are as in Figure 4.17. The Hβ, Mg$_b$ and <Fe> indices are in Å, and the <CN> indices are in magnitudes.
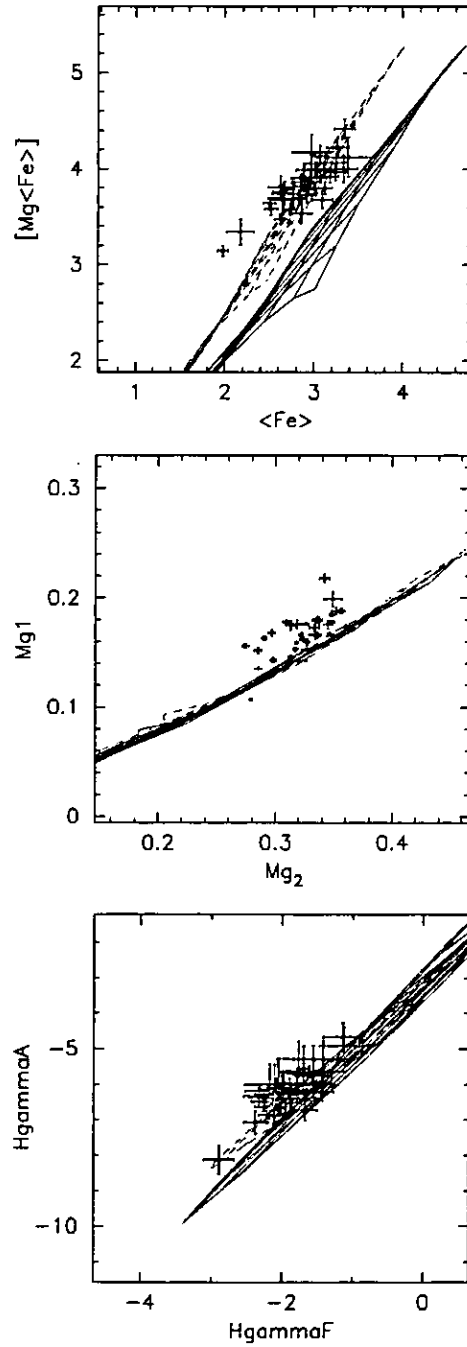
Figure 4.19: Example index-index plots: degenerate grids. The grids and colours are as in Figure 4.17. The $Mg_1$ and $Mg_2$ indices are in magnitudes, and all other indices are in Å.

| Galaxy | log (age) Gyr | [Z/H] | [E/Fe] |
|---|---|---|---|
| ESO146-028 | 0.97±0.18 | −0.12±0.06 | 0.60±0.03 |
| ESO202-043 | 0.58±0.18 | 0.58±0.06 | 0.45±0.03 |
| ESO303-005 | 0.81±0.23 | 0.34±0.05 | 0.41±0.03 |
| ESO346-003 | 0.63±0.43 | 0.43±0.09 | 0.30±0.03 |
| ESO349-010 | 0.89±0.22 | 0.21±0.08 | 0.30±0.05 |
| ESO444-046 | 1.25±0.20 | −0.18±0.12 | 0.59±0.05 |
| ESO488-027 | 0.85±0.13 | 0.42±0.08 | 0.32±0.03 |
| ESO541-013 | 0.75±0.38 | 0.30±0.09 | 0.49±0.04 |
| ESO552-020 | 1.12±0.19 | 0.02±0.07 | 0.48±0.03 |
| GSC555700266 | 0.66±0.37 | 0.40±0.05 | 0.41±0.03 |
| IC1101 | 0.70±0.15 | 0.41±0.08 | 0.27±0.04 |
| IC1633 | 0.94±0.19 | 0.38±0.06 | 0.44±0.04 |
| IC4765 | 1.01±0.23 | 0.36±0.07 | 0.30±0.04 |
| IC5358 | 0.92±0.32 | 0.28±0.10 | 0.41±0.05 |
| MCG-02-12-039 | 1.05±0.21 | 0.14±0.07 | 0.51±0.03 |
| NGC0533 | 1.25±0.10 | 0.14±0.10 | 0.38±0.05 |
| NGC0541 | 0.66±0.55 | 0.37±0.08 | 0.38±0.04 |
| NGC1399 | 0.93±0.10 | 0.42±0.09 | 0.45±0.05 |
| NGC1713 | 1.03±0.34 | 0.19±0.11 | 0.39±0.07 |
| NGC2832 | 0.93±0.02 | 0.48±0.06 | 0.38±0.04 |
| NGC3311 | 0.94±0.27 | 0.12±0.07 | 0.40±0.03 |
| NGC3842 | 1.10±0.17 | 0.11±0.09 | 0.47±0.05 |
| NGC4839 | 1.07±0.12 | 0.13±0.05 | 0.35±0.03 |
| NGC4874 | 0.89±0.12 | 0.35±0.05 | 0.46±0.05 |
| NGC4889 | 0.92±0.04 | 0.57±0.05 | 0.42±0.04 |
| NGC4946* | 0.92±0.20 | 0.28±0.06 | 0.33±0.03 |
| NGC6034 | 0.92±0.07 | 0.42±0.10 | 0.26±0.06 |
| NGC6086 | 1.00±0.14 | 0.28±0.07 | 0.39±0.04 |
| NGC6160 | 1.05±0.06 | 0.19±0.04 | 0.32±0.02 |
| NGC6173 | 0.90±0.14 | 0.20±0.05 | 0.39±0.02 |
| NGC6269 | 0.95±0.08 | 0.36±0.04 | 0.36±0.03 |
| NGC7012 | 0.69±0.19 | 0.51±0.08 | 0.39±0.03 |
| NGC7597 | 0.67±0.29 | 0.40±0.05 | 0.40±0.02 |
| NGC7647 | 0.86±0.11 | 0.48±0.12 | 0.54±0.07 |
| NGC7720 | 0.92±0.13 | 0.36±0.07 | 0.44±0.07 |
| NGC7768 | 1.02±0.24 | 0.29±0.10 | 0.38±0.04 |
| PGC004072 | 0.90±0.20 | 0.31±0.07 | 0.45±0.04 |
| PGC044257 | 0.63±0.19 | 0.50±0.10 | 0.31±0.04 |
| PGC071807 | 0.63±0.40 | 0.42±0.09 | 0.46±0.05 |
| PGC072804 | 0.69±0.37 | 0.48±0.05 | 0.38±0.03 |
| UGC00579 | 0.91±0.27 | 0.26±0.10 | 0.56±0.04 |
| UGC02232 | 0.99±0.17 | 0.13±0.06 | 0.54±0.03 |
| UGC05515 | 0.88±0.34 | 0.25±0.11 | 0.50±0.07 |
| UGC10143 | 0.93±0.21 | 0.45±0.09 | 0.28±0.06 |

Table 4.6: Central values for the SSP-equivalent parameters derived using H$\beta$, Mg$_b$, Fe5270 and Fe5335. NGC4946 marked ⋆ is known to be a normal elliptical galaxy.

| Parameter | $\sigma_{std}$ | $\sigma_{exp}$ | $\sigma_{res} = \sqrt{\sigma_{std}^2 - \sigma_{exp}^2}$ |
|---|---|---|---|
| log (age) | 0.1616 | 0.2016 | $\star$ |
| [Z/H] | 0.1669 | 0.0740 | 0.1496 |
| [E/Fe] | 0.0849 | 0.0393 | 0.0752 |

Table 4.7: Scatter of the SSP-parameters compared with that expected from the errors.

The errors on the parameters derived for PGC026269 are unusually high and, therefore, this galaxy is excluded from further analysis. NGC6047 does not have $Mg_b$, Fe5270 and Fe5335 measurements and is known to be a normal E/S0 galaxy, and is therefore also excluded from further analysis. As mentioned before, five galaxies (LEDA094683, NGC7649, NGC6166, PGC025714 and PGC030223) showed sky line or CCD gap residuals in $Mg_b$, Fe5270 or Fe5335. Hence the derived parameters using only four indices were deemed unreliable for these galaxies, and they were also excluded from further SSP-analysis. For the second ordinary elliptical galaxy, NGC4946, the SSP-parameters were derived but it was kept separate from the BCG SSP-analysis. Thus, 43 BCGs were analysed further.

Two galaxies (ESO444-046 and NGC0533 – neither of which show nebular emission) reached the upper age limit of the KMT models. Note that the oldest ages in certain SSP-models, such as the ones used here, are older than the current age of the Universe (this discrepancy has most recently been discussed in Sánchez-Blázquez et al. 2009). However, all the interpretations of this study are based on relative differences in ages which are much more reliable than absolute values.

It is important to remember that these are SSP-equivalent ages. If a galaxy has experienced a more complicated SFH than a single burst of star formation, the age derived here will be biased towards the age of the younger stars. The derived age should not be interpreted as the elapsed time since formation of most stars in the galaxy. On the other hand, Balmer-line based ages allow one to detect minor

amounts of recent star formation in generally old galaxies. The derived SSP-equivalent age depends primarily on the age of the younger population, whereas variations in the SSP-equivalent metallicity and $\alpha$-abundance ratio ([E/Fe]) are mostly driven by variations of these parameters in the older population (Serra & Trager 2007; Trager & Somerville 2009).

The presence of hot populations of stars (such as blue stragglers and horizontal branch stars) can also significantly affect the results (Maraston 2003; Trager et al. 2005). Trager et al. (2005) showed that these stars affect the inferred metallicities more than ages. On the other hand, Maraston (2003) claim that their models reproduce the Balmer line (i.e. age) observations only if warm horizontal branch stars are included.

The observed scatter in the parameters (age, [Z/H] and [E/Fe]) is compared with that expected from the errors (Table 4.7) to investigate if the distributions are compatible with a single value of age, [Z/H] and [E/Fe] for all the BCGs. $\sigma_{\mathrm{std}}$ is the standard deviation on the mean SSP-parameter value, $\sigma_{\mathrm{exp}}$ is the standard deviation expected from the mean errors on the parameter values, and $\sigma_{\mathrm{res}} = \sqrt{\sigma_{\mathrm{std}}^2 - \sigma_{\mathrm{exp}}^2}$ is the residual scatter not explained by the errors on the parameters. While the errors in the age explain the observed scatter, the scatter in [Z/H] and [E/Fe] is much larger, indicating a real variation in the mean stellar abundances in the BCG sample.

## 4.4.1 Comparison with ellipticals

Several authors have found a decreasing amount of scatter in the age and metallicity parameters with increasing velocity dispersion for early-type galaxies (Caldwell et al. 2003; Nelan et al. 2005; Sánchez-Blázquez et al. 2006b). Thus, more massive elliptical galaxies seem to be a much more homogeneous family of galaxies than less massive ones. Is this also true for the galaxies in the centre of the

clusters?

Figure 4.20 compares the distributions of SSP-equivalent parameters with those for ordinary ellipticals from Thomas et al. (2005 – T05 hereafter) and SB06. T05 derived ages and abundances for 124 early-type galaxies, 70 in low-density and 54 in high-density environments. The two different environments contain roughly the same fractions of elliptical and lenticular (S0) galaxies. To avoid artificial offsets between samples due to the use of different techniques to calculate the SSP-parameters, these parameters were recalculated using exactly the same indices and method as used for the present sample of BCGs. Nevertheless, small offsets can remain due to the use of different apertures. The T05 central indices were measured within the central 1/10 of the effective radius, and the SB06 indices within an equivalent aperture of $4.0''$ at a redshift of $z = 0.016$. As an example, the aperture correction for atomic indices (measured in Å)[5] is given by $\log(I_{norm}) = \log(I_{ab}) + \alpha \log(\frac{r_{ab}}{r_{norm}})$ (Jørgensen, Franx & Kjærgaard 1995), where $r_{ab}$ and $r_{norm}$ are the circular and normalised apertures, respectively, and $I$ the values of the indices for that aperture. For H$\beta$, Sánchez-Blázquez et al. (2009) derived $\alpha = -0.05 \pm 0.02$ from large samples of elliptical galaxies. The error introduced by assuming gradients for this correction is often bigger than the correction itself. This is as a consequence of the great variety of gradients found for elliptical galaxies. These gradients seem to be uncorrelated with other galaxy properties, such as mass, so mean gradients are calculated (Sánchez-Blázquez et al. 2009). For the samples used here, which all contain nearby galaxies, these aperture differences produce a negligible effect on the indices, and hence, given the uncertainties in the aperture corrections, these corrections were not applied here.

From the T05 and SB06 studies, galaxies with central velocity dispersions

[5]All the atomic indices with the exception of the higher order Balmer lines, where the same additive correction is used as for the molecular indices, as a result of the index ranges containing both positive and negative values.

between $\log \sigma = 2.3$ and $2.6$ km s$^{-1}$ were selected to match the same range as in the BCGs. Known BCGs (four in T05 and five in SB06) were also excluded. This left 65 and 45 elliptical galaxies for T05 and SB06, respectively. Note that the complete sample of T05 within the mass range (and excluding BCGs) was used here, whereas T05 themselves removed young massive galaxies in their analysis of the SSP-parameters. The distributions of velocity dispersions of the three samples within this mass range are shown in Figure 4.21.

Systematic differences were detected between the two samples of ordinary elliptical galaxies. The T05 and SB06 subsamples used here have 19 galaxies in common. In addition, the three Coma BCGs (NGC4839, NGC4874 and NGC4889) form part of both the present BCG sample and the original T05 and SB06 samples. Thus, offsets in H$\beta$, Mg$_b$ and <Fe> could be derived between the two samples of elliptical galaxies used. The indices of the three Coma BCGs measured here were in better agreement with the measurements from SB06 than from T05. For example, the average difference between the H$\beta$ measurements was $0.064$ Å compared with the SB06 sample and $0.35$ Å compared with the T05 sample. In addition, the SB06 sample is a closer match to the BCG sample in terms of velocity dispersion distribution (Table 4.8 and Figure 4.21). Thus, the following offsets in the indices (derived using the galaxies in common) were applied to the T05 data before the derivation of the SSP-parameters: $\Delta$H$\beta = -0.158$ Å; $\Delta$Mg$_b$ $= -0.139$ Å; $\Delta$ <Fe> $= +0.013$ Å. This normalisation placed the two elliptical samples in very good agreement, as confirmed by a Kolmogorov–Smirnov test (see the last column of Table 4.8, below).

Kolmogorov–Smirnov tests were performed on the distributions of the three samples, where the null hypothesis is that the distributions were drawn from an identical parent population. The critical value of the statistical test, at a 95 per

cent confidence level, is $D = 1.36\sqrt{\frac{m+n}{m\times n}}$, where $m$ and $n$ are the number of galaxies in the sample. Thus, if the test value is larger than $D$ (given in the heading in Table 4.8 for the three different comparisons: BCGs against each elliptical sample, and elliptical samples against each other), then the samples compared are significantly different from each other at the 95 per cent confidence level. It can be seen from Table 4.8 and Figure 4.21 that the velocity dispersion distributions of the two elliptical samples in fact agree quite well, but the distribution of the BCG sample compared with T05 is somewhat different. However, the range in velocity dispersion is narrow, and as shown in Section 4.4.2, the SSP-parameters do not depend on velocity dispersion over this mass range. Thus, this relatively small difference in the velocity dispersion distributions will not cause a bias in the comparison of the SSP-parameters between the BCG and elliptical samples because:

1. The difference between the BCG and elliptical samples' velocity dispersion distributions is only significant compared with one of the elliptical samples (T05), and all the differences between the SSP-parameters of the BCGs compared with the ellipticals (i.e. the differences in metallicity and $\alpha$-abundance discussed below) occur in both the elliptical samples;

2. The indices of the T05 sample were normalised to the SB06 sample, which is a better match to the BCG sample in velocity dispersion, as described above.

**Age**

The errors on the derived ages explain the observed scatter in the ages, as shown in Table 4.7. This indicates that there is no real variation in the mean ages in the BCG sample, and therefore, the age distribution will not be analysed further.
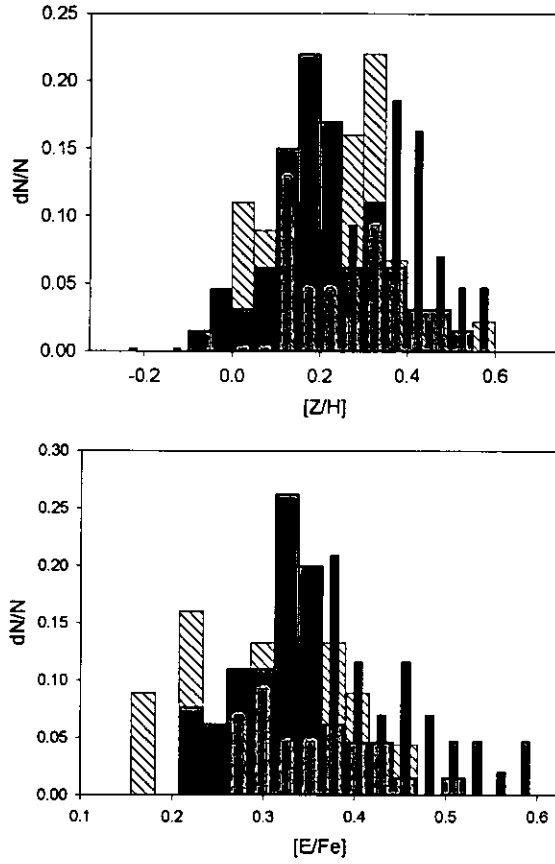
Figure 4.20: Distributions of the SSP-equivalent parameters for the BCGs (cyan), compared with those for ordinary ellipticals (T05 – grey; SB06 – red), over the same mass range.
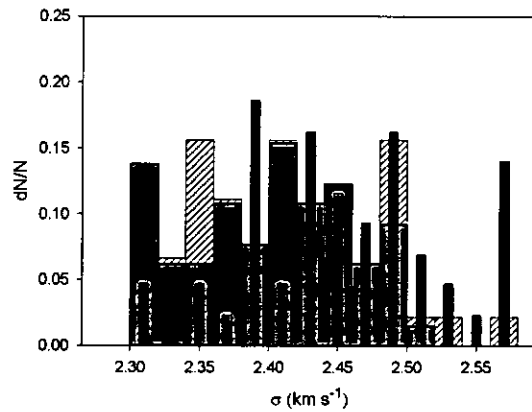


Figure 4.21: Distribution of the velocity dispersions of the BCGs (cyan), compared with those for ordinary ellipticals (T05 – grey; SB06 – red).

| Parameter | BCGs compared with SB06 | BCGs compared with T05 | SB06 compared with T05 |
|---|---|---|---|
| | $D = 0.290$ | $D = 0.267$ | $D = 0.264$ |
| log $(\sigma)$ | 0.260 | 0.320 | 0.140 |
| [Z/H] | 0.378 | 0.390 | 0.203 |
| [E/Fe] | 0.440 | 0.560 | 0.122 |

Table 4.8: Kolmogorov–Smirnov tests on the SSP-parameter distributions. If the test value is larger than $D$ (given in the heading), then the samples compared are significantly different from each other at the 95 per cent confidence level as described in the text. Thus, the distributions of all the parameters for the two elliptical samples (SB06 and T05) agree (column 4), whilst the [Z/H] and [E/Fe] distributions of the BCG sample are significantly different from both samples of ellipticals (last two values in column 2 and 3).

## [Z/H]

The KMT models provide an estimate of [Z/H] which includes all the elements heavier than H and He. The distribution of the BCG metallicities peaks at a higher value (mean [Z/H] and error on the mean: $0.31 \pm 0.03$) than the ordinary ellipticals (SB06 [Z/H] $= 0.24 \pm 0.02$; T05 [Z/H] $= 0.21 \pm 0.02$) in Figure 4.20. Table 4.8 confirms that the BCG metallicity distribution is significantly different from both elliptical samples.

## [E/Fe]

The $\alpha$-enhancement is parametrised as [E/Fe] and consists of the abundance ratios for the $\alpha$-elements (O, Ne, Mg, Si, S, Ar, Ca, Ti) plus N and Na. It serves as a crude estimation of the ratio of SNII (which produce $\alpha$-elements O, Na, Mg, Si, S, Ar, Ca, Ti when massive stars explode as well as the elements N and Ne) to SNIa (which are responsible for producing most of the Fe-peak elements like Fe and Cr when lower or intermediate mass stars explode in binary systems). Thus, the ratio will decrease with increasing time as the SNIa becomes more prominent (Worthey et al. 1992). The high values of [E/Fe] detected in massive early-type galaxies have been commonly interpreted in terms of star formation time-scales, i.e. the

star formation stops before SNIa have time to contribute significantly with their products (Tinsley 1980). However, a high [E/Fe] can also be the consequence of differences in the initial mass function (IMF) where it is skewed towards massive stars, differences in the binary fractions, or selective winds that drive most of the Fe-group elements to the intracluster medium (see discussion in Worthey 1998).

Figure 4.20 shows that the BCG sample has higher $\alpha$-enhancement values (mean BCG [E/Fe] = 0.41 ± 0.01; SB06 [E/Fe] = 0.30 ± 0.02; T05 [E/Fe] = 0.33 ± 0.02). Table 4.8 confirms that the BCG $\alpha$-enhancement distribution is significantly different from both elliptical samples.

This result agrees with the results of Von der Linden et al. (2007), who studied brightest group and cluster galaxies in the SDSS. They found that at the same stellar mass, the stellar populations of BCGs and non-BCGs are similar with the exception of their $\alpha$-element enhancement ratios, which were found to be higher in BCGs. Although these authors interpret their results in terms of star formation time-scales (star formation occurring in shorter time-scales in the BCGs than in ellipticals), it is possible that other mechanisms, related to the cluster environment and the privileged position of BCGs, are acting to influence their chemical abundances ratios. For example, it is possible that other elliptical galaxies loose their SNII products more readily than BCGs through early winds, due to the location of the BCGs in deep potential wells. This would lead to BCGs having a higher effective yield of SNII products, and also higher metallicities.

## 4.4.2 Correlations between derived properties and velocity dispersion

Figure 4.22 shows the derived SSP-parameters [Z/H] and [E/Fe] against the central velocity dispersion. The derived ages are not shown here as the scatter in the ages can be fully explained by the errors (see Table 4.7). To test for the
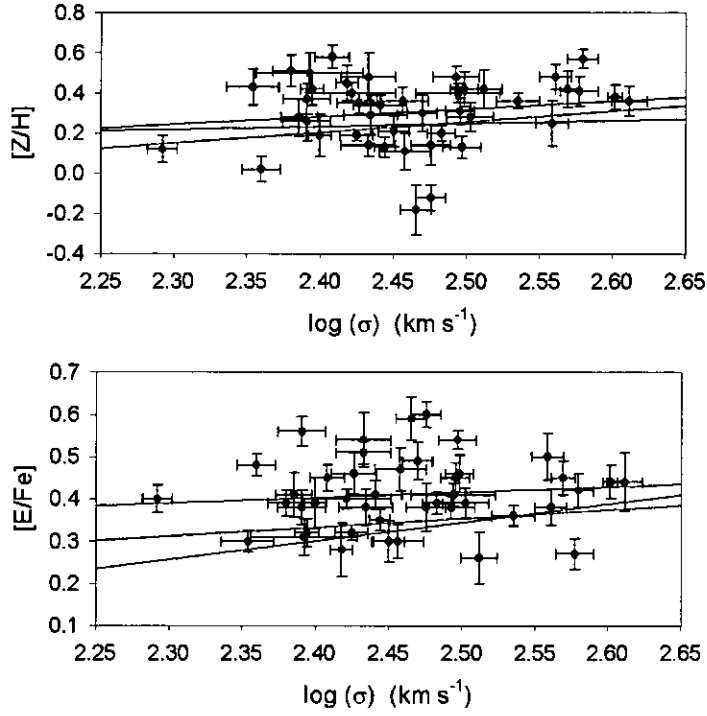
Figure 4.22: Correlation between derived SSP-parameters ([Z/H] and [E/Fe]) and velocity dispersion. The blue line denotes the best-fitting straight-line relations found for the BCGs whereas the red and green line denotes the relations found for the samples of T05 and SB06, respectively, over the same velocity dispersion range and using the same SSP-models and procedure.

| Relationship | $t$ | $P$ |
|---|---|---|
| [Z/H] $= -0.643 + 0.386 \log \sigma$ | 1.176 | 0.246 |
| [E/Fe] $= 0.098 + 0.127 \log \sigma$ | 0.755 | 0.455 |

Table 4.9: SSP-parameters: best-fitting straight-line relations with velocity dispersions derived for BCGs.

presence of correlations, linear relations of the form $P = a + b \times \log \sigma$ were fitted to the BCG data and t-tests were performed to test the null hypothesis $b = 0$ (see Table 4.9). In the following paragraphs, the relations derived for the BCG data are compared with those derived for the ordinary elliptical galaxy samples of T05 (red line) and SB06 (green line) in Figure 4.22. The SSP-parameters of the elliptical samples were recalculated using $H\beta$, $Mg_b$, Fe5270 and Fe5335 with the KMT models in exactly the same way as for the BCG data.

[Z/H]–velocity dispersion: No statistically significant correlation between metallicity and velocity dispersion is found for the BCGs (see Table 4.9), although the slope is very similar to that for normal elliptical galaxies over the same mass range. Several authors report a relationship for ordinary ellipticals which is dependent on the density of the environment (T05; Sánchez-Blázquez et al. 2006b; Trager et al. 2008). However, the mass range spanned by the BCG sample is too narrow to be able to see the differences found by these authors. Even if the BCGs were simply extensions of the massive end of normal elliptical galaxies, significant correlations in this mass range would not be detectable. Indeed, there is virtually no formal differences between the relationship obtained for the BCGs and those for the two normal elliptical samples shown in Figure 4.22.

[E/Fe]–velocity dispersion: Again, no correlation between the central $\alpha$-enhancement of the BCGs and velocity dispersion is found, but the slope is similar to that of ordinary ellipticals in the same mass range. Several authors have found the existence of a positive correlation between the degree of $\alpha$-enhancement in the central parts of early-type galaxies and (a bigger range of) velocity dispersions (Worthey et al. 1992; Kuntschner 2000; Trager et al. 2000b; T05; Sánchez-Blázquez et al. 2007). Figure 4.22 again shows that the BCGs have, on average,
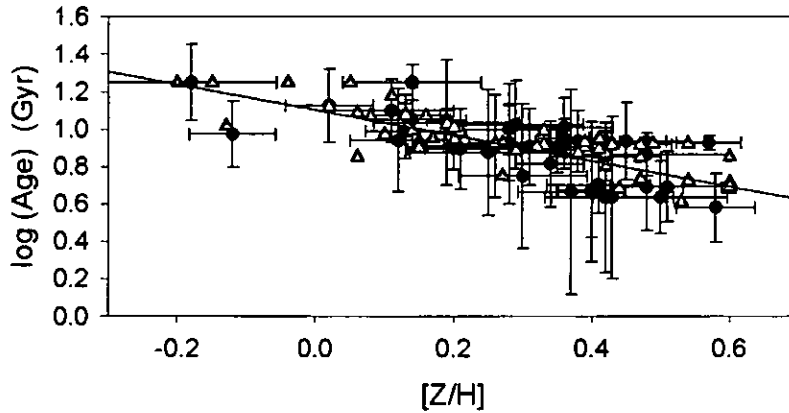
Figure 4.23: Correlation between derived SSP-equivalent age and metallicity. The black datapoints and the fitted straight line are for the BCG data, whilst the red points are the simulated data (described in the text).

higher [E/Fe] values than the ellipticals.

### 4.4.3 Age–metallicity

Several authors have noted the existence of an age–metallicity relation namely that younger galaxies are also more metal rich. This relation, being difficult to explain under the theories of passive evolution, also serves as evidence that galaxies have undergone several episodes of star formation in which the new stars formed from pre-enriched gas. Sánchez-Blázquez et al. (2006b) found that a real relation between age and metallicity only exists for low density environment early-type galaxies, and not for the early-type galaxies from a high density clustered environment, which show truncated SFHs. On the other hand, Brough et al. (2007) did not find any significant relation between age and metallicity for their sample of six brightest group and cluster galaxies. Figure 4.23 shows that a strong linear relationship between age and metallicity is found for the BCGs.

However, one has to be careful when interpreting any claimed age–metallicity relation as this can be an artifact of degeneracy between age and metallicity (Kuntschner et al. 2001). Because of the degeneracy, the errors on these stellar

population parameters are not independent and this causes an artificial anti-correlation between age and metallicity (Trager et al. 2000b; T05). To check this for the present study, 50 Monte–Carlo simulations of age and metallicity values were performed. The mean values of the indices were taken and moved randomly using a Gaussian distribution with a width equal to the typical error on the indices. The ages and metallicities were then derived with the same procedure used for the BCG data. The simulated data are plotted (red triangles) along with the real data points in Figure 4.23. The differences between the BCG data and the simulated data are marginal in both the slope of the best-fitting relation (BCG data –0.68, and simulated data –0.62) and the standard deviation from the relation (for example, BCG data 0.164, and simulated data 0.158 in the y-axis). Thus, the age–metallicity anti-correlation can almost entirely be explained by the correlation of the errors on the parameters. This also confirms the results in Table 4.7 where it was shown that there is no intrinsic scatter (other than expected from the errors) in the ages derived for the BCGs, whereas the metallicities do show inherent scatter.

## 4.4.4 Correlation between derived properties and magnitude

As discussed in Section 3.4, previous studies have shown that BCGs lie above the Faber–Jackson relation defined by ordinary elliptical galaxies. Their central velocity dispersions are almost constant with increasing luminosity. Therefore, despite the fact that no correlations were found between the stellar population parameters and velocity dispersion, it is possible that there might be correlations when the absolute magnitude is used instead.

Figure 4.24 shows plots of the total $K$-band magnitudes from the 2MASS catalogue versus the SSP-parameters ([Z/H] and [E/Fe]). None of the derived
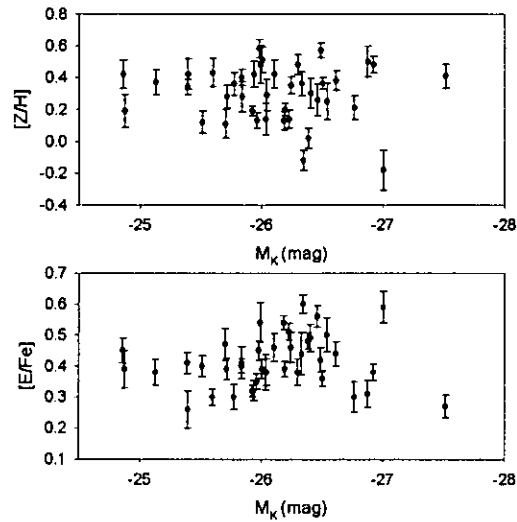
Figure 4.24: Correlations between derived parameters and absolute magnitude.

parameters shows any significant correlation with luminosity. The $K$-band is sensitive to the predominantly red populations in massive early-type galaxies and hence is a good measure of the total stellar mass. Also, Lauer et al. (2007) demonstrated that 2MASS photometry suffers least from possible errors caused by sky subtraction and crowding effects. These total $K$-band magnitudes were directly extracted from the 2MASS database, and no further corrections were applied.[6] Thus, they were not corrected for passive evolution. Brough et al. (2007) used the Bruzual & Charlot (2003) stellar population synthesis code with the assumption that the galaxies are 10 Gyr old and formed in an instantaneous burst, and found this correction to be only −0.2 mag for a galaxy at $z \sim 0.054$ (in the $K$-band). Thus, it will not make a significant difference to whether or not a correlation is found.

---

[6]The corrections applied to all 2MASS photometric data, including the extinction coefficients and uncertainties involved, are described at: http://www.ipac.caltech.edu/2mass/releases/allsky/doc/sec4_8.html.

## 4.5 Reconstructing star formation histories using full spectrum fitting

Spectral absorption features provide a direct test for the possible presence of a young stellar population in BCGs. There is an increasing amount of evidence that star formation is ongoing in BCGs, although at a very low rate, forming new stars that only account for a small mass fraction of the overall mass (for examples see the results of previous studies discussed in the introduction of Chapter 5). Investigating the full spectrum might lead to insight into the overall mass fraction of the new stars in BCGs.

Reconstruction methods to analyse the SFHs of galaxies using the full available spectrum are becoming increasingly popular, especially in studies involving large databases of spectra (such as SDSS), where galaxy spectra with similar properties can be stacked to achieve a high S/N ratio. However, the results should be interpreted with caution when the methods are applied to individual galaxies (Panter et al. 2003). These codes combine stellar evolution theory with stellar spectral libraries and assume an IMF to predict the SED for more complex populations with different SFHs. Some examples of such codes are: MOPED (Panter et al. 2003); STARLIGHT (Cid Fernandes et al. 2005); and VESPA (Tojeiro et al. 2007).

STECKMAP[7] (STEllar Content and Kinematics via Maximum A Posteriori likelihood) is such a method used to interpret the stellar populations of composite systems (Ocvirk et al. 2006a,b). It contains an inversion method for the interpretation of the integrated light spectra of galaxies and uses SSPs to reconstruct the stellar age distribution in a non-parametric way (i.e. no specific shape is assumed). STECKMAP is a "full spectrum fitting" code, i.e. it uses the full spectrum but is insensitive to extinction or flux calibration errors. Since the kinematics are

---

[7]http://astro.u-strasbg.fr/Obs/GALAXIES/stecmap_eng.html.
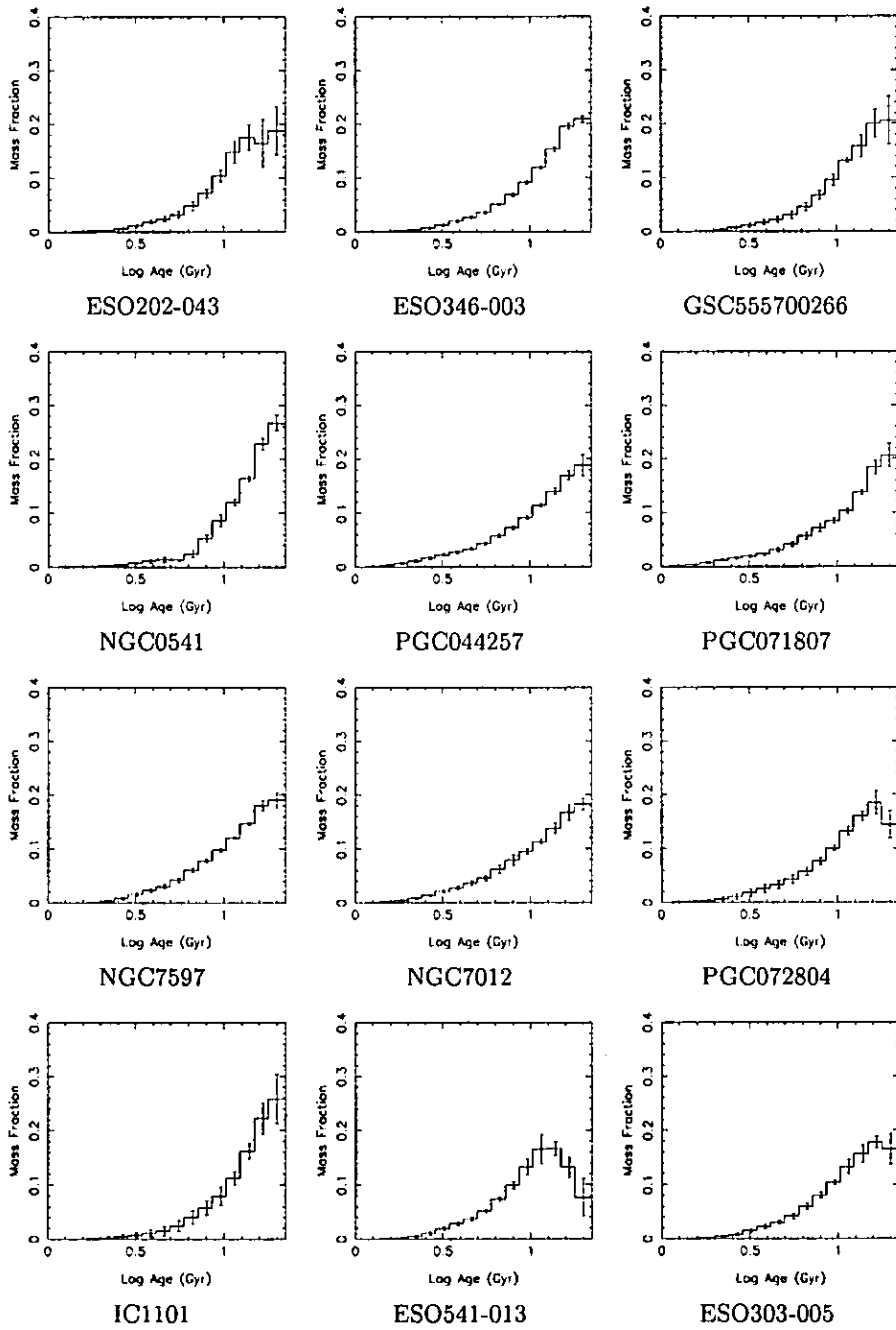
Figure 4.25: BCG SFHs: sorted by SSP-equivalent age from young to old.
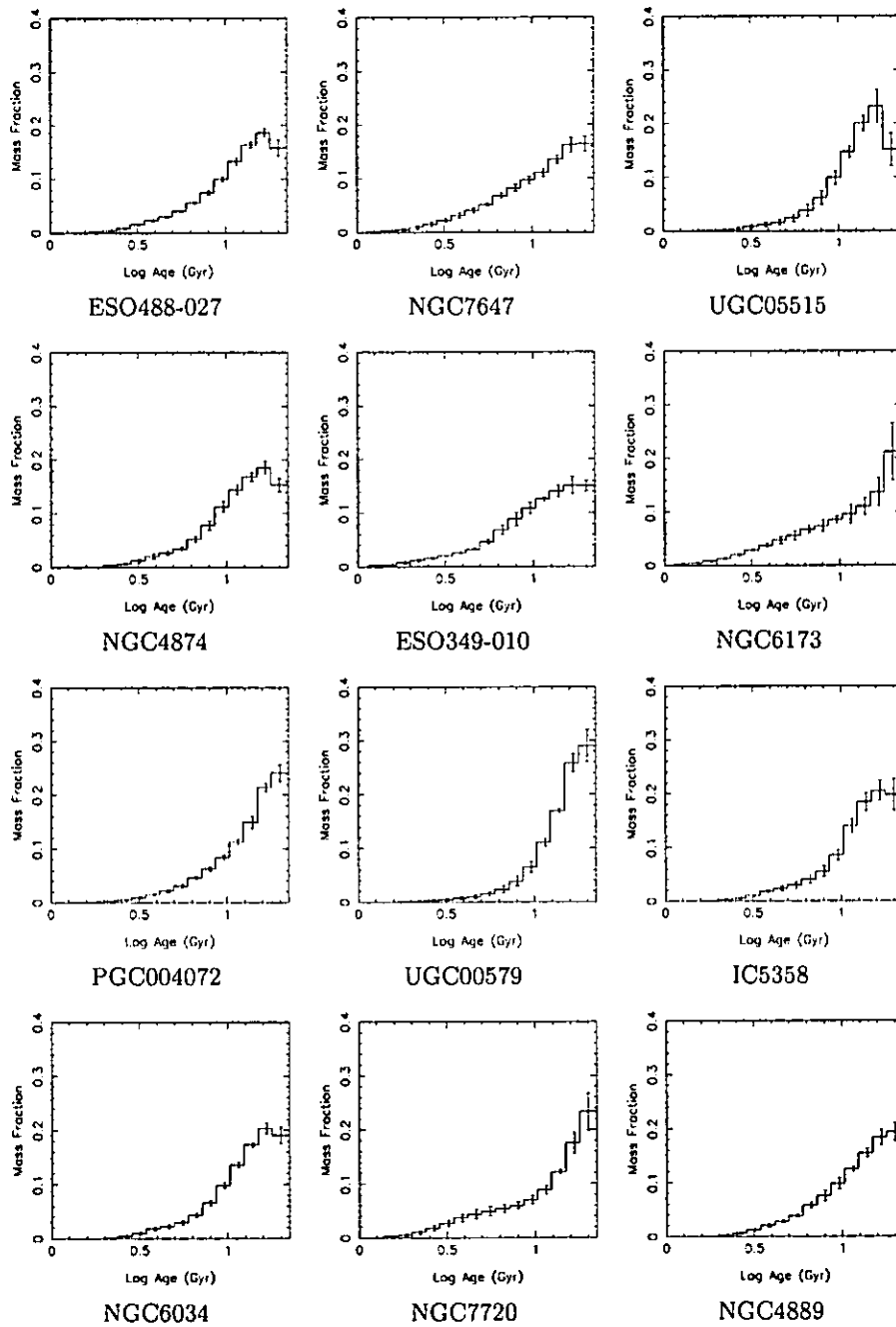
Figure 4.25 continued.

175

Figure 4.25 continued.

Figure 4.25 continued.

LEDA094683       NGC6166       NGC7649

PGC025714       PGC030223
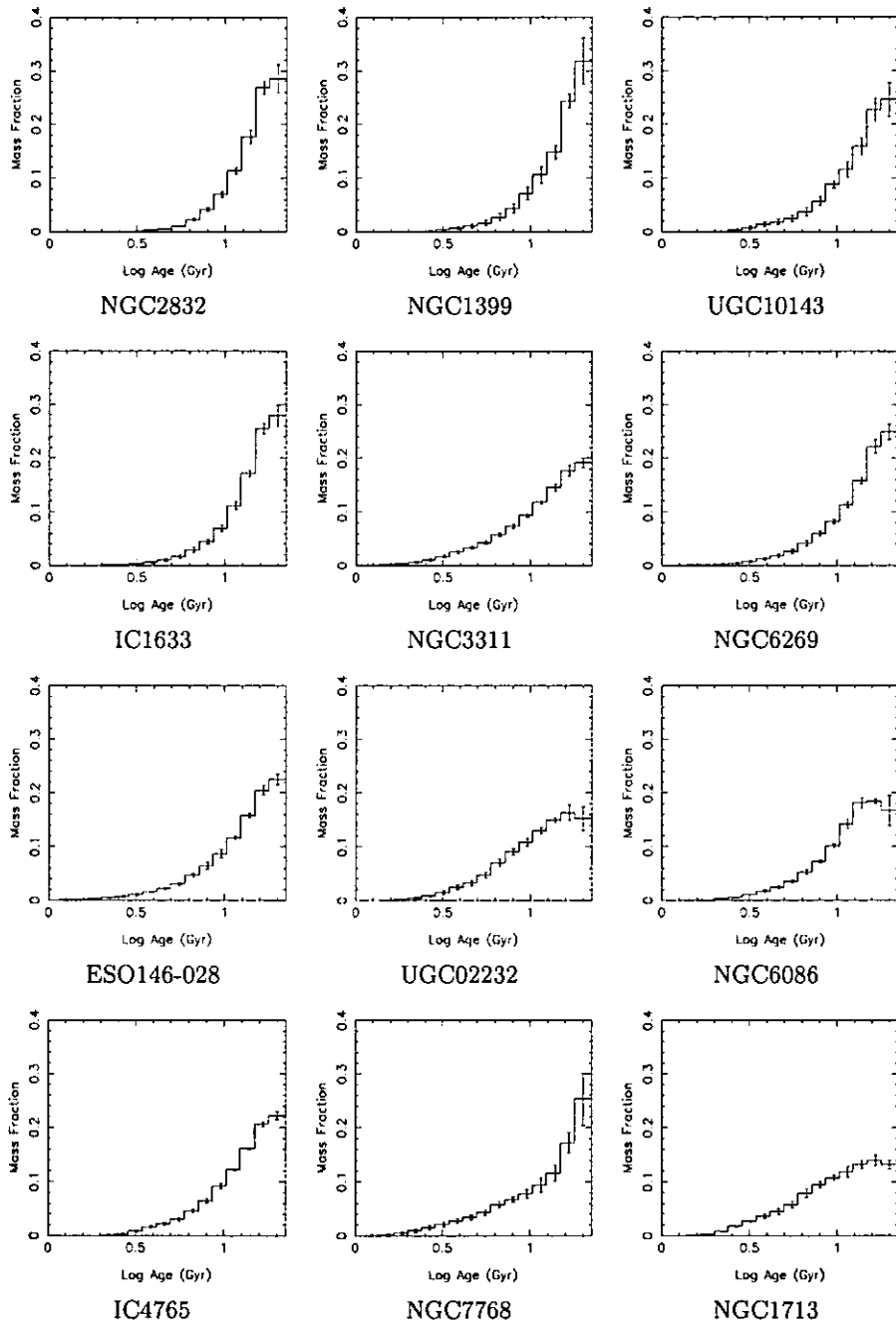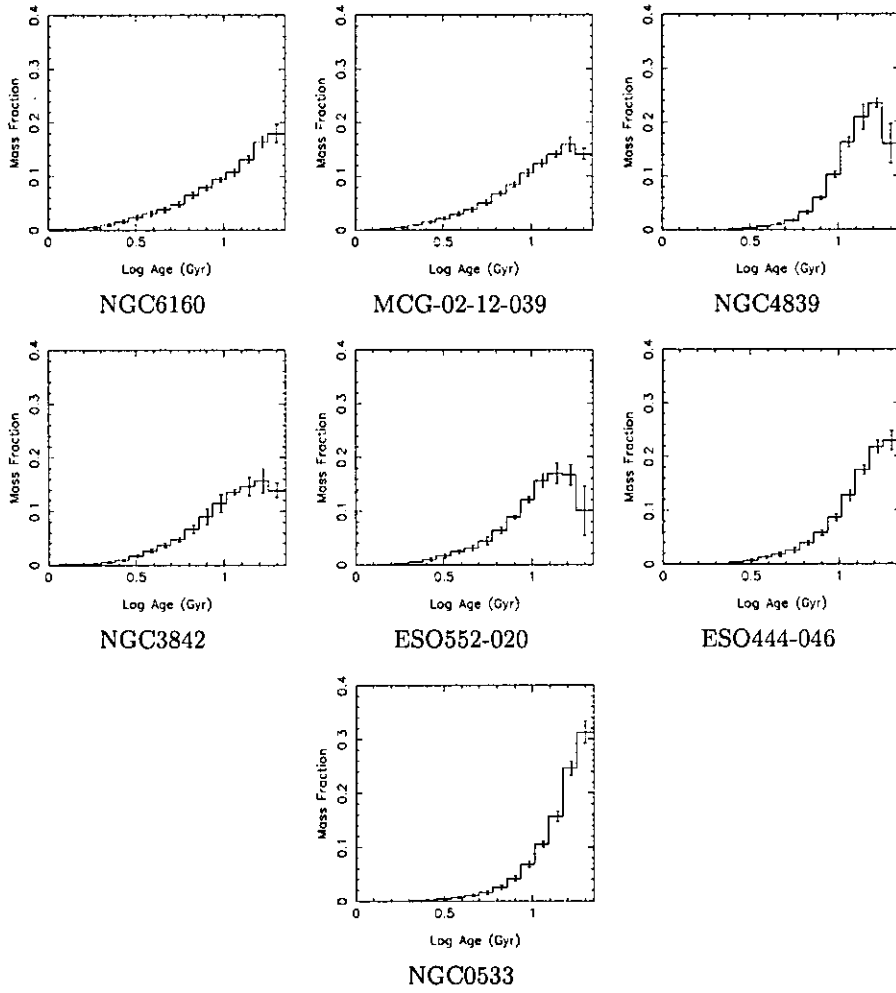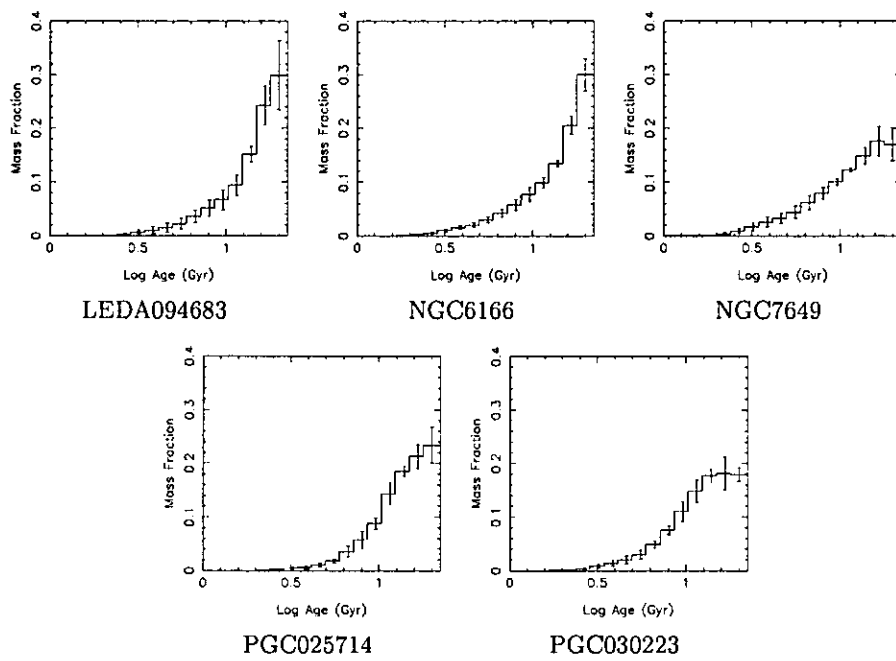
Figure 4.26: SFHs: five BCGs with unknown SSP-equivalent ages.



NGC4946       NGC6047
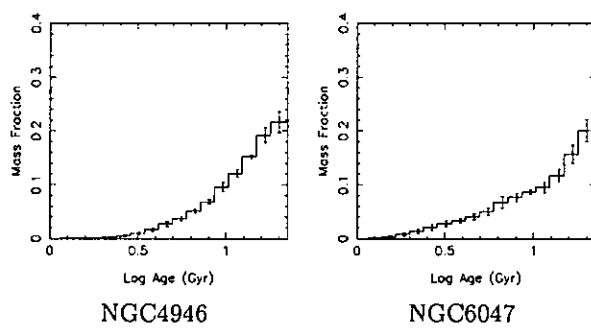
Figure 4.27: SFHs: ordinary ellipticals.

determined simultaneously with the stellar population parameters, the physical broadening of the spectral features is naturally taken into account.

In the present investigation, STECKMAP is used with the MILES stellar library (Sánchez-Blázquez et al. 2006d) with new models by Vazdekis (Vazdekis et al., in preparation)[8], and the Salpeter (1955) IMF, to find the mass fraction of new stars in each BCG. The age range was divided into 30 bins, from 100 Myr to 20 Gyr. The emission-line corrected spectra were used and all bad regions in the spectra (for example sky lines) were individually masked. For WHT spectra, the spectra from the 5300B dichroic were used in the fitting process since their wavelength range contains the largest number of indices.

Figure 4.25 shows the mass fractions of stars in each age bin for the BCGs for which SSP-equivalent ages were derived from the four indices (sorted from young to old SSP-equivalent age in the plot). Figure 4.26 shows the plots for the five BCGs for which SSP-equivalent ages could not be determined. Figure 4.27 shows the SFH of the two ordinary ellipticals.

The SFHs of the BCGs show considerable variety in shape, within a generally similar overall pattern. Decreasing the number of age bins used in the derivation of the SFHs did not alter the overall shapes significantly. No distinct difference was found in the SFHs of the younger and older-aged BCGs; or between those with high and low [E/Fe] ratios; or between those hosted by cooling-flow or non-cooling flow clusters (see Table 5.1).

Simulations show that a seed galaxy is required to build a BCG (Garijo, Athanassoula & Garciá-Gómez 1997). It is therefore predicted that a large proportion of stars in BCGs should be old. However, the BCGs should also have extended SFHs, and this is what can be seen in Figure 4.25.

Some of the SFHs show very subtle differences. For example, the SFH of

---

[8]The models are available at http://www.ucm.es/info/Astrof/miles/models/models.html

NGC0541 is unique amongst the BCGs, in that instead of gradually tapering down with time, there is a distinct change at $\sim$ 6 Gyr, followed by a very low fraction of the star formation which continues for the last several Gyrs (see the discussion on this object in Appendix A).

From the STECKMAP output, the luminosity-weighted mean ages were calculated by using the mass fractions derived and M/L ratios. These calculated ages, derived using the whole spectrum, were compared with the SSP-equivalent ages derived using only H$\beta$, Mg$_b$ and <Fe>. The results are given in Table 4.10 and Figure 4.28. The error bars on the age derivations are quite large, but despite this it is clear that the ages derived using only four key indices show a much larger range in values than the ages derived from the STECKMAP output for the BCGs. This could be due to a number of reasons. First, the Vazdekis models, incorporated into STECKMAP, do not yet include the appropriate enhancements necessary for non-solar abundances. This is essential in deriving ages for massive early-type galaxies, although it is not expected to cause significant differences with the ages derived using Lick indices H$\beta$, Mg$_b$ and <Fe>. It should also be noted that Von der Linden et al. (2007) concluded from the Kormendy relation for BCGs (which they found to be different from that of ordinary ellipticals of the same mass) that the M/L ratios of BCGs are different from ellipticals. However, it is likely that the main reason for the differences in ages between those derived using STECKMAP and those derived from SSP-analysis of Lick indices, is related to the method used by STECKMAP. This method is unlikely to be able to detect very small mass fractions of young stars, independent of the data quality or S/N ratio, because it penalises solutions that do not change smoothly with time (Ocvirk et al. 2006a). For this reason, the ages derived using the Lick indices (H$\beta$, Mg$_b$ and <Fe>) are considered to be more reliable, and no further tests were performed.
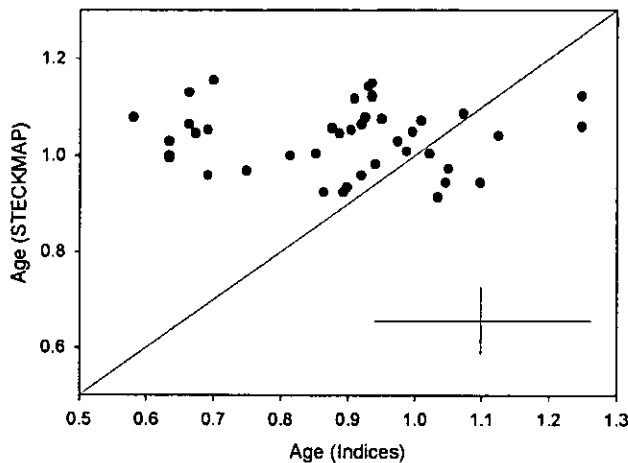
Figure 4.28: Comparison between the ages derived from Lick indices and those derived using full spectrum fitting (STECKMAP). The typical errors are shown in the bottom of the plot, and the line $x = y$ is also shown.

Full spectrum fitting methods are continuously being improved on to address some of the current limitations, and holds great promise for the future. Koleva et al. (2009) recently released a new code which is an improvement on the STECKMAP method.[9] The improved code addresses one of the main limitations in STECKMAP, which is the difficulty in assigning a degree of confidence on the solution, by constructing $\chi^2$ maps of the derived parameters.

## 4.6   Results and discussion

### Emission lines

- The GANDALF routine (Sarzi et al. 2006) was used, with realistic stellar templates, to carefully measure the small emission lines present in some of the BCGs. All the emission-line BCGs for which the H$\beta$, [OII]$\lambda$3727 and [OIII]$\lambda$5007 lines could be measured are star forming galaxies according to

---

[9]The code is called ULySS, and is available at http://ulyss.univ-lyon1.fr.

| Galaxy | Age (Gyr) (STECKMAP) | Age (Gyr) (Indices) | Galaxy | Age (Gyr) (STECKMAP) | Age (Gyr) (Indices) | Galaxy | Age (Gyr) (STECKMAP) | Age (Gyr) (Indices) |
|--------|--------|--------|--------|--------|--------|--------|--------|--------|
| ESO146-028 | 10.7 | 9.4 | NGC0541 | 11.6 | 4.6 | NGC7012 | 9.1 | 4.9 |
| ESO202-043 | 12.0 | 3.8 | NGC1399 | 14.1 | 8.6 | NGC7597 | 11.1 | 4.7 |
| ESO303-005 | 10.0 | 6.5 | NGC1713 | 8.2 | 10.8 | NGC7647 | 8.4 | 7.3 |
| ESO346-003 | 10.7 | 4.3 | NGC2832 | 13.9 | 8.5 | NGC7649 | 10.1 | – |
| ESO349-010 | 8.4 | 7.8 | NGC3311 | 9.6 | 8.7 | NGC7720 | 9.1 | 8.3 |
| ESO444-046 | 11.5 | 17.7 | NGC3842 | 8.8 | 12.5 | NGC7768 | 10.1 | 10.5 |
| ESO488-027 | 10.1 | 7.1 | NGC4839 | 12.2 | 11.8 | PGC004072 | 11.3 | 8.0 |
| ESO541-013 | 9.3 | 5.6 | NGC4874 | 11.1 | 7.7 | PGC025714 | 11.4 | – |
| ESO552-020 | 11.0 | 13.3 | NGC4889 | 12.0 | 8.4 | PGC030223 | 12.1 | – |
| GSC555700266 | 13.5 | 4.6 | NGC4946 | 10.4 | 8.4 | PGC044257 | 9.9 | 4.3 |
| IC1101 | 14.3 | 5.0 | NGC6034 | 11.8 | 8.3 | PGC071807 | 10.0 | 4.3 |
| IC1633 | 13.3 | 8.6 | NGC6047 | 8.7 | – | PGC072804 | 11.3 | 4.9 |
| IC4765 | 11.8 | 10.2 | NGC6086 | 11.2 | 9.9 | UGC00579 | 13.1 | 8.1 |
| IC5358 | 11.6 | 8.3 | NGC6160 | 8.8 | 11.1 | UGC02232 | 10.2 | 9.7 |
| LEDA094683 | 13.2 | – | NGC6166 | 12.5 | – | UGC05515 | 11.4 | 7.5 |
| MCG-02-12-039 | 9.4 | 11.2 | NGC6173 | 8.6 | 7.9 | UGC10143 | 13.2 | 8.6 |
| NGC0533 | 13.3 | 17.7 | NGC6269 | 11.9 | 8.9 | | | |

Table 4.10: Comparison between the luminosity-weighted ages derived using full spectrum fitting (STECKMAP) and using only four indices, for 50 galaxies. Typical errors are 0.7 Gyr in the STECKMAP ages and 1.6 Gyr in the ages derived from Lick indices (see Table 4.6).

the diagnostic diagram. This is in contrast with the results of Von der Linden et al. (2007) and Edwards et al. (2007), who found that most of the emission-line galaxies in their samples of BCGs showed LINER-type emission, similarly to normal giant elliptical galaxies (Yan et al. 2006). BCGs are known to be more likely to host radio-loud AGN than any other galaxy with the same stellar mass (Burns 1990; Best et al. 2007). However, it should be noted that Best et al. (2007) argued that radio-loud AGN and emission-line AGN (detectable through optical emission lines) are independent, unrelated phenomena.

The disagreement with earlier studies, may be partly due to the diagnostic diagram used here, which is much less effective at separating different sources of ionisation (Stasińska et al. 2006). However, [OIII]$\lambda5007$ is easier to measure than H$\beta$, so any bias in the measurements will usually be towards obtaining larger [OIII]$\lambda5007$/H$\beta$ values. The disagreement might also be due to different emission-line measurement methods, or it might also indicate that there is still some residual emission in the H$\beta$ index, even after careful emission correction using GANDALF. The fraction of the sample containing emission lines is too small, and the strengths of the emission lines detected are too weak, to draw detailed general conclusions on emission lines in BCGs.

- Of the emission-line galaxies in this sample for which cooling-flow information is available (Table 5.1), five are hosted by clusters with cooling flows and four are hosted by clusters without cooling flows. However, it is known that the fraction of BCGs with emission lines in cooling-flow clusters changes with the distance the BCG is located from the cluster X-ray centre (Edwards et al. 2007; Best et al. 2007). For example, Edwards et al. (2007) showed that emission lines in BCGs are rare in the absence of cooling flows,

when the BCGs are located close to the cluster centre ($\lesssim$ 50 kpc).

### Line-strength indices

- With the exception of G4300, no significant differences between the index relations with velocity dispersion of the BCG data and those of normal ellipticals in the same mass range were found. The Lick offsets do not explain the difference in the G4300 index. This index measures the G-band of CH at $\sim$ 4300 Å. It is relatively insensitive to metallicity, but the index is subject to interior-to-surface mixing in stars and the effect of this as a function of metallicity makes it difficult to calibrate it as an age indicator (Worthey 1994). G4300 can possibly be used, in conjunction with $C_24668$, to constrain oxygen abundance (Graves & Schiavon 2008). However, on its own, it is difficult to understand why this index is slightly higher in the BCG sample than in the comparison elliptical sample.

- Statistically significant linear relations between the line-strength indices and velocity dispersions were only found for six (Ca4227, H$\gamma_F$, Ca4455, Fe4531, $C_24668$ and Mg$_b$) out of 18 indices, revealing that at the high end of the galaxy mass scale, the indices are less dependent on mass (velocity dispersion). This is not specific to BCGs, but true for all massive early-type galaxies. Nelan et al. (2005), for example, show a clear non-linear relation for the age–velocity dispersion relation directly derived from the index–velocity dispersion relations of $\sim$ 4000 red sequence galaxies. Samples of more massive objects yield shallower SSP-parameter trends with velocity dispersion than samples in the low-mass regime.

- The BCG data are intrinsically more scattered (i.e. not explained by the errors) around the derived index–velocity dispersion relations than the data

for elliptical galaxies in that mass range.

**Derived properties**

- The peak of the metallicity distribution occurs at a higher value for the BCG data than for the samples of massive elliptical galaxies. This might indicate increased star formation efficiency in BCGs. The metallicity–velocity dispersion relation for the BCGs is similar in slope to that for the normal ellipticals. Future analysis of the stellar population gradients will reveal how much higher are the metallicities in the cores of the BCGs with respect to the rest of the galaxy. Metallicity gradients are an important signature of the different formation and evolution scenarios, and chemical evolution models offer clear predictions to compare with the observed gradients (as discussed below in Section 6.3).

- No significant [E/Fe]–velocity dispersion relation is found for the BCG sample in this mass range. The BCGs have higher [E/Fe] values than the comparison elliptical samples. This can naively be interpreted as a consequence of shorter formation time-scales in BCGs. However, other differences such as the IMF, differences in the binary fractions, or selective winds that drive most of the Fe-group elements to the intracluster medium cannot be conclusively eliminated. It will be very interesting to derive the abundances of individual elements when the new generation of SSP-models becomes available (Worthey et al., in preparation).

- No significant correlations between the derived SSP-parameters (metallicity and $\alpha$-abundance) and absolute magnitude were found for the BCG sample.

# Chapter 5

# CLUSTER ENVIRONMENT

Hierarchical models of galaxy formation predict that the formation of the central galaxy is closely connected with the evolution of the host cluster. In principle, this would not necessarily be reflected by differences in the SFH, as stars might have formed before the formation – or assembly – of the real galaxy. However, it is interesting to investigate whether, and to what extent, the characteristics of the host cluster play a role in the SFH of BCGs.

Various photometric studies and simulations of BCGs suggest that their evolution is closely connected to the properties of the host clusters, for example the cluster density (as manifested in the X-ray luminosity, $L_X$). As discussed in Section 1.2.1, the results of Brough et al. (2002; 2005) imply that the BCGs in high-$L_X$ clusters assembled their mass at $z > 1$ and have been passively evolving since. On the other hand, BCGs in low-$L_X$ clusters appear to be in the process of assembling their mass. The simulations of Miles et al. (2004) suggest that low-$L_X$ groups are the present sites of rapid dynamical evolution and that these groups would harbour younger stellar populations, in the case of dissipative merging, than their X-ray bright counterparts.

Whiley et al. (2008) found a correlation between the velocity dispersions of

the clusters and the $K$-band luminosities of the BCGs. Clusters with large velocity dispersions (masses) tend to host brighter BCGs (BCGs with larger stellar masses). It is also well-known that the optical and near-IR luminosities of BCGs are positively correlated with the X-ray luminosity of the cluster (Edge & Stewart 1991; Burke, Collins & Mann 2000; Stott et al. 2008). Taken together, the photometric observations point to an evolutionary history of BCGs which is closely connected to that of their host clusters, as predicted in the hierarchical models of galaxy formation. However, it is still not clear if the amount of galaxy growth due to accretion agrees with these models (as discussed in Section 1.2.1).

Another interesting aspect is the influence of cooling flows at low redshifts in shaping the stellar populations of these systems. Previous studies have reported several examples of ongoing star formation in BCGs, in particular those hosted by cooling-flow clusters (Cardiel et al. 1998a; Crawford et al. 1999; McNamara et al. 2006; Edwards et al. 2007; O'Dea et al. 2008; Bildfell et al. 2008; Pipino et al. 2009). However, the origin of the gas fuelling this star formation is not yet known. Possible explanations include processes involving cooling flows or cold gas deposited during a merging event (Bildfell et al. 2008). The lack of widespread detection of iron lines expected from cluster gas cooling below $1 - 2$ keV in *XMM-Newton* observations of cool-core clusters contradicted the model that these young stars are formed in cooling flows (as discussed in Section 1.2.1). However, it is possible that star formation is ongoing in cool-core clusters at a much reduced rate (Bildfell et al. 2008).

The X-ray properties of the host clusters are given in Table 5.1. All the values, with the exception of those from Ledlow et al. (2003), are from spectra observed in the $0.1 - 2.4$ keV band, and using the same cosmology, namely the Einstein de–Sitter model of $H_0 = 50$ km s$^{-1}$ Mpc$^{-1}$, $\Omega_m = 1$ and $\Omega_\Lambda = 0$. The values taken from Ledlow et al. (2003) are from spectra observed in the $0.5 - 2.0$ keV

band and were therefore not on the same scale as the rest of the values and were not used in subsequent analysis of correlations with stellar population properties. The X-ray luminosity values were converted to the concordance cosmological model ($\Omega_m = 0.3$ and $\Omega_\Lambda = 0.7$) by calculating the appropriate cosmological luminosity distances of the clusters, and are listed in Table 5.1 for completeness. The other X-ray properties used here, such as X-ray temperature, do not depend on the cosmological model assumed (White et al. 1999; Bohringer et al. 2004). The X-ray offset $R_{\text{off}}$ was calculated using $H_0 = 75$ km s$^{-1}$ Mpc$^{-1}$ (as used throughout this work). It is shown in Figure 5.1 that the assumed cosmological model does not influence the relative correlations between the parameters, and thus the previously most often used Einstein de–Sitter X-ray luminosity values are used to plot the correlations (as originally published from the *ROSAT* data).

The observations presented in Chen et al. (2007) were made with *ROSAT* and *ASCA*; those presented in Bohringer et al. (2004) are from the REFLEX cluster survey observed with *ROSAT*; and those in Bohringer et al. (2000) from the NORAS cluster survey observed with *ROSAT*. The data from Cruddace et al. (2002) are also from *ROSAT*. Values from the last three papers do not include error estimates.

| Galaxy | Cluster | $L_X$ (erg s$^{-1}$) | ref | $L_X$ (concordance) (erg s$^{-1}$) | $T_X$ (keV) | Cooling Flow | | ref | $\sigma_{cluster}$ (km s$^{-1}$) | ref | $R_{off}$ (Mpc) | ref |
|---|---|---|---|---|---|---|---|---|---|---|---|---|
| ESO146-028 | RXCJ2228.8-6053 | 0.17 | b | 0.09 | – | – | | – | – | – | 0.051 | cb |
| ESO202-043 | A S0479 | – | – | – | – | – | | – | – | – | – | – |
| ESO303-005 | RBS521 | 0.79 | b | 0.42 | – | – | | – | – | – | 0.010 | cb |
| ESO346-003 | A S1065 | 0.096 | r | 0.05 | – | – | | – | – | – | 0.032 | cr |
| ESO349-010 | A4059 | 2.80±0.06 | a | 1.50±0.06 | 3.5 | ✓ | | e | 845 | w | 0.019 | e |
| ESO444-046 | A3558 | 6.56±0.04 | a | 3.51±0.04 | 3.8 | X | | e | 986 | w | 0.019 | e |
| ESO488-027 | A0548 | 0.21 | b | 0.11 | 2.4 | ✓ | | w | 853 | w | ⋆ | cb |
| ESO541-013 | A0133 | 2.85±0.04 | a | 1.54±0.04 | 3.8 | ✓ | | w | 767 | w | 0.017 | e |
| ESO552-020 | CID 28 | 0.16 | b | 0.08 | – | – | | – | – | – | 0.013 | cb |
| GSC555700266 | A1837 | 1.28 | b | 0.70 | 2.4 | ✓ | | w | 596 | w | 0.020 | cb |
| IC1101 | A2029 | 17.07±0.18 | a | 9.39±0.18 | 7.8 | ✓ | | w | 786 | w | 0.131 | p |
| IC1633 | A2877 | 0.20 | b | 0.11 | 3.5 | X | | w | 738 | w | 0.015 | cb |
| IC4765 | A S0805 | 0.03 | b | 0.02 | – | – | | – | – | – | 0.007 | cb |
| IC5358 | A4038 | 1.92±0.04 | a | 1.01±0.04 | – | ✓ | | c | 891 | m | 0.002 | cb |
| LEDA094683 | A1809 | 2.44±0.32 | ⋆ | – | 3.7 | ✓ | | w | 249 | w | 0.044 | p |
| MCG-02-12-039 | A0496 | 3.77±0.05 | a | 1.99±0.05 | 4.7 | ✓ | | w,e | 705 | w | 0.031 | e |
| NGC0533 | A0189B | 0.04 | b | 0.02 | – | – | | – | – | – | 0.004 | cb |
| NGC0541 | A0194 | 0.14 | b | 0.07 | 1.9 | X | | w | 480 | w | 0.037 | cb |
| NGC1399 | RBS454 | 0.08±0.01 | a | 0.04±0.01 | – | X | | c | 240 | w | < 0.001 | cb |
| NGC1713 | CID 27 | – | – | – | – | – | | – | – | – | – | – |
| NGC2832 | A0779 | 0.07 | b | 0.04 | 1.5 | ✓ | | w | 503 | w | 0.038 | cl |
| NGC3311 | A1060 | 0.56±0.03 | a | 0.29±0.03 | 3.3 | ✓ | | w | 608 | w | 0.015 | pe |
| NGC3842 | A1367 | 1.20±0.02 | a | 0.63±0.02 | 3.5 | X | | w,e,g | 822 | w | 0.252 | e |
| NGC4839 | A1656 | – | – | – | – | – | | – | – | ⋆ | – | – |

Continued on Next Page...

Table 5.1 – Continued

| Galaxy | Cluster | $L_X$ | | $L_X$ (concordance) | $T_X$ | Cooling Flow | | $\sigma_{cluster}$ | | $R_{off}$ | |
|---|---|---|---|---|---|---|---|---|---|---|---|
| | | (erg s$^{-1}$) | ref | (erg s$^{-1}$) | (keV) | | ref | (km s$^{-1}$) | ref | (Mpc) | ref |
| NGC4874 | A1656 | 8.09±0.19 | a | 4.22±0.19 | 8.0 | X | e,g | 1010 | w | 0.038 | cb |
| NGC4889 | A1656 | 8.09±0.19 | a | 4.22±0.19 | 8.0 | X | e,g | 1010 | w | 0.169 | e |
| NGC4946 | A3526 | 1.19±0.04 | a | 0.62±0.04 | – | – | – | – | – | not BCG | |
| NGC6034 | A2151 | 0.98 | c | 0.52 | 3.5 | X | g | 827 | w | ⋆ | – |
| NGC6047 | A2151 | 0.98 | c | 0.52 | – | X | g | 827 | w | not BCG | |
| NGC6086 | A2162 | 0.14±0.03 | ⋆ | – | – | X | g | 323 | s | 0.053 | cl |
| NGC6160 | A2197 | 0.13 | c | 0.07 | 1.6 | ✓ | w,g | 564 | w | 0.017 | cc |
| NGC6166 | A2199 | 4.20±0.12 | a | 2.21±0.12 | 4.7 | ✓ | w,e,g | 794 | w | 0.007 | e |
| NGC6173 | A2197 | – | – | – | – | – | – | – | – | ⋆ | – |
| NGC6269 | AWM5 | 0.36 | c | 0.19 | – | – | – | – | – | 0.002 | cc |
| NGC7012 | A S0921 | – | – | – | – | – | – | – | – | – | – |
| NGC7597 | A2572 | 0.58 | c | 0.31 | – | – | – | 676 | st | 0.048 | cc |
| NGC7647 | A2589 | 1.87±0.04 | a | 0.99±0.04 | 3.7 | X | e | 500 | w | 0.073 | e |
| NGC7649 | A2593 | 1.44±0.23 | ⋆ | – | 3.1 | X | w | 690 | w | 0.020 | cl |
| NGC7720 | A2634 | 0.99±0.03 | a | 0.52±0.03 | 3.4 | X | e,g | 744 | w | 0.018 | e |
| NGC7768 | A2666 | 0.08±0.04 | ⋆ | – | 1.6 | X | g | 476 | w | 0.006 | cl |
| PGC004072 | A0151 | 0.99 | b | 0.53 | – | – | – | 715 | s | 0.006 | cb |
| PGC025714 | A0754 | 3.97±0.11 | a | 2.14±0.11 | 8.7 | X | e | 747 | w | 0.328 | e |
| PGC026269 | A0780 | 5.61 | b | 3.02 | – | ✓ | e | 641 | e | 0.015 | e |
| PGC030223 | A0978 | 0.50 | b | 0.27 | – | – | – | 498 | st | 0.027 | cb |
| PGC044257 | A1644 | 3.92±0.34 | a | 2.10±0.34 | 4.7 | ✓ | w | 933 | w | 0.009 | pe |
| PGC071807 | A2622 | 1.51±0.18 | ⋆ | – | – | – | – | 942 | s | 0.249 | cc |
| PGC072804 | A2670 | 2.70 | b | 1.48 | 3.9 | ✓ | w | 1038 | w | 0.035 | cb |

Continued on Next Page...

Table 5.1 – Continued

| Galaxy | Cluster | $L_X$ (erg s$^{-1}$) | ref | $L_X$ (concordance) (erg s$^{-1}$) | $T_X$ (keV) | Cooling Flow | ref | $\sigma_{cluster}$ (km s$^{-1}$) | ref | $R_{off}$ (Mpc) | ref |
|---|---|---|---|---|---|---|---|---|---|---|---|
| UGC00579 | A0119 | 3.34±0.05 | a | 1.78±0.05 | 5.1 | X | w,e | 863 | w | 0.054 | e |
| UGC02232 | A0376 | 1.36 | c | 0.73 | 5.1 | X | e | 903 | w | 0.136 | cc |
| UGC05515 | A0957 | 0.81 | b | 0.43 | 2.9 | X | w | 669 | w | 0.037 | cb |
| UGC10143 | A2147 | 2.87±0.15 | a | 1.52±0.15 | 4.4 | X | e,g | 1148 | w | 0.082 | e |

Table 5.1: X-ray properties and velocity dispersions of the host clusters for all 49 BCGs and two ellipticals. All $L_X$ values are $\times 10^{44}$, except those marked by $\star$ which are $\times 10^{43}$. The $L_X$ values marked by $\star$ (from Ledlow et al. 2003) were calculated assuming a third cosmological model (Friedmann–Walker), and measured in a different energy band than the rest of the $L_X$ values and were not used in the subsequent analysis (see text). The $L_X$ values which were used here, were also converted to the concordance cosmological model for completeness. The $\sigma_{cluster}$ values are in km s$^{-1}$ and the projected distance between the galaxy and the cluster X-ray peak ($R_{off}$) is in Mpc. The $\star$ marks at $R_{off}$ indicate that the galaxy is not in the centre of the cluster but closer to a local maximum X-ray density (see text). The references are: a = Chen et al. (2007); b = Bohringer et al. (2004); c = Bohringer et al. (2000); r = Cruddace et al. (2002); w = White, Jones & Forman (1997); e = Edwards et al. (2007); g = Giovannini, Liuzzo & Giroletti (2008); cc = Calculated from Bohringer et al. (2000); cl = Calculated from Ledlow et al. (2003); cb = Calculated from Bohringer et al. (2004); cr = Calculated from Cruddace et al. (2002); m = Mahdavi & Geller (2001); st = Struble & Rood (1999); s = Struble & Rood (1991); p = Patel et al. (2006); pe = Peres et al. (1998). All the values for X-ray temperature ($T_X$ in keV) are from White et al. (1997).
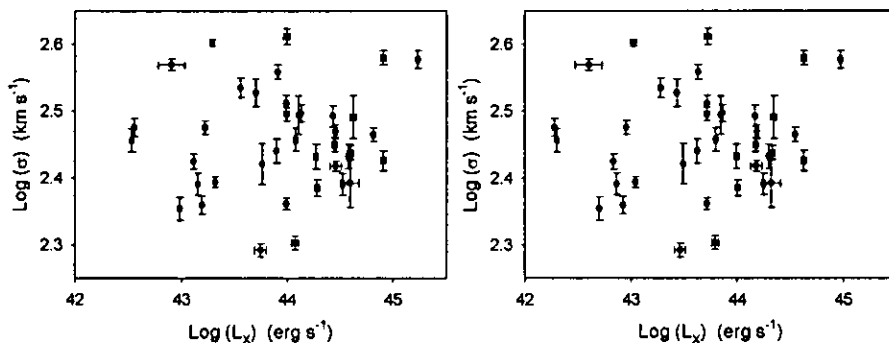
Figure 5.1: Velocity dispersion for the BCGs plotted against log $L_X$ for the host clusters assuming the Einstein de–Sitter cosmological model (left) and the concordance cosmological model (right). It can be seen that the relative correlation does not depend on the cosmological model assumed.

# 5.1 Cluster X-ray luminosity

## 5.1.1 Velocity dispersion versus log $L_X$

Cluster X-ray luminosity is directly proportional to the square of the density of the intracluster medium, as well as a function of X-ray temperature to a lesser extend (see Figure 5.7 this work; Mushotzky et al. 1978). Thus, X-ray luminosity can be used as a measure of environmental density (Reiprich & Bohringer 2002). In the present sample, no correlation is found between the X-ray luminosity of the cluster (i.e. density of the cluster) and the velocity dispersion of the BCG (i.e. the mass of the BCG) as shown in Figure 5.1.

Brough et al. (2007) noted a weak trend (only $2\sigma$) between these two properties, in the sense that galaxies in higher density clusters are more massive. However, their sample consisted of only six galaxies. It can be seen from Figure 5.1 that this correlation is not found when this much larger sample of BCGs is used. Nevertheless, it is well-known that BCG luminosity does correlate with host cluster mass (Lin & Mohr 2004; Hansen et al. 2007; Popesso et al. 2006; Whiley et al. 2008).

## 5.1.2   Indices versus log $L_X$

The mean SSP-equivalent [Z/H] and [E/Fe] of the BCGs are plotted against the X-ray luminosity of the host cluster in Figure 5.2, and no strong correlations are found. As previously, the derived ages are not shown here as the scatter in the ages can be fully explained by the errors (see Table 4.7).

If the true correlations between these parameters and the X-ray luminosity are only slight, they can be masked by systematic effects in the derivation of the parameters. For this reason, indices are also used here to explore possible correlations. Figure 5.3 shows some of the indices, including H$\beta$ measurements (where higher values imply lower age), as a function of the density of the host clusters. No significant correlations are found for any of the indices. The two oldest galaxies (NGC0533 and ESO444-046) are hosted by the least dense clusters, whilst the youngest galaxy is hosted by the most dense cluster. As discussed in the introduction to this chapter, previous photometric studies reported different evolutionary histories in X-ray bright and dim clusters. Brough et al. (2002) place this break at $L_X = 1.9 \times 10^{44}$ erg s$^{-1}$, and conclude that BCGs in high-$L_X$ clusters assembled their mass at $z > 1$ and have been passively evolving since, whereas BCGs in low-$L_X$ clusters appear to be in the process of assembling their mass. Unfortunately, the scatter in the measurements in Figure 5.3 is too large to clearly detect two different regimes in the $L_X$ and BCG line strength correlations. In the case of the Balmer lines, the scatter can be fully explained by the measurement errors (see analysis in Table 4.5).

The fact that no correlations are found between metallicity and $\alpha$-abundance ratio with the density of the host cluster is consistent with the result found for normal elliptical galaxies in earlier studies (e.g. T05). On the other hand, Bernardi et al. (2006) found higher [$\alpha$/Fe] values for early-type galaxies in higher density environments (although only larger by 0.02 compared with their counterparts
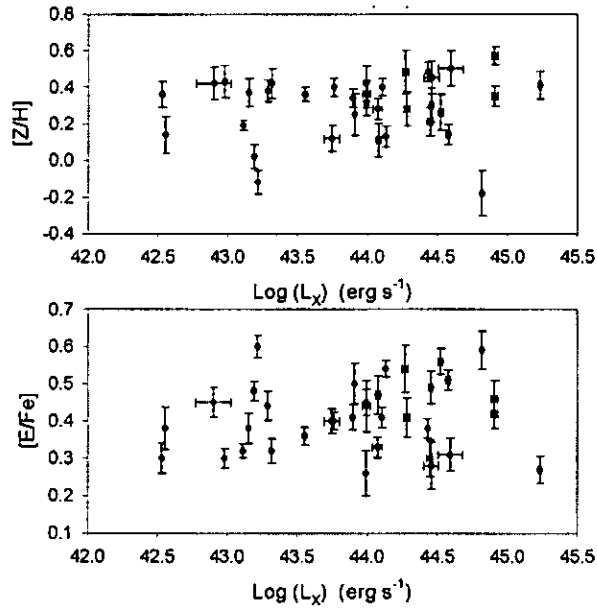
Figure 5.2: The derived SSP-parameters against log $L_X$ for the BCGs.

with the same velocity dispersion in less dense regions).

## 5.2 Cooling-flow clusters

It is well-known that the hot intracluster medium in galaxy clusters radiates large amounts of energy at X-ray wavelengths ($L_X \sim 10^{44} - 10^{46}$ erg s$^{-1}$), which implies that the gas is cooling and flowing inwards (as discussed in Bildfell et al. 2008). As mentioned in the introduction to this chapter, several studies reported examples of recent or ongoing star formation in BCGs hosted by cooling-flow clusters (Cardiel et al. 1998a; Crawford et al. 1999; McNamara et al. 2006; Edwards et al. 2007; O'Dea et al. 2008; Bildfell et al. 2008; Pipino et al. 2009). Most of these previous samples were photometric, and often had limited sample sizes or were biased exclusively towards cooling-flow clusters or emission-line galaxies.

Cooling-flow information was collected from the literature as shown in Table 5.1. The mean SSP-equivalent age of all the BCGs in cooling flow clusters is log
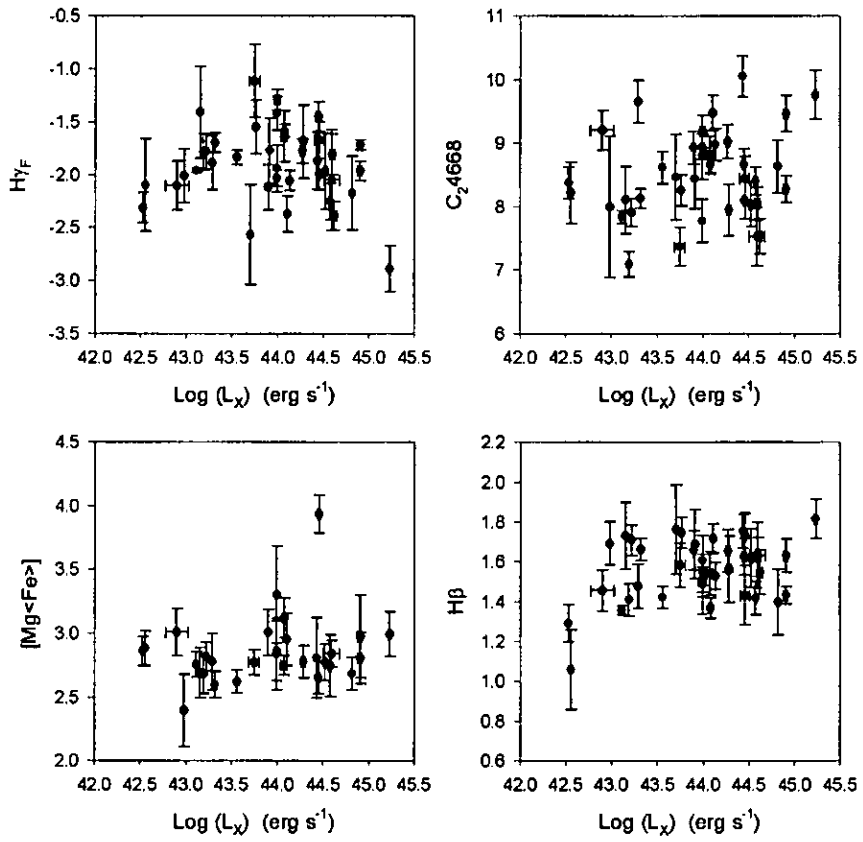
Figure 5.3: Examples of indices against log $L_X$ for the BCGs.

age = 0.843 ± 0.038 (mean ± error on mean), and 0.944 ± 0.028 for the BCGs in non-cooling flow clusters. A Kolmogorov–Smirnov test was performed on the distributions of the two samples, where as previously, the null hypothesis is that the distributions were drawn from an identical parent population. The critical value of the statistical test, at a 95 per cent confidence level, is $D = 0.52$, and the test value is 0.35. Thus, the age distributions of the two samples compared (those in cooling flow and non-cooling flow clusters) are not significantly different from each other at the 95 per cent confidence level.

Figure 5.4 shows the derived SSP-parameters against velocity dispersion for clusters with cooling-flow or non-cooling flow data available in the literature. It is interesting to note that a tendency is visible in the sense that five of the six BCGs with younger mean ages (log age < 0.8 Gyr) tend to be in clusters with cooling flows. However, it is possible that this is coincidental as the scatter in the age distribution can be fully explained by the errors (as shown previously in Table 4.7). Figure 5.5 shows the same tendency, where very high Hβ values imply lower ages. This, in principle, agrees with the results derived from photometric data (in an X-ray selected BCG sample) by Bildfell et al. (2008).

Figure 5.6 shows the Faber–Jackson relation for normal ellipticals, corresponding to $L \propto \sigma^4$, and data points for BCGs in cooling-flow and non-cooling flow clusters on the same graph. The lower panels in Figure 5.6 show the deviation from the Faber–Jackson relation against cluster X-ray luminosity and cluster velocity dispersion, respectively. No real difference can be seen between the location of the cooling and non-cooling clusters on the relation (this is also the case if 2MASS $K$-magnitudes are used). Hence, the presence of cooling flows in clusters does not affect the position of the BCG in this scaling relationship. This is to be expected, as the deviation from the Faber–Jackson relation by BCGs is naturally explained by models of dissipationless mergers of elliptical galaxies, provided that
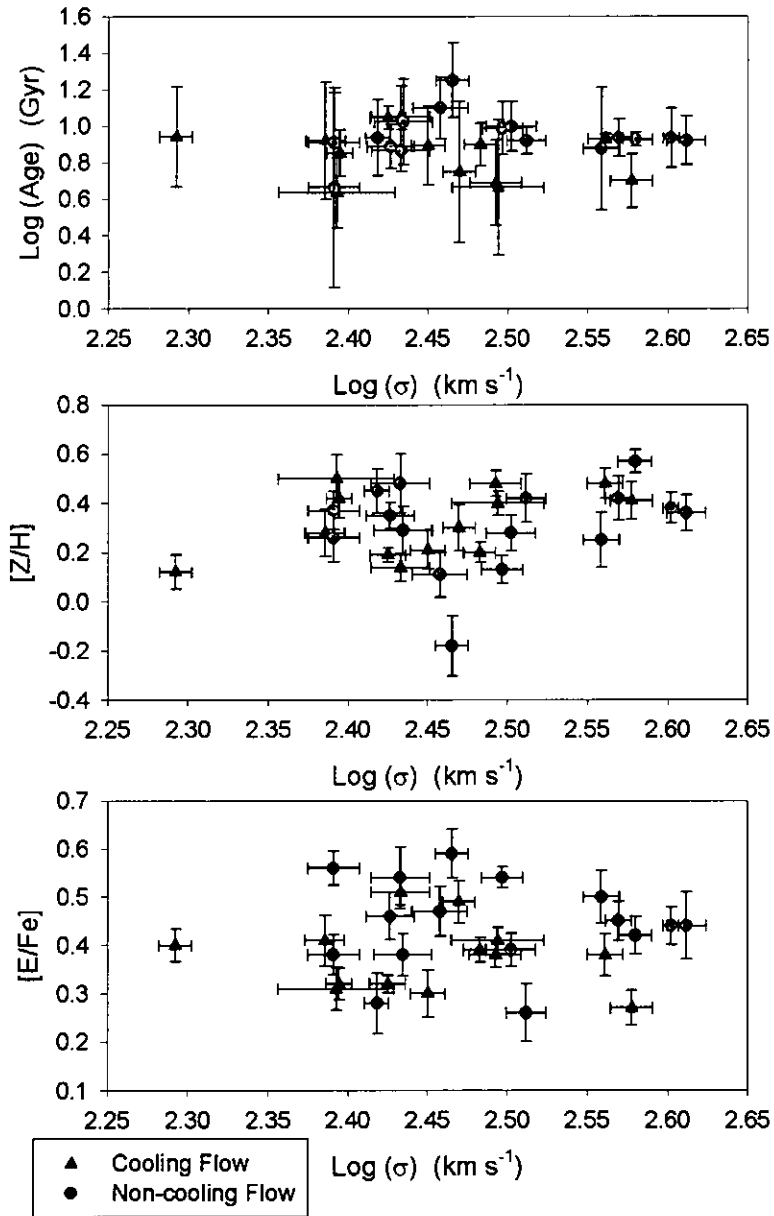
Figure 5.4: The derived SSP-parameters against velocity dispersion for the BCGs. The blue symbols are BCGs in host clusters with cooling flows, and the red symbols those in clusters without cooling flows.
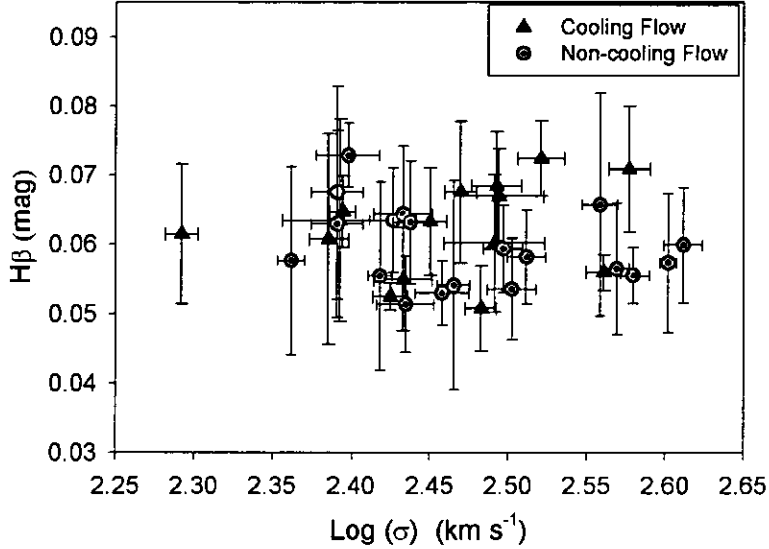
Figure 5.5: The measured H$\beta$ against velocity dispersion for the BCGs. The red symbols are BCGs in host clusters without cooling flows, and the blue symbols those in cooling-flow clusters.

the merger orbits become preferentially more radial for the most massive galaxies (Boylan-Kolchin et al. 2006). Hence, this deviation is not related to the presence of cooling flows in the cluster centre.

## 5.3  Log $L_X$ – log $T_X$ relation

It is believed that intrinsic scatter in the cluster X-ray luminosity–temperature ($L_X$–$T_X$) relation is physical in origin, caused by processes such as radiative cooling, and those associated with AGN (McCarthy et al. 2004; Bildfell et al. 2008).

Figure 5.7 shows the log $L_X$ – log $T_X$ plot for the host clusters for which the measurements of $T_X$ and $L_X$ were available in the literature. The X-ray luminosity ($L_X$) is normalised with $E(z) = [\Omega_m(1 + z)^3 + \Omega_\Lambda]^{\frac{1}{2}}$ to correct for the evolution of the mean background density, where $z$ is the redshift of the cluster. As in Bildfell et al. (2008), a power law of the form $\frac{L_X}{E(z)} = \beta T_X^\alpha$ was fitted to the normal (i.e. old) BCGs (the red dashed line in Figure 5.7 is fitted to the BCGs with an
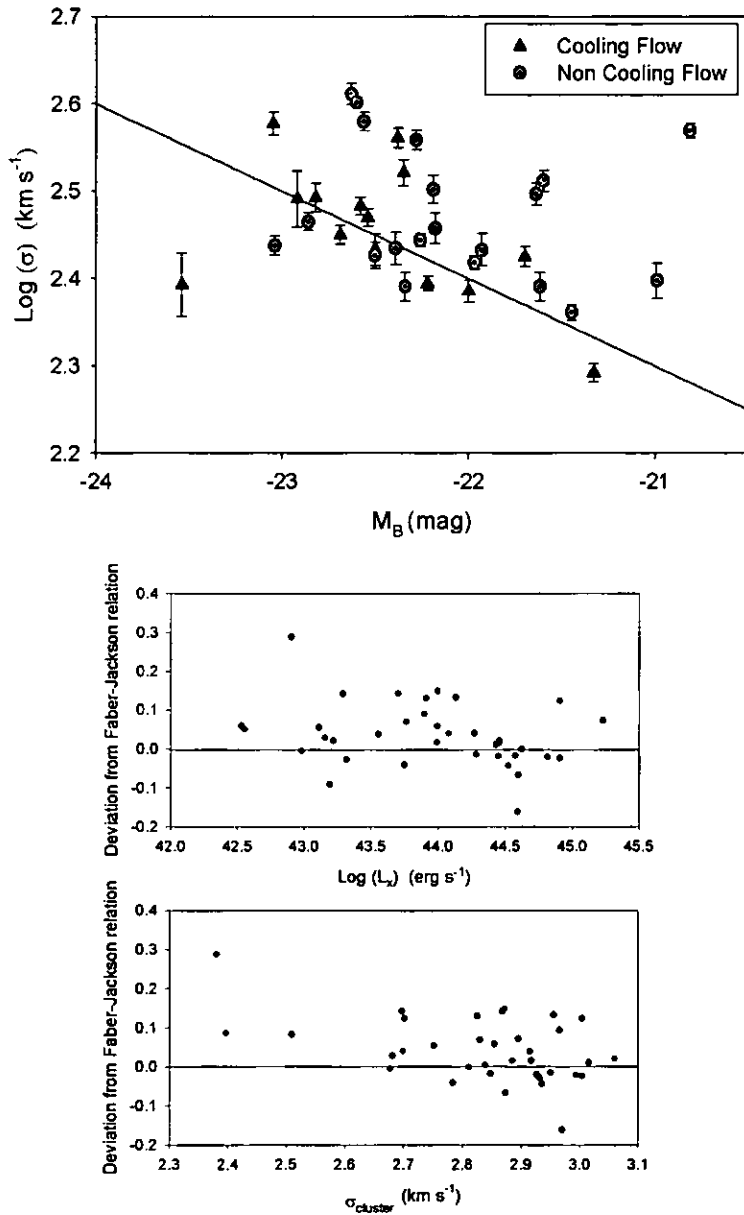
Figure 5.6: The $\log \sigma$ versus absolute $B$-band magnitude relation for BCGs in cooling-flow and non-cooling flow clusters. The straight line is the Faber–Jackson relation for normal ellipticals. The bottom two plots show the deviation from the Faber–Jackson relation as a function of host cluster X-ray luminosity and velocity dispersion (proxies for host cluster density and mass, respectively).

SSP-equivalent age older than 6 Gyr). A strong correlation with $t$ and $P$ values of 6.66 and $< 0.0001$, respectively, was found. Younger BCGs (blue datapoints) tend to be located above the line fitted to the older BCGs (red datapoints) in the diagram, i.e. it seems that they are predominantly in clusters with X-ray excess. It is interesting to note that the five young galaxies located above this line are the ones hosted by a cooling-flow cluster (denoted by a black circle). Only one of the younger galaxies, located at the bottom of the plot, NGC0541, is hosted by a cluster without cooling flows. However, this is speculative as no clear distinction can be made between younger and older BCGs in the present sample, and the young galaxies lies within the scatter of the old galaxies from the fitted function. Indeed, the correlation coefficients are only marginally different if the function is fitted to all the data instead of the older BCGs. Thus, the younger BCGs do not deviate significantly from the relation formed by the older BCGs in the diagram. The lower plot in Figure 5.7 shows the deviation from the fitted relation against age.

Using photometric data, Bildfell et al. (2008) showed that their star forming BCGs are exclusively located in clusters with a high-$L_X$ deviation from the $L_X$–$T_X$ relation – the region of the diagram usually populated by cool-core clusters. Their result implies that the origin of the cold gas fuelling the star formation may be linked to the processes that give rise to the $L_X$ excess, and points to cooling flows as the source of the cold gas in galaxies with young stellar populations.

Six of the older BCGs in this diagram are also located in cooling-flow clusters, but they did not experience recent star formation. The influence of cooling flows can be limited by either feedback processes or by the physical extent of the cooling flows. Rafferty, McNamara & Nulsen (2008), for example, set a criterion of an X-ray offset of $\sim 20$ kpc for star formation in the BCG to be as a result of the cooling flows.
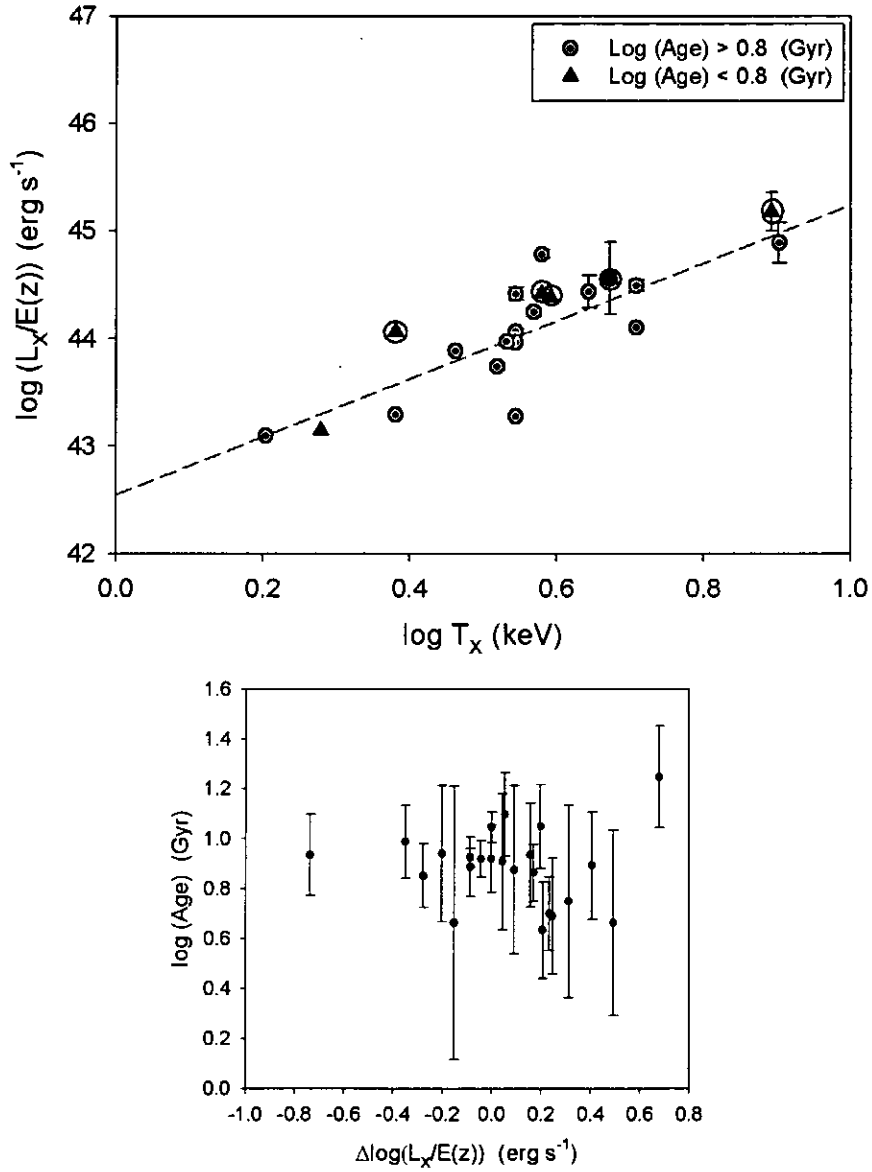
Figure 5.7: Log $(L_X/E(z))$ against log $T_X$ for the BCGs. The clusters hosting BCGs with ages log (age) $< 0.8$ Gyr are shown in blue, where the black circles denote young galaxies in cooling-flow clusters. The majority of the $L_X$ values from the literature does not have errorbars. The bottom plot shows the residuals of log $(L_X/E(z))$ compared with the fitted relation, plotted against age.

## 5.4 BCG offset from the X-ray peak

Numerical simulations predict that the offset of the BCG from the peak of the cluster X-ray emission is an indication of how close the cluster is to the dynamical equilibrium state, and that this decreases as the cluster evolves (Katayama et al. 2003). If the star formation in all young BCGs is a result of the presence of cooling flows, then the young BCGs are expected to be located exclusively at the centres of relaxed clusters, where the cold gas is deposited. Indeed, Bildfell et al. (2008) found that all the blue-core BCGs in their sample were located within $\sim$ 10 kpc of the peak of the cluster X-ray emission. Rafferty et al. (2008) used broadband imaging and X-ray data for a sample of 47 cluster central dominant galaxies. By comparing the near-UV colour gradients with the X-ray properties, they found that the central galaxy is likely to experience significant star formation when: 1) the X-ray and galaxy centroids are within $\sim$ 20 kpc of each other, and 2) the central cooling time of the hot atmosphere is much less than $\sim 8 \times 10^8$ yr (an entropy of less than $\sim$ 30 keV cm$^2$, Cavagnolo et al. 2008). Therefore, the younger BCGs need to be very close to the X-ray peaks, even though they are in cooling-flow clusters, for the recent star formation to be a result of the cooling flows.

For the present sample, the correlation between SSP-equivalent ages and off-sets from the X-ray peaks could be investigated as the ages are all consistent within their errors. Nevertheless, it is interesting to explore possible correlations between the derived metallicity and $\alpha$-enhancement with X-ray offset.

For the present sample, the projected angular separations between the BCGs and the peak of the cluster X-ray emission were collected from the literature and are listed in Table 5.1. These angular separations will be referred to as "X-ray offsets" in the following discussion. For the majority of the clusters this offset was

not already published, and it was then calculated from the BCG and published X-ray peak coordinates. However, this was not possible for those clusters, e.g. Coma, where a BCG is not in the centre and where the coordinates of a corresponding local X-ray maximum were not available. Figure 5.8 shows the derived SSP-parameters against the offsets for all BCGs for which the offsets were available, and no significant correlations can be seen.

The errors on the derived X-ray offsets are largely determined by the errors on the X-ray centres. The X-ray centres of the samples based on the *ROSAT* data are usually found by determining the two-dimensional centre of mass using the Voronoi tessellation and percolation method (Ebeling & Weidemann 1993; as described in Edwards et al. 2007). These X-ray centres are generally accurate to about 1.0 arcmin (Ebeling et al. 1998), corresponding to $\sim 90$ kpc at $z \sim 0.08$ (which is the highest redshift in this present sample). Therefore, the errors on the X-ray offsets are not negligibly small, but it makes no difference to the results in this section since it's clear that no correlations are found as the scatter is too large (larger than can be explained by the errors).

Figure 5.9 shows the X-ray offsets plotted against the galaxy velocity dispersion and absolute $K$-band magnitude. Bildfell et al. (2008) found a weak tendency for brightest BCGs to lie closest to their host cluster's X-ray peak while the faintest BCGs are the furthest. This might be expected since massive BCGs will locate at the centre of the cluster potential well on a shorter time-scale than less massive BCGs. They will also have an enhanced probability to merge with small galaxies and will grow more rapidly than BCGs further away form the centre and they will be close to where the cool gas is deposited (Bildfell et al. 2008). However, as can be seen in Figure 5.9, no such trend can be seen for the present sample, within the uncertainties.
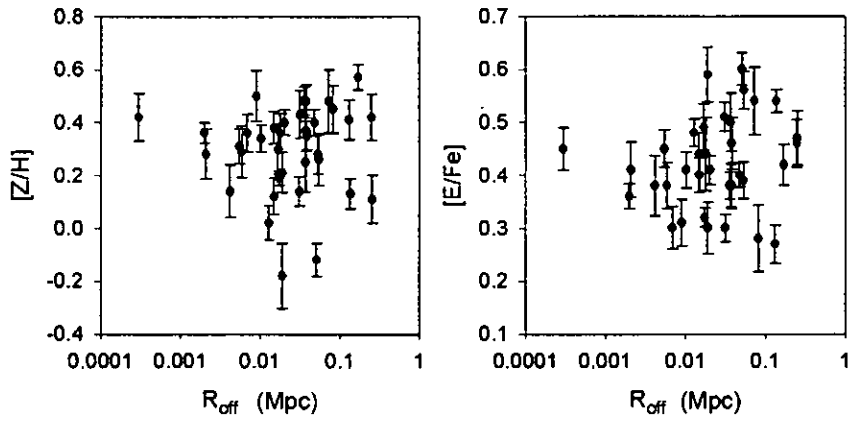
Figure 5.8: Derived SSP-parameters (metallicity and $\alpha$-enhancement) plotted against BCG offset from the X-ray peak for all BCGs for which the offsets were available.
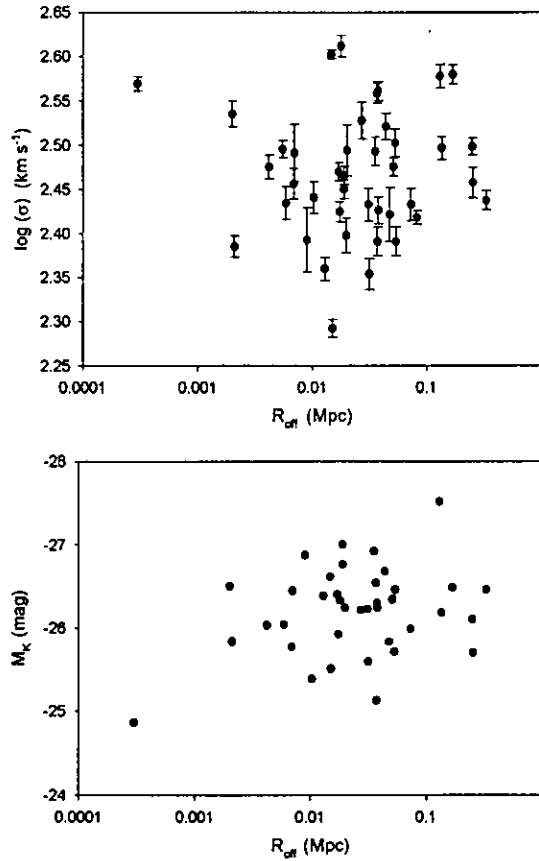


Figure 5.9: Galaxy velocity dispersion and absolute $K$-band magnitude plotted against X-ray offset.

## 5.5    Cluster velocity dispersion

Data on host cluster velocity dispersions were collected from the literature and listed in Table 5.1. The cluster velocity dispersions are plotted against various properties for the BCGs in Figures 5.10 and 5.11. No clear correlation between host cluster velocity dispersion (indicative of the mass of the host cluster) and any of the derived parameters was found.

## 5.6    Results and discussion

### Host cluster X-ray luminosity and velocity dispersion

- No correlation is found between the X-ray luminosity of the clusters and the velocity dispersion of the BCGs (Figure 5.1). Thus, galaxies in higher density clusters are not necessarily more massive, contrary to the findings of Brough et al. (2007) who studied a much smaller sample.

- No clear correlation between host cluster X-ray luminosity (cluster density) or host cluster velocity dispersion (cluster mass) and the derived parameters (metallicity and $\alpha$-abundance) were found.

### The origin of the cool gas fuelling recent star formation in BCGs

- Several sources of gas for fuelling the recent star formation in BCGs have been postulated (discussed by Pipino et al. 2009). These are: 1) cooling flows; 2) recycling of stellar ejecta; and 3) accretion of satellites.

  Because of the generally large errors on the derived ages, no clear distinction can be made between any galaxies which possibly experienced recent star formation and the older BCGs in the present sample. This makes it difficult to investigate if the young ages found for (some) BCGs is always
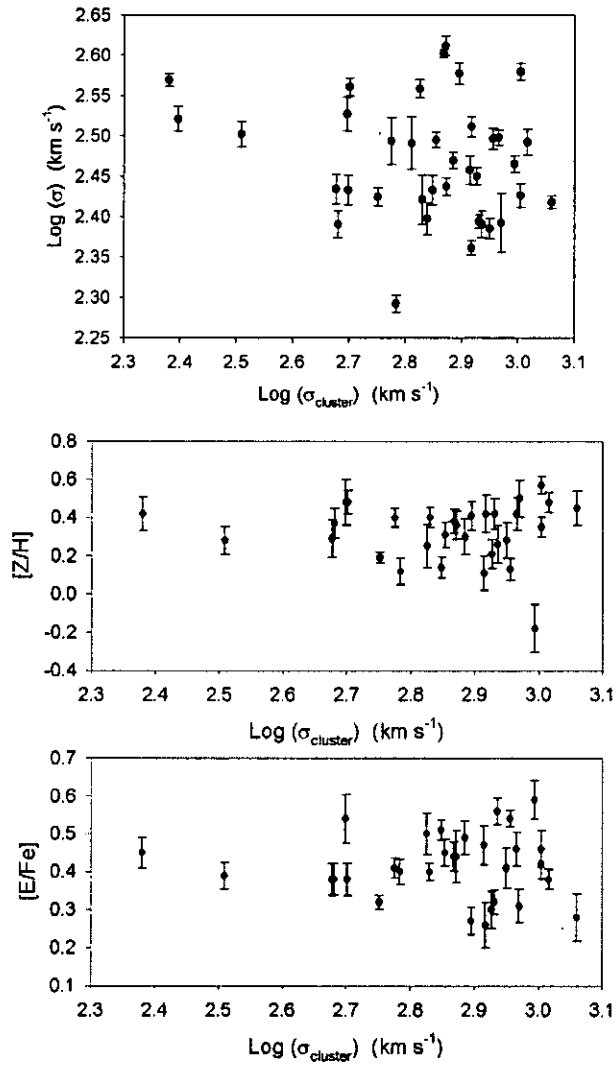
Figure 5.10: BCG velocity dispersion and SSP-parameters (metallicity and $\alpha$-abundance) against host cluster velocity dispersion.

Figure 5.11: The cluster velocity dispersion against BCG offset from the X-ray peak.

a consequence of cooling flows, as suggestions by previous authors (Bildfell et al. 2008; Pipino et al. 2009).

The second possible origin of the cool gas in the centre of BCGs, namely recycling of stellar ejecta (originally proposed by Menanteau, Abraham & Ellis 2001; Menanteau, Jimenez & Matteucci 2001), can also lead to blue cores of BCGs because of the increased potential well in the centre. This can cause star formation in the centre to be more extended in time (Pipino et al. 2009). However, it has been claimed that this internally recycled gas is not sufficient to produce UV-blue ellipticals (Kaviraj et al. 2007; Pipino et al. 2009). Pipino et al. (2009) dismissed this possibility for a source of cool gas based on the fact that this scenario implies that BCGs in non-cooling flow clusters can also have blue cores, and hence was in contrast with the findings of Bildfell et al. (2008).

The results discussed above are not yet conclusive, and the gradients of SSP-parameters with radius will provide a more conclusive test for these different scenarios (see Section 6.3). Even though the predicted signatures of gaseous mergers and dissipative models (such as cooling flows) are qualitatively similar in terms of metallicity gradients in that stars in the centre are more

metal rich, models by Kobayashi (2004) predict that dissipative processes will steepen the metallicity gradient, whilst major mergers are expected to flatten it.

# Chapter 6

# CONCLUSIONS AND FUTURE WORK

## 6.1 Conclusions

This thesis has presented the largest optical, spatially-resolved, spectroscopic sample of BCGs to date. The sample contains high signal-to-noise ratio, long-slit data for 49 BCGs in the nearby Universe, allowing possible connections between the kinematical, dynamical and stellar population properties to be studied using a statistically significant number of galaxies. Previous samples were either limited in numbers of galaxies, or concentrated on the photometric properties, or lacking in spatially-resolved information (e.g. SDSS data).

The spatially-resolved kinematic profiles for 49 BCGs were measured, and SSP-equivalent ages, metallicities and $\alpha$-abundance ratios in the centres of 43 BCGs were derived using the Lick/IDS system of absorption line indices. The indices measured and parameters derived for the BCGs are compared with those of ordinary ellipticals in the same mass range. They are also tested for possible correlations with the kinematic properties of the galaxies (velocity dispersion, rotation) and the properties of the host clusters (density, mass, distance to X-ray

209

peak, presence of cooling flows).

Clear rotation curves were found for a number of galaxies for which major axis spectra were obtained, and in particular, two galaxies were found to have rotational velocities exceeding 100 km s$^{-1}$. The large rotation is unexpected in the light of numerical simulations, which predict that the bombardment of small satellites without gas is very effective at heating the disc and creating a spheroid supported by velocity anisotropies (Boylan-Kolchin et al. 2006). However, in general the BCG data are consistent with the known trend for very massive elliptical galaxies to be supported by velocity anisotropy on the anisotropy–luminosity diagram, because of the large central velocity dispersions.

At least 31 per cent of the BCGs show very clear velocity substructure, which could be due to a merger event or because the galaxy is triaxial and supports different orbital types in the core and the main body. Despite the undeniably special nature of BCGs due to their extreme morphological properties and locations, the kinematic properties investigated here (rotation and incidence of velocity substructure) seem normal when compared with their ordinary giant elliptical counterparts. However, there are exceptions: 1) BCGs lie above the Faber–Jackson relation, which is naturally explained if the galaxies formed through dissipationless mergers of elliptical galaxies on radial orbits; and 2) the rising velocity dispersion profiles found for a small number of BCGs, which are generally not found in ordinary ellipticals, and might imply a rising M/L ratio.

The derived ages of these massive galaxies are consistently old, as expected. There are also differences – albeit small – between the stellar populations in BCGs and ordinary elliptical galaxies over the same mass range. The BCGs show higher metallicity and $\alpha$-enhancement values. The former possibly indicates more efficient star formation, and the latter is most commonly interpreted

as a consequence of shorter formation time-scales in BCGs, though other interpretations are possible including differences in the IMF, differences in the binary fractions, or selective winds. The SSP-equivalent parameters show very little dependence on the mass or brightness of the galaxies, or the mass or density of the host clusters.

The present BCG sample, and thus the findings discussed above, is biased towards cD galaxies. However, homogeneous photometry of the entire sample is needed to identify any non-cD BCGs in the sample. Only then will it be possible to conclusively say if any of the results discussed above is particularly relevant to cD galaxies, and if there is a clear distinction between the derived kinematics and stellar population properties of cD and non-cD galaxies.

Overall, the star formation histories in BCGs, and the connection to the processes in the cluster centres, are very complex. This sample of BCGs will also warrant further detailed analysis. Some of these possibilities are described in Section 6.3.

## 6.2 General recommendations for future work and limitations of the present study

The present sample, and the observational and analysis techniques presented in this thesis suffer from a number of limitations.

There exists a lot of confusion in the literature regarding the classification of cD galaxies, mostly because of the lack of deep photometry which would allow one to conclusively distinguish between BCGs with and without a halo. The present work initially aimed at compiling a representative cD sample and so rather broad selection criteria were adopted, although the sample is intrinsically a BCG sample. It is expected that deep, homogeneous photometric information will be added in

the future which will allow one to test for the presence of a faint halo and hence discriminate between cD and non-cD BCGs.

Another caveat regarding sample selection is that in the past optically selected samples have shown slightly different properties from X-ray selected samples. For example, Aragón-Salamanca et al. (1998) found a high rate of BCG evolution since $z \sim 1$ in their optically selected sample, whereas Collins & Mann (1998) found far less evolution for their X-ray selected sample. According to Burke et al. (2000), the properties derived from the two samples can be reconciled if luminosity-dependent evolution is taken into account. An example of a catalogue containing BCGs from an X-ray selected sample is the Brightest Cluster Survey (BCS) of Ebeling et al. (1998; 2000). Choosing a BCG sample from such a catalogue in future would guarantee that the BCG candidates are automatically the central galaxy closest to the X-ray peak, and eliminate systems with chance alignments of galaxies.

Stellar population studies suffer from some inherent difficulties, e.g.: they are luminosity-weighted; non-solar abundances have to be taken into account (especially in the case of massive ellipticals); and the age–metallicity degeneracy and the degeneracy between burst-age and burst-strength need to be broken. As a consequence, the results can be difficult to interpret and are subject to a number of uncertainties.

The most common technique employed so far in this kind of study, namely long-slit spectroscopy, is limited to just one or a few spectral directions per galaxy. Integral field spectrographs (IFUs), are becoming increasingly available, and provide both spectral and spatial information. Other observational limitations such as low S/N for higher redshift objects, and limited exposure times constrain the fraction of the galaxy (relative to the half-light radii) for which spatially resolved data can be obtained. For large, diffuse objects such as the BCGs, observations

are normally limited to only the very centre of the galaxy and do not normally extend out to the halo. Kinematics of the outer haloes of cD galaxies can be studied by using globular clusters and planetary nebulae as probes, though this is also limited by instrumental and magnitude constraints.

## 6.3 Specific areas of future work

### 6.3.1 Radial gradients of indices and SSP-parameters

All the indices and SSP-results discussed here relate only to the central regions of the BCGs. If significant radial gradients in age and metallicity are present, then these results will not necessarily be representative of the whole galaxy. It is therefore important to investigate the radial SSP-gradients in BCGs. These gradients will reveal even more information about the processes at work in galaxy formation, since gas dissipation and mergers will leave different radial signatures. Various authors have explored gradients in various types of galaxies (Gorgas, Efstathiou & Aragón-Salamanca 1990; Davies et al. 1993; González 1993; Fisher et al. 1995b; Gorgas et al. 1997; Cardiel et al. 1998a; Mehlert et al. 2003; Sánchez-Blázquez et al. 2006c; and many others), but studies involving BCGs have been limited to small samples.

Figure 6.1 shows a summary of the observational tests, involving gradients, for BCG formation scenarios. If galaxies undergo major mergers, then the stellar population signatures depend on the degree of gaseous dissipation and on the amount of triggered star formation (shown on the left side in Figure 6.1). If BCGs form in a dissipational process such as the cooling-flow scenario (shown on the right side in Figure 6.1), then metallicity gradients are expected in that stars in the centre being more metal rich. In addition, continuous enrichment of gas by evolving stars in the centre of the galaxy will lead to the centres being less
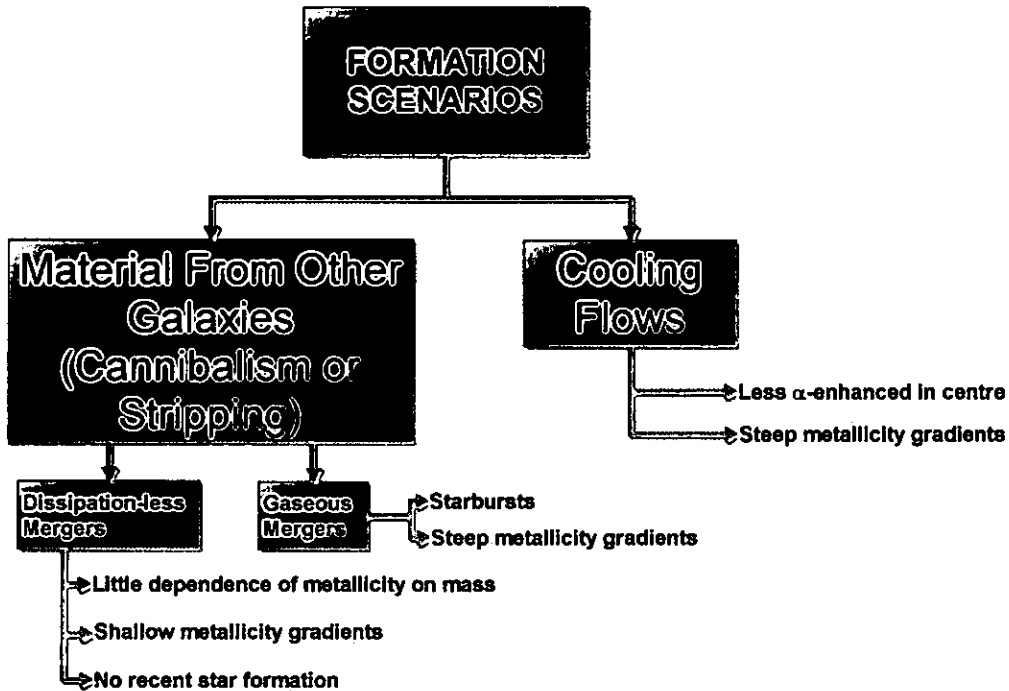
Figure 6.1: Summary of observational tests for BCG formation scenarios.

$\alpha$-enhanced in this scenario.

Figure 6.1 also shows that the predicted signatures of gaseous mergers and the cooling flow scenario are qualitatively similar in terms of metallicity gradients (stars in the centre will be more metal rich). However, models predict that dissipative processes will steepen the metallicity gradient, whilst major mergers are expected to flatten it (Bekki & Shioya 1999; Kobayashi 2004). In addition, formation by dissipative collapse predicts strong negative metallicity gradients that correlate with galaxy mass, negative $\alpha$-element enhancement gradients, and small positive to null age gradients. Stellar population gradients will, therefore, provide a powerful tool to distinguish between the different scenarios.

## 6.3.2 Surface brightness profiles and isophotes

### Surface brightness profiles

As mentioned in Section 6.2, it will be interesting to distinguish between cD and non-cD BCGs in this sample. To do that, surface brightness observations are needed, but the detection of cD envelopes is a very challenging task (Graham et al. 1996).

Many authors have adapted the generalised $r^{\frac{1}{n}}$ Sérsic surface brightness profile to characterise BCG surface brightness profiles, since the universality of the $r^{\frac{1}{4}}$ law is questionable (Patel et al. 2006, and references therein). In addition, Kormendy et al. (2009) argued that excess light over the $r^{\frac{1}{4}}$ law is present for all giant ellipticals that have $n > 4$. However, this makes it even more difficult to choose an appropriate range of radii over which the parametrised profile should be fitted, due to the extra degree of freedom.

Petrosian profiles are also used to characterise surface brightness profiles (Patel et al. 2006; Liu et al. 2008), but Hyde & Bernardi (2009) urged caution over the use of Petrosian profiles for BCGs, especially as they are often not corrected for the effects of seeing.

Therefore, it may be very difficult to unambiguously separate cD from non-cD BCGs based on surface brightness profiles alone (Seigar et al. 2007; Liu et al. 2008). It is still an open question as to whether the observed flux in cD galaxies is a distinct halo of material or just an artificial consequence of fitting of surface brightness profiles (as also discussed by Seigar et al. 2007).

Surface brightness studies are also severely limited in practice by redshift, since the surface brightness is proportional to $1/(1 + z)^4$ (Sandage 1994).

**Isophotes**

Another interesting aspect of BCG properties that can be studied using deep photometric observations is their isophotes. Liu et al. (2008) found that 51 per cent of their sample of 85 BCGs have "boxy" isophotes. This percentage is larger than the 31 per cent of normal ellipticals with boxy isophotes. However, they also find that some of the very luminous BCGs have "discy" isophotes. Such flattening can be a result of rotation or anisotropic motions. If BCGs experienced a recent merging event, and retain some of the orbital angular momentum from merging, then their isophotes may be discy (Liu et al. 2008).

## 6.3.3 Radio observations

The connection between the formation of a galaxy cluster and the formation of the BCG remains a mystery. As discussed in Chapter 1, it is still unresolved as to whether BCGs are products of cluster evolution, or form at the same time as the cluster, or whether these galaxies are the seeds around which clusters accreted. As such, BCGs are ideal objects for studying the heating and feedback mechanisms in cluster centres.

BCGs have long been known to show different radio properties from those of other cluster galaxies, being much more likely to be radio luminous than other non-dominant cluster ellipticals (Burns 1990; Best et al. 2007). This radio-loud AGN activity has been proposed as a potential solution to the well-known cooling flow problem. Future radio and submillimeter observations of the neutral and molecular gas content of the BCGs, in particular the ones with ongoing star formation, can be correlated with stellar kinematics and optical properties. Such studies would then yield important information on the possibility of recent mergers and tidal stripping events happening in the centres of the host clusters.

# CHAPTER 6

Many questions remain unsolved. However, an empirical approach to galaxy formation, using backwards-modelling of galaxy observations in combination with simulations of large-scale structure, holds great promise for the future. With more and improved data over the coming years, one can confidently expect to reduce or eliminate many of the uncertainties that currently exist in the subject area of galaxy formation.

# NOTES ON INDIVIDUAL GALAXIES

This section describes the individual objects in this study, primarily referring to the results obtained here, and then comparing it with the results published prior to this study. Figure A.1 shows the gallery of the galaxies and slit positions as obtained from the Digital Sky Survey.

## ESO146-028

The radial velocity profile of this galaxy is mostly flat and the velocity dispersion profile is decreasing outwards.

## ESO202-043

This galaxy shows moderate rotation, but no significant velocity substructure.

## ESO303-005

The radial kinematic profiles of this galaxy show no significant rotation or substructure.

## ESO346-003

The radial velocity profile shows clear rotation of the order of 51 km s$^{-1}$.
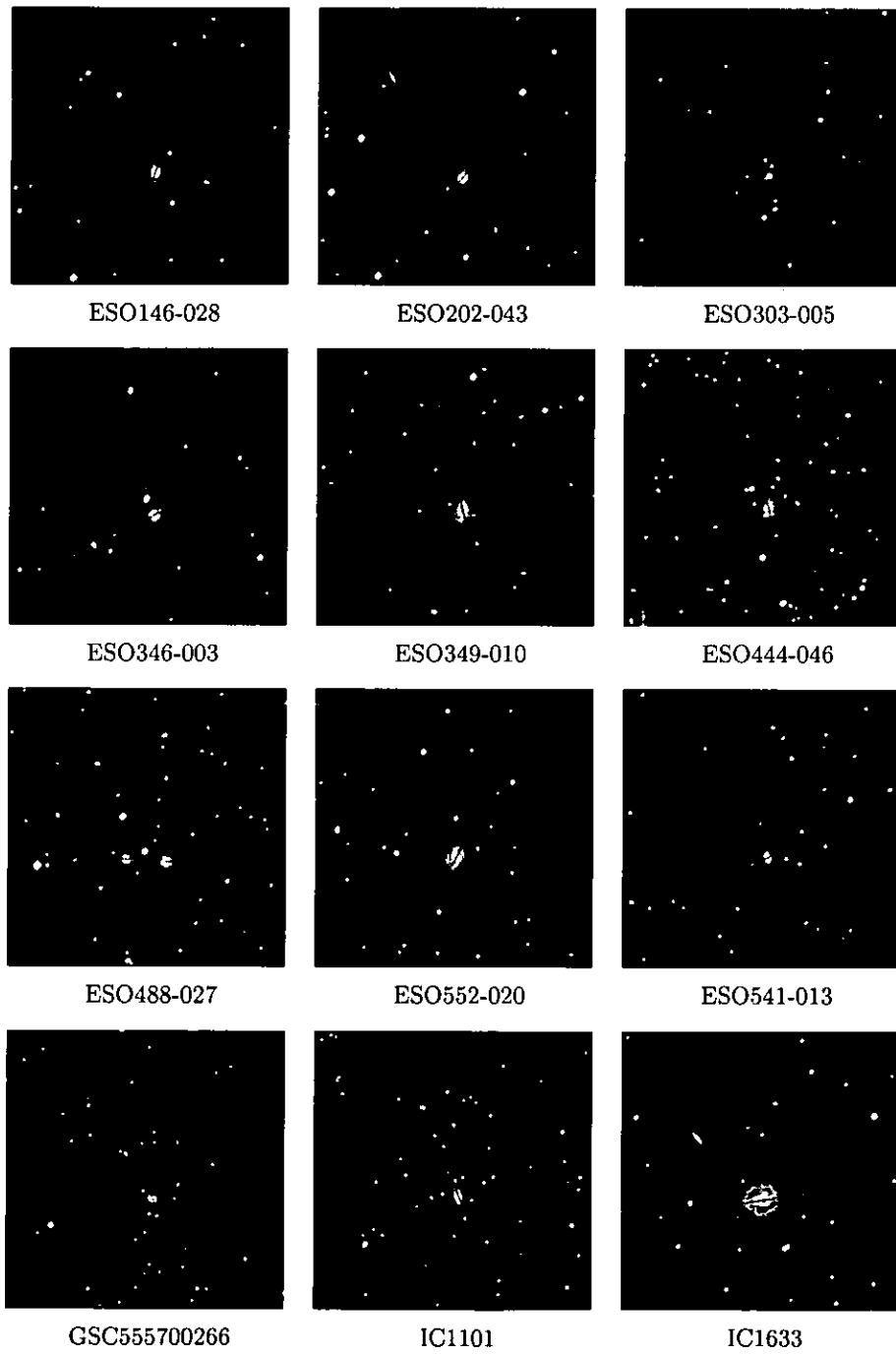
Figure A.1: Gallery: galaxy sample.

IC4765　　　　　　IC5358　　　　　　LEDA094683

MCG-02-12-039　　　NGC0533　　　　　NGC0541

NGC1399　　　　　NGC1713　　　　　NGC2832

NGC3311　　　　　NGC3842　　　　　NGC4839
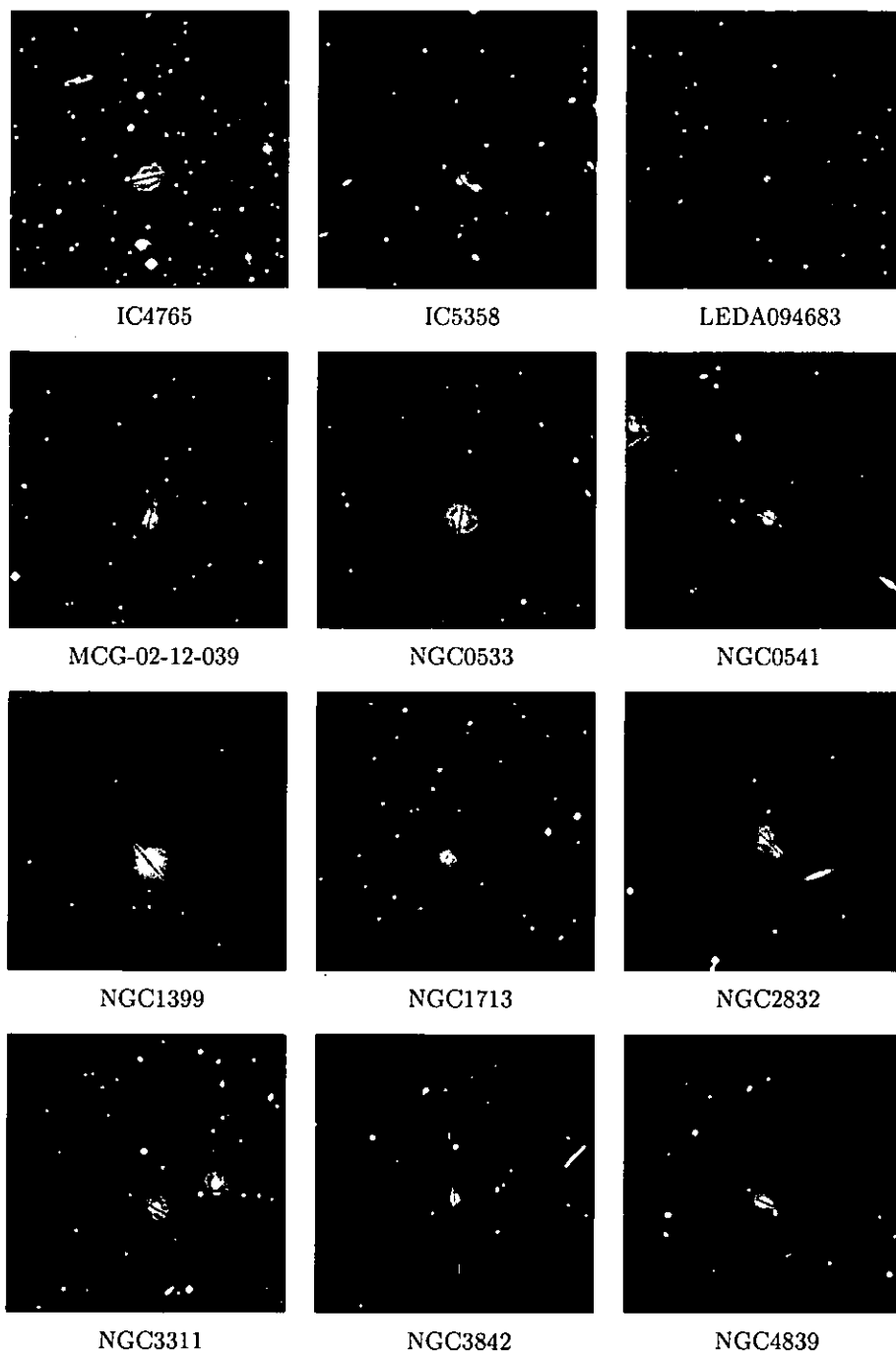
Figure A.1 continued.

APPENDIX A



NGC4874         NGC4889         NGC4946

NGC6034         NGC6047         NGC6086

NGC6160         NGC6166         NGC6173

NGC6269         NGC7012         NGC7597

Figure A.1 continued.

NGC7647     NGC7649     NGC7720

NGC7768     PGC004072     PGC025714

PGC026269     PGC030223     PGC044257

PGC071807     PGC072804     UGC00579

Figure A.1 continued.

UGC02232       UGC05515       UGC10143
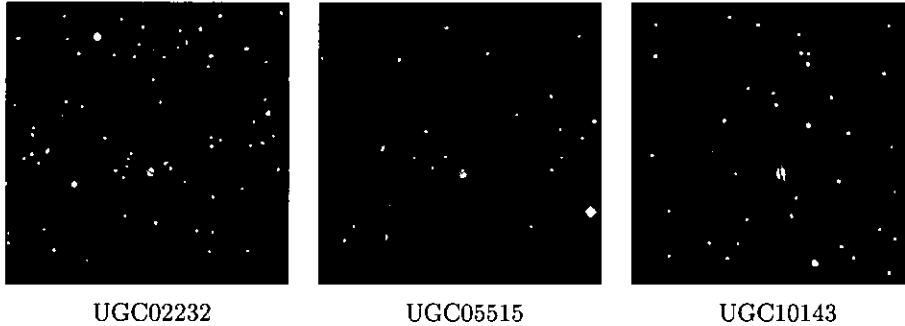
Figure A.1 continued.

## ESO349-010

HST imaging of this galaxy was published by Laine et al. (2003). The radial velocity profile shows no significant rotation and the velocity dispersion profile has a positive gradient. The spectrum of this galaxy contains emission lines originating from star formation.

## ESO444-046

No clear rotation or velocity substructure is visible in the kinematic profiles. The velocity dispersion profile has a positive gradient. This galaxy is one of the two oldest in the sample, where the derived ages reached the upper limit of the SSP-models.

## ESO488-027

The kinematic profiles show a KDC in the centre of this galaxy. Note that the slit was placed 2.20 arcsec from the centre of this galaxy during queue observations.

## ESO541-013

This galaxy shows rotation of $138 \pm 24$ km s$^{-1}$ (minor axis spectrum). Note that the slit was placed 1.50 arcsec from the centre of this galaxy during queue

APPENDIX A

observations.

## ESO552-020

The radial velocity profile is mostly flat and the velocity dispersion profile shows a small dip south-west of the centre of the galaxy which might indicate a colder component. The velocity dispersion profile has a positive gradient.

## GSC555700266

Slow rotation but no clear substructure can be seen in the kinematic profiles.

## IC1101

This galaxy is one of the few known BCGs that was previously found to have a rising velocity dispersion profile (Fisher et al. 1995a). This result cannot be confirmed here since the derived velocity dispersion profile was not measured to the same radius as in the above-mentioned study. No significant rotation was detected in the radial velocity profile.

## IC1633

This galaxy has an extended envelope with many companions. The surface brightness profile was published by Schombert (1986), and HST imaging by Laine et al. (2003). The radial velocity profile reveals some evidence for substructure at the centre of this galaxy. The SSP-equivalent parameters derived for the central $\frac{1}{8}R_e$ in this study (log (age) = 0.935 $\pm$ 0.187 Gyr; [E/Fe] = 0.440 $\pm$ 0.039; [Z/H] = 0.380 $\pm$ 0.061) can be compared with those presented in T05 for the central $\frac{1}{10}R_e$ (log (age) = 0.716 $\pm$ 0.308 Gyr; [E/Fe] = 0.366 $\pm$ 0.024; [Z/H] = 0.563 $\pm$ 0.057). Thus, the ages agree within the errors.

APPENDIX A

## IC4765

The radial velocity profile shows rotation in the centre of the galaxy which is possibly rotational substructure.

## IC5358

Both the radial kinematic profiles show the clear presence of a KDC in this galaxy.

## LEDA094683

No significant rotation but some evidence of substructure is visible from the radial velocity profile. Note that the slit was placed 2.00 arcsec from the centre of this galaxy during queue observations. The $Mg_b$ index of this galaxy is affected by a sky line and therefore no SSP-parameter derivation was made.

## MCG-02-12-039

Emission lines, originating from star formation, are present in the spectrum of this galaxy. The surface brightness profile was published by Schombert (1986), and HST imaging by Laine et al. (2003). The radial kinematic profiles show the presence of a KDC.

## NGC0533

A surface brightness profile was published by Malumuth & Kirshner (1985). This galaxy contains a KDC, and is one of the two oldest in the sample where the derived ages reached the upper limit of the SSP-models.

## NGC0541

This galaxy has been described as a cD S0 with a nuclear dust disc (Noel-Storr et al. 2003). No significant rotation or velocity substructure is visible from the radial

velocity profile. The spectrum of this galaxy contains emission lines originating from star formation (according to the emission-line diagnostic diagram). This galaxy has an SSP-equivalent age of log (age) < 0.8 Gyr. For the six intermediate-aged galaxies (SSP-equivalent age younger than ∼ 6 Gyr) for which cooling-flow information is available, this is the only galaxy not hosted by a cluster with cooling flows. This suggests that the recent star formation in this galaxy might have been fuelled by gas deposited in a merger event, or triggered by the radio jet originating from the galaxy's supermassive black hole. NGC0541 is known to be very peculiar and is associated with Minkowski's Object, an irregular dwarf located 16 kpc northeast from NGC0541 and in the path of the galaxy's radio jet. The radio jet is thought to have triggered the starburst in Minkowski's Object (Schaerer, Contini & Pindao 1999; Verdoes Kleijn et al. 1999; Croft et al. 2006). In addition, the SFH of NGC0541 is unique amongst all the BCGs – instead of gradually tapering down, the SFH has a distinct change at ∼ 6 Gyr, and then a very low rate of star formation continues for the last several Gyrs.

## NGC1399

The surface brightness profile was published by Schombert (1986). The central velocity dispersion of this galaxy was measured as $371 \pm 3$ km s$^{-1}$ in this study, and the velocity dispersion profile is steeply decreasing. Longo et al. (1994) found the velocity dispersion in the central region of this galaxy to be 388 km s$^{-1}$ decreasing to 200 km s$^{-1}$ at 10 arcseconds from the centre. Thus, the kinematics results of the two studies are in agreement. The radial velocity profile shows a dip in the very centre of the galaxy. Lyubenova, Kuntschner & Silva (2008) investigated the centres of the kinematic profiles of NGC1399 in much greater detail, and interpreted this dip ($r \leqslant 0.2$ arcsec) from high resolution $K$-band maps of the central kinematics as a dynamically cold subsystem in the centre.

APPENDIX A

This cold subsystem could be a central stellar disc or globular cluster having fallen into the centre on a purely radial orbit (Lyubenova et al. 2008). An age of $8.6 \pm 0.9$ Gyr was found for this galaxy in this study, which is consistent with the age of $10.0 \pm 2.0$ Gyr found by Forbes et al. (2001). This galaxy is located less than 1 kpc from the X-ray peak in the centre of the cluster.

## NGC1713

The radial velocity profile of this galaxy reveals a definite KDC in the centre of this galaxy. The spectrum contains emission lines originating from star formation.

## NGC2832

This galaxy is thought to be tidally interacting with its companion, NGC2831. Surface brightness profiles were published by Schombert (1986) and Jordán et al. (2004), and HST imaging by Laine et al. (2003). The radial velocity profile shows the presence of a KDC in the centre of this galaxy. The SSP-equivalent parameters derived for the central $\frac{1}{8}R_e$ in this study (log (age) $= 0.929 \pm 0.024$ Gyr; [E/Fe] $= 0.380 \pm 0.043$; [Z/H] $= 0.480 \pm 0.062$) are in very good agreement with those derived by other authors. Proctor & Sansom (2002) derived log (age) $= 0.875 \pm 0.069$ Gyr; [E/Fe] $= 0.300 \pm 0.025$; [Z/H] $= 0.457 \pm 0.074$ for the central $3.6 \times 1.25$ arcsec$^2$. Sánchez-Blázquez et al. (2006b) derived log (age) $= 0.995 \pm 0.007$ in the centre (equivalent aperture of $4''$ at a redshift of $z = 0.016$).

## NGC3311

Ferrari et al. (1999) found evidence of a dust cloud in the centre of the galaxy. HST imaging was published by Laine et al. (2003). No clear rotation or velocity substructure can be seen in the radial kinematic profiles, but the velocity dispersion profile has a positive gradient. The spectrum of this galaxy contains emission

APPENDIX A

lines.

## NGC3842

This galaxy belongs to a cluster which forms part of the Coma supercluster. The surface brightness profile was published by Schombert (1986), and HST imaging by Laine et al. (2003). The radial velocity profile of this galaxy reveals the presence of a KDC in the centre.

## NGC4839

The location of this BCG far from the centre of the Coma cluster is unusual. Surface brightness profiles were published by Schombert (1986), Oemler (1976) as well as Jordán et al. (2004), who all confirmed the presence of a very prominent cD envelope. Rotation of the order of 44 km s$^{-1}$ and a KDC in the centre of the galaxy were detected. Table A.1 shows the SSP-equivalent ages and metallicities for the three BCGs in the Coma cluster from the literature (as summarised by Trager et al. 2008). The central aperture in this study is $\frac{1}{8}R_e$. For Mehlert et al. (2000), Sánchez-Blázquez et al. (2006b) and Trager et al. (2008) the central aperture is 2.7″-diameter circular equivalent (by Trager et al. 2008), and for the other references as originally published. It can be seen that the literature SSP-equivalent age falls in a very large range, and the value derived in this study is within this range.

## NGC4874

This galaxy has a large, extended envelope. It is the second brightest galaxy of the famous pair of BCGs at the centre of the Coma cluster. The surface brightness profile was published by Peletier et al. (1990). No significant rotation or velocity substructure was detected. The spectrum of this galaxy contains emission lines.

| | NGC4889 | | |
|---|---|---|---|
| Reference | log (age) in Gyr | [Z/H] | [E/Fe] |
| This work | $0.92^{+0.04}_{-0.04}$ | $0.57^{+0.05}_{-0.05}$ | $0.42^{+0.04}_{-0.04}$ |
| Sánchez-Blázquez et al. 2006b | $1.08^{+0.27}_{-0.08}$ | $0.30^{+0.13}_{-0.14}$ | $0.18^{+0.04}_{-0.04}$ |
| Jørgensen 1999 | $0.23^{+0.05}_{-0.01}$ | $1.07^{+0.08}_{-0.04}$ | $0.29^{+0.01}_{-0.01}$ |
| Mehlert et al. 2000 | $0.12^{+0.16}_{-0.01}$ | $1.16^{+0.02}_{-0.19}$ | $0.39^{+0.01}_{-0.13}$ |
| Moore et al. 2002 | $0.14^{+0.02}_{-0.01}$ | $1.13^{+0.02}_{-0.01}$ | $0.38^{+0.04}_{-0.04}$ |
| Nelan et al. 2005 | $1.35^{+0.02}_{-0.01}$ | $-0.18^{+0.05}_{-0.07}$ | $0.27^{+0.01}_{-0.01}$ |
| Mean ± std. err. | 0.64 ± 0.54 | 0.68 ± 0.54 | 0.32 ± 0.09 |
| | NGC4874 | | |
| Reference | log (age) in Gyr | [Z/H] | [E/Fe] |
| This work | $0.89^{+0.12}_{-0.12}$ | $0.35^{+0.05}_{-0.05}$ | $0.46^{+0.05}_{-0.05}$ |
| Sánchez-Blázquez et al. 2006b | $1.02^{+0.20}_{-0.14}$ | $0.38^{+0.04}_{-0.01}$ | $0.17^{+0.01}_{-0.01}$ |
| Jørgensen 1999 | $0.31^{+0.23}_{-0.10}$ | $0.86^{+0.14}_{-0.16}$ | $0.25^{+0.04}_{-0.03}$ |
| Mehlert et al. 2000 | $0.12^{+0.02}_{-0.01}$ | $1.09^{+0.02}_{-0.01}$ | $0.35^{+0.04}_{-0.04}$ |
| Moore et al. 2002 | $0.62^{+0.29}_{-0.33}$ | $0.54^{+0.17}_{-0.16}$ | $0.18^{+0.04}_{-0.04}$ |
| Nelan et al. 2005 | $1.11^{+0.25}_{-0.22}$ | $0.08^{+0.25}_{-0.22}$ | $0.18^{+0.11}_{-0.08}$ |
| Trager et al. 2008 | $0.90^{+0.05}_{-0.04}$ | $0.21^{+0.11}_{-0.13}$ | $0.10^{+0.04}_{-0.04}$ |
| Mean ± std. err. | 0.71 ± 0.37 | 0.50 ± 0.36 | 0.24 ± 0.13 |
| | NGC4839 | | |
| Reference | log (age) in Gyr | [Z/H] | [E/Fe] |
| This work | $1.07^{+0.12}_{-0.12}$ | $0.13^{+0.05}_{-0.05}$ | $0.35^{+0.03}_{-0.03}$ |
| Sánchez-Blázquez et al. 2006b | $0.66^{+0.42}_{-0.39}$ | $0.05^{+0.22}_{-0.17}$ | $0.20^{+0.07}_{-0.07}$ |
| Jørgensen 1999 | $1.24^{+0.19}_{-0.75}$ | $0.21^{+0.22}_{-0.25}$ | $0.19^{+0.08}_{-0.06}$ |
| Mehlert et al. 2000 | $1.07^{+0.34}_{-0.75}$ | $0.63^{+0.27}_{-0.23}$ | $0.14^{+0.07}_{-0.06}$ |
| Mean ± std. err. | 1.01 ± 0.25 | 0.26 ± 0.26 | 0.22 ± 0.09 |

Table A.1: SSP-parameters of the Coma BCG galaxies compared with those in the literature (as summarised by Trager et al. 2008).

Trager et al. (2008) compiled a list of all the central Hβ measurements for this galaxy, and found an error weighted mean value of 1.57 ± 0.05 Å (including data from Fisher et al. 1995b; T98; Jørgensen 1999; Kuntschner et al. 2001; Moore et al. 2002; Nelan et al. 2005; Sánchez-Blázquez et al. 2006b). The Hβ index measured here (1.630 ± 0.082 Å) compares very well with the literature data. Table A.1 shows the SSP-equivalent parameters compared with those from the literature.

APPENDIX A

## NGC4889

This is a large BCG with a very extended envelope, and the brightest galaxy of the Coma cluster. The surface brightness profile was published by Peletier et al. (1990), and HST imaging by Laine et al. (2003). The radial velocity profile clearly shows a KDC. Table A.1 shows the SSP-equivalent parameters compared with those from the literature. Similarly to the other Coma BCGs, the ages fall in a very large range, and the value derived in this study is within this range.

## NGC4946

This is one of the two ordinary elliptical galaxies included in this thesis. The radial velocity profile of this galaxy reveals rotation of the order of 62 km s$^{-1}$ (major axis spectrum). The spectrum contains emission lines.

## NGC6034

The surface brightness profile of this galaxy was published by Schombert (1986). The radial velocity profile shows significant rotation of the order of 134 $\pm$ 15 km s$^{-1}$ (major axis spectrum). Thus it is unlikely that it formed through dissipationless mergers.

## NGC6047

This is one of the two elliptical galaxies. The surface brightness profile of this galaxy was published by Schombert (1986), and Schombert (1987) classified it as an E/S0 galaxy. The radial velocity profile shows rotation of 59 km s$^{-1}$ (with the slit rotated 29 degrees from the major axis).

APPENDIX A

## NGC6086

The surface brightness profile of this galaxy was published by Schombert (1986), and HST imaging by Laine et al. (2003). Carter et al. (1999) found this galaxy to have a KDC. Even though some evidence of substructure can be seen, this core cannot be confirmed since the profiles measured here do not cover the same radial extent as those in Carter et al. (1999).

## NGC6160

The radial velocity profile of this galaxy reveals no significant rotation or substructure.

## NGC6166

This is a classic multiple nucleus BCG in a rich cluster. The surface brightness profile was published by Schombert (1986). Carter et al. (1999) found the velocity dispersion to increase from 325 km s$^{-1}$ at the centre to 450 km s$^{-1}$ at 35 arcsec along the major axis. They also found the galaxy to show modest major-axis rotation (45 km s$^{-1}$ at 40 arcsec). The profiles derived here do not extent out to the radii necessary to confirm the positive velocity dispersion slope found by Carter et al. (1999). Rotation of the order of 31 km s$^{-1}$ is found in the centre of the galaxy although this is not a very clear rotation curve. Emission lines are present in the spectrum. The Fe5270 index of this galaxy is affected by a sky line or a CCD gap and therefore no SSP-parameter derivation was made.

## NGC6173

The surface brightness profile was published by Schombert (1986), and HST imaging by Laine et al. (2003). The derived radial kinematic profiles of this galaxy show no significant rotation or substructure. The spectrum contains emission

APPENDIX A

lines.

## NGC6269

Surface brightness profiles were published by Schombert (1986) and Malumuth & Kirshner (1985). The radial velocity profile shows some velocity substructure in the centre of this galaxy. It was observed at an angle of 46 degrees to the major axis.

## NGC7012

The radial velocity profile shows a small amount of rotation in the centre which might be a KDC. The spectrum contains emission lines originating from star formation.

## NGC7597

The surface brightness profile was published by Schombert (1986). The radial kinematic profiles show possible evidence for a KDC.

## NGC7647

This is a BCG with an extended red envelope and a large number of small companions (Vitores et al. 1996). The surface brightness profile was published by Schombert (1986), and HST imaging by Laine et al. (2003). The radial velocity profile of this galaxy shows a clear KDC in the centre.

## NGC7649

This is a BCG with an extended halo. The surface brightness profile was published by Schombert (1986), and HST imaging by Laine et al. (2003). A KDC is clearly visible in the centre of this galaxy. The Fe5335 index is affected by a sky line or

APPENDIX A

a CCD gap and therefore no SSP-parameter derivation was made. The spectrum contains emission lines originating from star formation.

## NGC7720

This is a multiple nuclei galaxy and has a massive, close companion, which is also an elliptical. The surface brightness profile was published by Lauer (1988), and HST imaging by Laine et al. (2003). The radial velocity profile reveals no significant rotation but there might be some substructure in this galaxy. Emission lines, originating from star formation, are present in the spectrum of this galaxy.

## NGC7768

Surface brightness profiles were published by Schombert (1986), Malumuth & Kirshner (1985) and Jordán et al. (2004) and HST imaging was published by Laine et al. (2003). The radial velocity profile of this galaxy shows significant rotation of the order of $114 \pm 11$ km s$^{-1}$ (major axis spectrum). This agrees with the $101 \pm 5$ km s$^{-1}$ and the 99 km s$^{-1}$ rotation found previously by Fisher et al. (1995a) and Prugniel & Simien (1996), respectively. Thus, it is unlikely that it formed through dissipationless mergers.

## PGC004072

This galaxy has rotation of the order of 93 km s$^{-1}$ (intermediate axis spectrum), and contains a KDC.

## PGC025714

No significant rotation or velocity substructure is visible from the radial profiles. The Fe5270 index of this galaxy is affected by a sky line or a CCD gap and therefore no SSP-parameter derivation was made.

APPENDIX A

## PGC026269

Also known as Hydra A. The radial kinematic profiles of this galaxy reveal rotation of the order of 51 km s$^{-1}$ (major axis spectrum), as well as a positive velocity dispersion profile. Emission lines are present in the spectrum of this galaxy.

## PGC030223

This galaxy has rotation of the order of 90 km s$^{-1}$ (intermediate axis spectrum), and contains a KDC in the centre. The Fe5270 index is affected by a sky line and therefore no SSP-parameter derivation was made.

## PGC044257

The data indicate that the velocity dispersion might increase with radius, although the large scatter and the small number of bins make it difficult to assess the slope. Emission lines, originating from star formation according to the emission-line diagnostic diagram, are present in the spectrum.

## PGC071807

No significant rotation or substructure can be seen in this galaxy.

## PGC072804

This galaxy has an extensive halo. The surface brightness profile was published by Malumuth & Kirshner (1985). The radial velocity profile shows rotation of the order of 50 km s$^{-1}$ (major axis spectrum).

## UGC00579

Surface brightness profiles were published by Schombert (1986) and Malumuth & Kirshner (1985), and HST imaging by Laine et al. (2003). The galaxy has

flat kinematic profiles, but with the large scatter it is not possible to exclude the presence of a KDC.

## UGC02232

This galaxy has an extended envelope and a large number of objects in the vicinity. HST imaging was published by Laine et al. (2003). No significant rotation or clear substructure was detected.

## UGC05515

The surface brightness profile was published by Schombert (1986). The radial velocity profile shows a KDC in the centre of this galaxy.

## UGC10143

This galaxy has a chain of companions. The surface brightness profile was published by Schombert (1986), and HST imaging by Laine et al. (2003). No significant rotation or substructure can be seen in the radial kinematic profiles.

# Appendix B

# RADIAL KINEMATICS

The spatially resolved kinematic data for all 51 galaxies follow here.

| Radius (arcsec) | $V$ (km s$^{-1}$) | $\sigma$ (km s$^{-1}$) |
|---|---|---|
| -9.71 | 12029±19 | 315±25 |
| -7.15 | 12083±16 | 232±26 |
| -5.84 | 12072±10 | 259±12 |
| -4.96 | 12063±12 | 276±14 |
| -4.31 | 12071±14 | 268±15 |
| -3.80 | 12065±12 | 285±14 |
| -3.36 | 12066±11 | 307±14 |
| -2.99 | 12067±15 | 306±13 |
| -2.70 | 12050±13 | 310±11 |
| -2.41 | 12067±11 | 283±10 |
| -2.12 | 12072±8 | 302±12 |
| -1.83 | 12064±9 | 276±12 |
| -1.61 | 12056±12 | 303±13 |
| -1.46 | 12048±9 | 286±11 |
| -1.31 | 12081±10 | 297±14 |
| -1.17 | 12067±8 | 286±11 |
| -1.02 | 12057±12 | 293±15 |
| -0.88 | 12050±19 | 298±11 |
| -0.73 | 12074±8 | 289±11 |
| -0.58 | 12049±10 | 301±14 |
| -0.44 | 12057±6 | 321±8 |
| -0.29 | 12055±9 | 289±10 |
| -0.15 | 12048±9 | 305±8 |
| 0.00 | 12063±8 | 289±10 |
| 0.15 | 12060±8 | 299±10 |
| 0.29 | 12061±7 | 298±13 |
| 0.44 | 12061±9 | 298±9 |
| 0.66 | 12065±6 | 303±9 |
| 0.73 | 12078±10 | 301±15 |
| 0.88 | 12061±10 | 289±10 |
| 1.02 | 12055±10 | 279±13 |
| 1.17 | 12050±11 | 314±12 |
| 1.31 | 12078±11 | 313±16 |
| 1.46 | 12058±9 | 297±15 |
| 1.61 | 12059±10 | 307±14 |
| 1.82 | 12064±8 | 290±9 |
| 1.90 | 12051±13 | 285±15 |
| 2.12 | 12065±9 | 301±8 |
| 2.41 | 12065±10 | 265±14 |
| 2.70 | 12072±9 | 285±12 |
| 2.99 | 12071±12 | 245±14 |
| 3.36 | 12058±9 | 252±14 |
| 3.80 | 12061±13 | 264±16 |
| 4.31 | 12068±11 | 233±12 |
| 4.96 | 12086±11 | 277±14 |
| 5.77 | 12071±13 | 284±26 |
| 6.93 | 12111±19 | 275±16 |
| 9.13 | 12066±18 | 294±26 |

Table B.1: Radial kinematics of ESO146-028.

| Radius (arcsec) | $V$ (km s$^{-1}$) | $\sigma$ (km s$^{-1}$) |
|---|---|---|
| -4.82 | 10937±12 | 234±18 |
| -2.26 | 10917±10 | 248±12 |
| -1.31 | 10931±6 | 262±12 |
| -0.95 | 10935±8 | 262±12 |
| -0.58 | 10935±9 | 256±13 |
| -0.29 | 10933±12 | 248±16 |
| 0.00 | 10950±9 | 269±14 |
| 0.15 | 10960±10 | 274±9 |
| 0.44 | 10942±8 | 257±9 |
| 0.73 | 10961±9 | 248±11 |
| 1.02 | 10952±10 | 248±11 |
| 1.39 | 10949±11 | 248±12 |
| 1.90 | 10964±10 | 247±17 |
| 2.77 | 10957±10 | 245±12 |

Table B.2: Radial kinematics of ESO202-043.

| Radius (arcsec) | $V$ (km s$^{-1}$) | $\sigma$ (km s$^{-1}$) |
|---|---|---|
| -2.92 | 14515±11 | 247±15 |
| -2.34 | 14524±9 | 240±23 |
| -1.97 | 14530±11 | 263±25 |
| -1.68 | 14552±11 | 259±13 |
| -1.39 | 14526±11 | 260±17 |
| -1.17 | 14551±11 | 268±16 |
| -1.02 | 14533±8 | 268±20 |
| -0.88 | 14535±7 | 259±17 |
| -0.73 | 14519±8 | 276±10 |
| -0.58 | 14535±8 | 270±14 |
| -0.44 | 14528±8 | 273±14 |
| -0.29 | 14535±9 | 265±12 |
| -0.15 | 14523±9 | 299±11 |
| 0.00 | 14524±9 | 281±17 |
| 0.15 | 14537±10 | 261±15 |
| 0.29 | 14530±9 | 267±15 |
| 0.44 | 14505±11 | 284±13 |
| 0.58 | 14533±10 | 268±17 |
| 0.73 | 14506±13 | 276±24 |
| 0.88 | 14525±14 | 274±29 |
| 1.02 | 14525±15 | 289±37 |
| 1.17 | 14508±9 | 248±18 |
| 1.39 | 14531±8 | 240±18 |
| 1.68 | 14529±9 | 238±15 |
| 2.04 | 14522±11 | 213±21 |
| 2.55 | 14510±10 | 227±34 |
| 3.28 | 14508±9 | 238±26 |

Table B.3: Radial kinematics of ESO303-005.

| Radius (arcsec) | $V$ (km s$^{-1}$) | $\sigma$ (km s$^{-1}$) |
|---|---|---|
| -2.92 | 8424±11 | 209±19 |
| -1.97 | 8396±11 | 209±12 |
| -1.46 | 8417±9 | 208±12 |
| -1.10 | 8427±10 | 224±17 |
| -0.80 | 8425±7 | 217±10 |
| -0.51 | 8441±9 | 223±10 |
| -0.22 | 8452±8 | 233±11 |
| 0.00 | 8475±12 | 257±13 |
| 0.22 | 8464±8 | 228±9 |
| 0.51 | 8480±10 | 234±16 |
| 0.80 | 8479±9 | 225±12 |
| 1.10 | 8486±12 | 219±17 |
| 1.46 | 8502±12 | 211±14 |
| 2.04 | 8485±10 | 188±15 |
| 3.50 | 8490±8 | 191±18 |

Table B.4: Radial kinematics of ESO346-003.

237

# APPENDIX B

| Radius (arcsec) | $V$ (km s$^{-1}$) | $\sigma$ (km s$^{-1}$) |
|---|---|---|
| -13.58 | 14421±20 | 346±21 |
| -10.88 | 14397±13 | 326±14 |
| -8.98 | 14363±12 | 295±9 |
| -7.81 | 14396±13 | 291±24 |
| -6.79 | 14437±19 | 310±24 |
| -5.99 | 14373±16 | 303±26 |
| -5.33 | 14420±14 | 331±16 |
| -4.74 | 14419±14 | 360±13 |
| -4.23 | 14415±12 | 292±14 |
| -3.80 | 14411±9 | 290±13 |
| -3.36 | 14407±16 | 316±30 |
| -2.99 | 14428±15 | 297±27 |
| -2.70 | 14397±11 | 257±11 |
| -2.41 | 14397±13 | 303±26 |
| -2.12 | 14415±15 | 274±48 |
| -1.82 | 14386±8 | 255±9 |
| -1.61 | 14421±12 | 331±29 |
| -1.46 | 14422±15 | 315±24 |
| -1.31 | 14403±19 | 280±33 |
| -1.17 | 14421±13 | 279±24 |
| -1.02 | 14449±11 | 292±12 |
| -0.88 | 14424±12 | 249±9 |
| -0.73 | 14446±11 | 285±16 |
| -0.58 | 14436±14 | 304±13 |
| -0.44 | 14434±10 | 273±11 |
| -0.29 | 14414±13 | 280±11 |
| -0.15 | 14437±13 | 294±9 |
| 0.00 | 14432±11 | 282±11 |
| 0.15 | 14426±10 | 282±11 |
| 0.29 | 14430±8 | 265±9 |
| 0.44 | 14436±9 | 275±12 |
| 0.58 | 14424±9 | 285±10 |
| 0.73 | 14415±13 | 278±10 |
| 0.88 | 14447±10 | 300±12 |
| 1.02 | 14430±11 | 264±11 |
| 1.17 | 14450±9 | 292±14 |
| 1.31 | 14444±11 | 272±8 |
| 1.46 | 14428±15 | 296±10 |
| 1.61 | 14443±10 | 277±10 |
| 1.83 | 14413±8 | 282±12 |
| 2.12 | 14389±10 | 250±11 |
| 2.41 | 14416±11 | 214±9 |
| 2.70 | 14435±12 | 282±14 |
| 2.99 | 14428±10 | 260±11 |
| 3.28 | 14414±10 | 270±13 |
| 3.65 | 14413±11 | 297±11 |
| 4.09 | 14400±11 | 271±12 |
| 4.60 | 14410±13 | 267±17 |
| 5.18 | 14380±14 | 262±14 |
| 5.84 | 14412±11 | 279±11 |
| 6.64 | 14353±16 | 303±22 |
| 7.67 | 14401±18 | 245±19 |
| 9.05 | 14353±14 | 316±18 |
| 10.88 | 14353±15 | 272±14 |
| 13.58 | 14400±18 | – |

Table B.5: Radial kinematics of ESO349-010.

| Radius (arcsec) | $V$ (km s$^{-1}$) | $\sigma$ (km s$^{-1}$) |
|---|---|---|
| -7.52 | 13730±28 | 352±18 |
| -4.89 | 13771±34 | 317±53 |
| -3.50 | 13725±21 | 292±35 |
| -2.63 | 13742±15 | 275±29 |
| -1.97 | 13755±18 | 310±22 |
| -1.39 | 13732±15 | 299±16 |
| -0.88 | 13751±15 | 275±24 |
| -0.44 | 13722±15 | 276±14 |
| 0.00 | 13752±15 | 301±18 |
| 0.29 | 13731±17 | 299±21 |
| 0.73 | 13748±12 | 287±11 |
| 1.17 | 13742±17 | 290±30 |
| 1.68 | 13745±16 | 307±19 |
| 2.34 | 13746±12 | 305±29 |
| 3.21 | 13741±15 | 287±25 |
| 4.53 | 13790±23 | 299±21 |
| 6.72 | 13789±37 | 315±33 |

Table B.6: Radial kinematics of ESO444-046.

# APPENDIX B

| Radius (arcsec) | $V$ (km s$^{-1}$) | $\sigma$ (km s$^{-1}$) |
|---|---|---|
| -6.57 | 11718±14 | 196±19 |
| -5.47 | 11708±15 | 187±18 |
| -4.75 | 11745±12 | 224±14 |
| -4.23 | 11726±13 | 221±28 |
| -3.80 | 11725±13 | 201±16 |
| -3.43 | 11723±15 | 245±15 |
| -3.14 | 11717±12 | 226±17 |
| -2.85 | 11762±8 | 214±12 |
| -2.56 | 11736±10 | 252±12 |
| -2.34 | 11717±8 | 220±17 |
| -2.19 | 11741±10 | 246±15 |
| -2.04 | 11742±10 | 248±14 |
| -1.90 | 11733±9 | 236±15 |
| -1.75 | 11728±8 | 257±17 |
| -1.61 | 11734±8 | 240±11 |
| -1.46 | 11739±8 | 237±9 |
| -1.31 | 11747±7 | 240±11 |
| -1.17 | 11730±7 | 247±9 |
| -1.02 | 11739±7 | 239±9 |
| -0.88 | 11730±5 | 241±8 |
| -0.73 | 11743±6 | 239±8 |
| -0.58 | 11745±6 | 240±9 |
| -0.44 | 11735±7 | 263±8 |
| -0.29 | 11742±6 | 252±6 |
| -0.15 | 11758±6 | 255±7 |
| 0.00 | 11752±6 | 247±8 |
| 0.15 | 11754±5 | 241±7 |
| 0.29 | 11759±6 | 243±7 |
| 0.44 | 11769±5 | 245±9 |
| 0.58 | 11775±4 | 244±10 |
| 0.73 | 11778±6 | 252±9 |
| 0.88 | 11785±8 | 248±6 |
| 1.02 | 11785±6 | 237±9 |
| 1.17 | 11796±6 | 227±8 |
| 1.31 | 11817±10 | 212±10 |
| 1.46 | 11800±9 | 246±11 |
| 1.61 | 11798±8 | 219±11 |
| 1.75 | 11785±8 | 220±10 |
| 1.90 | 11791±10 | 232±14 |
| 2.04 | 11799±12 | 229±15 |
| 2.19 | 11805±9 | 234±13 |
| 2.34 | 11819±11 | 235±20 |
| 2.48 | 11788±18 | 245±12 |
| 2.63 | 11822±12 | 218±13 |
| 2.85 | 11849±9 | 182±10 |
| 3.14 | 11801±12 | 235±16 |
| 3.43 | 11833±15 | 229±11 |
| 3.72 | 11789±13 | 240±17 |
| 4.09 | 11807±19 | 204±15 |
| 4.53 | 11807±15 | 205±19 |
| 5.04 | 11794±14 | 238±23 |
| 5.77 | 11831±22 | 211±15 |
| 6.94 | 11829±16 | 210±20 |
| 9.27 | 11865±14 | 179±18 |

Table B.7: Radial kinematics of ESO488-027.

| Radius (arcsec) | $V$ (km s$^{-1}$) | $\sigma$ (km s$^{-1}$) |
|---|---|---|
| -4.02 | 16453±10 | 299±11 |
| -2.85 | 16440±15 | 277±8 |
| -2.04 | 16427±14 | 299±11 |
| -1.39 | 16415±22 | 312±8 |
| -0.88 | 16408±23 | 304±11 |
| -0.44 | 16461±16 | 291±13 |
| 0.00 | 16438±15 | 291±10 |
| 0.29 | 16438±21 | 287±10 |
| 0.73 | 16451±21 | 295±11 |
| 1.17 | 16467±16 | 288±11 |
| 1.68 | 16500±17 | 302±9 |
| 2.34 | 16483±14 | 293±11 |
| 3.21 | 16546±24 | 301±14 |
| 4.82 | 16448±35 | 289±15 |

Table B.8: Radial kinematics of ESO541-013.

| Radius (arcsec) | $V$ (km s$^{-1}$) | $\sigma$ (km s$^{-1}$) |
|---|---|---|
| −16.05 | 9240±20 | 271±33 |
| −13.94 | 9245±12 | 275±15 |
| −12.33 | 9211±11 | 213±18 |
| −11.02 | 9264±14 | 261±11 |
| −9.92 | 9258±14 | 233±27 |
| −8.97 | 9258±15 | 256±14 |
| −8.17 | 9239±11 | 221±20 |
| −7.44 | 9280±11 | 244±25 |
| −6.78 | 9244±12 | 241±14 |
| −6.20 | 9254±9 | 238±14 |
| −5.69 | 9239±15 | 248±23 |
| −5.25 | 9244±11 | 246±11 |
| −4.81 | 9255±8 | 245±12 |
| −4.37 | 9233±12 | 251±23 |
| −3.94 | 9249±9 | 239±12 |
| −3.57 | 9262±11 | 245±15 |
| −3.28 | 9259±11 | 225±18 |
| −2.99 | 9262±11 | 243±12 |
| −2.69 | 9228±8 | 216±11 |
| −2.40 | 9259±7 | 216±11 |
| −2.11 | 9251±7 | 213±9 |
| −1.82 | 9243±6 | 204±10 |
| −1.53 | 9256±8 | 219±9 |
| −1.31 | 9246±10 | 240±14 |
| −1.16 | 9249±9 | 205±8 |
| −1.02 | 9260±7 | 227±12 |
| −0.87 | 9277±7 | 241±16 |
| −0.72 | 9259±11 | 219±12 |
| −0.58 | 9253±7 | 228±11 |
| −0.43 | 9252±11 | 238±15 |
| −0.29 | 9231±8 | 211±10 |
| −0.14 | 9246±9 | 215±7 |
| 0.01 | 9256±8 | 231±13 |
| 0.15 | 9243±11 | 251±11 |
| 0.30 | 9250±10 | 232±10 |
| 0.44 | 9243±10 | 229±10 |
| 0.59 | 9261±8 | 223±9 |
| 0.74 | 9249±10 | 244±11 |
| 0.88 | 9253±8 | 241±11 |
| 1.03 | 9243±9 | 217±13 |
| 1.17 | 9232±7 | 209±8 |
| 1.32 | 9260±12 | 255±12 |
| 1.47 | 9250±8 | 241±12 |
| 1.61 | 9248±11 | 246±11 |
| 1.76 | 9249±10 | 213±12 |
| 1.90 | 9245±8 | 186±18 |
| 2.12 | 9251±7 | 230±9 |
| 2.41 | 9253±8 | 241±9 |
| 2.71 | 9234±9 | 246±10 |
| 3.00 | 9224±11 | 246±15 |
| 3.29 | 9235±8 | 237±10 |
| 3.58 | 9233±9 | 230±17 |
| 3.87 | 9237±9 | 251±15 |
| 4.17 | 9251±16 | 249±29 |
| 4.53 | 9244±15 | 246±24 |
| 4.97 | 9245±10 | 213±10 |
| 5.41 | 9230±12 | 244±16 |
| 5.92 | 9266±12 | 243±24 |
| 6.50 | 9230±16 | 259±34 |
| 7.09 | 9259±18 | 257±29 |
| 7.74 | 9296±13 | 239±21 |
| 8.55 | 9265±14 | 288±11 |
| 9.50 | 9279±14 | 272±27 |
| 10.66 | 9272±12 | 269±19 |
| 12.12 | 9271±20 | 325±14 |
| 13.95 | 9232±13 | 239±13 |

Table B.9: Radial kinematics of ESO552-020.

| Radius (arcsec) | $V$ (km s$^{-1}$) | $\sigma$ (km s$^{-1}$) |
|---|---|---|
| −4.67 | 20134±18 | 290±21 |
| −3.43 | 20060±17 | 300±23 |
| −2.70 | 20095±14 | 293±20 |
| −2.19 | 20098±14 | 310±16 |
| −1.82 | 20106±11 | 267±14 |
| −1.53 | 20080±12 | 304±15 |
| −1.24 | 20066±11 | 293±11 |
| −1.02 | 20105±12 | 289±18 |
| −0.88 | 20069±13 | 342±17 |

Table B.10 – Continued

| Radius (arcsec) | $V$ (km s$^{-1}$) | $\sigma$ (km s$^{-1}$) |
|---|---|---|
| -0.73 | 20088±10 | 312±15 |
| -0.58 | 20077±13 | 273±11 |
| -0.44 | 20076±14 | 307±15 |
| -0.29 | 20083±11 | 365±14 |
| -0.15 | 20088±10 | 294±11 |
| 0.00 | 20079±13 | 290±13 |
| 0.15 | 20070±13 | 335±17 |
| 0.29 | 20077±14 | 313±13 |
| 0.44 | 20046±16 | 329±17 |
| 0.58 | 20081±12 | 301±13 |
| 0.73 | 20090±15 | 326±22 |
| 0.95 | 20085±10 | 298±21 |
| 1.24 | 20075±9 | 284±12 |
| 1.53 | 20083±15 | 313±24 |
| 1.90 | 20073±14 | 294±17 |
| 2.41 | 20056±13 | 267±23 |
| 3.14 | 20093±17 | 300±15 |
| 3.65 | 20036±15 | 379±17 |
| 4.38 | 20082±16 | 289±21 |

Table B.10: Radial kinematics of GSC555700266.

| Radius (arcsec) | $V$ (km s$^{-1}$) | $\sigma$ (km s$^{-1}$) |
|---|---|---|
| -4.23 | 22595±25 | 393±25 |
| -2.48 | 22605±21 | 372±25 |
| -1.46 | 22630±23 | 401±28 |
| -0.66 | 22575±16 | 361±25 |
| 0.00 | 22563±19 | 386±24 |
| 0.44 | 22626±16 | 384±27 |
| 1.09 | 22593±18 | 387±31 |
| 1.90 | 22567±19 | 352±22 |
| 2.92 | 22543±17 | 374±17 |
| 4.74 | 22552±22 | 373±18 |

Table B.11: Radial kinematics of IC1101.

| Radius (arcsec) | $V$ (km s$^{-1}$) | $\sigma$ (km s$^{-1}$) |
|---|---|---|
| -16.86 | 7049±35 | 329±49 |
| -15.55 | 7062±25 | 422±35 |
| -14.45 | 7041±18 | 307±43 |
| -12.99 | 7045±32 | 380±48 |
| -12.99 | 7041±30 | 384±70 |
| -11.97 | 7058±24 | 397±19 |
| -11.31 | 7095±23 | 354±64 |
| -10.73 | 7039±18 | 358±15 |
| -10.15 | 7066±21 | 355±37 |
| -9.64 | 7043±20 | 427±36 |
| -9.20 | 7060±22 | 354±25 |
| -8.76 | 7075±13 | 305±17 |
| -8.40 | 7068±33 | 384±46 |
| -8.10 | 7075±22 | 361±27 |
| -7.81 | 7063±17 | 346±28 |
| -7.52 | 7051±15 | 316±17 |
| -7.23 | 7037±13 | 343±18 |
| -6.93 | 7051±15 | 338±18 |
| -6.64 | 7059±12 | 341±15 |
| -6.35 | 7092±12 | 351±10 |
| -6.06 | 7056±14 | 344±18 |
| -5.77 | 7053±14 | 347±13 |
| -5.47 | 7064±9 | 333±18 |
| -5.18 | 7063±9 | 351±16 |
| -4.89 | 7058±11 | 380±14 |
| -4.60 | 7065±12 | 350±14 |
| -4.31 | 7065±7 | 353±8 |
| -4.09 | 7067±13 | 366±15 |
| -3.94 | 7047±11 | 352±17 |
| -3.80 | 7079±12 | 350±21 |
| -3.65 | 7045±14 | 367±15 |
| -3.50 | 7025±12 | 357±15 |
| -3.36 | 7073±10 | 357±15 |
| -3.21 | 7061±12 | 366±17 |
| -3.07 | 7064±13 | 388±16 |
| -2.92 | 7073±10 | 341±14 |

241

# APPENDIX B

Table B.12 – Continued

| Radius (arcsec) | V (km s$^{-1}$) | σ (km s$^{-1}$) |
|---|---|---|
| -2.77 | 7065±10 | 366±14 |
| -2.63 | 7060±10 | 387±11 |
| -2.48 | 7089±9 | 376±12 |
| -2.34 | 7071±8 | 376±15 |
| -2.19 | 7073±8 | 389±11 |
| -2.04 | 7042±7 | 394±8 |
| -1.90 | 7074±8 | 390±11 |
| -1.75 | 7057±7 | 406±12 |
| -1.61 | 7061±6 | 389±6 |
| -1.46 | 7062±7 | 391±6 |
| -1.31 | 7069±5 | 401±7 |
| -1.17 | 7059±6 | 388±8 |
| -1.02 | 7062±6 | 393±7 |
| -0.88 | 7063±5 | 395±6 |
| -0.73 | 7062±5 | 395±6 |
| -0.58 | 7073±5 | 408±7 |
| -0.44 | 7065±4 | 412±6 |
| -0.29 | 7065±5 | 411±7 |
| -0.15 | 7062±4 | 414±6 |
| 0.00 | 7056±4 | 414±5 |
| 0.15 | 7055±5 | 397±7 |
| 0.29 | 7055±5 | 404±6 |
| 0.44 | 7050±5 | 406±5 |
| 0.58 | 7069±6 | 402±7 |
| 0.73 | 7068±6 | 402±8 |
| 0.88 | 7052±6 | 407±7 |
| 1.02 | 7064±6 | 393±6 |
| 1.17 | 7052±7 | 382±8 |
| 1.31 | 7054±7 | 388±8 |
| 1.46 | 7058±8 | 397±8 |
| 1.61 | 7051±8 | 383±10 |
| 1.75 | 7049±7 | 379±8 |
| 1.90 | 7042±7 | 365±13 |
| 2.04 | 7037±8 | 362±12 |
| 2.19 | 7063±8 | 358±15 |
| 2.34 | 7052±9 | 363±10 |
| 2.48 | 7061±7 | 354±14 |
| 2.63 | 7045±9 | 352±18 |
| 2.77 | 7050±9 | 362±21 |
| 2.92 | 7071±9 | 370±14 |
| 3.07 | 7056±10 | 354±13 |
| 3.21 | 7071±10 | 357±16 |
| 3.36 | 7062±11 | 332±22 |
| 3.50 | 7060±12 | 349±25 |
| 3.65 | 7060±11 | 357±11 |
| 3.80 | 7055±11 | 331±37 |
| 3.94 | 7045±14 | 345±27 |
| 4.09 | 7050±13 | 339±22 |
| 4.23 | 7044±8 | 335±17 |
| 4.45 | 7071±9 | 335±12 |
| 4.75 | 7057±9 | 313±18 |
| 5.04 | 7059±10 | 329±23 |
| 5.33 | 7058±9 | 323±13 |
| 5.62 | 7056±14 | 343±18 |
| 5.91 | 7035±14 | 313±21 |
| 6.20 | 7048±13 | 319±40 |
| 6.64 | 7042±15 | 323±32 |
| 6.93 | 7053±17 | 297±69 |
| 7.23 | 7058±14 | 322±26 |
| 7.52 | 7069±18 | 296±43 |
| 7.81 | 7047±18 | 314±52 |
| 8.10 | 7045±23 | 304±50 |
| 8.39 | 7027±16 | 312±36 |
| 8.76 | 7043±18 | 313±69 |
| 9.20 | 7013±27 | 352±65 |
| 9.64 | 7033±22 | 316±41 |
| 10.07 | 6969±19 | 343±35 |
| 10.59 | 7049±16 | 287±31 |
| 11.17 | 7077±15 | 266±24 |
| 11.75 | 7021±31 | 348±62 |
| 12.41 | 7014±20 | 367±46 |
| 13.21 | 7024±19 | 249±37 |
| 14.09 | 7056±26 | 344±22 |
| 15.04 | 7035±26 | 410±56 |
| 16.21 | 7065±44 | 288±99 |
| 17.67 | 7024±16 | 286±36 |

Table B.12: Radial kinematics of IC1633.

| Radius (arcsec) | $V$ (km s$^{-1}$) | $\sigma$ (km s$^{-1}$) |
|---|---|---|
| -4.96 | 4366±23 | 284±16 |
| -3.21 | 4415±13 | 255±24 |
| -2.26 | 4404±17 | 305±17 |
| -1.61 | 4405±17 | 306±24 |
| -1.10 | 4412±10 | 268±17 |
| -0.66 | 4411±12 | 288±17 |
| -0.29 | 4467±13 | 281±18 |
| 0.00 | 4411±18 | 326±30 |
| 0.29 | 4406±16 | 260±20 |
| 0.44 | 4423±13 | 313±28 |
| 0.73 | 4362±15 | 280±23 |
| 1.10 | 4386±14 | 311±21 |
| 1.53 | 4375±11 | 291±15 |
| 1.97 | 4372±14 | 271±17 |
| 2.48 | 4397±19 | 296±21 |
| 3.14 | 4403±17 | 262±12 |
| 4.09 | 4422±15 | 245±13 |
| 5.84 | 4418±23 | 313±23 |

Table B.13: Radial kinematics of IC4765.

| Radius (arcsec) | $V$ (km s$^{-1}$) | $\sigma$ (km s$^{-1}$) |
|---|---|---|
| -7.74 | 8530±15 | 221±38 |
| -5.55 | 8507±15 | 222±17 |
| -4.45 | 8503±17 | 228±31 |
| -3.72 | 8534±14 | 199±23 |
| -3.21 | 8532±15 | 208±21 |
| -2.77 | 8521±8 | 210±16 |
| -2.41 | 8516±10 | 204±21 |
| -2.12 | 8527±10 | 207±12 |
| -1.90 | 8525±12 | 192±16 |
| -1.75 | 8507±8 | 183±17 |
| -1.61 | 8520±8 | 187±13 |
| -1.46 | 8530±8 | 191±9 |
| -1.31 | 8532±6 | 184±11 |
| -1.17 | 8514±8 | 193±8 |
| -1.02 | 8522±6 | 192±7 |
| -0.88 | 8513±6 | 206±9 |
| -0.73 | 8507±5 | 222±7 |
| -0.58 | 8508±5 | 227±8 |
| -0.44 | 8512±4 | 233±7 |
| -0.29 | 8510±4 | 241±6 |
| -0.15 | 8528±4 | 253±5 |
| 0.00 | 8541±4 | 252±6 |
| 0.15 | 8558±3 | 243±4 |
| 0.29 | 8562±4 | 245±5 |
| 0.44 | 8566±5 | 237±4 |
| 0.58 | 8560±4 | 232±9 |
| 0.73 | 8551±4 | 215±5 |
| 0.88 | 8558±5 | 222±7 |
| 1.02 | 8569±6 | 214±9 |
| 1.17 | 8559±6 | 208±10 |
| 1.31 | 8537±8 | 214±10 |
| 1.46 | 8538±10 | 230±10 |
| 1.61 | 8538±9 | 213±11 |
| 1.75 | 8527±14 | 215±14 |
| 1.90 | 8515±12 | 231±16 |
| 2.12 | 8510±9 | 219±10 |
| 2.41 | 8524±15 | 236±18 |
| 2.77 | 8520±14 | 225±12 |
| 3.21 | 8479±15 | 265±12 |
| 3.72 | 8511±17 | 274±26 |
| 4.38 | 8485±17 | 233±21 |
| 5.26 | 8474±24 | 284±49 |
| 6.57 | 8462±47 | 284±46 |
| 8.61 | 8536±52 | 317±87 |

Table B.14: Radial kinematics of IC5358.

243

| Radius (arcsec) | $V$ (km s$^{-1}$) | $\sigma$ (km s$^{-1}$) |
|---|---|---|
| -2.19 | 22772±16 | 321±19 |
| -1.82 | 22759±14 | 318±22 |
| -1.53 | 22775±17 | 339±31 |
| -1.24 | 22765±11 | 339±16 |
| -1.02 | 22793±17 | 307±23 |
| -0.88 | 22769±16 | 327±26 |
| -0.73 | 22742±15 | 359±14 |
| -0.58 | 22752±16 | 340±17 |
| -0.44 | 22730±12 | 319±20 |
| -0.29 | 22744±12 | 346±18 |
| -0.15 | 22762±12 | 328±14 |
| 0.00 | 22732±13 | 336±12 |
| 0.15 | 22749±14 | 333±24 |
| 0.29 | 22775±14 | 328±22 |
| 0.44 | 22786±14 | 308±11 |
| 0.58 | 22766±14 | 339±38 |
| 0.73 | 22776±14 | 306±20 |
| 0.88 | 22771±16 | 310±32 |
| 1.02 | 22771±20 | 317±43 |
| 1.24 | 22765±14 | 327±23 |
| 1.53 | 22754±14 | 324±31 |
| 1.90 | 22770±15 | 305±29 |
| 2.41 | 22777±17 | 287±21 |
| 3.21 | 22783±18 | 284±38 |

Table B.15: Radial kinematics of LEDA094683.

| Radius (arcsec) | $V$ (km s$^{-1}$) | $\sigma$ (km s$^{-1}$) |
|---|---|---|
| -13.21 | 9672±32 | 321±32 |
| -10.66 | 9636±30 | 420±30 |
| -9.05 | 9650±27 | 257±25 |
| -7.88 | 9633±22 | 289±20 |
| -6.93 | 9613±16 | 333±14 |
| -6.13 | 9647±22 | 282±42 |
| -5.47 | 9630±14 | 228±16 |
| -4.89 | 9647±13 | 258±24 |
| -4.38 | 9680±21 | 287±30 |
| -3.94 | 9654±16 | 242±28 |
| -3.50 | 9641±20 | 328±18 |
| -3.14 | 9627±12 | 242±17 |
| -2.85 | 9665±8 | 250±11 |
| -2.56 | 9635±13 | 270±13 |
| -2.26 | 9649±11 | 295±26 |
| -1.97 | 9646±11 | 249±13 |
| -1.75 | 9629±8 | 295±15 |
| -1.61 | 9658±9 | 254±16 |
| -1.46 | 9632±10 | 251±12 |
| -1.31 | 9642±10 | 290±16 |
| -1.17 | 9639±8 | 268±13 |
| -1.02 | 9668±8 | 280±12 |
| -0.88 | 9648±9 | 277±14 |
| -0.73 | 9616±9 | 270±18 |
| -0.58 | 9665±8 | 249±13 |
| -0.44 | 9653±7 | 246±13 |
| -0.29 | 9662±8 | 255±19 |
| -0.15 | 9642±10 | 263±14 |
| 0.00 | 9648±8 | 278±17 |
| 0.15 | 9655±9 | 304±20 |
| 0.29 | 9641±8 | 293±12 |
| 0.44 | 9642±10 | 278±19 |
| 0.58 | 9646±8 | 252±12 |
| 0.73 | 9655±12 | 272±15 |
| 0.88 | 9650±8 | 282±19 |
| 1.02 | 9650±8 | 280±13 |
| 1.17 | 9680±11 | 288±10 |
| 1.31 | 9661±11 | 294±19 |
| 1.46 | 9629±11 | 261±18 |
| 1.61 | 9671±10 | 391±25 |
| 1.75 | 9642±10 | 264±14 |
| 1.97 | 9648±11 | 278±12 |
| 2.26 | 9622±7 | 261±14 |
| 2.55 | 9636±10 | 262±16 |
| 2.85 | 9618±11 | 260±16 |
| 3.14 | 9624±14 | 236±21 |
| 3.43 | 9604±17 | 265±25 |
| 3.80 | 9616±13 | 250±26 |
| 4.23 | 9598±11 | 257±26 |
| 4.67 | 9642±8 | 230±16 |
| 5.18 | 9566±11 | 221±26 |

Table B.16 – Continued

| Radius (arcsec) | $V$ (km s$^{-1}$) | $\sigma$ (km s$^{-1}$) |
|---|---|---|
| 5.77 | 9650±18 | 306±25 |
| 6.42 | 9624±14 | 298±20 |
| 7.23 | 9635±21 | 300±24 |
| 8.25 | 9621±26 | 349±27 |
| 9.49 | 9652±29 | 289±29 |
| 11.02 | 9651±14 | 253±15 |
| 13.14 | 9618±25 | 282±25 |
| 16.57 | 9620±23 | 272±23 |

Table B.16: Radial kinematics of MCG-02-12-039.

| Radius (arcsec) | $V$ (km s$^{-1}$) | $\sigma$ (km s$^{-1}$) |
|---|---|---|
| -8.18 | 5454±9 | 302±11 |
| -6.13 | 5472±8 | 266±17 |
| -5.04 | 5485±9 | 264±15 |
| -4.31 | 5490±8 | 279±14 |
| -3.72 | 5463±8 | 240±24 |
| -3.36 | 5483±8 | 291±14 |
| -2.99 | 5489±8 | 274±15 |
| -2.70 | 5481±8 | 283±11 |
| -2.41 | 5472±11 | 285±11 |
| -2.12 | 5473±10 | 272±15 |
| -1.83 | 5479±11 | 274±12 |
| -1.61 | 5491±11 | 280±22 |
| -1.46 | 5475±7 | 268±21 |
| -1.31 | 5491±10 | 313±15 |
| -1.17 | 5479±10 | 311±12 |
| -1.02 | 5495±9 | 294±14 |
| -0.88 | 5500±9 | 278±18 |
| -0.73 | 5498±8 | 317±14 |
| -0.58 | 5483±8 | 308±8 |
| -0.44 | 5486±14 | 273±20 |
| -0.29 | 5491±8 | 308±10 |
| -0.15 | 5497±9 | 326±11 |
| 0.00 | 5491±6 | 288±11 |
| 0.15 | 5490±9 | 303±10 |
| 0.29 | 5468±12 | 289±14 |
| 0.44 | 5485±10 | 301±11 |
| 0.58 | 5486±7 | 303±9 |
| 0.73 | 5483±7 | 299±13 |
| 0.88 | 5483±9 | 298±11 |
| 1.02 | 5482±7 | 269±12 |
| 1.17 | 5484±16 | 278±12 |
| 1.31 | 5474±9 | 290±12 |
| 1.46 | 5479±10 | 284±11 |
| 1.61 | 5486±12 | 301±15 |
| 1.83 | 5499±9 | 277±13 |
| 2.12 | 5485±9 | 292±9 |
| 2.41 | 5478±8 | 286±9 |
| 2.70 | 5490±9 | 279±10 |
| 2.99 | 5495±10 | 286±11 |
| 3.36 | 5494±8 | 276±12 |
| 3.80 | 5491±10 | 288±13 |
| 4.31 | 5465±10 | 260±14 |
| 5.04 | 5484±10 | 278±15 |
| 6.21 | 5487±10 | 281±8 |
| 8.61 | 5481±10 | 282±14 |

Table B.17: Radial kinematics of NGC0533.

| Radius (arcsec) | $V$ (km s$^{-1}$) | $\sigma$ (km s$^{-1}$) |
|---|---|---|
| -5.18 | 5338±7 | 212±12 |
| -3.72 | 5333±7 | 212±8 |
| -2.99 | 5337±6 | 226±10 |
| -2.48 | 5334±4 | 233±9 |
| -2.12 | 5342±5 | 225±8 |
| -1.83 | 5343±6 | 210±8 |
| -1.53 | 5346±6 | 234±10 |
| -1.24 | 5347±6 | 243±6 |
| -1.02 | 5335±7 | 241±12 |
| -0.88 | 5339±5 | 233±14 |
| -0.73 | 5338±6 | 262±9 |
| -0.58 | 5328±7 | 240±11 |

Table B.18 – Continued

| Radius (arcsec) | $V$ (km s$^{-1}$) | $\sigma$ (km s$^{-1}$) |
|---|---|---|
| -0.44 | 5338±6 | 238±12 |
| -0.29 | 5338±6 | 263±7 |
| -0.15 | 5347±7 | 242±8 |
| 0.00 | 5343±5 | 235±12 |
| 0.15 | 5343±5 | 253±9 |
| 0.29 | 5341±6 | 273±8 |
| 0.44 | 5335±7 | 259±11 |
| 0.58 | 5348±6 | 237±11 |
| 0.73 | 5337±8 | 230±13 |
| 0.88 | 5333±6 | 232±18 |
| 1.02 | 5347±8 | 248±9 |
| 1.02 | 5342±7 | 256±9 |
| 1.17 | 5348±7 | 234±8 |
| 1.39 | 5338±6 | 237±9 |
| 1.68 | 5340±5 | 240±12 |
| 1.97 | 5345±8 | 245±11 |
| 2.34 | 5342±7 | 226±9 |
| 2.85 | 5346±8 | 231±10 |
| 3.50 | 5340±8 | 216±10 |
| 4.60 | 5343±10 | 216±11 |

Table B.18: Radial kinematics of NGC0541.

| Radius (arcsec) | $V$ (km s$^{-1}$) | $\sigma$ (km s$^{-1}$) |
|---|---|---|
| -20.22 | – | 263±30 |
| -19.93 | – | 292±40 |
| -19.64 | – | 251±40 |
| -19.34 | – | 167±47 |
| -19.05 | – | 202±52 |
| -18.76 | – | 189±37 |
| -18.47 | 1445±30 | 251±47 |
| -18.18 | 1413±32 | 225±18 |
| -17.88 | 1410±21 | 252±29 |
| -17.59 | 1433±17 | 265±24 |
| -17.30 | 1406±14 | 271±17 |
| -17.01 | 1386±11 | 229±21 |
| -16.72 | 1397±11 | 236±19 |
| -16.42 | 1417±9 | 209±20 |
| -16.13 | 1401±11 | 273±15 |
| -15.84 | 1402±11 | 274±12 |
| -15.55 | 1401±8 | 255±21 |
| -15.26 | 1401±13 | 301±11 |
| -14.96 | 1426±15 | 286±11 |
| -14.67 | 1416±11 | 296±15 |
| -14.38 | 1386±16 | 265±10 |
| -14.09 | 1417±11 | 280±11 |
| -13.80 | 1432±13 | 255±17 |
| -13.58 | 1412±11 | 272±11 |
| -13.43 | 1441±8 | 272±12 |
| -13.29 | 1419±9 | 260±15 |
| -13.14 | 1415±13 | 287±15 |
| -12.99 | 1409±15 | 265±26 |
| -12.85 | 1402±12 | 287±11 |
| -12.70 | 1401±12 | 291±14 |
| -12.56 | 1416±10 | 263±10 |
| -12.41 | 1404±10 | 222±14 |
| -12.26 | 1427±10 | 282±13 |
| -12.12 | 1431±11 | 278±13 |
| -11.97 | 1411±8 | 280±14 |
| -11.83 | 1431±13 | 282±10 |
| -11.68 | 1426±9 | 245±11 |
| -11.53 | 1394±10 | 279±15 |
| -11.39 | 1419±10 | 278±18 |
| -11.24 | 1450±12 | 270±10 |
| -11.10 | 1468±11 | 201±16 |
| -10.95 | 1435±9 | 259±18 |
| -10.80 | 1440±10 | 262±18 |
| -10.66 | 1413±8 | 268±11 |
| -10.51 | 1419±9 | 277±14 |
| -10.37 | 1419±10 | 299±11 |
| -10.22 | 1422±9 | 319±17 |
| -10.07 | 1421±9 | 252±19 |
| -9.93 | 1406±8 | 291±10 |
| -9.78 | 1411±8 | 286±10 |
| -9.64 | 1431±10 | 288±16 |
| -9.49 | 1421±13 | 288±10 |
| -9.34 | 1409±11 | 277±14 |
| -9.20 | 1412±10 | 261±9 |

246

Table B.19 – Continued

| Radius (arcsec) | $V$ (km s$^{-1}$) | $\sigma$ (km s$^{-1}$) |
|---|---|---|
| -9.05 | 1417±9 | 276±13 |
| -8.91 | 1424±9 | 292±11 |
| -8.76 | 1422±9 | 290±10 |
| -8.61 | 1429±7 | 269±14 |
| -8.47 | 1409±6 | 286±9 |
| -8.32 | 1427±6 | 278±9 |
| -8.18 | 1430±7 | 290±8 |
| -8.03 | 1408±10 | 313±10 |
| -7.88 | 1413±9 | 316±14 |
| -7.74 | 1416±9 | 306±9 |
| -7.59 | 1405±8 | 288±9 |
| -7.45 | 1439±14 | 275±11 |
| -7.30 | 1416±10 | 287±12 |
| -7.15 | 1427±8 | 300±9 |
| -7.01 | 1454±16 | 310±11 |
| -6.86 | 1431±17 | 393±23 |
| -6.72 | 1419±7 | 314±8 |
| -6.57 | 1422±7 | 302±13 |
| -6.42 | 1414±8 | 307±9 |
| -6.28 | 1427±8 | 303±8 |
| -6.13 | 1420±8 | 308±9 |
| -5.99 | 1430±5 | 299±7 |
| -5.84 | 1420±8 | 318±9 |
| -5.69 | 1417±7 | 303±9 |
| -5.55 | 1414±9 | 300±12 |
| -5.40 | 1401±10 | 319±8 |
| -5.26 | 1422±11 | 303±11 |
| -5.11 | 1425±6 | 316±11 |
| -4.96 | 1413±8 | 339±10 |
| -4.82 | 1426±7 | 297±10 |
| -4.67 | 1432±7 | 321±13 |
| -4.53 | 1404±12 | 318±11 |
| -4.38 | 1424±11 | 311±13 |
| -4.23 | 1419±11 | 327±8 |
| -4.09 | 1414±10 | 320±10 |
| -3.94 | 1419±8 | 329±8 |
| -3.80 | 1413±6 | 325±6 |
| -3.65 | 1425±6 | 321±8 |
| -3.50 | 1430±8 | 332±6 |
| -3.36 | 1425±9 | 327±0 |
| -3.21 | 1426±9 | 347±12 |
| -3.07 | 1414±10 | 328±9 |
| -2.92 | 1408±10 | 338±9 |
| -2.77 | 1419±10 | 344±10 |
| -2.63 | 1421±11 | 354±14 |
| -2.48 | 1423±9 | 354±7 |
| -2.34 | 1412±6 | 324±13 |
| -2.19 | 1404±8 | 349±7 |
| -2.04 | 1402±7 | 342±12 |
| -1.90 | 1411±6 | 350±7 |
| -1.75 | 1417±6 | 368±6 |
| -1.61 | 1395±9 | 367±9 |
| -1.46 | 1408±6 | 354±7 |
| -1.31 | 1400±10 | 337±6 |
| -1.17 | 1416±6 | 381±6 |
| -1.02 | 1399±12 | 373±7 |
| -0.88 | 1406±8 | 364±6 |
| -0.73 | 1418±8 | 377±6 |
| -0.58 | 1383±11 | 387±6 |
| -0.44 | 1404±7 | 379±7 |
| -0.29 | 1406±8 | 381±7 |
| -0.15 | 1413±10 | 390±6 |
| 0.00 | 1399±6 | 394±6 |
| 0.15 | 1409±9 | 393±8 |
| 0.29 | 1390±8 | 392±6 |
| 0.44 | 1390±9 | 401±7 |
| 0.58 | 1401±11 | 387±8 |
| 0.73 | 1401±8 | 379±14 |
| 0.88 | 1408±11 | 375±8 |
| 1.02 | 1393±8 | 396±10 |
| 1.17 | 1405±7 | 398±9 |
| 1.31 | 1408±7 | 359±9 |
| 1.46 | 1401±7 | 360±6 |
| 1.61 | 1415±7 | 373±6 |
| 1.75 | 1412±9 | 371±9 |
| 1.90 | 1409±7 | 369±7 |
| 2.04 | 1417±7 | 372±13 |
| 2.19 | 1411±8 | 367±9 |
| 2.34 | 1402±7 | 341±12 |
| 2.48 | 1418±7 | 343±6 |
| 2.63 | 1409±6 | 355±6 |
| 2.77 | 1410±8 | 344±9 |

# APPENDIX B

| Radius (arcsec) | $V$ (km s$^{-1}$) | $\sigma$ (km s$^{-1}$) |
|---|---|---|
| 2.92 | 1412±5 | 353±10 |
| 3.07 | 1405±7 | 341±5 |
| 3.21 | 1396±8 | 327±8 |
| 3.36 | 1398±10 | 337±7 |
| 3.50 | 1403±6 | 328±8 |
| 3.65 | 1421±7 | 320±7 |
| 3.80 | 1403±9 | 334±7 |
| 3.94 | 1393±16 | 332±7 |
| 4.09 | 1414±8 | 344±7 |
| 4.23 | 1410±11 | 306±8 |
| 4.38 | 1409±6 | 307±7 |
| 4.53 | 1396±6 | 348±11 |
| 4.67 | 1414±7 | 305±8 |
| 4.82 | 1421±6 | 296±8 |
| 4.96 | 1435±10 | 297±9 |
| 5.11 | 1445±14 | 293±10 |
| 5.26 | 1423±13 | 298±8 |
| 5.40 | 1409±8 | 315±8 |
| 5.55 | 1411±7 | 289±9 |
| 5.69 | 1400±7 | 287±10 |
| 5.84 | 1407±6 | 291±8 |
| 5.99 | 1387±14 | 286±8 |
| 6.13 | 1424±7 | 317±17 |
| 6.28 | 1398±7 | 288±10 |
| 6.42 | 1398±8 | 263±15 |
| 6.57 | 1408±7 | 277±10 |
| 6.72 | 1391±6 | 285±7 |
| 6.86 | 1405±7 | 290±8 |
| 7.01 | 1413±8 | 296±9 |
| 7.15 | 1409±9 | 290±11 |
| 7.30 | 1417±9 | 270±17 |
| 7.45 | 1426±11 | 267±12 |
| 7.59 | 1398±8 | 270±10 |
| 7.74 | 1399±7 | 276±9 |
| 7.88 | 1413±7 | 268±15 |
| 8.03 | 1407±7 | 260±12 |
| 8.18 | 1423±11 | 263±13 |
| 8.32 | 1405±7 | 266±11 |
| 8.47 | 1403±5 | 266±10 |
| 8.61 | 1402±8 | 258±16 |
| 8.76 | 1406±8 | 285±12 |
| 8.91 | 1402±9 | 255±11 |
| 9.05 | 1414±7 | 262±22 |
| 9.20 | 1387±7 | 286±8 |
| 9.34 | 1396±8 | 257±13 |
| 9.49 | 1402±8 | 272±10 |
| 9.64 | 1405±10 | 257±14 |
| 9.78 | 1395±8 | 281±8 |
| 9.93 | 1404±10 | 245±13 |
| 10.07 | 1385±7 | 257±13 |
| 10.22 | 1404±7 | 272±9 |
| 10.37 | 1396±7 | 285±12 |
| 10.51 | 1412±8 | 255±22 |
| 10.66 | 1421±8 | 255±19 |
| 10.80 | 1396±9 | 341±26 |
| 11.10 | 1384±8 | 245±14 |
| 11.24 | 1368±8 | 234±34 |
| 11.39 | 1415±12 | 279±14 |
| 11.53 | 1413±7 | 245±12 |
| 11.68 | 1411±8 | 258±9 |
| 11.90 | 1385±6 | 247±22 |
| 12.12 | 1415±7 | 251±13 |
| 12.26 | 1372±9 | 261±12 |
| 12.41 | 1390±8 | 260±13 |
| 12.56 | 1403±10 | 279±11 |
| 12.70 | 1425±11 | 260±21 |
| 12.85 | 1413±10 | 236±13 |
| 12.99 | 1384±9 | 253±15 |
| 13.14 | 1393±14 | 239±25 |
| 13.29 | 1390±11 | 254±16 |
| 13.43 | 1381±10 | 244±12 |
| 13.58 | 1392±11 | 201±17 |
| 13.72 | 1399±8 | 285±13 |
| 13.87 | 1412±12 | 252±18 |
| 14.02 | 1392±11 | 245±19 |
| 14.16 | 1389±9 | 257±16 |
| 14.38 | 1414±9 | 266±11 |
| 14.67 | 1394±9 | 228±13 |
| 14.97 | 1390±8 | 243±13 |
| 15.26 | 1405±9 | 231±11 |
| 15.55 | 1401±8 | 241±9 |
| 15.84 | 1403±8 | 248±11 |

# APPENDIX B

Table B.19 – Continued

| Radius (arcsec) | $V$ (km s$^{-1}$) | $\sigma$ (km s$^{-1}$) |
| --- | --- | --- |
| 16.13 | 1402±9 | 217±17 |
| 16.42 | 1386±7 | 239±20 |
| 16.72 | 1394±11 | 257±14 |
| 17.01 | 1405±13 | 203±20 |
| 17.30 | 1404±11 | 252±18 |
| 17.59 | 1404±16 | 241±18 |
| 17.88 | 1363±13 | 273±15 |
| 18.18 | 1404±12 | 273±18 |
| 18.47 | 1423±12 | 265±13 |
| 18.76 | 1412±10 | 215±26 |
| 19.05 | 1441±15 | 305±18 |
| 19.42 | 1405±12 | 234±21 |
| 19.86 | 1462±14 | 199±28 |

Table B.19: Radial kinematics of NGC1399.

| Radius (arcsec) | $V$ (km s$^{-1}$) | $\sigma$ (km s$^{-1}$) |
| --- | --- | --- |
| -16.21 | 4481±16 | 267±28 |
| -14.24 | 4464±11 | 205±25 |
| -12.78 | 4459±11 | 242±20 |
| -11.24 | 4506±14 | 237±17 |
| -10.07 | 4468±10 | 188±20 |
| -9.13 | 4495±11 | 219±14 |
| -8.32 | 4474±9 | 234±15 |
| -7.67 | 4505±12 | 222±23 |
| -7.08 | 4484±10 | 215±8 |
| -6.57 | 4476±9 | 221±11 |
| -6.13 | 4482±10 | 194±15 |
| -5.77 | 4465±10 | 204±13 |
| -5.48 | 4490±8 | 199±10 |
| -5.18 | 4476±7 | 194±10 |
| -4.89 | 4474±9 | 213±13 |
| -4.60 | 4481±8 | 243±10 |
| -4.31 | 4474±6 | 206±9 |
| -4.09 | 4495±10 | 199±16 |
| -3.94 | 4493±8 | 173±12 |
| -3.80 | 4475±10 | 226±12 |
| -3.65 | 4477±9 | 210±11 |
| -3.50 | 4465±12 | 207±13 |
| -3.36 | 4460±7 | 178±13 |
| -3.21 | 4463±7 | 193±13 |
| -2.99 | 4460±5 | 212±7 |
| -2.92 | 4459±7 | 199±10 |
| -2.70 | 4480±5 | 216±6 |
| -2.63 | 4482±7 | 210±9 |
| -2.48 | 4465±6 | 211±12 |
| -2.34 | 4442±8 | 206±5 |
| -2.19 | 4456±6 | 223±11 |
| -2.04 | 4461±5 | 238±8 |
| -1.90 | 4468±5 | 217±7 |
| -1.75 | 4468±5 | 226±7 |
| -1.61 | 4473±6 | 239±7 |
| -1.46 | 4471±4 | 204±6 |
| -1.31 | 4454±4 | 223±6 |
| -1.17 | 4459±5 | 227±4 |
| -1.02 | 4474±4 | 255±4 |
| -0.88 | 4459±4 | 246±5 |
| -0.73 | 4455±4 | 247±6 |
| -0.58 | 4465±4 | 242±6 |
| -0.44 | 4468±3 | 246±5 |
| -0.29 | 4478±4 | 247±5 |
| -0.15 | 4478±4 | 253±5 |
| 0.00 | 4470±4 | 259±4 |
| 0.15 | 4477±4 | 257±4 |
| 0.29 | 4479±3 | 261±6 |
| 0.44 | 4477±4 | 255±5 |
| 0.58 | 4472±4 | 255±6 |
| 0.73 | 4478±4 | 255±5 |
| 0.88 | 4465±4 | 241±5 |
| 1.02 | 4482±4 | 235±5 |
| 1.02 | 4482±5 | 235±6 |
| 1.17 | 4493±5 | 235±7 |
| 1.31 | 4467±4 | 240±6 |
| 1.46 | 4477±6 | 226±9 |
| 1.61 | 4481±4 | 217±9 |
| 1.75 | 4480±5 | 226±5 |
| 1.90 | 4465±5 | 224±7 |
| 2.04 | 4488±6 | 215±10 |

Continued on Next Page...

Table B.20 – Continued

| Radius (arcsec) | $V$ (km s$^{-1}$) | $\sigma$ (km s$^{-1}$) |
|---|---|---|
| 2.19 | 4472±6 | 217±10 |
| 2.34 | 4460±6 | 231±9 |
| 2.48 | 4478±6 | 203±11 |
| 2.63 | 4484±8 | 209±8 |
| 2.77 | 4475±7 | 210±16 |
| 2.92 | 4462±9 | 215±10 |
| 3.07 | 4467±7 | 213±9 |
| 3.21 | 4455±9 | 221±15 |
| 3.36 | 4489±11 | 218±15 |
| 3.50 | 4487±10 | 226±10 |
| 3.65 | 4472±8 | 222±11 |
| 3.80 | 4489±9 | 223±13 |
| 4.01 | 4472±6 | 191±9 |
| 4.31 | 4480±6 | 180±9 |
| 4.60 | 4476±7 | 212±12 |
| 4.89 | 4459±9 | 200±11 |
| 5.18 | 4449±8 | 226±13 |
| 5.47 | 4473±13 | 225±13 |
| 5.84 | 4479±10 | 220±21 |
| 6.28 | 4475±6 | 175±10 |
| 6.72 | 4489±11 | 275±16 |
| 7.23 | 4503±12 | 175±23 |
| 7.81 | 4467±11 | 208±14 |
| 8.47 | 4462±10 | 226±11 |
| 9.27 | 4463±9 | 187±12 |
| 10.29 | 4465±9 | 212±13 |
| 11.61 | 4447±13 | 255±19 |
| 13.36 | 4497±14 | 182±20 |
| 15.91 | 4442±16 | 228±18 |

Table B.20: Radial kinematics of NGC1713.

| Radius (arcsec) | $V$ (km s$^{-1}$) | $\sigma$ (km s$^{-1}$) |
|---|---|---|
| -15.91 | -- | 185±66 |
| -15.33 | -- | 186±27 |
| -14.75 | 6847±29 | 326±52 |
| -14.16 | 6894±24 | 258±32 |
| -13.58 | 6828±22 | 219±16 |
| -12.99 | 6825±20 | 281±34 |
| -12.41 | 6841±39 | 386±61 |
| -11.83 | 6912±31 | 387±45 |
| -11.24 | 6867±38 | 300±55 |
| -10.66 | 6857±26 | 353±35 |
| -9.78 | 6829±20 | 341±31 |
| -9.34 | 6834±17 | 321±36 |
| -8.91 | 6903±24 | 345±26 |
| -8.47 | 6861±17 | 270±16 |
| -8.03 | 6870±16 | 325±18 |
| -7.59 | 6842±17 | 303±22 |
| -7.30 | 6886±16 | 285±20 |
| -7.01 | 6862±17 | 353±24 |
| -6.72 | 6899±21 | 287±21 |
| -6.42 | 6897±20 | 334±17 |
| -6.13 | 6845±15 | 293±14 |
| -5.84 | 6859±18 | 311±16 |
| -5.55 | 6880±17 | 341±20 |
| -5.26 | 6871±16 | 339±24 |
| -4.96 | 6896±24 | 363±18 |
| -4.82 | 6825±15 | 264±39 |
| -4.67 | 6852±24 | 266±23 |
| -4.53 | 6876±20 | 329±20 |
| -4.38 | 6873±17 | 299±36 |
| -4.23 | 6834±18 | 345±22 |
| -4.09 | 6879±23 | 336±19 |
| -3.94 | 6838±17 | 359±29 |
| -3.80 | 6850±14 | 349±20 |
| -3.65 | 6897±13 | 392±14 |
| -3.50 | 6867±13 | 332±15 |
| -3.36 | 6830±19 | 382±13 |
| -3.21 | 6879±12 | 330±28 |
| -3.07 | 6864±11 | 302±12 |
| -2.92 | 6841±12 | 324±12 |
| -2.77 | 6823±12 | 341±13 |
| -2.63 | 6867±12 | 342±10 |
| -2.48 | 6891±23 | 321±11 |
| -2.34 | 6876±15 | 329±28 |
| -2.19 | 6818±20 | 341±17 |
| -2.04 | 6826±14 | 349±14 |

Table B.21 – Continued

| Radius (arcsec) | $V$ (km s$^{-1}$) | $\sigma$ (km s$^{-1}$) |
|---|---|---|
| -1.90 | 6843±11 | 355±16 |
| -1.75 | 6877±9 | 333±13 |
| -1.61 | 6843±15 | 312±12 |
| -1.46 | 6857±9 | 347±12 |
| -1.31 | 6836±9 | 356±11 |
| -1.17 | 6880±12 | 399±15 |
| -1.02 | 6839±18 | 355±12 |
| -0.88 | 6841±13 | 350±23 |
| -0.73 | 6869±11 | 372±13 |
| -0.58 | 6853±8 | 359±11 |
| -0.44 | 6828±12 | 352±15 |
| -0.29 | 6861±13 | 368±8 |
| -0.15 | 6830±9 | 368±10 |
| 0.00 | 6848±9 | 369±9 |
| 0.15 | 6852±9 | 358±10 |
| 0.29 | 6848±8 | 351±8 |
| 0.44 | 6833±12 | 379±12 |
| 0.58 | 6828±11 | 394±13 |
| 0.73 | 6825±8 | 357±9 |
| 0.88 | 6846±15 | 364±8 |
| 1.02 | 6811±16 | 352±9 |
| 1.17 | 6821±9 | 330±19 |
| 1.31 | 6832±12 | 370±10 |
| 1.46 | 6825±12 | 340±11 |
| 1.61 | 6827±12 | 368±15 |
| 1.75 | 6796±10 | 347±17 |
| 1.90 | 6819±12 | 355±17 |
| 2.04 | 6811±11 | 371±11 |
| 2.19 | 6813±15 | 346±15 |
| 2.34 | 6808±13 | 340±17 |
| 2.48 | 6821±12 | 317±17 |
| 2.63 | 6808±9 | 351±19 |
| 2.77 | 6841±15 | 330±13 |
| 2.92 | 6806±14 | 357±16 |
| 3.07 | 6769±11 | 327±16 |
| 3.21 | 6828±9 | 298±10 |
| 3.36 | 6756±17 | 379±15 |
| 3.50 | 6800±13 | 316±14 |
| 3.65 | 6796±14 | 259±28 |
| 3.80 | 6721±13 | 369±17 |
| 3.94 | 6820±14 | 287±22 |
| 4.09 | 6815±25 | 357±33 |
| 4.23 | 6785±14 | 264±51 |
| 4.38 | 6835±16 | 321±19 |
| 4.53 | 6816±18 | 327±27 |
| 4.67 | 6824±16 | 328±24 |
| 4.96 | 6755±20 | 293±11 |
| 5.26 | 6813±12 | 335±21 |
| 5.55 | 6845±17 | 310±22 |
| 5.84 | 6825±18 | 326±19 |
| 6.13 | 6817±17 | 254±22 |
| 6.42 | 6780±20 | 378±15 |
| 6.72 | 6844±19 | 261±39 |
| 7.01 | 6765±13 | 320±23 |
| 7.30 | 6818±17 | 323±17 |
| 7.74 | 6804±15 | 325±19 |
| 8.18 | 6856±26 | 368±30 |
| 8.61 | 6795±26 | 340±50 |
| 9.20 | 6775±15 | 326±20 |
| 9.78 | 6822±18 | 319±23 |
| 10.37 | 6884±27 | 356±40 |
| 11.10 | 6829±15 | 290±31 |
| 11.97 | 6774±17 | 360±29 |
| 12.85 | 6808±20 | 303±31 |
| 13.87 | 6842±27 | 243±51 |
| 15.04 | 6860±44 | 382±39 |
| 16.35 | 6897±33 | 302±42 |
| 17.96 | 6789±18 | 257±24 |
| 19.86 | 6810±19 | 177±73 |
| 22.05 | 6774±21 | – |
| 28.47 | 6802±28 | – |

Table B.21: Radial kinematics of NGC2832.

| Radius (arcsec) | $V$ (km s$^{-1}$) | $\sigma$ (km s$^{-1}$) |
|---|---|---|
| -13.58 | 3706±14 | 212±22 |
| -10.22 | 3722±12 | 243±24 |
| -8.61 | 3738±10 | 211±15 |

# APPENDIX B

Table B.22 – Continued

| Radius (arcsec) | $V$ (km s$^{-1}$) | $\sigma$ (km s$^{-1}$) |
|---|---|---|
| -7.45 | 3719±9 | 205±15 |
| -6.50 | 3704±10 | 212±14 |
| -5.69 | 3719±8 | 198±12 |
| -5.04 | 3715±7 | 193±17 |
| -4.45 | 3713±7 | 188±16 |
| -3.94 | 3692±9 | 198±13 |
| -3.50 | 3704±9 | 190±12 |
| -3.07 | 3712±10 | 199±21 |
| -2.63 | 3720±8 | 185±12 |
| -2.19 | 3719±8 | 188±11 |
| -1.75 | 3700±8 | 189±11 |
| -1.31 | 3722±8 | 182±16 |
| -0.88 | 3703±8 | 194±13 |
| -0.44 | 3716±8 | 195±13 |
| 0.00 | 3715±8 | 193±13 |
| 0.29 | 3704±9 | 207±15 |
| 0.73 | 3704±7 | 184±12 |
| 1.17 | 3697±8 | 193±10 |
| 1.61 | 3701±8 | 201±12 |
| 2.04 | 3709±7 | 193±15 |
| 2.56 | 3709±7 | 199±12 |
| 3.14 | 3712±7 | 202±13 |
| 6.79 | 3723±7 | 204±14 |
| 8.61 | 3691±10 | 216±16 |
| 11.75 | 3715±10 | 225±14 |

Table B.22: Radial kinematics of NGC3311.

| Radius (arcsec) | $V$ (km s$^{-1}$) | $\sigma$ (km s$^{-1}$) |
|---|---|---|
| -16.40 | 6205±11 | 252±14 |
| -11.60 | 6207±15 | 279±21 |
| -8.80 | 6182±11 | 264±13 |
| -7.20 | 6197±12 | 254±17 |
| -6.00 | 6210±10 | 268±12 |
| -5.00 | 6190±10 | 242±9 |
| -4.20 | 6204±9 | 259±13 |
| -3.60 | 6215±10 | 244±12 |
| -3.20 | 6208±12 | 260±10 |
| -2.80 | 6209±7 | 279±11 |
| -2.40 | 6205±7 | 281±8 |
| -2.00 | 6208±6 | 274±7 |
| -1.60 | 6212±6 | 279±7 |
| -1.20 | 6208±7 | 277±6 |
| -0.80 | 6215±6 | 272±6 |
| -0.40 | 6205±5 | 279±5 |
| 0.00 | 6211±5 | 293±4 |
| 0.40 | 6207±6 | 298±4 |
| 0.80 | 6217±5 | 292±5 |
| 1.20 | 6201±6 | 282±5 |
| 1.60 | 6203±6 | 286±6 |
| 2.00 | 6199±7 | 285±6 |
| 2.40 | 6201±7 | 267±6 |
| 2.80 | 6201±8 | 266±9 |
| 3.20 | 6183±12 | 278±10 |
| 3.60 | 6204±11 | 278±12 |
| 4.20 | 6196±9 | 261±9 |
| 5.00 | 6197±9 | 249±8 |
| 5.80 | 6201±10 | 264±13 |
| 6.80 | 6216±11 | 253±8 |
| 8.20 | 6214±11 | 265±14 |
| 10.20 | 6203±12 | 262±12 |
| 13.40 | 6220±14 | 307±14 |
| 20.80 | 6195±12 | 268±13 |

Table B.23: Radial kinematics of NGC3842.

| Radius (arcsec) | $V$ (km s$^{-1}$) | $\sigma$ (km s$^{-1}$) |
|---|---|---|
| -10.44 | 7377±7 | 291±12 |
| -7.88 | 7363±15 | 274±23 |
| -6.35 | 7352±11 | 270±19 |
| -5.33 | 7400±9 | 239±26 |
| -4.53 | 7389±10 | 234±17 |
| -3.87 | 7364±12 | 237±22 |

Continued on Next Page...

252

Table B.24 – Continued

| Radius (arcsec) | $V$ (km s$^{-1}$) | $\sigma$ (km s$^{-1}$) |
|---|---|---|
| -3.36 | 7374±12 | 252±20 |
| -2.92 | 7385±8 | 260±11 |
| -2.56 | 7392±10 | 267±17 |
| -2.26 | 7372±13 | 273±16 |
| -1.97 | 7385±11 | 269±12 |
| -1.68 | 7370±10 | 257±11 |
| -1.39 | 7388±8 | 258±11 |
| -1.17 | 7383±8 | 266±10 |
| -1.02 | 7386±12 | 281±13 |
| -0.88 | 7390±9 | 280±11 |
| -0.73 | 7381±10 | 259±13 |
| -0.58 | 7382±10 | 280±12 |
| -0.44 | 7380±8 | 272±14 |
| -0.29 | 7371±9 | 282±12 |
| -0.15 | 7364±10 | 293±12 |
| 0.00 | 7376±10 | 282±10 |
| 0.15 | 7371±8 | 278±13 |
| 0.29 | 7380±10 | 280±11 |
| 0.44 | 7372±9 | 272±9 |
| 0.58 | 7382±10 | 279±13 |
| 0.73 | 7387±11 | 274±13 |
| 0.88 | 7386±11 | 281±13 |
| 1.09 | 7389±7 | 274±10 |
| 1.39 | 7385±8 | 268±10 |
| 1.61 | 7389±11 | 269±16 |
| 1.97 | 7393±10 | 263±11 |
| 2.26 | 7392±9 | 263±16 |
| 2.55 | 7387±12 | 262±15 |
| 3.07 | 7400±9 | 251±14 |
| 3.58 | 7392±11 | 255±15 |
| 4.23 | 7393±10 | 260±17 |
| 5.04 | 7386±11 | 255±26 |
| 6.06 | 7410±14 | 249±18 |
| 7.59 | 7419±14 | 278±21 |
| 10.00 | 7442±14 | 301±32 |

Table B.24: Radial kinematics of NGC4839.

| Radius (arcsec) | $V$ (km s$^{-1}$) | $\sigma$ (km s$^{-1}$) |
|---|---|---|
| -10.40 | 6919±12 | 240±16 |
| -7.60 | 6915±11 | 215±10 |
| -6.00 | 6952±9 | 208±13 |
| -5.00 | 6944±7 | 213±11 |
| -4.20 | 6956±7 | 228±8 |
| -3.40 | 6953±8 | 244±9 |
| -2.80 | 6953±8 | 243±8 |
| -2.40 | 6948±10 | 247±9 |
| -2.00 | 6930±9 | 259±10 |
| -1.60 | 6949±9 | 267±8 |
| -1.20 | 6955±9 | 278±9 |
| -0.80 | 6958±9 | 280±11 |
| -0.40 | 6953±9 | 267±9 |
| 0.00 | 6958±8 | 268±10 |
| 0.40 | 6944±13 | 268±10 |
| 1.00 | 6950±8 | 269±8 |
| 1.80 | 6942±9 | 267±9 |
| 2.60 | 6961±10 | 241±9 |
| 3.40 | 6968±9 | 234±11 |
| 4.40 | 6966±9 | 230±10 |
| 5.80 | 6963±9 | 230±11 |
| 7.80 | 6942±8 | 235±14 |
| 11.80 | 6940±10 | 248±16 |

Table B.25: Radial kinematics of NGC4874.

| Radius (arcsec) | $V$ (km s$^{-1}$) | $\sigma$ (km s$^{-1}$) |
|---|---|---|
| -23.00 | 6291±36 | 313±36 |
| -18.80 | 6266±54 | 249±74 |
| -16.20 | 6314±27 | 317±25 |
| -14.00 | 6218±18 | 337±17 |
| -12.20 | 6239±17 | 401±25 |
| -10.80 | 6270±15 | 335±29 |
| -9.80 | 6251±10 | 328±25 |

Continued on Next Page...

253

# APPENDIX B

| Radius (arcsec) | $V$ (km s$^{-1}$) | $\sigma$ (km s$^{-1}$) |
|---|---|---|
| -9.00 | 6272±14 | 331±14 |
| -8.20 | 6261±20 | 343±16 |
| -7.40 | 6302±16 | 353±14 |
| -6.80 | 6300±16 | 334±21 |
| -6.40 | 6297±18 | 329±16 |
| -6.00 | 6258±14 | 331±15 |
| -5.60 | 6265±17 | 361±18 |
| -5.20 | 6289±12 | 359±14 |
| -4.80 | 6293±10 | 359±12 |
| -4.40 | 6285±13 | 374±10 |
| -4.00 | 6262±10 | 355±9 |
| -3.60 | 6286±9 | 369±9 |
| -3.20 | 6299±10 | 380±10 |
| -2.80 | 6285±9 | 357±7 |
| -2.40 | 6291±7 | 362±8 |
| -2.00 | 6285±7 | 384±7 |
| -1.60 | 6282±7 | 388±8 |
| -1.20 | 6270±7 | 382±7 |
| -0.80 | 6291±8 | 396±8 |
| -0.40 | 6269±10 | 395±6 |
| 0.00 | 6267±7 | 379±6 |
| 0.40 | 6269±9 | 369±5 |
| 0.80 | 6252±8 | 377±9 |
| 1.20 | 6258±8 | 369±8 |
| 1.60 | 6238±16 | 366±7 |
| 2.00 | 6254±9 | 359±11 |
| 2.40 | 6244±9 | 368±9 |
| 2.80 | 6279±11 | 357±11 |
| 3.20 | 6275±12 | 350±13 |
| 3.60 | 6291±16 | 358±16 |
| 4.00 | 6277±16 | 372±17 |
| 4.40 | 6268±14 | 351±18 |
| 5.00 | 6288±11 | 339±11 |
| 5.80 | 6262±12 | 325±11 |
| 6.60 | 6272±15 | 347±12 |
| 7.40 | 6265±13 | 355±13 |
| 8.20 | 6292±15 | 313±14 |
| 9.20 | 6225±18 | 339±11 |
| 10.40 | 6319±20 | 350±18 |
| 11.80 | 6278±17 | 353±25 |
| 13.80 | 6277±15 | 311±18 |
| 16.80 | 6261±16 | 318±17 |
| 22.00 | 6338±37 | 330±62 |

Table B.26: Radial kinematics of NGC4889.

| Radius (arcsec) | $V$ (km s$^{-1}$) | $\sigma$ (km s$^{-1}$) |
|---|---|---|
| -11.10 | 3098±8 | 200±13 |
| -9.49 | 3101±9 | 207±10 |
| -8.32 | 3074±8 | 161±15 |
| -7.45 | 3085±7 | 173±7 |
| -6.79 | 3079±12 | 192±25 |
| -6.21 | 3089±7 | 181±10 |
| -5.69 | 3087±8 | 175±11 |
| -5.26 | 3088±8 | 173±11 |
| -4.89 | 3077±8 | 188±15 |
| -4.60 | 3093±5 | 173±10 |
| -4.31 | 3074±6 | 193±8 |
| -4.01 | 3085±5 | 179±9 |
| -3.72 | 3100±7 | 172±11 |
| -3.43 | 3095±4 | 180±7 |
| -3.21 | 3093±9 | 200±10 |
| -3.07 | 3105±6 | 189±9 |
| -2.92 | 3078±8 | 200±13 |
| -2.77 | 3111±8 | 195±11 |
| -2.63 | 3092±7 | 190±9 |
| -2.48 | 3094±6 | 202±9 |
| -2.34 | 3094±5 | 191±10 |
| -2.19 | 3092±6 | 212±9 |
| -2.04 | 3080±4 | 196±16 |
| -1.90 | 3084±5 | 208±11 |
| -1.75 | 3096±5 | 203±7 |
| -1.61 | 3102±5 | 202±6 |
| -1.46 | 3093±4 | 204±7 |
| -1.31 | 3099±4 | 192±6 |
| -1.17 | 3097±5 | 203±7 |
| -1.02 | 3093±4 | 192±5 |
| -0.88 | 3106±4 | 209±6 |

Table B.27 – Continued

| Radius (arcsec) | $V$ (km s$^{-1}$) | $\sigma$ (km s$^{-1}$) |
|---|---|---|
| -0.73 | 3106±3 | 197±6 |
| -0.58 | 3112±6 | 215±5 |
| -0.44 | 3127±4 | 198±5 |
| -0.29 | 3131±3 | 202±6 |
| -0.15 | 3130±6 | 200±5 |
| 0.00 | 3161±4 | 208±5 |
| 0.15 | 3153±4 | 199±4 |
| 0.29 | 3173±4 | 198±6 |
| 0.44 | 3171±4 | 207±6 |
| 0.58 | 3183±4 | 209±5 |
| 0.73 | 3185±3 | 195±4 |
| 0.88 | 3197±7 | 202±5 |
| 1.02 | 3190±5 | 190±5 |
| 1.17 | 3185±4 | 196±6 |
| 1.31 | 3181±5 | 200±5 |
| 1.46 | 3194±4 | 190±7 |
| 1.61 | 3198±5 | 190±7 |
| 1.75 | 3185±5 | 205±6 |
| 1.90 | 3194±6 | 198±7 |
| 2.04 | 3187±5 | 196±6 |
| 2.19 | 3190±5 | 198±8 |
| 2.34 | 3193±5 | 207±8 |
| 2.48 | 3190±6 | 214±10 |
| 2.63 | 3191±5 | 183±8 |
| 2.85 | 3188±5 | 190±6 |
| 3.14 | 3188±5 | 183±9 |
| 3.43 | 3188±8 | 190±6 |
| 3.72 | 3174±6 | 160±9 |
| 4.01 | 3174±8 | 180±7 |
| 4.31 | 3184±6 | 174±9 |
| 4.67 | 3168±6 | 182±10 |
| 5.11 | 3197±6 | 149±11 |
| 5.55 | 3177±5 | 148±14 |
| 6.06 | 3166±5 | 142±19 |
| 6.72 | 3163±7 | 145±14 |
| 7.52 | 3168±5 | 133±11 |
| 8.54 | 3173±6 | 148±14 |
| 9.93 | 3163±6 | 172±9 |
| 12.04 | 3133±11 | 203±21 |

Table B.27: Radial kinematics of NGC4946.

| Radius (arcsec) | $V$ (km s$^{-1}$) | $\sigma$ (km s$^{-1}$) |
|---|---|---|
| -6.00 | 10179±16 | 272±18 |
| -4.00 | 10205±14 | 274±22 |
| -3.00 | 10229±11 | 250±9 |
| -2.40 | 10229±16 | 280±20 |
| -2.00 | 10225±12 | 294±11 |
| -1.60 | 10247±22 | 284±16 |
| -1.20 | 10224±10 | 325±13 |
| -0.80 | 10178±14 | 300±11 |
| -0.40 | 10160±9 | 320±9 |
| 0.00 | 10116±8 | 322±14 |
| 0.40 | 10063±11 | 333±9 |
| 0.80 | 10036±10 | 327±8 |
| 1.20 | 10008±11 | 317±12 |
| 1.60 | 10002±11 | 282±17 |
| 2.00 | 9993±12 | 288±23 |
| 2.40 | 9977±13 | 283±18 |
| 2.80 | 9983±10 | 257±25 |
| 3.40 | 10016±13 | 256±22 |
| 4.40 | 9977±18 | 255±46 |
| 6.60 | 10039±17 | 260±16 |

Table B.28: Radial kinematics of NGC6034.

| Radius (arcsec) | $V$ (km s$^{-1}$) | $\sigma$ (km s$^{-1}$) |
|---|---|---|
| -4.40 | 9075±18 | 232±13 |
| -2.40 | 9068±9 | 195±8 |
| -1.40 | 9010±11 | 211±11 |
| -0.80 | 9052±13 | 212±9 |
| -0.40 | 9020±13 | 233±10 |
| 0.00 | 9027±8 | 230±9 |

Table B.29 – Continued

| Radius (arcsec) | $V$ (km s$^{-1}$) | $\sigma$ (km s$^{-1}$) |
|---|---|---|
| 0.40 | 9046±16 | 226±11 |
| 0.80 | 9017±9 | 233±8 |
| 1.40 | 8995±10 | 217±14 |
| 2.40 | 8966±9 | 212±15 |
| 4.40 | 8963±14 | 215±12 |

Table B.29: Radial kinematics of NGC6047.

| Radius (arcsec) | $V$ (km s$^{-1}$) | $\sigma$ (km s$^{-1}$) |
|---|---|---|
| -2.48 | 9480±10 | 283±12 |
| -1.61 | 9468±11 | 287±11 |
| -1.10 | 9477±10 | 299±11 |
| -0.73 | 9483±10 | 319±12 |
| -0.44 | 9487±7 | 334±11 |
| -0.15 | 9485±7 | 332±14 |
| 0.00 | 9487±7 | 329±13 |
| 0.29 | 9484±8 | 314±11 |
| 0.58 | 9479±10 | 305±9 |
| 0.88 | 9477±8 | 297±14 |
| 1.17 | 9469±9 | 303±14 |
| 1.75 | 9492±9 | 288±11 |
| 2.56 | 9483±11 | 290±14 |
| 4.16 | 9495±14 | 273±13 |

Table B.30: Radial kinematics of NGC6086.

| Radius (arcsec) | $V$ (km s$^{-1}$) | $\sigma$ (km s$^{-1}$) |
|---|---|---|
| -3.01 | 9430±10 | 221±22 |
| -2.02 | 9418±9 | 240±17 |
| -1.45 | 9431±7 | 236±15 |
| -1.02 | 9413±7 | 258±14 |
| -0.66 | 9431±9 | 260±14 |
| -0.36 | 9435±9 | 257±13 |
| -0.15 | 9432±9 | 272±10 |
| 0.15 | 9435±8 | 277±9 |
| 0.36 | 9430±10 | 273±11 |
| 0.66 | 9420±10 | 266±10 |
| 1.02 | 9430±8 | 263±14 |
| 1.45 | 9437±8 | 264±12 |
| 2.17 | 9421±9 | 247±20 |
| 3.66 | 9435±10 | 255±12 |

Table B.31: Radial kinematics of NGC6160.

| Radius (arcsec) | $V$ (km s$^{-1}$) | $\sigma$ (km s$^{-1}$) |
|---|---|---|
| -13.00 | 9093±34 | 297±53 |
| -9.80 | 9103±15 | 260±17 |
| -7.80 | 9093±18 | 242±39 |
| -6.40 | 9083±18 | 313±19 |
| -5.20 | 9125±10 | 284±16 |
| -4.20 | 9108±15 | 278±24 |
| -3.40 | 9097±9 | 283±14 |
| -2.60 | 9090±13 | 294±21 |
| -2.00 | 9074±16 | 296±47 |
| -1.60 | 9104±13 | 307±13 |
| -1.20 | 9091±14 | 312±14 |
| -0.80 | 9102±15 | 321±18 |
| -0.40 | 9092±18 | 295±33 |
| 0.00 | 9095±15 | 309±29 |
| 0.40 | 9114±15 | 327±17 |
| 0.80 | 9095±15 | 306±28 |
| 1.20 | 9102±11 | 280±13 |
| 1.60 | 9085±19 | 300±16 |
| 2.00 | 9095±15 | 284±33 |
| 2.40 | 9079±14 | 275±21 |
| 3.00 | 9095±10 | 284±13 |
| 3.80 | 9098±10 | 260±22 |
| 4.60 | 9074±13 | 284±14 |
| 5.40 | 9064±17 | 277±26 |

Table B.32 – Continued

| Radius (arcsec) | $V$ (km s$^{-1}$) | $\sigma$ (km s$^{-1}$) |
|---|---|---|
| 6.40 | 9077±15 | 278±20 |
| 7.60 | 9079±20 | 267±38 |
| 9.00 | 9090±28 | 300±53 |
| 10.60 | 9074±41 | 274±63 |

Table B.32: Radial kinematics of NGC6166.

| Radius (arcsec) | $V$ (km s$^{-1}$) | $\sigma$ (km s$^{-1}$) |
|---|---|---|
| -4.60 | 8780±13 | 274±14 |
| -3.07 | 8763±12 | 282±18 |
| -2.26 | 8745±10 | 314±13 |
| -1.75 | 8762±10 | 290±12 |
| -1.39 | 8777±8 | 295±10 |
| -1.10 | 8768±11 | 302±9 |
| -0.80 | 8759±7 | 306±12 |
| -0.58 | 8764±14 | 301±17 |
| -0.44 | 8766±11 | 271±22 |
| -0.29 | 8758±8 | 300±11 |
| -0.15 | 8762±7 | 302±11 |
| 0.00 | 8756±7 | 298±13 |
| 0.15 | 8779±10 | 310±15 |
| 0.29 | 8765±8 | 312±17 |
| 0.44 | 8769±10 | 315±16 |
| 0.66 | 8765±8 | 309±12 |
| 0.95 | 8767±8 | 314±9 |
| 1.24 | 8772±10 | 315±10 |
| 1.61 | 8753±8 | 298±8 |
| 2.12 | 8769±8 | 274±10 |
| 2.85 | 8783±10 | 274±15 |
| 4.09 | 8758±13 | 288±15 |
| 7.01 | 8734±14 | 279±22 |

Table B.33: Radial kinematics of NGC6173.

| Radius (arcsec) | $V$ (km s$^{-1}$) | $\sigma$ (km s$^{-1}$) |
|---|---|---|
| -6.50 | 10367±11 | 320±13 |
| -5.26 | 10354±12 | 302±24 |
| -4.38 | 10355±14 | 315±13 |
| -3.72 | 10344±13 | 309±16 |
| -3.21 | 10346±15 | 324±15 |
| -2.77 | 10352±11 | 327±13 |
| -2.41 | 10345±11 | 328±15 |
| -2.12 | 10348±11 | 326±15 |
| -1.82 | 10356±9 | 314±11 |
| -1.53 | 10350±8 | 325±11 |
| -1.31 | 10343±13 | 367±11 |
| -1.17 | 10349±12 | 348±11 |
| -1.02 | 10370±11 | 331±14 |
| -0.88 | 10370±11 | 344±7 |
| -0.73 | 10376±10 | 330±11 |
| -0.58 | 10354±12 | 336±13 |
| -0.44 | 10356±13 | 361±12 |
| -0.29 | 10378±10 | 337±11 |
| -0.15 | 10379±11 | 352±10 |
| 0.00 | 10362±9 | 359±13 |
| 0.15 | 10360±11 | 375±25 |
| 0.29 | 10357±10 | 337±14 |
| 0.44 | 10352±12 | 333±12 |
| 0.58 | 10364±8 | 330±10 |
| 0.73 | 10357±12 | 327±13 |
| 0.88 | 10339±11 | 351±12 |
| 1.10 | 10356±10 | 334±14 |
| 1.39 | 10338±10 | 342±13 |
| 1.68 | 10342±10 | 323±15 |
| 1.97 | 10344±12 | 327±20 |
| 2.34 | 10346±11 | 313±19 |
| 2.77 | 10342±14 | 331±20 |
| 3.28 | 10339±14 | 303±16 |
| 3.94 | 10347±11 | 305±11 |
| 4.82 | 10377±12 | 305±12 |
| 6.13 | 10328±19 | 336±13 |
| 8.39 | 10348±14 | 305±15 |

Table B.34: Radial kinematics of NGC6269.

# APPENDIX B

| Radius (arcsec) | $V$ (km s$^{-1}$) | $\sigma$ (km s$^{-1}$) |
|---|---|---|
| -14.60 | 8637±20 | 177±40 |
| -11.97 | 8645±15 | 207±22 |
| -10.37 | 8693±21 | 180±88 |
| -9.20 | 8664±19 | 234±28 |
| -8.25 | 8697±24 | 209±65 |
| -7.45 | 8613±19 | 232±56 |
| -6.79 | 8657±14 | 213±28 |
| -6.21 | 8608±18 | 285±21 |
| -5.69 | 8635±14 | 248±18 |
| -5.26 | 8646±14 | 235±22 |
| -4.82 | 8641±13 | 234±53 |
| -4.45 | 8636±14 | 222±23 |
| -4.16 | 8621±49 | 230±94 |
| -3.87 | 8660±33 | 245±60 |
| -3.58 | 8650±20 | 232±17 |
| -3.29 | 8645±15 | 253±15 |
| -2.99 | 8603±18 | 310±56 |
| -2.70 | 8603±12 | 290±16 |
| -2.48 | 8637±13 | 231±20 |
| -2.34 | 8631±12 | 248±15 |
| -2.19 | 8635±11 | 246±15 |
| -2.04 | 8641±9 | 218±18 |
| -1.90 | 8649±9 | 221±17 |
| -1.75 | 8655±10 | 235±14 |
| -1.61 | 8646±9 | 223±18 |
| -1.46 | 8651±9 | 237±10 |
| -1.31 | 8637±10 | 238±16 |
| -1.17 | 8651±10 | 242±18 |
| -1.02 | 8656±10 | 248±22 |
| -0.88 | 8638±11 | 231±13 |
| -0.73 | 8646±9 | 236±13 |
| -0.58 | 8653±9 | 233±14 |
| -0.44 | 8649±6 | 252±14 |
| -0.29 | 8663±7 | 228±9 |
| -0.15 | 8638±6 | 254±11 |
| 0.00 | 8647±6 | 235±12 |
| 0.15 | 8640±7 | 237±10 |
| 0.29 | 8655±9 | 253±10 |
| 0.44 | 8659±6 | 237±10 |
| 0.58 | 8667±8 | 231±13 |
| 0.73 | 8664±8 | 254±7 |
| 0.88 | 8667±8 | 250±10 |
| 1.02 | 8639±8 | 260±8 |
| 1.17 | 8667±8 | 236±9 |
| 1.31 | 8657±8 | 228±14 |
| 1.46 | 8650±8 | 249±12 |
| 1.61 | 8658±7 | 216±11 |
| 1.75 | 8665±7 | 223±13 |
| 1.90 | 8655±9 | 286±11 |
| 2.04 | 8654±10 | 239±12 |
| 2.19 | 8669±11 | 246±12 |
| 2.34 | 8667±12 | 236±14 |
| 2.48 | 8658±11 | 260±14 |
| 2.63 | 8663±11 | 242±11 |
| 2.77 | 8674±11 | 226±12 |
| 2.99 | 8664±8 | 260±14 |
| 3.28 | 8666±9 | 239±11 |
| 3.58 | 8665±11 | 239±17 |
| 3.87 | 8641±11 | 231±12 |
| 4.16 | 8634±13 | 264±17 |
| 4.45 | 8660±13 | 215±27 |
| 4.74 | 8640±12 | 203±16 |
| 5.26 | 8721±15 | 256±16 |
| 5.77 | 8659±10 | 274±13 |
| 6.35 | 8641±13 | 233±40 |
| 7.01 | 8673±11 | 191±18 |
| 7.81 | 8632±15 | 254±19 |
| 8.83 | 8668±13 | 311±21 |
| 10.29 | 8585±13 | 239±42 |
| 12.48 | 8600±14 | 287±17 |

Table B.35: Radial kinematics of NGC7012.

| Radius (arcsec) | $V$ (km s$^{-1}$) | $\sigma$ (km s$^{-1}$) |
|---|---|---|
| -4.89 | 10972±15 | 184±12 |
| -3.58 | 10924±20 | 233±15 |
| -2.85 | 10925±14 | 234±32 |
| -2.34 | 10928±9 | 241±10 |
| -1.97 | 10902±9 | 229±20 |

Continued on Next Page...

258

Table B.36 - Continued

| Radius (arcsec) | $V$ (km s$^{-1}$) | $\sigma$ (km s$^{-1}$) |
|---|---|---|
| -1.68 | 10924±11 | 243±16 |
| -1.39 | 10920±9 | 248±21 |
| -1.17 | 10909±16 | 221±57 |
| -1.02 | 10925±10 | 257±16 |
| -0.88 | 10852±27 | 227±46 |
| -0.73 | 10913±15 | 300±17 |
| -0.58 | 10927±10 | 290±23 |
| -0.44 | 10925±9 | 235±12 |
| -0.29 | 10925±8 | 264±14 |
| -0.15 | 10900±10 | 257±9 |
| 0.00 | 10900±11 | 295±12 |
| 0.15 | 10903±9 | 291±28 |
| 0.29 | 10903±9 | 247±9 |
| 0.44 | 10895±14 | 264±18 |
| 0.58 | 10891±8 | 257±12 |
| 0.73 | 10924±10 | 257±13 |
| 0.88 | 10911±10 | 287±15 |
| 1.02 | 10918±11 | 244±13 |
| 1.24 | 10925±8 | 232±8 |
| 1.53 | 10912±9 | 273±11 |
| 1.82 | 10954±12 | 210±14 |
| 2.12 | 10910±9 | 207±10 |
| 2.48 | 10923±11 | 205±17 |
| 2.99 | 10952±11 | 241±22 |
| 3.72 | 10910±10 | 203±12 |
| 5.91 | 10933±9 | 190±12 |

Table B.36: Radial kinematics of NGC7597.

| Radius (arcsec) | $V$ (km s$^{-1}$) | $\sigma$ (km s$^{-1}$) |
|---|---|---|
| -4.80 | 11838±18 | 240±18 |
| -3.20 | 11878±10 | 251±20 |
| -2.20 | 11879±11 | 280±12 |
| -1.60 | 11861±10 | 248±12 |
| -1.20 | 11845±8 | 251±13 |
| -0.80 | 11848±9 | 272±8 |
| -0.40 | 11834±11 | 285±9 |
| 0.00 | 11839±10 | 281±7 |
| 0.40 | 11842±7 | 273±7 |
| 0.80 | 11847±7 | 276±8 |
| 1.20 | 11842±9 | 258±14 |
| 1.60 | 11831±11 | 240±13 |
| 2.20 | 11808±9 | 243±19 |
| 3.20 | 11819±18 | 243±11 |

Table B.37: Radial kinematics of NGC7647.

| Radius (arcsec) | $V$ (km s$^{-1}$) | $\sigma$ (km s$^{-1}$) |
|---|---|---|
| -6.64 | 12278±17 | 277±22 |
| -5.33 | 12277±17 | 265±33 |
| -4.31 | 12263±13 | 237±23 |
| -3.58 | 12261±14 | 221±24 |
| -3.07 | 12236±12 | 220±32 |
| -2.63 | 12249±11 | 213±27 |
| -2.26 | 12250±11 | 216±18 |
| -1.97 | 12295±12 | 236±34 |
| -1.68 | 12281±8 | 238±6 |
| -1.46 | 12262±11 | 229±23 |
| -1.31 | 12266±14 | 229±26 |
| -1.17 | 12271±12 | 264±24 |
| -1.02 | 12260±9 | 243±13 |
| -0.88 | 12248±10 | 242±23 |
| -0.73 | 12257±8 | 234±10 |
| -0.58 | 12263±8 | 229±9 |
| -0.44 | 12276±9 | 274±11 |
| -0.29 | 12266±8 | 258±20 |
| -0.15 | 12253±8 | 263±9 |
| 0.00 | 12246±8 | 262±10 |
| 0.15 | 12291±9 | 242±18 |
| 0.29 | 12246±9 | 254±19 |
| 0.44 | 12254±9 | 246±13 |
| 0.58 | 12234±9 | 238±8 |
| 0.73 | 12255±10 | 239±16 |

# APPENDIX B

Table B.38 – Continued

| Radius (arcsec) | $V$ (km s$^{-1}$) | $\sigma$ (km s$^{-1}$) |
|---|---|---|
| 0.88 | 12222±7 | 237±11 |
| 1.02 | 12247±11 | 224±13 |
| 1.17 | 12231±9 | 227±12 |
| 1.39 | 12238±7 | 233±12 |
| 1.68 | 12246±8 | 215±13 |
| 2.26 | 12215±17 | 221±21 |
| 2.63 | 12213±12 | 243±20 |
| 3.14 | 12239±10 | 216±16 |
| 3.80 | 12238±12 | 201±16 |
| 4.67 | 12238±22 | 224±34 |
| 5.91 | 12254±18 | 276±36 |
| 7.66 | 12214±34 | 285±30 |
| 10.29 | 12237±16 | 262±17 |

Table B.38: Radial kinematics of NGC7649.

| Radius (arcsec) | $V$ (km s$^{-1}$) | $\sigma$ (km s$^{-1}$) |
|---|---|---|
| −7.40 | 8993±24 | 344±42 |
| −5.60 | 9003±14 | 288±30 |
| −4.60 | 9034±17 | 317±18 |
| −3.80 | 9020±14 | 307±21 |
| −3.20 | 9006±15 | 325±14 |
| −2.80 | 9034±13 | 305±28 |
| −2.40 | 9026±16 | 309±20 |
| −2.00 | 9005±23 | 318±39 |
| −1.60 | 9021±10 | 349±14 |
| −1.20 | 9017±10 | 361±15 |
| −0.80 | 9032±11 | 379±11 |
| −0.40 | 9064±15 | 402±14 |
| 0.00 | 9024±14 | 419±26 |
| 0.40 | 9014±17 | 407±11 |
| 0.80 | 9015±12 | 353±10 |
| 1.20 | 9003±13 | 361±18 |
| 1.60 | 8965±23 | 324±13 |
| 2.00 | 9004±11 | 330±22 |
| 2.40 | 9000±13 | 328±21 |
| 2.80 | 9017±15 | 325±14 |
| 3.20 | 9022±21 | 327±33 |
| 3.80 | 9019±14 | 287±50 |
| 4.60 | 8988±27 | 354±42 |
| 5.60 | 8943±25 | 450±34 |

Table B.39: Radial kinematics of NGC7720.

| Radius (arcsec) | $V$ (km s$^{-1}$) | $\sigma$ (km s$^{-1}$) |
|---|---|---|
| −11.40 | 7818±13 | 264±10 |
| −8.00 | 7784±10 | 233±10 |
| −6.40 | 7764±9 | 231±9 |
| −5.40 | 7759±10 | 230±11 |
| −4.60 | 7784±10 | 243±11 |
| −3.80 | 7739±11 | 261±11 |
| −3.20 | 7759±10 | 237±12 |
| −2.80 | 7746±9 | 248±9 |
| −2.40 | 7752±11 | 249±13 |
| −2.00 | 7754±6 | 255±7 |
| −1.60 | 7752±8 | 272±8 |
| −1.20 | 7778±8 | 272±9 |
| −0.80 | 7807±6 | 275±7 |
| −0.40 | 7842±5 | 285±6 |
| 0.00 | 7870±5 | 278±5 |
| 0.40 | 7919±7 | 262±5 |
| 0.80 | 7934±6 | 260±6 |
| 1.20 | 7945±9 | 262±9 |
| 1.60 | 7945±7 | 251±6 |
| 2.00 | 7977±7 | 250±7 |
| 2.40 | 7964±10 | 257±10 |
| 2.80 | 7964±8 | 234±11 |
| 3.20 | 7976±8 | 233±10 |
| 3.80 | 7950±6 | 228±7 |
| 4.60 | 7942±10 | 268±12 |
| 5.60 | 7948±11 | 242±8 |
| 7.20 | 7940±8 | − |

Table B.40: Radial kinematics of NGC7768.

# APPENDIX B

| Radius (arcsec) | $V$ (km s$^{-1}$) | $\sigma$ (km s$^{-1}$) |
|---|---|---|
| -3.58 | 15362±24 | 352±28 |
| -2.48 | 15389±20 | 328±14 |
| -1.90 | 15441±20 | 302±20 |
| -1.53 | 15458±20 | 320±18 |
| -1.24 | 15442±20 | 318±17 |
| -0.95 | 15463±22 | 301±16 |
| -0.73 | 15427±32 | 329±21 |
| -0.58 | 15471±16 | 299±18 |
| -0.44 | 15481±17 | 301±18 |
| -0.29 | 15473±13 | 312±14 |
| -0.15 | 15454±13 | 311±13 |
| 0.00 | 15476±14 | 324±16 |
| 0.15 | 15440±18 | 322±16 |
| 0.29 | 15458±16 | 307±14 |
| 0.44 | 15433±20 | 306±25 |
| 0.58 | 15449±15 | 323±17 |
| 0.73 | 15416±26 | 329±23 |
| 0.95 | 15450±15 | 323±14 |
| 1.24 | 15434±17 | 323±17 |
| 1.61 | 15447±12 | 280±15 |
| 2.12 | 15447±21 | 286±14 |
| 2.99 | 15455±19 | 308±18 |

Table B.41: Radial kinematics of PGC004072.

| Radius (arcsec) | $V$ (km s$^{-1}$) | $\sigma$ (km s$^{-1}$) |
|---|---|---|
| -2.12 | 15986±6 | 237±9 |
| -1.53 | 15075±16 | 205±17 |
| -0.95 | 15980±13 | 274±16 |
| -0.58 | 15989±8 | 270±16 |
| -0.29 | 15991±8 | 279±13 |
| 0.00 | 15989±9 | 264±16 |
| 0.15 | 15986±10 | 283±13 |
| 0.44 | 15984±10 | 283±10 |
| 0.73 | 15982±10 | 263±17 |
| 1.10 | 15974±10 | 254±24 |
| 1.61 | 15964±16 | 271±17 |
| 2.41 | 15962±11 | 180±19 |

Table B.42: Radial kinematics of PGC025714.

| Radius (arcsec) | $V$ (km s$^{-1}$) | $\sigma$ (km s$^{-1}$) |
|---|---|---|
| -3.72 | 15805±16 | 266±21 |
| -2.99 | 15778±21 | 282±26 |
| -2.48 | 15792±18 | 241±21 |
| -2.12 | 15780±23 | 273±29 |
| -1.82 | 15789±19 | 228±22 |
| -1.53 | 15805±18 | 256±19 |
| -1.24 | 15808±22 | 235±23 |
| -0.95 | 15813±15 | 227±19 |
| -0.73 | 15769±13 | 232±20 |
| -0.58 | 15781±22 | 269±18 |
| -0.44 | 15808±26 | 211±23 |
| -0.29 | 15830±21 | 253±15 |
| -0.15 | 15781±23 | 176±24 |
| 0.00 | 15838±14 | 263±19 |
| 0.15 | 15804±22 | 216±25 |
| 0.29 | 15840±16 | 219±23 |
| 0.44 | 15807±15 | 218±20 |
| 0.58 | 15837±23 | 206±21 |
| 0.73 | 15824±20 | 199±24 |
| 0.88 | 15818±20 | 205±25 |
| 1.02 | 15859±17 | 262±21 |
| 1.17 | 15850±18 | 280±19 |
| 1.39 | 15844±25 | 247±20 |
| 1.68 | 15848±22 | 251±19 |
| 1.97 | 15866±15 | 256±23 |
| 2.26 | 15869±18 | 268±25 |
| 2.55 | 15822±22 | 358±25 |
| 2.92 | 15810±25 | 290±23 |
| 3.36 | 15815±20 | 327±25 |
| 3.87 | 15831±15 | 246±26 |

Table B.43: Radial kinematics of PGC026269.

# APPENDIX B

| Radius (arcsec) | $V$ (km s$^{-1}$) | $\sigma$ (km s$^{-1}$) |
|---|---|---|
| -4.89 | 15816±30 | 241±36 |
| -3.43 | 15859±29 | 188±38 |
| -2.70 | 15825±21 | 218±44 |
| -2.19 | 15828±18 | 210±23 |
| -1.83 | 15817±27 | 230±26 |
| -1.53 | 15801±12 | 216±40 |
| -1.31 | 15808±14 | 214±18 |
| -1.17 | 15805±13 | 248±19 |
| -1.02 | 15796±15 | 236±16 |
| -0.88 | 15789±21 | 311±26 |
| -0.73 | 15765±29 | 290±17 |
| -0.58 | 15830±29 | 321±28 |
| -0.44 | 15808±17 | 334±17 |
| -0.29 | 15830±26 | 349±21 |
| -0.15 | 15801±16 | 342±20 |
| 0.00 | 15814±13 | 312±17 |
| 0.15 | 15796±27 | 371±32 |
| 0.29 | 15790±14 | 322±20 |
| 0.44 | 15800±19 | 329±17 |
| 0.58 | 15769±18 | 328±18 |
| 0.73 | 15792±14 | 295±17 |
| 0.88 | 15777±10 | 276±18 |
| 1.02 | 15762±13 | 273±22 |
| 1.17 | 15793±14 | 271±25 |
| 1.31 | 15776±17 | 262±23 |
| 1.46 | 15768±20 | 251±25 |
| 1.68 | 15707±35 | 450±52 |
| 1.97 | 15761±14 | 229±24 |
| 2.34 | 15769±22 | 191±19 |
| 2.85 | 15827±45 | 180±20 |
| 3.58 | 15707±30 | 180±23 |
| 5.04 | 15669±28 | 230±33 |

Table B.44: Radial kinematics of PGC030223.

| Radius (arcsec) | $V$ (km s$^{-1}$) | $\sigma$ (km s$^{-1}$) |
|---|---|---|
| -3.72 | 14028±29 | 240±34 |
| -2.04 | 13987±25 | 301±24 |
| -1.17 | 14034±16 | 252±27 |
| -0.51 | 14038±22 | 272±19 |
| 0.00 | 14022±16 | 250±29 |
| 0.29 | 14001±15 | 217±22 |
| 0.80 | 14010±16 | 233±17 |
| 1.46 | 13999±20 | 221±30 |
| 2.34 | 13998±18 | 242±34 |
| 4.09 | 14007±17 | 295±24 |

Table B.45: Radial kinematics of PGC044257.

| Radius (arcsec) | $V$ (km s$^{-1}$) | $\sigma$ (km s$^{-1}$) |
|---|---|---|
| -4.43 | 17915±12 | 269±13 |
| -2.55 | 17919±11 | 295±15 |
| -1.76 | 17908±10 | 280±19 |
| -1.25 | 17913±11 | 293±12 |
| -0.88 | 17915±9 | 293±15 |
| -0.60 | 17928±10 | 310±12 |
| -0.29 | 17909±8 | 310±14 |
| 0.00 | 17900±12 | 319±11 |
| 0.14 | 17915±12 | 323±19 |
| 0.44 | 17901±9 | 312±16 |
| 0.73 | 17912±8 | 341±12 |
| 1.00 | 17933±10 | 312±34 |
| 1.38 | 17919±13 | 280±35 |
| 1.90 | 17905±11 | 305±23 |
| 2.75 | 17918±13 | 284±16 |
| 3.93 | 17938±16 | 285±29 |

Table B.46: Radial kinematics of PGC071807.

262

| Radius (arcsec) | $V$ (km s$^{-1}$) | $\sigma$ (km s$^{-1}$) |
|---|---|---|
| -3.29 | 22460±19 | 295±20 |
| -2.41 | 22449±17 | 319±23 |
| -1.90 | 22441±19 | 350±17 |
| -1.53 | 22447±18 | 332±48 |
| -1.24 | 22436±12 | 283±22 |
| -1.02 | 22447±14 | 340±26 |
| -0.88 | 22434±12 | 324±18 |
| -0.73 | 22442±13 | 306±12 |
| -0.58 | 22438±12 | 297±13 |
| -0.44 | 22437±14 | 320±27 |
| -0.29 | 22451±10 | 299±17 |
| -0.15 | 22421±10 | 317±33 |
| 0.00 | 22432±8 | 311±17 |
| 0.15 | 22427±12 | 296±33 |
| 0.29 | 22429±11 | 322±21 |
| 0.44 | 22407±13 | 309±13 |
| 0.58 | 22398±11 | 321±17 |
| 0.73 | 22394±13 | 310±20 |
| 0.88 | 22426±12 | 269±18 |
| 1.02 | 22397±22 | 291±21 |
| 1.17 | 22419±15 | 277±37 |
| 1.39 | 22407±12 | 302±15 |
| 1.68 | 22392±26 | 300±33 |
| 2.04 | 22380±15 | 330±20 |
| 2.55 | 22368±21 | 332±41 |
| 3.36 | 22360±30 | 354±67 |
| 5.40 | 22377±24 | 296±32 |

Table B.47: Radial kinematics of PGC072804.

| Radius (arcsec) | $V$ (km s$^{-1}$) | $\sigma$ (km s$^{-1}$) |
|---|---|---|
| -2.99 | 13036±18 | 249±21 |
| -1.97 | 13047±14 | 230±19 |
| -1.39 | 13030±10 | 228±18 |
| -0.95 | 13047±13 | 242±14 |
| -0.58 | 13008±12 | 241±18 |
| -0.29 | 13015±8 | 241±17 |
| 0.00 | 13021±11 | 243±14 |
| 0.15 | 12985±21 | 262±17 |
| 0.44 | 13044±13 | 274±20 |
| 0.80 | 13052±13 | 260±15 |
| 1.24 | 13012±10 | 232±12 |
| 1.83 | 13011±15 | 255±18 |
| 2.85 | 13053±13 | 245±22 |

Table B.48: Radial kinematics of UGC00579.

| Radius (arcsec) | $V$ (km s$^{-1}$) | $\sigma$ (km s$^{-1}$) |
|---|---|---|
| -7.74 | 14291±18 | 244±19 |
| -7.01 | 14212±20 | 246±20 |
| -6.28 | 14184±16 | 290±16 |
| -5.62 | 14199±15 | 172±23 |
| -5.04 | 14205±12 | 226±17 |
| -4.53 | 14235±12 | 228±17 |
| -4.09 | 14206±15 | 263±12 |
| -3.65 | 14262±12 | 260±14 |
| -3.29 | 14225±14 | 269±28 |
| -2.99 | 14202±8 | 226±13 |
| -2.70 | 14217±11 | 280±25 |
| -2.41 | 14218±8 | 251±16 |
| -2.12 | 14212±8 | 240±20 |
| -1.90 | 14220±13 | 285±23 |
| -1.75 | 14212±14 | 263±29 |
| -1.61 | 14199±14 | 274±29 |
| -1.46 | 14200±11 | 297±17 |
| -1.31 | 14258±7 | 251±15 |
| -1.17 | 14223±8 | 271±11 |
| -1.02 | 14209±7 | 266±13 |
| -0.88 | 14226±10 | 300±17 |
| -0.73 | 14202±8 | 278±11 |
| -0.58 | 14220±7 | 297±10 |
| -0.44 | 14211±9 | 302±9 |
| -0.29 | 14205±8 | 324±10 |
| -0.15 | 14198±12 | 318±10 |

Table B.49 – Continued

| Radius (arcsec) | $V$ (km s$^{-1}$) | $\sigma$ (km s$^{-1}$) |
|---|---|---|
| 0.00 | 14217±8 | 310±10 |
| 0.15 | 14191±8 | 326±11 |
| 0.29 | 14214±7 | 333±11 |
| 0.44 | 14208±8 | 315±10 |
| 0.58 | 14209±7 | 308±10 |
| 0.73 | 14206±7 | 309±12 |
| 0.88 | 14209±8 | 291±12 |
| 1.02 | 14221±7 | 309±11 |
| 1.17 | 14225±8 | 266±11 |
| 1.31 | 14190±8 | 286±20 |
| 1.46 | 14217±8 | 280±14 |
| 1.61 | 14222±9 | 245±16 |
| 1.75 | 14200±10 | 275±13 |
| 1.90 | 14208±15 | 298±44 |
| 2.04 | 14188±13 | 294±27 |
| 2.26 | 14219±9 | 277±11 |
| 2.55 | 14196±10 | 291±10 |
| 2.85 | 14194±12 | 276±31 |
| 3.14 | 14204±10 | 240±17 |
| 3.43 | 14224±11 | 282±18 |
| 3.80 | 14249±12 | 268±11 |
| 4.23 | 14224±12 | 309±43 |
| 4.67 | 14223±26 | 294±26 |
| 5.18 | 14271±15 | 270±20 |
| 5.77 | 14219±16 | 280±58 |
| 6.35 | 14308±28 | 274±55 |
| 7.01 | 14239±23 | 301±26 |
| 7.74 | 14256±21 | 332±31 |

Table B.49: Radial kinematics of UGC02232.

| Radius (arcsec) | $V$ (km s$^{-1}$) | $\sigma$ (km s$^{-1}$) |
|---|---|---|
| −4.38 | 13017±18 | 332±18 |
| −2.99 | 13037±15 | 329±16 |
| −2.26 | 13018±11 | 334±17 |
| −1.75 | 13017±12 | 322±14 |
| −1.39 | 13033±11 | 346±18 |
| −1.09 | 13107±11 | 373±17 |
| −0.80 | 13085±9 | 363±16 |
| −0.58 | 13134±17 | 385±18 |
| −0.44 | 13129±13 | 372±20 |
| −0.29 | 13123±12 | 385±19 |
| −0.15 | 13119±11 | 365±17 |
| 0.00 | 13101±11 | 348±15 |
| 0.15 | 13119±12 | 362±19 |
| 0.29 | 13087±11 | 346±19 |
| 0.44 | 13094±12 | 360±17 |
| 0.58 | 13079±10 | 350±15 |
| 0.73 | 13062±17 | 349±16 |
| 0.88 | 13061±15 | 332±15 |
| 1.02 | 13062±15 | 348±19 |
| 1.24 | 13054±14 | 338±13 |
| 1.53 | 13043±12 | 328±20 |
| 1.83 | 13049±17 | 312±28 |
| 2.19 | 13023±12 | 298±20 |
| 2.70 | 13038±16 | 322±29 |
| 3.43 | 13044±15 | 328±18 |
| 4.60 | 13037±17 | 319±26 |

Table B.50: Radial kinematics of UGC05515.

| Radius (arcsec) | $V$ (km s$^{-1}$) | $\sigma$ (km s$^{-1}$) |
|---|---|---|
| −9.00 | 10329±10 | 218±14 |
| −5.20 | 10341±12 | 217±12 |
| −3.60 | 10341±9 | 220±10 |
| −2.60 | 10320±9 | 242±9 |
| −1.80 | 10354±9 | 249±14 |
| −1.20 | 10334±10 | 231±9 |
| −0.80 | 10349±11 | 270±14 |
| −0.40 | 10334±8 | 268±12 |
| 0.00 | 10349±7 | 274±12 |
| 0.40 | 10347±9 | 266±15 |
| 0.80 | 10335±12 | 255±22 |

# APPENDIX B

| Table B.51 – Continued | | |
|---|---|---|
| Radius (arcsec) | $V$ (km s$^{-1}$) | $\sigma$ (km s$^{-1}$) |
| 1.20 | 10350±8 | 255±10 |
| 1.60 | 10358±10 | 245±9 |
| 2.20 | 10354±9 | 251±16 |
| 3.00 | 10336±8 | 248±19 |
| 4.00 | 10342±10 | 224±14 |
| 5.60 | 10352±9 | 227±10 |
| 10.20 | 10324±10 | 214±10 |

Table B.51: Radial kinematics of UGC10143.

# Appendix C

# CENTRAL INDEX MEASUREMENTS

Table C.1 contains the index measurements from $H\delta_A$ to $C_24668$, and Table C.2 from $H\beta$ to $TiO_2$, for all 51 galaxies (49 BCG and 2 ellipticals). The first line for each galaxy is the index measurement, and the second is the error on the index measurement.

| Object | $H\delta_A$ | $H\delta_F$ | $CN_1$ | $CN_2$ | Ca4227 | G4300 | $H\gamma_A$ | $H\gamma_F$ | Fe4383 | Ca4455 | Fe4531 | $C_24668$ |
|---|---|---|---|---|---|---|---|---|---|---|---|---|
| Name | Å | Å | mag | mag | Å | Å | Å | Å | Å | Å | Å | Å |
| ESO146-028 | −2.582 | 0.242 | 0.102 | 0.143 | 1.375 | 5.808 | −5.969 | −1.783 | 4.193 | 2.228 | 3.562 | 7.903 |
|  | 0.407 | 0.285 | 0.009 | 0.011 | 0.145 | 0.204 | 0.314 | 0.166 | 0.314 | 0.142 | 0.159 | 0.220 |
| ESO202-043 | −3.117 | 0.394 | 0.140 | 0.189 | 1.331 | 5.861 | −6.102 | −1.999 | 5.888 | 2.293 | 3.517 | 7.892 |
|  | 0.559 | 0.396 | 0.012 | 0.013 | 0.219 | 0.439 | 0.345 | 0.198 | 0.329 | 0.165 | 0.218 | 0.287 |
| ESO303-005 | −3.642 | 0.070 | 0.130 | 0.167 | 1.385 | 5.868 | −6.853 | −2.122 | 5.256 | 1.563 | 3.796 | 8.925 |
|  | 0.376 | 0.250 | 0.008 | 0.010 | 0.142 | 0.216 | 0.403 | 0.214 | 0.180 | 0.135 | 0.172 | 0.259 |
| ESO346-003 | −3.039 | −0.185 | 0.067 | 0.107 | 1.359 | 5.703 | −6.384 | −2.015 | 5.672 | 1.435 | 3.151 | 7.993 |
|  | 0.613 | 0.401 | 0.013 | 0.015 | 0.192 | 0.291 | 0.411 | 0.255 | 0.352 | 0.176 | 0.261 | 1.109 |
| ESO349-010 | −3.574 | −0.478 | 0.127 | 0.154 | 1.457 | 5.595 | −5.977 | −1.449 | 5.046 | 1.697 | 3.796 | 8.665 |
|  | 0.241 | 0.163 | 0.005 | 0.006 | 0.100 | 0.158 | 0.282 | 0.140 | 0.170 | 0.129 | 0.160 | 0.249 |
| ESO444-046 | −3.379 | −0.275 | 0.130 | 0.177 | 1.389 | 5.466 | −6.193 | −2.175 | 5.138 | 1.977 | 3.439 | 8.632 |
|  | 0.842 | 0.615 | 0.018 | 0.021 | 0.297 | 0.422 | 0.774 | 0.347 | 0.511 | 0.304 | 0.330 | 0.419 |
| ESO488-027 | −2.573 | 0.144 | 0.109 | 0.148 | 1.334 | 5.597 | −5.554 | −1.701 | 3.655 | 2.537 | 3.511 | 8.130 |
|  | 0.190 | 0.126 | 0.004 | 0.005 | 0.072 | 0.115 | 0.156 | 0.089 | 0.200 | 0.101 | 0.100 | 0.151 |
| ESO541-013 | −4.073 | −0.491 | 0.129 | 0.162 | 1.176 | 5.917 | −6.215 | −2.000 | 5.179 | 1.644 | 2.889 | 8.097 |
|  | 0.203 | 0.156 | 0.005 | 0.006 | 0.108 | 0.182 | 0.289 | 0.146 | 0.233 | 0.188 | 0.208 | 0.292 |
| ESO552-020 | −3.306 | −0.278 | 0.148 | 0.197 | 1.307 | 5.668 | −6.236 | −1.790 | 5.490 | 2.302 | 3.838 | 7.090 |
|  | 0.384 | 0.257 | 0.008 | 0.010 | 0.135 | 0.206 | 0.281 | 0.172 | 0.313 | 0.134 | 0.178 | 0.199 |
| GSC555700266 | −3.562 | −0.104 | 0.142 | 0.161 | 1.194 | 5.954 | −7.071 | −2.375 | 5.382 | 2.158 | 3.648 | 9.468 |
|  | 0.407 | 0.286 | 0.009 | 0.015 | 0.148 | 0.207 | 0.314 | 0.167 | 0.326 | 0.141 | 0.161 | 0.274 |
| IC1101 | −4.312 | −0.008 | 0.183 | 0.223 | 1.635 | 8.486 | −8.126 | −2.891 | 4.787 | 1.871 | 3.970 | 9.759 |
|  | 0.380 | 0.251 | 0.008 | 0.010 | 0.168 | 0.235 | 0.408 | 0.214 | 0.204 | 0.140 | 0.179 | 0.387 |
| IC1633 | −5.445 | −0.527 | 0.192 | 0.239 | 1.557 | 5.667 | −6.243 | −1.893 | 5.939 | 2.125 | 3.462 | 9.651 |
|  | 0.615 | 0.401 | 0.013 | 0.015 | 0.226 | 0.294 | 0.413 | 0.255 | 0.406 | 0.206 | 0.283 | 0.332 |
| IC4765 | −4.223 | −0.395 | 0.139 | 0.181 | 1.421 | 5.835 | −6.360 | −2.317 | 4.623 | 1.677 | 4.529 | 8.370 |
|  | 0.241 | 0.166 | 0.005 | 0.006 | 0.100 | 0.159 | 0.282 | 0.141 | 0.173 | 0.139 | 0.170 | 0.251 |
| IC5358 | −4.479 | −0.293 | 0.192 | 0.241 | 1.196 | 5.365 | −5.690 | −1.692 | 4.925 | 2.178 | 3.779 | 7.943 |

Continued on Next Page...

Table C.1 – Continued

| Object Name | Hδ$_A$ Å | Hδ$_F$ Å | CN$_1$ mag | CN$_2$ mag | Ca4227 Å | G4300 Å | Hγ$_A$ Å | Hγ$_F$ Å | Fe4383 Å | Ca4455 Å | Fe4531 Å | C$_2$4668 Å |
|---|---|---|---|---|---|---|---|---|---|---|---|---|
| | 0.842 | 0.615 | 0.018 | 0.021 | 0.297 | 0.422 | 0.774 | 0.347 | 0.509 | 0.302 | 0.327 | 0.407 |
| LEDA094683 | −3.953 | 0.214 | 0.157 | 0.215 | 1.250 | 5.987 | −6.726 | −2.095 | 5.641 | 1.795 | 3.882 | 10.093 |
| | 0.194 | 0.127 | 0.004 | 0.005 | 0.088 | 0.126 | 0.156 | 0.090 | 0.235 | 0.122 | 0.116 | 0.203 |
| MCG-02-12-039 | −4.326 | −0.521 | 0.196 | 0.236 | 1.691 | 5.741 | −6.476 | −2.255 | 5.933 | 1.623 | 3.192 | 8.400 |
| | 0.385 | 0.257 | 0.008 | 0.010 | 0.135 | 0.208 | 0.281 | 0.172 | 0.315 | 0.142 | 0.182 | 0.217 |
| NGC0533 | −4.236 | −0.312 | 0.131 | 0.165 | 1.411 | 5.508 | −6.333 | −2.100 | 5.446 | 1.965 | 3.670 | 8.215 |
| | 0.917 | 0.629 | 0.019 | 0.022 | 0.313 | 0.449 | 0.890 | 0.436 | 0.566 | 0.365 | 0.373 | 0.486 |
| NGC0541 | −3.602 | 0.097 | 0.118 | 0.146 | 1.350 | 5.321 | −5.298 | −1.413 | 5.162 | 1.818 | 3.324 | 8.101 |
| | 1.434 | 0.941 | 0.028 | 0.032 | 0.504 | 0.855 | 0.518 | 0.432 | 0.859 | 0.323 | 0.435 | 0.531 |
| NGC1399 | −3.126 | 0.011 | 0.137 | 0.188 | 1.552 | 5.343 | −6.643 | −2.107 | 5.823 | 2.124 | 3.846 | 9.201 |
| | 0.577 | 0.420 | 0.012 | 0.013 | 0.231 | 0.317 | 0.271 | 0.230 | 0.511 | 0.179 | 0.229 | 0.311 |
| NGC1713 | −2.970 | 0.164 | 0.112 | 0.148 | 1.335 | 5.471 | −5.642 | −1.560 | 5.175 | 1.681 | 2.252 | 8.386 |
| | 1.109 | 0.752 | 0.023 | 0.027 | 0.441 | 0.805 | 0.729 | 0.450 | 0.697 | 0.349 | 0.469 | 0.604 |
| NGC2832 | −5.004 | −0.389 | 0.190 | 0.232 | 1.355 | 5.416 | −6.582 | −2.108 | 6.099 | 2.194 | 4.481 | 9.494 |
| | 0.082 | 0.046 | 0.001 | 0.003 | 0.078 | 0.061 | 0.056 | 0.035 | 0.199 | 0.130 | 0.138 | 0.166 |
| NGC3311 | −3.547 | 0.000 | 0.108 | 0.134 | 1.105 | 5.050 | −6.022 | −1.642 | 5.226 | 1.851 | 3.885 | 7.364 |
| | 0.923 | 0.530 | 0.018 | 0.021 | 0.322 | 0.357 | 0.526 | 0.345 | 0.451 | 0.214 | 0.281 | 0.307 |
| NGC3842 | −2.583 | −0.399 | 0.136 | 0.181 | 1.227 | 5.615 | −6.031 | −1.592 | 5.451 | 1.960 | 3.557 | 8.658 |
| | 0.107 | 0.076 | 0.003 | 0.003 | 0.045 | 0.077 | 0.094 | 0.062 | 0.146 | 0.106 | 0.109 | 0.147 |
| NGC4839 | −4.649 | −0.276 | 0.160 | 0.202 | 1.203 | 5.520 | −5.734 | −1.790 | 5.138 | 1.822 | 3.344 | 7.980 |
| | 0.110 | 0.077 | 0.003 | 0.003 | 0.047 | 0.079 | 0.090 | 0.056 | 0.125 | 0.075 | 0.096 | 0.150 |
| NGC4874 | −2.547 | −0.137 | 0.100 | 0.135 | 1.203 | 6.076 | −6.822 | −1.968 | 5.578 | 2.046 | 3.623 | 8.272 |
| | 0.155 | 0.099 | 0.004 | 0.004 | 0.066 | 0.112 | 0.150 | 0.092 | 0.177 | 0.108 | 0.137 | 0.208 |
| NGC4889 | −2.970 | −0.422 | 0.139 | 0.181 | 1.435 | 5.758 | −6.277 | −1.720 | 5.412 | 2.061 | 3.649 | 9.463 |
| | 0.094 | 0.057 | 0.002 | 0.003 | 0.127 | 0.084 | 0.080 | 0.048 | 0.133 | 0.096 | 0.142 | 0.282 |
| NGC4946 | −3.209 | −0.107 | 0.065 | 0.095 | 1.463 | 5.053 | −6.022 | −1.642 | 5.953 | 1.991 | 3.761 | 8.819 |

Continued on Next Page...

Table C.1 – Continued

| Object Name | Hδ$_A$ Å | Hδ$_F$ Å | CN$_1$ mag | CN$_2$ mag | Ca4227 Å | G4300 Å | Hγ$_A$ Å | Hγ$_F$ Å | Fe4383 Å | Ca4455 Å | Fe4531 Å | C$_2$4668 Å |
|---|---|---|---|---|---|---|---|---|---|---|---|---|
| | 0.585 | 0.444 | 0.012 | 0.014 | 0.217 | 0.410 | 0.370 | 0.240 | 0.355 | 0.180 | 0.240 | 0.288 |
| NGC6034 | −2.662 | −0.362 | 0.104 | 0.143 | 1.529 | 5.967 | −6.651 | −2.036 | 6.009 | 2.020 | 3.905 | 8.936 |
| | 0.127 | 0.086 | 0.003 | 0.004 | 0.085 | 0.106 | 0.124 | 0.077 | 0.209 | 0.114 | 0.130 | 0.197 |
| NGC6047 | −2.255 | −0.274 | 0.090 | 0.123 | 1.396 | 6.165 | −6.213 | −1.427 | 5.715 | 1.367 | 3.377 | 7.771 |
| | 0.261 | 0.171 | 0.007 | 0.008 | 0.110 | 0.195 | 0.258 | 0.159 | 0.293 | 0.152 | 0.222 | 0.339 |
| NGC6086 | −4.578 | −0.156 | 0.187 | 0.221 | 1.227 | 5.909 | −6.632 | −2.210 | 5.847 | 1.998 | 3.887 | 8.689 |
| | 0.369 | 0.241 | 0.008 | 0.009 | 0.118 | 0.199 | 0.264 | 0.169 | 0.360 | 0.146 | 0.208 | 0.267 |
| NGC6160 | −3.479 | −0.128 | 0.137 | 0.189 | 1.607 | 5.391 | −6.011 | −1.963 | 5.155 | 1.848 | 3.735 | 7.829 |
| | 0.054 | 0.039 | 0.001 | 0.001 | 0.021 | 0.033 | 0.036 | 0.023 | 0.052 | 0.070 | 0.047 | 0.103 |
| NGC6166 | −3.129 | −0.818 | 0.116 | 0.160 | 1.610 | 5.739 | −6.790 | −2.390 | 5.719 | 1.909 | 3.404 | 7.525 |
| | 0.236 | 0.158 | 0.006 | 0.007 | 0.102 | 0.166 | 0.220 | 0.136 | 0.260 | 0.160 | 0.194 | 0.278 |
| NGC6173 | −2.800 | −0.194 | 0.085 | 0.183 | 1.148 | 5.626 | −5.648 | −1.627 | 5.689 | 2.580 | 3.572 | 7.857 |
| | 0.539 | 0.119 | 0.004 | 0.005 | 0.084 | 0.126 | 0.167 | 0.125 | 0.172 | 0.096 | 0.116 | 0.171 |
| NGC6269 | −3.195 | 0.040 | 0.161 | 0.208 | 1.478 | 5.888 | −6.282 | −1.839 | 5.583 | 2.015 | 3.085 | 8.619 |
| | 0.133 | 0.087 | 0.003 | 0.004 | 0.078 | 0.101 | 0.108 | 0.067 | 0.166 | 0.105 | 0.095 | 0.254 |
| NGC7012 | −4.502 | −0.464 | 0.188 | 0.240 | 1.270 | 5.873 | −6.291 | −2.085 | 5.450 | 1.243 | 2.844 | 8.237 |
| | 0.711 | 0.433 | 0.015 | 0.017 | 0.245 | 0.325 | 0.444 | 0.291 | 0.397 | 0.198 | 0.273 | 0.339 |
| NGC7597 | −2.931 | −0.110 | 0.082 | 0.111 | 1.634 | 4.945 | −5.747 | −1.554 | 6.322 | 2.848 | 3.958 | 8.249 |
| | 0.810 | 0.487 | 0.015 | 0.017 | 0.227 | 0.309 | 0.389 | 0.254 | 0.356 | 0.219 | 0.206 | 0.242 |
| NGC7647 | −2.976 | −0.036 | 0.099 | 0.136 | 1.496 | 5.321 | −6.188 | −1.779 | 5.935 | 1.813 | 3.786 | 9.016 |
| | 0.197 | 0.126 | 0.005 | 0.006 | 0.094 | 0.147 | 0.183 | 0.115 | 0.219 | 0.131 | 0.170 | 0.264 |
| NGC7649 | −3.293 | 0.111 | 0.137 | 0.170 | 1.263 | 5.097 | −5.231 | −1.201 | 5.447 | 1.297 | 3.404 | 8.043 |
| | 0.391 | 0.254 | 0.008 | 0.009 | 0.107 | 0.180 | 0.239 | 0.152 | 0.197 | 0.105 | 0.144 | 0.170 |
| NGC7720 | −2.664 | −0.149 | 0.143 | 0.181 | 1.603 | 5.981 | −6.009 | −1.296 | 5.712 | 2.307 | 3.860 | 9.183 |
| | 0.188 | 0.116 | 0.004 | 0.006 | 0.123 | 0.147 | 0.169 | 0.099 | 0.217 | 0.132 | 0.159 | 0.254 |
| NGC7768 | −2.494 | −0.401 | 0.104 | 0.139 | 1.280 | 5.745 | −6.430 | −1.862 | 5.170 | 1.877 | 3.577 | 8.538 |

Continued on Next Page...

Table C.1 – Continued

| Object Name | $H\delta_A$ Å | $H\delta_F$ Å | $CN_1$ mag | $CN_2$ mag | Ca4227 Å | G4300 Å | $H\gamma_A$ Å | $H\gamma_F$ Å | Fe4383 Å | Ca4455 Å | Fe4531 Å | $C_2$4668 Å |
|---|---|---|---|---|---|---|---|---|---|---|---|---|
| | 0.140 | 0.092 | 0.003 | 0.004 | 0.063 | 0.109 | 0.134 | 0.085 | 0.177 | 0.117 | 0.132 | 0.203 |
| PGC004072 | −3.710 | −0.028 | 0.144 | 0.187 | 1.472 | 6.192 | −6.530 | −1.943 | 5.249 | 1.869 | 3.688 | 8.807 |
| | 0.512 | 0.336 | 0.011 | 0.013 | 0.194 | 0.284 | 0.404 | 0.220 | 0.425 | 0.187 | 0.253 | 0.379 |
| PGC025714 | −3.787 | −0.064 | 0.147 | 0.184 | 1.259 | 5.775 | −7.904 | −1.808 | 7.167 | 2.182 | 3.461 | 8.044 |
| | 0.456 | 0.318 | 0.010 | 0.012 | 0.167 | 0.222 | 0.394 | 0.193 | 0.353 | 0.169 | 0.188 | 0.256 |
| PGC026269 | 0.137 | 1.107 | 0.020 | 0.042 | 0.496 | 2.461 | −4.088 | −1.139 | 4.843 | 1.421 | 3.021 | 4.551 |
| | 1.379 | 0.815 | 0.026 | 0.030 | 0.408 | 0.522 | 0.715 | 0.460 | 0.903 | 0.374 | 0.428 | 0.390 |
| PGC030223 | −3.723 | 0.174 | 0.096 | 0.133 | 1.390 | 5.895 | −4.497 | −2.569 | 1.932 | 1.810 | 3.547 | 8.459 |
| | 1.834 | 0.437 | 0.072 | 0.072 | 0.914 | 0.987 | 1.456 | 0.969 | 1.196 | 0.488 | 0.583 | 0.675 |
| PGC044257 | −2.695 | 0.108 | 0.088 | 0.118 | 1.191 | 5.863 | −6.006 | −2.052 | 3.741 | 1.192 | 2.847 | 7.526 |
| | 1.262 | 0.800 | 0.026 | 0.030 | 0.393 | 0.570 | 0.747 | 0.476 | 0.914 | 0.419 | 0.503 | 0.460 |
| PGC071807 | −4.517 | −0.076 | 0.199 | 0.232 | 1.774 | 5.319 | −4.672 | −1.142 | 5.619 | 2.758 | 3.549 | 8.614 |
| | 0.935 | 0.675 | 0.020 | 0.023 | 0.403 | 0.699 | 0.409 | 0.273 | 0.663 | 0.420 | 0.271 | 0.458 |
| PGC072804 | −4.175 | −0.253 | 0.158 | 0.196 | 1.253 | 5.470 | −6.425 | −1.869 | 5.263 | 1.905 | 3.875 | 10.052 |
| | 0.799 | 0.508 | 0.016 | 0.018 | 0.240 | 0.334 | 0.422 | 0.267 | 0.552 | 0.255 | 0.287 | 0.322 |
| UGC00579 | −2.932 | −0.052 | 0.144 | 0.187 | 1.125 | 5.642 | −6.154 | −1.969 | 4.419 | 1.754 | 3.673 | 8.030 |
| | 0.420 | 0.290 | 0.011 | 0.013 | 0.214 | 0.338 | 0.376 | 0.359 | 0.334 | 0.169 | 0.238 | 0.343 |
| UGC02232 | −3.909 | −0.053 | 0.155 | 0.196 | 1.450 | 5.962 | −6.746 | −2.059 | 5.765 | 2.018 | 3.920 | 8.976 |
| | 0.188 | 0.126 | 0.004 | 0.005 | 0.089 | 0.125 | 0.152 | 0.096 | 0.211 | 0.104 | 0.157 | 0.250 |
| UGC05515 | −2.411 | 0.213 | 0.112 | 0.166 | 1.305 | 5.535 | −5.281 | −1.773 | 2.507 | 1.807 | 3.789 | 8.437 |
| | 0.723 | 0.472 | 0.016 | 0.018 | 0.255 | 0.400 | 0.496 | 0.308 | 0.676 | 0.349 | 0.348 | 0.473 |
| UGC10143 | −2.304 | −0.404 | 0.096 | 0.141 | 1.293 | 6.218 | −6.729 | −1.673 | 5.611 | 2.273 | 3.737 | 8.438 |
| | 0.307 | 0.198 | 0.007 | 0.009 | 0.129 | 0.214 | 0.287 | 0.174 | 0.317 | 0.160 | 0.233 | 0.349 |

Table C.1: Index measurements: $H\delta_A$ to $C_2$4668.

| Object | Hβ | Fe5015 | Mg₁ | Mg₂ | Mgᵦ | Fe5270 | Fe5335 | Fe5406 | Fe5709 | Fe5782 | NaD | TiO₁ | TiO₂ |
|--------|-----|--------|------|------|------|--------|--------|--------|--------|--------|------|------|------|
| Name | Å | Å | mag | mag | Å | Å | Å | Å | Å | Å | Å | mag | mag |
| ESO146-028 | 1.707 | 5.570 | 0.178 | 0.336 | 5.004 | 2.923 | 1.035 | 1.832 | 0.740 | 0.944 | 5.130 | 0.009 | — |
|  | 0.075 | 0.220 | 0.001 | 0.002 | 0.099 | 0.075 | 0.083 | 0.077 | 0.034 | 0.038 | 0.039 | 0.001 | — |
| ESO202-043 | 1.849 | 5.325 | 0.177 | 0.346 | 5.285 | 3.061 | 2.983 | 2.684 | 0.745 | 1.011 | 5.062 | −0.011 | — |
|  | 0.109 | 0.227 | 0.002 | 0.002 | 0.116 | 0.106 | 0.155 | 0.099 | 0.046 | 0.047 | 0.047 | 0.002 | — |
| ESO303-005 | 1.655 | 5.942 | 0.178 | 0.309 | 5.026 | 2.890 | 2.914 | 2.034 | 0.942 | 1.030 | 5.857 | 0.057 | — |
|  | 0.097 | 0.234 | 0.002 | 0.003 | 0.122 | 0.158 | 0.162 | 0.134 | 0.073 | 0.074 | 0.088 | 0.002 | — |
| ESO346-003 | 1.691 | 5.514 | 0.160 | 0.327 | 4.626 | 3.345 | 2.899 | 0.293 | 0.711 | 0.973 | 5.254 | 0.022 | — |
|  | 0.109 | 0.229 | 0.002 | 0.002 | 0.104 | 0.101 | 0.124 | 0.085 | 0.055 | 0.047 | 0.050 | 0.001 | — |
| ESO349-010 | 1.625 | 5.890 | 0.163 | 0.290 | 4.379 | 2.908 | 2.799 | 1.948 | 0.927 | 0.842 | 6.010 | 0.054 | — |
|  | 0.092 | 0.196 | 0.002 | 0.002 | 0.171 | 0.156 | 0.193 | 0.128 | 0.066 | 0.071 | 0.077 | 0.002 | — |
| ESO444-046 | 1.397 | 4.891 | 0.175 | 0.313 | 5.134 | 2.171 | 2.184 | 1.809 | 0.990 | 0.785 | 4.892 | 0.034 | — |
|  | 0.165 | 0.355 | 0.004 | 0.004 | 0.192 | 0.206 | 0.232 | 0.132 | 0.080 | 0.077 | 0.085 | 0.002 | — |
| ESO488-027 | 1.661 | 5.337 | 0.198 | 0.358 | 4.835 | 2.812 | 3.545 | 1.876 | 0.896 | 0.922 | 4.804 | 0.000 | — |
|  | 0.056 | 0.152 | 0.001 | 0.001 | 0.093 | 0.079 | 0.173 | 0.087 | 0.041 | 0.046 | 0.051 | 0.001 | — |
| ESO541-013 | 1.731 | 4.643 | 0.156 | 0.274 | 5.110 | 2.756 | 2.538 | 1.956 | 0.978 | 0.688 | 5.019 | −0.361 | — |
|  | 0.111 | 0.254 | 0.002 | 0.003 | 0.166 | 0.158 | 0.190 | 0.107 | 0.067 | 0.068 | 0.088 | 0.005 | — |
| ESO552-020 | 1.409 | 5.240 | 0.153 | 0.317 | 5.092 | 2.764 | 2.273 | 2.144 | 1.227 | 0.811 | 4.795 | 0.011 | — |
|  | 0.081 | 0.179 | 0.002 | 0.002 | 0.096 | 0.095 | 0.116 | 0.111 | 0.057 | 0.059 | 0.070 | 0.002 | — |
| GSC555700266 | 1.716 | 4.475 | 0.112 | 0.264 | 4.976 | 2.615 | 3.259 | 1.660 | 0.911 | 0.720 | 5.533 | −0.793 | — |
|  | 0.074 | 0.172 | 0.001 | 0.002 | 0.102 | 0.073 | 0.128 | 0.074 | 0.033 | 0.034 | 0.043 | 0.007 | — |
| IC1101 | 1.814 | 5.367 | 0.106 | 0.253 | 4.384 | 3.190 | 2.994 | 1.881 | 0.575 | 0.675 | 1.818 | — | — |
|  | 0.098 | 0.232 | 0.002 | 0.003 | 0.127 | 0.159 | 0.173 | 0.114 | 0.073 | 0.070 | 0.196 | — | — |
| IC1633 | 1.477 | 5.500 | 0.174 | 0.360 | 5.461 | 3.112 | 2.904 | 2.056 | 0.756 | 0.711 | 6.303 | 0.054 | — |
|  | 0.109 | 0.234 | 0.002 | 0.002 | 0.140 | 0.103 | 0.240 | 0.182 | 0.055 | 0.047 | 0.073 | 0.001 | — |
| IC4765 | 1.290 | 5.561 | 0.167 | 0.346 | 5.078 | 3.441 | 3.065 | 1.950 | 0.942 | 0.403 | 5.957 | 0.107 | — |
|  | 0.094 | 0.240 | 0.002 | 0.002 | 0.148 | 0.162 | 0.207 | 0.129 | 0.065 | 0.078 | 0.089 | 0.002 | — |
| IC5358 | 1.562 | 5.084 | 0.176 | 0.345 | 5.014 | 3.003 | 2.703 | 2.520 | 0.672 | 0.838 | 5.638 | 0.017 | — |

Continued on Next Page...

Table C.2 – Continued

| Object | Hβ | Fe5015 | Mg₁ | Mg₂ | Mgb | Fe5270 | Fe5335 | Fe5406 | Fe5709 | Fe5782 | NaD | TiO₁ | TiO₂ |
|---|---|---|---|---|---|---|---|---|---|---|---|---|---|
| Name | Å | Å | mag | mag | Å | Å | Å | Å | Å | Å | Å | mag | mag |
| | 0.165 | 0.342 | 0.004 | 0.004 | 0.157 | 0.203 | 0.234 | 0.147 | 0.078 | 0.073 | 0.074 | 0.002 | — |
| LEDA094683 | 1.852 | 5.751 | 0.105 | 0.280 | 4.898 | 3.250 | 3.233 | 1.920 | 0.689 | 0.928 | 0.516 | — | — |
| | 0.059 | 0.215 | 0.001 | 0.001 | 0.162 | 0.077 | 0.132 | 0.084 | 0.042 | 0.061 | 0.202 | — | — |
| MCG-02-12-039 | 1.417 | 5.628 | 0.185 | 0.348 | 5.395 | 2.789 | 2.454 | 1.983 | 1.238 | 0.935 | 5.363 | −0.004 | — |
| | 0.083 | 0.193 | 0.002 | 0.002 | 0.110 | 0.097 | 0.122 | 0.115 | 0.057 | 0.060 | 0.073 | 0.002 | — |
| NGC0533 | 1.057 | 4.569 | 0.166 | 0.334 | 5.037 | 3.131 | 2.409 | 1.805 | 0.879 | 1.036 | 5.740 | 0.100 | — |
| | 0.201 | 0.405 | 0.004 | 0.005 | 0.182 | 0.231 | 0.269 | 0.155 | 0.098 | 0.090 | 0.101 | 0.002 | — |
| NGC0541 | 1.729 | 4.869 | 0.162 | 0.324 | 4.762 | 3.152 | 2.688 | 1.861 | 0.835 | 1.149 | 5.575 | 0.099 | — |
| | 0.169 | 0.313 | 0.002 | 0.003 | 0.131 | 0.130 | 0.148 | 0.099 | 0.040 | 0.042 | 0.042 | 0.002 | — |
| NGC1399 | 1.456 | 6.313 | 0.178 | 0.349 | 5.576 | 3.023 | 3.114 | 1.921 | 0.765 | 0.892 | 6.459 | 0.084 | — |
| | 0.103 | 0.277 | 0.002 | 0.002 | 0.246 | 0.122 | 0.142 | 0.094 | 0.044 | 0.064 | 0.113 | 0.002 | — |
| NGC1713 | 1.381 | 5.112 | 0.153 | 0.327 | 5.015 | 2.927 | 2.777 | 1.775 | 1.059 | 0.426 | 5.431 | 0.098 | — |
| | 0.226 | 0.446 | 0.004 | 0.005 | 0.228 | 0.211 | 0.255 | 0.172 | 0.101 | 0.087 | 0.101 | 0.007 | — |
| NGC2832 | 1.442 | 5.514 | 0.166 | 0.349 | 5.458 | 3.225 | 3.308 | 1.931 | 0.838 | 0.929 | 6.492 | 0.060 | — |
| | 0.028 | 0.120 | 0.001 | 0.001 | 0.191 | 0.097 | 0.234 | 0.143 | 0.032 | 0.058 | 0.105 | 0.001 | — |
| NGC3311 | 1.581 | 5.030 | 0.166 | 0.322 | 4.608 | 2.773 | 2.473 | 1.532 | 0.876 | 0.851 | 5.463 | 0.114 | — |
| | 0.111 | 0.228 | 0.002 | 0.002 | 0.091 | 0.088 | 0.099 | 0.072 | 0.050 | 0.068 | 0.051 | 0.001 | — |
| NGC3842 | 1.367 | 2.876 | 0.199 | 0.397 | 5.253 | 2.722 | 2.617 | −0.556 | −0.773 | 0.035 | 4.545 | −0.013 | 0.141 |
| | 0.051 | 0.158 | 0.003 | 0.003 | 0.228 | 0.165 | 0.211 | 0.052 | 0.033 | 0.031 | 0.141 | 0.001 | 0.001 |
| NGC4839 | 1.371 | 4.916 | 0.140 | 0.311 | 4.814 | 2.992 | 2.666 | 1.810 | 0.732 | 0.702 | 5.214 | 0.044 | — |
| | 0.045 | 0.134 | 0.001 | 0.001 | 0.081 | 0.067 | 0.144 | 0.096 | 0.035 | 0.036 | 0.044 | 0.001 | — |
| NGC4874 | 1.630 | 2.667 | 0.195 | 0.392 | 5.273 | 2.916 | 2.862 | 2.073 | 0.833 | 0.807 | 4.970 | 0.021 | 0.151 |
| | 0.082 | 0.206 | 0.003 | 0.004 | 0.183 | 0.190 | 0.236 | 0.128 | 0.060 | 0.062 | 0.084 | 0.002 | 0.001 |
| NGC4889 | 1.431 | 2.968 | 0.200 | 0.395 | 5.832 | 3.244 | 3.445 | 2.036 | 0.835 | 0.959 | 6.303 | 0.022 | 0.136 |
| | 0.044 | 0.113 | 0.002 | 0.003 | 0.170 | 0.128 | 0.203 | 0.083 | 0.037 | 0.054 | 0.119 | 0.001 | 0.001 |
| NGC4946 | 1.539 | 5.878 | 0.146 | 0.313 | 4.725 | 3.176 | 2.775 | 2.110 | 0.988 | 0.937 | 5.516 | 0.099 | — |

Continued on Next Page...

Table C.2 – Continued

| Object | Hβ | Fe5015 | Mg₁ | Mg₂ | Mgb | Fe5270 | Fe5335 | Fe5406 | Fe5709 | Fe5782 | NaD | TiO₁ | TiO₂ |
|---|---|---|---|---|---|---|---|---|---|---|---|---|---|
| Name | Å | Å | mag | mag | Å | Å | Å | Å | Å | Å | Å | mag | mag |
| | 0.108 | 0.202 | 0.002 | 0.002 | 0.094 | 0.087 | 0.106 | 0.069 | 0.042 | 0.039 | 0.044 | 0.003 | — |
| NGC6034 | 1.498 | 5.406 | 0.240 | 0.418 | 4.802 | 3.177 | 3.487 | 1.795 | 0.728 | 0.570 | 5.952 | 0.008 | −0.223 |
| | 0.074 | 0.249 | 0.003 | 0.004 | 0.255 | 0.186 | 0.255 | 0.110 | 0.065 | 0.077 | 0.186 | 0.001 | 0.005 |
| NGC6047 | 1.485 | 3.298 | — | — | — | — | — | 1.520 | 1.248 | 0.856 | 5.396 | 0.010 | 0.056 |
| | 0.148 | 0.364 | — | — | — | — | — | 0.152 | 0.103 | 0.096 | 0.120 | 0.003 | 0.004 |
| NGC6086 | 1.381 | 5.338 | 0.166 | 0.336 | 5.171 | 3.143 | 2.775 | 0.870 | 1.302 | 0.859 | 5.687 | 0.009 | — |
| | 0.080 | 0.192 | 0.002 | 0.002 | 0.113 | 0.119 | 0.195 | 0.106 | 0.062 | 0.056 | 0.071 | 0.002 | — |
| NGC6160 | 1.355 | 5.326 | 0.143 | 0.300 | 4.824 | 3.053 | 2.863 | 1.652 | 0.866 | 0.919 | 4.965 | 0.006 | — |
| | 0.021 | 0.136 | 0.000 | 0.000 | 0.065 | 0.049 | 0.085 | 0.049 | 0.016 | 0.023 | 0.026 | 0.000 | — |
| NGC6166 | 1.547 | 1.067 | 0.221 | 0.389 | 5.469 | 2.271 | 3.223 | 1.803 | 0.767 | 0.364 | 5.420 | 0.009 | 0.037 |
| | 0.112 | 0.274 | 0.004 | 0.005 | 0.233 | 0.245 | 0.372 | 0.148 | 0.077 | 0.075 | 0.110 | 0.002 | 0.004 |
| NGC6173 | 1.635 | 5.442 | 0.135 | 0.285 | 4.680 | 2.877 | 2.587 | 1.491 | 0.819 | 0.809 | 4.976 | 0.017 | — |
| | 0.067 | 0.141 | 0.001 | 0.003 | 0.073 | 0.083 | 0.125 | 0.084 | 0.047 | 0.038 | 0.059 | 0.001 | — |
| NGC6269 | 1.420 | 4.698 | 0.159 | 0.318 | 5.120 | 2.865 | 3.372 | 0.184 | 0.662 | 0.789 | 4.965 | −0.002 | — |
| | 0.053 | 0.130 | 0.001 | 0.001 | 0.098 | 0.066 | 0.126 | 0.136 | 0.054 | 0.036 | 0.047 | 0.001 | — |
| NGC7012 | 1.750 | 5.240 | 0.188 | 0.356 | 5.120 | 3.407 | 2.812 | 1.055 | 0.714 | 0.841 | 5.974 | 0.022 | — |
| | 0.121 | 0.242 | 0.002 | 0.003 | 0.114 | 0.113 | 0.132 | 0.083 | 0.054 | 0.055 | 0.056 | 0.001 | — |
| NGC7597 | 1.744 | 5.623 | 0.143 | 0.326 | 4.919 | 2.702 | 3.162 | 2.717 | 0.338 | 0.968 | 5.145 | 0.003 | — |
| | 0.078 | 0.193 | 0.001 | 0.001 | 0.084 | 0.064 | 0.106 | 0.088 | 0.018 | 0.026 | 0.037 | 0.000 | — |
| NGC7647 | 1.654 | 7.712 | 0.250 | 0.440 | 5.865 | 3.649 | 2.284 | 2.109 | 0.963 | 0.934 | 6.180 | 0.009 | −0.270 |
| | 0.106 | 0.298 | 0.005 | 0.006 | 0.251 | 0.269 | 0.354 | 0.145 | 0.081 | 0.081 | 0.107 | 0.002 | 0.002 |
| NGC7649 | 1.863 | 5.255 | 0.156 | 0.298 | 4.755 | 2.635 | 4.634 | 2.116 | 0.872 | 0.893 | 5.329 | 0.017 | — |
| | 0.050 | 0.145 | 0.001 | 0.001 | 0.085 | 0.063 | 0.185 | 0.083 | 0.023 | 0.028 | 0.028 | 0.001 | — |
| NGC7720 | 1.541 | 1.113 | 0.240 | 0.393 | 5.348 | 2.864 | 3.080 | −0.199 | 0.105 | −0.755 | −2.887 | −0.011 | 0.034 |
| | 0.094 | 0.222 | 0.004 | 0.004 | 0.320 | 0.220 | 0.262 | 0.096 | 0.075 | 0.102 | 0.196 | 0.002 | 0.004 |
| NGC7768 | 1.326 | 2.728 | 0.203 | 0.395 | 5.245 | 3.040 | 3.040 | 1.773 | 0.623 | 0.958 | 5.116 | 0.022 | 0.172 |

Continued on Next Page...

Table C.2 – Continued

| Object Name | Hβ Å | Fe5015 Å | Mg1 mag | Mg2 mag | Mgb Å | Fe5270 Å | Fe5335 Å | Fe5406 Å | Fe5709 Å | Fe5782 Å | NaD Å | TiO1 mag | TiO2 mag |
|---|---|---|---|---|---|---|---|---|---|---|---|---|---|
| | 0.076 | 0.192 | 0.003 | 0.004 | 0.169 | 0.186 | 0.280 | 0.119 | 0.056 | 0.081 | 0.082 | 0.001 | 0.001 |
| PGC004072 | 1.605 | 6.272 | 0.168 | 0.297 | 5.206 | 2.671 | 3.044 | 2.005 | 0.791 | 0.911 | 5.997 | −0.123 | — |
| | 0.127 | 0.279 | 0.003 | 0.003 | 0.140 | 0.131 | 0.172 | 0.135 | 0.073 | 0.072 | 0.087 | 0.004 | — |
| PGC025714 | 1.623 | 5.634 | 0.153 | 0.276 | 4.614 | 1.084 | 2.402 | 1.879 | 0.923 | 0.672 | 5.554 | −0.234 | — |
| | 0.096 | 0.208 | 0.002 | 0.002 | 0.105 | 0.096 | 0.128 | 0.100 | 0.048 | 0.045 | 0.049 | 0.004 | — |
| PGC026269 | 1.278 | 3.507 | 0.127 | 0.195 | 4.122 | 1.844 | 1.685 | 1.409 | 1.006 | 0.799 | 4.251 | −0.196 | — |
| | 0.139 | 0.250 | 0.002 | 0.002 | 0.103 | 0.091 | 0.103 | 0.093 | 0.029 | 0.033 | 0.046 | 0.003 | — |
| PGC030223 | 1.761 | 6.275 | 0.164 | 0.281 | 4.753 | 6.406 | 3.636 | 2.213 | 1.083 | 1.023 | 4.708 | −0.190 | — |
| | 0.224 | 0.364 | 0.004 | 0.004 | 0.186 | 0.188 | 0.216 | 0.152 | 0.086 | 0.084 | 0.094 | 0.004 | — |
| PGC044257 | 1.631 | 3.339 | 0.152 | 0.285 | 4.861 | 2.949 | 3.531 | 1.806 | 0.636 | 0.931 | 4.560 | 0.041 | — |
| | 0.164 | 0.297 | 0.003 | 0.003 | 0.131 | 0.124 | 0.177 | 0.127 | 0.041 | 0.047 | 0.049 | 0.001 | — |
| PGC071807 | 1.718 | 6.109 | 0.143 | 0.298 | 5.169 | 2.997 | 2.759 | 1.583 | 0.735 | 1.058 | 5.869 | −0.820 | — |
| | 0.137 | 0.273 | 0.002 | 0.002 | 0.156 | 0.126 | 0.205 | 0.128 | 0.052 | 0.046 | 0.062 | 0.001 | — |
| PGC072804 | 1.753 | 6.129 | 0.107 | 0.279 | 4.997 | 3.144 | 2.992 | 1.751 | 0.872 | 0.827 | 4.240 | — | — |
| | 0.085 | 0.198 | 0.001 | 0.001 | 0.098 | 0.071 | 0.121 | 0.078 | 0.021 | 0.034 | 0.156 | — | — |
| UGC00579 | 1.617 | 4.574 | 0.188 | 0.352 | 5.514 | 2.664 | 2.595 | 1.760 | 0.772 | 0.821 | 5.612 | 0.021 | — |
| | 0.146 | 0.316 | 0.003 | 0.004 | 0.154 | 0.184 | 0.220 | 0.151 | 0.103 | 0.099 | 0.131 | 0.003 | — |
| UGC02232 | 1.527 | 5.818 | 0.176 | 0.326 | 5.297 | 2.863 | 2.141 | 1.948 | 0.840 | 0.920 | 5.641 | 0.053 | — |
| | 0.068 | 0.177 | 0.001 | 0.002 | 0.106 | 0.085 | 0.106 | 0.136 | 0.050 | 0.050 | 0.062 | 0.001 | — |
| UGC05515 | 1.687 | 5.453 | 0.176 | 0.318 | 5.142 | 3.002 | 2.302 | 1.815 | 0.567 | 0.774 | 5.390 | 0.027 | — |
| | 0.174 | 0.369 | 0.004 | 0.004 | 0.236 | 0.187 | 0.289 | 0.221 | 0.111 | 0.102 | 0.137 | 0.003 | — |
| UGC10143 | 1.430 | 5.144 | 0.219 | 0.408 | 5.019 | 3.433 | 3.337 | 2.409 | 0.901 | 0.821 | 5.076 | 0.005 | −0.240 |
| | 0.148 | 0.362 | 0.007 | 0.008 | 0.315 | 0.343 | 0.409 | 0.142 | 0.099 | 0.094 | 0.123 | 0.003 | 0.005 |

Table C.2: Index measurements: Hβ to TiO2

# Appendix D

# PUBLICATIONS APPENDED

The following publications are appended to this thesis:

Loubser S.I., Sansom A.E., Sánchez-Blázquez P., Soechting I.K. & Bromage G. *Radial kinematics of brightest cluster galaxies.* 2008, MNRAS, 391, 1009 – 1028.

Loubser S.I., Sánchez-Blázquez P., Sansom A.E. & Soechting I.K. *Stellar populations is the centres of brightest cluster galaxies.* 2009, MNRAS, 398, 133 – 156.

Note that the first publication only contains data for 41 BCGs, whereas the second publication includes the data from the last Gemini observing semester (2007B), and therefore contains data for all 49 BCGs. The kinematics data for the eight BCGs observed in Gemini semester 2007B are included in Chapter 3.

# Radial kinematics of brightest cluster galaxies

S. I. Loubser,[1]⋆ A. E. Sansom,[1] P. Sánchez-Blázquez,[1] I. K. Soechting[2] and G. E. Bromage[1]

[1]*Centre for Astrophysics, University of Central Lancashire, Preston PR1 2HE*
[2]*Oxford Astrophysics, Department of Physics, University of Oxford, Oxford OX1 3RH*

## ABSTRACT

This is the first of a series of papers devoted to the investigation of a large sample of brightest cluster galaxies (BCGs), their kinematic and stellar population properties, and the relationships between those and the properties of the cluster. We have obtained high signal-to-noise ratio, long-slit spectra of these galaxies with Gemini and William Herschel Telescope with the primary purpose of investigating their stellar population properties. This paper describes the selection methods and criteria used to compile a new sample of galaxies, concentrating on BCGs previously classified as containing a halo (cD galaxies), together with the observations and data reduction. Here, we present the full sample of galaxies, and the measurement and interpretation of the radial velocity and velocity dispersion profiles of 41 BCGs. We find clear rotation curves for a number of these giant galaxies. In particular, we find rapid rotation ($>100\,\mathrm{km\,s^{-1}}$) for two BCGs, NGC 6034 and 7768, indicating that it is unlikely that they formed through dissipationless mergers. Velocity substructure in the form of kinematically decoupled cores is detected in 12 galaxies, and we find five galaxies with velocity dispersion increasing with radius. The amount of rotation, the velocity substructure and the position of BCGs on the anisotropy–luminosity diagram are very similar to those of 'ordinary' giant ellipticals in high-density environments.

**Key words:** galaxies: elliptical and lenticular, cD – galaxies: kinematics and dynamics.

## 1 INTRODUCTION

The galaxies in the centres of clusters are unique. They are usually the dominant, brightest and most massive galaxies in their clusters. A wealth of imaging data has been accumulated for these intriguing objects (Malumuth & Kirshner 1985; Schombert 1986, 1987, 1988; Postman & Lauer 1995; Collins & Mann 1998; Brough et al. 2002; Laine et al. 2003); however the spectroscopic data are limited to very small samples or narrow wavelength coverage.

Tonry (1984), Tonry (1985), Gorgas, Efstathiou & Aragon-Salamanca (1990), Fisher, Illingworth & Franx (1995a), Fisher, Franx & Illingworth (1995b), Cardiel, Gorgas & Aragon-Salamanca (1998) and Carter, Bridges & Hau (1999) each investigated 18 or less galaxies, and, moreover, measured only three or less indices. Brough et al. (2007) used a wide wavelength range but included only three brightest cluster galaxies (BCGs). Von der Linden et al. (2007) studied BCGs from the Sloan Digital Sky Survey, however the spatial information is lacking since fibres were used.

Among BCGs, there exists a special class of galaxies catalogued as cD galaxies, although there exists a great deal of confusion over

the exact meaning of the classifications gE, D and cD. Matthews, Morgan & Schmidt (1964) outlined the following definition: 'D galaxies have an elliptical-like nucleus surrounded by an extensive envelope. The supergiant D galaxies observed near the centre of a number of Abell's rich clusters have diameters three to four times as great as the ordinary lenticulars in the same clusters. These very large D galaxies observed in clusters are given the prefix 'c', in a manner similar to the notation for supergiant stars in stellar spectroscopy'. Later, Schombert (1987) defined gE galaxies as distinct from other early-type galaxies by their large size; D galaxies as being gE galaxies with a shallow surface brightness profile slope and cD galaxies as D galaxies with large extended stellar haloes. The last are also more diffuse than normal ellipticals (Schombert 1986). Because of the confusion surrounding the definition of D galaxies, and the fact that they are rarely regarded as a separate type of object in the modern literature, this study will only refer to cD and non-cD BCGs (i.e. BCGs containing a halo or not). For BCGs, we adopt the definition to comply with recent literature (e.g. Von der Linden et al. 2007), where BCG refers to the central, dominant galaxy in a cluster. For a small fraction of clusters, the BCG might not strictly be the brightest galaxy in the cluster.

Approximately 20 per cent of the rich clusters of galaxies contain a dominant central cD galaxy (Dressler 1984; Oegerle & Hill 2001),

---

although they can be found in poor clusters as well (Giacintucci et al. 2007). Some clusters have more than one cD galaxy, but a cD galaxy is always the dominant member of a local subcluster. The surface–brightness profiles of cD galaxies are displaced above the de Vaucouleurs law (de Vaucouleurs 1948) at large radii. The break in the cD galaxy surface-brightness profile typically occurs between 24 and 26 mag arcsec$^{-2}$ in the $V$ band (Sarazin 1988). The interpretation of this deviation is that the galaxy is embedded in an extensive luminous stellar halo. Three main theories have been proposed over the last four decades to explain the properties of BCGs, and in particular cD galaxies.

*Theory 1.* In the first theory, BCG formation is caused by the presence of *cooling flows* in clusters of galaxies (Cowie & Binney 1977). Cooling flow clusters are common in the local Universe, and BCGs are most often found at the centres of these systems (Edwards et al. 2007). If the central cluster density is high enough, intracluster gas can condense and form stars at the bottom of the potential well. Observations that support this idea are blue- and ultraviolet-colour excesses observed in the central galaxy of Abell 1795 (indicative of star formation) by McNamara et al. (1996) and molecular gas detected in 10 out of 32 central cluster galaxies by Salomé & Combes (2003). Cardiel et al. (1998) obtained radial gradients for the $D_{4000}$ and $Mg_2$ spectral features in 11 central cluster galaxies. Their observations were consistent with an evolutionary sequence in which radio-triggered star formation bursts take place several times during the lifetime of the cooling flow in the centre of the cluster. However, McNamara & O'Connell (1992) find only small colour anomalies with small amplitudes, implying star formation rates that account for at most a few per cent of the material that is cooling and accreting on to the central galaxy.

More recently, *XMM–Newton* observations showed that the X-ray gas in cluster centres does not cool significantly below a threshold temperature of $kT \sim 1-2$ keV (Jordán 2004, and references therein). The central cluster galaxies often host radio-loud active galactic nuclei (AGN), which may account for the necessary heating to counteract radiative cooling (Von der Linden et al. 2007). Although BCGs are probably not completely formed in the cooling flows, the flows play an important role in regulating the rate at which gas cools at the centres of groups and clusters.

*Theory 2.* The second theory was proposed by Merritt (1983) and suggests that the essential properties of BCGs, and in particular those with haloes, are determined when the clusters collapse (*primordial origin*). Thereafter, frequent mergers of galaxies would be inhibited by the relatively high velocities between galaxies. Merritt (1983) argued that all galaxies had large haloes early in the life of the cluster. These haloes were then removed by the mean cluster tidal field during the initial collapse and returned to the cluster potential, except for the central member which remained unaffected because of its special position with respect to the cluster potential.

*Theory 3.* The third, and most widely accepted, theory is in the context of the $\Lambda$ cold dark matter ($\Lambda$CDM) cosmology and relates the formation of the central galaxy to mergings with or captures of less massive galaxies, and is known as '*galactic cannibalism*'. It was first proposed by Ostriker & Tremaine (1975) and developed by Ostriker & Hausman (1977).

The most complete quantitative prediction of the formation of BCGs in the now standard CDM model of structure formation is by De Lucia & Blaizot (2007). They used $N$-body and semi-analytic

techniques to study the formation and evolution of BCGs and found that, in a model where cooling flows are suppressed at late times by AGN activity, the stars of BCGs are formed very early (50 per cent at $z \sim 5$ and 80 per cent at $z \sim 3$) and in many small galaxies. They also found that BCGs assemble late: half of their final mass is typically locked up in a single galaxy after $z \sim 0.5$ (illustrated in their fig. 9). A very similar conclusion was reached by Romeo et al. (2008), who performed $N$-body and hydrodynamical simulations of the formation and evolution of galaxy groups and clusters in a $\Lambda$CDM cosmology to follow the build up of two clusters and 12 groups. Observationally, Aragon-Salamanca, Baugh & Kauffmann (1998) examined the $K$-band Hubble diagram for BCGs up to a redshift of $z = 1$. They found that the BCGs had grown by a factor of 2 to 4 since $z = 1$. Brough et al. (2002) found a similar result but discovered that the mass growth depended on the X-ray luminosity of the host cluster. They found that BCGs in high X-ray luminosity clusters showed no mass accretion since $z = 1$ as opposed to BCGs in low X-ray luminosity clusters which grew by a factor of 4. However, the recent near-infrared photometric study of 42 BCGs by Whiley et al. (2008) in the $0.2 < z < 1$ range contradicts this. They studied the colour and rest-frame $K$-band luminosity evolution of BCGs and found it to be in good agreement with the population synthesis models of stellar populations which formed at $z \sim 2$ and evolved passively thereafter.

Using the Millennium Simulation, De Lucia et al. (2006) studied how formation histories, ages and metallicities of elliptical galaxies depend on environment and on stellar mass. Their fig. 9 shows the effective number of progenitors of early-type galaxies as a function of galaxy stellar mass. The number of effective progenitors is less than two for galaxies up to stellar masses of $\simeq 10^{11}$ M$_\odot$. This function suddenly increases up to the value of approximately five effective progenitors for the mass of a typical BCG.

A related theory, called *tidal stripping*, was first proposed by Gallagher & Ostriker (1972). Cluster galaxies that pass near the gravitational centre of the cluster may be stripped of some of their material by the tidal forces from the cluster potential or the central galaxy potential. The stripped material falls to the centre of the potential well, and could contribute to the observed haloes of cD galaxies. The most massive galaxies surrounding the central galaxy would be preferentially depleted as they are most strongly affected by dynamical friction (Jordán 2004). The difference between stripping and primordial origin is that stripping (and cD halo formation) begins after the cluster collapse, whereas primordial origin assumes that the tidal events occur before the collapse, and that the cD halo is not a consequence of tidal stripping (Schombert 1988).

The observation of multiple nuclei in central galaxies favours the cannibalism theory (Postman & Lauer 1995). Tonry (1984) observed the velocity and velocity dispersion profiles of NGC 6166 and 7720 and their multiple nuclei. He found that the stellar velocity dispersion of the central galaxy demonstrated that the multiple nuclei are not following circular orbits. This was followed by a bigger sample of 14 multiple nuclei BCGs for which the redshifts and stellar velocity dispersions are presented in Tonry (1985). Yamada et al. (2002) showed that the BCG in a cluster at $z = 1.26$ is composed of two distinct subunits that are likely to fully merge on a time-scale of $10^8$ years. Jordán (2004) studied the globular cluster systems in BCGs with confirmed haloes from *Hubble Space Telescope (HST)* observations. They concluded that the observed globular cluster metallicity distributions are consistent with those expected if BCGs galaxies form through cannibalism of numerous galaxies and protogalactic fragments that formed their stars and globular clusters before capture and disruption, although they state

that the cannibalism scenario is not the only possible mechanism to explain these observations. The Jordán (2004) globular cluster data also suggest that BCGs experienced their mergers prior to cluster virialization, yet the presence of tidal streams suggests otherwise (Seigar, Graham & Jerjen 2007).

Carter & Metcalfe (1980) and West (1989) showed that the major axis (MA) of BCGs tends to be aligned with the MA of the cluster galaxy distribution. Recent studies of the Coma cluster (Torlina, De Propris & West 2007) show strong evidence that there are no other large-scale galaxy alignments other than for the BCGs. This also confirms that BCGs form via mechanism related to collimated infall of galaxies along the filaments and the growth of the cluster from the surrounding large-scale structure (Boylan-Kolchin, Ma & Quataert 2006).

In the CDM cosmology, it is now understood that the local massive cluster galaxies assemble late through the merging of smaller systems. In this picture, cooling flows are the main fuel for galaxy mass growth at high redshift. This source is removed only at low redshifts in group or cluster environments, due to AGN feedback (De Lucia & Blaizot 2007).

Some of the outstanding issues are: whether BCGs have a different formation mechanism than elliptical galaxies and if the formation of BCGs is controlled by environment. To address these issues the present project was initiated, and long-slit spectra of a large and statistically significant sample of BCGs were obtained. These data provide a set of spectral indices, covering a wide wavelength range. The luminous central galaxies will be contrasted with other early-type galaxies to look for relative differences in their evolution, using features sensitive to stellar population age and abundances of various elements.

The first part of this project entails the determination of the stellar kinematics through derivation of velocity and velocity dispersion profiles. A forthcoming paper will be devoted to the measurement and analysis of the line strengths for this sample of BCGs.

This paper is organized as follows. Section 2 details the sample and the selection criteria, followed by a description of the observations and data reductions in Section 3. The kinematical measurements are described in Section 4, and the individual galaxy kinematic profiles and notes are presented in Section 5. Section 6 discusses the kinematic properties of BCGs as a class, compared to other Hubble types. Conclusions and future work are given in Section 7.

## 2 SAMPLE

The initial intention of this project was to study cD galaxies in particular. However, the confusion regarding the classification of the cD galaxies and the lack of deep photometry, which would allow to conclusively distinguish between BCGs with and without a halo, made the sample selection extremely challenging. Aiming at maximizing the completeness of the cD sample and inclusion of any potential subpopulation, we adopted rather broad selection criteria when restricting an intrinsic BCG sample. We expect to add deep photometric information in future publications, which will allow us to test the presence of a faint halo and discriminate between cD and non-cD BCGs. For the purpose of this publication, we refer to our sample of 63 galaxies as a BCG sample and present kinematics results for 41 observed members. Two ordinary elliptical galaxies were also observed (one E and one E/SO) and their kinematics presented here. They will be used as a control sample in this study, where relevant.

The sample selection combines three methods making the best use of available information from literature and astronomical data bases. The three search methods are described below.

*Method 1.* Two well-known galaxy cluster classification systems that distinguish clusters containing a cD galaxy in the centre from other galaxy clusters are those of Rood & Sastry (1971, hereafter RS) and Bautz & Morgan (1970, hereafter BM). The RS classification is based on the projected distribution of the brightest 10 members, and the BM classification is based on the brightness contrast between first- and second-ranked galaxies (i.e. the slope of the luminosity function at the bright end).

Hoessel, Gunn & Thuan (1980) derived the BM types for all the nearby Abell clusters of galaxies, which made it possible to obtain a list of all nearby Abell clusters with BM types I and I-II (classified to contain a cD galaxy). Struble & Rood (1987) compiled a catalogue of the morphological properties of 2712 Abell clusters, derived from a visual inspection of the KPNO photographic plates. This made it possible to obtain a list of Abell clusters with RS cluster classification type cD. The NASA/IPAC Extragalactic Data base (NED)[1] was used to search for the brightest galaxies close to the centre of each cluster. If the brightest member was classified as either a cD or a D galaxy in NED (in the NED morphology or notes of previous observations), it was included in our list of BCGs. The RS and/or BM classifications are frequently used as a method to identify possible cD galaxies (e.g. Hill & Oegerle 1992; Baier & Wipper 1995; Giacintucci et al. 2007).

*Method 2.* The second search was carried out by performing an all-sky search in the HyperLEDA[2] data base for galaxies with the following properties: T type between $-3.7$ and $-4.3$ [the de Vaucouleurs Third Reference Catalogue (RC3) classifies cD galaxies as T type $= -4$]; apparent $B$ magnitude brighter than 16; distance closer than 340 Mpc and further than 15° from the Galactic plane.[3] It was found that T type alone is not a reliable classification of galaxy types (in both the RC3 and HyperLeda catalogues), as various low-luminosity galaxies are also categorized as galaxies with T type $= -4$. This prompted an absolute magnitude cut-off of $M_B = -20$ to be applied throughout the sample selection. The galaxies obtained with this search were added to our list of BCGs if they were classified as cD galaxies in NED.

*Method 3.* The third search was undertaken by choosing galaxies with published surface brightness profiles that had a slope consistent with cD galaxies, and in the case of cD galaxies broke the de Vaucouleurs $r^{\frac{1}{4}}$ law at large radii. Galaxies were chosen from the series of papers by Schombert (1986, 1987, 1988) and from Malumuth & Kirshner (1985). These are all optical photometric studies of the brightest cluster members of clusters. Galaxies with the surface brightness slopes and profiles conforming to the cD/D criteria set in Schombert (1987) were included in our list since that forms the basis of most definitions of cD galaxies.

The complete list of galaxies and their properties is given in Table 1. The following global criteria were applied to the sample: apparent $B$ magnitude brighter than 16; distance closer than 340 Mpc and the absolute magnitude cut-off at $M_B = -20$. Method 1 delivered 13 galaxies, Method 2 delivered 32 galaxies and Method 3

---

[1] http://nedwww.ipac.caltech.edu/.

[2] http://leda.univ-lyon1.fr/.

[3] An $H_0$ value of 75 km s$^{-1}$ Mpc$^{-1}$ is assumed throughout this work.

**Table 1.** The new sample of BCGs, including the two ordinary ellipticals (marked as ⋆). Columns 2, 3, 6–9 are from the HyperLeda catalogue and 4 and 5 from NED. PA is the position angle of the galaxy MA. Refs 1,2 and 3 correspond to the three search methods for objects (Column 10). Run (Column 11) 1 = WHT, 2 = Gemini − N 2006B, 3 = Gemini − S 2006B, 4 = Gemini − N 2007A, 5 = Gemini S2007Aand 6 = Gemini − S 2007B (the data from Run 6 are not presented in this paper.). Besides the galaxies classified as cD/D in the NED morphology (Column 5), NGC 6034, UGC 05515 and NGC 1129 were classified as cD/D in Schombert (1987); NGC 7012, ESO 146-028, ESO 346-003, ESO 202-043, NGC 3842, PGC 026269 and IC 1634 were classified as cD/D in the NED notes by previous observations.

| Object name | α(J2000) | δ(J2000) | Cluster | NED type | T type | PA (deg) | $m_B$ | $M_B$ | Refs | Run |
|---|---|---|---|---|---|---|---|---|---|---|
| IC 1565 | 0 39 26.3 | 06 44 03 | A0076 | cD;E | −3.9 ± 1.2 | – | 14.41 | −21.96 | 2 | |
| UGC 00579 | 0 56 16.2 | -01 15 22 | A0119 | cD;E | −4.8 ± 0.4 | 41 | 14.40 | −22.34 | 3 | 6 |
| ESO 541-013 | 1 02 41.8 | −21 52 55 | A0133 | cD;E+3 pec | −4.0 ± 0.7 | 16 | 14.71 | −22.54 | 2 | 6 |
| PGC 004072 | 1 08 50.8 | −15 24 31 | A0151 | D | −4.2 ± 1.0 | 83 | 14.75 | −22.37 | 2 | 6 |
| IC 1633 | 1 09 55.6 | −45 55 52 | A2877 | cD;E+1 | −3.9 ± 0.5 | 97 | 12.57 | −22.60 | 2, 3 | 3 |
| IC 1634 | 1 11 02.9 | 17 39 46 | A0154 | MLT SYS | −4.1 ± 1.0 | 153 | 15.27 | −22.64 | 1 | |
| IC 1695 | 1 25 07.6 | 08 41 58 | A0193 | cD;S? | – | 103 | 14.87 | −21.98 | 1 | |
| NGC 0533 | 1 25 31.5 | 01 45 33 | A0189B | cD;E3: | −4.8 ± 0.6 | 50 | 12.45 | −22.25 | 3 | 6 |
| NGC 0541 | 1 25 44.3 | −01 22 46 | A0194 | cD;SO-: | −3.9 ± 0.9 | 69 | 13.09 | −21.62 | 2 | 6 |
| IC 1733 | 1 50 42.9 | 33 04 55 | A0260 | cD;E: | −4.9 ± 0.8 | – | 14.14 | −22.16 | 1 | |
| NGC 0708 | 1 52 46.3 | 36 09 12 | A0262 | cD;E | −4.9 ± 0.4 | 39 | 13.63 | −20.98 | 3 | |
| UGC 02232 | 2 46 03.9 | 36 54 19 | A0376 | cD;E/D | −3.9 ± 1.3 | – | 15.50 | −21.64 | 2 | 2 |
| NGC 1129 | 2 54 27.4 | 41 34 46 | AWM7 | E;BrClG | −4.7 ± 1.2 | 73 | 13.34 | −21.67 | 3 | |
| UGC 02450 | 2 58 57.8 | 13 34 59 | A0401 | cD | 2.8 ± 5.0 | 29 | 15.24 | −23.50 | 1 | |
| NGC 1275 | 3 19 48.2 | 41 30 42 | A0426 | cD;pec;NLRG | −2.2 ± 1.7 | 110 | 12.55 | −22.69 | 3 | |
| NGC 1399 | 3 38 29.0 | −35 26 58 | RBS454 | cD;E1 pec | −4.5 ± 0.5 | – | 10.42 | −20.81 | 3 | 3 |
| ESO 303-005 | 4 13 58.8 | −38 05 50 | RBS512 | cD? | −4.0 ± 0.5 | – | 15.38 | −21.51 | 2 | 3 |
| MCG-02-12-039 | 4 33 37.8 | −13 15 40 | A0496 | cD;E+? | −3.9 ± 0.9 | 180 | 13.95 | −22.50 | 2, 3 | 3 |
| ESO 202-043 | 4 37 47.6 | −51 25 23 | A S0479 | E+ | −3.8 ± 0.8 | 133 | 14.45 | −21.72 | 2 | 6 |
| ESO 552-020 | 4 54 52.3 | −18 06 53 | CID 28 | cD;E+ | −3.9 ± 0.7 | 148 | 13.54 | −22.51 | 2 | 3 |
| NGC 1713 | 4 58 54.6 | 00 29 20 | CID 27 | cD;E+ | −4.3 ± 0.6 | 39 | 13.88 | −20.71 | 2 | 2 |
| UGC 03197 | 4 59 55.8 | 80 10 43 | A0505 | cD | −4.9 ± 0.9 | 85 | 15.25 | −22.26 | 3 | |
| ESO 488-027 | 5 48 38.5 | −25 28 44 | A0548 | cD;E+1 | −3.8 ± 0.6 | 68 | 14.22 | −22.22 | 2 | 3 |
| PGC 025714 | 9 08 32.4 | −09 37 47 | A0754 | D | −4.2 ± 1.4 | 122 | 14.32 | −23.04 | 2 | 6 |
| PGC 026269 | 9 18 05.7 | −12 05 44 | A0780 | (R')SAO-:;BrClGSy3 | −2.6 ± 1.0 | 133 | 14.38 | −22.84 | 1 | 3 |
| NGC 2832 | 9 19 46.9 | 33 44 59 | A0779 | E+2:;cD | −4.3 ± 0.6 | 172 | 12.79 | −22.38 | 2, 3 | 2 |
| UGC 05515 | 10 13 38.3 | 00 55 32 | A0957 | E+pec: | −4.0 ± 0.7 | 83 | 14.49 | −22.28 | 2, 3 | 5 |
| PGC 030223 | 10 20 26.6 | −06 31 35 | A0978 | D | −3.9 ± 1.2 | 1 | 15.40 | −21.85 | 2 | 6 |
| NGC 3311 | 10 36 42.9 | −27 31 37 | A1060 | cD;E+2 | −3.3 ± 1.3 | – | 12.69 | −21.33 | 1 | 5 |
| NGC 3842 | 11 44 02.2 | 19 56 59 | A1367 | E;BrClG | −4.8 ± 0.7 | 177 | 12.80 | −22.18 | 3 | 1 |
| PGC 044257 | 12 57 11.4 | −17 24 36 | A1644 | cD;E+4 | −4.1 ± 1.0 | 44 | 13.50 | −23.54 | 1, 2 | 5 |
| NGC 4839 | 12 57 24.2 | 27 29 54 | A1656 | cD;SAO | −4.0 ± 0.8 | 64 | 13.05 | −22.26 | 2, 3 | 4 |
| NGC 4874 | 12 59 35.5 | 27 57 36 | A1656 | cD;Di | −3.7 ± 0.9 | 45 | 12.75 | −22.50 | 2, 3 | 1 |
| NGC 4884(9) | 13 00 07.9 | 27 58 41 | A1656 | cD;E4;Db | −4.3 ± 0.5 | 82 | 12.48 | −22.56 | 2 | 1 |
| NGC 4946⋆ | 13 05 29.4 | −43 35 28 | A3526 | E+? | −3.8 ± 0.8 | 135 | 13.41 | −20.27 | | 5 |
| ESO 444-046 | 13 27 56.9 | −31 29 44 | A3558 | cD;E+4 | −3.7 ± 1.0 | 161 | 14.07 | −22.86 | 2, 3 | 5 |
| LEDA094683 | 13 53 06.4 | 05 08 59 | A1809 | cD | −2.3 ± 5.0 | 46 | 15.30 | −22.35 | 1 | 5 |
| GSC555700266 | 14 01 36.4 | −11 07 43 | A1837 | cD | – | – | 14.59 | – | 1 | 5 |
| NGC 5539 | 14 17 37.8 | 08 10 46 | A1890 | cD | 0.7 ± 5.0 | 39 | 14.92 | −22.62 | 1 | |
| IC 1101 | 15 10 56.1 | 05 44 41 | A2029 | cD;SO-: | −2.9 ± 1.1 | 25 | 15.10 | −23.05 | 3 | 5 |
| UGC 09799 | 15 16 44.6 | 07 01 16 | A2052 | cD;E | −4.7 ± 1.3 | 30 | 14.34 | −21.84 | 3 | |
| PGC 054913 | 15 23 05.3 | 08 36 33 | A2063 | cD;S | −3.8 ± 1.6 | – | 14.71 | −21.46 | 2 | |
| UGC 09958 | 15 39 39.1 | 21 46 58 | A2107 | cD;SO-: | −2.9 ± 0.7 | 98 | 14.76 | −22.00 | 3 | |
| UGC 10012 | 15 44 59.0 | 36 06 36 | A2124 | cD;E | −4.9 ± 0.6 | 143 | 14.54 | −23.15 | 3 | |
| UGC 10143 | 16 02 17.3 | 15 58 28 | A2147 | cD;E+ | −4.0 ± 0.8 | 12 | 14.27 | −21.97 | 2, 3 | 1 |
| NGC 6034 | 16 03 32.1 | 17 11 55 | A2151 | E+ | −4.0 ± 0.4 | 59 | 14.58 | −21.60 | 2, 3 | 1 |
| NGC 6047⋆ | 16 05 09.1 | 17 43 48 | A2151 | E+ | −3.5 ± 0.8 | 117 | 14.58 | −21.45 | | 1 |
| NGC 6086 | 16 12 35.6 | 29 29 06 | A2162 | cD;E | −4.8 ± 0.6 | 3 | 13.81 | −22.19 | 3 | 4 |
| NGC 6160 | 16 27 41.1 | 40 55 37 | A2197 | cD;E | −4.8 ± 0.6 | 72 | 14.17 | −21.70 | 3 | 4 |
| NGC 6166 | 16 28 38.5 | 39 33 04 | A2199 | cD;E | −4.2 ± 1.4 | 38 | 12.88 | −22.92 | 2, 3 | 1 |
| NGC 6173 | 16 29 44.9 | 40 48 42 | A2197 | cD;E | −4.8 ± 0.6 | 138 | 13.13 | −22.58 | 3 | 4 |
| NGC 6269 | 16 57 58.1 | 27 51 16 | AWM5 | cD;E | −4.7 ± 0.7 | 80 | 13.38 | −22.98 | 3 | 4 |
| IC 4765 | 18 47 18.5 | −63 19 50 | A S0805 | cD;E+4 | −3.9 ± 0.5 | 123 | 12.46 | −21.97 | 2 | 5 |
| NGC 7012 | 21 06 45.8 | −44 48 49 | A S0921 | E+4 pec | −3.9 ± 0.5 | 100 | 13.93 | −21.79 | 2 | 3 |
| ESO 146-028 | 22 28 51.1 | −60 52 55 | RXCJ2228.8-6053 | E+3 | −3.8 ± 0.8 | 154 | 13.94 | −22.54 | 2 | 5 |
| ESO 346-003 | 22 49 22.0 | −37 28 20 | A S1065 | E+2 pec: | −3.8 ± 0.8 | 118 | 14.00 | −21.59 | 2 | 5 |
| NGC 7597 | 23 18 30.3 | 18 41 20 | A2572 | cD;S? | −2.0 ± 0.8 | 133 | 15.00 | −21.52 | 1 | 2 |
| NGC 7647 | 23 23 57.4 | 16 46 38 | A2589 | cD;E | −4.7 ± 0.8 | 174 | 14.61 | −21.93 | 3 | 1 |

**Table 1** – *continued.*

| Object name | α(J2000) | δ(J2000) | Cluster | NED type | T type | PA (deg) | $m_B$ | $M_B$ | Refs | Run |
|---|---|---|---|---|---|---|---|---|---|---|
| NGC 7649 | 23 24 20.1 | 14 38 49 | A2593 | cD;E | −4.6 ± 1.1 | 78 | 15.65 | −20.99 | 3 | 2 |
| PGC 071807 | 23 35 01.5 | 27 22 20 | A2622 | cD | – | 138 | 15.28 | −22.05 | 1 | 4 |
| NGC 7720 | 23 38 29.5 | 27 01 51 | A2634 | cD;E+pec: | −4.3 ± 0.6 | – | 13.43 | −22.63 | 2 | 1 |
| IC 5358 | 23 47 45.0 | −28 08 26 | A4038 | cD;E+4 pec | −3.8 ± 1.1 | 114 | 13.64 | −22.00 | 2 | 3 |
| NGC 7768 | 23 50 58.3 | 27 08 51 | A2666 | cD;E | −4.9 ± 0.5 | 55 | 13.28 | −22.39 | 3 | 1 |
| PGC 072804 | 23 54 13.7 | −10 25 09 | A2670 | cD;XBONG | −4.4 ± 2.4 | 76 | 15.32 | −22.82 | 1 | 5 |
| ESO 349-010 | 23 57 00.7 | −34 45 33 | A4059 | cD;E+4 | −3.7 ± 1.2 | 155 | 14.18 | −22.69 | 2 | 3 |

contributed 29 galaxies (indicated in Table 1). With 11 of the merged list being duplicates presented from more than one method, this provided an all-sky list of the 63 galaxies.

In summary: these 63 galaxies were classified as cD/D in NED (in the morphological classification or in the notes of previous observations) and/or have profiles breaking the $r^{\frac{1}{4}}$ law. With the exception of NGC 4946 and 6047, which are included in the sample as control galaxies but known to be an E and E/S0 galaxy, respectively, all galaxies have thus been previously classified in the literature to contain a halo, albeit very inhomogeneously. Despite the confusion regarding the halo classification, all these galaxies are the dominant central galaxies in clusters or groups. If selection methods 1 and 3 above are assumed to be more robust methods of identifying a BCG with a halo, then 67 per cent of the BCG sample are confirmed cD galaxies. 10 galaxies in the BCG sample are in common with the Fisher et al. (1995a) sample of 13 BCGs. For four Abell clusters, the choice of BCG differs from that by Postman & Lauer (1995). These are: Abell 0194, 0548, 4038 and 2151. In each of the first three cases, the choice of BCG in this sample is more dominant than the BCG in the Postman & Lauer (1995) sample. In the case of Abell 2151, we followed previous authors (e.g. Aragon-Salamanca et al. 1998) who have chosen NGC 6034 to be the BCG as it has a very prominent cD halo (Schombert 1987, 1988) and is close to an X-ray peak.

Some of our clusters are known to have substructure (Rines et al. 2002; Adami et al. 2005) and, in these cases, there may be more than one local X-ray maximum, which can host a dominant galaxy central to that substructure. Hence, according to the definition adopted here, there can be more than one BCG per cluster. In particular, three of the selected BCGs (NGC 4889, 4874 and 4839) are hosted by the Coma cluster, all of them showing pronounced envelopes (Schombert 1987; Andreon et al. 1996). The first two are the dominant galaxies in the cluster (it is not clear which one is the original central galaxy of the main cluster; see e.g. Adami et al. 2005), while NGC 4839 is the dominant galaxy of a group that appears to be infalling into the main cluster (Neumann et al. 2001). Two galaxies (NGC 6173 and 6160) from the cluster Abell 2197 are also included in the sample. These two galaxies are believed to be the dominant galaxies of two main groups in the process of merging (Abell 2197E and Abell 2197W; Schombert 1987).

An internally consistent photometric study of this BCG sample will be done before investigating the properties of the cD galaxies as a separate class. Liu et al. (2008) measured the extended envelopes of a sample of BCGs using Petrosian profiles (Patel et al. 2006). There is a distinct signature of a plateau in the Petrosian profiles of cD galaxies with an extended stellar halo, which is not present for normal elliptical galaxies. However, they find that the devia-

tion of the surface brightness profiles from a single Sérsic profile does not have any sharp transitions. Therefore, it is very difficult to unambiguously separate cD from non-cD BCGs based on surface brightness profiles alone (Liu et al. 2008), and confirming the presence or absence of cD haloes depends on choices of profiles fitted to the surface brightness as a function of radius.

In all the conclusions of this study, it will be clearly stated whether it applies to BCGs or includes the two normal elliptical galaxies. The 43 galaxies discussed further in this first paper are indicated in the last column of Table 1 (numbered 1 to 5 according to observing run), and range from $M_B = -23.54$ to $-20.71$ for the BCGs.

# 3 OBSERVATIONS AND DATA REDUCTION

## 3.1 WHT observations

Spectroscopic observations of 10 of the 43 galaxies presented here (listed in Table 2) were carried out during the period 2006 June 23 to June 26, using the 4.2-m William Herschel Telescope (WHT) equipped with the ISIS double spectrograph mounted at the *f*/11 Cassegrain focus. The Marconi2 CCD was employed on the red arm and the EEV12 on the blue. The spatial scale of both CCDs was 0.4 arcsec pixel$^{-1}$ (with 2 × 2 binning) and the slit width was 1 arcsec. Comparison spectra were provided by Cu/Ar and Cu/Ne arcs and the flat-field illumination by a tungsten lamp.

Two different dichroics were used. The 5300 Å dichroic was used for three nights and delivered an unvignetted spectral range of 3900–5460 Å in the blue arm and 5730–6960 Å in the red arm. The 6100 Å dichroic was used for one night, delivering an unvignetted spectral range of 4500–6120 Å in the blue arm and 7950–9600 Å in the red arm. The exposure times are listed in Table 2. This combination made it possible to observe 29 absorption indices consisting of the original 21 Lick indices from CN to TiO$_2$ (Burstein et al. 1984; Faber et al. 1985; Worthey et al. 1994), the four Hδ and Hγ indices contributed by Worthey & Ottaviani (1997), the near-infrared Ca II triplet at ∼8600 Å and the Mg I index. This collection of 29 indices will be referred to as the Lick indices in this study.

Dispersion in the blue arm was 0.90 Å pixel$^{-1}$ (grating R600B) and 0.88 Å pixel$^{-1}$ (grating R600R) in the red. The spectral resolution ranged between 3.3 and 4.0 Å, depending on the dichroic and arm used. Seeing was typically better than 1 arcsec, and all necessary calibration frames were obtained. In most cases, the slit was placed on the MA of the galaxy. Exceptions occurred if there was another early-type galaxy (unrelated to the sample) in close proximity, in which case the slit was positioned to go through the centres of both galaxies, to allow a control sample of ellipticals with

Table 2. Exposure times in each of the two dichroics and PAs for the WHT BCGs. The PA is given as deg E of N. The half-light radii ($r_e$) were calculated from the 2MASS catalogue, except NGC 6166 and NGC 7720 for which they were calculated with the VAUCOUL task in the REDUCEME package. The last column lists the fraction of the effective half-light radii spanned by the radial profiles measured in this work. Table 1 contains more detailed properties for the galaxies.

| Object | Exposure (5300 Å) (s) | Exposure (6100 Å) (s) | Slit PA (deg) | Major axis (deg) | $r_e$ (arcsec) | $\epsilon$ | $a_e$ (arcsec) | Fraction times $a_e$ |
|---|---|---|---|---|---|---|---|---|
| NGC 3842 | 6 × 1200 | 2 × 900 | 5 | 177 | 16.4 | 0.29 | 16.3 | 1.22 |
| NGC 4874 | 6 × 1200 | 3 × 900 | 82 | 45 | 20.0 | 0.00 | 20.0 | 0.60 |
| NGC 4889 | 6 × 1200 | 2 × 900 | 80 | 82 | 25.7 | 0.34 | 25.7 | 0.89 |
| NGC 6034 | 6 × 1200 | 3 × 900 | 50 | 59 | 8.2 | 0.27 | 8.1 | 1.23 |
| NGC 6047 | 3 × 1200 | – | 88 | 117 | 7.4 | 0.27 | 7.0 | 0.61 |
| NGC 6166 | 6 × 1200 | 3 × 900 | 35 | 38 | 22.6 | 0.26 | 22.6 | 0.22 |
| NGC 7647 | 6 × 1200 | 3 × 900 | 174 | 174 | 11.2 | 0.49 | 11.2 | 1.21 |
| NGC 7720 | 6 × 1200 | 3 × 900 | 10 | – | 9.3 | 0.19 | 9.3 | 0.65 |
| NGC 7768 | 3 × 1200 | 3 × 900 | 60 | 55 | 14.7 | 0.19 | 14.7 | 0.82 |
| UGC 10143 | 6 × 1200 | 3 × 900 | 12 | 12 | 10.5 | 0.41 | 10.5 | 0.65 |

the same observational setup (two control sample ellipticals were observed but are not used in the present paper.). Five spectrophotometric standard stars were also observed for flux calibration.

A total of 22 Lick calibration stars (*G*- and *K*-type stars which are considered the main contributors to the visible light in early-type galaxies) were observed with the 5300 Å dichroic and 10 with the 6100 Å dichroic. A neutral density filter was used for the Lick stars with both dichroics. These stars are used as the templates for velocity dispersion measurements as well as to transform the line-strength indices to the Lick system. Before and/or after every standard star or object spectrum, an arc spectrum and flat-field frame were obtained in the red and blue arm at each telescope pointing, to allow accurate wavelength calibration as well as the removal of the response function of the dichroics.

### 3.2 Gemini observations

The Gemini Multi-object Spectrograph (GMOS) observations were performed in queue scheduling mode. The B600 grating was used (2.7 Å resolution) with a 0.5 arcsec slit width to match the observations of the Lick stars described below. Dispersion was 0.914 Å pixel$^{-1}$, and the spatial scale was 0.146 arcsec pixel$^{-1}$ (with 2 × 2 binning). 10 galaxies were observed at Gemini South in semester 2006B (2006 August to 2007 January) and five galaxies at Gemini North in the same observing semester. A further 12 galaxies were observed at Gemini South and six at Gemini North in 2007A (2007 February to 2007 August).

Bryan Miller et al. (private communication) performed a series of observing programmes from 2002 to 2004 in which they acquired long-slit spectroscopic data of 'Lick stars'. These are well suited as calibration data for our observing programmes, and our instrumental setup corresponded to the setup used for observations of the Lick stars. Spectral dithering was carried out with two central wavelengths at 5080 and 5120 Å for the Lick stars as well as the galaxy data described here. This is done in order to obtain the full spectrum uninterrupted by the gaps between the three CCDs. The three CCDs mosaicked together delivered a spectral range from 3700 to 6500 Å. Exposure times were 2 × 900 s at each position, which amounts to an hour (mostly along the MA) for each galaxy, except in the case of ESO 444-046 where only one 900 s exposure at each position was taken. Imaging sequences (3 × 20 s with the *g* and *r* filter)

were performed to allow insight into the possible presence and location of dust lanes or gas relative to the slit position. Standard stars were observed for relative flux calibration. The observations were mostly executed in dark time. The seeing typically ranged from 0.6 to 1.2 arcsec, and very rarely went up to 2.2 arcsec. Calibration arc (CuAr) and flat-field spectra were also frequently observed at the two different central wavelengths. General bias frames and imaging flat-field frames were also obtained.

For the Gemini data, information on the slit placements during observations was used to reconstruct the slit position on images of the galaxies. The slit location on the targets was determined using the slit acquisition images and the target positions from the imaging sequences. The images were taken with the same telescope pointing, and used to measure the offsets of the slit position from the galaxy centre (Table 3). In the few cases where the same galaxy was observed on two different nights, this was done for both nights. Offsets from the galaxy centres are shown in Table 3. The majority of the galaxies were centred correctly or with very small offsets. There are no offsets indicated for the WHT observations, because these were carried out in visiting observer mode, and all offsets were zero.

### 3.3 Data reduction

All the WHT data reductions were performed with the IRAF[4] and STARLINK[5] reduction packages. The blue and red spectra and spectra taken using the 5300 and 6100 Å dichroics were treated in similar parallel streams of data reduction. Overscan correction, ADU conversion, bias subtraction and trimming of the image edges were done first. Flat-field spectra were normalized by correcting for the lamp response function, and all star and galaxy spectra were appropriately flat-fielded. The dichroics introduced an intermediate-frequency pattern, which varied with the position of the telescope. This was successfully removed by flat-fielding, using the flat-field

---

[4] IRAF is distributed by the National Optical Astronomy Observatories, which are operated by the Association of Universities for Research in Astronomy, Inc., under cooperative agreement with the National Science Foundation.
[5] STARLINK is an interactive reduction and analysis facility that was developed in the UK, funded by the PPARC/STFC Research Council.

**Table 3.** Galaxies observed with the Gemini-North and South telescopes. Table 1 contains more detailed properties for the galaxies. The PA is given as deg E of N. The half-light radii ($r_e$) were calculated from the 2MASS catalogue, except ESO 303-005 for which it was calculated with the VAUCOUL task in the REDUCEME package. The second last column lists the fraction of the effective half-light radii spanned by the radial profiles measured in this work and the last column lists the offsets as described in the text.

| Object | Slit PA | Major axis | $r_e$ (arcsec) | $\epsilon$ | $a_e$ (arcsec) | Fraction $a_e$ | Offset (arcsec) |
|---|---|---|---|---|---|---|---|
| *2006B South* | | | | | | | |
| ESO303-005 | 55 | – | 9.1 | 0.25 | 9.1 | 0.50 | 0.70 |
| ESO 349-010 | 14 | 155 | 15.3 | 0.52 | 12.3 | 1.18 | 0.30 |
| ESO 488-027 | 88 | 68 | 10.3 | 0.15 | 10.1 | 0.94 | 2.20 |
| ESO 552-020 | 148 | 148 | 18.3 | 0.43 | 18.3 | 0.76 | 0.64 |
| IC 1633 | 97 | 97 | 23.9 | 0.17 | 23.9 | 0.75 | 0.00 |
| IC 5358 | 40 | 114 | 17.4 | 0.60 | 8.3 | 1.44 | 0.26 |
| MCG-02-12-039 | 166 | 180 | 15.2 | 0.19 | 15.1 | 1.13 | 0.64 |
| NGC 1399 | 222 | – | 42.2 | 0.06 | 42.2 | 0.44 | 0.45 |
| NGC 7012 | 289 | 100 | 15.8 | 0.44 | 15.6 | 0.96 | 0.00 |
| PGC 026269 | 313 | 133 | 7.3 | 0.00 | 7.3 | 0.89 | 0.00 |
| *2006B North* | | | | | | | |
| NGC 1713 | 330 | 39 | 15.5 | 0.14 | 14.0 | 1.07 | 0.00 |
| NGC 2832 | 226 | 172 | 21.2 | 0.17 | 19.6 | 1.12 | 0.50 |
| NGC 7597 | 46 | 133 | 9.4 | 0.00 | 9.4 | 0.64 | 0.00 |
| NGC 7649 | 78 | 78 | 12.8 | 0.31 | 12.8 | 0.82 | 0.20 |
| UGC 02232 | 60 | – | 9.7 | 0.00 | 9.7 | 0.82 | 0.00 |
| *2007A South* | | | | | | | |
| ESO 146-028 | 154 | 154 | 12.4 | 0.35 | 12.4 | 0.48 | 0.15 |
| ESO 346-003 | 297 | 118 | 11.9 | 0.18 | 11.9 | 0.29 | 0.15 |
| ESO 444-046 | 196 | 161 | 16.0 | 0.29 | 14.9 | 0.24 | 0.45 |
| GSC555700266 | 204 | – | 10.6 | 0.30 | 10.6 | 0.47 | 0.00 |
| IC 1101 | 204 | 25 | 12.2 | 0.50 | 12.2 | 0.39 | 0.20 |
| IC 4765 | 287 | 123 | 28.0 | 0.46 | 27.1 | 0.13 | 0.75 |
| LEDA094683 | 226 | 46 | 7.3 | 0.33 | 7.3 | 0.54 | 2.00 |
| NGC 3311 | 63 | – | 26.6 | 0.17 | 26.6 | 0.53 | 0.40 |
| NGC 4946 | 134 | 135 | 17.0 | 0.20 | 17.0 | 0.74 | 0.00 |
| PGC 044257 | 267 | 44 | 15.3 | 0.63 | 10.5 | 0.38 | 0.00 |
| PGC 072804 | 76 | 76 | 7.6 | 0.16 | 7.6 | 0.52 | 0.00 |
| UGC 05515 | 293 | 83 | 12.0 | 0.13 | 11.8 | 0.38 | 0.00 |
| *2007A North* | | | | | | | |
| NGC 4839 | 63 | 64 | 17.2 | 0.52 | 17.2 | 0.61 | 0.00 |
| NGC 6086 | 270 | 3 | 11.2 | 0.29 | 8.1 | 0.51 | 0.10 |
| NGC 6160 | 140 | 72 | 13.9 | 0.47 | 9.0 | 0.41 | 0.00 |
| NGC 6173 | 139 | 138 | 15.0 | 0.26 | 15.0 | 0.47 | 0.10 |
| NGC 6269 | 306 | 80 | 14.1 | 0.20 | 13.1 | 0.50 | 0.35 |
| PGC 071807 | 138 | 138 | 6.7 | 0.70 | 6.7 | 0.71 | 0.10 |

images taken directly before and/or after the science frames (i.e. at the same telescope pointing). It was necessary to make an illumination correction using normalized twilight flat-field spectra to correct for spatial gradients in the star and galaxy spectra. Full two-dimensional wavelength calibration was performed and star and galaxy spectra were transformed to equal linear spectral bin sizes.

All the flux calibration and Lick stars were sky-subtracted and S-distortion-corrected before one-dimensional spectra were extracted. All one-dimensional Lick star spectra were flux calibrated and corrected for atmospheric extinction.

A cosmic ray cleaning algorithm was applied to all the two-dimensional galaxy spectra before they were background-subtracted and S-distortion-corrected. For each individual galaxy frame, a sky region consisting of 40 rows was chosen on each side of the galaxy and averaged together to obtain a one-dimensional sky spectrum. The sky spectrum was grown into a two-dimensional spectrum and

subtracted from the data frame. Flux calibration and extinction corrections were also applied to the two-dimensional spectra. The galaxy frames were then co-added (also removing any remaining cosmic ray effects in the process) to form a single frame for each galaxy in each of the blue and red arms and for each of the two dichroics.

The basic Gemini data reductions were performed with the Gemini-specific GMOS data reduction package that can be added on to the standard IRAF reduction package. Spectra with different central wavelengths (5080 and 5120 Å) and spectra taken with GMOS-North and GMOS-South were treated in similar parallel streams of data reduction. The raw Lick star data were obtained from the Gemini Science Archive.[6] The basic data reductions were

[6] http://www4.cadc-ccda.hia-iha.nrc-cnrc.gc.ca/gsa/

conducted in a similar manner as for the WHT data. For each of the two central wavelength settings, a bad pixel spectrum was made in order to avoid interpolation between the gaps. When the spectra of the two different wavelength settings were combined, these bad pixel masks were used to ensure that only true data were averaged.

Proctor et al. (2005) and Brough et al. (2007) also used GMOS data to measure Lick indices, and found negligble scattered light that influenced their results. Nevertheless, as a test of the effect of scattered light in the GMOS spectrograph on our data, bright sky-lines were used to extract flat-field profiles that could be compared to the shape of the dome flats that were used. It was found that scattered light effects did not influence the regions where galaxy data were extracted or the regions used for background subtraction.

An error analysis was completed to account for both Poisson (photonic) noise and systematic errors in the data. Variance frames were created from the data frames after bias subtraction and ADU conversion, and reduced in a way similar to the data frames, but the arithmetic manipulations were performed by incorporating the usual error propagation laws. Thus, the variance frames represent the square of the Poisson noise at the start of this reduction process, and all other systematic noise effects are added on to the variance frames in quadrature.

Flat-fielding produced negligible errors with the exception of the WHT flat-field spectra taken in the upper wavelength region (red spectra of dichroic 6100 Å on night four), which contained fringe patterns. This contributed about 4 per cent to the errors, and these were appropriately propagated in the variance frame. Errors contributed by the illumination correction proved negligible. Wavelength calibration was accurate to within 0.1 Å in all cases. After that, the variance frames were also *S*-distortion-corrected, following the procedure used for the corresponding data frames. The sky subtraction process added to the uncertainty in the data and was properly taken into account by calculating the following for each variance frame:

$$[\Delta \text{Sky}(\lambda)]^2 = [\frac{1}{\sqrt{N}} \Delta A(\lambda)]^2, \tag{1}$$

where $\Delta$ Sky is the error contribution of the sky subtraction being taken into account, $N$ is the number of spatial cross-sections averaged for the sky determination and $A$ is the Poisson error on the average one-line sky spectrum. This one-dimensional spectrum was then grown into a two-dimensional spectrum with the proper dimensions and added on to the variance frames in all cases.

Relative flux calibration was accurate to within 5 to 10 per cent, and the variance frames were also co-added so that they could be treated alongside the galaxy data in further analysis. For the Gemini data, variance frames were co-added for each galaxy by dealing with the gaps in the same manner as the data (described above) to avoid any interpolation. The fact that only $N/2$ frames were added in the regions where the gaps occur, instead of $N$ individual frames per galaxy in all the other regions, was taken into account in the variance frame combination procedure. At the end of this reduction process, each two-dimensional galaxy data frame had an associated two-dimensional variance array.

As mentioned, some of the galaxies were observed at a position angle (PA) other than the MA, due to the two control elliptical galaxies in the WHT observations and the availability of suitably bright guide stars in the Gemini observations. This had an effect on the relative half-light radii ($r_e$), which had to be taken into account. Tables 2 and 3 list the $r_e$ along the semimajor axis of the galaxies, computed from the Two-Micron All Sky Survey (2MASS) $K$-band 20th magnitude arcsec$^{-2}$ isophotal radius using the formula by

Jarrett et al. (2003): $\log r_e \sim \log r_{K20} - 0.4$. Using the ellipticities ($\epsilon$) of the galaxies (data from NED), the effective half-light radii at PA were computed according to

$$a_e = \frac{r_e(1 - \epsilon)}{1 - \epsilon \mid \cos(\mid \text{PA} - \text{MA} \mid) \mid}. \tag{2}$$

The fraction of $a_e$ which the radial profiles measured in this work spans is also listed in Tables 2 and 3. For those galaxies for which a MA angle is not available in HyperLeda, the PA is assumed to be the same as the MA (as intended during the observation preparations).

## 4 CENTRAL KINEMATICAL MEASUREMENTS

The central radial velocity and velocity dispersion values of the galaxies were derived for regions with the size of $a_e/8$, and with the galaxy centres defined as the luminosity peaks. Thus, the central values are for an aperture of $1 \times a_e/8$ arcsec$^2$ for the WHT data and $0.5 \times a_e/8$ arcsec$^2$ for the Gemini data.

The Lick stars were shifted to zero radial velocity before using them as templates. Radial velocities and velocity dispersions of the galaxies were measured using the MOVEL and OPTEMA algorithms described by González (1993) and integrated into the REDUCEME data reduction package.[7] This routine is an improvement of the classic Fourier Quotient Technique described by Sargent et al. (1977). It is an iterative procedure in which a galaxy model is processed in parallel with the galaxy spectrum. In this way, a comparison between the input and recovered broadening functions for the model allows one to correct the galaxy power spectrum for any imperfections of the data handling procedures in Fourier Space. The procedure uses an algorithm that obtains the linear combination of individual templates that best matches the observed galaxy spectrum. The best template is scaled, shifted and broadened to match the galaxy kinematic parameters and is feeded to the MOVEL algorithm. The output kinematic parameters are then used to create and improve composite templates, and the process continues until it converges. This OPTEMA algorithm is able to overcome the typical template mismatch problem (see van der Marel & Franx 1993) by constructing an optimal template as a linear combination of stellar spectra of different spectral types and luminosity classes for each galaxy (González 1993; Sánchez-Blázquez et al. 2006). A new optimal template was constructed with each spatial bin in the kinematical measurements.

Skyline residuals and emission lines were masked. Emission lines were detected in 13 galaxies: ESO 349-010, MCG-02-12-039, NGC 0541, NGC 1713, NGC 3311, NGC 4874, NGC 4946, NGC 6166, NGC 6173, NGC 7012, NGC 7649, NGC 7720 and PGC 044257. The detection thresholds and emission-line correction will be described in a future paper devoted to the stellar populations.

For the Gemini data, 20 stars were used to make the optimal template (excluding the stars not of $G$ or $K$ spectral type), and 22 stars for the WHT data. Fig. 1 shows a typical fit between the observed central spectrum of a galaxy and the optimal template for that galaxy corrected by the derived kinematic parameters.[8]

---

[7] REDUCEME is an astronomical data reduction package, specially devoted to the analysis of the long-slit spectroscopy data. It was developed by N. Cardiel and J. Gorgas (Cardiel 1999). http://www.ucm. es/info/Astrof/software/reduceme/reduceme.html

[8] The derived recession velocities were automatically corrected for the standard special relativistic correction $z = (1 + \frac{V_{nr}}{c})\gamma - 1$, where $\gamma = \frac{c}{\sqrt{c^2 - v^2}}$, $V_{nr}$ is the non-relativistic radial velocity and $c$ is the speed of light.
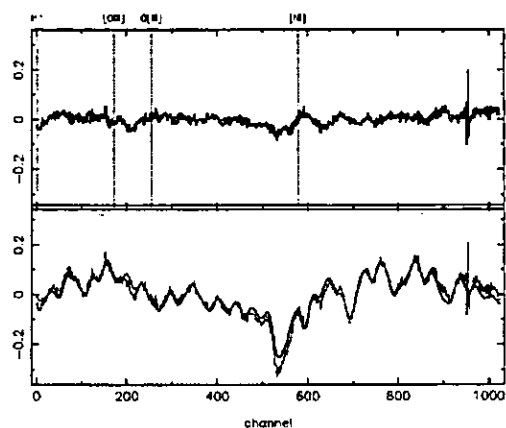
**Figure 1.** A typical example of the calculation of the derived kinematics for NGC 7768 with the MOVEL algorithm. In the lower panel, the smooth line corresponds to the optimal template spectrum, plotted together with the galaxy spectrum which has been shifted and broadened to the derived parameters. The upper panel shows the residuals of fit (in relative flux units), with the dotted lines indicating the positions of typical emission lines. This illustration spans 4900 to 5400 Å.

The errors were computed through Monte Carlo numerical simulations and using the appropriate error spectra. In each simulation, Gaussian noise was added to the galaxy spectra in accordance with the error spectra and the radial velocity and velocity dispersion derived. Errors in the radial velocities and velocity dispersions were calculated as the unbiased standard deviation of the different solutions. The errors computed in this manner are expected to incorporate all the uncertainties, from the basic reduction process (which is accounted for in the error spectra) to the final measurement of the parameters.

When comparing measured central velocity dispersion values with those from the literature, emphasis must be placed on the fact that published values are measurements from within different apertures, which can have a systematic effect on the values. Accurate comparison is further limited because of different effective spatial resolution, data of different quality and different analysis techniques.

Fig. 2 shows the rough comparison (not taking into account the above differences) between the velocity dispersion values from HyperLeda (if available) and those derived in this study. For most of the galaxies, more than one velocity dispersion values are listed in HyperLeda (in which case the most recent was used for this comparison). In the case of NGC 1399, for example, published values range between 233 and 420 km s$^{-1}$, which shows the effect different apertures and measurements have (this can be seen in the steep change in the measured velocity dispersion profile of NGC 1399 in Fig. 4). The absolute mean difference between the values measured here and the literature is $|\sigma(\text{here}) - \sigma(\text{lit, uncorrected})| = 33 \pm 29$ km s$^{-1}$, which is acceptable for the purposes of this paper.

# 5 KINEMATICS OF INDIVIDUAL GALAXIES

The galaxy spectra were binned in the spatial direction to ensure a minimum signal-to-noise ratio of 20 per Å in the H$\beta$ region of the spectrum for kinematical measurements as a function of radius. Thus, the spatial cross-sections are broader with increasing radius from the centre of the galaxy. The radial kinematics (radial velocities and velocity dispersions) were measured with the same MOVEL and OPTEMA algorithms in the REDUCEME package and with the same
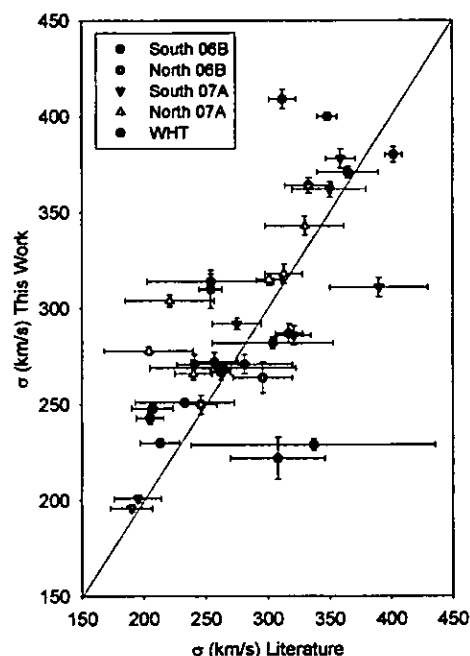


**Figure 2.** Velocity dispersion results compared to literature values. The latter values are the most recent ones from HyperLeda as described in the text.

optimal Lick star templates as the central kinematics. The values of the kinematic parameters are evaluated at the luminosity-weighted centres of the spatial bins used to derive the parameters.

Dark time at both Gemini telescopes is highly oversubscribed. To speed up the completion of this multi-semester project, we relaxed the observing conditions to accept grey time as well. However, as a consequence, it was not possible to extract radial profiles to very large radii for those targets observed during grey time, but the central values are still accurate. Eight galaxies (three WHT and five Gemini) could be extracted to radii $> 1a_e$ and 12 galaxies (one WHT and 11 Gemini) could only be extracted to radii $< 0.5a_e$. The rotational velocity $V_{\text{max}}$ was measured as half the difference between the peaks of the rotation curve.

## 5.1 Notes on individual objects

This section describes the individual objects and their radial kinematic profiles as shown in Figs 3–7. We refer to results published prior to this study, as well as the results obtained here. The radial kinematic profiles of NGC 4839, NGC 4889, NGC 6166 and IC 1101 are compared to previous measurements from the literature in Appendix A. Appendix B contains the radial kinematics of the individual galaxies in tabular form, which is available in the online version of this article.

ESO 146-028: the radial velocity of this galaxy is mostly flat and the velocity dispersion profile is decreasing outwards.

ESO 303-005: the radial kinematic profiles of this galaxy show no significant rotation or substructure.

ESO 346-003: the radial velocity profile shows clear rotation of the order of 51 km s$^{-1}$.

ESO 349-010: *HST* imaging of this galaxy was published by Laine et al. (2003). The radial velocity profile of this galaxy shows

(a) ESO146-028.

(b) ESO303-005.

(c) ESO346-003.

(d) ESO349-010.

(e) ESO444-046.

(f) ESO488-027.

(g) ESO552-020

(h) GSC555700266

(i) IC1101
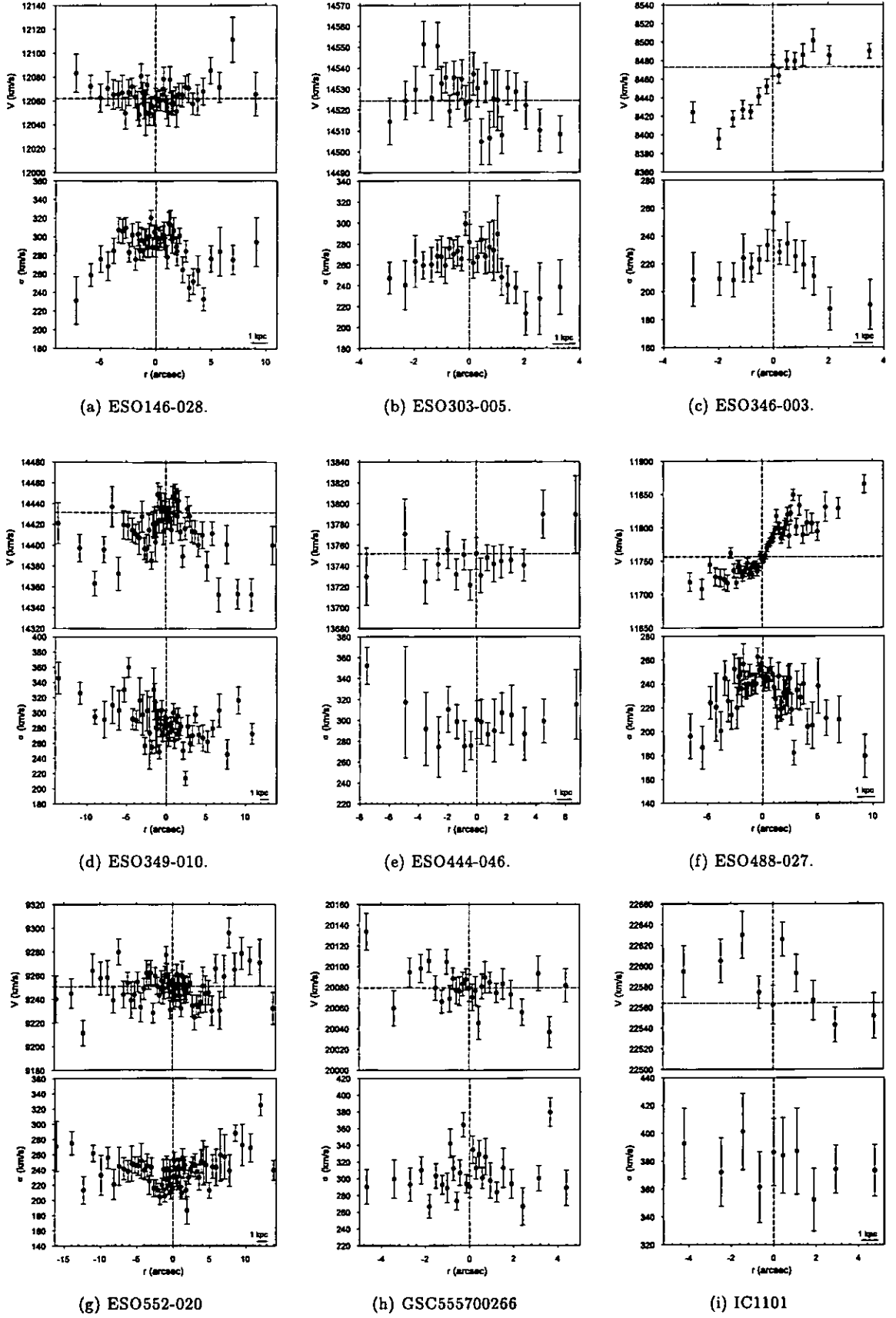
**Figure 3.** Radial profiles of velocities (*V*) and velocity dispersion (σ). The vertical lines indicate the centre of the galaxy and the horizontal line the radial velocity of the central bin.
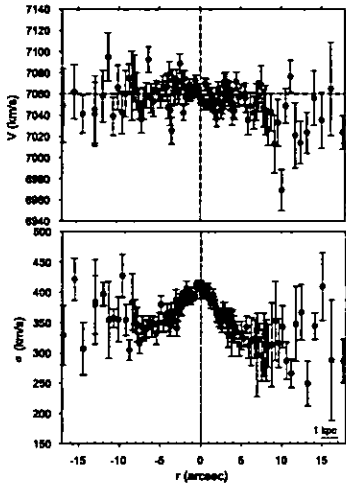
(a) IC1633.
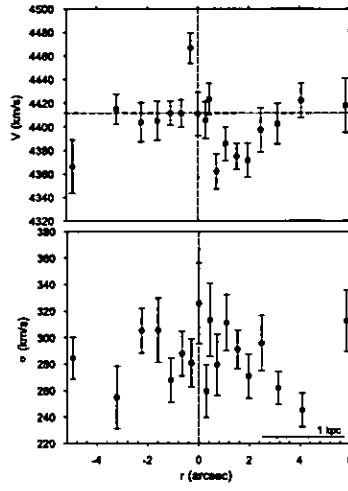
(b) IC4765.
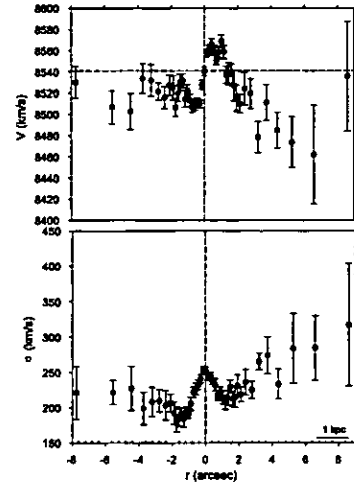
(c) IC5358.
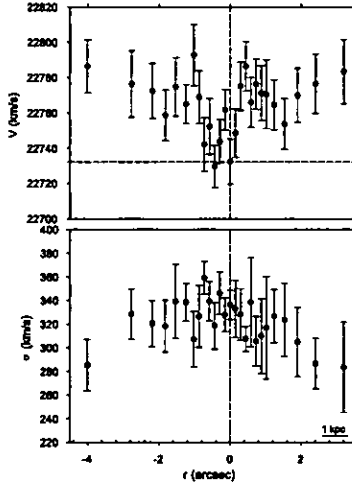
(d) Leda094683.
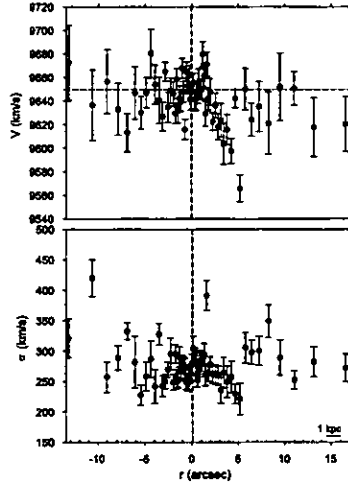
(e) MCG-02-12-039.
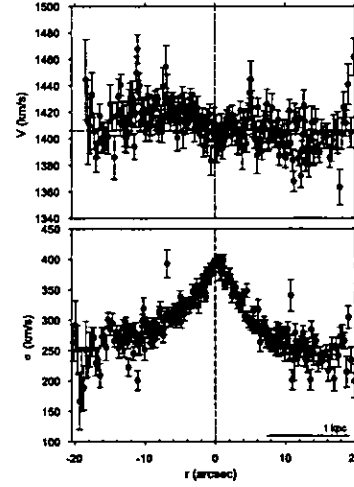
(f) NGC1399.
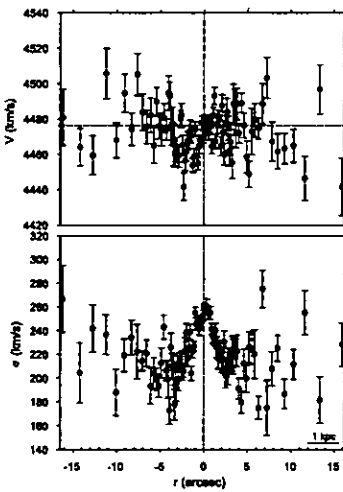
(g)NGC1713
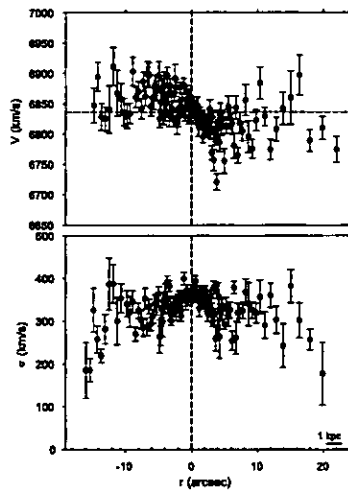
(h) NGC2832
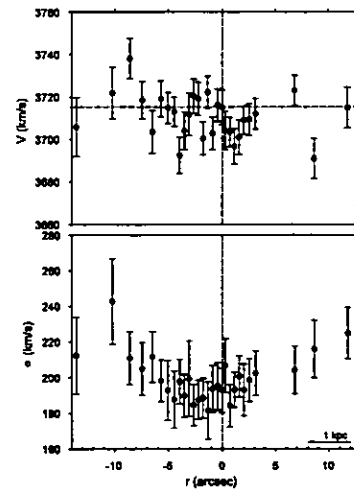
(i) NGC3311

**Figure 4.** Radial profiles of velocities (*V*) and velocity dispersion ($\sigma$). The dashed lines are as in Fig. 3.

(a) NGC3842.

(b) NGC4839.

(c) NGC4874.

(d) NGC4889.

(e) NGC4946.

(f) NGC6034.

(g) NGC6047

(h) NGC6086

(i) NGC6160
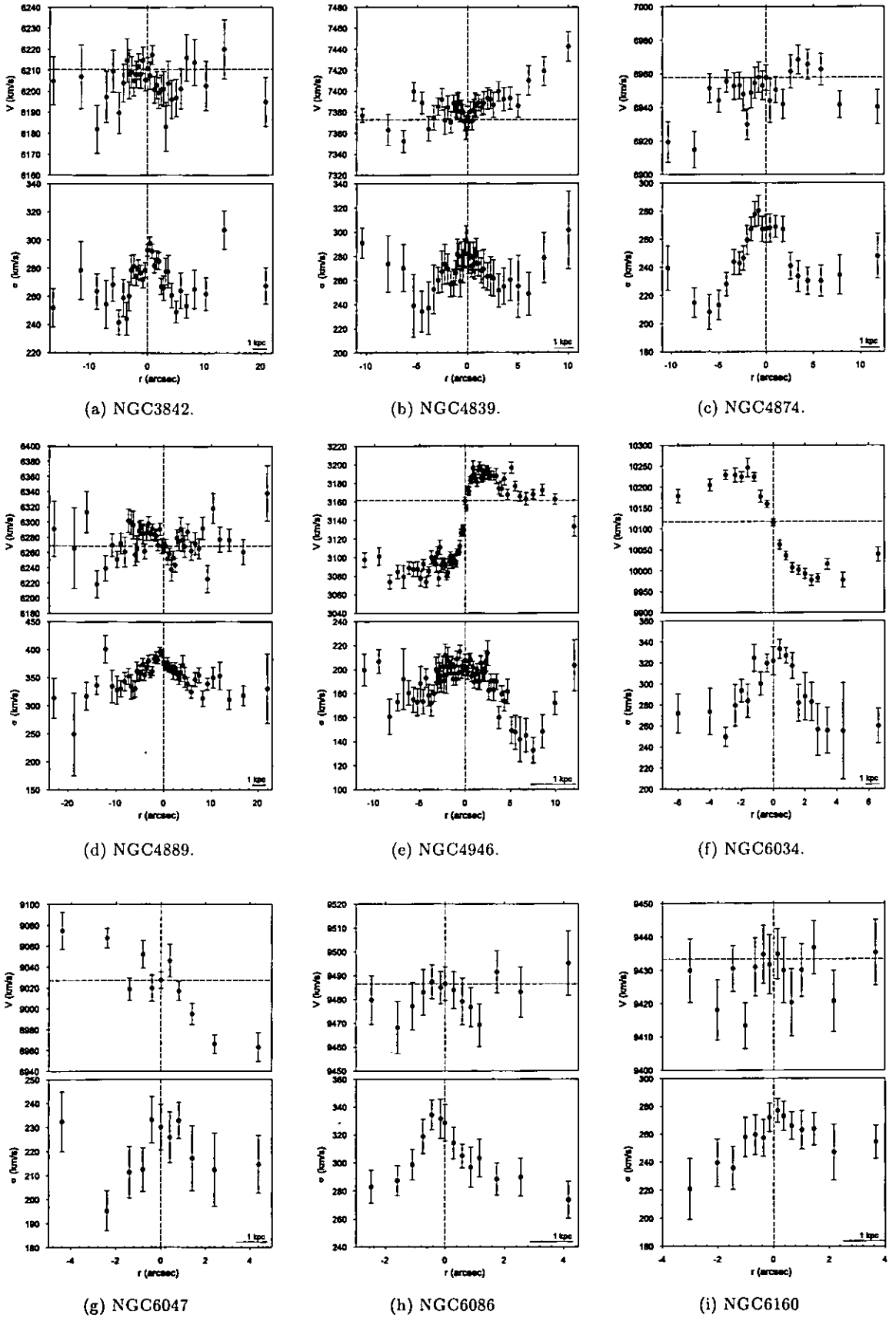
**Figure 5.** Radial profiles of velocities ($V$) and velocity dispersion ($\sigma$). The dashed lines are as in Fig. 3.

(a) NGC6166.

(b) NGC6173.

(c) NGC6269.

(d) NGC7012.

(e) NGC7597.

(f) NGC7647.

(g) NGC7649

(h) NGC7720

(i) NGC7768
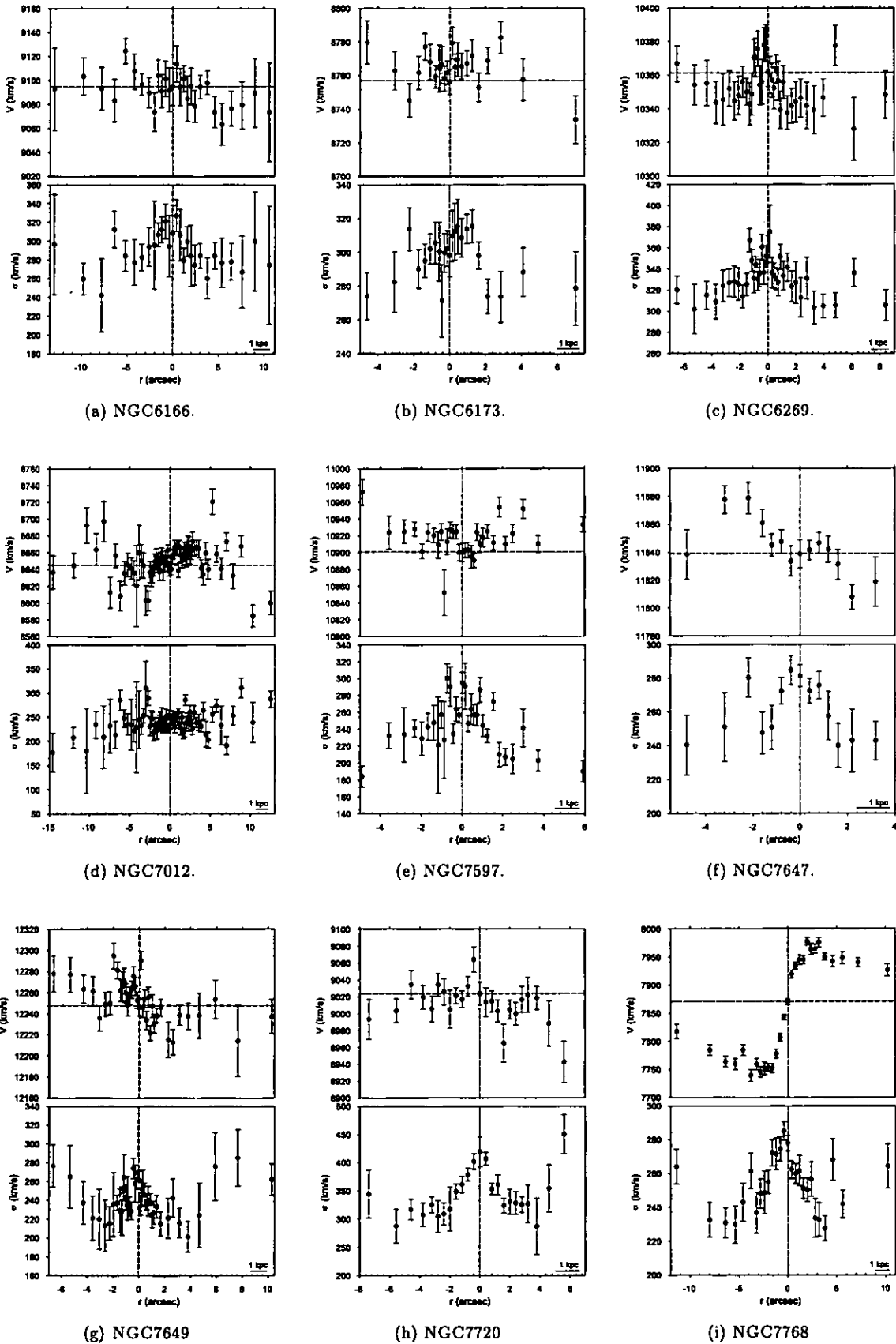
**Figure 6.** Radial profiles of velocities (*V*) and velocity dispersion ($\sigma$). The dashed lines are as in Fig. 3.
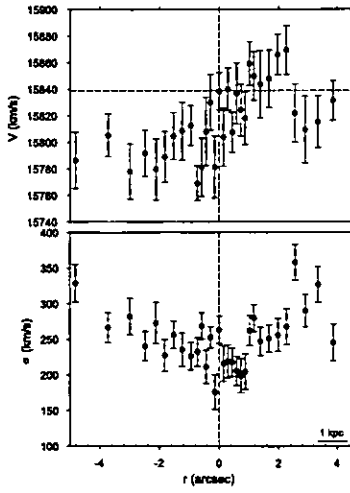
(a) PGC026269.
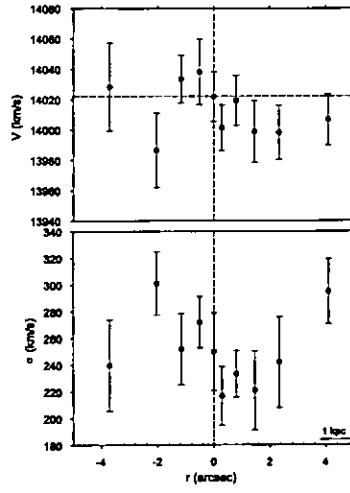
(b) PGC044257.
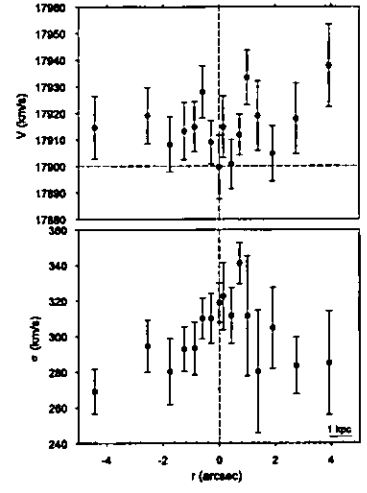
(c) PGC071807.
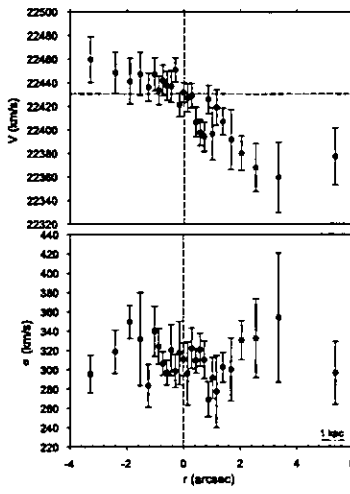
(d) PGC072804.
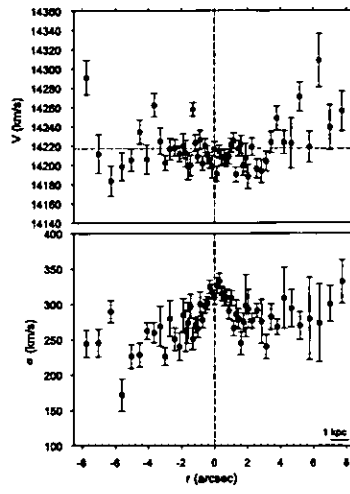
(e) UGC02232.
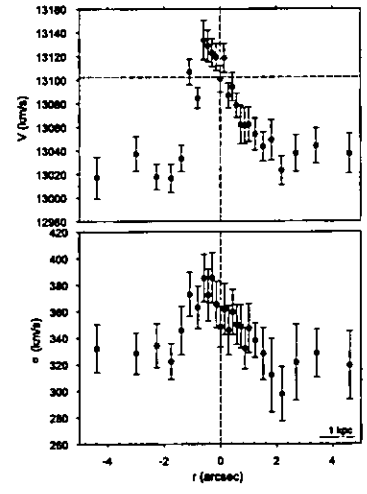
(f) UGC05515.
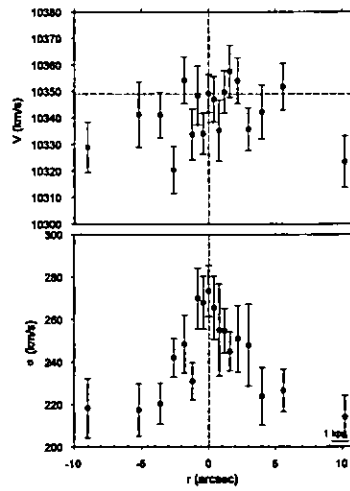
(g) UGC10143

**Figure 7.** Radial profiles of velocities (*V*) and velocity dispersion (σ). The dashed lines are as in Fig. 3.

no significant rotation, and the velocity dispersion profile has a positive gradient.

ESO 444-046: no clear rotation or velocity substructure is visible in the kinematic profiles.

ESO 488-027: the kinematic profiles show a kinematically decoupled core (KDC) in the centre of this galaxy.

ESO 552-020: the radial velocity profile is mostly flat and the velocity dispersion profile shows a small dip south-west of the centre of the galaxy, which might indicate a colder component.

GSC555700266: slow rotation but no clear substructure can be seen in the kinematic profiles.

IC 1101: this galaxy is one of the few known BCGs that were previously found to have a rising velocity dispersion profile (Fisher et al. 1995a). This result cannot be confirmed here since the derived velocity dispersion profile is not measured to the same radius as in the above-mentioned study. No significant rotation is detected in the radial velocity profile.

IC 1633: the surface brightness profile was published by Schombert (1986) and *HST* imaging by Laine et al. (2003). The radial velocity profile reveals some evidence for substructure at the centre of this galaxy.

IC 4765: the radial velocity profile shows rotation in the centre of the galaxy, which is possibly rotational substructure.

IC 5358: both the radial kinematic profiles show the clear presence of a KDC in this galaxy.

LEDA094683: no significant rotation but some evidence of substructure is visible from the radial velocity profile.

MCG-02-12-039: this BCG is a weak line emitter. The surface brightness profile was published by Schombert (1986) and *HST* imaging by Laine et al. (2003). A KDC is detected in the radial kinematic profiles.

NGC 1399: the surface brightness profile was published by Schombert (1986). The velocity dispersion in the central region of this galaxy was found to be 388 km s$^{-1}$ decreasing to 200 km s$^{-1}$ at 10 arcsec from the centre by Longo et al. (1994). The central radial velocity dispersion of this galaxy was measured in this study as 371 $\pm$ 3 km s$^{-1}$. Thus, the central velocity dispersion measured in this study corresponds to that measured by Longo et al. (1994), and the steep decreasing velocity dispersion profile is confirmed as well. This galaxy has a flat radial velocity profile.

NGC 1713: the radial velocity profile of this galaxy reveals a definite KDC in the centre of this galaxy.

NGC 2832: this galaxy is thought to be tidally interacting with its companion, NGC 2831. The surface brightness profile was published by Schombert (1986) and Jordán (2004) and the *HST* imaging by Laine et al. (2003). The radial velocity profile shows the presence of a KDC in the centre of this galaxy.

NGC 3311: the *HST* imaging was published by Laine et al. (2003). No clear rotation or velocity substructure can be seen in the radial kinematic profiles, but the velocity dispersion profile has a positive gradient.

NGC 3842: this galaxy belongs to a cluster, which forms a part of the Coma supercluster. The surface brightness profile was published by Schombert (1986) and the *HST* imaging by Laine et al. (2003). The radial velocity profile of this galaxy reveals the presence of a KDC in the centre.

NGC 4839: the location of this cD galaxy far from the centre of the Coma cluster is unusual. Surface brightness profiles were published by Schombert (1986), Oemler (1976) as well as Jordán (2004), who all confirm the presence of a very prominent cD envelope. Rotation of the order of 44 km s$^{-1}$ and a KDC in the centre of the galaxy are detected.

NGC 4874: this galaxy has a large, extended envelope. It is the second brightest galaxy of the famous pair of cDs at the centre of the Coma cluster. The surface brightness profile was published by Peletier et al. (1990). No significant rotation or velocity substructure is detected for this galaxy.

NGC 4889: a large cD galaxy with a very extended envelope. This is the brightest galaxy of the Coma cluster. The surface brightness profile was published by Peletier et al. (1990) and the *HST* imaging by Laine et al. (2003). The radial velocity profile clearly shows a KDC.

NGC 4946: this is an ordinary elliptical galaxy. The radial velocity profile of this galaxy reveals rotation of the order of 62 km s$^{-1}$ along the MA.

NGC 6034: the surface brightness profile was published by Schombert (1986). The radial velocity profile of this galaxy shows a significant rotation of the order of 134 $\pm$ 15 km s$^{-1}$ along the MA.

NGC 6047: the surface brightness profile was published by Schombert (1986), and Schombert (1987) classified it as an E/S0 galaxy. The radial velocity profile of this galaxy shows rotation of the order of 59 km s$^{-1}$ (with the slit placement 29° from the MA).

NGC 6086: the surface brightness profile was published by Schombert (1986) and the *HST* imaging by Laine et al. (2003). Carter et al. (1999) found this galaxy to have a KDC. Even though some evidence of substructure can be seen, this core cannot be confirmed since the profiles measured here do not cover the same radial extend as those in Carter et al. (1999).

NGC 6160: the radial velocity profile of this galaxy reveals no significant rotation or substructure.

NGC 6166: this is a classic multiple nucleus cD galaxy in a rich cluster. The surface brightness profile was published by Schombert (1986). Carter et al. (1999) found the velocity dispersion of this galaxy to increase from 325 km s$^{-1}$ at the centre to 450 km s$^{-1}$ at 35 arcsec along the MA. They also found the galaxy to show modest MA rotation (45 km s$^{-1}$ at 40 arcsec). The profiles derived here do not extend out to the radii necessary to confirm the positive velocity dispersion slope found by Carter et al. (1999). Rotation of the order of 31 km s$^{-1}$ is found in the centre of the galaxy, although this is not a very clear rotation curve.

NGC 6173: the surface brightness profile was published by Schombert (1986) and the *HST* imaging by Laine et al. (2003). The derived radial kinematic profiles of this galaxy show no significant rotation or substructure.

NGC 6269: surface brightness profiles were published by Schombert (1986) and by Malumuth & Kirshner (1985). The radial velocity profile shows some velocity substructure in the centre of this galaxy. This galaxy was observed at an angle of 46° away from the MA.

NGC 7012: the radial velocity profile shows a small amount of rotation in the centre which might be a KDC.

NGC 7597: the surface brightness profile was published by Schombert (1986). The radial kinematic profiles show possible evidence for a KDC.

NGC 7647: this is a cD galaxy with a red envelope and a large number of small companions (Vitores et al. 1996). The surface brightness profile was published by Schombert (1986) and the *HST* imaging by Laine et al. (2003). The radial velocity profile of this galaxy shows a clear KDC in the centre.

NGC 7649: the surface brightness profile was published by Schombert (1986) and the *HST* imaging by Laine et al. (2003). A KDC is clearly visible in the centre of this galaxy.

NGC 7720: this is a multiple nuclei galaxy and has a massive close companion galaxy, also an elliptical. The surface brightness

profile was published by Lauer (1988) and the *HST* imaging by Laine et al. (2003). The radial velocity profile reveals no significant rotation but there might be some substructure in this galaxy.

NGC 7768: surface brightness profiles were published by Schombert (1986), Malumuth & Kirshner (1985) and Jordán (2004) and the *HST* imaging was published by Laine et al. (2003). The radial velocity profile of this galaxy shows significant rotation of the order of $114 \pm 11$ km s$^{-1}$ along the MA. This agrees with the $101 \pm 5$ and the 99 km s$^{-1}$ rotations found previously by Fisher et al. (1995a) and Prugniel & Simien (1996), respectively.

PGC 026269: also known as Hydra A. The radial kinematic profiles of this galaxy reveal rotation of the order of 51 km s$^{-1}$ along the MA, as well as an increasing velocity dispersion profile.

PGC 044257: the data indicate that the velocity dispersion might increase with radius, although the large scatter and the small number of bins make it difficult to assess the slope.

PGC 071807: no significant rotation or substructure can be seen in this galaxy.

PGC 072804: the surface brightness profile was published by Malumuth & Kirshner (1985). The radial velocity profile of this galaxy shows rotation of the order of 50 km s$^{-1}$ along the MA.

UGC 02232: this galaxy has an extended envelope and a large number of objects in the vicinity. The *HST* imaging was published by Laine et al. (2003). No significant rotation or clear substructure is detected.

UGC 05515: the surface brightness profile was published by Schombert (1986). The radial velocity profile shows a KDC in the centre of this galaxy.

UGC 10143: this galaxy has a chain of companions. The surface brightness profile was published by Schombert (1986) and the *HST* imaging by Laine et al. (2003). No significant rotation or substructure can be inferred from the radial kinematic profiles of this galaxy.

## 6 DISCUSSION

(i) *Five out of 41 BCGs (ESO 349-010, ESO 444-046, ESO 552-020, NGC 3311, PGC 026269) were found to have a positive velocity dispersion gradient.*

The radial kinematic studies done so far on early-type galaxies are mostly limited to normal ellipticals, for which flat or decreasing velocity dispersion profiles are found. The majority of the results previously obtained for very small samples of BCGs are similar to those of normal ellipticals. Fisher et al. (1995a) found one galaxy (IC 1101) in their sample of 13 BCGs with a positive velocity dispersion gradient. Carter et al. (1999) found one (NGC 6166) of their sample of three BCGs to have a positive velocity dispersion gradient, although Fisher et al. (1995a) did not find it for this galaxy. Brough et al. (2007) found negative velocity dispersion gradients in five out of their sample of six brightest cluster and group galaxies (the other one had a zero velocity dispersion gradient).

Both IC 1101 and NGC 6166 form part of the sample of BCGs studied here, but in both cases the measured velocity dispersion profiles do not reach the radius achieved in the much smaller samples in the above-mentioned studies. Thus, the positive velocity dispersion gradient could not be confirmed for IC 1101 or NGC 6166 (see Figs A3 and A4). However, five other BCGs were found to have a positive velocity dispersion gradient, though admittedly the slope is marginally positive in some cases. If these positive velocity dispersion gradients are not caused by systematic errors in the various data reduction or velocity dispersion measurements by different authors, then they imply a rising mass-to-light ratio.

(ii) *At least 12 BCGs (NGC 3842, NGC 4889, NGC 7647, ESO 488-027, IC 5358, MCG-02-12-039, NGC 1713, NGC 2832, NGC 4839, NGC 6269, NGC 7649 and UGC 05515) show clear velocity substructure in their profiles.*

From studies of elliptical galaxies in high-density environments (e.g. Koprolin & Zeilinger 2000), the incidence of KDCs is observed to be about 33 per cent, rising to 50 per cent when projection effects are considered. Hau & Forbes (2006) find KDCs in 40 per cent of their isolated elliptical galaxies. For BCGs, we have found at least 12 of the 41 BCGs show clear velocity substructure, amounting to 29 per cent of the sample (intermediate- and minor-axis data included).

KDCs can be the result of a merger event (Koprolin & Zeilinger 2000), but can also occur when the galaxy is triaxial and supports different orbital types in the core and main body (Statler 1991). The fact that the incidence of KDCs in BCGs compares with that found for normal elliptical galaxies in high-density environments suggests that the two classes share the same fraction of galaxies with triaxial shapes.

(iii) *NGC 6034 and 7768 possess significant rotation (134 and 114 km s$^{-1}$, respectively) along the MA. Several other BCGs show rotation that is >40 km s$^{-1}$ and more than three times the standard error: ESO 346-003, GSC555700266 and NGC 4839 (MA spectra); ESO 488-027, IC 5358 and UGC 05515 (intermediate axis spectra), as do the two elliptical galaxies NGC 4946 (MA spectra) and NGC 6047 (intermediate axis spectra).*

Carter et al. (1999) found small rotation along the MA at large radii (30–40 arcsec) for their sample of three BCGs, which is consistent with the nearly complete lack of rotation found near the centres of the sample of 13 BCGs by Fisher et al. (1995a). According to Fisher et al. (1995a), the lack of rotation found in samples of BCGs is in agreement with the expectation of declining importance of rotation with increasing luminosity for elliptical galaxies. The lack of rotation is also compatible with the idea that these objects formed through dissipationless mergers (Boylan-Kolchin et al. 2006). The remnants left by mergers with or without dissipation are expected to differ in their kinematical structure. In a merger which involves gas-rich galaxies, the gas will form a disc. After the gas has been removed from the system at the end of the merger (through ejection and converted into stars), the remnant will show rotation (Bournaud, Jog & Combes 2005). Whereas in a merger where dissipationless processes dominate, the remnant will show little or no rotation (Naab & Burkert 2003; Cox et al. 2006). In this study, clear rotation above 100 km s$^{-1}$ was found for NGC 6034 and 7768, while most BCGs showed little or no rotation. This kinematical differentiation (the existence of slow and fast rotators) in early-type galaxies is also clearly visible in the SAURON data presented by Emsellem et al. (2007).

The amount of flattening that is expected due to the rotation in a galaxy depends on the balance between ordered and random motions, and this can be quantified using the anisotropy parameter. The rotation of elliptical galaxies is conventionally expressed as the anisotropy parameter, defined as $(V_{max}/\sigma_0)^* = (V_{max}/\sigma_0)/\sqrt{\epsilon/1-\epsilon}$ (Kormendy 1982), where the rotational velocity $V_{max}$ is measured as in Section 5 and the central velocity dispersion $\sigma_0$ is taken as the measurement for the central velocity dispersion in Table 4. A value of $(V_{max}/\sigma_0)^* \approx 1$ would be expected if a galaxy is flattened by rotation. The anisotropy parameter $(V_{max}/\sigma_0)^*$ can be used to separate galaxies that are rotationally supported from those that are supported by $\sigma$ anisotropy where the

**Table 4.** Central velocity dispersions ($\sigma$) and radial velocities ($V$) of the galaxies. The measurement and determination of $V_{max}$ and $(V_{max}/\sigma_0)^*$ are described in Section 6.

| Galaxy | $\sigma$ (km s$^{-1}$) Observed | $V$ (km s$^{-1}$) Observed | $V_{max}$ (km s$^{-1}$) | $\log(V_{max}/\sigma_0)^*$ |
|---|---|---|---|---|
| ESO 146-028 | $299 \pm 3$ | $12\,061 \pm 3$ | $14 \pm 18$ | $-1.2 \pm 0.9$ |
| ESO 303-005 | $276 \pm 5$ | $14\,526 \pm 4$ | $23 \pm 17$ | $-0.8 \pm 0.4$ |
| ESO 346-003 | $226 \pm 4$ | $8459 \pm 9$ | $51 \pm 13$ | $-0.3 \pm 0.1$ |
| ESO 349-010 | $282 \pm 3$ | $14\,420 \pm 3$ | $46 \pm 19$ | $-0.8 \pm 0.4$ |
| ESO 444-046 | $292 \pm 3$ | $13\,741 \pm 3$ | $26 \pm 16$ | $-0.9 \pm 0.4$ |
| ESO 488-027 | $248 \pm 2$ | $11\,754 \pm 4$ | $53 \pm 12$ | $-0.3 \pm 0.1$ |
| ESO 552-020 | $229 \pm 3$ | $9128 \pm 5$ | $20 \pm 19$ | $-1.0 \pm 0.8$ |
| GSC555700266 | $312 \pm 9$ | $20\,059 \pm 6$ | $49 \pm 14$ | $-0.6 \pm 0.2$ |
| IC 1101 | $378 \pm 5$ | $22\,585 \pm 9$ | $41 \pm 31$ | $-1.0 \pm 0.8$ |
| IC 1633 | $400 \pm 2$ | $7061 \pm 2$ | $20 \pm 17$ | $-1.0 \pm 0.4$ |
| IC 4765 | $286 \pm 5$ | $4403 \pm 6$ | $50 \pm 28$ | $-0.8 \pm 0.6$ |
| IC 5358 | $243 \pm 3$ | $8539 \pm 9$ | $55 \pm 13$ | $-0.7 \pm 0.3$ |
| Leda094683 | $332 \pm 5$ | $22\,748 \pm 5$ | $32 \pm 26$ | $-0.9 \pm 0.6$ |
| MCG-02-12-039 | $271 \pm 5$ | $9648 \pm 3$ | $59 \pm 28$ | $-0.3 \pm 0.3$ |
| NGC 1399 | $371 \pm 3$ | $1406 \pm 2$ | $24 \pm 11$ | $-0.6 \pm 0.1$ |
| NGC 1713 | $251 \pm 2$ | $4472 \pm 2$ | $30 \pm 11$ | $-0.5 \pm 0.1$ |
| NGC 2832 | $364 \pm 4$ | $6841 \pm 4$ | $64 \pm 22$ | $-0.4 \pm 0.2$ |
| NGC 3311 | $196 \pm 2$ | $3709 \pm 2$ | $25 \pm 9$ | $-0.6 \pm 0.2$ |
| NGC 3842 | $287 \pm 5$ | $6211 \pm 2$ | $11 \pm 13$ | $-1.2 \pm 0.8$ |
| NGC 4839 | $278 \pm 2$ | $7380 \pm 2$ | $44 \pm 14$ | $-0.8 \pm 0.3$ |
| NGC 4874 | $267 \pm 4$ | $6953 \pm 2$ | $15 \pm 12$ | $-0.4 \pm 0.1$ |
| NGC 4889 | $380 \pm 4$ | $6266 \pm 5$ | $40 \pm 19$ | $-0.8 \pm 0.3$ |
| NGC 4946 | $201 \pm 2$ | $3148 \pm 9$ | $62 \pm 9$ | $-0.2 \pm 0.1$ |
| NGC 6034 | $325 \pm 4$ | $10\,113 \pm 28$ | $134 \pm 15$ | $-0.2 \pm 0.1$ |
| NGC 6047 | $230 \pm 2$ | $9031 \pm 8$ | $59 \pm 16$ | $-0.4 \pm 0.2$ |
| NGC 6086 | $318 \pm 5$ | $9483 \pm 2$ | $13 \pm 18$ | $-1.2 \pm 0.9$ |
| NGC 6160 | $266 \pm 3$ | $9428 \pm 3$ | $12 \pm 18$ | $-1.3 \pm 1.4$ |
| NGC 6166 | $310 \pm 10$ | $9100 \pm 2$ | $31 \pm 20$ | $-0.7 \pm 0.4$ |
| NGC 6173 | $304 \pm 3$ | $8766 \pm 2$ | $24 \pm 16$ | $-0.9 \pm 0.4$ |
| NGC 6269 | $343 \pm 5$ | $10\,363 \pm 3$ | $26 \pm 35$ | $-0.8 \pm 0.7$ |
| NGC 7012 | $240 \pm 3$ | $8653 \pm 3$ | $24 \pm 16$ | $-0.9 \pm 0.6$ |
| NGC 7597 | $264 \pm 8$ | $10\,907 \pm 5$ | $63 \pm 20$ | $0.2 \pm 0.1$ |
| NGC 7647 | $271 \pm 5$ | $11\,842 \pm 7$ | $36 \pm 14$ | $-0.9 \pm 0.4$ |
| NGC 7649 | $250 \pm 5$ | $12\,258 \pm 5$ | $41 \pm 14$ | $-0.6 \pm 0.2$ |
| NGC 7720 | $409 \pm 5$ | $9034 \pm 5$ | $50 \pm 18$ | $-0.6 \pm 0.2$ |
| NGC 7768 | $272 \pm 5$ | $7875 \pm 24$ | $114 \pm 11$ | $-0.1 \pm 0.1$ |
| PGC 026269 | $222 \pm 11$ | $15\,816 \pm 8$ | $51 \pm 20$ | $0.2 \pm 0.1$ |
| PGC 044257 | $247 \pm 9$ | $14\,014 \pm 6$ | $20 \pm 16$ | $-1.2 \pm 1.0$ |
| PGC 071807 | $315 \pm 3$ | $17\,911 \pm 5$ | $16 \pm 13$ | $-1.5 \pm 1.2$ |
| PGC 072804 | $311 \pm 5$ | $22\,433 \pm 4$ | $50 \pm 24$ | $-0.4 \pm 0.2$ |
| UGC 02232 | $314 \pm 4$ | $14\,208 \pm 3$ | $42 \pm 18$ | $0.0 \pm 0.1$ |
| UGC 05515 | $362 \pm 4$ | $13\,103 \pm 7$ | $56 \pm 18$ | $-0.4 \pm 0.1$ |
| UGC 10143 | $262 \pm 2$ | $10\,344 \pm 5$ | $19 \pm 11$ | $-1.1 \pm 0.5$ |

value is substantially less than unity. The division occurs at about $(V_{max}/\sigma_0)^* = 0.7$ (Bender, Burstein & Faber 1992).

Fig. 8 shows the anisotropy parameter as a function of galaxy $B$-band luminosity, where the above-mentioned division is indicated by the horizontal dashed line. Note that the errors indicated are only propagated from the errors on the velocity measurements taken to be the extreme radial velocity points, and the errors on the central velocity dispersion. They do not take into account the general uncertainties involved in determining the most extreme velocity measurements. Therefore, care has to be taken when interpreting the individual points on the diagram. The only notable BCG data point that lies significantly above the dashed line is for the galaxy PGC 026269, which possesses moderate rotation (51 km s$^{-1}$) and
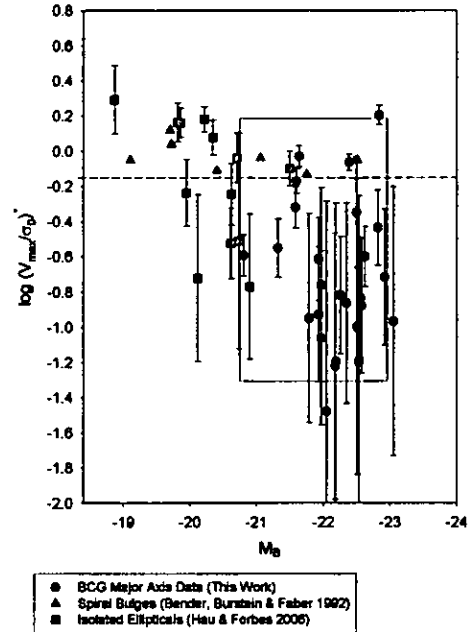


**Figure 8.** The anisotropy–luminosity diagram. The horizontal dashed line separates the rotationally supported galaxies from the anisotropic galaxies as described in the text. Only the BCGs for which MA spectra were taken (within 10°) are plotted. The box plotted in the figure outlines the region containing data on giant ellipticals from Bender et al. (1992).

surprisingly low central velocity dispersion (222 km s$^{-1}$). However, the ellipticity of this galaxy is zero and it is not rotationally supported.

Another factor that complicates the dynamical interpretation of individual points is that the observed ellipticity is a global property of the galaxy, whereas the kinematic measurements taken here only reflect the kinematics along the axis where the slit was placed, and only close to the centre of the galaxy. For example, a disc component may dominate the measured kinematics but will have little effect on the ellipticity, making the galaxy appear to rotate faster than its global ellipticity would suggest (Merrifield 2004).

For comparison, the sample of isolated ellipticals from Hau & Forbes (2006) is also plotted in Fig. 8. Of this sample, 11 galaxies were observed along the MA, and the central velocity dispersions were derived from the bins closest to the galaxy cores. The BCGs show less rotational support than the isolated elliptical galaxies as a class. Spiral bulge (typically rotationally supported) and giant elliptical data from Bender et al. (1992) are also plotted. Their central velocity dispersions were derived over the whole half-light radii of the galaxies. Even though large rotation velocities were found for a few individual cases, the BCGs are consistent with the general trend for very massive galaxies.

## 7 SUMMARY

In this paper, we have presented the largest optical spectroscopic sample of BCGs with radial information to date. We have derived the rotational velocity and velocity dispersion profiles for 41 BCGs. We find clear rotation curves for a number of galaxies for which we have obtained MA spectra and two galaxies with rotational velocities exceeding 100 km s$^{-1}$. However, because of the generally large central velocity dispersions, the BCG data are consistent with

the trend for very massive elliptical galaxies on the anisotropy–luminosity diagram. At least 29 per cent of the galaxies show very clear velocity substructure.

A future paper will be devoted to the stellar population properties of this galaxy sample. Despite the undeniably special nature of BCGs due to their extreme morphological properties and locations, the kinematic properties investigated here (rotation and incidence of velocity substructure) seem normal compared with their ordinary giant elliptical counterparts.

## ACKNOWLEDGMENTS

## REFERENCES

Adami C., Biviano A., Durret F., Mazure A., 2005, A&A, 443, 17
Andreon S., Davoust E., Michard R., Nieto J. L., Poulain P., 1996, A&AS, 116, 429
Aragon-Salamanca A., Baugh C. M., Kauffmann G., 1998, MNRAS, 297, 427
Baier F. W., Wipper H., 1995, AN, 316, 319
Bautz L. P., Morgan W. W., 1970, BAAS, 2, 294 (BM)
Bender R., Burstein D., Faber S. M., 1992, ApJ, 399, 462
Bournaud F., Jog C. J., Combes F., 2005, A&A, 437, 69
Boylan-Kolchin M., Ma C., Quataert E., 2006, MNRAS, 369, 1081
Brough S., Collins C. A., Burke D. J., Mann R. G., Lynam P. D., 2002, MNRAS, 329, 533
Brough S., Proctor R., Forbes D. A., Couch W. J., Collins C. A., Burke D. J., Mann R. G., 2007, MNRAS, 378, 1507
Burstein D., Faber S. M., Gaskell C. M., Krumm N., 1984, ApJ, 287, 586
Cardiel N., 1999, PhD thesis, Universidad Complutense de Madrid
Cardiel N., Gorgas J., Aragon-Salamanca A., 1998, MNRAS, 298, 977
Carter D., Metcalfe N., 1980, MNRAS, 191, 325
Carter D., Bridges T. J., Hau G. K. T., 1999, MNRAS, 307, 131
Collins C. A., Mann R. G., 1998, MNRAS, 297, 128
Cowie L. L., Binney J., 1977, ApJ, 215, 723
Cox T. J., Dutta S. N., Di Matteo T., Hernquist L., Hopkins P. F., Robertson B., Springel V., 2006, ApJ, 650, 791
De Vaucouleurs G., 1948, JO, 31, 113
De Lucia G., Blaizot J., 2007, MNRAS, 375, 2
De Lucia G., Springer V., White S. D. M., Croton D., Kauffmann G., 2006, MNRAS, 366, 499
Dressler A., 1984, ApJ, 281, 512
Edwards L. O. V., Hudson M. J., Balogh M. L., Smith R. J., 2007, MNRAS, 379, 100
Emsellem E. et al., 2007, MNRAS, 379, 401
Faber S. M., Friel E. D., Burstein D., Gaskell C. M., 1985, ApJS, 57, 711
Fisher D., Illingworth G., Franx M., 1995a, ApJ, 438, 539
Fisher D., Franx M., Illingworth G., 1995b, ApJ, 448, 119
Gallagher J. S., Ostriker J. P., 1972, AJ, 77, 288
Giacintucci S., Venturi T., Murgia M., Dallacasa D., Athreya R., Bardelli S., Mazzotta P., Saikia D. J., 2007, A&A, 476, 99
González J. J., 1993, PhD thesis, Univ. California
Gorgas J., Efstathiou G., Aragon-Salamanca A., 1990, MNRAS, 245, 217
Hau G. K. T., Forbes D. A., 2006, MNRAS, 371, 633
Hill J. M., Oegerle W. R., 1992, A&AS, 18, 1413
Hoessel J. G., Gunn J. E., Thuan T. X., 1980, ApJ, 241, 486
Jarrett T. H., Chester T., Cutri R., Schneider S. E., Huchra J. P., 2003, AJ, 125, 525
Jordán A., Côté P., West M. J., Marzke R. O., Minniti D., Rejkuba M., 2004, AJ, 127, 24
Kormendy J., 1982, in Martinet L., Major M., eds, Morphology and Dynamics of Galaxies. Geneva Observatory, Sauverny, p. 115
Koprolin W., Zeilinger W., 2000, A&A, 145, 71
Laine S., van der Marel R. P., Lauer T. R., Postman M., O'Dea C. P., Owen F. N., 2003, AJ, 125, 478
Lauer T. R., 1988, ApJ, 325, 49
Liu F. S., Xia X. Y., Mao S., Wu H., Deng Z. G., 2008, MNRAS, 385, 23
Longo G., Zaggio S. R., Brusarello G., Richter G., 1994, A&AS, 105, 433
McNamara B. R., O'Connell R. W., 1992, ApJ, 393, 579
McNamara B. R., Wise M., Sarazin C. L., Jannuzi B. T., Elston R., 1996, ApJ, 466, L9
Malumuth E. M., Kirshner R. P., 1985, ApJ, 291, 8
Matthews T. A., Morgan W. W., Schmidt M., 1964, ApJ, 140, 35
Mehlert D., Saglia R. P., Bender R., Wegner G., 2000, A&AS, 141, 449
Merrifield M., 2004, MNRAS, 353, L13
Merritt D., 1983, ApJ, 264, 24
Naab T., Burkert A., 2003, ApJ, 597, 893
Neumann D. M. et al., 2001, A&A, 365, 74
Oegerle W. R., Hill J. M., 2001, AJ, 122, 2858
Oemler A., 1976, ApJ, 209, 693
Ostriker J. P., Hausman M. A., 1977, ApJ, 217, 125
Ostriker J. P., Tremaine S. D., 1975, ApJ, 202, 113
Patel P., Maddox S., Pearce F. R., Aragón-Salamanca A., Conway E., 2006, MNRAS, 370, 851
Peletier R. F., Davies R. L., Illingworth G. D., Davis L. E., Cawson M., 1990, AJ, 100, 1091
Postman M., Lauer T. R., 1995, ApJ, 440, 28
Proctor R. N., Forbes D. A., Forestell A., Gebhardt K., 2005, MNRAS, 362, 857
Prugniel Ph., Simien F., 1996, A&A, 309, 749
Rines K., Geller M. J., Diaferio A., Mahdavi A., Mohr J. J., Wegner G., 2002, AJ, 124, 1266
Romeo A. D., Napolitano N. R., Covone G., Sommer-Larsen J., Antonuccio-Delogu V., Capacciolo M., 2008, MNRAS, 389, 13
Rood H. J., Sastry G. N., 1971, PASP, 83, 313 (RS)
Salomé P., Combes F., 2003, A&A, 412, 657
Sánchez-Blázquez P., Gorgas J., Cardiel N., González J. J., 2006, A&A, 457, 787
Sarazin C. L., 1988, X-ray Emission from Clusters of Galaxies. Cambridge Univ. Press, Cambridge
Sargent W., Schechter P., Boksenberg A., Shortridge K., 1977, ApJ, 212, 326
Schombert J. M., 1986, ApJS, 60, 603
Schombert J. M., 1987, ApJS, 64, 643
Schombert J. M., 1988, ApJ, 328, 475

Seigar M. S., Graham A. W., Jerjen H., 2007, MNRAS, 378, 1575

Statler T. S., 1991, AJ, 102, 882

Struble M. F., Rood H. J., 1987, ApJS, 63, 555

Tonry J. L., 1984, ApJ, 279, 13

Tonry J. L., 1985, AJ, 90, 2431

Torlina L., De Propris R., West M. J., 2007, ApJ, 660, L97

Van der Marel R. P., Franx M., 1993, ApJ, 407, 525

Vitores A. G., Zamorano J., Rego M., Alonso O., Gallego J., 1996, A&AS, 118, 7

Von der Linden A., Best P. N., Kauffmann G., White S. D. M., 2007, MNRAS, 379, 867

West M. J., 1989, ApJ, 344, 535

Whiley I. M. et al., 2008, MNRAS, 387, 1253

Worthey G., Ottaviani D. L., 1997, ApJS, 111, 377

Worthey G., Faber S. M., González J. J., Burstein D., 1994, ApJS, 94, 687

Yamada T., Koyama Y., Nakata F., Kajisawa M., Tanaka I., Kodama T., Okamura S., De Propis R., 2002, ApJ, 577, 89

## APPENDIX A: KINEMATIC PROFILES: COMPARISON WITH LITERATURE

The kinematic radial profiles of some of the galaxies could be compared to previous measurements in the literature. Four comparisons are shown in Figs A1 to A4. Two of the Coma cluster cD galaxies (NGC 4839 and NGC 4889) were compared to the data from Fisher et al. (1995a) and Mehlert et al. (2000). The third Coma cD (NGC 4874) was not compared as it was observed at a different slit PA than in the other studies. No systematic differences are found (within the error bars) for the measurements of this study compared to the previous studies. The velocity dispersion measurements of NGC 4889 in Fisher et al. (1995a) are lower than the other studies. This discrepancy was already reported in Mehlert et al. (2000). NGC 6166 was compared to Fisher et al. (1995a) and agree within the errors. IC



**Figure A2.** NGC 4889. Kinematic profile compared to the previous literature.
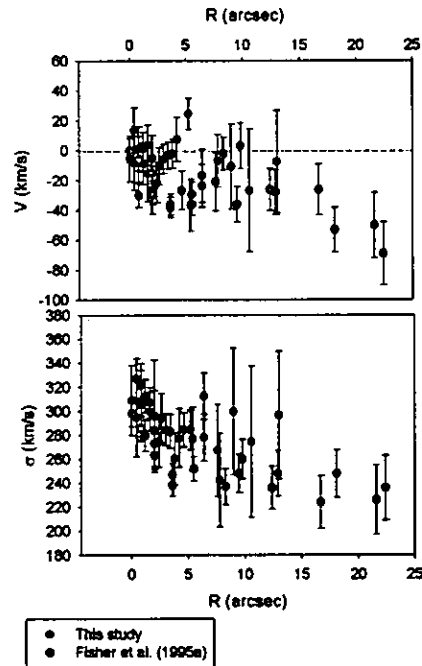


**Figure A3.** NGC 6166. Kinematic profile compared to the previous literature.



**Figure A1.** NGC 4839. Kinematic profile compared to previous literature. The data are folded with respect to the centre of the galaxy, and the radial velocities are given as relative to the central radial velocity.

1101 was compared to Fisher et al. (1995a), who found the velocity dispersion profile to be increasing. As can be seen from Fig. A4, the velocity dispersion profile measured here does not extend out to the same radius as that from Fisher et al. (1995a), but the central measurements are in good agreement.
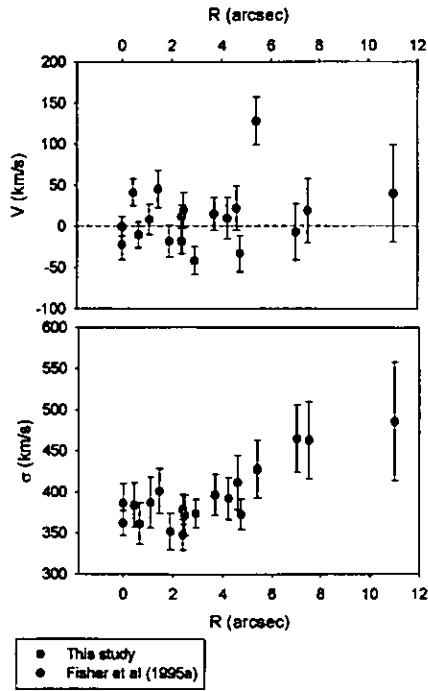
**Figure A4.** IC 1101. Kinematic profile compared to previous literature.

## APPENDIX B: SUPPORTING INFORMATION

Additional supporting information may be found in the online version of this article.

**Table B1.** Radial kinematics of ESO 146-028.
**Table B2.** Radial kinematics of ESO 303-005.
**Table B3.** Radial kinematics of ESO 346-003.
**Table B4.** Radial kinematics of ESO 349-010.
**Table B5.** Radial kinematics of ESO 444-046.
**Table B6.** Radial kinematics of ESO 488-027.
**Table B7.** Radial kinematics of ESO 552-020.
**Table B8.** Radial kinematics of GSC555700266.
**Table B9.** Radial kinematics of IC 1101.
**Table B10.** Radial kinematics of IC 1633.

**Table B11.** Radial kinematics of IC 4765.
**Table B12.** Radial kinematics of IC 5358.
**Table B13.** Radial kinematics of Leda094683.
**Table B14.** Radial kinematics of MCG-02-12-039.
**Table B15.** Radial kinematics of NGC 1399.
**Table B16.** Radial kinematics of NGC 1713.
**Table B17.** Radial kinematics of NGC 2832.
**Table B18.** Radial kinematics of NGC 3311.
**Table B19.** Radial kinematics of NGC 3842.
**Table B20.** Radial kinematics of NGC 4839.
**Table B21.** Radial kinematics of NGC 4874.
**Table B22.** Radial kinematics of NGC 4889.
**Table B23.** Radial kinematics of NGC 4946.
**Table B24.** Radial kinematics of NGC 6034.
**Table B25.** Radial kinematics of NGC 6047.
**Table B26.** Radial kinematics of NGC 6086.
**Table B27.** Radial kinematics of NGC 6160.
**Table B28.** Radial kinematics of NGC 6166.
**Table B29.** Radial kinematics of NGC 6173.
**Table B30.** Radial kinematics of NGC 6269.
**Table B31.** Radial kinematics of NGC 7012.
**Table B32.** Radial kinematics of NGC 7597.
**Table B33.** Radial kinematics of NGC 7647.
**Table B34.** Radial kinematics of NGC 7649.
**Table B35.** Radial kinematics of NGC 7720.
**Table B36.** Radial kinematics of NGC 7768.
**Table B37.** Radial kinematics of PGC 026269.
**Table B38.** Radial kinematics of PGC 044257.
**Table B39.** Radial kinematics of PGC 071807.
**Table B40.** Radial kinematics of PGC 072804.
**Table B41.** Radial kinematics of UGC 02232.
**Table B42.** Radial kinematics of UGC 05515.
**Table B43.** Radial kinematics of UGC 10143.

Please note: Wiley-Blackwell are not responsible for the content or functionality of any supporting information supplied by the authors. Any queries (other than missing material) should be directed to the corresponding author for the article.

This paper has been typeset from a TEX/LATEX file prepared by the author.

# Stellar populations in the centres of brightest cluster galaxies

S. I. Loubser,[1,2]* P. Sánchez-Blázquez,[1,3] A. E. Sansom[1] and I. K. Soechting[4]

[1]*Jeremiah Horrocks Institute for Astrophysics and Supercomputing, University of Central Lancashire, Preston, PR1 2HE*
[2]*Physics Department, University of the Western Cape, Cape Town 7535, South Africa*
[3]*Instituto de Astrofísica de Canarias, Via Lactea S/N, 38205, La Laguna, Tenerife, Spain*
[4]*Oxford Astrophysics, Department of Physics, University of Oxford, Oxford OX1 3RH*

## ABSTRACT

This paper is part of a series devoted to the study of the stellar populations in brightest cluster galaxies (BCGs), aimed at setting constraints on the formation and evolution of these objects. We have obtained high signal-to-noise ratio, long-slit spectra of 49 BCGs in the nearby Universe. Here, we derive single stellar population (SSP)-equivalent ages, metallicities and $\alpha$-abundance ratios in the centres of the galaxies using the Lick system of absorption line indices. We systematically compare the indices and derived parameters for the BCGs with those of large samples of ordinary elliptical galaxies in the same mass range. We find no significant differences between the index-velocity dispersion relations of the BCG data and those of normal ellipticals, but we do find subtle differences between the derived SSP parameters. The BCGs show, on average, higher metallicity ([Z/H]) and $\alpha$-abundance ([E/Fe]) values. We analyse possible correlations between the derived parameters and the internal properties of the galaxies (velocity dispersion, rotation, luminosity) and those of the host clusters (density, mass, distance from BCG to X-ray peak, presence of cooling flows), with the aim of dissentangling if the BCG properties are more influenced by their internal or host cluster properties. The SSP parameters show very little dependence on the mass or luminosity of the galaxies, or the mass or density of the host clusters. Of this sample, 26 per cent show luminosity-weighted ages younger than 6 Gyr, probably a consequence of recent – if small – episodes of star formation. In agreement with previous studies, the BCGs with intermediate ages tend to be found in cooling-flow clusters with large X-ray excess.

**Key words:** galaxies: elliptical and lenticular, cD – galaxies: formation – galaxies: stellar content.

## 1 INTRODUCTION

The assembly history of the most massive galaxies in the Universe and the influence of the cluster environment are very important, but poorly understood, aspects of galaxy formation. The most direct route to investigate the evolution of early-type galaxies is to observe them at different redshifts. Unfortunately, it is very difficult to find the progenitors of early-type galaxies by direct observations, and this method also demands large amounts of observing time even on the current generation of telescopes. An alternative approach is to infer the star formation histories (SFHs) of large samples of nearby galaxies by studying their stellar population properties and the relationships between these and the structural and kinematic properties of the galaxies.

In the context of the, now widely accepted, $\Lambda$ cold dark matter ($\Lambda$CDM) model of structure formation, Dubinski (1998) showed

that a central cluster galaxy forms naturally when a cluster collapses along the filaments. Gao et al. (2004), using numerical simulations, predicted that central galaxies in clusters experienced a significant number of mergers since $z \sim 1$. De Lucia & Blaizot (2007) provided a complete quantitative estimate of the formation of brightest cluster galaxies (BCGs) using the Millennium simulation. They predicted that the stars that will end up in a BCG formed at high redshift (with 50 per cent of the stars already formed $\sim 12.5$ Gyr ago). However, the BCG continues to assemble at much lower redshifts (with 50 per cent of the mass assembling after $z \sim 0.5$). The nature of these mergers (or accretion) is dissipationless and, therefore, no new stars are formed in the process. Thus, according to these simulations, we expect to see evidence of dissipationless mergers, little dependence of metallicity on mass, and old stellar populations in these galaxies.

Because of their position in the cluster, the mergers forming BCGs are expected to be with preferentially radial orbits. Boylan-Kolchin, Ma & Quataert (2006) showed that these types of mergers, in absence of dissipation, create systems that depart from the Faber–Jackson relationship in the same way as BCGs do (Tonry 1984;

*E-mail: 2971873@uwc.ac.za

Oegerle & Hoessel 1991; Bernardi et al. 2007; Desroches et al. 2007; Lauer et al. 2007; Von der Linden et al. 2007). Observations that support BCG formation by predominantly radial mergers include those of Bernardi et al. (2008), who showed that the shapes of the most massive ($\sigma \geq 350\,km\,s^{-1}$), high-luminosity objects (with properties similar to BCG properties) are consistent with those expected if the objects formed through radial mergers. Observations of the luminosity functions of clusters put additional constraints on BCG evolution. Loh & Strauss (2006) found the luminosity gap between the first and second brightness-ranked galaxies to be large ($\sim 0.8$ mag), larger than could be explained by an exponentially decaying luminosity function of galaxies. Loh & Strauss (2006) found that the large luminosity gap showed little evolution with redshift since $z = 0.4$, and suggest that the BCGs must have become the dominant cluster members by $z > 0.4$.

Various photometric studies have found correlations between the luminosity of the BCG and the mass or density of the host cluster, measured through the cluster velocity dispersion and X-ray luminosity (e.g. Edge & Stewart 1991; Burke, Collins & Mann 2000; Brough et al. 2002; Stott et al. 2008; Whiley et al. 2008). Taken together, these observations point to an evolutionary history of BCGs which are closely connected to the evolution of the cluster, as predicted by the hierarchical models of galaxy formation, although it is not clear if the amount of galaxy growth due to accretion agrees with these models (e.g. Whiley et al. 2008).

The mass growth of BCGs with redshift have been well studied. Aragón-Salamanca, Baugh & Kauffmann (1998) investigated the evolution of $K$ magnitudes since $z \sim 1$ and found the lack of evolution in the magnitudes compatible with mass growth of a factor of 2 to four since $z \sim 1$. However, other studies have found a more modest stellar mass growth of BCGs since those redshifts (e.g. Collins & Mann 1998; Whiley et al. 2008), although it is known that the amount of mass growth in BCGs depends on the luminosity of the host clusters (Burke et al. 2000; Brough et al. 2002). No significant BCG stellar mass growth is observed in the most X-ray luminous clusters ($L_X > 1.9 \times 10^{44}\,erg\,s^{-1}$) since $z \sim 1$, whereas BCGs in less X-ray luminous clusters experience an increase in their mass by a factor of 4 in that redshift range (Brough et al. 2002). However, more recent studies, using the velocity dispersion of the cluster instead of X-ray luminosity, have not confirmed this trend (Whiley et al. 2008).

The contradictory results might be partially due to the difficulty in the sample selection and in the comparison between aperture magnitudes (observations) and total magnitudes (models; e.g. Whiley et al. 2008). Aperture magnitudes used so far in the literature include less than 50 per cent of the total mass of the BCGs. Furthermore, it is not clear if intracluster light should be considered when comparing with the models (González, Zaritsky & Zubladoff 2007).

An alternative to measuring the BCG mass growth with redshift to study their evolution is to analyse their dynamical, structural and stellar population properties, and investigate if these are compatible with that expected from remnants of multiple dry mergers over a large redshift range.

Cooling flows are very common at low redshifts (Chen et al. 2007; Edwards et al. 2007), but their role in shaping the stellar populations of BCGs is not fully understood. The lack of widespread detection of iron lines, expected from cluster gas cooling below 1–2 keV in *XMM–Newton* observations of cool-core clusters, contradicted the model that BCG formation is a consequence of cooling flows (Jordán et al. 2004; see also discussion in Loubser et al. 2008, hereafter Paper 1). However, it is possible that star formation is ongoing in cool-core clusters at a much reduced rate (Bildfell et al.

2008). Several studies reported examples of recent or ongoing star formation in BCGs hosted by cooling-flow clusters (Cardiel, Gorgas & Aragón-Salamanca 1998a; Crawford et al. 1999; McNamara et al. 2006; Edwards et al. 2007; O'Dea et al. 2008; Bildfell et al. 2008; Pipino et al. 2009). However, the origin of the gas fuelling the recent star formation in some BCGs is not yet known. The competing explanations include cooling flows, or cold gas deposited during a merging event (Bildfell et al. 2008).

This paper is the second in a series of papers investigating a new, large sample of BCGs, their kinematic and stellar population properties and the relationships between these and the properties of the host clusters. The first paper was devoted to the spatially resolved kinematics of 41 BCGs (Paper 1). Here, we measure and interpret BCG spectral line strengths to gain insights into their stellar populations. The stellar populations in early-type galaxies have been studied by numerous authors (González 1993; Fisher, Franx & Illingworth 1995; Jørgensen 1999; Mehlert et al. 2000; Trager et al. 2000a,b; Kuntschner et al. 2001; Moore et al. 2002; Caldwell, Rose & Concannon 2003; Nelan et al. 2005; Thomas et al. 2005, T05 hereafter; Sánchez-Blázquez et al. 2006a,b; Sánchez-Blázquez, Gorgas & Cardiel 2006c; Ogando et al. 2008; Trager, Faber & Dressler 2008 and many others). However, as discussed in detail in Paper 1, very little is known about the stellar population properties of BCGs. Recently, Von der Linden et al. (2007) carried out a study of 625 brightest group and cluster galaxies, taken from the Sloan Digital Sky Survey (SDSS), to contrast their stellar population properties with those of elliptical galaxies with the same mass. They found that stellar populations of BCGs are not different from the stellar populations of ordinary elliptical galaxies, except for the $\alpha$-enhancement, which is higher in BCGs. Brough et al. (2007), with a much smaller sample, did not find this difference.

The study of Von der Linden et al. (2007) constitutes a benchmark in the study of stellar populations in BCGs. However, they did not have spatial information. The merger history of a galaxy determines the kinematical and stellar population properties and these can, therefore, be used as a probe for the assembly history of those galaxies. Brough et al. (2007) showed that BCGs present a large spread in their metallicity gradients, probably reflecting differences in their assembly history and the dissipation during the interactions. In Paper 1, we showed that our sample of BCGs shows great variety in the galaxies' dynamical and kinematic properties (see also Brough et al. 2007).

In this paper, we concentrate on the central properties of these galaxies. The stellar population gradients and reconstructed SFHs will be investigated in future papers in the series. This paper is structured as follows: Section 2 contains the details of the sample selection, observations and data reduction. Section 3 contains the central index measurements and their relations with the velocity dispersions of the BCGs. The single stellar populations (SSPs) are derived, and compared with those of ordinary elliptical galaxies in Section 4. Section 5 shows the relations of the derived properties with the galaxy kinematics, and Section 6 details the context of the cluster environment. The conclusions are summarized in Section 7.

## 2 SAMPLE, OBSERVATIONS AND DATA REDUCTION

This study was initially intended to investigate a subsample of BCGs with extended haloes (cD galaxies). However, due to the difficulties in the classification of cD galaxies and the very inhomogeneous definitions in the literature, we cannot be confident that all the galaxies in our sample are cD galaxies. Instead, we can say that our sample

comprises of the dominant galaxies closest to the X-ray peaks in the centres of clusters. For consistency, we call these galaxies BCGs to comply with recent literature (e.g. De Lucia & Blaizot 2007; Von der Linden et al. 2007). For a small fraction of clusters, the BCG might not strictly be the brightest galaxy in the cluster, but they are always the galaxy closer to the X-ray peak. The sample selection, observations and data reduction procedures were detailed in Paper 1. In summary, these 49 galaxies were classified as cD either in NASA/IPAC Extragalactic Data base (NED) (in the morphological classification or in the notes of previous observations) and/or have profiles breaking the $r^{\frac{1}{4}}$ law in the external parts. In addition, NGC 4946 (an ordinary elliptical) and NGC 6047 (an E/S0) were also observed with the same observational set-up, and are included in this project as control galaxies.

The galaxies were observed on the William Herschel Telescope (WHT) and Gemini North and South telescopes. In addition to the 41 BCGs described in Paper 1, long-slit spectra were obtained for eight more BCGs with Gemini South in the 2007B (2007 July to 2008 January) observing semester. Thus, 49 BCGs were observed in total (for details of these galaxies see table 1, Paper 1). The instrumental set-up and data reduction procedure for the Gemini South 2007B observations were the same as used for the data taken in the previous semesters. The data reduction procedures are described in Paper 1 and will not be repeated here.

To analyse the central parts of the BCGs, we extracted spectra inside apertures of $a_e/8$ along the slit. The effective half-light radius was calculated as $a_e = \frac{r_e(1-\epsilon)}{1-\epsilon|\cos(|PA-MA|)|}$, with $\epsilon$ the ellipticity (data from NED), $r_e$ the radius containing half the light of the galaxy [computed from the Two Micron All Sky Survey (2MASS) $K$ band 20th magnitude arcsec$^{-2}$ isophotal radius as described in Paper 1], PA the slit position axis and MA the major axis. For old stellar populations, these half-light radii do not differ much from those derived using the optical bands (Jarrett et al. 2003). The central values are for an aperture of $1 \times a_e/8$ arcsec$^2$ for the WHT data and $0.5 \times a_e/8$ arcsec$^2$ for the Gemini data, as the slit widths were 1 and 0.5 arcsec, respectively. The signal-to-noise ratios (S/N) per Å around the H$\beta$ region of the central spectra ranged between 16 (ESO541-013) and 502 (NGC 1399), with an average of 87. The central kinematics used in the present paper are taken from our BCG kinematic study in Paper 1 (Table 4).

### 2.1 Transformation to the Lick/IDS system

A widely used set of spectral absorption indices is the Lick system based on a large survey of individual stars in the solar neighbourhood carried out with the image dissecting scanner (IDS) at the Lick Observatory (Burstein et al. 1984; Faber et al. 1985; Gorgas et al. 1993; Worthey et al. 1994). The original Lick system consisted of 21 indices from CN$_1$, at $\sim$4150 Å, to TiO$_2$, at $\sim$6230 Å (Faber et al. 1985; Worthey 1994; Trager et al. 1998). Worthey & Ottaviani (1997) later contributed four more indices centred on the Balmer lines H$\delta$ and H$\gamma$. This collection of 25 indices will be referred to as the Lick indices in this study. The advantages of using this set of indices are: they are well calibrated against globular clusters; the indices are not affected by dust (MacArthur 2005); and their sensitivity to different chemical elements have been calculated using model atmospheres (Tripicco & Bell 1995; Korn, Maraston & Thomas 2005).

Line-strength indices depend on the broadening of lines caused by the velocity dispersion of the galaxies and the instrumental resolution. In order to use model predictions based on the Lick/IDS
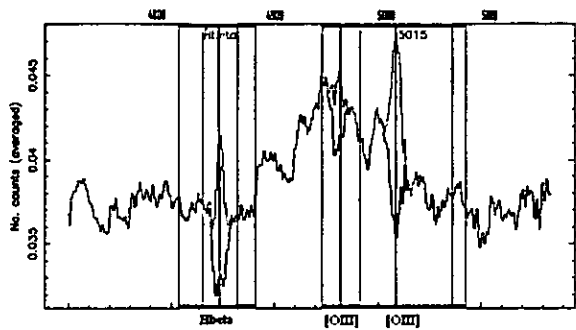


**Figure 1.** Illustration of emission-line correction of NGC 6166. The original spectrum is plotted over the emission-corrected spectrum with the affected indices (H$\beta$ and Fe5015) and their sidebands indicated. The H$\beta$ and [O iii]$\lambda\lambda$ 4958, 5007 emission lines are also indicated by vertical lines.

system, spectra need to be degraded to the wavelength dependent resolution of the Lick/IDS spectrograph and indices need to be corrected for the broadening caused by the velocity dispersion of the galaxies. This has been done using the prescriptions of Worthey & Ottaviani (1997). The detailed procedure follows in Appendix A.

### 2.2 Emission correction

The presence of emission lines leads to problems in analysing the absorption lines in stellar populations. Key absorption indices like H$\beta$, H$\gamma$ and H$\delta$ suffer from emission line in-filling. Fe5015 is also affected by [O iii]$\lambda$5007[1] emission, while Mg$_b$ is affected by [N i]$\lambda$5199 emission. In the case of the Balmer lines, emission fill-in can weaken the line strength and lead to older derived ages.

To measure the emission-line fluxes of the BCGs in this study, the GANDALF routine (Sarzi et al. 2006) was used. This software treats the emission lines as additional Gaussian templates, and solves linearly at each step for their amplitudes and the optimal combination of stellar templates, which are convolved by the best stellar line-of-sight velocity distribution. The stellar continuum and emission lines are fitted simultaneously. The stellar templates used were based on the MILES stellar library (Medium-resolution Isaac Newton Telescope Library of Empirical Spectra; Sánchez-Blázquez et al. 2006d). The [O iii]$\lambda$5007 line was fitted first. Where H$\beta$ emission was relatively weak, the kinematics of all the other lines were tied to [O iii]$\lambda$5007, following the procedure described in Sarzi et al. (2006). This was done to avoid any spurious detections of H$\beta$ lines that might have been caused by the presence of a number of metal features around 4870 Å. However, in cases where H$\beta$ was strong enough to measure its kinematics, this was calculated independently as there is no a priori reason to expect the kinematics measured from the [O iii]$\lambda$5007 and H$\beta$ lines to be the same (as they can originate in different regions). This procedure was used in order to derive the best-fitting emission-line spectrum in the galaxies where emission was detected, and enables us to derive a purely-stellar spectrum for these galaxies. The spectra of ESO349-010, MCG-02-12-039, NGC 0541, NGC 1713, NGC 3311, NGC 4874, NGC 4946, NGC 6166, NGC 6173, NGC 7012, NGC 7649, NGC 7720 and PGC044257 have detectable emission lines. For these galaxies, a purely stellar spectrum was derived by subtracting the best-fitting emission-line spectrum from the observed one. Fig. 1 shows the H$\beta$

---

[1] The standard notation is used, where the spectral identification is written between two square brackets for forbidden lines.
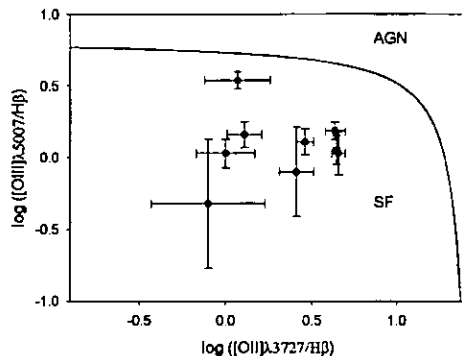
**Figure 2.** Diagnostic diagram using emission lines to separate star-forming galaxies from AGN. Star-forming galaxies are below the line (given by Lamareille et al. 2004).

region of the spectrum of NGC 6166 before and after the emission-line correction.

Emission lines originate from the hot ionized gas in the galaxies which can indicate an active galaxy [such as active galactic nuclei (AGN), LINER] or active star formation in the galaxy. We could not measure [N II]λ6584 or Hα, as they were outside our wavelength range. Therefore, we use the diagnostic diagram [O III]λ5007/Hβ against [O II]λ3727/Hβ to separate the two major origins of emission: star formation and AGN (Baldwin, Phillips & Terlevich 1981; Lamareille et al. 2004). Fig. 2 shows the galaxies for which the Hβ, [O II]λ3727 and [O III]λ5007 lines could be measured (within at least 2σ detections) on the diagnostic plot.

All nine emission-line galaxies in the present work for which these three lines could be measured should be star-forming galaxies according to this test. BCGs are known to be more likely to host radio-loud AGN than any other galaxy with the same stellar mass (Burns 1990; Best et al. 2007). This is especially true if they are hosted by cooling-flow clusters (Burns et al. 1997). However, Best et al. (2007) argue that radio-loud AGN and emission-line AGN (detectable through optical emission lines) are independent, unrelated phenomena. Edwards et al. (2007) found, in their sample of BCGs, that the emission was mostly LINER-like or a combination of LINER and star formation, and concluded that this emission was directly related to the cooling of X-ray gas at the cluster centre. Von der Linden et al. (2007) found emission lines in more than 50 per cent of their sample, although the four lines that they used as a diagnostic could only be measured with a S/N > 3 in 30 per cent of their sample. From this subsample, only 6 per cent were star-forming galaxies, 70 per cent LINERs and 24 per cent composite objects (star-forming and LINER).

Because the diagnostic diagram used here in Fig. 2 is much less effective at separating different sources of ionization (Stasińska et al. 2006), and because the fraction of the current sample containing emission lines is relatively small, and with weak emission lines, it is too early to draw detailed conclusions about the nature of emission lines in BCGs.

## 3 CENTRAL BCG INDICES

We measured line-strength indices from the flux-calibrated spectra and calculated the index errors according to the error equations presented in Cardiel et al. (1998b), Vazdekis & Arimoto (1999) and Cenarro et al. (2001).

The wavelength coverage allowed us to measure all the Lick indices, with the exception of TiO$_2$ for most galaxies (and in

a few cases also TiO$_1$) in the Gemini data and five indices of NGC 6047 (Mg$_1$ to Fe5335). TiO$_1$ is very close to the edge of the spectrum and therefore not reliable. On very close inspection, five galaxies (Leda094683, NGC 7649, NGC 6166, PGC025714 and PGC030223) showed either residuals of skyline removal or residuals where the gaps in between the GMOS CCDs were inside the band definitions of the indices used to derive the SSP parameters, hence they were also excluded from any further analysis using those indices.

The derived errors on the indices take the Poisson and systematic errors (flux calibration effects, velocity dispersion corrections, sky subtraction uncertainties, wavelength calibration and radial velocity errors) into account. We do not take into account the errors derived on the offsets to transform the indices to the Lick system (shown in Table A1). The central index measurements compared very well with previous measurements from the literature, as shown in Appendix B.

Lick offsets are applied to correct measurements that were flux calibrated using the spectrophotometric system to the Lick/IDS system and, therefore, should be identical for all flux-calibrated studies. Thus, we compare our derived offsets with other sources to test the robustness of the Lick transformation. The Lick offsets derived here for the Gemini data were compared to independently derived offsets from the same Lick star data set (M. Norris, private communication), as described in Appendix A. Most of the offsets are in agreement, with the exception of C$_2$4668 and Ca4455 which are marginally higher in this study. Since the BCG data are being compared with SB06 (Section 3.1), the Lick offsets were also compared. All the Lick offsets agree within the errors, and no real outliers were found. As a final test, we also compare our offsets with the offsets derived by comparing all the stars in common between the flux-calibrated MILES library (Sánchez-Blázquez et al. 2006d, 2009) and the Lick/IDS library. Any remaining systematics would not have been corrected by the usual Lick calibration offsets, as the systematic would have had a different effect on stars and on galaxies (at different redshifts).

### 3.1 Results: index – velocity dispersion relations

Following various other authors, and to compare with Sánchez-Blázquez et al. (2006a, hereafter SB06), the atomic indices will be expressed in magnitudes when correlated with the velocity dispersion. These will be denoted by the name followed by a prime sign, and were obtained using $I_{Mag} = 2.5 \log[\frac{-I_{Ang}}{(\lambda_1 - \lambda_2)} - 1]$, where the wavelength range is $\lambda_1$–$\lambda_2$ in the central bandpass, and $I_{Ang}$ and $I_{Mag}$ are the index measurement in Å and magnitudes, respectively.

Straight line fits ($I' = a + b \times \log\sigma$) were made to the BCG data with a least-squares fitting routine, and are shown in Figs 3 and 4 and given in Table 1. Statistical $t$-tests were run to explore the presence of correlations. Only six out of 18 indices possess a statistically significant slope different from zero (as can be seen from Table 1). These are Ca4227, Hγ$_F$, Ca4455, Fe4531, C$_2$4668 and Mg$_b$.

The scatter in the CN$_1$, CN$_2$, Mg$_1$, Mg$_2$, NaD and TiO$_1$ indices were found to be large. The molecular indices are known to show only a small amounts of scatter, but are frequently affected by flux calibration uncertainties, since the index definitions span a broad wavelength range. For 15 of the indices plotted, the index–velocity dispersion relations found by SB06 for a large sample of elliptical galaxies are also indicated. The complete SB06 sample consists of 98 galaxies, of which 35 belong to the Coma cluster, and the rest are galaxies in the field, in groups or in the Virgo cluster. Two
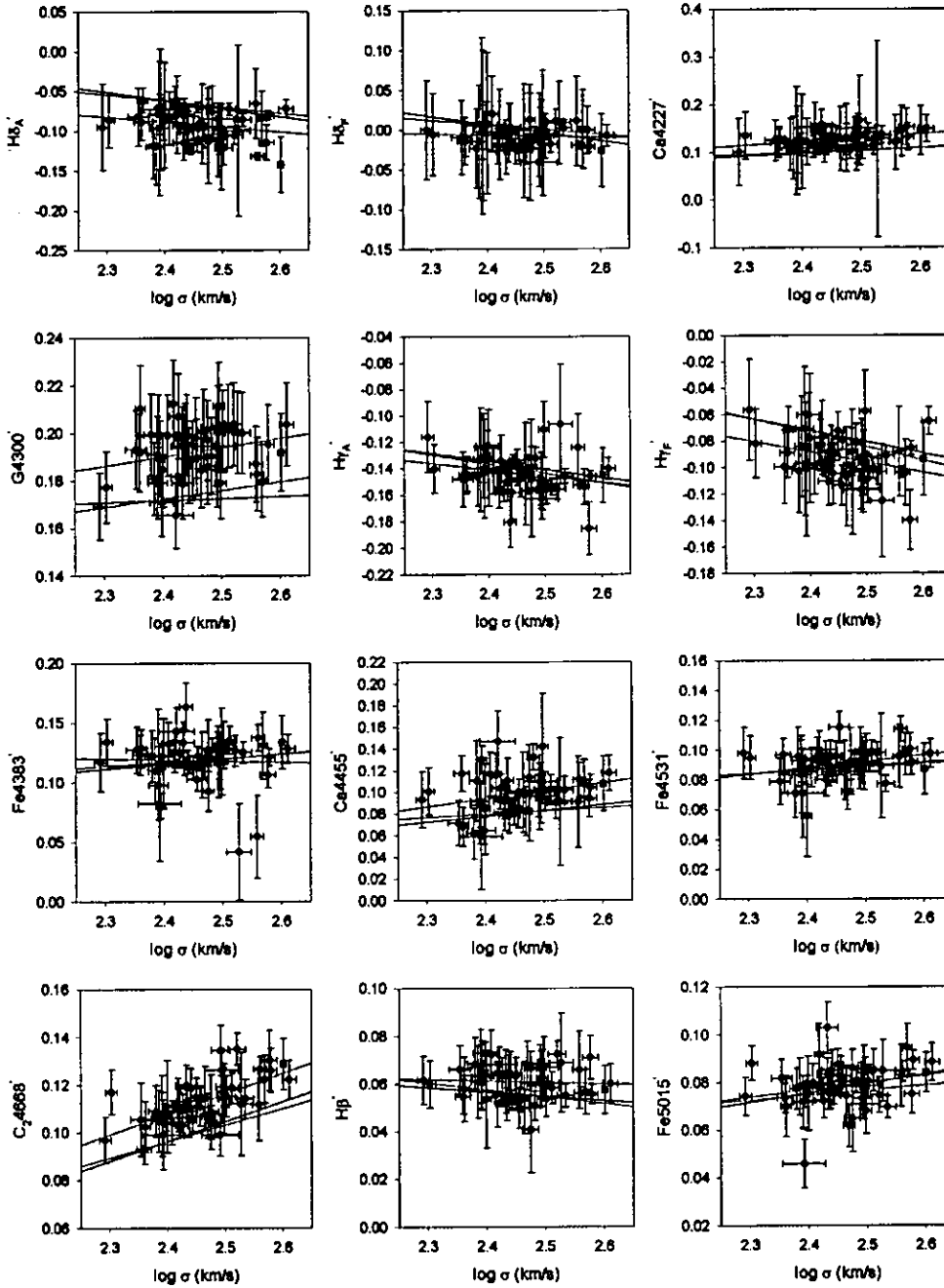
**Figure 3.** Central index measurements against velocity dispersion. The straight lines fitted to the BCG data are in red. The blue lines denote the relations found for the SB06 elliptical sample in the same mass range, and the green line the relations for the complete SB06 elliptical sample (high- and low-density samples combined).

relations per index were derived by SB06: one for ellipticals in a higher density environment, and one for ellipticals in a lower density environment. Here, both the higher and lower density samples are combined for comparison with the BCG data, since some of the BCGs are in Virgo-equivalent environments. As mentioned in Appendix B, five galaxies were in common with SB06. Four of those are in the higher density sample and one in the lower density sample. The BCG data are spread over a narrower range in velocity dispersion ($\log \sigma = 2.3$ to $2.6$ km s$^{-1}$) than the SB06 sample ($\log \sigma = 1.4$ to $2.6$ km s$^{-1}$), which meant that their slopes could possibly be heavily influenced by the lower velocity dispersion galaxies. The velocity dispersion distributions of the two samples

are shown in Fig. 5. We performed a Kolmogorov–Smirnov test on the velocity dispersion distributions of the two samples within the $\log \sigma = 2.3$ to $2.6$ km s$^{-1}$ range, where the null hypothesis is that the distributions were drawn from an identical parent population. Within this limited range, the two velocity dispersion distributions are consistent (the test value is $0.260$, where a test value larger than $D = 0.290$ indicates that the two samples compared are significantly different from each other at the 95 per cent confidence level). New relationships between the indices and velocity dispersion were derived for the SB06 sample to compare with the BCG data, only including the elliptical galaxies in the same mass range and excluding the five known BCGs. These new relations and their errors,
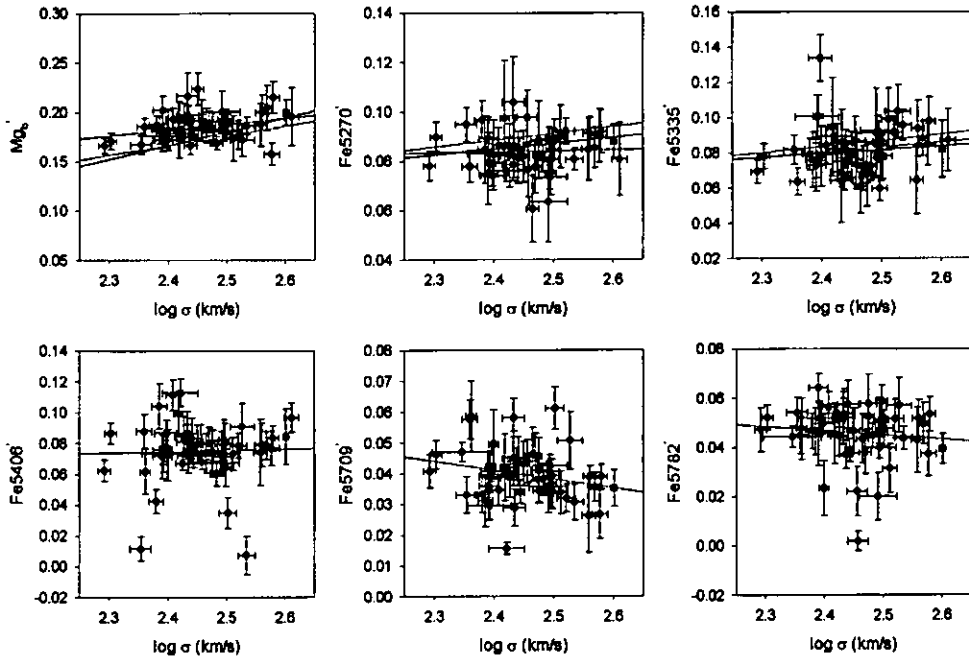
**Figure 4.** Central index measurements against velocity dispersion. The lines are as in Fig. 3.

derived using a subsample of 45 galaxies from SB06, are given in Table 1. Two relations derived for the SB06 sample are shown in Figs 3 and 4: the relation found for the SB06 elliptical sample in the same mass range (blue line), as well as the relation for the complete SB06 elliptical sample (green line). Both lines are for the high- and low-density samples combined.

Most of the fitted relations agree with those of elliptical galaxies. The only indices where a notable difference is detected are G4300, Ca4455 and $C_2$4668 where the zero points of the BCG data are higher than for the SB06 elliptical data. For Ca4455 and $C_2$4668,

this is explained by the offsets applied to the data to transform it on to the Lick system. But, this does not explain the discrepancy in the G4300 index. Thus, there are no significant discrepancies between the index–velocity dispersion relations of the BCG data and that of normal ellipticals in the same mass range, with the exception of G4300.

We calculate the intrinsic scatter (not explained by the errors) for both the BCGs and the SB06 elliptical sample in the mass range considered here. All the indices, for which the intrinsic scatter around the slope could be calculated for both samples, showed

**Table 1.** Parameters of the indices against velocity dispersion comparison between the BCGs and elliptical galaxies. $T$-tests were run on all the slopes to assess if a real slope was present or if $b = 0$ (as a null hypothesis). A $t$ value larger than 1.96 means that there is a true correlation between the variables ($b \neq 0$), at a 95 per cent confidence level. $P$ is the probability of being wrong in concluding that there is a true correlation (i.e. the probability of falsely rejecting the null hypothesis). The average index measurements (mean ± Std err) for the BCGs are also given.

| Index | BCG Galaxies | | | | | Ellipticals | |
|---|---|---|---|---|---|---|---|
| | $a \pm$ Std err($a$) | $b \pm$ Std err($b$) | $t$ | $P$ | Mean ± Std err | $a \pm$ Std err($a$) | $b \pm$ Std err($b$) |
| H$\delta'_A$ | $0.0598 \pm 0.0903$ | $-0.0620 \pm 0.0368$ | 1.687 | 0.098 | $-0.093 \pm 0.020$ | $0.184 \pm 0.016$ | $-0.102 \pm 0.007$ |
| H$\delta'_F$ | $0.0280 \pm 0.0592$ | $-0.0145 \pm 0.0241$ | 0.603 | 0.550 | $-0.008 \pm 0.016$ | $0.251 \pm 0.018$ | $-0.102 \pm 0.008$ |
| Ca4227$'$ | $-0.0700 \pm 0.0681$ | $0.0800 \pm 0.0277$ | 2.887 | 0.006 | $0.127 \pm 0.016$ | $-0.044 \pm 0.015$ | $0.059 \pm 0.007$ |
| G4300$'$ | $0.0973 \pm 0.0500$ | $0.0385 \pm 0.0204$ | 1.893 | 0.065 | $0.192 \pm 0.011$ | $0.152 \pm 0.016$ | $0.008 \pm 0.007$ |
| H$\gamma'_A$ | $-0.0261 \pm 0.0669$ | $-0.0479 \pm 0.0272$ | 1.758 | 0.085 | $-0.144 \pm 0.015$ | $0.009 \pm 0.017$ | $-0.060 \pm 0.007$ |
| H$\gamma'_F$ | $0.0991 \pm 0.0746$ | $-0.0781 \pm 0.0304$ | 2.570 | 0.013 | $-0.093 \pm 0.017$ | $0.135 \pm 0.023$ | $-0.086 \pm 0.010$ |
| Fe4383$'$ | $0.1403 \pm 0.0950$ | $-0.0091 \pm 0.0387$ | 0.235 | 0.815 | $0.118 \pm 0.020$ | $0.014 \pm 0.008$ | $0.042 \pm 0.003$ |
| Ca4455$'$ | $-0.0826 \pm 0.0843$ | $0.0735 \pm 0.0343$ | 2.142 | 0.037 | $0.098 \pm 0.019$ | $-0.049 \pm 0.009$ | $0.053 \pm 0.004$ |
| Fe4531$'$ | $-0.0140 \pm 0.0460$ | $0.0424 \pm 0.0187$ | 2.266 | 0.028 | $0.090 \pm 0.010$ | $0.027 \pm 0.005$ | $0.025 \pm 0.002$ |
| $C_2$4668$'$ | $-0.0985 \pm 0.0334$ | $0.0859 \pm 0.0136$ | 6.317 | <0.001 | $0.113 \pm 0.009$ | $-0.103 \pm 0.011$ | $0.083 \pm 0.005$ |
| H$\beta'$ | $0.0754 \pm 0.0327$ | $-0.0060 \pm 0.0133$ | 0.448 | 0.656 | $0.061 \pm 0.001$ | $0.100 \pm 0.012$ | $-0.018 \pm 0.005$ |
| Fe5015$'$ | $0.0035 \pm 0.0413$ | $0.0306 \pm 0.0168$ | 1.819 | 0.075 | $0.079 \pm 0.010$ | $-0.018 \pm 0.013$ | $0.039 \pm 0.006$ |
| Mg$'_b$ | $0.0405 \pm 0.0606$ | $0.0588 \pm 0.0247$ | 2.383 | 0.021 | $0.185 \pm 0.014$ | $-0.169 \pm 0.015$ | $0.140 \pm 0.007$ |
| Fe5270$'$ | $0.0738 \pm 0.0396$ | $0.0041 \pm 0.0161$ | 0.253 | 0.801 | $0.084 \pm 0.008$ | $0.029 \pm 0.007$ | $0.023 \pm 0.003$ |
| Fe5335$'$ | $0.0128 \pm 0.0632$ | $0.0281 \pm 0.0257$ | 1.093 | 0.280 | $0.082 \pm 0.014$ | $0.030 \pm 0.009$ | $0.021 \pm 0.004$ |
| Fe5406$'$ | $0.0545 \pm 0.0913$ | $0.0084 \pm 0.0372$ | 0.225 | 0.823 | $0.075 \pm 0.019$ | | |
| Fe5709$'$ | $0.1109 \pm 0.0401$ | $-0.0291 \pm 0.0163$ | 1.783 | 0.081 | $0.040 \pm 0.009$ | | |
| Fe5782$'$ | $0.0877 \pm 0.0517$ | $-0.0171 \pm 0.0210$ | 0.812 | 0.421 | $0.046 \pm 0.011$ | | |
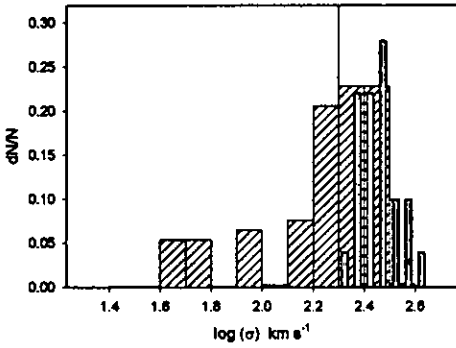
**Figure 5.** The velocity dispersion distributions of the complete SB06 (red) and the BCG sample (cyan). The vertical line indicates the lower limit in velocity dispersion (log $\sigma = 2.3$ km s$^{-1}$) of the SB06 subsample used here for comparison.

that the BCGs are intrinsically more scattered than the ellipticals (column 5 compared to column 6 in Table 2). This might indicate that the BCGs are more affected by properties other than mass, than elliptical galaxies over this mass range.

# 4 DERIVATION OF LUMINOSITY-WEIGHTED PROPERTIES

To calculate the ages, metallicities ([Z/H]) and $\alpha$-enhancement ratios ([E/Fe]), we compare our derived line-strength indices with the predictions of Thomas, Maraston & Bender (2003) and Thomas, Maraston & Korn (2004). These models are based on the evolutionary population synthesis models of Maraston (1998, 2005). Variations of the indices with chemical partitions departing from solar are computed with the Tripicco & Bell (1995) and Korn et al. (2005) model atmospheres, with a slightly modified method from the one presented by Trager et al. (2000a). The models are presented for six different metallicities [Z/H] $= -2.25, -1.35, -0.33, 0.0, 0.35,$ 0.67, ages between 1 and 15 Gyr, evenly spaced in logarithmic steps of 0.025, and [E/Fe] $= 0.0, 0.3$ and 0.5. The 'E' group contains O, Ne, Mg, Si, S, Ar, Ca, Ti, Na and N. The models are computed at constant metallicity in such a way that an increase in the 'E' group is compensated by a decrease of the abundances of the elements Fe and Cr (see Thomas et al. 2003; Trager et al. 2000a for a more detailed discussion), because the total metallicity is dominated by oxygen (included in the E group).

Ages, [Z/H] and [E/Fe], were derived using the indices $\langle$Fe$\rangle^2$, H$\beta$ and Mg$_b$. We started by interpolating the model grids in increments of 0.05 in [Z/H] and [E/Fe] and 0.1 dex in age. Then, we applied a $\chi^2$ technique to find the combination of SSP that best reproduced the four indices simultaneously. Errors in the parameters were calculated performing 50 Monte Carlo simulations in which, each time, the indices were displaced by an amount given by a Gaussian probability distribution with a width equal to the errors on these indices.

All SSP parameter results are shown in Table 3. The errors for the galaxy PGC026269 are unusually high and, therefore, this galaxy is excluded from further analysis. As mentioned before, five galaxies (Leda094683, NGC 7649, NGC 6166, PGC025714 and PGC030223) showed skyline or CCD gap residuals in Mg$_b$, Fe5270 or Fe5335. Hence, the derived parameters using these indices were deemed unreliable for these galaxies, and they were

also excluded from the SSP analysis. Thus, with NGC 6047 and NGC 4946 (the two ordinary elliptical galaxies) already excluded, our final sample for which SSP analyses are carried out, contains 43 BCGs. Index–index plots are shown in Fig. 6.[3]

Two galaxies (ESO444-046 and NGC 0533 – neither of which show nebular emission) reached the upper age limit of the Thomas et al. models, and 11 galaxies have log (age) $< 0.8$ Gyr: ESO202-043, ESO346-003, ESO541-013, GSC555700266, IC1101, NGC 0541, NGC 7012, NGC 7597, PGC044257, PGC071807 and PGC072804. Emphasis is placed on the fact that these are SSP-equivalent ages. If a galaxy has experienced a more complicated SFH than a single burst of star formation, then the age derived here will be biased towards the age of the younger stars and not the dominating stellar populations by mass (Li & Han 2007). On the other hand, the SSP metallicity will be more biased to the metallicity of the old population, depending on the mass fraction of the burst (Sánchez-Blázquez et al. 2007; Serra & Trager 2007). Thus, the derived age should not be interpreted as the time that passed since formation of most stars in that galaxy. However, Balmer-line-based ages allow us to detect minor amounts of recent star formation in generally old galaxies. Several authors (Maraston et al. 2003; Trager et al. 2005) pointed out that another complication to the age and metallicity analysis of non-star-forming galaxies is the possible presence of hot populations of stars not included in the models (such as blue stragglers and horizontal branch stars). However, Trager et al. (2005) showed that these stars affect the inferred metallicities more than ages.

Fig. 7 shows the age, [Z/H] and [E/Fe] distributions for our sample of BCGs. We compare the observed scatter with that expected from the errors (see Table 4) to investigate if the distributions are compatible with a single value of age, [Z/H] and [E/Fe] for all the BCGs. We found that, while the errors in the age explain the observed scatter, the scatter in [Z/H] and [E/Fe] is much larger, possibly indicating a real variation in the mean stellar abundances of these galaxies.

## 4.1 SSP-equivalent parameters: comparison with ellipticals

Several authors have found a decreasing amount of scatter in the age and metallicity parameters with increasing velocity dispersion for early-type galaxies (Caldwell et al. 2003; Nelan et al. 2005; Sánchez-Blázquez et al. 2006b). Thus, more massive elliptical galaxies seem to be a much more homogeneous family of galaxies than less massive ones. Is this also true for the galaxies in the centre of the clusters?

Fig. 7 compares the distribution of SSP-equivalent parameters with that of ordinary ellipticals from T05 and SB06. To avoid artificial offsets between samples due to the use of different techniques to calculate the SSP parameters, we recalculated these parameters using exactly the same indices and method as used for our sample of BCGs. Nevertheless, small offsets can remain due the use of different apertures. The T05 central indices were measured within 1/10 of the effective radius, and the SB06 indices within an equivalent aperture of 4 arcsec at a redshift of $z = 0.016$. The uncertainties in assuming gradients to perform these aperture corrections are large because of the great variety of gradients found for elliptical galaxies. These gradients seem to be uncorrelated with other galaxy properties, such as mass, and mean gradients are usually calculated (Sánchez-Blázquez et al. 2009). For the samples

---

[2] Where $\langle$Fe$\rangle$ is defined as (Fe5270+Fe5335)/2 (González 1993).

[3] [Mg(Fe)] $= \sqrt{\text{Mg}_b \times \langle$Fe$\rangle}$.

used here, which all contain nearby galaxies, these aperture differences produce a negligible effect in the indices, and hence, given the uncertainties in the aperture corrections, these corrections were not applied here. From the T05 and SB06 studies, we select those galaxies with central velocity dispersions between $\log \sigma = 2.3$ and 2.6 km s$^{-1}$ to match the same range as in our BCGs. We also excluded their known BCGs (four in T05 and five in SB06). This left subsamples of 65 and 45 elliptical galaxies from T05 and SB06, respectively.

Systematic differences were detected between the two samples of ordinary elliptical galaxies. The T05 and SB06 samples used here have 19 galaxies in common. In addition, the three Coma BCGs (NGC 4839, NGC 4874 and NGC 4889) form part of the BCG sample and the original T05 and SB06 samples. Thus, offsets in H$\beta$, Mg$_b$ and $\langle$Fe$\rangle$ could be derived between the two samples of elliptical galaxies used. The indices of the three Coma BCGs measured here were in better agreement with the measurements from SB06 than from T05. For example, the average difference between the H$\beta$ measurements was 0.064 Å compared to the SB06 sample and 0.35 Å compared to the T05 sample. Thus, the following offsets in the indices (derived using the galaxies in common) were applied to the data from T05: H$\beta$ $-0.158$ Å; Mg$_b$ $-0.139$; $\langle$Fe$\rangle$ $+0.013$ before the derivation of the SSP parameters. This normalization placed the two elliptical samples in very good agreement, as confirmed by a Kolmogorov–Smirnov test (see the last column of Table 5, described below).

We explore possible differences in the distributions of the SSP parameters derived for BCGs and elliptical galaxies by performing a Kolmogorov–Smirnov test on the three samples (see Table 5), where the null hypothesis is that the distributions were drawn from an identical parent population. We comment on the results in the following paragraphs.

*Age.* As can be seen in Fig. 7, and confirmed in Table 5, the peaks and dispersions of the age distributions of all three samples coincide. Nevertheless, the BCG age distribution shows a second,

smaller peak at $\log$ (age) $\sim 0.65$, which although not statistically significant, is absent in the elliptical galaxy distributions.

*Metallicity.* The models provide an estimate of [Z/H] which includes all the elements heavier than H and He. The distribution of the BCG metallicities peaks at a higher value (average [Z/H] $= 0.31 \pm 0.03$) than the ordinary ellipticals (average SB06 [Z/H] $= 0.24 \pm 0.02$; T05 [Z/H] $= 0.21 \pm 0.02$). Table 5 confirms that the BCG metallicity distribution is significantly different from both elliptical samples.

*$\alpha$-enhancement.* The [E/Fe] ratio is often used as an indicator for the time-scales of star formation (Worthey, Faber & González 1992; Trager 2006), as it serves as a crude estimation of the ratio of Type II supernova (SNII) to Type Ia supernova (SNIa). The high values of [E/Fe] detected in massive early-type galaxies has been commonly interpreted in terms of star formation time-scales, i.e. the star formation stop before SNIa has time to contribute significantly with their products (Tinsley 1980). However, a high [E/Fe] can also be the consequence of differences in the initial mass function (IMF) where it is skewed towards massive stars, differences in the binary fractions or to selective winds that drive most of the Fe-group elements to the intracluster medium.

Fig. 7 shows that the BCG sample has slightly higher $\alpha$-enhancement values (average BCG [E/Fe] $= 0.41 \pm 0.01$; SB06 [E/Fe] $= 0.30 \pm 0.02$; T05 [E/Fe] $= 0.33 \pm 0.02$). Table 5 confirms that the BCG $\alpha$-enhancement distribution is significantly different from both elliptical samples.

This result agrees with that of Von der Linden et al. (2007), who studied brightest group and cluster galaxies in the SDSS. They found that at the same stellar mass, the stellar populations of BCGs and non-BCGs are similar with the exception of their $\alpha$-element enhancement ratios, which were found to be higher in BCGs. These authors interpret their results in terms of star formation time-scales (star formation occurring in shorter time-scales in the BCGs than in ellipticals), but it is possible that other mechanisms, related to the cluster environment and the privileged position of BCGs are

**Table 2.** Scatter of the index measurements (in magnitudes) compared to that expected from the errors. $\sigma_{Std}$ is the standard deviation on the mean index value, $\sigma_{exp}$ is the standard deviation expected from the mean errors on the index values, and $\sigma_{res} = \sqrt{\sigma_{Std}^2 - \sigma_{exp}^2}$ is the residual scatter not explained by the errors on the index measurements. The indices marked with $*$ have $\sigma_{Std} \leq \sigma_{exp}$. The first three columns are for the scatter in the BCG data points. The last two columns are for the intrinsic scatter around the slope for the BCG and elliptical data, respectively, over the same mass range.

| Index | Scatter in BCG data points | | | Scatter around the slope (BCGs) | Scatter around the slope (ellipticals) |
|---|---|---|---|---|---|
| | $\sigma_{Std}$ | $\sigma_{exp}$ | $\sigma_{res} = \sqrt{\sigma_{Std}^2 - \sigma_{exp}^2}$ | $\sigma_{res}$ | $\sigma_{res}$ |
| H$\delta'_A$ | 0.020 | 0.029 | $*$ | 0.023 | 0.005 |
| H$\delta'_F$ | 0.016 | 0.036 | $*$ | $*$ | 0.006 |
| Ca4227' | 0.016 | 0.042 | $*$ | $*$ | 0.006 |
| G4300' | 0.011 | 0.016 | $*$ | 0.013 | 0.006 |
| H$\gamma'_A$ | 0.015 | 0.017 | $*$ | 0.021 | 0.006 |
| H$\gamma'_F$ | 0.017 | 0.022 | $*$ | 0.021 | 0.008 |
| Fe4383' | 0.020 | 0.019 | 0.006 | 0.034 | $*$ |
| Ca4455' | 0.019 | 0.023 | $*$ | 0.025 | $*$ |
| Fe4531' | 0.010 | 0.016 | $*$ | 0.010 | $*$ |
| C$_2$ 4668' | 0.009 | 0.010 | $*$ | 0.009 | $*$ |
| H$\beta'$ | 0.001 | 0.010 | $*$ | 0.009 | 0.004 |
| Fe5015' | 0.010 | 0.009 | 0.004 | 0.014 | 0.005 |
| Mg$'_b$ | 0.014 | 0.014 | $*$ | 0.020 | $*$ |
| Fe5270' | 0.008 | 0.009 | $*$ | 0.013 | $*$ |
| Fe5335' | 0.014 | 0.013 | 0.005 | 0.022 | $*$ |
| Fe5406' | 0.019 | 0.011 | 0.015 | 0.036 | $*$ |
| Fe5709' | 0.009 | 0.006 | 0.007 | 0.015 | |
| Fe5782' | 0.011 | 0.008 | 0.008 | 0.019 | |

**Figure 6.** Index–index plots. The grids correspond to the Thomas et al. (2003) models, with $\alpha$-enhancement [E/Fe] = 0 (solid) and 0.3 (dashed). Age lines are 15, 12, 8, 5 and 3 Gyr (from the bottom) and metallicities from [Z/H] = 0.80 decreasing in steps of 0.25 dex towards the left. All index measurements are in Å. The galaxy point which lies below the H$\beta$ grid is that of NGC 0533, which reached the upper age limit of the models but does not contain emission.

**Table 3.** Central values for the SSP-equivalent parameters derived using H$\beta$, Mg$_b$, Fe5270 and Fe5335.

| Galaxy | $\log(\sigma)$ (km s$^{-1}$) | $\log$ (age) (Gyr) | [Z/H] | [E/Fe] |
|---|---|---|---|---|
| ESO146-028 | 299 ± 3 | 0.97 ± 0.18 | −0.12 ± 0.06 | 0.60 ± 0.03 |
| ESO202-043 | 256 ± 3 | 0.58 ± 0.18 | 0.58 ± 0.06 | 0.45 ± 0.03 |
| ESO303-005 | 276 ± 5 | 0.81 ± 0.23 | 0.34 ± 0.05 | 0.41 ± 0.03 |
| ESO346-003 | 226 ± 4 | 0.63 ± 0.43 | 0.43 ± 0.09 | 0.30 ± 0.03 |
| ESO349-010 | 282 ± 3 | 0.89 ± 0.22 | 0.21 ± 0.08 | 0.30 ± 0.05 |
| ESO444-046 | 292 ± 3 | 1.25 ± 0.20 | −0.18 ± 0.12 | 0.59 ± 0.05 |
| ESO488-027 | 248 ± 2 | 0.85 ± 0.13 | 0.42 ± 0.08 | 0.32 ± 0.03 |
| ESO541-013 | 295 ± 3 | 0.75 ± 0.38 | 0.30 ± 0.09 | 0.49 ± 0.04 |
| ESO552-020 | 229 ± 3 | 1.12 ± 0.19 | 0.02 ± 0.07 | 0.48 ± 0.03 |
| GSC555700266 | 312 ± 9 | 0.66 ± 0.37 | 0.40 ± 0.05 | 0.41 ± 0.03 |
| IC1101 | 378 ± 5 | 0.70 ± 0.15 | 0.41 ± 0.08 | 0.27 ± 0.04 |
| IC1633 | 400 ± 2 | 0.94 ± 0.19 | 0.38 ± 0.06 | 0.44 ± 0.04 |
| IC4765 | 286 ± 5 | 1.01 ± 0.23 | 0.36 ± 0.07 | 0.30 ± 0.04 |
| IC5358 | 243 ± 3 | 0.92 ± 0.32 | 0.28 ± 0.10 | 0.41 ± 0.05 |
| MCG-02-12-039 | 271 ± 5 | 1.05 ± 0.21 | 0.14 ± 0.07 | 0.51 ± 0.03 |
| NGC 0533 | 299 ± 4 | 1.25 ± 0.10 | 0.14 ± 0.10 | 0.38 ± 0.05 |
| NGC 0541 | 246 ± 4 | 0.66 ± 0.55 | 0.37 ± 0.08 | 0.38 ± 0.04 |
| NGC 1399 | 371 ± 3 | 0.93 ± 0.10 | 0.42 ± 0.09 | 0.45 ± 0.05 |
| NGC 1713 | 251 ± 2 | 1.03 ± 0.34 | 0.19 ± 0.11 | 0.39 ± 0.07 |
| NGC 2832 | 364 ± 4 | 0.93 ± 0.02 | 0.48 ± 0.06 | 0.38 ± 0.04 |
| NGC 3311 | 196 ± 2 | 0.94 ± 0.27 | 0.12 ± 0.07 | 0.40 ± 0.03 |
| NGC 3842 | 287 ± 5 | 1.10 ± 0.17 | 0.11 ± 0.09 | 0.47 ± 0.05 |
| NGC 4839 | 278 ± 2 | 1.07 ± 0.12 | 0.13 ± 0.05 | 0.35 ± 0.03 |
| NGC 4874 | 267 ± 4 | 0.89 ± 0.12 | 0.35 ± 0.05 | 0.46 ± 0.05 |
| NGC 4889 | 380 ± 4 | 0.92 ± 0.04 | 0.57 ± 0.05 | 0.42 ± 0.04 |
| NGC 6034 | 325 ± 4 | 0.92 ± 0.07 | 0.42 ± 0.10 | 0.26 ± 0.06 |
| NGC 6086 | 318 ± 5 | 1.00 ± 0.14 | 0.28 ± 0.07 | 0.39 ± 0.04 |
| NGC 6160 | 266 ± 3 | 1.05 ± 0.06 | 0.19 ± 0.04 | 0.32 ± 0.02 |
| NGC 6173 | 304 ± 3 | 0.90 ± 0.14 | 0.20 ± 0.05 | 0.39 ± 0.02 |
| NGC 6269 | 343 ± 5 | 0.95 ± 0.08 | 0.36 ± 0.04 | 0.36 ± 0.03 |
| NGC 7012 | 240 ± 3 | 0.69 ± 0.19 | 0.51 ± 0.08 | 0.39 ± 0.03 |
| NGC 7597 | 264 ± 8 | 0.67 ± 0.29 | 0.40 ± 0.05 | 0.40 ± 0.02 |
| NGC 7647 | 271 ± 5 | 0.86 ± 0.11 | 0.48 ± 0.12 | 0.54 ± 0.07 |
| NGC 7720 | 409 ± 5 | 0.92 ± 0.13 | 0.36 ± 0.07 | 0.44 ± 0.07 |
| NGC 7768 | 272 ± 5 | 1.02 ± 0.24 | 0.29 ± 0.10 | 0.38 ± 0.04 |
| PGC004072 | 313 ± 3 | 0.90 ± 0.20 | 0.31 ± 0.07 | 0.45 ± 0.04 |
| PGC044257 | 247 ± 9 | 0.63 ± 0.19 | 0.50 ± 0.10 | 0.31 ± 0.04 |
| PGC071807 | 315 ± 3 | 0.63 ± 0.40 | 0.42 ± 0.09 | 0.46 ± 0.05 |
| PGC072804 | 311 ± 5 | 0.69 ± 0.37 | 0.48 ± 0.05 | 0.38 ± 0.03 |
| UGC00579 | 246 ± 4 | 0.91 ± 0.27 | 0.26 ± 0.10 | 0.56 ± 0.04 |
| UGC02232 | 314 ± 4 | 0.99 ± 0.17 | 0.13 ± 0.06 | 0.54 ± 0.03 |
| UGC05515 | 362 ± 4 | 0.88 ± 0.34 | 0.25 ± 0.11 | 0.50 ± 0.07 |
| UGC10143 | 262 ± 2 | 0.93 ± 0.21 | 0.45 ± 0.09 | 0.28 ± 0.06 |
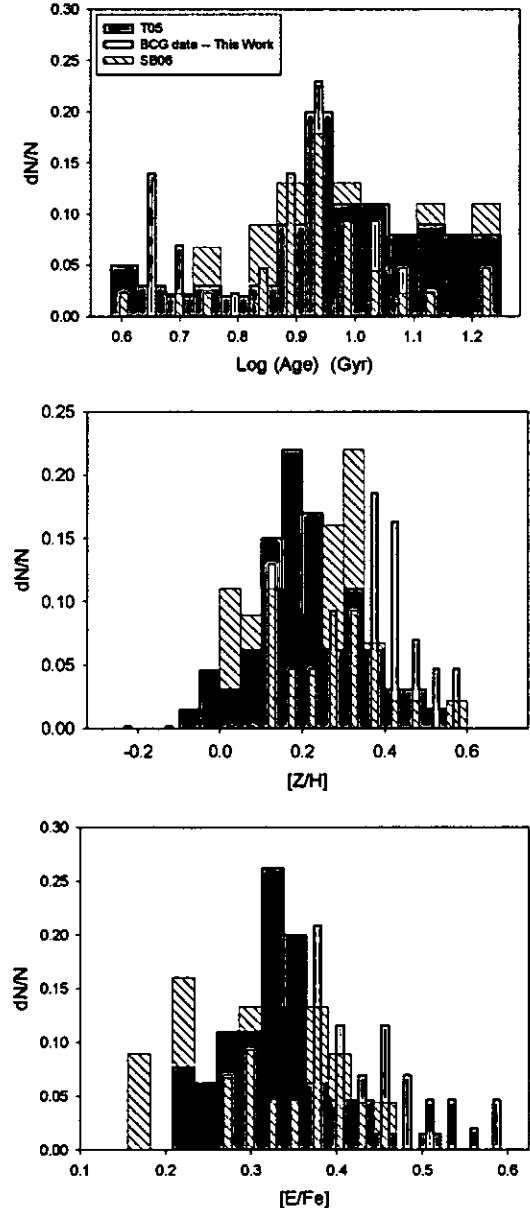
**Figure 7.** Distributions of the SSP-equivalent parameters of the BCGs (cyan), compared to that of ordinary ellipticals (T05 – grey; SB06 – red), over the same mass range.

**Table 4.** Scatter of the SSP parameters compared to that expected from the errors. $\sigma_{Std}$ is the standard deviation on the mean SSP-parameter value, $\sigma_{exp}$ is the standard deviation expected from the mean errors on the parameter values, and $\sigma_{res} = \sqrt{\sigma_{Std}^2 - \sigma_{exp}^2}$ is the residual scatter not explained by the errors on the parameters.

| Parameter | $\sigma_{Std}$ | $\sigma_{exp}$ | $\sigma_{res} = \sqrt{\sigma_{Std}^2 - \sigma_{exp}^2}$ |
|---|---|---|---|
| log (age) | 0.1616 | 0.2016 | * |
| [Z/H] | 0.1669 | 0.0740 | 0.1496 |
| [E/Fe] | 0.0849 | 0.0393 | 0.0752 |

**Table 5.** Kolmogorov–Smirnov tests on the SSP parameter distributions. The critical value of the statistical test, at a 95 per cent confidence level, is $D = 1.36\sqrt{\frac{m+n}{m \times n}}$, where $m$ and $n$ are the number of galaxies in the sample. Thus, if the test value is larger than $D$ (given in the heading of the table for the three different comparisons), then the samples compared are significantly different from each other at a 95 per cent confidence level.

| | BCGs compared to SB06 $D = 0.290$ | BCGs compared to T05 $D = 0.267$ | SB06 compared to T05 $D = 0.264$ |
|---|---|---|---|
| log (age) | 0.197 | 0.236 | 0.097 |
| [Z/H] | 0.378 | 0.390 | 0.203 |
| [E/Fe] | 0.440 | 0.560 | 0.122 |

acting to influence their chemical abundance ratios. Other scenarios causing higher [E/Fe] values such as differences in the IMF, or in the binary fractions, or selective winds cannot be conclusively eliminated.

# 5 CORRELATION BETWEEN KINEMATICS AND DERIVED PROPERTIES

Recent studies have shown that the lack of rotation found in massive ellipticals is compatible with the idea that these objects formed through dissipationless mergers (e.g. Naab & Burkert 2003; Boylan-Kolchin et al. 2006). The remnants left by mergers with or without dissipation are expected to differ in their kinematical structure. For example, in a merger where dissipationless processes dominate, the remnant will show little or no rotation, whereas rotation is expected in remnants left by mergers involving gas (Paper 1, and references therein). In Paper 1, we showed that our sample of BCGs have great variety in their kinematical and dynamical properties, and that a number of BCGs show clear rotation contrary to what is expected if all BCGs formed by radial accretion of satellites without gas. If rotating BCGs are the consequence of dissipational mergers, and these happened relatively recently, we would expect younger ages for these systems. As numerical simulations have shown, when the gas is present in merging systems, it is very effectively funnelled towards the centre of the remnant where star formation occurs (e.g. Mihos & Hernquist 1994).

Fig. 8 shows the anisotropy parameters (where $V_{max}$ is half the difference between the peaks of the rotation curve) of the BCGs for which major axis spectra were observed against the ages. No real difference is visible in the ages of rotating and non-rotating galaxies, and a whole range of ages were found for galaxies showing a lack
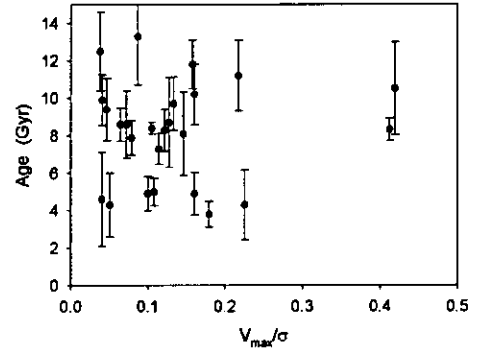


**Figure 8.** The derived ages versus anisotropy parameters for the BCGs (major axis data).
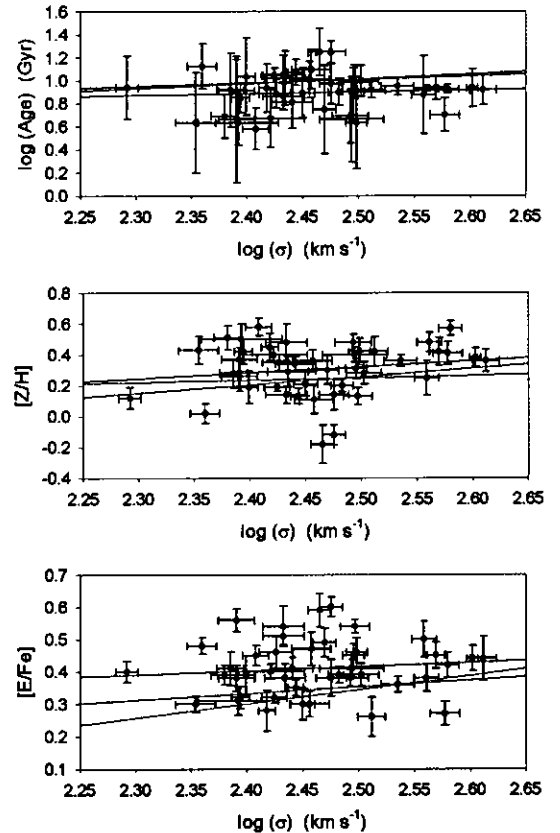


**Figure 9.** Correlations between derived SSP-equivalent parameters and velocity dispersions. The blue line denotes the correlation found for the BCGs whereas the red and green line denotes the correlations found for the samples of T05 and SB06, respectively, over the same mass range and using the same SSP models and procedure.

of rotation. In fact, the two galaxies rotating the fastest are amongst the oldest in our sample.

Fig. 9 shows the derived SSP parameters log (age), [Z/H] and [E/Fe] against the central velocity dispersion. To test for the presence of correlations, linear relations of the form $P = a + b \times \log \sigma$ were fitted to the BCG data and $t$-tests were performed to test the null hypothesis $b = 0$ (see Table 6). The $t$ and $P$ values have the same meaning as previously (in Table 1). The relations derived for the BCG data are compared with those derived for the ordinary elliptical galaxy samples of T05 (red line) and SB06 (green line) in Fig. 9. The SSP parameters of the elliptical samples were

**Table 6.** SSP parameters: best-fitting straight-line relations with velocity dispersions derived for BCGs.

| Relationship | $t$ | $P$ |
|---|---|---|
| $\log(\text{age}) = 0.530 + 0.148 \log \sigma$ | 0.461 | 0.648 |
| $[Z/H] = -0.643 + 0.386 \log \sigma$ | 1.176 | 0.246 |
| $[E/Fe] = 0.098 + 0.127 \log \sigma$ | 0.755 | 0.455 |

recalculated using H$\beta$, Mg$_b$, Fe5270 and Fe5335 with the KMT models in exactly the same way as for the BCG data.

It can be seen in Fig. 9 and Table 6 that we do not find significant relations between the derived SSP parameters and the velocity dispersions in our sample of galaxies, although the slopes are similar to that of normal elliptical galaxies over the same mass range. This result, in principle, contrasts with the relationships obtained for normal elliptical galaxies, for which several authors have found an increase in the mean age with the velocity dispersion (T05; Nelan et al. 2005; Sánchez-Blázquez et al. 2006b). However, the mass range spanned by our sample is too narrow to be able to see the differences. Even if the BCG were simply the extension towards the massive end of normal elliptical galaxies, we would not be able to detect significant correlations in this mass range. Indeed, there are virtually no differences between the relationship obtained for the BCGs and those for the two normal elliptical samples shown in Fig. 9. Several authors have also found the existence of a positive correlation between the degree of $\alpha$-enhancement in the central parts of early-type galaxies and velocity dispersion (Worthey et al. 1992; Kuntschner 2000; Trager et al. 2000b; Sánchez-Blázquez et al. 2007), which is not visible here because of the narrow mass range. Fig. 9 again shows that the BCGs have, on average, higher [E/Fe] values than the ellipticals.

We also investigated the possibility of correlations with the SSP parameters when the total magnitude is used instead of velocity dispersion. None of the derived parameters show a potential correlation with $K$-band magnitudes from 2MASS, and this was not investigated further.

*Other correlations: age–metallicity*

A strong age–metallicity anticorrelation was found for the BCG sample, but is likely to be an artefact of the degeneracy between age and metallicity since the errors on these stellar population parameters are not independent (Kuntschner et al. 2001). To check this for the present study, 50 Monte Carlo simulations were performed. The mean values of the indices were taken and moved randomly using a Gaussian distribution with a width equal to the typical error on the indices. The ages and metallicities were then derived with the same procedure used for the BCG data. The differences between the BCG data and the simulated data are marginal in both the slope of the best-fitting correlation as well as the standard deviation from the relation. Thus, the age–metallicity anticorrelation can almost entirely be explained by the correlation of the errors on the parameters. Table 4 also showed that there is no intrinsic scatter (other than expected from the errors) in the ages derived for the BCGs, whereas the metallicities do show inherent scatter.

# 6 CONTEXT OF THE ENVIRONMENT

Hierarchical models of galaxy formation predict that the formation of the central galaxy is closely connected with the evolution of the host cluster. In principle, this would not necessarily be reflected by

differences in the SFH, as stars might have formed before the formation – or assembly – of the real galaxy. However, it is interesting to investigate whether, and to what extent, the characteristics of the host cluster influence the stellar populations of the BCG.

The X-ray properties of the host clusters are given in Table 7. All the X-ray luminosity and temperature ($L_X$ and $T_X$) values are from spectra observed in the 0.1–2.4 keV band, and using the same cosmology namely $H_0 = 50\,\text{km}\,\text{s}^{-1}\,\text{Mpc}^{-1}$, $\Omega_m = 1$ and $\Omega_\Lambda = 0$.

## 6.1 Velocity dispersion – $\log L_X$

Cluster X-ray luminosity is directly proportional to the square of the density of the intracluster medium and thus provides a measure of environmental density (Reiprich & Bohringer 2002). We do not find a correlation between the X-ray luminosities of the clusters (i.e. density of the cluster) and the velocity dispersions of the BCGs (i.e. the mass of the BCG), as shown in Fig. 10. Brough et al. (2007) noted a weak trend (only $2\sigma$) between these two properties, in the sense that galaxies in higher density clusters are more massive. However, their sample consisted of only six galaxies. It can be seen from Fig. 10 that this correlation is not found when this much larger sample of BCGs is used. Nevertheless, it is well known that BCG luminosity does correlate with host cluster mass (Lin & Mohr 2004; Popesso et al. 2006; Hansen et al. 2007; Whiley et al. 2008).

## 6.2 Indices – $\log L_X$

Fig. 11 shows the relations of some of the central Lick/IDS indices measured in our sample of BCGs with the host cluster X-ray luminosity. We do not find any significant correlation for any of the indices. However, the plots of the Balmer lines against X-ray luminosity seem to suggest a break in the relationships at $\log L_X \sim 44\,\text{erg}\,\text{s}^{-1}$. For low-$L_X$ clusters, Balmer-line strengths seem to increase with X-ray luminosity. However, for clusters with X-ray luminosity greater than $\log L_X \sim 44\,\text{erg}\,\text{s}^{-1}$, this trend seems to reverse (with the exception of the most dense cluster). However, this is a weak trend, and not confirmed by the relationship between the derived age with cluster X-ray luminosity (not shown here). As discussed in the introduction, previous photometric studies reported different evolutionary histories in X-ray bright and dim clusters. Brough et al. (2002) places this break at $L_X = 1.9 \times 10^{44}\,\text{erg}\,\text{s}^{-1}$, and conclude that BCGs in high-$L_X$ clusters assemble their mass at $z > 1$ and have been passively evolving since, whereas BCGs in low-$L_X$ clusters appear to be in the process of assembling their mass. Fig. 11 suggests two different regimes in the cluster X-ray luminosity and the BCG line strengths, but this is not conclusive due to the scatter and large errors on the measurements.

Host cluster velocity dispersion data were also collected from the literature as shown in Table 7, and no clear correlations between host cluster velocity dispersion (indicative of the mass of the host cluster) and any of the derived parameters were found.

## 6.3 Cooling-flow clusters

A very interesting aspect in the evolution of BCGs is the influence of cluster cooling flows. Several studies reported examples of recent or ongoing star formation in BCGs hosted by cooling-flow clusters (Cardiel et al. 1998a; Crawford et al. 1999; McNamara et al. 2006; Edwards et al. 2007; O'Dea et al. 2008; Bildfell et al. 2008; Pipino et al. 2009). Cooling-flow information was collected from the literature as shown in Table 7. Fig. 12 shows the derived SSP

**Table 7.** X-ray properties and velocity dispersions of the host clusters for all 49 BCGs and two ellipticals. The $\sigma_{cluster}$ values are in km s$^{-1}$ and the projected distance between the galaxy and the cluster X-ray peak ($R_{off}$) is in Mpc.

| Galaxy | Cluster | $L_X \times 10^{44}$ (erg s$^{-1}$) | Ref. | $T_X$ (keV) | cooling flow | Ref. | $\sigma_{cluster}$ (km s$^{-1}$) | Ref. | $R_{off}$ (Mpc) | Ref. |
|---|---|---|---|---|---|---|---|---|---|---|
| ESO146-028 | RXCJ2228.8-6053 | 0.17 | b | – | – | – | – | – | 0.051 | cb |
| ESO202-043 | A S0479 | – | – | – | – | – | – | – | – | – |
| ESO303-005 | RBS521 | 0.79 | b | – | – | – | – | – | 0.010 | cb |
| ESO346-003 | A S1065 | 0.096 | r | – | – | – | – | – | 0.032 | cr |
| ESO349-010 | A4059 | 2.80 ± 0.06 | a | 3.5 | √ | e | 845 | w | 0.019 | e |
| ESO444-046 | A3558 | 6.56 ± 0.04 | a | 3.8 | X | e | 986 | w | 0.019 | e |
| ESO488-027 | A0548 | 0.21 | b | 2.4 | √ | w | 853 | w | ⋆ | cb |
| ESO541-013 | A0133 | 2.85 ± 0.04 | a | 3.8 | √ | w | 767 | w | 0.017 | e |
| ESO552-020 | CID 28 | 0.16 | b | – | – | – | – | – | 0.013 | cb |
| GSC555700266 | A1837 | 1.28 | b | 2.4 | √ | w | 596 | w | 0.020 | cb |
| IC1101 | A2029 | 17.07 ± 0.18 | a | 7.8 | √ | w | 786 | w | 0.131 | p |
| IC1633 | A2877 | 0.20 | b | 3.5 | X | w | 738 | w | 0.015 | cb |
| IC4765 | A S0805 | 0.03 | b | – | – | – | – | – | 0.007 | cb |
| IC5358 | A4038 | 1.92 ± 0.04 | a | – | √ | c | 891 | m | 0.002 | cb |
| Leda094683 | A1809 | – | – | 3.7 | √ | w | 249 | w | 0.044 | p |
| MCG-02-12-039 | A0496 | 3.77 ± 0.05 | a | 4.7 | √ | w, e | 705 | w | 0.031 | e |
| NGC 0533 | A0189B | 0.04 | b | – | – | – | – | – | 0.004 | cb |
| NGC 0541 | A0194 | 0.14 | b | 1.9 | X | w | 480 | w | 0.037 | cb |
| NGC 1399 | RBS454 | 0.08 ± 0.01 | a | – | X | c | 240 | w | <0.001 | cb |
| NGC 1713 | CID 27 | – | – | – | – | – | – | – | – | – |
| NGC 2832 | A0779 | 0.07 | b | 1.5 | √ | w | 503 | w | 0.038 | cl |
| NGC 3311 | A1060 | 0.56 ± 0.03 | a | 3.3 | √ | w | 608 | w | 0.015 | pe |
| NGC 3842 | A1367 | 1.20 ± 0.02 | a | 3.5 | X | w, e, g | 822 | w | 0.252 | e |
| NGC 4839 | A1656 | – | – | – | – | – | – | – | ⋆ | – |
| NGC 4874 | A1656 | 8.09 ± 0.19 | a | 8.0 | X | e, g | 1010 | w | 0.038 | cb |
| NGC 4889 | A1656 | 8.09 ± 0.19 | a | 8.0 | X | e, g | 1010 | w | 0.169 | e |
| NGC 4946 | A3526 | 1.19 ± 0.04 | a | – | – | – | – | – | not BCG | |
| NGC 6034 | A2151 | 0.98 | c | 3.5 | X | g | 827 | w | ⋆ | |
| NGC 6047 | A2151 | 0.98 | c | – | X | g | 827 | w | not BCG | |
| NGC 6086 | A2162 | – | – | – | X | g | 323 | s | 0.053 | cl |
| NGC 6160 | A2197 | 0.13 | c | 1.6 | √ | w, g | 564 | w | 0.017 | cc |
| NGC 6166 | A2199 | 4.20 ± 0.12 | a | 4.7 | √ | w, e, g | 794 | w | 0.007 | e |
| NGC 6173 | A2197 | – | – | – | – | – | – | – | ⋆ | – |
| NGC 6269 | AWM5 | 0.36 | c | – | – | – | – | – | 0.002 | cc |
| NGC 7012 | A S0921 | – | – | – | – | – | – | – | – | – |
| NGC 7597 | A2572 | 0.58 | c | – | – | – | 676 | st | 0.048 | cc |
| NGC 7647 | A2589 | 1.87 ± 0.04 | a | 3.7 | X | e | 500 | w | 0.073 | e |
| NGC 7649 | A2593 | – | – | 3.1 | X | w | 690 | w | 0.020 | cl |
| NGC 7720 | A2634 | 0.99 ± 0.03 | a | 3.4 | X | e, g | 744 | w | 0.018 | e |
| NGC 7768 | A2666 | – | – | 1.6 | X | g | 476 | w | 0.006 | cl |
| PGC004072 | A0151 | 0.99 | b | – | – | – | 715 | s | 0.006 | cb |
| PGC025714 | A0754 | 3.97 ± 0.11 | a | 8.7 | X | e | 747 | w | 0.328 | e |
| PGC026269 | A0780 | 5.61 | b | – | √ | e | 641 | e | 0.015 | e |
| PGC030223 | A0978 | 0.50 | b | – | – | – | 498 | st | 0.027 | cb |
| PGC044257 | A1644 | 3.92 ± 0.34 | a | 4.7 | √ | w | 933 | w | 0.009 | pe |
| PGC071807 | A2622 | – | – | – | – | – | 942 | s | 0.249 | cc |
| PGC072804 | A2670 | 2.70 | b | 3.9 | √ | w | 1038 | w | 0.035 | cb |
| UGC00579 | A0119 | 3.34 ± 0.05 | a | 5.1 | X | w, e | 863 | w | 0.054 | e |
| UGC02232 | A0376 | 1.36 | c | 5.1 | X | e | 903 | w | 0.136 | cc |
| UGC05515 | A0957 | 0.81 | b | 2.9 | X | w | 669 | w | 0.037 | cb |
| UGC10143 | A2147 | 2.87 ± 0.15 | a | 4.4 | X | e, g | 1148 | w | 0.082 | e |

*Note.* The ⋆ marks at $R_{off}$ indicate the galaxy is not in the centre of the cluster but closer to a local maximum X-ray density, different from the X-ray coordinates given in the literature. The references are: a = Chen et al. (2007); b = Bohringer et al. (2004); c = Bohringer et al. (2000); r = Cruddace et al. (2002); w = White, Jones & Forman (1997); e = Edwards et al. (2007); g = Giovannini, Liuzzo & Giroletti (2008); cc = Calculated from Bohringer et al. (2000); cl = Calculated from Ledlow et al. (2003); cb = Calculated from Bohringer et al. (2004); cr = Calculated from Cruddace et al. (2002); m = Mahdavi & Geller (2001); st = Struble & Rood (1999); s = Struble & Rood (1991); p = Patel et al. (2006); pe = Perez et al. (1998). All the values for $T_X$ are from White et al. (1997).

parameters against velocity dispersion for clusters with cooling-flow or non-cooling-flow data available in the literature. For the six intermediate-aged galaxies (younger than ~6 Gyr) for which cooling-flow information is available, only one is hosted by a cluster without a cooling flow. Thus, there is a tendency that the BCGs with younger mean ages tend to be in clusters with cooling flows, in agreement with the previous photometric results by Bildfell et al. (2008).
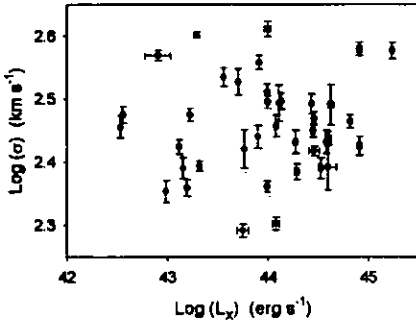
**Figure 10.** Velocity dispersion for the BCGs plotted against log $L_X$ for the host clusters.
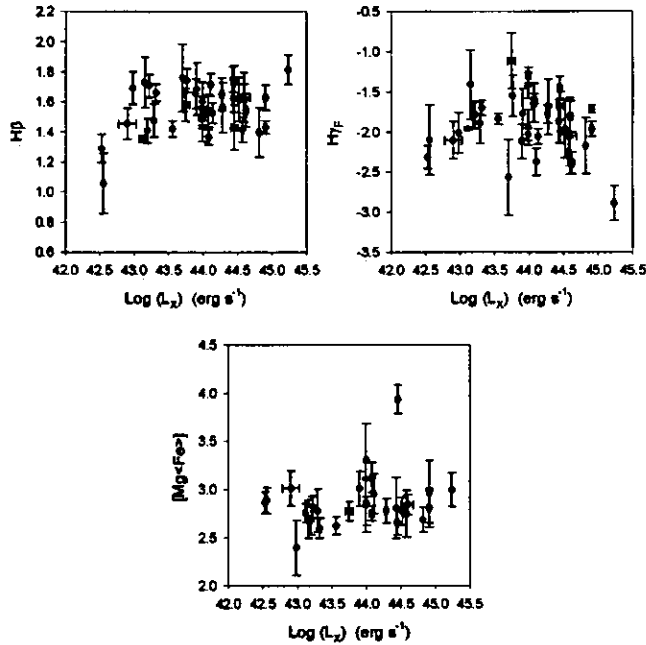


**Figure 11.** Examples of indices against log $L_X$ for the BCGs.



**Figure 12.** The derived SSP-parameters against velocity dispersion for the BCGs. The blue symbols are BCGs in host clusters with cooling flows, and the red symbols those in clusters without cooling flows.

Several previous studies have shown that BCGs lie above the Faber–Jackson relation (Faber & Jackson 1976) defined by ordinary elliptical galaxies (Tonry 1984; Oegerle & Hoessel 1991; Bernardi et al. 2007; Desroches et al. 2007; Lauer et al. 2007; Von der Linden et al. 2007). Fig. 13 shows the Faber–Jackson relation for normal ellipticals, corresponding to $L \propto \sigma^4$, and data points for BCGs in cooling-flow and non-cooling-flow clusters on the same graph. The lower panels in Fig. 13 show the deviation from the Faber–Jackson relation against cluster X-ray luminosity and cluster velocity dispersion, respectively. No real difference can be seen between the location of the cooling and non-cooling clusters on the relation (this is also the case if 2MASS $K$ magnitudes are used). Hence, the presence of cooling flows in clusters does not affect the position of the BCG in this scaling relationship. This is to be expected, as the deviation from the Faber–Jackson relation by BCGs is naturally explained by models of dissipationless mergers of elliptical galaxies, provided that the merger orbits become preferentially more radial for the most massive galaxies (Boylan-Kolchin, Ma & Quataert 2006). Hence, this deviation is not related to the presence of cooling flows in the cluster centre.

Of the nine emission-line galaxies in this sample for which cooling-flow information is available (see Table 7), five are hosted

by clusters with cooling flows and four are hosted by clusters without cooling flows. Edwards et al. (2007) found that the frequency of BCGs showing optical emission lines in their sample increased in cooling-flow clusters (70 versus 10 per cent in non-cooling-flow clusters), regardless of the mass density or velocity dispersion of the cluster. This is also true here, where the corresponding fractions are 33 per cent in cooling-flow clusters and 21 per cent in non-cooling clusters, although the difference in the fractions is not as pronounced. One possible cause of this difference could be that the fraction of BCGs with emission lines changes with the distance between the BCG and the cluster X-ray centre (Best et al. 2007; Edwards et al. 2007).

### 6.4 Log $L_X$–log $T_X$

It is believed that intrinsic scatter in the cluster X-ray luminosity–temperature ($L_X$–$T_X$) relation is physical in origin, caused by processes such as radiative cooling, and those associated with AGN (McCarthy et al. 2004; Bildfell et al. 2008).

Fig. 14 shows the log $L_X$–log $T_X$ plot for the host clusters for which the measurements of $T_X$ and $L_X$ were available in the literature. We normalize $L_X$ with $E(z) = [\Omega_m(1 + z)^3 + \Omega_\Lambda]^{\frac{1}{2}}$ to correct for the evolution of the mean background density, where $z$ is the redshift of the cluster. We follow Bildfell et al. (2008) and fit a power law of the form $\frac{L_X}{E(z)} = \beta T_X^\alpha$ to the regular (i.e. old) BCGs (red-dashed line in Fig. 14). We find a strong correlation with $t$ and $P$ values of 6.66 and <0.0001, respectively. Younger BCGs tend to be located above older BCGs in the diagram, i.e. they are
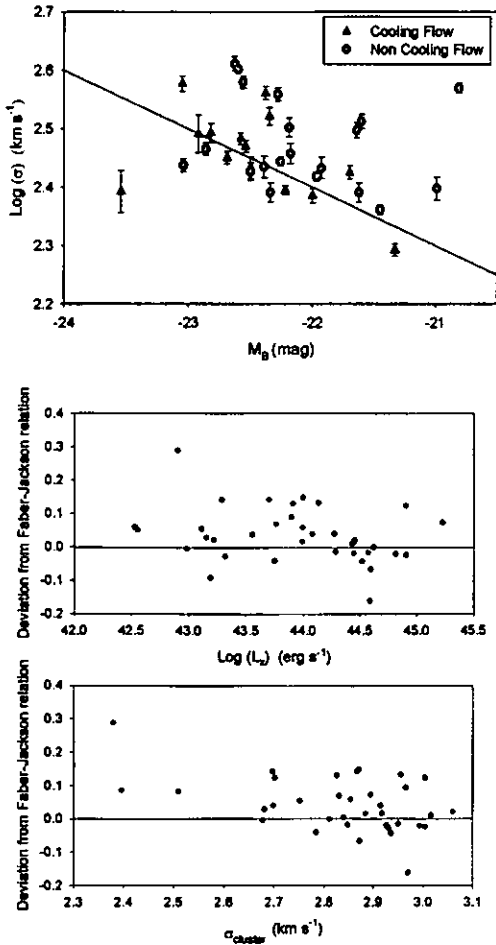
Figure 13. The $\log\sigma$ versus absolute $B$-band magnitude relation for BCGs in cooling-flow and non-cooling-flow clusters. The straight line is the Faber–Jackson relation for normal ellipticals. The bottom two plots show the deviation from the Faber–Jackson relation as a function of host cluster X-ray luminosity and velocity dispersion (proxies for host cluster density and mass, respectively).
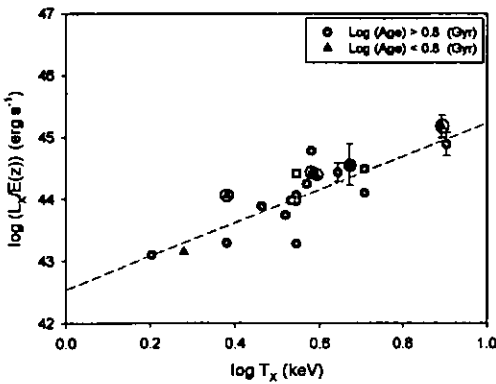


Figure 14. $\log[L_X/E(z)]$ against $\log T_X$ for the BCGs. The clusters hosting BCGs with ages $\log$ (age) $< 0.8$ Gyr are shown in blue, where the black circles denote young galaxies in cooling-flow clusters. The majority of the $L_X$ values from the literature does not have errorbars.

predominantly in clusters with X-ray excess. Five of the young galaxies for which the host cluster information is available are hosted by cooling-flow clusters (denoted by a black circle). Only one of the younger galaxies, located at the bottom of the plot, NGC

0541, is hosted by a cluster without cooling flows. The result that younger BCGs tend to be hosted by clusters with X-ray excess agrees with the photometric result from Bildfell et al. (2008) who showed that their star-forming BCGs are exclusively located in clusters with a high-$L_X$ deviation from the $L_X$–$T_X$ relation – the region of the diagram usually populated by cool-core clusters. This implies that the origin of the cold gas fuelling the star formation may be linked to the processes that give rise to the $L_X$ excess, and points to cooling flows as the source of the cold gas in galaxies with young stellar populations.

### 6.5  BCG offset from X-ray peak

If the star formation in all young BCGs is a result of cooling flows, then the young BCGs are expected to be located exclusively at the centres of relaxed clusters, where the cold gas is deposited. Furthermore, numerical simulations predict that the offset of the BCG from the peak of the cluster X-ray emission is an indication of how close the cluster is to the dynamical equilibrium state, and decreases as the cluster evolves (Katayama et al. 2003).

We collected the projected angular separations between BCGs and the peak of the X-ray emission from the literature as shown in Table 7. For those clusters for which it was not available, we calculated it from the BCG and published X-ray peak coordinates. However, this was not possible for those clusters, e.g. Coma, where a BCG is not in the centre and where the coordinates of a corresponding local X-ray maximum were not available.

Fig. 15 shows the derived ages plotted against the X-ray offsets, with separate symbols for galaxies in cooling and non-cooling-flow clusters, as well as plots of the derived SSP parameters against the offsets for all BCGs for which the offsets were available. Contrary to what was found by Bildfell et al. (2008), there is no significant difference in mean X-ray offsets for young and old galaxies. Thus, the younger BCGs are preferentially found in cooling-flow clusters, but they are not necessarily closer to the centres of the clusters,
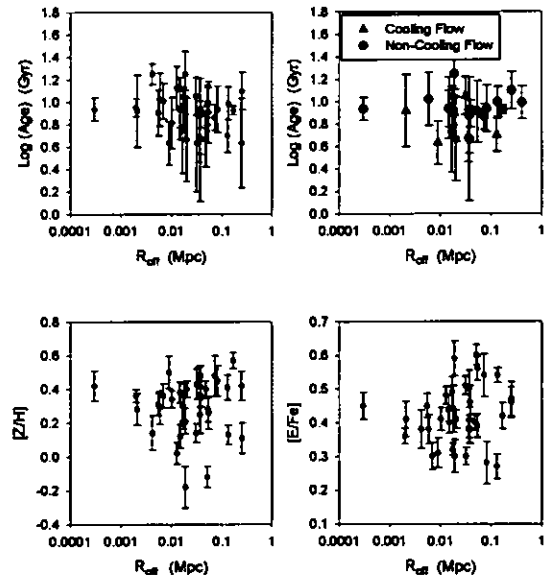


Figure 15. Derived SSP parameters plotted against BCG offset from the X-ray peak. The upper right plot shows the derived ages plotted against the X-ray offsets, with separate symbols for galaxies in cooling and non-cooling-flow clusters. The other three plots show the derived SSP parameters against the offsets for all BCGs for which the offsets were available.
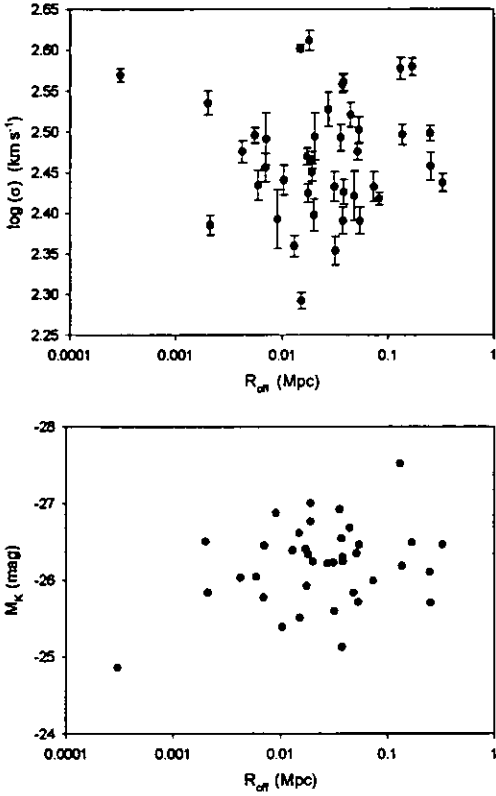
**Figure 16.** Galaxy velocity dispersion and absolute $K$-band magnitude plotted against X-ray offset.

where the cooling flows are deposited, than galaxies with old stellar populations.

Rafferty, McNamara & Nulsen (2008) found that the central galaxy is likely to experience significant star formation when: (i) the X-ray and galaxy centroids are within $\sim 20$ kpc of each other and (ii) the central cooling time of the hot atmosphere is much less than $\sim 8 \times 10^8$ yr (an entropy of less than $\sim 30$ keV cm$^2$). Therefore, the younger BCGs need to be very close to the X-ray peaks, even though they are in cooling-flow clusters, for the recent star formation to be a result of the cooling flows. As only three of the five younger galaxies hosted by cooling-flow clusters are located within $\sim 20$ kpc of the X-ray peak in the present sample, all the recent star formation found in this sample is not necessarily a consequence of the cooling flows.

Fig. 16 shows the X-ray offsets plotted against the galaxy velocity dispersion and absolute $K$-band magnitude. Bildfell et al. (2008) found a weak tendency for brightest BCGs to lie closest to their host cluster's X-ray peak while the faintest BCGs are the farthest. This might be expected since massive BCGs will locate at the centre of the cluster potential well on a shorter time-scale than less massive BCGs. They will also have an enhanced probability to merge with small galaxies and will grow more rapidly than BCGs further away from the centre and they will be close to where the cool gas is deposited (Bildfell et al. 2008). However, as can be seen in Fig. 16, no such trend can be seen for the present sample, within the uncertainties.

# 7 CONCLUSIONS

We have obtained high S/N, long-slit spectra of 49 BCGs in the nearby Universe, and derived SSP-equivalent ages, metallicities and

$\alpha$-enhancements in the centres of 43 galaxies using the Lick/IDS system of absorption line indices. We compared the indices and parameters derived for these BCGs with those of ordinary ellipticals in the same mass range. We tested the derived properties for possible correlations with the kinematic properties (velocity dispersion, rotation) and luminosity of the galaxies and the X-ray properties of the host clusters (density, mass, distance to X-ray peak, presence of cooling flows).

(i) With the exception of G4300, we find no significant discrepancies between the index relations with velocity dispersion of the BCG data and those of normal ellipticals in the same mass range. Only six (Ca4227, H$\gamma_F$, Ca4455, Fe4531, C$_2$4668 and Mg$_b$) out of 18 indices possess a statistically significant slope different from zero. The BCG data are much more scattered around the derived index–velocity dispersion slopes than the elliptical galaxies in that mass range.

(ii) In general, most BCGs are very old. However, 11 galaxies (26 per cent of the sample for which ages were derived) were found with SSP-equivalent ages log (age) $< 0.8$ (in Gyr). Young BCGs are not unusual. Other examples of observational signs of recent star formation and accretion activity in massive central galaxies in clusters are young globular clusters in NGC 1275 and multiple nuclei in NGC 6166 (Trager et al. 2008, and references therein). Bildfell et al. (2008) also found 25 per cent of the 48 BCGs in their photometric sample to have blue cores. Active star formation in BCGs pose a challenge for simulations, which predict virtually no recent star formation due to the assumption of extremely efficient AGN feedback (e.g. De Lucia & Blaizot 2007).

(iii) No significant age–velocity dispersion relation is found for the BCG sample in this mass range. The peaks of the age distributions, and the slope of the age–velocity dispersion relation of the BCG and elliptical samples are similar. However, the BCG age distribution also shows a smaller second peak at log (age) $\sim 0.65$ which, although not statistically significant according to a Kolmogorov–Smirnov test, is absent in the elliptical galaxy distributions. Thus, it can be argued that the mean, generally old ages of BCGs are similar to normal giant elliptical galaxies, but there is a weak indication that for a small fraction of BCGs, recent star formation occurred as a result of their privileged location in the centre of the cluster.

(iv) The peak of the metallicity distribution occurs at a higher value for the BCGs than for the samples of massive elliptical galaxies. The BCG metallicity–velocity dispersion relation is similar in slope than that of normal ellipticals (Figs 7 and 9).

(v) No significant [E/Fe]–velocity dispersion relation is found for the BCG sample in this mass range. The BCGs have higher [E/Fe] values than the comparison elliptical samples (Figs 7 and 9). This can naively be interpreted as a consequence of shorter formation time-scales in BCGs. However, other differences such as the IMF, differences in the binary fractions or selective winds that drive most of the Fe-group elements to the intracluster medium cannot be conclusively eliminated.

(vi) No real difference is visible in the ages of rotating and non-rotating BCGs, and a wide range of ages were derived for galaxies that show a lack of rotation. No relations between the derived parameters and absolute magnitude were found for the BCG sample. The strong age–metallicity relation found for BCGs is almost entirely due to the correlation between errors on the parameters.

(vii) No correlation is found between the X-ray luminosity of the clusters and the velocity dispersion of the BCGs (Fig. 10). Thus, galaxies in higher density clusters are not necessarily more massive. BCGs with younger SSP-equivalent ages are found in both dense

and less dense host clusters; however, the relationships between the Balmer-line indices and cluster X-ray luminosity possibly suggest two different regimes, and therefore an evolutionary history which is dependent on environment (Fig. 11).

(viii) No clear correlation between host cluster velocity dispersion (cluster mass) and any of the derived parameters (age, metallicity and $\alpha$-abundance) were found.

(ix) Several sources of gas for fuelling the recent star formation in BCGs have been postulated (discussed by Pipino et al. 2009). These are: (i) cooling flows, (ii) recycling of stellar ejecta and (iii) accretion of satellites. For the six young galaxies (younger than $\sim 6$ Gyr) for which cooling flow information is available, only one is hosted by a cluster without a cooling flow. This suggests that the recent star formation in this galaxy (NGC 0541) might have been fuelled by gas deposited in a merger event, or perhaps triggered by the radio jet originating from the galaxy's supermassive black hole. NGC 0541 is known to be very peculiar and is associated with Minkowski's Object, an irregular dwarf located 16 kpc from NGC 0541 and in the path of the galaxy's radio jet. The radio jet is thought to have triggered the starburst in Minkowski's Object (Schaerer, Contini & Pindao 1999; Verdoes Kleijn et al. 1999; Croft et al. 2006).

(x) As mentioned above, there is a tendency that the younger galaxies in this BCG sample are hosted by clusters with cooling flows. In addition, the $L_X$–$T_X$ cluster relation shows that the younger BCGs are located in clusters with large values of X-ray excess. However, some of the younger galaxies were found to be slightly further away from the X-ray peak of the cluster. This will limit the influence of the cluster cooling flows, which in turn suggests that the possibility that the gas fuelling the star formation had its origin in mergers cannot be discarded. On the other hand, potential merging and capturing of less massive galaxies would be enhanced by the galaxy being close to the cluster potential well.

In summary, there are differences – albeit small – between the stellar populations in BCGs and ordinary elliptical galaxies over the same mass range. The BCGs show higher metallicity and $\alpha$-enhancement values. The former possibly indicates more efficient star formation, and the latter is most commonly interpreted as a consequence of shorter formation time-scales in BCGs. The SSP-equivalent parameters show very little dependence on the mass or brightness of the galaxies, or the mass or density of the host clusters. No real differences are found between the ages of rotating and non-rotating BCGs. Most of BCGs are very old, as expected. However, 11 galaxies (26 per cent of the sample for which ages were derived) were found to have intermediate ages (SSP-equivalent ages of <6 Gyr). We have shown that the younger BCGs tend to be found in cooling-flow clusters which lies above the $L_X$–$T_X$ relation. However, this is not exclusively the case. In at least one of the young BCGs (NGC 0541 – hosted by a cluster without cooling flows), the gas must have a different origin. This means that there is likely to be more than one process responsible for the recent star formation in BCGs. In addition, the younger BCGs seem to be slightly further away from the cluster X-ray peak, limiting the influence of the cooling flows. As a result, the possibility that more of the young BCGs experienced recent mergers or accretion events involving gas, and leading to star formation, should not be discounted. Overall, the recent star formation in BCGs, and the connection with the processes in the cluster centres, is very complex.

All the indices and SSP results discussed here are only for the central regions of the galaxies. The radial SSP gradients in BCGs will be investigated in a subsequent paper.

## REFERENCES

Aragón-Salamanca A., Baugh C. M., Kauffmann G., 1998, MNRAS, 297, 427
Baldwin J. A., Phillips M. M., Terlevich R., 1981, PASP, 93, 5
Bernardi M., Hyde J. B., Sheth R. K., Miller C. J., Nichol R. C., 2007, AJ, 133, 1741
Bernardi M., Hyde J. B., Fritze A., Sheth R. K., Gebhardt K., Nichol R. C., 2008, MNRAS, 391, 1191
Best P. N., Von der Linden A., Kauffmann G., Heckman T. M., Kaiser C. R., 2007, MNRAS, 379, 894
Bildfell C., Hoekstra H., Babul A., Mahdavi A., 2008, MNRAS, 389, 1637
Bohringer H. et al., 2000, ApJS, 129, 435
Bohringer H. et al., 2004, A&A, 425, 367
Boylan-Kolchin M., Ma C., Quataert E., 2006, MNRAS, 369, 1081
Brough S., Collins C. A., Burke D. J., Mann R. G., Lynam P. D., 2002, MNRAS, 329, 533
Brough S., Proctor R., Forbes D. A., Couch W. J., Collins C. A., Burke D. J., Mann R. G., 2007, MNRAS, 378, 1507
Burke D. J., Collins C. A., Mann R. G., 2000, ApJ, 532, 105
Burns J. O., 1990, AJ, 99, 14
Burns J. O., Loken C., Gómez P., Rizza E., Bliton M., Ledlow M., Owen F. N., 1997, in Soker N., ed., ASP Conf. Ser. Vol. 115, Galactic and Cluster Cooling Flows. Astron. Soc. Pac., San Francisco, p. 21
Burstein D., Faber S. M., Gaskell C. M., Krumm N., 1984, ApJ, 287, 586
Caldwell N., Rose J. A., Concannon K. D., 2003, AJ, 125, 289
Cardiel N., Gorgas J., Aragón-Salamanca A., 1998a, MNRAS, 298, 977
Cardiel N., Gorgas J., Cenarro J., González J. J., 1998b, A&AS, 127, 597
Cenarro A. J., Gorgas J., Cardiel N., Pedraz S., Peletier R. F., Vazdekis A., 2001, MNRAS, 326, 981
Chen Y., Reiprich T. H., Bohringer H., Ikebe Y., Zhang Y. Y., 2007, A&A, 466, 805
Collins C. A., Mann R. G., 1998, MNRAS, 297, 128
Crawford C. S., Allen S. W., Ebeling H., Edge A. C., Fabian A. C., 1999, MNRAS, 306, 857
Croft S. et al., 2006, ApJ, 647, 1040
Cruddace R. et al., 2002, ApJS, 140, 239
De Lucia G., Blaizot J., 2007, MNRAS, 375, 2

Desroches L., Quataert E., Ma C., West A. A., 2007, MNRAS, 377, 402

Dubinski J., 1998, ApJ, 502, 141

Edge A. C., Stewart G. C., 1991, MNRAS, 252, 428

Edwards L. O. V., Hudson M. J., Balogh M. L., Smith R. J., 2007, MNRAS, 379, 100

Faber S. M., Jackson R. E., 1976, ApJ, 204, 668

Faber S. M., Friel E. D., Burstein D., Gaskell C. M., 1985, ApJS, 57, 711

Fisher D., Franx M., Illingworth G., 1995, ApJ, 448, 119

Forbes D. A., Beasley M. A., Brodie J. P., Kissler-Patig M., 2001, ApJ, 563, 143

Gao L., Loeb A., Peebles P. J. E., White S. D. M., Jenkins A., 2004, ApJ, 614, 17

Giovannini G., Liuzzo E., Giroletti M., 2008, in Hagiwara Y., Fomalont E., Tsuboi M., Murata Y., eds, Approaching Micro-Arcsecond Resolution with VSOP-2: Astrophysics and Technology. Astron. Soc. Pac., San Francisco, in press (arXiv:0802.3574)

González J. J., 1993, PhD thesis, Univ. California

González A. H., Zaritsky D., Zubladoff A. I., 2007, ApJ, 666, 147

Gorgas J., Faber S. M., Burstein D., González J. J., Courteau S., Prosser C., 1993, ApJS, 86, 153

Hansen S. M., Sheldon E. S., Wechsler R. H., Koester B. P., 2007, preprint (arXiv:0710.3780)

Jarrett T. H., Chester T., Cutri R., Schneider S. E., Huchra J. P., 2003, AJ, 125, 525

Jordán A., Côté P., West M. J., Marzke R. O., Minniti D., Rejkuba M., 2004, AJ, 127, 24

Jørgensen I., 1999, MNRAS, 306, 607

Katayama H., Hayashida K., Takahara F., Fukita Y., 2003, ApJ, 585, 687

Korn A. J., Maraston C., Thomas D., 2005, A&A, 438, 685

Kuntschner H., 2000, MNRAS, 315, 184

Kuntschner H., 2004, A&A, 426, 737

Kuntschner H., Lucey J. R., Smith R. J., Hudson M. J., Davies R. L., 2001, MNRAS, 323, 615

Laine S., van der Marel R. P., Lauer T. R., Postman M., O'Dea C. P., Owen F. N., 2003, AJ, 125, 478

Lamareille F., Mouchine M., Contini T., Lewis I., Maddox S., 2004, MNRAS, 350, 396

Lauer T. R. et al., 2007, ApJ, 662, 808

Ledlow M. J., Voges W., Owen F. N., Burns J. O., 2003, AJ, 126, 2740

Lee H., Worthey G., 2005, ApJS, 160, 176 (LW05)

Li Z., Han Z., 2007, A&A, 471, 795

Lin Y. T., Mohr J. J., 2004, ApJ, 617, 879

Loh Y. S., Strauss M. A., 2006, MNRAS, 366, 373

Loubser S. I., Sansom A. E., Sánchez-Blázquez P., Soechting I. K., Bromage G., 2008, MNRAS, 391, 1009 (Paper 1)

Lyubenova M., Kuntschner H., Silva D. R., 2008, A&A, 485, 425

MacArthur L., 2005, ApJ, 623, 795

Mahdavi A., Geller M. J., 2001, ApJ, 554, 129

Maraston C., 1998, MNRAS, 300, 872

Maraston C., 2005, MNRAS, 362, 799

Maraston C., Greggio L., Renzini A., Ortolani S., Saglia R. P., Puzia T. H., Kissler-Patig M., 2003, A&A, 400, 823

McCarthy I. G., Balogh M. L., Babul A., Pool G. B., 2004, ApJ, 613, 811

McNamara B. R. et al., 2006, ApJ, 648, 164

Mehlert D., Saglia R. P., Bender R., Wegner G., 2000, A&AS, 141, 449

Mihos J. C., Hernquist L., 1994, ApJ, 425, L13

Moore S. A. W., Lucey J. R., Kuntschner H., Colless M., 2002, MNRAS, 336, 382

Naab T., Burkert A., 2003, ApJ, 597, 893

Nelan J. E., Smith R. J., Hudson M. J., Wegner G. A., Lucey J. R., Moore S. A. W., Quinney S. J., Suntzeff N. B., 2005, ApJ, 632, 137

O'Dea C. P. et al., 2008, ApJ, 681, 1035

Oegerle W. R., Hoessel J. G., 1991, ApJ, 375, 15

Oemler A., 1976, ApJ, 209, 693

Ogando R. L. C., Maia M. A. G., Pellegrini P. S., da Costa L. N., 2008, AJ, 135, 2424 (OG08)

Patel P., Maddox S., Pearce F. R., Aragón-Salamanca A., Conway E., 2006, MNRAS, 370, 851

Peletier R. F., Davies R. L., Illingworth G. D., Davis L. E., Cawson M., 1990, AJ, 100, 1091

Perez C. B., Fabian A. C., Edge A. C., Allen S. W., Johnstone R. M., White D. A., 1998, MNRAS, 298, 416

Pipino A., Kaviraj S., Bildfell C., Hoekstra H., Babul A., Silk J., 2009, MNRAS, 395, 462

Popesso P., Biviano A., Bohringer H., Romaniello M., 2006, A&A, 445, 29

Proctor R. N., Sansom A. E., 2002, MNRAS, 333, 517

Rafferty D. D., McNamara B. R., Nulsen P. E. J., 2008, ApJ, 687, 899

Reiprich T. H., Bohringer H., 2002, ApJ, 567, 716

Sánchez-Blázquez P., Gorgas J., Cardiel N., González J. J., 2006a, A&A, 457, 787 (SB06)

Sánchez-Blázquez P., Gorgas J., Cardiel N., González J. J., 2006b, A&A, 457, 809

Sánchez-Blázquez P., Gorgas J., Cardiel N., 2006c, A&A, 457, 823

Sánchez-Blázquez P. et al., 2006d, MNRAS, 371, 703

Sánchez-Blázquez P., Forbes D. A., Strader J., Brodie J., Proctor R., 2007, MNRAS, 377, 759

Sánchez-Blázquez P. et al., 2009, A&A, 499, 47

Sarzi M. et al., 2006, MNRAS, 366, 1151

Schaerer D., Contini T., Pindao M., 1999, A&AS, 136, 35

Schombert J. M., 1986, ApJS, 60, 603

Serra P., Trager S. C., 2007, MNRAS, 374, 769

Stasińska G., Cid Fernandes R., Mateus A., Sodré L., Asari N. V., 2006, MNRAS, 371, 972

Stott J. P., Edge A. C., Smith G. P., Swinbank A. M., Ebeling H., 2008, MNRAS, 384, 1502

Struble M. F., Rood H. J., 1991, ApJS, 77, 363

Struble M. F., Rood H. J., 1999, ApJS, 125, 35

Thomas D., Maraston C., Bender R., 2003, MNRAS, 343, 279

Thomas D., Maraston C., Korn A. J., 2004, MNRAS, 351, 19

Thomas D., Maraston C., Bender R., de Oliviera C. M., 2005, ApJ, 621, 673 (T05)

Tinsley B. M., 1980, Fund. Cosmic Phys., 5, 287

Tonry J. L., 1984, ApJ, 279, 13

Trager S. C., 2006, preprint (arXiv:0611378)

Trager S. C., Worthey G., Faber S. M., Burstein D., González J. J., 1998, ApJS, 116, 1 (T98)

Trager S. C., Faber S. M., Worthey G., González J. J., 2000a, AJ, 119, 164

Trager S. C., Faber S. M., Worthey G., González J. J., 2000b, AJ, 120, 165

Trager S. C., Worthey G., Faber S. M., Dressler A., 2005, MNRAS, 362, 2

Trager S. C., Faber S. M., Dressler A., 2008, MNRAS, 386, 715

Tripicco M. J., Bell R. A., 1995, AJ, 110, 3035

Vazdekis A., Arimoto N., 1999, ApJ, 525, 144

Verdoes Kleijn G. A., Baum S. A., De Zeeuw P. T., O'Dea C. P., 1999, AJ, 118, 2592

Von der Linden A., Best P. N., Kauffmann G., White S. D. M., 2007, MNRAS, 379, 867

Whiley I. M. et al., 2008, MNRAS, 387, 1253

White D. A., Jones C., Forman W., 1997, MNRAS, 292, 419

Worthey G., 1994, ApJS, 95, 107

Worthey G., Ottaviani D. L., 1997, ApJS, 111, 377

Worthey G., Faber S. M., González J. J., 1992, ApJ, 398, 69

Worthey G., Faber S. M., González J. J., Burstein D., 1994, ApJS, 94, 687

# APPENDIX A: CONVERTING TO THE LICK/IDS SYSTEM

Index measurements depend on the broadening of the absorption lines caused by both the instrumental spectral resolution and the line-of-sight velocities of the stars. In order to use model predictions based on the Lick system, the observed spectra need to be degraded to the wavelength-dependent resolution of the Lick/IDS spectrograph, and the indices need to be corrected for the broadening caused by the velocity dispersion of the galaxies.

This section entails the calibration to the Lick/IDS system which consists of three effects that should be accounted for to compare the observed values with those predicted by models:

(i) The difference in spectral resolution between the observational data, and that of the Lick stars observed with the Lick set-up (Faber et al. 1985).

(ii) The internal velocity dispersion of the galaxies.

(iii) Small systematic differences caused by the fact that the Lick/IDS spectra were not flux calibrated.

## A1 Correction to Lick spectral resolution and velocity dispersion corrections

A total of 22 Lick calibration stars were observed with the 5300 Å dichroic and 10 with the 6100 Å dichroic at the WHT, as described in Paper 1. The Lick stars used for the Gemini data are from the Gemini Science Archive and were observed with an observational set-up corresponding to that of the galaxy data presented here (PI: Bryan Miller, private communication).

As the first step, the Lick star spectra observed with both sets of observations in this work (the WHT and the Gemini data) were shifted to zero radial velocity (Doppler correction), and broadened to the wavelength-dependent resolution of the original Lick/IDS spectra (Worthey & Ottaviani 1997).

The instrumental broadening ($\sigma_1$) of the WHT telescope and ISIS CCD as well as that of the Gemini telescopes and GMOS-N and GMOS-S were measured from the emission lines of the arc spectra. The lines were fitted by Gaussian functions from which the FWHMs were measured.

The stellar velocity dispersion weakens the strength of most absorption features. To calculate the effects of velocity dispersion on the index measurements, the Lick star spectra were smoothed to varying widths in the range $\sigma_c = 0$ to 300 km s$^{-1}$, in intervals of 20 km s$^{-1}$, where $\sigma_c$ is the width of the broadening Gaussian. Following Proctor & Sansom (2002), correction factors $C_i(\sigma_c)$ were determined.

For molecular line indices ($CN_1$, $CN_2$, $Mg_1$, $Mg_2$, $TiO_1$ and $TiO_2$) and for indices with ranges which include negative values (i.e. H$\gamma$ and H$\delta$):

$$C_i(\sigma_c) = I_L - I_{\text{Measured}}, \tag{A1}$$

where $I_L$ is the index value at the calibration resolution and $I_{\text{Measured}}$ the index value measured in the broadened star spectrum.

For all the other atomic line indices

$$C_i(\sigma_c) = I_L / I_{\text{Measured}}. \tag{A2}$$

For each of the indices, $C_i$ was plotted against $\sigma_c$, and a third order polynomial ($C_i = x_0 + x_1\sigma_c + x_2\sigma_c^2 + x_3\sigma_c^3$) was fitted. The value of $x_0$ was fixed at zero for the molecular, H$\gamma$ and H$\delta$ indices and at one for the other atomic indices.

Fig. A1 shows the broadening functions of the Gemini data as an example, and the plots illustrate how the index measurements are affected by velocity dispersion broadening. The derived WHT broadening functions agreed very well when compared with those published by Proctor & Sansom (2002) and Kuntschner (2004).

Depending on whether galaxies have a total broadening ($\sqrt{\sigma_i^2 + \sigma_V^2}$) greater or smaller than $\sigma_L$, where $\sigma_I$ is the instrumental broadening, $\sigma_V$ is the galaxy velocity dispersion and $\sigma_L$ is the Lick resolution, their spectra were effectively debroadened or broadened to the Lick resolution, as well as corrected for the broadening caused by the velocity dispersion of the galaxies.

## A2 Corrections to the Lick flux scale

The original Lick/IDS spectra were not flux calibrated by means of spectrophotometric standard stars but instead were normalized to a calibration lamp. This causes small differences in the indices compared with those measured from flux-calibrated data. By comparing the measured indices in the observed, flux-calibrated stars with those in the Lick/IDS database, the mean differences in index measurements caused by this flux scale difference can be derived for all the indices.

Index values were measured from the Lick star spectra observed in this work (WHT and Gemini data) broadened up to the Lick/IDS resolution. Comparisons to the Lick star data presented in Worthey (1994) and Worthey & Ottaviani (1997) for the same stars enabled the calculation of the mean Lick index differences (hereafter called offsets, $\Delta I$). For all the Lick index measurements presented here, the flux calibration correction was performed by adding the appropriate $\Delta I$ to the measured index value.

All the offsets derived for the WHT and Gemini data were independent of the strength of the index itself, with the exception of the two Gemini CN indices. For all other indices, the average differences were computed and used as final corrections. For the CN indices, correlations between the offsets and the measured index values (from this work) were found:

$$\Delta I = -0.0109 + 0.201 \times CN_1 \tag{A3}$$

$$\Delta I = -0.0150 + 0.184 \times CN_2. \tag{A4}$$

For all indices, the error in calibration to the Lick system was calculated as rms/$\sqrt{N-1}$, where $N$ is the number of calibration stars ($N = 17$ for the Gemini data, $N = 20$ for the WHT data 5300 dichroic and $N = 10$ for the WHT data 6100 dichroic). The Gemini offsets are shown in Fig. A2 as an example. As can be seen in the plots, the offsets are typically smaller than the error on the index measurement. A comparison was made between the Gemini offsets derived in this work with those derived by M. Norris (private communication), using the same archive data of the Lick stars. No systematic differences between the two sets of offsets were visible. Most of the offsets used here are in agreement, with the exception of C$_2$4668 and Ca4455 which are slightly higher than those derived by M. Norris.

Table A1 shows all the parameters of the calibration to the Lick system for the Gemini data as an example, and similar parameters were derived for the WHT data.

## APPENDIX B: INDICES: COMPARISON WITH PREVIOUS MEASUREMENTS

The central index measurements were compared to those of Trager (1998, hereafter T98) for 14 galaxies which the samples had in common. The measurements of the original 21 Lick indices were presented in T98, and the four higher order Balmer indices (of the same galaxy sample) in Lee & Worthey (2005) (hereafter LW05). The central values of the T98 sample were measured in an aperture of $1.4 \times 4$ arcsec$^2$. Only one of the 14 galaxies had TiO$_2$ measurements in both T98 and this sample, so no comparison of TiO$_2$ measurements were made. Galaxies with large differences in certain indices (e.g. a few Fe5270 measurements) were compared on an individual basis (S. Trager, private communication), and can be attributed to lower S/N data.

The central index measurements were also compared to those of SB06 for five galaxies in common (also indicated in Fig. B1).
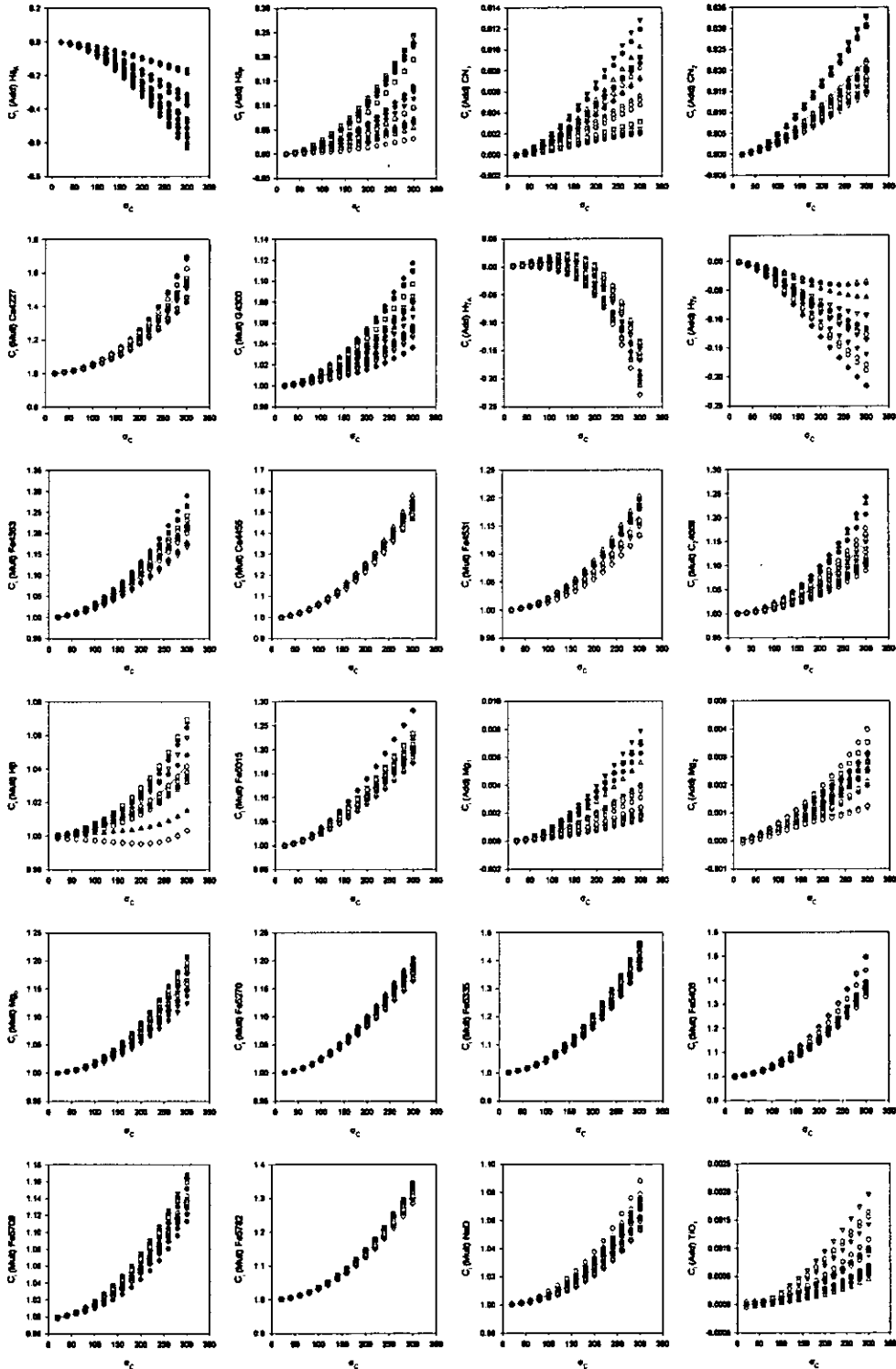
**Figure A1.** Broadening functions: $C_i$ plotted as a function of $\sigma_c$ (Gemini data) for all the indices. The best-fitting third order polynomial is indicated in each figure by the continuous curve. The different symbols represent the different stars used to obtain the best-fitting curve. The abbreviations 'Add' and 'Mult' indicate whether the index values were added (molecular and higher order Balmer indices) or multiplied (atomic indices) to calculate $C_i$, and $\sigma_c$ is in km s$^{-1}$.

For this comparison, the same central aperture of the galaxies was extracted, and 15 indices measured from the SB06 data. Nine index measurements for five galaxies were also compared with those measured by Ogando et al. (2008, hereafter OG08). The indices from OG08 were measured within a metric circular aperture equivalent

to 1.19 kpc at the distance of the Coma cluster. No flux calibration was applied to these galaxies. No comparison between the six different observing runs (WHT, Gemini North 06B and 07A, Gemini South 06B, 07A and 07B) and T98, SB06 or OG08 could be made since there were too few galaxies in common. In total, index
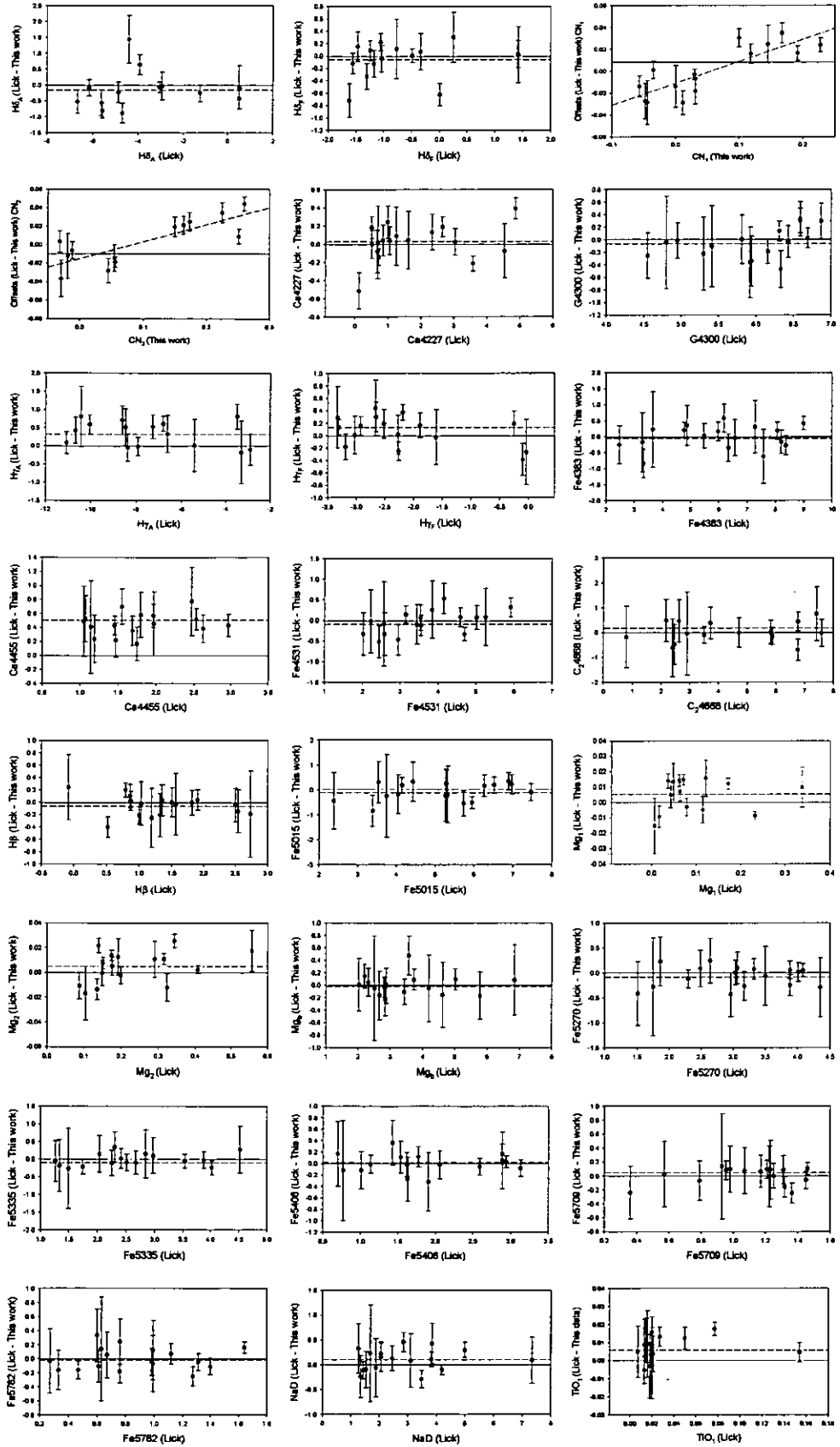
**Figure A2.** Gemini offsets derived from index measurements (original Lick data – this work) plotted against the original Lick measurements. The dashed horizontal line represents the Lick offset.

**Table A1.** Values for the calibration of the Gemini data to Lick resolution and offsets. The values of the Lick spectral resolution ($\sigma_L$) were taken from Worthey & Ottaviani (1997) and are given as FWHM values, where FWHM = 2.35 $\sigma_L$ (in Å). The values of $\Delta I$ are Lick − this work, and the rms are the error on the mean. *Relations were derived for the two CN offsets (as described in Section A2), whereas all the other offsets were found to be independent of the strength of the index.

| Index | FWHM ($\sigma_L$) | $x_0$ | $x_1$ | $x_2$ | $x_3$ | $\Delta I$ | rms |
|---|---|---|---|---|---|---|---|
| H$\delta_A$ | 10.9 | 0 | 3.5695e-5 | −7.7694e-6 | 8.5777e-9 | −0.139 | 0.154 |
| H$\delta_F$ | 10.9 | 0 | −3.0135e-5 | 1.7720e-6 | −5.6082e-10 | −0.065 | 0.073 |
| CN$_1$ | 10.6 | 0 | −1.3830e-6 | 1.4721e-7 | −2.0204e-10 | * | 0.013 |
| CN$_2$ | 10.6 | 0 | −3.6741e-6 | 4.2346e-7 | −5.5390e-10 | * | 0.015 |
| Ca4227 | 10.2 | 1 | 1.7865e-4 | 2.9655e-6 | 9.0006e-9 | 0.021 | 0.050 |
| G4300 | 9.8 | 1 | 3.2797e-5 | 6.4488e-7 | 1.7805e-10 | −0.058 | 0.061 |
| H$\gamma_A$ | 9.5 | 0 | 2.8251e-6 | 2.0551e-6 | −1.3255e-8 | 0.344 | 0.087 |
| H$\gamma_F$ | 9.5 | 0 | −1.4965e-5 | −3.3005e-6 | 6.6191e-9 | 0.071 | 0.061 |
| Fe4383 | 9.2 | 1 | 4.7860e-6 | 2.7446e-6 | −1.2824e-9 | −0.016 | 0.094 |
| Ca4455 | 9.1 | 1 | 5.0919e-5 | 5.8155e-6 | −8.1350e-10 | 0.452 | 0.041 |
| Fe4531 | 9.0 | 1 | 3.1621e-5 | 1.5188e-6 | 8.8514e-10 | −0.045 | 0.072 |
| C$_2$4668 | 8.8 | 1 | −1.9459e-6 | 1.3580e-6 | 1.0041e-9 | 0.018 | 0.106 |
| H$\beta$ | 8.5 | 1 | 4.5530e-5 | 2.4319e-9 | 1.0960e-9 | −0.051 | 0.041 |
| Fe5015 | 8.4 | 1 | 1.5787e-5 | 3.2697e-6 | −3.0301e-9 | −0.066 | 0.090 |
| Mg$_1$ | 8.4 | 0 | −2.9836e-7 | 6.4496e-8 | −6.1692e-11 | 0.005 | 0.003 |
| Mg$_2$ | 8.4 | 0 | 1.0236e-6 | 3.3235e-8 | −3.0902e-11 | 0.005 | 0.003 |
| Mg$_b$ | 8.4 | 1 | −4.1861e-5 | 2.0200e-6 | 4.1426e-11 | −0.001 | 0.042 |
| Fe5270 | 8.4 | 1 | −8.9369e-6 | 2.8442e-6 | −2.4675e-9 | −0.073 | 0.053 |
| Fe5335 | 8.4 | 1 | 2.0324e-5 | 4.1990e-6 | 1.1364e-9 | −0.017 | 0.045 |
| Fe5406 | 8.4 | 1 | 3.1157e-5 | 3.2510e-6 | 3.1952e-9 | 0.001 | 0.043 |
| Fe5709 | 9.1 | 1 | 5.4235e-5 | 1.0542e-6 | 1.2787e-9 | 0.005 | 0.030 |
| Fe5782 | 9.3 | 1 | 3.3839e-5 | 2.9915e-6 | 1.3392e-9 | −0.003 | 0.041 |
| NaD | 9.5 | 1 | 3.0030e-5 | 3.4807e-7 | 9.2784e-10 | 0.097 | 0.055 |
| TiO$_1$ | 9.7 | 0 | −2.8748e-7 | 1.4645e-8 | −7.8336e-12 | 0.006 | 0.002 |
| TiO$_2$ | 10.3 | 0 | 2.7041e-7 | −1.8201e-9 | 1.1353e-11 | −0.007 | 0.003 |

measurements of 15 galaxies (some of the galaxies being in common with more than one of the above-mentioned samples) could be compared, and are all shown in Fig. B1. This comparison shows that the H$\delta_A$ index measurements in the Gemini data are systematically higher (by 1–2 Å) compared with previous measurements, and shows a large amount of scatter. No other systematic differences were found. With the exception of the TiO$_1$ index, which was often very close to the edge of the spectrum in the BCG data, all the index comparison plots show scatter that is smaller than that expected from the errors on the index measurements.

# APPENDIX C: NOTES ON INDIVIDUAL OBJECTS

This section contains notes of some of the individual objects that could be compared with existing SSP-equivalent measurements from the literature.

## IC1633

The surface brightness profile of this galaxy was published by Schombert (1986) and *HST* imaging by Laine et al. (2003). The radial velocity profile reveals some evidence for substructure at the centre of this galaxy (Paper 1). The SSP equivalent parameters derived for the central $\frac{1}{8} R_e$ in this study (log (age) = 0.935 ± 0.187; [E/Fe] = 0.440 ± 0.039; [Z/H] = 0.380 ± 0.061) could be compared with those presented in T05 for the central $\frac{1}{10} R_e$ (log (age) = 0.716 ± 0.308; [E/Fe] = 0.366 ± 0.024; [Z/H] = 0.563 ± 0.057).

## NGC 1399

The surface brightness profile was published by Schombert (1986). Paper 1 showed a steep decreasing velocity dispersion profile and a flat radial velocity profile with a small dip in the centre. Lyubenova, Kuntschner & Silva (2008) were able to investigate the centres of the kinematic profiles of NGC 1399 in much more detail, and interpreted this dip ($r \leqslant 0.2$ arcsec) from high-resolution $K$-band maps of the central kinematics as a dynamically cold subsystem in the centre. This cold subsystem could be a central stellar disc or globular cluster having fallen into the centre on a purely radial orbit (Lyubenova et al. 2008). An age of 8.6 ± 0.9 Gyr was found for this galaxy in this study, which is consistent with the age of 10 ± 2 Gyr found by Forbes et al. (2001).

## NGC 2832

The surface brightness profiles were published by Schombert (1986) and Jordán et al. (2004), and HST imaging by Laine et al. (2003). The radial velocity profile shows the presence of a kinematic decoupled core (KDC) in the centre of this galaxy (Paper 1). The SSP equivalent parameters derived for the central $\frac{1}{8} R_e$ in this study [log (age) = 0.929 ± 0.024; [E/Fe] = 0.380 ± 0.043; [Z/H] = 0.480 ± 0.062] are in very good agreement with that derived by other authors. Proctor & Sansom (2002) derived log (age) = 0.875 ± 0.069; [E/Fe] = 0.300 ± 0.025; [Z/H] = 0.457 ± 0.074 for the central 3.6 × 1.25 arcsec$^2$. Sánchez-Blázquez et al. (2006b) derived log (age) = 0.995 ± 0.007 in the centre (equivalent aperture of 4 arcsec at a redshift of $z = 0.016$).
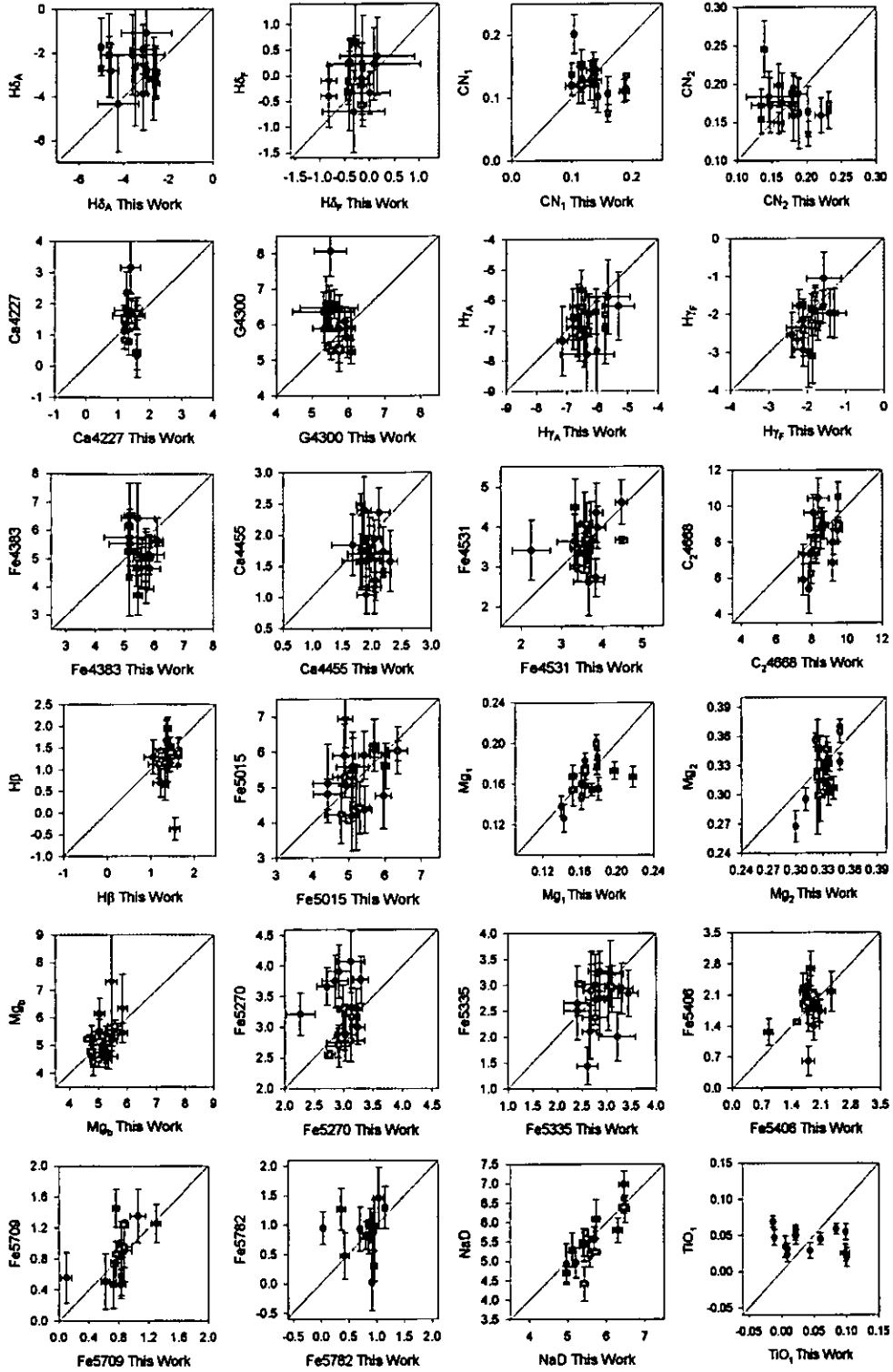
**Figure B1.** Central index measurements compared to T98 and LW05 (black circles) for 14 galaxies in common, SB06 (red triangles) for five galaxies in common and OG08 (green circles) for five galaxies in common. All index measurements are in Å, except CN, Mg and TiO which are in magnitudes.

## NGC 4839

Surface brightness profiles were published by Schombert (1986), Oemler (1976) as well as Jordán et al. (2004), who all confirm the presence of a very prominent cD envelope. Rotation of the order 44 km s$^{-1}$ and a KDC in the centre of the galaxy are detected

(Paper 1). Table C1 shows the SSP-equivalent ages and metallicities for the three BCGs in the Coma cluster from the literature (as summarized by Trager et al. 2008). The data from this study is for $\frac{1}{8} R_e$. For Mehlert et al. (2000), Sánchez-Blázquez et al. (2006b) and Trager et al. (2008), the data is for 2.7 arcsec diameter equivalent circular apertures (by Trager et al. 2008), and for the other

**Table C1.** SSP parameters of the Coma BCG galaxies compared to that in the literature (as summarized by Trager et al. 2008).

| Reference | log (age) | [Z/H] | [E/Fe] |
|---|---|---|---|
| NGC 4889 | | | |
| This work | $0.92^{+0.04}_{-0.04}$ | $0.57^{+0.05}_{-0.05}$ | $0.42^{+0.04}_{-0.04}$ |
| Sánchez-Blázquez et al. (2006b) | $1.08^{+0.27}_{-0.08}$ | $0.30^{+0.13}_{-0.14}$ | $0.18^{+0.04}_{-0.04}$ |
| Jørgensen (1999) | $0.23^{+0.05}_{-0.01}$ | $1.07^{+0.08}_{-0.04}$ | $0.29^{+0.01}_{-0.01}$ |
| Mehlert et al. (2000) | $0.12^{+0.16}_{-0.01}$ | $1.16^{+0.02}_{-0.19}$ | $0.39^{+0.01}_{-0.13}$ |
| Moore et al. (2002) | $0.14^{+0.02}_{-0.01}$ | $1.13^{+0.02}_{-0.01}$ | $0.38^{+0.04}_{-0.04}$ |
| Nelan et al. (2005) | $1.35^{+0.02}_{-0.01}$ | $-0.18^{+0.05}_{-0.07}$ | $0.27^{+0.01}_{-0.01}$ |
| Mean ± Std err | $0.64 \pm 0.54$ | $0.68 \pm 0.54$ | $0.32 \pm 0.09$ |
| NGC 4874 | | | |
| This work | $0.89^{+0.12}_{-0.12}$ | $0.35^{+0.05}_{-0.05}$ | $0.46^{+0.05}_{-0.05}$ |
| Sánchez-Blázquez et al. (2006b) | $1.02^{+0.20}_{-0.14}$ | $0.21^{+0.11}_{-0.13}$ | $0.10^{+0.04}_{-0.04}$ |
| Jørgensen (1999) | $0.31^{+0.23}_{-0.10}$ | $0.86^{+0.14}_{-0.16}$ | $0.25^{+0.04}_{-0.03}$ |
| Mehlert et al. (2000) | $0.12^{+0.02}_{-0.01}$ | $1.09^{+0.02}_{-0.01}$ | $0.35^{+0.04}_{-0.04}$ |
| Moore et al. (2002) | $0.62^{+0.29}_{-0.33}$ | $0.54^{+0.17}_{-0.16}$ | $0.18^{+0.04}_{-0.04}$ |
| Nelan et al. (2005) | $1.11^{+0.25}_{-0.22}$ | $0.08^{+0.25}_{-0.22}$ | $0.18^{+0.11}_{-0.08}$ |
| Trager et al. (2008) | $0.90^{+0.05}_{-0.04}$ | $0.38^{+0.04}_{-0.01}$ | $0.17^{+0.01}_{-0.01}$ |
| Mean ± Std err | $0.71 \pm 0.37$ | $0.50 \pm 0.36$ | $0.24 \pm 0.13$ |
| NGC 4839 | | | |
| This work | $1.07^{+0.12}_{-0.12}$ | $0.13^{+0.05}_{-0.05}$ | $0.35^{+0.03}_{-0.03}$ |
| Sánchez-Blázquez et al. (2006b) | $0.66^{+0.42}_{-0.39}$ | $0.63^{+0.27}_{-0.23}$ | $0.14^{+0.07}_{-0.06}$ |
| Jørgensen (1999) | $1.24^{+0.19}_{-0.75}$ | $0.05^{+0.22}_{-0.17}$ | $0.20^{+0.07}_{-0.07}$ |
| Mehlert et al. (2000) | $1.07^{+0.34}_{-0.75}$ | $0.21^{+0.22}_{-0.25}$ | $0.19^{+0.08}_{-0.06}$ |
| Mean ± Std err | $1.01 \pm 0.25$ | $0.26 \pm 0.26$ | $0.22 \pm 0.09$ |

references as originally published. It can be seen that the literature SSP-equivalent age falls in a very large range, and the value derived in this study is within this range.

## NGC 4874

This galaxy has a large, extended envelope, and is the second brightest galaxy of the famous pair of BCGs at the centre of the Coma cluster. The surface brightness profile was published by Peletier et al. (1990). No significant rotation or velocity substructure is detected for this galaxy (Paper 1). Trager et al. (2008) compiled a list of all the central H$\beta$ measurements for this galaxy, and found an error weighted mean value of $1.57 \pm 0.05$ Å (including data from

Fisher et al. 1995; Trager et al. 1998; Jørgensen 1999; Kuntschner et al. 2001; Moore et al. 2002; Nelan et al. 2005; Sánchez-Blázquez et al. 2006b). The H$\beta$ index measured here ($1.630 \pm 0.082$ Å) compares very well with the literature data. Table C1 shows the SSP-equivalent parameters compared with those from the literature.

## NGC 4889

A large BCG with a very extended envelope, and the brightest galaxy of the Coma cluster. The surface brightness profile was published by Peletier et al. (1990), and *HST* imaging by Laine et al. (2003). The radial velocity profile clearly shows a KDC (Paper 1).

**Table D1.** The index measurements from H$\delta_A$ to C$_2$4668 for all 51 galaxies (49 BCG and 2 ellipticals). The first line for each galaxy is the index measurement, and the second is the error on the index measurement. The complete table is available in the online version of the paper (see Supporting Information).

| Object Name | H$\delta_A$ (Å) | H$\delta_F$ (Å) | CN$_1$ (mag) | CN$_2$ (mag) | Ca4227 (Å) | G4300 (Å) | H$\gamma_A$ (Å) | H$\gamma_F$ (Å) | Fe4383 (Å) | Ca4455 (Å) | Fe4531 (Å) | C$_2$4668 (Å) |
|---|---|---|---|---|---|---|---|---|---|---|---|---|
| ESO146-028 | −2.582 | 0.242 | 0.102 | 0.143 | 1.375 | 5.808 | −5.969 | −1.783 | 4.193 | 2.228 | 3.562 | 7.903 |
| | 0.407 | 0.285 | 0.009 | 0.011 | 0.145 | 0.204 | 0.314 | 0.166 | 0.314 | 0.142 | 0.159 | 0.220 |
| ESO202-043 | −3.117 | 0.394 | 0.140 | 0.189 | 1.331 | 5.861 | −6.102 | −1.999 | 5.888 | 2.293 | 3.517 | 7.892 |
| | 0.559 | 0.396 | 0.012 | 0.013 | 0.219 | 0.439 | 0.345 | 0.198 | 0.329 | 0.165 | 0.218 | 0.287 |
| ESO303-005 | −3.642 | 0.070 | 0.130 | 0.167 | 1.385 | 5.868 | −6.853 | −2.122 | 5.256 | 1.563 | 3.796 | 8.925 |
| | 0.376 | 0.250 | 0.008 | 0.010 | 0.142 | 0.216 | 0.403 | 0.214 | 0.180 | 0.135 | 0.172 | 0.259 |
| ESO346-003 | −3.039 | −0.185 | 0.067 | 0.107 | 1.359 | 5.703 | −6.384 | −2.015 | 5.672 | 1.435 | 3.151 | 7.993 |
| | 0.613 | 0.401 | 0.013 | 0.015 | 0.192 | 0.291 | 0.411 | 0.255 | 0.352 | 0.176 | 0.261 | 1.109 |
| ESO349-010 | −3.574 | −0.478 | 0.127 | 0.154 | 1.457 | 5.595 | −5.977 | −1.449 | 5.046 | 1.697 | 3.796 | 8.665 |
| | 0.241 | 0.163 | 0.005 | 0.006 | 0.100 | 0.158 | 0.282 | 0.140 | 0.170 | 0.129 | 0.160 | 0.249 |

**Table D2.** Index measurements: $H\beta$ to $TiO_2$ for all 51 galaxies (49 BCG and 2 ellipticals). The first line for each galaxy is the index measurement, and the second is the error on the index measurement. The complete table is available in the online version of the paper (see Supporting Information).

| Object Name | $H\beta$ (Å) | Fe5015 (Å) | $Mg_1$ (mag) | $Mg_2$ (mag) | $Mg_b$ (Å) | Fe5270 (Å) | Fe5335 (Å) | Fe5406 (Å) | Fe5709 (Å) | Fe5782 (Å) | NaD (Å) | $TiO_1$ (mag) | $TiO_2$ (mag) |
|---|---|---|---|---|---|---|---|---|---|---|---|---|---|
| ESO146-028 | 1.707 | 5.570 | 0.178 | 0.336 | 5.004 | 2.923 | 1.035 | 1.832 | 0.740 | 0.944 | 5.130 | 0.009 | – |
|  | 0.075 | 0.220 | 0.001 | 0.002 | 0.099 | 0.075 | 0.083 | 0.077 | 0.034 | 0.038 | 0.039 | 0.001 | – |
| ESO202-043 | 1.849 | 5.325 | 0.177 | 0.346 | 5.285 | 3.061 | 2.983 | 2.684 | 0.745 | 1.011 | 5.062 | −0.011 | – |
|  | 0.109 | 0.227 | 0.002 | 0.002 | 0.116 | 0.106 | 0.155 | 0.099 | 0.046 | 0.047 | 0.047 | 0.002 | – |
| ESO303-005 | 1.655 | 5.942 | 0.178 | 0.309 | 5.026 | 2.890 | 2.914 | 2.034 | 0.942 | 1.030 | 5.857 | 0.057 | – |
|  | 0.097 | 0.234 | 0.002 | 0.003 | 0.122 | 0.158 | 0.162 | 0.134 | 0.073 | 0.074 | 0.088 | 0.002 | – |
| ESO346-003 | 1.691 | 5.514 | 0.160 | 0.327 | 4.626 | 3.345 | 2.899 | 0.293 | 0.711 | 0.973 | 5.254 | 0.022 | – |
|  | 0.109 | 0.229 | 0.002 | 0.002 | 0.104 | 0.101 | 0.124 | 0.085 | 0.055 | 0.047 | 0.050 | 0.001 | – |
| ESO349-010 | 1.625 | 5.890 | 0.163 | 0.290 | 4.379 | 2.908 | 2.799 | 1.948 | 0.927 | 0.842 | 6.010 | 0.054 | – |
|  | 0.092 | 0.196 | 0.002 | 0.002 | 0.171 | 0.156 | 0.193 | 0.128 | 0.066 | 0.071 | 0.077 | 0.002 | – |

Table C1 shows the SSP-equivalent parameters compared to that of the literature. Similarly, to the other Coma BCGs, the ages fall in a very large range, and the value derived in this study is within this range.

## APPENDIX D: CENTRAL INDEX MEASUREMENTS

Table D1 contains the index measurements from $H\delta_A$ to $C_24668$, and Table D2 from $H\beta$ to $TiO_2$ for all the galaxies. The complete tables are available as Supporting Information.

## SUPPORTING INFORMATION

Additional Supporting Information may be found in the online version of this article:

**Table D1.** The index measurements from $H\delta_A$ to $C_24668$ for all 51 galaxies (49 BCG and two ellipticals). The first line for each galaxy

is the index measurement, and the second is the error on the index measurement.

**Table D2.** Index measurements: $H\beta$ to $TiO_2$ for all 51 galaxies (49 BCG and two ellipticals). The first line for each galaxy is the index measurement, and the second is the error on the index measurement.

Please note: Wiley-Blackwell are not responsible for the content or functionality of any supporting materials supplied by the authors. Any queries (other than missing material) should be directed to the corresponding author for the article.

This paper has been typeset from a TeX/LaTeX file prepared by the author.

# Bibliography

[1] Adami C., Biviano A., Durret F., Mazure A., 2005, A&A, 443, 17

[2] Andreon S., Davoust E., Michard R., Nieto J.L., Poulain P., 1996, A&AS, 116, 429

[3] Aragón-Salamanca A., Baugh C.M., Kauffmann G., 1998, MNRAS, 297, 427

[4] Athanassoula E., Garijo A., García-Gómez C., 2001, MNRAS, 321, 353

[5] Baier F.W., Wipper H., 1995, AN, 316, 319

[6] Baldwin J.A., Phillips M.M., Terlevich R., 1981, PASP, 93, 5

[7] Bautz L.P., Morgan W.W., 1970, BAAS, 2, 294

[8] Bekki K., Shioya Y., 1999, ApJ, 513, 108

[9] Bender R., 1988, A&A, 229, 441

[10] Bender R., Burstein D., Faber S.M., 1992, ApJ, 399, 462

[11] Bender R., Saglia R., Gerhard O., 1994, MNRAS, 269, 785

[12] Bernardi M., 2009, MNRAS, 395, 1491

[13] Bernardi M., Renzini A., da Costa L.N., Wegner G., Alonso M.V., Pellegrini P.S., Rité C., Willmer C.N.A., 1998, ApJ, 508, L143

[14] Bernardi M., Nichol R.C., Sheth R.K., Miller C.J., Brinkmann J., 2006, AJ, 131, 1288

[15] Bernardi M., Hyde J.B., Sheth R.K., Miller C.J., Nichol R.C., 2007, AJ, 133, 1741

[16] Bernardi M., Hyde J.B., Fritze A., Sheth R.K., Gebhardt K., Nichol R.C. 2008, MNRAS, 391, 1191

[17] Best P.N., Von der Linden A., Kauffmann G., Heckman T.M., Kaiser C.R., 2007, MNRAS, 379, 894

[18] Bildfell C., Hoekstra H., Babul A., Mahdavi A., 2008, MNRAS, 389, 1637

[19] Blumenthal G.R., Faber S.M., Primack J.R., Rees M.J., 1984, Nature, 311, 517

[20] Bohringer H. et al., 2000, ApJS, 129, 435

[21] Bohringer H. et al., 2004, A&A, 425, 367

[22] Bournaud F., Jog C.J., Combes F., 2005, A&A, 437, 69

[23] Boylan-Kolchin M., Ma C., Quataert E., 2006, MNRAS, 369, 1081

[24] Brough S., Collins C.A., Burke D.J., Mann R.G., Lynam P.D., 2002, MNRAS, 329, 533

[25] Brough S., Collins C.A., Burke D.J., Lynam P.D., Mann R.G., 2005, MNRAS, 364, 1354

[26] Brough S., Proctor R., Forbes D.A., Couch W.J., Collins C.A., Burke D.J., Mann R.G., 2007, MNRAS, 378, 1507

[27] Bruzual G., 1983, ApJ, 273, 105

[28] Bruzual G., Charlot S., 2003, MNRAS, 344, 1000

[29] Burke D.J., Collins C.A., Mann R.G., 2000, ApJ, 532, 105

[30] Burns J.O., 1990, AJ, 99, 14

[31] Burns J.O., Loken C., Gómez P., Rizza E., Bliton M., Ledlow M., Owen F.N., 1997, in ASP Conf. Ser. Vol. 115: "Galactic and Cluster Cooling Flows", ed. Soker N.

[32] Burstein D., Faber S.M., Gaskell C.M., Krumm N., 1984, ApJ, 287, 586

[33] Caldwell N., Rose J.A., Concannon K.D., 2003, AJ, 125, 289

[34] Cappellari M., Emsellem E., 2004, PASP, 116, 138

[35] Cardiel N., 1999, PhD thesis, Universidad Complutense de Madrid

[36] Cardiel N., Gorgas J., Aragón-Salamanca A., 1998a, MNRAS, 298, 977

[37] Cardiel N., Gorgas J., Cenarro J., González J.J., 1998b, A&ASS, 127, 597

[38] Carter D., Metcalfe N., 1980, MNRAS, 191, 325

[39] Carter D., Bridges T.J., Hau G.K.T., 1999, MNRAS, 307, 131

[40] Cassisi S., 2007, in IAU Symp. 241: "Stellar Populations as Building Blocks of Galaxies", ed. Vazdekis A., Peletier R.F.

[41] Cavagnolo K.W., Donahue M., Voit G.M., Sun M., 2008, ApJ, 683, 107

[42] Cenarro A.J., Gorgas J., Cardiel N., Pedraz S., Peletier R.F., Vazdekis A., 2001, MNRAS, 326, 981

278

[43] Chen Y., Reiprich T.H., Bohringer H., Ikebe Y., Zhang Y.Y., 2007, A&A, 466, 805

[44] Cid Fernandes R., Mateus A., Sodré L., Stasińska G., Gomes J.M., 2005, MNRAS, 358, 363

[45] Collins C.A., Mann R.G., 1998, MNRAS, 297, 128

[46] Concannon K.D., Rose J.A., Caldwell N., 2000, ApJ, 536, 19

[47] Cowie L.L., Binney J., 1977, ApJ, 215, 723

[48] Cox T.J., Dutta S.N., Di Matteo T., Hernquist L., Hopkins P.F., Robertson B., Springel V., 2006, ApJ, 650, 791

[49] Crawford C.S., Allen S.W., Ebeling H., Edge A.C., Fabian A.C., 1999, MNRAS, 306, 857

[50] Croft S. et al., 2006, ApJ, 647, 1040

[51] Cruddace R. et al., 2002, ApJS, 140, 239

[52] Davies R.L., Sadler E.M., Peletier R.F., 1993, MNRAS, 262, 650

[53] De Bruyne V., Vauterin P., De Rijcke S., Dejonghe H., 2003, MNRAS, 339, 215

[54] De Lucia G., Blaizot J., 2007, MNRAS, 375, 2

[55] De Lucia G., Springer V., White S.D.M., Croton D., Kauffmann G., 2006, MNRAS, 366, 499

[56] De Vaucouleurs G., 1948, Ann. Astrophys., 11, 247

[57] De Vaucouleurs G., De Vaucouleurs A., Corwin H.G., Buta R.J., Paturel G., Fouque P., 1995, VizieR On-line Data Catalogue, 7155, 0

[58] Desroches L., Quataert E., Ma C., West A.A., 2007, MNRAS, 377, 402

[59] Diaz A.I., Terlevich E., Terlevich R., 1989, MNRAS, 239, 325

[60] Dressler A., 1984, ApJ, 281, 512

[61] Dubinski J., 1998, ApJ, 502, 141

[62] Ebeling H., Weidemann G., 1993, PhRvE, 47, 704

[63] Ebeling H., Edge A.C., Bohringer H., Allen S.W., Crawford C.S., Fabian A.C., Voges W., Huchra J.P., 1998, MNRAS, 301, 881

[64] Ebeling H., Edge A.C., Allen S.W., Crawford C.S., Fabian A.C., Huchra J.P., 2000, MNRAS, 318, 333

[65] Edge A.C., Stewart G.C., 1991, MNRAS, 252, 428

[66] Edwards L.O.V., Hudson M.J., Balogh M.L., Smith R.J., 2007, MNRAS, 379, 100

[67] Edwards L.O.V., Robert C., Mollá M., McGee S.L., 2009, MNRAS, 396, 1953

[68] Emsellem E. et al., 2007, MNRAS, 379, 401

[69] Faber S.M., Jackson R.E., 1976, ApJ, 204, 668

[70] Faber S.M., Friel E.D., Burstein D., Gaskell C.M., 1985, ApJS, 57, 711

[71] Ferrari F., Pastoriza M.G., Macchetto F., Caon N., 1999, A&AS, 136, 269

[72] Fisher D., Illingworth G., Franx M., 1995a, ApJ, 438, 539

[73] Fisher D., Franx M., Illingworth G., 1995b, ApJ, 448, 119

[74] Forbes D.A., Beasley M.A., Brodie J.P., Kissler-Patig M., 2001, ApJ, 563, 143

[75] Franx M., Illingworth G., Heckman T., 1989, AJ, 98, 538

[76] Fuller T.M., West M.J., Bridges T.J., 1999, ApJ, 519, 22

[77] Gallagher J.S., Ostriker J.P., 1972, AJ, 77, 288

[78] Gao L., Loeb A., Peebles P.J.E., White S.D.M., Jenkins A., 2004, ApJ, 614, 17

[79] Garijo A., Athanassoula E., García-Gómez C., 1997, A&A, 327, 930

[80] Giacintucci S., Venturi T., Murgia M., Dallacasa D., Athreya R., Bardelli S., Mazzotta P., Saikia D.J., 2007, A&A, 476, 99

[81] Giovannini G., Liuzzo E., Giroletti M., 2008, in "Approaching Micro-Arcsecond Resolution with VSOP-2: Astrophysics and Technology", ed. Hagiwara Y., Fomalont E., Tsuboi M., Murata Y.

[82] Graham A., Lauer T.R., Colless M., Postman M., 1996, ApJ, 465, 534

[83] Graves G.J., Schiavon R.P., 2008, ApJS, 177, 446

[84] González A.H., Zaritsky D., Zubladoff A.I., 2007, ApJ, 666, 147

[85] González J.J., 1993, PhD thesis, Univ. California

[86] Gorgas J., Efstathiou G., Aragón-Salamanca A., 1990, MNRAS, 245, 217

[87] Gorgas J., Faber S.M., Burstein D., González J.J., Courteau S., Prosser C., 1993, ApJS, 86, 153

[88] Gorgas J., Pedras S., Guzmán R., Cardiel N., González, J.J., 1997, ApJ, 481, 19

[89] Hansen S.M., Sheldon E.S., Wechsler R.H., Koester B.P., 2007, arXiv:0710.3780

[90] Hau G.K.T., Forbes D.A., 2006, MNRAS, 371, 633

[91] Hill J.M., Oegerle W.R., 1992, AAS, 18, 1413

[92] Hoessel J.G., Gunn J.E., Thuan T.X., 1980, ApJ, 241, 486

[93] Houdashelt M.L., Trager S.C., Worthey G., Bell R.A., 2002, BAAS, 201, 1405

[94] Hyde J.B., Bernardi M., 2009, MNRAS, 396, 1171

[95] Jarrett T.H., Chester T., Cutri R., Schneider S.E., Huchra J.P., 2003, AJ, 125, 525

[96] Jordán A., Côté P., West M.J., Marzke R.O., Minniti D., Rejkuba M., 2004, AJ, 127, 24

[97] Jørgensen I., 1999, MNRAS, 306, 607

[98] Jørgensen I., Franx M., Kjærgaard P., 1995, MNRAS, 276, 1341

[99] Katayama H., Hayashida K., Takahara F., Fukita Y., 2003, ApJ, 585, 687

[100] Kaviraj S. and GALEX Collaboration., 2007, ApJS, 173, 619

[101] Kelson D.D., Illingworth G.D., Franx M., Van Dokkum P.G., 2006, ApJ, 653, 159

[102] Kobayashi C., 2004, MNRAS, 347, 740

[103] Koleva M., Prugniel Ph., Ocvirk P., Le Borgne D., Soubiran C., 2008, MNRAS, 385, 1998

[104] Koleva M., Prugniel Ph., Bouchard A., Wu Y., 2009, A&A, 501, 1269

[105] Koprolin W., Zeilinger W., 2000, A&A, 145, 71

[106] Kormendy J., 1982, in "Morphology and Dynamics of Galaxies", ed. Martinet L., Major M.

[107] Kormendy J., Fisher D.B., Cornell M.E., Bender R., 2009, ApJS, 182, 216

[108] Korn A.J., Maraston C., Thomas D., 2005, A&A, 438, 685

[109] Kuntschner H., 2000, MNRAS, 315, 184

[110] Kuntschner H., 2004, A&A, 426, 737

[111] Kuntschner H., Lucey J.R., Smith R.J., Hudson M.J., Davies R.L., 2001, MNRAS, 323, 615

[112] Laine S., Van der Marel R.P., Lauer T.R., Postman M., O'Dea C.P., Owen F.N., 2003, AJ, 125, 478

[113] Lamareille F., Mouchine M., Contini T., Lewis I., Maddox S., 2004, MNRAS, 350, 396

[114] Lauer T.R., 1988, ApJ, 325, 49

[115] Lauer T.R. et al., 2007, ApJ, 662, 808

[116] Ledlow M.J., Voges W., Owen F.N., Burns J.O., 2003, AJ, 126, 2740

[117] Lee H., Worthey, G., 2005, ApJS, 160, 176 (LW05)

[118] Li Z., Han Z., 2007, A&A, 471, 795

[119] Lin Y.T., Mohr J.J., 2004, ApJ, 617, 879

[120] Liu F.S., Xia X.Y., Mao S., Wu H., Deng Z.G., 2008, MNRAS, 385, 23

283

[121] Loh Y.S., Strauss M.A., 2006, MNRAS, 366, 373

[122] Longo G., Zaggio S.R., Brusarello G., Richter, G., 1994, A&AS, 105, 433

[123] Lyubenova M., Kuntschner H., Silva D.R., 2008, A&A, 485, 425

[124] MacArthur L., 2005, ApJ, 623, 795

[125] Mahdavi A., Geller M.J., 2001, ApJ, 554, 129

[126] Malumuth E.M., Kirshner R.P., 1985, ApJ, 291, 8

[127] Maraston C., 1998, MNRAS, 300, 872

[128] Maraston C., 2003, in "Extragalactic globular cluster systems", ed. Kissler-Patig M.

[129] Maraston C., 2005, MNRAS, 362, 799

[130] Matthews T.A., Morgan W.W., Schmidt M., 1964, ApJ, 140, 35

[131] McCarthy I.G., Balogh M.L., Babul A., Pool G.B., 2004, ApJ, 613, 811

[132] McNamara B.R., O'Connell R.W., 1992, ApJ, 393, 579

[133] McNamara B.R., Wise M., Sarazin C.L., Jannuzi B.T., Elston R., 1996, ApJL, 466, 9

[134] McNamara B.R. et al., 2006, ApJ, 648, 164

[135] Mehlert D., Saglia R., Bender R., Wegner G., 1998, A&A, 332, 33

[136] Mehlert D., Saglia R.P., Bender R., Wegner G., 2000, A&AS, 141, 449

[137] Mehlert D., Thomas D., Saglia R.P., Bender R., Wegner G., 2003, A&A, 407, 423

[138] Menanteau F., Abraham R.G., Ellis R.S., 2001, MNRAS, 322, 1

[139] Menanteau F., Jimenez R., Matteucci F., 2001, ApJ, 562, 23

[140] Merrifield, M., 2004, MNRAS, 353, L13

[141] Merritt D., 1983, ApJ, 264, 24

[142] Mihos J.C., Hernquist L., 1994, ApJ, 425, L13

[143] Miles T.A., Raychaudhury S., Forbes D.A., Goudfrooij P., Ponman T.J., Kozhurina-Platais V., 2004, MNRAS, 355, 785

[144] Moore S.A.W., Lucey J.R., Kuntschner H., Colless M., 2002, MNRAS, 336, 382

[145] Mushotzky R.F., Serlemitsos P.J., Smith B.H., Boldt E.A., Holt S.S., 1978, ApJ, 225, 21

[146] Naab T., Burkert A., 2003, ApJ, 597, 893

[147] Nelan J.E., Smith R.J., Hudson M.J., Wegner G.A., Lucey J.R., Moore S.A.W., Quinney S.J., Suntzeff N.B., 2005, ApJ, 632, 137

[148] Neumann D.M. et al., 2001, A&A, 365, 74

[149] Noel-Storr J., Baum S.A., Verdoes Kleijn G., Van der Marel R.P., O'Dea C.P., De Zeeuw P.T., Carollo C.M., 2003, ApJS, 148, 419

[150] Ocvirk P., Pichon C., Lançon A., Thiébaut E., 2006a, MNRAS, 365, 46

[151] Ocvirk P., Pichon C., Lançon A., Thiébaut E., 2006b, MNRAS, 365, 74

[152] O'Dea C.P. et al., 2008, ApJ, 681, 1035

[153] Oegerle W.R., Hill, J.M., 2001, AJ, 122, 2858

[154] Oegerle W.R., Hoessel J.G., 1991, ApJ, 375, 15

[155] Oemler A., 1976, ApJ, 209, 693

[156] Ogando R.L.C., Maia M.A.G., Pellegrini P.S., da Costa L.N., 2008, AJ, 135, 2424 (OG08)

[157] Ostriker J.P., Hausman M.A., 1977, ApJ, 217, 125

[158] Ostriker J.P., Tremaine S.D., 1975, ApJ, 202, 113

[159] Panter B., Heavens A.F., Jimenez R., 2003, MNRAS, 343, 1145

[160] Patel P., Maddox S., Pearce F.R., Aragón-Salamanca A., Conway E., 2006, MNRAS, 370, 851

[161] Peletier R.F., Davies R.L., Illingworth G.D., Davis L.E., Cawson M., 1990, AJ, 100, 1091

[162] Peres C.B., Fabian A.C., Edge A.C., Allen S.W., Johnstone R.M., White D.A., 1998, MNRAS, 298, 416

[163] Pipino A., Kaviraj S., Bildfell C., Hoekstra H., Babul A., Silk J., 2009, MNRAS, 395, 462

[164] Popesso P., Biviano A., Bohringer H., Romaniello M., 2006, A&A, 445, 29

[165] Postman M., Lauer T.R., 1995, ApJ, 440, 28

[166] Proctor R.N., 2002, Ph.D thesis, University of Central Lancashire

[167] Proctor R.N., Sansom A.E., 2002, MNRAS, 333, 517

[168] Proctor R.N., Forbes D.A., Beasley M.A., 2004, MNRAS, 255, 1327

[169] Prugniel Ph., Simien F., 1996, A&A, 309, 749

[170] Rafferty D.D., McNamara B.R., Nulsen P.E.J., 2008, ApJ, 687, 899

[171] Reiprich T.H., Bohringer H., 2002, ApJ, 567, 716

[172] Renzini A., 2007, ASPC, 380, 309

[173] Rines K., Geller M.J., Diaferio A., Mahdavi A., Mohr J.J., Wegner G., 2002, AJ, 124, 1266

[174] Rix H., White S.D.M., 1992, MNRAS, 254, 389

[175] Romeo A.D., Napolitano N.R., Covone G., Sommer-Larsen J., Antonuccio-Delogu V., Capacciolo M., 2008, MNRAS, 389, 13

[176] Rood H.J., Sastry G.N., 1971, PASP, 83, 313

[177] Ruszkowski M., Springel V., 2009, ApJ, 696, 1094

[178] Salaris M., Cassisi S., 2005, "Evolution of Stars and Stellar Populations" (England: John Wiley & Sons)

[179] Salomé P., Combes F., 2003, A&A, 412, 657

[180] Salpeter E.E., 1955, ApJ, 121, 161

[181] Sánchez-Blázquez P., Gorgas J., Cardiel N., González J.J., 2006a, A&A, 457, 787 (SB06)

[182] Sánchez-Blázquez P., Gorgas J., Cardiel N., González J.J., 2006b, A&A, 457, 809

[183] Sánchez-Blázquez P., Gorgas J., Cardiel N., 2006c, A&A, 457, 823

[184] Sánchez-Blázquez P. et al., 2006d, MNRAS, 371, 703

[185] Sánchez-Blázquez P., Forbes D.A., Strader J., Brodie J., Proctor R., 2007, MNRAS, 377, 759

[186] Sánchez-Blázquez P. et al., 2009, A&A, 499, 47

[187] Sandage A., 1972, ApJ, 178, 1

[188] Sandage A., 1994, ApJ, 430, 1

[189] Sarazin C.L., 1988, "X-ray Emission in Clusters of Galaxies" (Cambridge Astrophysical Series, Cambridge, CUP)

[190] Sargent W., Schechter P., Boksenberg A., Shortridge K., 1977, ApJ, 212, 326

[191] Sarzi M. et al., 2006, MNRAS, 366, 1151

[192] Schaerer D., Contini T., Pindao M., 1999, A&AS, 136, 35

[193] Schiavon R.P., 2007, ApJS, 171, 146

[194] Schiavon R.P., Barbuy B., Bruzual G., 2000, ApJ, 532, 453

[195] Schneider D.P., Gunn J.E., Hoessel J.G., 1983, ApJ, 268, 476

[196] Schombert J.M., 1986, ApJS, 60, 603

[197] Schombert J.M., 1987, ApJS, 64, 643

[198] Schombert J.M., 1988, ApJ, 328, 475

[199] Schweizer F., 1998, in "Galaxies: Interactions and Induced Star Formation", ed. Kennicutt R.C., Schweizer F., Barnes J.E., Friedli D., Martinet L., Pfenniger D.

[200] Seigar M.S., Graham A.W., Jerjen H., 2007, MNRAS, 378, 1575

[201] Serra P., Trager S.C., 2007, MNRAS, 374, 769

[202] Stasińska G., Cid Fernandes R., Mateus A., Sodré L., Asari N.V., 2006, MNRAS, 371, 972

[203] Statler T.S., 1991, AJ, 102, 882

[204] Stott J.P., Edge A.C., Smith G.P., Swinbank A.M., Ebeling H., 2008, MN-RAS, 384, 1502

[205] Struble M.F., Rood H.J., 1987, ApJS, 63, 555

[206] Struble M.F., Rood H.J., 1991, ApJS, 77, 363

[207] Struble M.F., Rood H.J., 1999, ApJS, 125, 35

[208] Tantalo R., Chiosi C., 2004, MNRAS, 353, 917

[209] Thomas D., Maraston C., Bender R., 2003, MNRAS, 343, 279

[210] Thomas D., Maraston C., Korn A.J., 2004, MNRAS, 351, 19

[211] Thomas D., Maraston C., Bender R., De Oliviera C.M., 2005, ApJ, 621, 673 (T05)

[212] Tinsley B.M., 1968, ApJ, 151, 547

[213] Tinsley B.M., 1980, Fund. Cosmic Phys., 5, 287

[214] Tojeiro R., Heavens A.F., Jimenez R., Panter B., 2007, MNRAS, 381, 1252

[215] Tonry J.L., 1984, ApJ, 279, 13

[216] Tonry J.L., 1985, AJ, 90, 2431

[217] Torlina L., De Propris R., West M.J., 2007, ApJ, 660L, 97

[218] Trager S.C., Somerville R.S., 2009, MNRAS, 395, 608

[219] Trager S.C., Worthey G., Faber S.M., Burstein D., González J.J., 1998, ApJS, 116, 1 (T98)

[220] Trager S.C., Faber S.M., Worthey G., González J.J., 2000a, AJ, 119, 164

[221] Trager S.C., Faber S.M., Worthey G., González J.J., 2000b, AJ, 120, 165

[222] Trager S.C., Worthey G., Faber S.M., Dressler A., 2005, MNRAS, 362, 2

[223] Trager S.C., Faber S.M., Dressler A., 2008, MNRAS, 386, 715

[224] Tripicco M.J., Bell R.A., 1995, AJ, 110, 3035

[225] Van der Marel R.P., Franx M., 1993, ApJ, 407, 525

[226] Van Dokkum P.G., Franx M., Fabricant D., Illingworth G.D., Kelson D., 2000, ApJ, 541, 95

[227] Vazdekis A., 1999, ApJ, 513, 224

[228] Vazdekis A., 2005, RevMexAA, 24, 129

[229] Vazdekis A., Arimoto N., 1999, ApJ, 525, 144

[230] Verdoes Kleijn G.A., Baum S.A., De Zeeuw P.T., O'Dea C.P., 1999, AJ, 118, 2592

[231] Vitores A.G., Zamorano J., Rego M., Alonso O., Gallego J., 1996, A&AS, 118, 7

[232] Voit G.M., Cavagnolo K.M., Donahue M., Rafferty D.A., McNamara B.R., Nulsen P.E.J., 2008, ApJ, 681, 5

[233] Von der Linden A., Best P.N., Kauffmann G., White S.D.M., 2007, MN-RAS, 379, 867

[234] Weiss A., Cassisi S., Dotter A., Han Z., Lebreton Y., 2007, in IAU Symp. 241: "Stellar Populations as Building Blocks of Galaxies", ed. Vazdekis A., Peletier R.F.

[235] West M.J., 1989, ApJ, 344, 535

[236] Whiley I.M. et al., 2008, MNRAS, 387, 1253

[237] White D.A., Jones C., Forman W., 1997, MNRAS, 292, 419

[238] Worthey G., 1994, ApJS, 95, 107

[239] Worthey G., 1998, PASP, 110, 888

[240] Worthey G., 2001, "Synthetic Stellar Populations", The Encyclopedia of Astronomy and Astrophysics, ed. Murdin P (IoP Publishing)

[241] Worthey G., Ottaviani D.L., 1997, ApJS, 111, 377

[242] Worthey G., Faber S.M., González J.J., 1992, ApJ, 398, 69

[243] Worthey G., Faber S.M., González J.J., Burstein D., 1994, ApJS, 94, 687

[244] Yan R., Newman J.A., Faber S.M., Konidaris N., Koo D., Davis M., 2006, ApJ, 648, 281

*"Moenie te ver vorentoe kyk nie,*

*ook nie te ver agtertoe nie,*

*maar kyk altyd Op."*